BEHAVIOR OF SUCTION CAISSON FOUNDATIONS

FINAL REPORT

submitted to:

MIT Sea Grant College Program
Minerals Management Services
Offshore Technology Research Center,
University of Texas at Austin
and
JOINT OIL INDUSTRY CONSORTIUM:
Amoco Corporation
BP International Ltd.
Chevron Petroleum Technology Company
Conoco Inc.
Exxon Production Research Company
Shell Development Company
Texaco Inc.

by

Andrew J. Whittle
John T. Germaine
Douglas F. Cauble
Michael A. Geer
Boonchai Ukritchon
Henry L. Pierce Engineering Laboratory
Department of Civil and Environmental Engineering
Massachusetts Institute of Technology

August 1996

EXECUTIVE SUMMARY

This report describes the main findings of a three year, joint industry funded research project which addresses geotechnical problems associated with the design of large diameter caissons as permanent anchors for tension leg platforms in deep water applications. The work focuses on the caisson behavior during installation by underbase suction, and on the axial load response of single caisson cells in clay for short-term (undrained) pullout and sustained tensile loading conditions.

The project has generated three major analytical developments: 1) The formulation and implementation of the Shallow Strain Path Method (SSPM) to estimate disturbances caused by undrained shallow penetration of piles and caissons in clay. 2) The application of non-linear finite element analyses (using the ABAQUS program with customized cubic strain elements), which incorporate the MIT-E3 effective stress soil model, to predict the axial load-displacement response. All of the finite element calculations assume wished-in-place initial conditions. The analyses include parametric studies of performance for prototype caisson geometries and predictions of experimental data for model caissons. 3) Upper and lower bound estimates of undrained pullout capacity have been obtained using numerical limit analyses. The validation of analytical predictions is supported by a program of experimental measurements in the Caisson Element Test (CET) cell, which was designed, fabricated and proof tested as part of this project. The CET experiments use a miniature two-piece model caisson (2.54cm radius) installed in a homogeneous specimen of normally consolidated BBC. The program of 14 experiments includes detailed measurements of cap and wall forces and displacements, pore pressures and ground deformations during caisson installation, equilibration, monotonic pullout testing and sustained tensile loading.

Installation forces measured in the CET experiments are consistent with previous predictions of pile installation in BBC. The data show that all of the volume of soil displaced by the wall moves inside the soil plug, generating very low effective stresses beneath the cap. The proposed SSPM analysis is able to describe measurements of surface heave around a thick-walled open-ended caisson in centrifuge tests (performed by Delft Geotechnics) but greatly underestimates the CET cap displacements. This discrepancy is attributed to the effects of confining pressures applied in the CET experiments.

The axial load-deformation behavior in CET pullout experiments measure a maximum caisson capacity (F_{TOT} = -23±1kg) and wall resistance (F_w = -13±1.5kg) at a cap displacement δ_c = 0.2±0.05cm. The maximum cap resistance is lower than the theoretical limit expected for cavitation, probably due to air trapped in the annular space between the caisson cap and wall. Finite element analyses using the MIT-E3 model give excellent predictions of the wall resistance versus cap displacement, but overestimate the measured cap resistance.

Finite element analyses for prototype caissons (in BBC) predict a well defined yield displacement, at which the full frictional resistance is mobilized on the external surface of the caisson. Continued loading generates additional shear forces along the inner wall surface, while the predicted cap forces increase linearly with displacement. The report presents calculations showing the effect of the wall embedment length, caisson diameter, soil type and stress history.

Finite element predictions of have also been compared with results from centrifuge model tests in kaolin (provided by EPR), using model input parameters selected from published data. The analysis underestimates the measured caisson resistance by about 10% (at displacement of 20cm), while the predicted pore pressures are in good agreement with measurements from inside the caisson.

The undrained pullout capacities have also been estimated by numerical solutions of upper and lower bound collapse loads. These calculations overestimate the measured capacity of the CET model caissons, but are in excellent agreement with results from EPR centrifuge tests, and match the failure load from a field test performed by NGI.

The behavior of the CET model caissons in sustained tensile loading has been measured in a series of 5 experiments. These data show that the maximum tensile force that can be sustained by the caisson is very similar to the maximum wall resistance in undrained pullout experiments, and give detailed measurements of the release of underbase suction at stable tensile load levels. Finite element predictions for prototype caisson geometries predict similar mechanisms of failure in sustained tensile loading. The results also show that there is a characteristic breakthrough time after tensile load application, before the excess pore pressures start to dissipate beneath the cap of the caisson.

ACKNOWLEDGMENTS

The Authors would like to acknowledge the valuable contributions of several individuals who have participated in this study. Two sabbatical visitors, Professor Michael Kavvadas (Technical University of Athens) and Professor César Sagaseta (University of Cantabria) have contributed significantly in the analytical developments described in Chapter 2. Professor Scott Sloan (University of Newcastle) generously provided copies of his programs for numerical limit analyses. Graduate students Marika Santagata and Twarath Sutabutr worked on the development of the SSPM analyses, while Stacey Sonnenberg and Amy Varney asssisted in the CET exepriments through MIT's Undergraduate Research Opportunities Program (UROP). Dr Youssef Hashash and Lucy Jen have assisted in the finite element analyses. Dr Ed Clukey hosted the first annual technical review meeting at EPR in Houston, and assisted in the interpretation of the EPR centrifuge tests. Dirk Lugar and Peter van den Berg provided information on the centrifuge model tests performed by Delft Geotechnics.

Finally the Authors would like to acknowledge the technical monitors of this project for their input and support. This project occurred at a time of upheaval in the oil industry with many changes in the offshore geotechnical community. We would like to thank the following individuals in particular; Richard Beck, William McCarron and Philippe Jeanjean, Amoco Corporation; Duncan Eastland, Mike Sweeney and Jim Clarke, BP International Ltd.; Glen Andersen, Jen-Hwa Chen and J-R. Hsu, Chevron Production Technology Company; Tom Ramsey, Jack Chan, Wen-Jeng Wang, Conoco Inc.; Ed Clukey and Patrick Wong, Exxon Production Research Company; John Pelletier, Shell Development Company; and Don Woodford, Texaco Inc..

TABLE OF CONTENTS

EXECUTIVE SUMMARY	i
ACKNOWLEDGMENTS	iii
Table of Contents	iv
List of Tables	x
List of Figures	xi
1. INTRODUCTION	**1**
2. DEVELOPMENT OF ANALYSIS CAPABILITIES	**3**
2.1 PROBLEM DESCRIPTION	3
2.2 DEVELOPMENTS OF FINITE ELEMENT CAPABILITIES	5
2.2.1 Numerical Difficulties Posed by Incompressibility	5
2.2.2 User Element Subroutines for ABAQUS Program	8
2.2.3 Validation of Cubic Strain Elements	8
2.3 MODELING OF INSTALLATION DISTURBANCE FOR CAISSONS	10
2.3.1 Formulation of the Shallow Strain Path Method	12
2.3.2 Predictions of Deformations and Strains for Caisson Penetration	14
2.4 NUMERICAL LIMIT ANALYSES FOR PULLOUT CAPACITY	17
2.4.1 Methods of Stability Analysis	17
2.4.2 Limit Analyses by Finite Elements and Linear Programming	18
2.4.3 Bearing Capacity of a Footing on Clay	19
3. DESIGN OF CET CELL	**47**
3.1 THE CAISSON ELEMENT TEST CELL	47
3.1.1 Consolidation Chamber	47
3.1.2 Model Caisson	49
3.1.3 Driving System	50
3.1.4 Control System	52
3.1.4.1 Hardware	53
3.1.4.2 Software	54
3.1.5 Instrumentation	57
3.2 RESEDIMENTED BOSTON BLUE CLAY	60
3.2.1 Origin and Processing	60

3.2.2 Index Properties 61
3.2.3 Engineering Properties 62
3.2.3.1 Compression, Consolidation and Flow Properties 62
3.2.3.2 Undrained Triaxial Shear Behavior 63
3.2.3.3 Undrained Direct Simple Shear Behavior 64
3.3 CAISSON TESTING PROCEDURE 64
3.3.1 Resedimentation of BBC 64
3.3.2 RBBC Consolidation Using Rigid Cap 65
3.3.3 RBBC Consolidation In CET Apparatus 65
3.3.4 Model Caisson Test Events 66

4. EVALUATION OF CET CELL 96
4.1 EQUIPMENT DEVELOPMENT CHRONOLOGY 96
4.1.1 Cylindrical Slip Ring Assembly Modifications 96
4.1.2 Model Caisson Improvements 97
4.1.3 Driving System Modifications 98
4.1.4 Control Software Changes 98
4.1.5 Instrumentation Improvement 99
4.2 CONSOLIDATION CHAMBER 100
4.2.1 Boundary Total Stress 101
4.2.2 Cylindrical Slip Ring Assembly 102
4.3 MODEL CAISSON 103
4.3.1 Clay Surface Stability Through Soil Arching 103
4.3.2 External and Internal Model Caisson Friction 104
4.4 DRIVING SYSTEM 105
4.5 CONTROL SYSTEM 106
4.5.1 Constant Total Stress 106
4.5.2 Constant Total Force During Installation by Underbase Suction 106
4.5.3 Constant Total Force During Equilibration and Sustained Load 106
4.5.4 Constant Rate Withdrawal During Monotonic Pullout 107
4.6 INSTRUMENTATION 107
4.6.1 Primary Transducers and Clay Surface LVDT's 108
4.6.2 Pore Pressure Measuring Devices 108
4.6.3 Cap Pore Pressure Sensor 111

5. RESULTS OF CET CELL EXPERIMENTS 134

5.1 THE TESTING PROGRAM 134
5.1.1 The Program Objectives 134
5.1.1 Test Geometry and Instrumentation 135
5.1.3 Test Loading Schedule 135
5.1.4 Test Quality Assessment 137
5.2 SUCTION INSTALLATION 138
5.2.1 Caisson Force Distribution 138
5.2.1.1 Total Force 138
5.2.1.2 Wall Force 138
5.2.1.3 Cap Force 142
5.2.2 Pore Pressure Generation Beneath Cap 143
5.2.3 Cap Displacement 144
5.2.4 Pore Pressure Generation in Soil Mass 145
5.2.5 Soil Surface Displacement 146
5.3 OTHER INSTALLATION METHODS 147
5.3.1 CET-6 Partial Slow Rate Suction Installation 148
5.3.2 CET-13, 14 - Fixed Cap Force, Cap Displacement Installation 150
5.4 EQUILIBRATION 153
5.4.1 Caisson Force Distribution 153
5.4.1.1 Total Force 154
5.4.1.2 Wall Force 154
5.4.1.3 Cap Force 155
5.4.2 Pore Pressure Dissipation 155
5.4.3 Caisson Displacement 156
5.4.4 Soil Surface Settlement 157
5.5 MONOTONIC PULLOUT 1 158
5.5.1 Caisson Force Distribution 158
5.5.1.1 Total Force 159
5.5.1.2 Wall Force 159
5.5.1.3 Cap Force 160
5.5.1.4 Best Estimate of Component Force Behavior 160
5.5.1.5 Fast Rate Monotonic Pullout 161
5.5.2 Pore Pressure Generation 162
5.5.2.1 Fast Rate Monotonic Pullout 163
5.5.3 Soil Surface Displacement 163
5.5.3.1 Fast Rate Monotonic Pullout 164

5.6 SUSTAINED LOAD 164
5.6.1 Caisson Force Distribution 165
5.6.2 Caisson Displacement 166
5.6.3 Excess Pore Pressure 166
5.6.4 Soil Surface Displacement 168
5.7 RE-EQUILIBRATION 169
5.7.1 Caisson Force Distribution 170
5.7.2 Pore Pressure Dissipation 171
5.7.3 Caisson Displacement 171
5.7.4 Soil Surface Displacement 172
5.8 MONOTONIC PULLOUT II 172
5.8.1 Caisson Force Distribution 173
5.8.1.1 Total Force 173
5.8.1.2 Wall Force 173
5.8.1.3 Cap Force 174
5.8.1.4 Fast Rate Monotonic Pullout #2 174
5.8.2 Pore Pressure Generation 175
5.8.2.1 Fast Rate Monotonic Pullout #2 176
5.8.3 Soil Surface Displacement 176
5.8.3.1 Fast Rate Monotonic Pullout #2 177

6. ANALYSIS OF CAISSON BEHAVIOR IN AXIAL TENSILE LOADING 276
6.1 INTRODUCTION 276
6.2 EFFECT OF SOIL MODEL FOR UNDRAINED AXIAL LOADING 277
6.2.1 Finite Element Model 277
6.2.2 Results for the MCC Model 279
6.2.3 MIT-E3 Analysis for Base Case Geometry 280
6.2.4 Undrained Capacity of Suction Caissons 281
6.2.4.1 Limit Equilibrium Calculation for Base Case Geometry 281
6.2.4.2 Numerical Limit Analysis for Base Case Geometry 283
6.2.4.3 Generalization of Collapse Loads for Offshore Caissons 284
6.3 PARAMETRIC ANALYSES FOR UNDRAINED AXIAL LOADING 285
6.3.1 Cell Geometry 285
6.3.2 Effect of Wall Length 285
6.3.3 Effect of Caisson Diameter 286
6.3.4 Effect of Stress History 287

6.3.5 Effect of Soil Type 288
6.4 SUSTAINED TENSILE LOADING 289
6.4.1 Introduction 289
6.4.2 Caisson Response at Selected Levels of Sustained Tensile Load 290

7. EVALUATION OF MEASURED CAISSON PERFORMANCE 340
7.1 INTRODUCTION 340
7.2 INSTALLATION PHASE 340
7.2.1 Installation Disturbance Due To Underbase Suction 340
7.2.2 Interpretation of Installation Forces 343
7.2.3 Interpretation of Ground Deformations by SSPM 344
7.2.3.1 SSPM Predictions for Delft Centrifuge Tests 346
7.3 EQUILIBRATION PHASE 346
7.4 UNDRAINED AXIAL LOADING TO FAILURE 347
7.4.1 Results of CET Tests 347
7.4.2 Interpretation of CET Model Caison Capacity 349
7.4.2.1 Limit Equilibrium 349
7.4.2.2 Numerical Limit Analysis 350
7.4.3 FE Predictions for Undrained Axial Loading of CET Caisson 352
7.4.4 Finite Element Predictions of EPR Centrifuge Model Test 355
7.4.4.1 Description of EPR Centrifuge Model and Data from Test 355
7.4.4.2 Selection of MIT-E3 Input Parameters for Kaolin 355
7.4.4.3 Predictions of Load-Deformation and Caisson Capacity 358
7.4.5 Caisson Capacity with Inclined Loading 360
7.5 BEHAVIOR OF CAISSONS UNDER SUSTAINED TENSILE LOADING 362
7.5.1 Experimental Data 362
7.5.2 Finite Element Simulation of Sustained Loading for CET Caisson 363

8. SUMMARY AND CONCLUSIONS 419
8.1 SUMMARY 419
8.1.1 Analytical Framework 419
8.1.2 Experimental Behavior of CET Model Caissons 421
8.1.3 Evaluation of Predicted and Measured Caisson Behavior 422
8.2 CONCLUSIONS 423
8.2.1 Caisson Installation and Equilibration 423
8.2.2 Undrained Axial Pullout Behavior 424

8.2.2.1 Measurement and Prediction for CET Model Caissons 424
8.2.2.2 Finite Element Predictions of Prototype Caisson Behavior 425
8.2.2.3 Measurement and Prediction for EPR Centrifuge Model 426
8.2.2.4 Caisson Capacity by Numerical Limit Analysis 426
8.2.3 Behavior Under Sustained Tensile Loading 427

REFERENCES **428**

LIST OF TABLES

2.1 Net Degrees of Freedom for Triangular Finite Elements with Low Order Displacement Interpolation

2.2 Capabilities of Finite Elements for Predicting Collapse (after Sloan & Randolph, 1982)

2.3 User Defined Elements for ABAQUS Program

2.4 Summary of Previous Finite Element Studies of Axial Pile Loading in Clays

2.5 Formulation of Numerical Limit Analyses

3.1 Characteristics of Instrumentation for a Typical Caisson Element Test (CET10)

3.2 Index Properties of Resedimented Boston Blue Clay Batches and Powder from Series IV Boston Blue Clay

4.1 CET Equipment Modification Chronology

4.2 Important Physical Characteristics of the Three Probe Tranducers

4.3 Time Response to Applied Pressure of Pore Pressure Probes and Cap Sensor in Water and Soil: Theoretical vs. Measured Values

5.1 Individual Test Geometry and Instrumentation

5.2 Individual Test Loading Phases

5.3 Quality Assessment for Individual Test Control and Instrumentation

a) Test Control, Installation Phase Instrumentation

b) Equilibration and Montonic Pullout Phase 1 Instrumentation

c) Sustained Load and Re-Equilibration Phase Instrumentation

d) Monotonic Pullout 2 Phase Instrumentation

5.4 Guidelines for Quality Assessment Code

5.5a Caisson Force Characteristics During Installation: Initial and Transition Zones

5.5b Caisson Force Characteristics During Installation: Deep Zone

6.1 Input Parameters for BBC using the MIT-E3 and MCC Models

6.2 Summary of Collapse Loads for Vertically Loaded Planar Caisssons

6.3 Summary of Wall and Cap Forces from Lower Bound Analyses of Planar Caissons

6.4 Summary of Parametric Study for Undrained Axial Loading of Caissons

6.5 Normalized Engineering Properties of BBC from MIT-E3 Soil Model

6.6 Summary of Sustained Loading Analyses

7.1 Input Parameters for Speswhite Kaolin using the MIT-E3 Model

7.2 MIT-E3 Predictions of Deformation and Strength Properties of K_0-Normally Consolidated Clays

7.3 Comparison of MIT-E3 Predictions of Shaft Parameters of Piles Installed in Three K_0-Normally Consolidated Clays

LIST OF FIGURES

2.1 Discretization Around Pile Tip using 15-Noded Triangular Finite Elements

2.2 Evaluation of Tip Resistance Factors for Finite Element Analyses of Piles in Elasto-Plastic Soils

2.3 Effect of Element Type on Elasto-Plastic Predictions of Stress Fields Around Pile Tip

a) Octahedral Shear Stress, 8-Noded Quadrilateral Elements

b) Mean Total Stress, 8-Noded Quadrilateral Elements

c) Octahedral Shear Stress, 15-Noded Triangular Elements

d) Mean Total Stress, 15-Noded Triangular Elements

2.4 Comparison of Pile Tip Resistance with Results of DeBorst and Vermeer (1984)

2.5 Comparison of Pile Tip Resistance with Results of Teh and Houlsby (1991)

2.6 Conceptual Model for Simulation of Penetration with Stress-Free Surface

2.7 Problem Geometry and Notation

2.8a. Displacement Contours Around Simple Tube with R/w = 40, at L/R = 2

2.8b. Displacement Contours Around Simple Tube with R/w = 40, at L/R = 5

2.9a. Deformation Paths of Soil Elements Inside Simple Tube with R/w = 40 and L/R = 2

2.9b. Deformation Paths of Soil Elements Outside Simple Tube with R/w = 40 and L/R = 2

2.10 Wall Shape of Simple Tube with Aspect Ratio, R/w = 40

2.11 Approximate Corrections of Centerline Strains for Simple Tube Geometry

2.12 Average Clearance for Shallow Penetration of Simple Tubes

2.13 Contours of Octahedral Shear Strain Around Simple Tube with R/w = 40

2.14 Finite Element Discretization for Lower Bound Stress Analysis

2.15 Linearization of Mohr-Coulomb Yield Function

2.16 Typical Meshes Used in Limit Analyses for Vertically Loaded Footing on Clay

2.17 Lower Bound Solutions for Vertically Loaded Footing on Deep Homogeneous Clay Layer

2.18 Upper Bound Solutions for Vertically Loaded Footing on Deep Homogeneous Clay Layer

3.1 Schematic Diagram of the Caisson Element Test Cell Illustrating the Five Main Components

3.2 Original Chamber for 1-D Consolidation of Clay Samples

3.3 Modified Consolidation Chamber: Cross Sectional Side and Plan Views

3.4 New Consolidation Chamber Top Assembly for Caisson Element Experiments

3.5 Model Caisson: Cross Sectional Side Views of Wall and Cap Components

3.6 Caisson Cap with Pressure Transducer: Cross Sectional Side Views

3.7 Schematic Diagram of the Caisson Element Test Cell with Highlights of the Three Driving Subsystems

3.8 Total Stress Driving Subsystem

3.9 Caisson Wall Driving Subsystem
3.10 Caisson Cap Driving Subsystem
3.11 Schematic Drawing of the Control System Hardware Components
3.12 Schematic Drawing of the Control System Software Components
3.13 Schematic Drawing of Consolidation Chamber Air/Soil Interface Illustrating the Control Methodology for the CONS Module
3.14 Schematic Drawing of Consolidation Chamber Air/Soil Interface Illustrating the Control Methodology for the HOLDSTS Module
3.15 Schematic Drawing of Consolidation Chamber Air/Soil Interface Illustrating the Control Methodology for the SUCDRV Module
3.16 Schematic Drawing of Consolidation Chamber Air/Soil Interface Illustrating the Control Methodology for the MONPULL Module
3.17 Schematic Drawing of CET Cell Showing Typical Instrumentation Package Used for CET Test: Primary Transducers
3.18 Consolidation Chamber Cross Sectional Side View Showing Typical Instrumentation Package Used for CET Test: Chamber Transducers for CET 10
3.19 Consolidation Chamber Cross Section Showing Side and Top Views of Clay Surface LVDTs with Mounting Bracket
3.20 Pore Pressure Probe with Kulite Transducer: Cross Sectional Views
3.21 Consolidation Chamber Baseplate Showing Radial Location of Pore Pressure Probe Ports and a Probe in Place: Cross Sectional Side and Top Views
3.22 Consolidation Chamber Sidewalls Showing Location of Total Stress and Pore Pressure Ports: Cross Sectional Side and Top Views
3.23 Grain Size Distribution of Series IV Boston Blue Clay
3.24 Atterberg Limits for Series IV Boston Blue Clay
a) Plastic and Liquid Limits for BBC IV Powder and RBBC 401-411, 413-417
b) Plasticity Chart with Data from Series IV BBC
3.25 RBBC Consolidation with Rigid Cap: Compression, Consolidation, and Flow Characteristics
3.26 Schematic Diagram of the Residimentation Equipment for Boston Blue Clay (from Germaine 1982)
4.1 Slip Ring Assembly Modification: Replacement of O-rings with X-rings in Outer Slip Ring to Prevent Air Leaks
4.2 Slip Ring Assembly Modification: Three Surface Drainage Improvements
4.3 Slip Ring Assembly Modification: Two Modifications to Improve Caisson Wall Passage
4.4 Two Model Caisson Modifications

4.5 Pore Pressure Probe Development: Five Different Probes
4.6 Cross-section of the Consolidation Chamber for CET6 Showing Instrumentation, Including Horizontal Total Stress Transducer
4.7 Horizontal Total Stress Record for Five Test Phases of CET6
4.8 Chamber Air Pressure for Five Test Phases of CET6
4.9 Air Leak Path Through Cylindrical Slip Ring Assembly
4.10 Time Curves (vertical strain vs. log time) for Consolidation in CET Apparatus During Load Increment from σ'_v=0.67 to 0.73 ksc for tests CET 3-14
4.11 Slip Ring Assembly and Model Caisson in Position Prior to Wall Installation to Illustrate Annular Gaps Between Slip Ring and Wall and Between Wall and Cap
4.12 Slip Ring Assembly and Model Caisson in Position Prior to Wall Installation to Illustrate Four Locations of Model Caisson Friction
4.13 Chamber Air Pressure versus Log Time for Suction Installation, Equilibration, and Monotonic Pullout for CET8
4.14 Theoretical Time Response of Three Pore Pressure Probes in Water
4.15 Theoretical Time Response of Three Pore Pressure Probes Inserted into a Triaxial Specimen of Clay
4.16 Theoretical Time Response of Kulite Probe Inserted into a Triaxial Specimen of Clay at Three Different Soil Hydraulic Conductivities
4.17 Measured Time Response of Three Probes Inserted into a Triaxial Specimen of Clay
4.18 Theoretical Time Response of Cap Sensor in Water and Soil
5.1 Schematic Cross Section of CET Chamber with Caisson Fully Penetrated to Illustrate Test Geometry and Instrumentation
5.2a Individual Test Force and Displacement Timelines for CET-3-10
5.2b Individual Test Force and Displacement Timelines for CET-11-14
5.3 Measured Forces on Caisson Components During Suction Driving in CET-9
5.4 Measured Total Force on Caisson During Suction Driving for CET-3-5, 7-12 at Large Scale (-5 to 25 kg)
5.5 Measured Total Force on Caisson During Suction Driving for CET-3-5, 7-12 at Small Scale (14 to 19 kg)
5.6 Measured Wall Force Component During Suction Driving for CET-3-5, 7-12
5.7 Measured Wall Force Component During Suction Driving for CET-3-5, 7-12: Initial and Transition Zones
5.8 Measured Wall Force Component During Suction Driving for CET-3-5, 7-12: Deep Zone
5.9 Most Representative Measured Wall Force During Initial and Deep Penetration of Suction Driving
5.10 Best Estimate of Wall Force versus Wall Tip Penetration During Suction Driving

5.11 Measured Cap Force Component During Suction Driving for CET-3-5, 7-12
5.12 Measured Cap Force Component During Suction Driving for CET-3-5, 7-12: Initial and Deep Zones
5.13 Measured Excess Pore Pressure Beneath Cap During Suction Driving for CET-4-5,7-12
5.14 Measured Excess Pore Pressure Beneath Cap During Suction Driving for CET-4-5, 7-12: Initial and Transition Zones
5.15 Measured Cap Displacement During Suction Driving for CET-3-5,7-12
5.16 Measured Excess Pore Pressure by Probes P1, P2, and P3 During Suction Driving for CET-7-12
5.17 Measured Soil Surface Displacement at Three Radial Locations During Suction Driving for CET-8
5.18 Measured Soil Surface Displacement by S1-S5 During Suction Driving for CET-3-5, 7-10
5.19 Measured Total Force on Caisson During Installation for CET-6, 13, 14
5.20 Measured Wall Force Component During Installation for CET-6, 13, 14
5.21 Measured Cap Force Component During Installation for CET-6, 13, 14
5.22 Measured Excess Pore Pressure Beneath Cap During Installation for CET-6, 13, 14
5.23 Measured Excess Pore Pressure by P1-P4 During Installation for CET-6, 13, 14
5.24 Measured Cap Displacement During Installation for CET-6, 13, 14
5.25 Measured Soil Surface Displacement by S1-S5 During Installation for CET-6, 13, 14
5.26 Measured Forces on Caisson Components During Post-Installation Equilibration in CET-9
5.27 Measured Total, Wall, and Cap Force on Caisson During Post-Installation Equilibration for CET-3, 8-9, 11-14
5.28 Measured Excess Pore Pressure Beneath Cap and by P1-P4 During Post-Installation Equilibration for CET-4, 8-9, 11-14
5.29 Measured Caisson Settlement During Post-Installation Equilibration for CET-8
5.30 Measured Wall and Cap Settlement During Post-Installation Equilibration for CET-3-6, 8-9, 12-13
5.31 Measured Caisson Settlement During Post-Installation Equilibration for CET-14
5.32 Measured Soil Surface Displacement at Five Radial Locations During Post-Installation Equilibration for CET-8
5.33 Measured Soil Surface Displacement by S1-S5 During Post-Installation Equilibration for CET-3-6, 8-9, 11-13
5.34 Measured Soil Surface Displacement at Five Radial Locations During Post-Installation Equilibration for CET-14
5.35 Measured Force Components During Monotonic Pullout 1 for CET-8
5.36 Measured Total, Wall, and Cap Force on Caisson During Monotonic Pullout 1 for CET-3-6, 8
5.37 Measured Force Components During Early (0.0 to 0.02 cm) Monotonic Pullout 1 for CET-6, 8-14
5.38 Best Estimate of Total, Wall, and Cap Force versus Wall Displacement During Monotonic Pullout 1
5.39 Measured Total, Wall, and Cap Force on Caisson During Monotonic Pullout 1 at Two Pullout Rates for CET-3-4, 8

5.40 Measured Excess Pore Pressure Beneath Cap During Monotonic
Pullout 1 for CET-5-6, 9-14
5.41 Measured Excess Pore Pressure by P1-P4 During Monotonic Pullout 1 for CET-5-6, 9-14
5.42 Measured Excess Pore Pressure Beneath Cap and by P2-P3 During Monotonic Pullout 1 at Two Pullout Rates for CET-4, 8
5.43 Measured Soil Surface Displacement at Five Radial Locations During Monotonic Pullout 1 for CET-8
5.44 Measured Soil Surface Displacement by S1-S5 During Monotonic Pullout 1 for CET-8-11, 13-14.
5.45 Measured Soil Surface Displacement by S1-S5 During Monotonic Pullout 1 at Two Pullout Rates for CET-4, 8
5.46 Measured Force Components During Sustained Load for CET-9, 10
5.47 Measured Force Components During Sustained Load for CET-11
5.48 Measured Force Components During Sustained Load for CET-12
5.49 Measured Force Components During Sustained Load for CET-13
5.50 Measured Force Components During Sustained Load for CET-14
5.51 Measured Caisson Displacement During Sustained Load for CET-9, 10
5.52 Measured Caisson Displacement During Sustained Load for CET-11
5.53 Measured Caisson Displacement During Sustained Load for CET-12
5.54 Measured Caisson Displacement During Sustained Load for CET-13
5.55 Measured Caisson Displacement During Sustained Load for CET-14
5.56 Measured Excess Pore Pressure Beneath Cap and by P1-P3 During Sustained Load for CET-9, 10
5.57 Measured Excess Pore Pressure Beneath Cap and by P1 During Sustained Load for CET-11
5.58 Measured Excess Pore Pressure Beneath Cap and by P1-P4 During Sustained Load for CET-12
5.59 Measured Excess Pore Pressure Beneath Cap and by P1-P4 During Sustained Load for CET-13
5.60 Measured Excess Pore Pressure Beneath Cap and by P1-P4 During Sustained Load for CET-14
5.61 Measured Soil Surface Displacement by S1-S5 During Sustained Load for CET-9, 10
5.62 Measured Soil Surface Displacement by S1-S5 During Sustained Load for CET-11
5.63 Measured Soil Surface Displacement by S2-S5 During Sustained Load for CET-12
5.64 Measured Soil Surface Displacement by S1-S5 During Sustained Load for CET-13
5.65 Measured Soil Surface Displacement by S1-S5 During Sustained Load for CET-14
5.66 Measured Total, Wall, and Cap Forces on Caisson During Re-Equilibration for CET-5-6, 12-14
5.67 Measured Excess Pore Pressure Beneath Cap and by P1-P4 During Re-Equilibration for CET-5-6, 12-14
5.68 Measured Wall and Cap Settlement During Re-Equilibration for CET-5-6, 12-14
5.69 Measured Soil Surface Displacement by S1-S5 During Re-Equilibration for CET-5-6, 12-14

5.70 Measured Total, Wall, and Cap Force on Caisson During Monotonic Pullout 2 for CET-5-6, 9, 12-14

5.71 Measured Force Components During Monotonic Pullout 2 for CET-6, 9, 12-14 (0.0 - 0.02 cm)

5.72 Measured Total, Wall, and Cap Force on Caisson During Monotonic Pullout 2 at Two Pullout Rates for CET-12-14

5.73 Measured Excess Pore Pressure Beneath Cap During Monotonic Pullout 2 for CET-5-6, 9, 12-14

5.74 Measured Excess Pore Pressure by P1-P4 During Monotonic Pullout 2 for CET-5-6, 9, 12, 14

5.75 Measured Excess Pore Pressure Beneath Cap During Monotonic Pullout 2 at Two Pullout Rates for CET-12-14

5.76 Measured Excess Pore Pressure by P1-P4 During Monotonic Pullout 2 at Two Pullout Rates for CET-12, 14

5.77 Measured Soil Surface Displacement by S1-S5 During Monotonic Pullout 2 for CET-5-6, 9, 12-14 (Wall Tip Displacement, z_w=0 to 0.4 cm)

5.78 Measured Soil Surface Displacement by S1-S5 During Monotonic Pullout 2 at Two Pullout Rates for CET-12-14

6.1 Detail of Finite Element Mesh and Shear Strength Profile of Clay for Base Case Analyses

6.2 Comparison of Predicted and Measured Undrained Shear Behavior of K_0-Normally Consolidated BBC

6.3 Predictions of Load-Deformation Response for Base Case Geometry using the MCC Soil Model

6.4 Excess Pore Pressure and Vertical Strains from Base Case Analysis with MCC Soil Model

6.5 Radial Effective Stress and Shear Tractions on Caisson Wall for Base Case Analysis with MCC Soil Model

6.6 Contours of Shear Stresses for Base Case Analysis with MCC Soil Model

a) Triaxial Shear Stress, $q/\sigma'_{v0} = (\sigma_v - \sigma_h)/2\ \sigma'_{v0}$ b) Direct Shear Stress τ/σ'_{v0}

6.7 Predictions of Load-Deformation Response for Base Case Geometry using the MIT-E3 Soil Model

6.8 Excess Pore Pressure and Vertical Strains from Base Case Analysis with MIT-E3 Soil Model

6.9 Radial Effective Stress and Shear Tractions on Caisson Wall for Base Case Analysis with MIT-E3 Soil Model

6.10 Contours of Shear Stresses for Base Case Analysis with MIT-E3 Soil Model

a) Triaxial Shear Stress, $q/\sigma'_{v0} = (\sigma_v - \sigma_h)/2\ \sigma'_{v0}$ b) Direct Shear Stress τ/σ'_{v0}

6.11 Bearing Capacity Factors for Footings on Non-Homogeneous Clay (Davis & Booker, 1973)

6.12 Results of Lower Bound Analysis for Base Case Caisson Geometry

6.13 Results of Upper Bound Analysis for Base Case Caisson Geometry

6.14 Pullout Loads from Planar Limit Analyses of Caissons in Non-Homogeneous Clay

6.15 Results of Lower Bound Analysis of a Deep Caisson with Embedment Ratio, L/B = 3
6.16 Results of Upper Bound Analysis of a Deep Caisson with Embedment Ratio, L/B = 3
6.17 Results of Lower Bound Analysis of a Shallow Caisson with Embedment Ratio, L/B = 0.25
6.18 Results of Upper Bound Analysis of a Shallow Caisson with Embedment Ratio, L/B = 0.25
6.19 Lower Bound Calculations of Wall and Cap Forces for Planar Caissons in Non-Homogeneous Clay
6.20a Effect of Wall Length on Predicted Load-Deformation Response
6.20b Effect of Wall Length on Mobilization of Total, Wall and Cap Forces
6.21 Effect of Caisson Diameter on Mobilization of Total, Wall and Cap Forces
6.22 Parameters for Estimating the Cap Force-Displacement Behavior of Caissons in BBC
6.23 Comparison of Predicted and Measured Undrained Shear Behavior of BBC at OCR = 2.0
6.24 Comparison of Predicted Load-Deformation Response in BBC at OCR = 1.0 and 2.0 for Base Case Geometry
6.25 Radial Effective Stress and Shear Tractions on Caisson Wall in BBC at OCR = 2.0 for Base Case Geometry
6.26 Comparison of Predicted and Measured Undrained Shear Behavior for K_0-Normally Consolidated Empire Clay
6.27 Comparison of Undrained Shear Stress-Strain Behavior Predicted by MIT-E3 for BBC and Empire Clay
6.28 Comparison of Predicted Load-Deformation Response for Base Case Caisson Geometry in Normally Consolidated BBC and Empire Clay
6.29 Excess Pore Pressure Ratio and Vertical Strains Predicted for Base Case Caisson Geometry in in Normally Consolidated BBC and Empire Clay
6.30 Summary of Load-Deformation Response for Four Sustained Load Tests with Base Case Caisson Geometry
6.31 Time Dependent Response at Load Level I for the Base Case Geometry
6.32 Development of Wall Shear Tractions During Sustained Loading at Level I
6.33 Time Dependent Response at Load Level II for the Base Case Geometry
6.34 Development of Wall Shear Tractions During Sustained Loading at Level II
6.35 Time Dependent Response at Load Level III for the Base Case Geometry
6.36 Development of Wall Shear Tractions During Sustained Loading at Level III
6.37 Time Dependent Response at Load Level IV for the Base Case Geometry
6.38 Development of Wall Shear Tractions During Sustained Loading at Level IV
6.39 Summary of Cap and Wall Forces for Sustained Load Tests on Base Case Geometry
7.1 Summary of CET Penetration Force Measurements
7.2 Stress Conditions Beneath Caisson Cap in CET Penetration Tests

7.3 Summary of Pore Pressures in Clay During Penetration of CET Model Caisson
7.4 Summary of CET Cap Displacements During Caisson Installation
7.5 Summary of CET Clay Surface Displacements During Caisson Installation
7.6 Comparison of Predicted and Measured Surface Heave in CET Cell at End of Installation
7.7 Comparison of Predicted and Measured Surface Displacements During CET Caisson Penetration
7.8 Delft Geotechnics Centrifuge Model of Thick-Walled Open-Ended Pile (from Hjortnaes-Pedersen & Bezuijen, 1992)
7.9 Comparison of Predicted and Measured Surface Heave Profile in Delft Centrifuge Test
7.10 Comparison of Predicted and Measured Surface Displacements During Penetration of Thick-Walled Open-Ended Pile in Delft Centrifuge Tests
7.11 Summary of Equilibration Data for CET Model Caissons
7.12 Summary of CET Model Caisson Behavior in First Time Axial Pullout Tests
7.13 Behavior of CET Model Caissons in Axial Pullout Tests at Small Displacements
7.14 Best Estimate of Force-Displacement Behavior in First Time Axial Pullout Tests
7.15 Measurements of Pore Pressures Inside CET Model Caissons During First Time Axial Pullout
7.16 Comparison of Average Total Stresses and Excess Pore Pressures Below Cap in First Time Axial Pullout Tests
7.17 Measurements of Pore Pressure Outside CET Model Caissons During First Time Axial Pullout
7.18 Comparison of Force-Deformation Response of CET Model Caissons in First and Second Time Axial Pullout Experiments
7.19 Static Equilibrium for Vertically Loaded Suction Anchors (from Clukey & Morrison, 1993)
7.20 Spatial Discretization of CET Cell for Numerical Limit Analyses
a) Lower Bound Analysis, b) Upper Bound Analysis
7.21 Results of Lower Bound Analysis for CET Model Caisson
a) Shear Stress, q/s_u; b) Mean Stress, p/s_u;
c) Inclination of Major Principal Stress to Vertical, δ (^{0})
7.22 Results of Upper Bound Analysis for CET Model Caisson
a) Deformed Mesh; b) Location of Plastic Failure Zone; c) Velocity Vectors
7.23 Finite Element Mesh and Boundary Conditions for Finite Element Analysis of CET Tests
7.24 Finite Element Predictions of Undrained Axial Load-Deformation Response for CET Model Caisson
7.25 Finite Element Predictions of Displacements, Shear Stresses and Pore Pressures for Undrained Axial Loading of CET Model Caisson at dv = 0.1cm

a) Triaxial Shear Stress, q/σ'_{v0}; b) Direct Simple Shear Stress, τ/σ'_{v0};
c) Excess Pore Pressures; d) Displacements

7.26 Comparison of Predicted and Measured Force-Displacement Behavior for Axial Pullout of CET Model Caissons

7.27 Geometry and Instrumentation for EPR Centrifuge Model Caisson Experiments

7.28a. One-Dimensional Compression Behavior of Speswhite Kaolin

7.28b. One-Dimensional Swelling Behavior of Speswhite Kaolin

7.29a. Comparison of Computed and Measured Effective Stress Paths in Undrained Triaxial Shear Tests on K_0-Consolidated Kaolin

7.29b. Comparison of Computed and Measured Shear Stress-Strain Behavior in Undrained Triaxial Tests on K_0-Consolidated Kaolin

7.30a. Comparison of Predicted and Measured Effective Stress Paths for Undrained Direct Simple Shear Tests on Speswhite Kaolin

7.30b. Comparison of Predicted and Measured Shear Stress-Strain Behavior for Undrained Direct Simple Shear Tests on Speswhite Kaolin

7.31 Comparison of Predicted and Measured Behavior for Axial Pullout of EPR Centrifuge Model Caisson: a) Pore Pressures Inside Caisson; b) Force-Displacement Response

7.32 Finite Element Prediction of Surface Tractions on Wall of EPR Centrifuge Model Caisson at $\delta_v = 0.2$m

7.33 Lower Bound Limit Analysis for Axial Pullout of EPR Centrifuge Model Caisson
a) Shear Stress, q/s_u; b) Mean Stress, p/s_u;
c) Inclination of Major Principal Stress to Vertical, δ (^{0})

7.34 Upper Bound Limit Analysis for Axial Pullout of EPR Centrifuge Model Caisson
a) Deformed Mesh; b) Location of Plastic Failure Zone; c) Velocity Vectors

7.35 Calculation of Lower Bound Inclined Loads for EPR Centrifuge Model Caisson

7.36 Results of Lower Bound Limit Analysis for Inclined Pullout of EPR Centrifuge Model Caisson: a) Shear Stress, q/s_u; b) Mean Stress, p/s_u; c) Traction Distributions on Caisson

7.37 Results of Upper Bound Limit Analysis for Inclined Pullout of EPR Centrifuge Model Caisson: a) Deformed Mesh; b) Location of Plastic Failure Zone; c) Velocity Vectors

7.38a. NGI Four Cell Caisson Model (Andersen et al., 1993)

7.38b. Prediction and Observation of Failure in NGI Caisson Test (Andersen et al., 1993)

7.38c. Geometry and Strength Profile Used in Numerical Limit Analysis of NGI Field Test

7.39 Results of Lower Bound Limit Analysis for Inclined Loading of NGI Field Test

7.40 Results of Upper Bound Limit Analysis for Inclined Loading of NGI Field Test

7.41 Summary of Force-Deformation Measurements for Sustained Tensile Loading of CET Model Caissons
7.42 Typical Stable Behavior of CET Model Caisson Under Sustained Tensile Loading
7.43 Failure of CET Model Caisson in First Stage Sustained Tensile Load Test
7.44 Failure of CET Model Caisson in Subsequent Sustained Tensile Load Test
7.45 Measurements of Pore Pressure Dissipation During First Stage of Sustained Tensile Loading
7.46 Finite Element Prediction of CET Model Force-Displacement Response in Four-Stage Sustained Tensile Load Test
7.47 Summary of Predicted CET Model Caisson Response in Sustained Tensile Load Tests

1. INTRODUCTION

Large diameter caissons, installed using underbase suction, have been developed recently as foundations for both large offshore gravity platforms and as anchorages for tension leg platforms in the North Sea. Experience with suction caisson foundations is extremely limited and involves significant uncertainties associated with: a) the prediction of penetration resistance; b) the effects of installation and set-up behavior on subsequent foundation performance; and c) estimation of ultimate caisson capacity. The overall goal of this three year research project is to develop a better understanding of the geotechnical aspects of behavior which affect the performance of suction caissons and hence, provide a basis for more efficient foundation design. The research comprises an integrated program of analytical modeling, supporting laboratory experiments, and evaluations of predictive capabilities using data from available model caisson tests. The three main components of the proposed research were as follows:

1. Development of an analytical framework to describe systematically the changes in soil stresses and pore water pressures during caisson installation and set-up (pore pressure equilibration). The goal of these analyses is to establish how the caisson performance (load-deformation response) is affected by individual caisson geometry, cell configuration and load duration. The study focuses on axial loading conditions encountered in tension leg platform applications. The analyses use and extend the modeling capabilities developed previously at MIT, including: a) the Strain Path Method, an approximate analytical technique which quantifies the effects of severe soil disturbances caused by pile installation; and b) MIT-E3, a generalized effective stress soil model with proven capabilities for describing the nonlinear and anisotropic stress-strain behavior of soft clays in both monotonic and cyclic shearing conditions.
2. Laboratory verification using data from element level on miniature caissons in order to assess specific aspects of caisson performance under well controlled laboratory conditions, including: a) the effects of caisson geometry on installation pore pressures and set-up rates; and b) the release of suction pressures under conditions of sustained tensile loading. This task involves the design, fabrication and proof testing of an automated Caisson Element Test (CET) cell. The test material is resedimented Boston Blue Clay, a material whose manufacture and engineering properties are well documented from previous MIT research. These experiments will provide data for detailed evaluations of the analytical predictions.
3. Evaluation of the analytical framework. Analytical predictions will also be compared with results of other available tests on instrumented model caissons including: 1) Centrifuge model tests performed by the Laboratoire Central des Ponts et Chausées in Nantes, and supplied to this project by Exxon Production Research Company (Clukey & Morrison, 1993). The three tests available scale a single prototype caisson cell of length, L = 35.7m, diameter, D = 15.2m and wall thickness, 2w = 6cm, installed in K_0-normally consolidated speswhite kaolin. Delft

Geotechnics have also published results of centrifuge tests (in kaolin) for a thick-walled caisson (L = 36.0m, D = 13.0m and 2w = 1.3m) (Hjortnaes-Pedersen and Bezuijen, 1992a, b). 2) The Norwegian Geotechnical Institute have now published results of field experiments (1-g) on a four cell model caisson unit (each cell with length, L = 0.9m, D = 0.91m and 2w = 2.3cm) in overconsolidated Lysaker clay.

Results from this project have been presented in two Annual Technical Reports (October 1993; November 1994), three Technical Progress Reports (March 1993, April 1994, July 1995) and an MIT Research Report (R94-09) on Deformation Analysis of Shallow Penetration in Clays (November 1995). The core material for this project has been developed as part of two PhD theses (Douglas Cauble, Michael Geer), which are still in progress.

This report synthesizes the main findings of the project. Chapter 2 summarizes the main analytical developments used in predicting the performance of caissons these comprise: 1) a library of finite elements (mixed elements with high order interpolation of displacements) for accurate undrained analyses of axisymmetric piles and caissons; 2) the formulation and validation of the Shallow Strain Path Method for predicting disturbances caused by caisson installation; and 3) the application of numerical limit analyses which are used to compute undrained pullout capacities. Chapters 3 and 4 describe the design of the Caisson Element Test (CET) apparatus and the subsequent development refinement of its control and measurement capabilities. The CET experiments use a unique two-piece model caisson with independent control of the caisson wall and cap. Chapter 5 documents the results from a program of 14 CET experiments which include detailed measurements during successive phases of caisson installation (by underbase suction in most tests), equilibration and axial loading. The test data include repeatable high quality measurements of the load-deformation response in monotonic pullout tests as well as sustained tensile load sequences. Chapter 6 presents finite element predictions of caisson response in undrained pullout and sustained tensile loading. The calculations use the MIT-E3 model, but assume no installation disturbance. Parametric studies show the effects of caisson cell geometry, soil properties and compare results for a Gulf of Mexico clay with predictions for Boston Blue Clay. Chapter 7 compares finite element predictions of axial load-deformation response with measured data from CET experiments and an EPR centrifuge model test. The chapter also interprets penetration and equilibration data from CET experiments, and applies SSPM analyses to evaluate measurements of ground deformations. Limit analyses are used to estimate undrained pullout capacities for the CET tests, EPR centrifuge models and a field test performed by NGI. Chapter 8 gives a summary of the project and the main conclusions from this work.

2. DEVELOPMENT OF ANALYSIS CAPABILITIES

2.1 PROBLEM DESCRIPTION

One of the main goals of this research is the development of a rational analytical framework that can predict the changes in stress pore pressures and properties of the soil around a suction caisson through the successive stages of installation, equilibration and loading. This type of analysis was originally proposed for the study of long offshore friction piles in clay (Esrig et al., 1977; Randolph et al., 1979; Baligh & Kavvadas, 1980), and has led to significant advances in the understanding of set-up and shaft capacity (e.g., Azzouz et al., 1990; Whittle, 1992). The proposed research for suction caissons uses and extends the theoretical models developed in the study of pile performance, including a) the Strain Path Method (Baligh, 1985), an approximate analytical technique used to predict the effects of disturbances caused by pile installation; and b) MIT-E3 (Whittle, 1987; Whittle & Kavvadas, 1994), a generalized effective stress soil model with well documented capabilities for describing the nonlinear and anisotropic stress-strain behavior of soft clays in both monotonic and cyclic shearing conditions. The MIT-E3 model has been used in conjunction with non-linear finite element methods to predict pile shaft set-up (due to radial dissipation of installation excess pore pressures) and was previously integrated in the ABAQUS™ program (through unrelated research on the performance of deep excavations, Hashash, 1992).

The development of an integrated analytical framework for suction caisson foundations introduces several new technical challenges:

1. The proposed cell geometries for caisson anchorages have embedment-to-diameter ratios ranging from $0.25 \leq L/B \leq 3$. A complete analysis of caisson installation involves the transition from a shallow penetration process, in which the displaced soil moves towards the stress free ground surface, to a kinematically constrained deep penetration problem, where the displaced material is accommodated by deformations within the soil mass. Furthermore, caisson installation is achieved through a combination of self-weight penetration and 'underbase suction'. Disturbances caused by these installation processes can affect the shear resistance of soil around the caisson, and hence, affect its caisson capacity (in both short-term/undrained and sustained loading situations). Previous Strain Path analyses were developed for deep penetration problems, and do not account for the proximity of the mudline.
2. A complete analysis framework must combine the calculation of installation stresses, pore pressures and soil properties as initial conditions in a subsequent finite element analysis of caisson response performance. Previous studies have managed to integrate deep penetration predictions with finite element analyses in predictions of cone tip resistance (Teh & Houlsby, 1992) and coupled pore pressure dissipation for piezocone penetrometers (Aubeny, 1992;

Whittle et al., 1991). However, no previous studies have made a complete model of installation disturbance including the mudline and depth variations of soil properties.

3. Non-linear finite element analyses of the tensile load capacity will require special modeling of soil-caisson interfaces (to account for sliding and separation). Possible formulations include: a) quasi-continuum elements; b) linkage elements; c) joint elements of finite thickness; and d) interface elements of zero thickness.

During the first year of the project, two important unforeseen problems were identified (Whittle & Germaine, 1993):

1. Undrained analyses of axisymmetric piles (and caissons) caused severe numerical difficulties in the finite element analyses, generating unrealistic predictions of stress fields around the tip of closed-ended and open-ended piles.
2. Reliable calculations of stresses and pore pressures inside the soil plug cannot be achieved using the strain path method (due to equilibrium errors and assumptions of steady penetration conditions).

These problems have completely re-shaped the direction and progress of the analytical work in this project. This chapter summarizes the main analytical developments which relate to three different methods of analysis: Section 7.2 describes the implementation of special finite elements, with high order interpolation of displacements (after Sloan & Randolph, 1982), in the ABAQUS code[1] (full documentation of these user element [UEL] subroutines was supplied with the 1993 Annual Technical Report) These elements mitigate the numerical problems associated with undrained axisymmetric analyses and have been used in all subsequent finite element calculations of caisson performance.

Problems associated with modeling installation disturbance have been tackled through the development of the Shallow Strain Path Method (SSPM), which incorporates the stress-free ground surface (mudline). Section 7.3 summarizes the formulation and illustrates key results of SSPM analyses for open-ended (unplugged) caisson penetration. An MIT research report (R94-09; Sagaseta et al. 1995), which gives full details of the SSPM analysis and compares predictions with measured ground movements for piles and caissons, was submitted to the sponsors of this project in 1995. At present, only soil deformations and strains have been computed from the SSPM analyses, and extensive work is still necessary 1) to validate predictions of effective stresses and excess pore pressures; and 2) to link these results to subsequent finite element analyses. As a result, all of the finite element calculations in this report assume that the caissons are initially wished-in-place (i.e., no effects of installation disturbance).

In principle, the calculation of undrained caisson capacity can be achieved by non-linear

[1] Several commercially available geotechnical finite element programs (PLAXIS, CRISP-90) have also implemented these types of element.

finite element methods. However, the results (cf., chapters 6 and 7) show that relatively large cap displacements are necessary to mobilize the full base resistance of the underlying clay. Alternative calculations of capacity rely on approximate limit equilibrium methods. This project has implemented numerical techniques for solving (rigorous) upper and lower bound collapse loads (for rigid perfectly-plastic materials) for general planar soil-structure problems. These analyses are based on formulations presented by Sloan (1988) and Sloan & Kleeman (1995). Numerical limit analyses provide an independent calculation of caisson capacity for comparison with results of the finite element analyses in chapters 6 and 7. Section 7.4 summarizes the formulation of numerical limit analyses and illustrates their application for a simple bearing capacity problem.

2.2 DEVELOPMENT OF FINITE ELEMENT CAPABILITIES

2.2.1 Numerical Difficulties Posed by Incompressibility

The installation (by driving or underbase suction) of piles or caissons in low permeability clays occurs rapidly, such that there is minimal migration of pore water within the surrounding soil and hence, the process is undrained. Similarly, the capacity of these foundations during critical axial loading conditions (during storms) are also controlled by the undrained response of the surrounding soil. Both of these situations impose an important constraint of incompressible material behavior, which is well known to cause numerical difficulties in finite element analyses (Nagtegaal et al., 1974). Specific difficulties associated with incompressibility include: 1) spurious oscillations in the stresses computed across an individual finite element; and 2) inadequate calculation of collapse loads in elasto-plastic analyses. In soil mechanics there are two methods which have been traditionally used to by-pass these problems:

1. Total stress formulations with nearly-incompressible elasticity.

Displacement-based finite element algorithms (i.e., where the displacements $\mathbf{u}$ are the only independent solution variables) compute the tangent material stiffness matrix $\mathbf{C}$, such that $\dot{\sigma} = \mathbf{C}:\dot{\varepsilon}$. If the material response is incompressible, the matrix $\mathbf{C}$ cannot be formed as its inverse, the flexibility matrix $\mathbf{S}$ is singular and cannot be inverted. By definition, the incompressibility condition can be written:

$$\dot{\varepsilon}_{vol} = \mathbf{I}:\dot{\varepsilon} = 0 \tag{2.1a}$$

where $\mathbf{I}$ is the identity matrix, and hence:

$$\dot{\varepsilon}_{vol} = \mathbf{I}:\mathbf{S}:\dot{\sigma} = 0 \tag{2.1b}$$

which implies that the matrix $\mathbf{S}$ is not positive definite and cannot be inverted. As a result, it is common in the displacement-based finite element method to relax the incompressibility condition using a value of Poisson's ratio, $\nu < 0.5$ (say $\nu = 0.49$). The finite element model then describes a nearly incompressible response which can also be applied in conjunction with incompressible plastic models (e.g., Mises type plasticity).

2. Effective stress, mixed formulations.

In mixed formulations for saturated soils, the constitutive model describes the response of the soil skeleton which is compressible, while the pore water is incompressibile (this is consistent with basic definitions of effective stress). Strains of the soil skeleton are associated with changes in effective stresses:

$$\dot{\varepsilon} = \mathbf{S}' : \dot{\sigma}' \tag{2.2a}$$

$$\dot{\sigma}' = \dot{\sigma} - \dot{p}\mathbf{I} \tag{2.2b}$$

Mixed formulations assume that the displacements, $\mathbf{u}$, and pore water pressures, p, are independent solution variables. In this case, the pore pressure can always be computed when there is no volume change in the soil (i.e., eqn. 2.1a is satisfied):

$$\dot{p} = \frac{\mathbf{I}:\mathbf{S}':\dot{\sigma}}{\mathbf{I}:\mathbf{S}':\mathbf{I}} \tag{2.3}$$

This result shows the incompressible pore pressure response, $\dot{p}$, for an increment of total stress, $\dot{\sigma}$. The tangent flexibility of the soil skeleton, $\mathbf{S}'$ is always positive definite. In the mixed formulation, undrained loading is simulated by applying the loads over a very short time period such that there is no migration of pore water within the soil.

The incompressibility requirement imposes an important constraint on the displacement field. For two-dimensional analysis of a continuum, the incompressibility condition can be written:

$$\text{Plane Strain:} \quad \frac{\partial u_x}{\partial x} + \frac{\partial u_y}{\partial y} = 0 \tag{2.4a}$$

$$\text{Axisymmetry:} \quad \frac{\partial u_r}{\partial r} + \frac{u_r}{r} + \frac{\partial u_z}{\partial z} = 0 \tag{2.4b}$$

In the finite element formulation, the incompressibility constraint must be satisfied by the displacement interpolation. For example, linear displacement interpolations for a plane strain element are given as (cf., Zienkiewicz & Cheung, 1967):

$$u_x = \alpha_1 + \alpha_2 x + \alpha_3 y \tag{2.5a}$$

$$u_y = \beta_1 + \beta_2 x + \beta_3 y \tag{2.5b}$$

where α_i and β_i are generalized amplitudes. The incompressibility requirement imposes one constraint (C = 1) in the interpolation functions (from eqn. 2.4a):

$$\alpha_2 + \beta_3 = \frac{\partial u_x}{\partial x} + \frac{\partial u_y}{\partial y} = 0 \tag{2.6}$$

Hence, the displacements are described by only 5 independent unknowns (instead of 6).

For axisymmetric problems, with linear displacement interpolations,

$$u_r = \alpha_1 + \alpha_2 r + \alpha_3 z \tag{2.7a}$$

$$u_z = \beta_1 + \beta_2 r + \beta_3 z \tag{2.7b}$$

the incompressibility constraint requires:

$$2\alpha_2 + \beta_3 + \frac{\alpha_1}{r} + \alpha_3 \frac{z}{r} = 0 \tag{2.8a}$$

Hence:

$$2\alpha_2 + \beta_3 = 0 \; ; \; \alpha_1 = \alpha_3 = 0 \tag{2.8b}$$

In this case, the displacements are described by only three independent unknowns per element (i.e., there are three constraints, C = 3). Table 2.1 gives a second example which shows that for quadratic interpolation of displacements, incompressibility imposes 3 constraints in plane strain and six constraints in axisymmetry.

In a large array of finite elements (i.e., infinite extent with no constraints imposed by boundary conditions), the number of unconstrained degrees of freedom (DOF) per element (N) is less than the number of generalized amplitudes (for a given interpolation scheme) as the nodes are shared among neighboring elements. For example, in a regular mesh of triangular elements, each corner node (with two degrees of freedom, u_x, u_y) is shared among six elements, while a mid-side node is shared between two elements. Thus, triangular elements with linear displacement interpolation (constant strain, 3 corner nodes) have $3x(2/6) = 1$ unconstrained DOF per element, while quadratic interpolation (linear strain, 3 corner nodes and 3 mid-side nodes) have $[3x(2/6) + 3x(2/2)] = 4$ free DOF's.

Incompressibility provides an additional constraint within each element according to the basic results described above. Hence, the net number of degrees of freedom per element (NDOF) can be estimated by subtracting the number of incompressibility constraints from the number of free DOF's per element (i.e., NDOF = N-C). Table 2.1 shows that the linear interpolation (constant strain) triangular elements are overconstrained (i.e., NDOF < 0) by the incompressibility conditions for both plane strain and axisymmetric geometries. Hence, the incompressibility condition cannot be satisfied at every point within the element. In contrast, with higher order quadratic interpolation (6-noded triangular elements), the plane strain elements have one net DOF available per element and can satisfy the incompressibility condition. Quadratic interpolation of displacements is not adequate for axisymmetric problems (NDOF<0).

In the implementation of the finite element method, the incompressibility constraints need only be satisfied at the Gauss points where numerical integration is performed. If the number of Gauss points within a given element is larger than the number of constraints required for continuous interpolation, then the incompressibility condition is guaranteed at all points in the element. However, if the number of Gauss points is less than the number of incompressibility conditions in the continuum problem, then there is a reduction in the number of constraints per element. Thus, if the order of the numerical integration (number of Gauss points) is reduced, the

incompressibility constraint is relaxed and hence, problems of overconstrained elements can be avoided. Although techniques of reduced integration are widely used (e.g., Griffiths, 1982), they introduce approximations in the numerical integration which are difficult to evaluate.

An alternative approach proposed by Sloan and Randolph (1982) is to use higher order interpolation functions. In this approach there are more nodes per element and hence, more degrees of freedom, however, there are also more constraints associated with incompressibility. Thus, appropriate finite elements must be selected carefully to achieve accurate solutions for incompressible materials. Table 2.2 shows the summary of element capabilities reported by Sloan and Randolph (1982) for total stress analyses (the criterion for acceptance is $N/C \geq 1$ in this case). Of all the elements considered in this table, only the 15-noded triangle with cubic strain interpolation is adequate for undrained axisymmetric problems.

2.2.2 User Element Subroutines for ABAQUS Program

The implementation of user-defined elements in ABAQUS represents a formidable task as the user must provide the complete set of matrices at the element level comprising 1) the Jacobian stiffness, 2) the residual load vector, and 3) the material constitutive model (UMAT subroutines for MCC and MIT-E3 models). The formulation of these matrices and proof testing of the new elements for non-linear material response and coupled flow-deformation required a substantial effort during the first year of this project. Full details of the UEL subroutines, which include 34 types of elements (Table 2.3), were given in Appendix B of Whittle & Germaine (1993). Refined versions of the subroutines are available on request.

Geer (1996) gives full details of step sizes and convergence tolerances used to control the non-linear finite element analyses of caissons (in both undrained axial loading, and for coupled consolidation simulation of sustained loading events) using the UEL subroutines and MIT-E3 soil model.

2.2.3 Validation of Cubic Strain Elements

In order to evaluate the numerical accuracy of finite element analyses for describing stress changes around a pile during undrained axial loading, a series of numerical experiments were performed for closed-ended piles loaded to failure in a homogeneous, elasto-plastic soil. The main characteristics of the analyses are as follows:

1. The calculations compare the performance of different types of finite element using the UEL subroutines implemented in the ABAQUS code. All of the calculations assume small strain conditions with total vertical displacements, $\delta/R \leq 40\%$ (where R is the radius of the pile).
2. The calculations use a total stress formulation and approximate incompressibility using $\nu = 0.49$. Soil behavior is described by a linearly-elastic, perfectly-plastic soil model (EPP) with a

von Mises generalization of the yield function.

3. The pile is modeled as an elastic material using similar finite elements as the soil (with stiffness ratio, $E_p/G=\lambda$). Calculations have been performed for a variety of tip geometries (see Figure 2.1), however, most of the calculations use a rounded tip in order to minimize the effects of singularities associated with corner conditions. Figure 2.1 illustrates the finite element discretization of the tip region using 15-noded (cubic strain) triangular elements. The interface between the soil and pile shaft is modeled as either perfectly rough (no slip) or smooth (no interface shear traction).
4. The initial conditions assume that the pile is wished-in-place (with embedment length, L), with no disturbance of the surrounding soil, and hydrostatic stress conditions at all points.

There are no closed form analytical solutions for the tip resistance of long axisymmetric piles (or penetrometers). However, previous studies of deep penetration problems (Vesic, 1977; Baligh, 1975; Baligh, 1986) have shown that the tip resistance factor, $N_c = (q_b - \sigma_0)/s_u$ (where q_b is the average bearing stress, σ_0 is the initial mean stress, and s_u is the undrained, plane strain shear strength), in an isotropic EPP soil ranges from N_c = 5-15. The actual tip resistance factor is affected by a variety of factors including the yield strain (G/s_u), in-situ shear stress (σ_{h0}/σ_{v0}), interface friction/adhesion and tip geometry. Figure 2.2 compares the computed N_c values for Wished-In-Place axisymmetric piles and plane strain pile walls as a function of the embedment length-to-radius ratio, L/R. In all cases, failure is defined as the load at which the local gradient of the computed load-displacement response, $Q' \le 0.01Q'_0$ ($Q' = dQ/d\delta$; $Q'_0=Q'|_{\delta->0}$, where Q is the load applied at the top of the pile) as proposed by DeBorst and Vermeer (1984). This ad hoc definition is unavoidable as the analyses do not exhibit well defined collapse loads (cf. Figs. 2.4 and 2.5).

For a given pile tip geometry and soil properties, the tip resistance factor in Figure 2.2 should be independent of the embedment length for long piles (say L/R > 10). Small variations in tip resistance factor as a function of L/R reflect differences in the tip geometry, shaft friction and relative pile-soil stiffness. However, large changes in the computed value of N_c are caused by numerical inaccuracies associated with analysis of a nearly incompressible material. Reasonable values of tip resistance factor (N_c = 8-13) are obtained for plane strain pile walls using 8-noded isoparametric, quadrilateral elements (standard elements available in ABAQUS). However, for axisymmetric piles the tip resistance factor computed using these same elements suggest a linear variation in N_c with embedment length. Subsequent calculations using high order 15-noded triangular elements clearly show that these solutions are spurious and confirm that N_c = 10-15 for piles with rounded tip geometry.

Figures 2.3a through d compare contours of octahedral shear stress, S (where $S^2=1/3s_{ij}s_{ij}$, and s_{ij} are the deviatoric stress components) and mean stress, σ_0 (= $1/3\sigma_{kk}$), for a very long pile

(L/R = 100) with rounded tip geometry, using 8-noded quadrilateral and 15-noded triangular elements. Although the two solutions show very similar results for shear stress around the pile tip, there are large differences in the mean stress. The results for 8-noded quadrilateral elements show a very erratic field associated with locking of elements ahead of the pile, while the pressure distribution is acceptably smooth for the high order triangular elements.

Similar numerical analyses have been reported in the literature by a number of authors, as shown in Table 2.4. The studies of cone penetration (60^0 tip geometry) by DeBorst and Vermeer (1984) are particularly similar to the current analyses, but use an EPP model with a Tresca yield surface. Figure 2.4 compares predictions of tip resistance-deformation response for a pile of length L/D = 10 with results of DeBorst and Vermeer (there is no slip along the pile shaft). Although the two soil models (von Mises vs Tresca plasticity) describe different magnitudes of the intermediate principal stress at failure the two solutions are in excellent agreement throughout the loading (for $\delta/D \leq 20\%$). Figure 2.5 shows similar comparisons with analyses reported by Teh and Houlsby (1991) for wished-in-place cone penetrometers (L/D = 10) with rough (no-slip) and smooth shaft-soil interface conditions. Teh and Houlsby (1991) use von Mises type plasticity together with a formulation for large strains (using Jaumann stress rates), but model the penetrometer as a rigid body through prescribed boundary displacements. Although the results in Figure 2.5 show close agreement in the initial stiffness and overall magnitude of the tip resistance factor, there are significant differences in the load-displacement response for $\delta/D \geq 2\%$. Teh and Houlsby's results for a rough pile shaft, are qualitatively very similar to the current analysis, however, their solutions for a smooth shaft show a well defined collapse (with small post peak brittleness). Although these authors do not comment on this particular feature of their results, it is related to the assumed cone tip geometry which has a sharp corner at the base of the cone. Overall, the comparisons in Figures 2.4 and 2.5 confirm that the analyses of wished-in-place piles (using 15-noded triangular elements) achieve numerical accuracy which is comparable to the results reported in the literature.

2.3 MODELING OF INSTALLATION DISTURBANCE FOR CAISSONS

The theoretical analysis of penetration mechanics represents a very challenging problem due to a) the high gradients of the field variables around the penetrometer; b) the large deformations and strains which develop in the soil; c) the complexity of the constitutive behavior of soils; and d) non-linear pile-soil interface characteristics. Previous development of the Strain Path Method (SPM; Baligh, 1985) was based on the hypothesis that soil deformations and strains induced by penetration are essentially independent of its shearing resistance, and can be estimated with reasonable accuracy based only on kinematic considerations and boundary conditions. To date, the applications of the Strain Path Method have focused on penetration in low permeability clays and

assume: i) there is no migration of pore water during penetration and hence, the soil is sheared in an undrained mode; ii) the analyses consider steady[2], 'deep' penetration process where there is no effect of the ground surface or underlying soil/rock layers on the deformations within the clay; and iii) soil deformations and strains can be estimated from the steady, irrotational flow of an incompressible, inviscid fluid. Strain Path Analyses have been applied to a variety of penetrometer geometries including cone penetrometers, cylindrical closed and open-ended piles, and thin plates (Baligh & Levadoux, 1980; Baligh et al., 1987; Whittle et al., 1991). By considering two (or three) dimensional deformations of soil elements, the Strain Path analyses provide a more realistic framework for describing the mechanics of penetration than one-dimensional, cavity expansion methods (CEM; e.g., Randolph et al., 1979). On the other hand, the assumptions of strain controlled behavior used in SPM analyses greatly simplify the penetration problem and avoid the complexities of large deformation finite element analyses (e.g., Kiousis et al., 1988; van den Berg, 1994).

The restriction of the Strain Path Method to steady, deep penetration has a number of important limitations:

1. Deep penetration considers an idealized situation where the penetrometer tip is at infinite depth. This approach can be useful for the analysis of strains near the tip, but has no physical meaning for far field conditions, where the presence of the ground surface is likely to affect soil deformations. For example, in the SPM analysis of pile penetration, all soil elements undergo net downward movements, whereas there are many published field observations of ground surface heave caused by pile driving.
2. The penetration of caissons proceeds from the ground surface and hence, there is a transition from a shallow mechanism, where most of the soil displaces towards the stress free ground surface, to the limiting deep penetration case where the displaced material is accommodated by deformations in the soil surrounding the tip of the penetrometer. There is very limited information available for assessing the depth required to approximate the deep penetration conditions assumed in SPM analyses. Further complications arise for caisson foundations where the total penetration depth is of similar magnitude to the cell diameter and hence, the ground surface can represent an important factor in estimating the installation disturbance.

This research has developed a new method of analysis for estimating the deformations and strains caused by shallow undrained penetration of piles and caissons in clay. The formulation combines previous analyses for steady, deep penetration, with methods used to compute soil deformations due to near-surface ground loss (Sagaseta, 1987), and is referred to as the Shallow

[2]By inference, the analyses are quasi-static and hence, do not differentiate between different methods of achieving penetration such as pile driving vs jacking etc.

Strain Path Method (SSPM).

2.3.1 Formulation of the Shallow Strain Path Method

Sagaseta (1987) proposed a method for dealing with near-surface problems, where the principal focus was the prediction of ground deformations. The analysis assumed small strain conditions and formulated equations in terms of the final state of deformation (as opposed to the velocities occurring during penetration). According to this method, a point source discharging a volume, V, at some depth, z = h, below the ground surface can be modeled by the following three steps (Figure 2.6):

1. The ground surface is ignored, and solutions are obtained for the displacements and strains corresponding to a source, S, within an infinite, full space.

2. A sink, S', absorbing an equal and opposite volume to the source (i.e., -V) is located at an elevation z = -h above the ground surface. At points along the ground surface, z = 0 (plane of reflective symmetry), the virtual sink will cancel out the horizontal displacements due to the point source, but will double the vertical displacements.

3. For specified stress-strain properties of the medium, the source induces normal and shear tractions ($\sigma_{zz}[r]$, $\sigma_{rz}[r]$) at all points along the ground surface, while the image sink generates components ($-\sigma_{zz}[r]$, $\sigma_{zz}[r]$) along the same surface. Hence, by superimposing the source and image sink solutions, the ground surface experiences shear tractions of magnitude $2\sigma_{rz}[r]$ (Fig. 2b).

4. In order to simulate a stress free surface, a distribution of corrective shear tractions is applied to the surface (Fig. 2c). This involves the following steps: a) evaluate the shear strains due to the source and image sink (S, S'; steps 1 and 2), b) assume a given stress-strain behavior for the soil and hence, find the shear stresses associated with the strains occurring at points along the ground surface; c) apply a field of equal and opposite shear stresses (referred to as corrective shear tractions) over the surface and compute the distribution of shear strains which these generate in the underlying soil; and d) add this strain distribution to the previous solutions from steps 1 and 2.

   In contrast to the preceding steps, the calculation of corrective shear tractions requires a specific stress-strain relation for the soil. Analytic solutions for step 3c are only possible for linear, elastic behavior. In this case, the deformations resulting from step 3d are inversely proportional to the soil modulus, while the corrective stresses themselves are computed using the same soil modulus (step 3b). As a result, the soil modulus will cancel out in performing step 3, and the resulting soil deformations are independent of the modulus. Nevertheless, the

solution is based on the assumption of homogeneous, linear, isotropic behavior.

Due to the presence of the stress free surface, penetration is no longer a steady state process. Instead, the analysis assumes that the pile/caisson penetrates from the surface at a constant velocity, U, such that the depth of embedment at time t is given by: $h = Ut$.

$$h = U\,t \quad ; \quad 0 \le h \le L \tag{2.9}$$

where L is the final depth of penetration.

Sagaseta et al. (1995) have analyzed three geometries (Fig. 2.7): 1) simple wall generated by an infinite line source discharging a volume q per unit time, which generates a wall with half-thickness, $w = q/(2U)$; 2) a simple pile generated by a point source discharging a volume Q per unit time, which produces a pile of radius, $R=Q/\sqrt{(\pi U)}$; and 2) a simple tube (open-ended caisson) formed by a ring source of radius, R, discharging a volume Q per unit time. The open-ended caisson has a nominal radius, R, and wall thickness $2w = Q/(2\pi RU)$.

The analysis is purely kinematical, so that the only dimensions are the length [L] and time scale [T]. The simple pile radius, R (or half thickness of the open-ended pile wall, w) is taken as the length scale, while the time scale can be written R/U (or w/U) for penetration at constant velocity, U. All of the geometric dimensions can be scaled by R (or w), the velocities by U, and the strain rates by R/U (or w/U).

Sagaseta et al. (1995) give complete expressions for the velocities (v_i) and strain rates ($\dot{\varepsilon}_{ij}$) at any point (x_i) for the source at depth h ($0 \le h \le L$) for the wall, pile and tube geometries. In each case, the solution (velocities and strain rates) is given as the sum of three components (Fig. 2.6); 1) source, S; 2) image sink, S'; 3) corrective shear tractions.

Once the velocities and strain rates are defined, the displacements are obtained by integration of the velocities along the particle path[3]. The position (x,z) of a particle initially located at a point (x_0, z_0), when the source is at a depth h is:

$$\begin{Bmatrix} x(h) \\ z(h) \end{Bmatrix} = \begin{Bmatrix} x_0 \\ z_0 \end{Bmatrix} + \int_0^t \begin{Bmatrix} v_x(x,z,h) \\ v_z(x,z,h) \end{Bmatrix} \cdot dt = \begin{Bmatrix} x_0 \\ z_0 \end{Bmatrix} + \int_0^h \begin{Bmatrix} v_x(x,z,h) \\ v_z(x,z,h) \end{Bmatrix} \cdot \frac{1}{U} \cdot dh \tag{2.10}$$

The strains can then be obtained by integration of the strain rates along the particle paths:

$$\varepsilon_{ij} = \int_0^t \dot{\varepsilon}_{ij}\,(x,z,h) \cdot dt = \int_0^h \frac{1}{U} \cdot \dot{\varepsilon}_{ij}\,(x,z,h) \cdot dh \tag{2.11}$$

Integration of equations (1) and (2) must be performed numerically, because the current

[3] This enables the analyses to give partial representation of large strains in accounting for the volume displaced by the penetrometer. However, the corrective shear tractions are based on small strain elastic theory.

coordinates (x, z) in the integrands are variable. If the changes of geometry are neglected (small strains), then the initial coordinates (x_0, z_0) can be used in eqn 1, and some useful closed-form expressions can be obtained for estimating ground displacements (Sagaseta et al., 1995).

2.3.2 Predictions of Deformations and Strains for Caisson Penetration

Shallow Strain Path solutions for the simple tube geometry (Fig. 2.7c) simulate the unplugged penetration of open-ended piles and caissons. Figures 2.8a, b show contours of the radial and vertical displacements (δ_r/w and δ_z/w) caused by a simple tube of aspect ratio, R/w = 40, with penetration depths, L/R = 2 and L/R = 5, respectively. Most of the soil around the tube experiences net upward displacement ($\delta_z/w < 0$). Vertical deformations are relatively uniform across the pile plug over most of the embedded length of the tube. At any given depth, the heave is always larger inside the tube than outside. For thin walled caissons, the surface heave at the center of the soil plug can be estimated from the following small strain SSPM solution:

$$\delta_z(0, 0) = -2wR \cdot \left(\frac{1}{R} - \frac{1}{\sqrt{R^2 + L^2}} \right) = -\frac{\Omega}{2\pi} \cdot \left(\frac{1}{R} - \frac{1}{\sqrt{R^2 + L^2}} \right) \qquad (2.12)$$

where Ω is the cross-sectional area of the tube.

The zone of soil settlement comprises a thin veneer around the walls of the tube connecting to a bulb shaped region. For L/R = 2 (Fig. 2.8a), this bulb extends to a depth $\Delta z/L \approx 0.30$ below the tip of the tube (source elevation) with a maximum radial dimension of $\Delta r/L \approx 0.25$. When the tube penetrates to a depth L/R = 5 (Fig. 2.8b), the settlement bulb expands across the entire base of the soil plug, extending outside the tube to a radius $\Delta r/L = 0.3$ and vertically ahead of the tip (source elevation) $\Delta z/L = 0.5$ (i.e., approaching the conditions for a closed-ended simple pile geometry).

The contour of $\delta_z/w = 0$ delineates the zone of net inward soil movement and forms a locus which is similar to the geometry of an equivalent simple pile of radius R, and is largely independent of the embedment depth. All other points in the soil experience net outward movements ($\delta_z/w > 0$) with magnitudes controlled by the volume of soil displaced by the walls of the tube.

Figures 2.9a and b show the deformation paths of selected soil elements located close to the tube wall at four different initial depths $z_o/L = 0.1, 0.5, 0.9$ and 1.0, as the tube penetrates from the surface to a total embedment depth L/R = 2, for elements which move inside and outside the tube, respectively. For the soil elements which are displaced outside the tube (Fig. 2.9b), the radial displacements increase continuously with embedment depth. For elements which move inside the tube (Fig. 2.9a), there is a characteristic pattern of small outward displacements, which then

reverse direction when the wall tip approaches the depth of the element. All elements inside the caisson have a net inward radial displacement. For elements initially located at z_o/L = 0.1, 0.5, there is a second reversal in the direction of the radial displacements and continuous outward movement with subsequent penetration of the tube. This behavior can be explained from a detailed study of the simple tube geometry.

Figure 2.10 shows the geometry of a thin-walled simple tube with aspect ratio, R/w = 40, generated by the proposed SSPM analysis at a penetration depth L/R = 5 (L/w = 200). The shaft of the simple tube is not perfectly straight, but instead the mean radius increases slightly moving from the tip towards the free surface. The radius increases from R/w ≈ 40.0 at the tip to R/w ≈ 40.4 over most of the shaft length and then flares out further to R/w ≈ 40.7 near the free surface. The wall itself is almost constant in thickness (R_o - R_i ≈ 2w) over most of the shaft length. These subtle details of the tube geometry have only a minor influence on the soil outside the tube, but can represent a significant factor in computing the deformations and strains within the soil plug, especially for thick-walled tubes or long embedment to radius (L/R) ratios.

Previous results of SPM analyses for deep penetration (Chin, 1986) also show continuous expansion of the simple tube with distance above the tip (location of the ring source). For deep penetration, the tube expansion approaches an asymptotic limit, ΔR/w = 0.5, referred to as the 'inherent clearance' (Baligh et al., 1987), which generates an additional radial strain, $d\varepsilon_{rr}$ (= ΔR/R) = -1.25% (extension) for R/w = 40. Thus, the effects of the inherent clearance can be corrected by applying an increment of compressive radial strain to compensate for the difference between the simple tube and the ideal straight-shafted tube. Figure 2.11 illustrates this procedure for three points along the centerline for shallow penetration of the simple tube (with R/w = 40; cf. Fig. 22). As the tip of the tube penetrates below the elevation of the soil element, the correction factor inhibits the tendency of the soil to expand laterally (and hence, compress in the vertical direction). In the corrected solution, the vertical strain remains almost constant once the soil reaches an elevation Δz/w ≈ 50 above the current tip elevation.

Further studies (Sagaseta et al., 1995) have established that the inherent clearance can be represented by the average clearance over the embedded length, L, which occurs at mid-depth. Figure 2.12 shows that the average clearance, ΔR/w, is independent of the tube aspect ratio, R/w (in the range $10 \le R/w \le 80$) but is a function of the embedment length ratio, λ = L/R. The numerical solutions in Figure 2.12 are well represented by the following empirical function:

$$\frac{\Delta R}{w} \approx \frac{\lambda}{2\sqrt{6+\lambda^2}} \qquad (2.13)$$

As the embedment ratio λ increases, the clearance tends to the value obtained by Chin (1986) for infinite depth (ΔR/w = 0.5). The ground surface only affects the average clearance

calculation for λ less than 15 - 20.

Once the average clearance of the simple tube has been evaluated, it is possible to estimate the additional surface heave caused by the inherent clearance of the tube. For points inside the tube, a uniform triaxial strain ($\varepsilon_{zz} = -2.\varepsilon_{rr}$) is added to cancel the average inherent clearance shown in Figure 2.12.

$$\varepsilon_{zz} = -2\varepsilon_{rr} = -2\frac{\Delta R}{w}\frac{w}{R} \approx -\frac{w}{R}\frac{\lambda}{\sqrt{6+\lambda^2}} \tag{2.14}$$

By assuming that this average strain applies over the embedded length of the tube, the additional heave can be computed in a simple closed-form expression:

$$\frac{\Delta\delta_z}{w} = -\varepsilon_{zz}\frac{L}{w} \approx 2\lambda\frac{\lambda}{2\sqrt{6+\lambda^2}} \approx \frac{\lambda^2}{\sqrt{6+\lambda^2}} \tag{2.15}$$

For a thin walled tube, the total vertical surface heave is the obtained by adding eqns. 2.12 and 2.15.

The inherent clearance has a much smaller effect on movements outside the caisson where the ground surface heave of an ideal cylindrical tube is smaller than that of the simple tube. In this case, the correction for inherent clearance assumes a uniform contraction of the caisson wall (R) by an amount ΔR. The ground loss associated with this contraction in volume can be estimated by assuming that an equivalent volume change occurs at the centerline axis, producing a correction factor:

$$\frac{\Delta\delta_z}{w} = -\frac{\lambda}{2\sqrt{6+\lambda^2}}\left(\frac{1}{\rho} - \frac{1}{\sqrt{\rho^2+\lambda^2}}\right) \tag{2.16}$$

where $\rho = r/R$

Section 7.2.3 presents predictions of ground movements for penetration of open-ended caissons (centrifuge models and CET experiments). These results show the importance of the inherent clearance correction for conditions inside the soil plug. As in previous penetration analyses, it is convenient to characterize the distortions caused by penetration using the second invariant of the deviatoric strain, E (= $1/\sqrt{3\varepsilon_{ij}\varepsilon_{ij}}$). Figures 2.13a and b compare contours of the octahedral shear strain, E, for shallow penetration of the thin-walled simple tube (R/w = 40) at a depth L/R = 2.0, with previous SPM solutions (Chin, 1986) for deep penetration (the elevations are reported relative to the wall tip).

For shallow penetration (Fig. 2.13a), the zone of intense soil shearing ($E \geq 10\%$) is restricted to a thin annulus around the wall of the tube (with characteristic dimension comparable to w). All points inside the soil plug undergo significant amounts of shearing ($E \geq 1\%$). Outside the tube, the zone of intermediate strains ($0.1 \leq E \leq 10\%$), extends radially to $\Delta r/w \approx 150$ and a

similar distance below the wall tip. At points in the exterior region around the wall of the tube, all soil elements undergo monotonically increasing levels of shear strain with continued penetration (i.e., similar to conditions around the simple pile).

A comparison of the two analyses (Fig. 2.13a and b) shows that the zone of intense shearing ($E \geq 10\%$) is largely unaffected by the embedment depth and is controlled by the wall thickness. However, the embedment depth does affect the extent of the zone of intermediate strains levels, both around the outside of the tube and in the region below the wall tip. It is very difficult to compare the strain levels inside the soil plug due to reversals in the magnitude of E predicted in the deep penetration analyses. The results in Figure 2.13b imply that most of the soil elements within the tube ($r/w \leq 30$) experience maximum shear strains, $E \leq 1\%$ while they are still below the tip of the penetrating tube. After reaching a local minimum strain close to the tip elevation, subsequent strains inside the soil plug are largely controlled by the inherent clearance of the simple tube geometry. In contrast, the shallow penetration analysis (Fig. 2.13a) predicts larger shear strains throughout the soil plug, whose distribution is clearly related to the deformations occurring at the stress free ground surface.

2.4 NUMERICAL LIMIT ANALYSES FOR PULLOUT CAPACITY

2.4.1 Methods of Stability Analysis

In principle, the finite element method provides a comprehensive analysis capability which is capable of predicting the complete load-deformation response of caissons for general loading and drainage conditions. However, large computation times are required in order to achieve accurate calculations of the complete non-linear equilibrium load path through to failure, while the reliability of these predictions depends on the ability of the constitutive model to describe generalized stress-strain-strength properties of the soil. In practice, calculations of stability are usually based on much simpler limit equilibrium analyses, which ignore pre-failure deformations.

Limit equilibrium calculations for undrained caisson pullout capacity have been presented by several authors (e.g., Clukey & Morrison, 1993; Fuglsang & Steensen-Bach, 1993; Andersen et al., 1993). For undrained axial loading, most authors assume that the soil plug displaces with the caisson. The failure mechanism is then approximated as the sum of the external wall friction and reverse end bearing forces (cf. section 7.4.2). Bearing capacity factors are based on solutions for shallow foundations in compression, modified by empirical factors to account for the embedment depth and axisymmetric geometry. More complex limit equilibrium calculations have been used by Andersen et al. (1993) to interpret caisson capacity with inclined and cyclic loading. These calculations[4] search for a critical failure surface (Fig. 7.38 shows a typical composite failure

[4] In theory, corrections factors are also required for these analyses to account for axisymmetric geometries.

surface geometry) assuming specified distributions of undrained shear strength (which account for anisotropy, cyclic loading). Although, these limit equilibrium calculations can achieve good agreement with measured pullout capacities, they require much subjective judgment in the selection of failure mechanisms and search procedures. Furthermore, there is no theoretical basis for establishing the accuracy of the solutions.

This research has applied a third method for estimating undrained caisson capacity through numerical analyses based on the upper and lower bound theorems of plasticity. These theorems are very well known in structural mechanics where they are widely used to bracket true collapse loads. Historically, the bound theorems have not been widely used in geotechnical engineering as the solution techniques (e.g., method of characteristics) were difficult to apply, except in the case of very simple geometries (e.g., earth pressure charts of Caquot & Kérisel, 1949, used in DM7). However, research conducted during the last ten years has led to robust numerical solutions of the bound theorems using finite element type discretization and formulating the analysis as a linear programming problem, as first suggested by Lysmer (1970). A major limitation of this original formulation was the large computational time required to solve the large system of constraint equations, arising primarily from the linearization of the yield function. Sloan (1988a, b) developed a more robust lower bound formulation for plane strain problems, which solves the linear programming problem efficiently using an active set algorithm. More recently, Sloan and Kleeman (1995) have applied the same algorithm to solve the dual upper bound linear programming problem.

Ukritchon (1995) has applied and extended these lower and upper bound formulations to study the undrained stability of surface footings on clay subject to inclined and eccentric loading, and has recently (Ukritchon, 1996) incorporated structural elements in order to study soil-structure interaction problems. The current programs are restricted to plane strain conditions (the same restriction applies to most limit equilibrium calculations), with an isotropic Tresca failure criterion for the clay ($s_u = [\sigma_1 - \sigma_3]/2$), but can model generalized strength profiles. The following sections summarize the main components of the numerical limit analyses, and demonstrate their applicability for the vertical bearing capacity of a footing on clay. Chapters 6 and 7 apply numerical limit analyses to estimate the undrained pullout capacity of caissons (including CET experiments, centrifuge models and prototype scale caissons).

2.4.2 Limit Analyses by Finite Elements and Linear Programming

The lower bound analysis discretizes the soil mass into 3-noded triangular elements ('extension' elements are introduced to model infinite boundaries of a half-space) and assumes a linear variation of the unknown stresses (σ_x, σ_y, τ_{xy}) within each element. In contrast to conventional finite element methods, each node is unique to a particular element such that stress

discontinuities can occur along shared edges between elements, Figure 2.14. The unknown nodal stresses are subject to constraints which ensure that the stress field is statically admissible at all points. This is achieved by imposing i) the static equilibrium equations at all points inside each element and along each stress discontinuity; ii) prescribed surface (normal and/or shear) traction boundary conditions; and iii) the yield function, $F(\sigma_x, \sigma_y, \tau_{xy})$ must not be violated at any point (i.e., $F \leq 0$). For a cohesive clay layer, the non-linear Tresca criterion is transformed $F([\sigma_x-\sigma_y]/2, \tau_{xy})$ to form a circular locus, Figure 2.15, which is then replaced by a series of linear inequalities in the form of an n-sided, interior polygon (the examples in this paper all use n = 24). The lower bound collapse load is found by maximizing the force $\mathbf{Q} = \mathbf{C}^T\boldsymbol{\sigma}$ applied over some specified part of the boundary (where $\boldsymbol{\sigma}$ is the global vector of nodal stresses), subject to the constraints that the stress field is statically admissible. Sloan (1988) solves this linear programming problem (Table 2.5) in the canonical form used by the active set algorithm:

The upper bound analysis (after Sloan & Kleeman, 1995) assumes a linear variation of the velocity field (v_x, v_y) within each triangular element, with velocity discontinuities permitted along edges of adjacent elements. The conditions for a kinematically admissible velocity field are imposed through a set of linear constraints which impose: i) compatibility between velocities and strains; ii) the associated flow rule is based on the linearized form of the Tresca failure criterion, where the plastic strain rates, $\dot{\varepsilon}^p_{ij} = \dot{\lambda}\,\partial F/\partial\sigma_{ij}$ (where $\dot{\lambda}$ is the plastic multiplier); and iii) prescribed velocity boundary conditions. The plastic strains are constant within each element (for linear variation of velocities). Sloan and Kleeman (1995) also describe an algorithm to ensure that the associated flow rule is also satisfied along all velocity discontinuities where the relative tangential velocity is not known a priori (this introduces additional constraints shown in Table 2.5).

The principle of virtual work links the kinematically admissible velocity field with the applied external load, by equating the rate of work done by the external loads with the power dissipated in the plastically deformed region (within the elements and along the velocity discontinuities). The upper bound collapse load can then be obtained by minimizing the power dissipation for the kinematically admissible velocity field as shown in Table 2.5 ($\mathbf{u}$ and $\dot{\lambda}$ are the global vectors of nodal point velocities and plastic multiplier rates).

2.4.3 Bearing Capacity of a Footing on Clay

This section illustrates the application of numerical limit analyses for estimating the bearing capacity of a smooth rigid footing on the surface of a deep homogeneous clay layer. The exact solution of this problem was first presented by Prandtl (1920): $q_f = N_c s_u$, where $N_c = (2 + \pi) = 5.14$.

Figures 2.16a and b show the meshes used to discretize the clay layer for lower and upper

bound analyses[5]. The mesh for the lower bound stress calculation has a high concentration of elements emanating in a radial fan from the edge of the footing, where stress discontinuities are expected. Far field boundaries of the discretized domain are modeled using extension elements which ensure that the computed stresses are statically admissible for all points in the half-space (in order to guarantee a rigorous lower bound solution). The analysis imposes stress free conditions along the ground surface, and zero shear tractions along the axis of symmetry and beneath the base of the smooth footing. The lower bound calculation maximizes the total load, Max.{Q} = $\int\sigma_n dx$ (where σ_n are the normal tractions at points below the base of the footing).

The upper bound solution is much less sensitive to mesh arrangement. Figure 2.16b presents a regular grid, in which each rectangular cell is sub-divided into four triangular finite elements with a common apex at the center. Upper bound solutions are not affected by the extent of the mesh provided that the failure mechanism is fully contained within the discretized domain. The upper bound analysis imposes zero velocities at the far field boundaries, and a unit vertical velocity at all points along the rigid footing.

Figure 2.17 and 2.18 present the results of the lower and upper bond analyses for the footing. which show that the bearing capacity factor is bounded within the range $5.042 \leq Q/Bs_u = N_c \leq 5.201$. Thus the exact collapse load is bracketed within 3.3%. The computation times for each calculation are less than 10mins (CPU time for analyses performed on a Dec Alpha 3000-300x workstation).

The lower bound solutions include contours of the major and minor principal stresses (Figs. 2.17a, b), the directions of the major principal stress to the vertical (Fig. 2.17c), and the locations of the failure zone ($[\sigma_1 - \sigma_3]/2s_u$; Fig. 2.17d). As expected from the know solutions, the stress field can be divided into three zones: 1) active failure occurring beneath the footing with $\delta = 0^0$ and $\sigma_1/s_u \approx 5.0$; 2) radial shear zone where the major principal stress direction rotates from the vertical to the horizontal direction ($\delta = 0^0 \rightarrow 90^0$) and the major principal stress reduces from $\sigma_1/s_u = 5.0$ to 2.0; and 3) passive failure, extending from a line at 45^0 from the edge of the footing to the ground surface, where $\sigma_1/s_u = 5.0$ and $\delta = 90^0$.

The upper bound results in Figure 2.18 include the deformed mesh, based on relative velocities of individual finite elements (Fig. 2.18a); the plastic failure zone which shows the zone where the full shear strength of the soil is mobilized (Fig. 2.18b); velocity field and velocity trajectories (characteristics) which show the directions of movement for the collapse mechanism (Figs. 2.18c and d). The results show that the predicted failure mechanism (with maximum width from the edge of the footing, $x/B \approx 1.25$; and maximum depth, $z/B \approx 0.875$) and velocity characteristics match very closely the slip line mechanism solved by Prandtl.

---

[5] For the record, the lower bound mesh has 699 nodes, 222 triangular elements and 330 stress discontinuities; while the upper bound example uses 1536 nodes, 512 elements and 744 velocity discontinuities.

Ukritchon (1995) has applied numerical limit analyses to predict the collapse of footings on non-homogeneous clays with inclined and eccentric loading, for which there are no published exact solutions. The analyses have shown different failure mechanisms associated with bearing capacity, separation between the footing and soil, interface sliding etc. In all cases, the collapse loads are predicted within ±4-5%, with computation times in the range of 30-45minutes (CPU on Dec Alpha 3000-300x workstation). These studies have confirmed the capabilities of numerical limit analyses for predicting complex failure mechanisms and have motivated their current application for estimating the undrained pullout capacity of caissons in clays.

1. Linear Interpolation

$$u_x = \alpha_1 + \alpha_2 x + \alpha_3 y \quad \text{(a)}$$

$$u_y = \beta_1 + \beta_2 x + \beta_3 y \quad \text{(b)}$$

Incompressibility Constraints:

Plane Strain: $\alpha_2 + \beta_3 = 0$ (c)

Axisymmetry: $2\alpha_2 + \beta_3 = \alpha_1 = \alpha_3 = 0$ (d)

2.Quadratic Interpolation:

$$u_x = \alpha_1 + \alpha_2 x + \alpha_3 y + \alpha_4 xy + \alpha_5 x^2 + \alpha_6 y^2 \quad \text{(a)}$$

$$u_y = \beta_1 + \beta_2 x + \beta_3 y + \beta_4 xy + \beta_5 x^2 + \beta_6 y^2 \quad \text{(b)}$$

Incompressibility Constraints:

Plane Strain: $\alpha_2 + \beta_3 = 2\alpha_5 + \beta_4 = \alpha_4 + 2\beta_6 = 0$ (c)

Axisymmetry: $\alpha_1 = 2\alpha_2 + \beta_3 = \alpha_3 = 2\alpha_4 + 2\beta_6 = 3\alpha_5 + \beta_4 = \alpha_6 = 0$ (d)

Displacement Interpolation:	Linear	Linear	Quadratic	Quadratic
Geometry:	Plane Strain	Axisymmetric	Plain Strain	Axisymmetric
Free DOF/element[1], N (large regular mesh)	1	1	4	4
No. of Incompressibility Constraints/element[2], C	1	3	3	6
Net DOF/element, NDOF	0	<0	1	<0

Notes:

1. There are additional Free DOF associated with the edge elements of a mesh of finite dimension. However, the number of edge elements is generally small compared to the total number of elements within the mesh.
2. There are additional constraints imposed by kinematically constrained boundary conditions. However, the total number of kinematic constraints is generally small compared to the number of elements within the mesh.

Table 2.1 Net Degrees of Freedom for Triangular Finite Elements with Low Order Displacement Interpolation

Element Type	Degrees of Freedom per Element	Plane Strain				Axisymmetric			
		Integration Rule	Constraints per Element	Ratio $\frac{\text{Degrees of Freedom}}{\text{Constraints}}$	Suitable	Integration Rule	Constraints per Element	Ratio $\frac{\text{Degrees of Freedom}}{\text{Constraints}}$	Suitable
 constant strain triangle*	1	1-point	1	1	Yes	3-point	3	$\frac{1}{3}$	No
 linear strain triangle*	4	3-point	3	$\frac{4}{3}$	Yes	6-point	6	$\frac{2}{3}$	No
 quadratic strain triangle	9	6-point	6	$\frac{3}{2}$	Yes	12-point	10	$\frac{9}{10}$	No
 cubic strain triangle	16	12-point	10	$\frac{8}{5}$	Yes	16-point	15	$\frac{16}{15}$	Yes
 4-noded quadrilateral*	2	2×2	3	$\frac{2}{3}$	No	3×3	5	$\frac{2}{5}$	No
 8-noded quadrilateral*	6	3×3	6	1	Yes	3×3	9	$\frac{2}{3}$	No
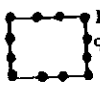 12-noded quadrilateral	10	4×4	10	1	Yes	4×4	13	$\frac{10}{13}$	No
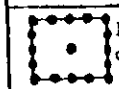 17-noded quadrilateral	16	5×5	14	$\frac{8}{7}$	Yes	5×5	19	$\frac{16}{19}$	No

Notes: - All results for rectangular quadrilaterals and straight-sided triangles. The number of constraints per element shown are minima for quadrilateral and triangular elements of arbitary shape.
- * Row entries after Nagtegaal, Parks and Rice[1].
- Integration rules for triangles from Laursen and Gellert[13].

Table 2.2 Capabilities of Finite Elements for Predicting Collapse (Sloan & Randolph, 1982)

Code No., n (Un)	Element Shape	Geometry	No. Displ. Node	No. Pore Pressure Nodes	Total No. of Nodes
1	Triangular	Axisymmetric	6	3	6
2*	Triangular	Axisymmetric	6	-	6
3	Triangular	Plane Strain	6	3	6
4*	Triangular	Plane Strain	6	-	6
5*	Quadrilateral	Axisymmetric	8	4	8
6*	Quadrilateral	Axisymmetric	8	-	8
7*	Quadrilateral	Plane Strain	8	4	8
8*	Quadrilateral	Plane Strain	8	-	8
9	Triangular	Axisymmetric	10	6	13
10	Triangular	Axisymmetric	10	-	10
11	Triangular	Plane Strain	10	6	13
12	Triangular	Plane Strain	10	-	10
13	Quadrilateral	Axisymmetric	13	9	17
14	Quadrilateral	Axisymmetric	13	-	13
15	Quadrilateral	Plane Strain	13	9	17
16	Quadrilateral	Plane Strain	13	-	13
17	Triangular	Axisymmetric	15	3	15
18	Triangular	Axisymmetric	15	-	15
19	Triangular	Plane Strain	15	3	15
20	Triangular	Plane Strain	15	-	15
21	Quadrilateral	Axisymmetric	13	3I	16
22	Quadrilateral	Axisymmetric	13	3I	16
23	Quadrilateral	Plane Strain	13	3I	16
24	Quadrilateral	Plane Strain	13	3I	16
25	Quadrilateral	Axisymmetric	13	4	13
26	Quadrilateral	Axisymmetric	13	4	13
27	Quadrilateral	Axisymmetric	16	4	16
28	Quadrilateral	Axisymmetric	16	-	16
29	Quadrilateral	Plane Strain	16	4	16
30	Quadrilateral	Plane Strain	16	-	16
31	Triangular	Axisymmetric	15	6	15
32	Triangular	Plane Strain	15	6	15
33	Triangular	Axisymmetric	15	10	22
34	Triangular	Plain Strain	15	10	22

* Elements previously available in ABAQUS

Table 2.3 User Defined Elements in Subroutine UEL

Element Type	F.E. Formulation	Pile	Interface	Soil Model	Initial Conditions	Notes	Reference
8Q	- Small strain - Reduced int. - Total stress	Open Hole	---	-EPP (Tresca)	Unstressed	- Tip factor for pile only	Griffiths (1982)
15T	-Small strain -Full integration -Total stress	Rigid 60^0 Tip	Rough	- EPP(Tresca)	Unstressed	- Deep incremented load - $\delta/D \leq 20\%$ - 1% rule for Limit Load	DeBorst & Vermeer (1984)
8Q-4P	- large strain (up. Lagrange) - Mixed form.	Rigid	Rough	MCC[1] - OCR=1.0(K_0)	CEM[2] (approx.)	- Installation disturbance - Partially drained (compressible) - Load rate	Nystrom (1984)
8Q	-Large strain (up. Lagrange) -Mixed form -Int.?.	Rigid 60^0 Tip	Approx. Displ. Control	MCC -OCR=1.0(K_0)	Cone at base of hole	- Large displacement $\delta/D \geq 300\%$	Budhu & Bond (1987)
8Q-4P	- Large strain - Mixed form.	60^0 Tip	Approx. Displ. Control	- Cap-EP	Unstressed	- Deep-incremented load - $\delta/D \leq 20\%$ - Accuracy?	Kiousis et al. (1988)
15T	-Large strain Large Displacement (Eulerian) - Total stress	Rigid 60^0 Tip	Tip: rough Shaft: smooth rough	- EPP (von Mises) - Init. shear stress	Unstressed SPM[3]	- Deep-incremented load - $\delta/D \leq 20\%$	Teh & Houlsby (1991)
15T	Large strain Large displacement Total stress	Rigid Flat tip	Frictional elements	- EPP (Mohr-Coulomb) - Implicit Int.	Unstressed	- Deep - large load inc. - δ/D-> 300% - Singular point elements	van Langen & Vermeer (1991)
4Q	Large strain: ALE[4] Total stress	Rigid 60^0 Tip	Frictional elements	- EPP (von Mises)	Unstressed	- Large surface penetration	van den Berg et al. (1992)

Notes:
1. Particular version of MCC with J_3 shear stress invariant in yield surface.
2. Cylindrical cavity expanded in finite steps with some partial drainage.
3. First application of SPM in conjunction with FE analyses.
4. Arbitrary Lagrangian Eulerian formulation

Table 2.4 Summary of Previous Finite Element Studies of Axial Pile Loading in Clays

	LOWER BOUND (Sloan 1988)	UPPER BOUND (Sloan & Kleeman 1994)
Unknowns	Nodal Point Stresses, σ	Nodal Point Velocities, u Plastic Multipliers, $\dot{\lambda}$
F.E. Approximation	Triangular Elements Linear Stress Variation	Triangular Elements Linear Velocity Variation
Linear Programming Form	*Minimize* $-C^T\sigma$ *Subject to* $A_1\sigma = B_1$, $A_2\sigma \leq B_2$	*Minimize* $\{C_1^T\dot{\lambda} + C_2^T u\}$ *Subject to* $A_1\dot{\lambda} + A_2 u + A_3 u_i^+ + A_4 u_i^- = 0$, $u_i^+, u_i^-, \dot{\lambda} \geq 0$
Optimization Function	Applied Boundary Load	Total Power Dissipated
Constraints	Equilibrium Mohr-Coulomb Yield Stress BC's	Compatibility Associated Flow Velocity BC's

Table 2.5 Formulation of Numerical Limit Analyses

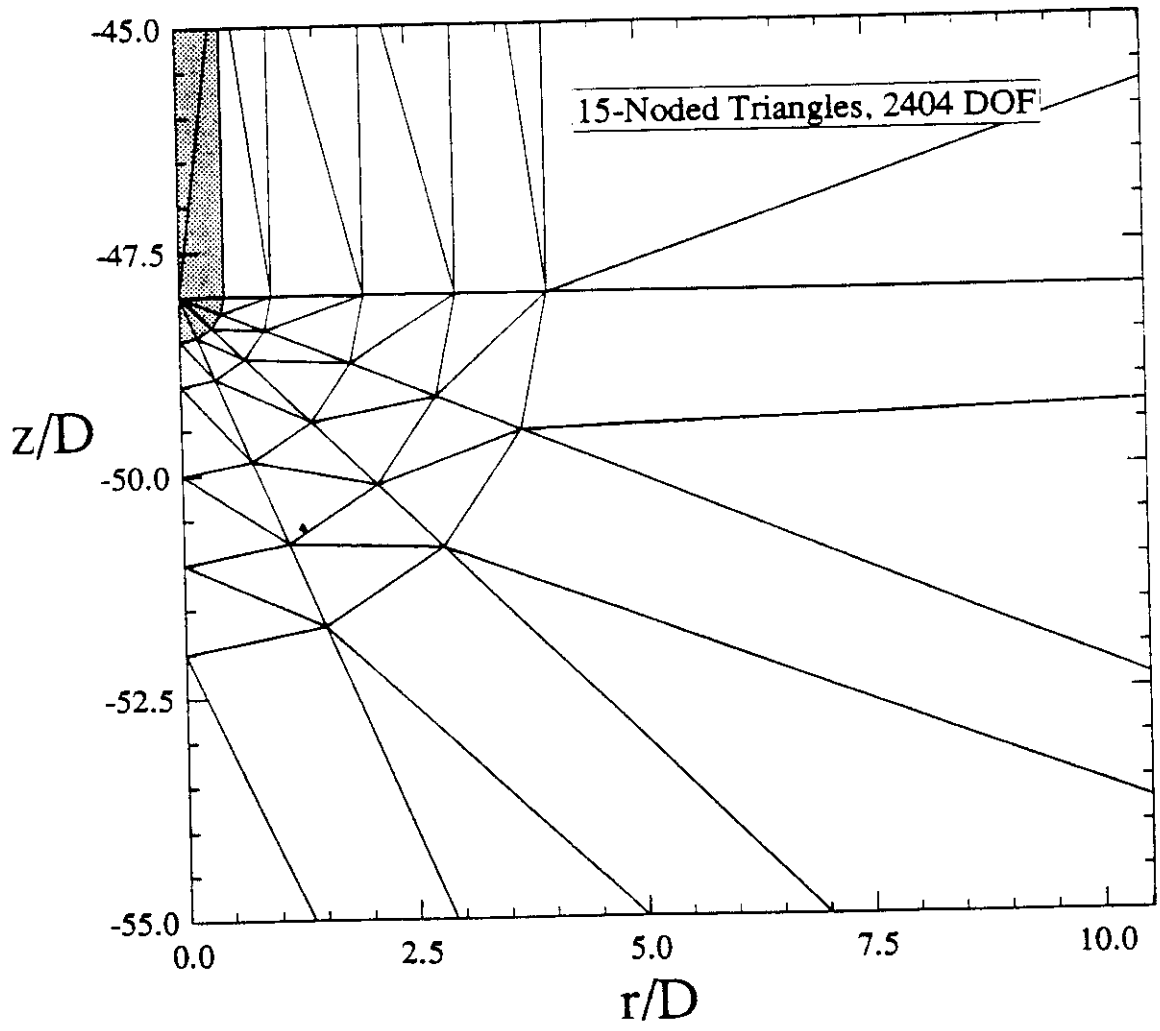

Figure 2.1 Discretization Around Pile Tip using 15-Noded Triangular Finite Elements

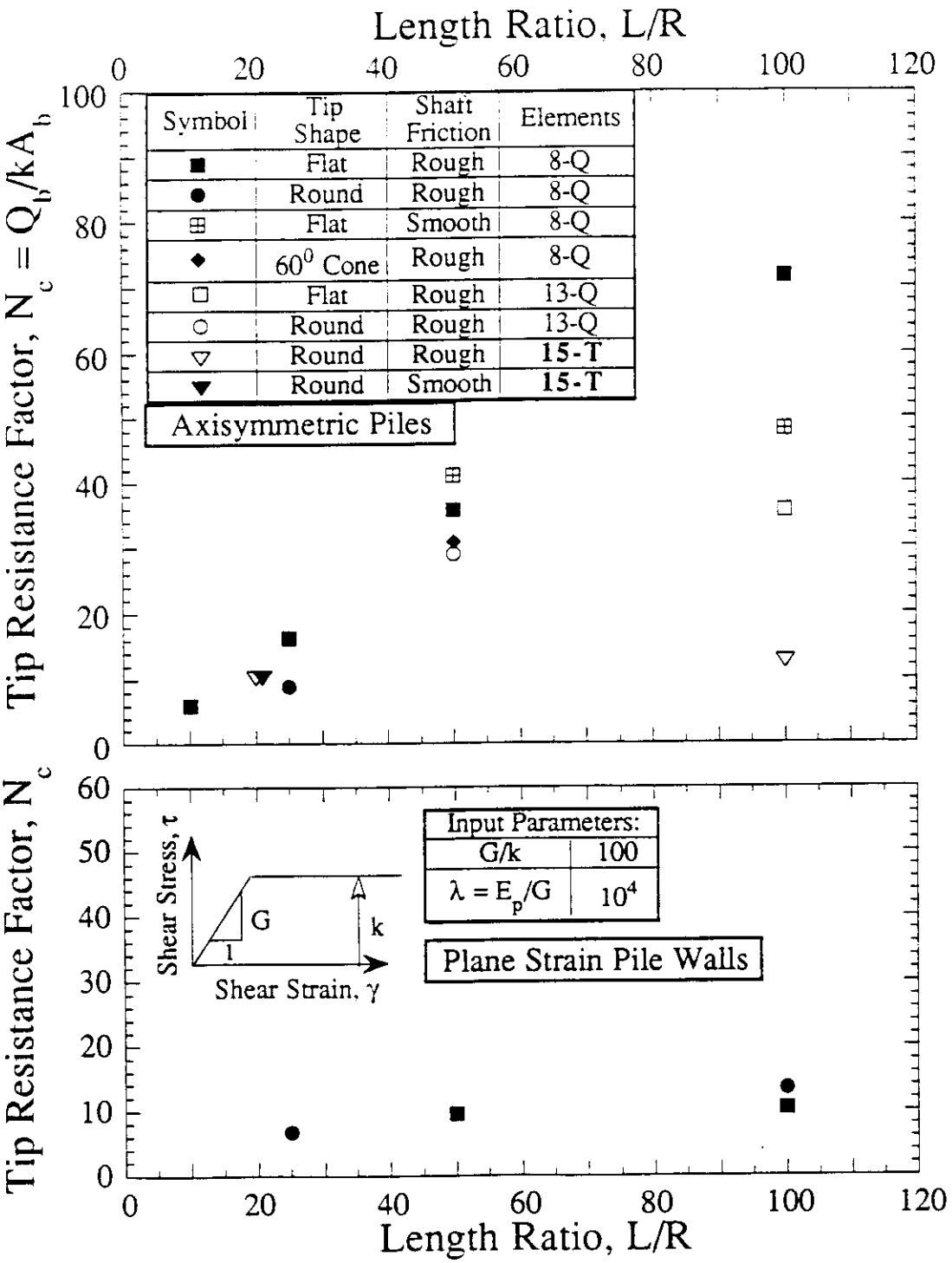

Figure 2.2 Evaluation of Tip Resistance Factors for Finite Element Analyses of Piles in Elasto-Plastic Soils

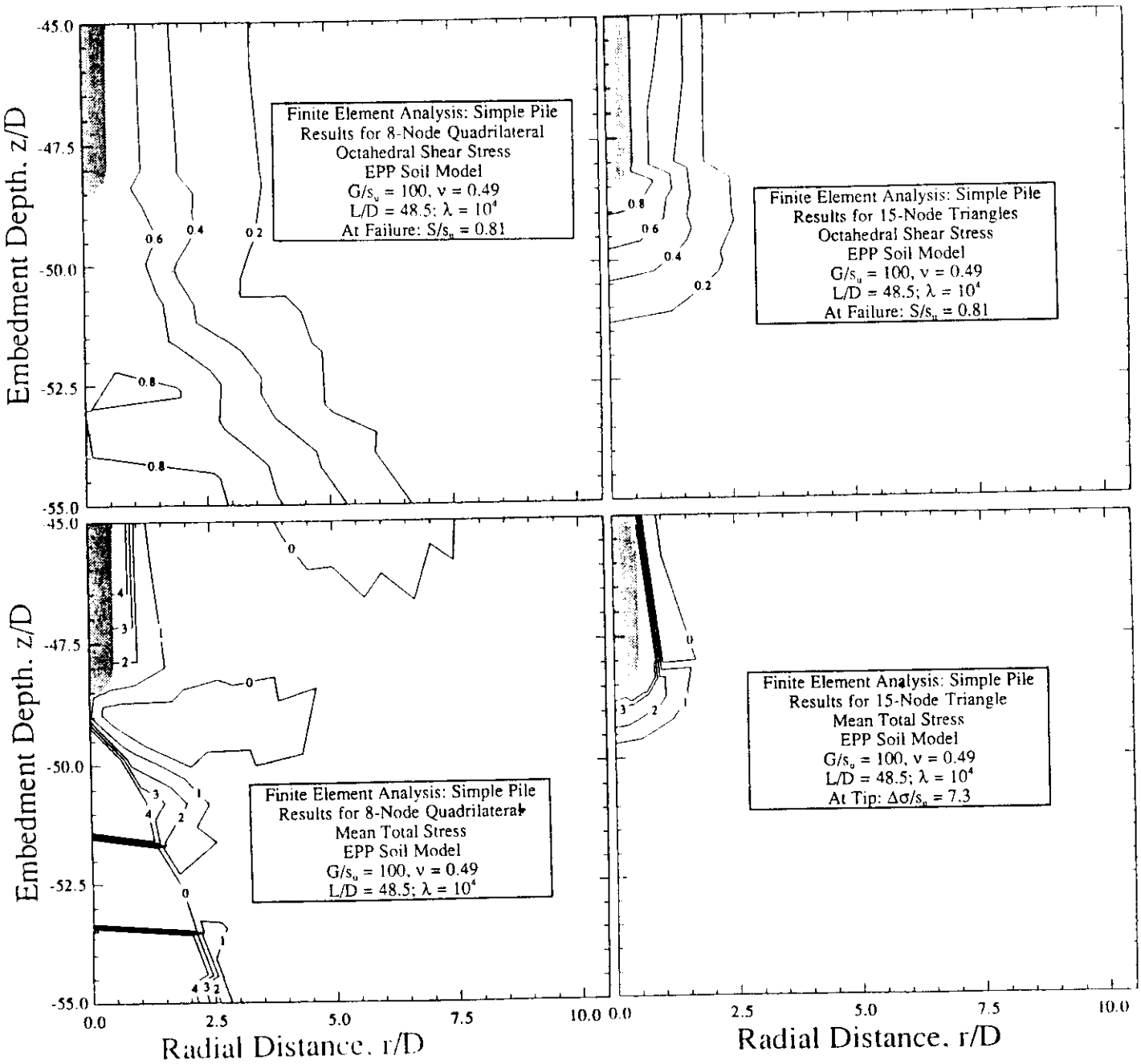

Figure 2.3 Effect of Element Type on Elasto-Plastic Predictions of Stress Fields Around Pile Tip

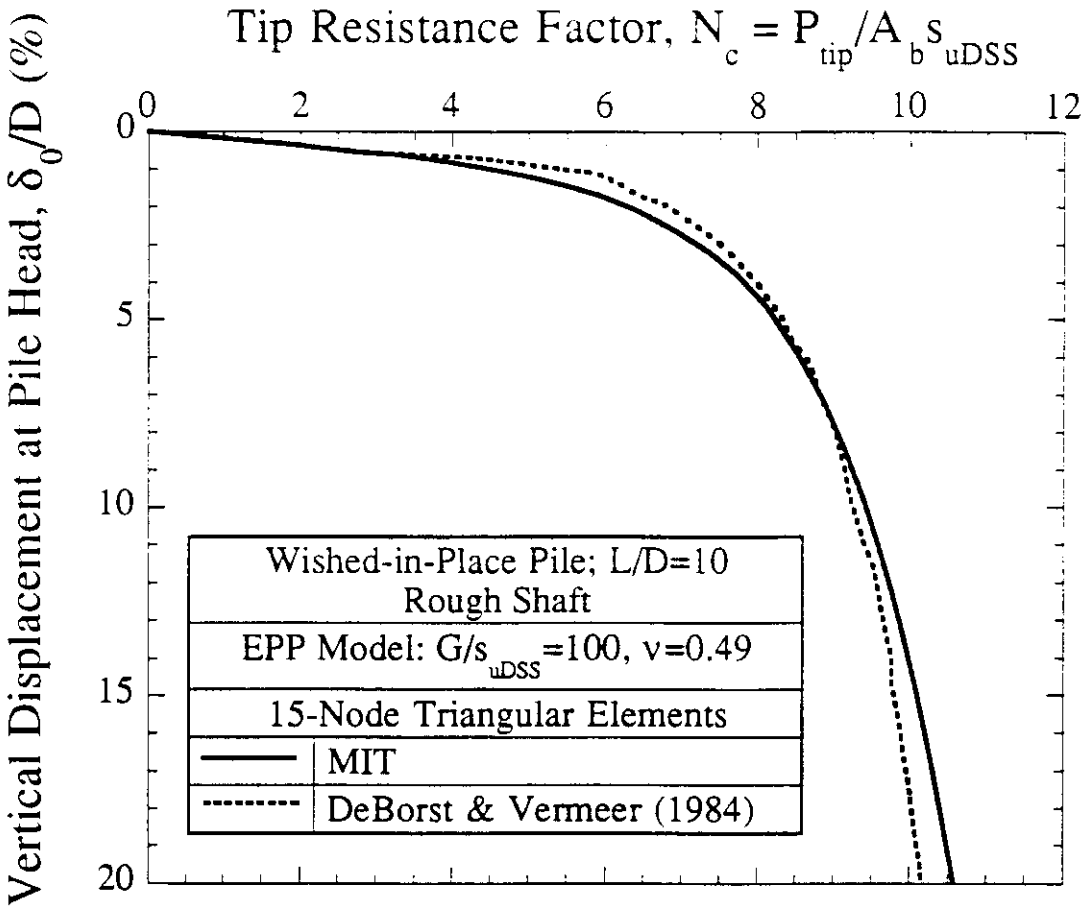

Figure 2.4 Comparison of Pile Tip Resistance with Results of DeBorst and Vermeer (1984)

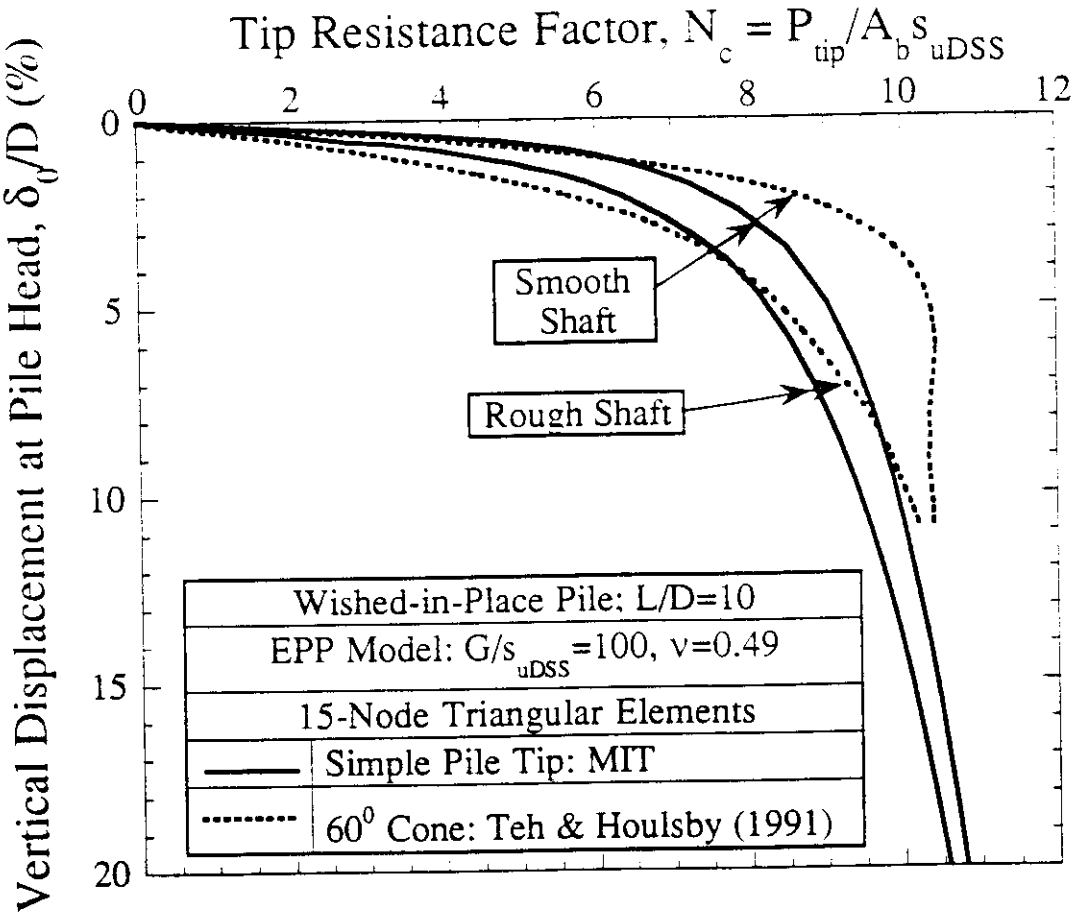

Figure 2.5 Comparison of Pile Tip Resistance with Results of Teh and Houlsby (1991)

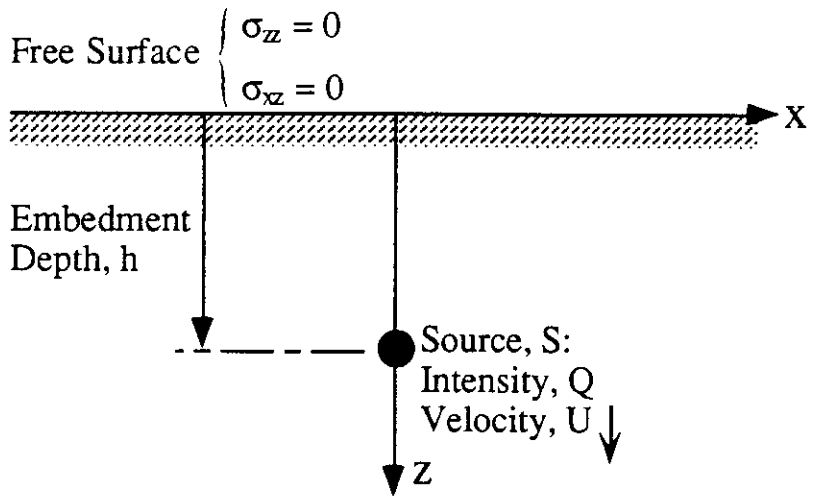

a) SSPM Representation of Shallow Penetration Problem

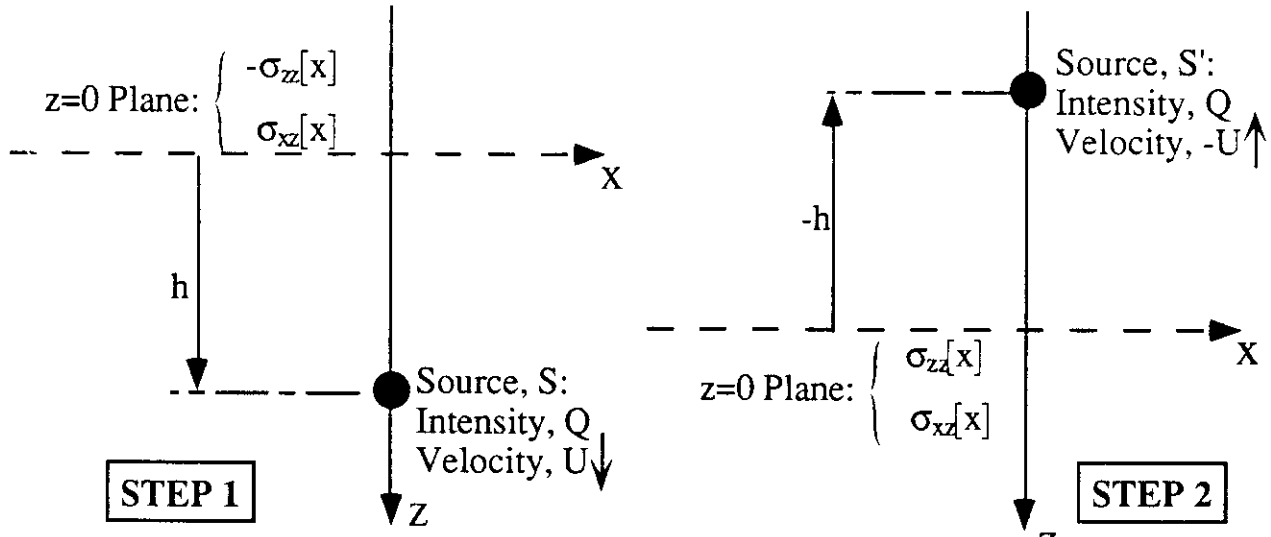

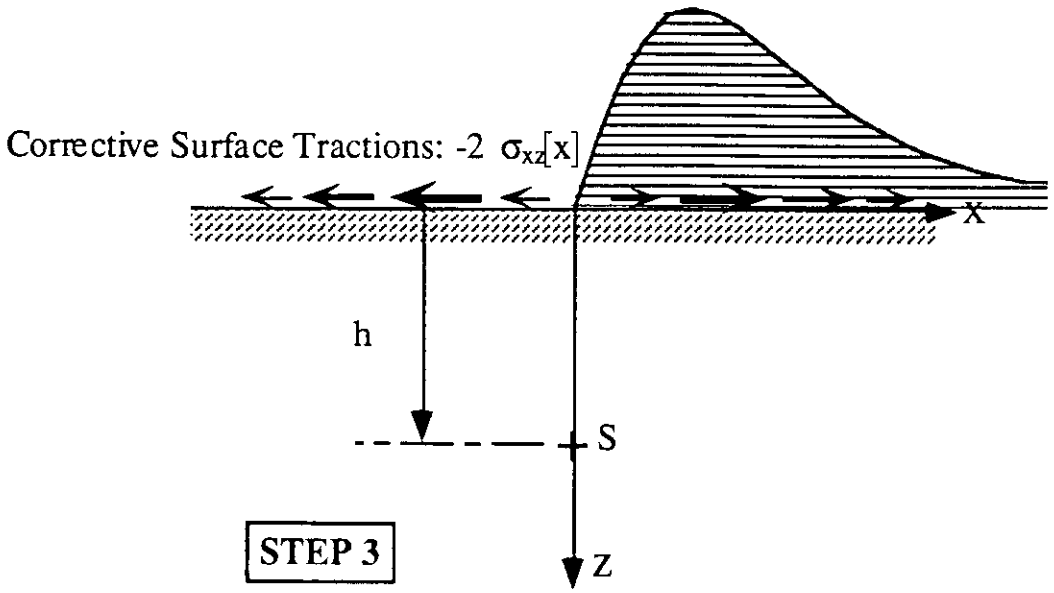

c) Equivalent Solution (Steps 1+2+3)

Figure 2.6 Conceptual Model for Simulation of Penetration with Stress-Free Surface

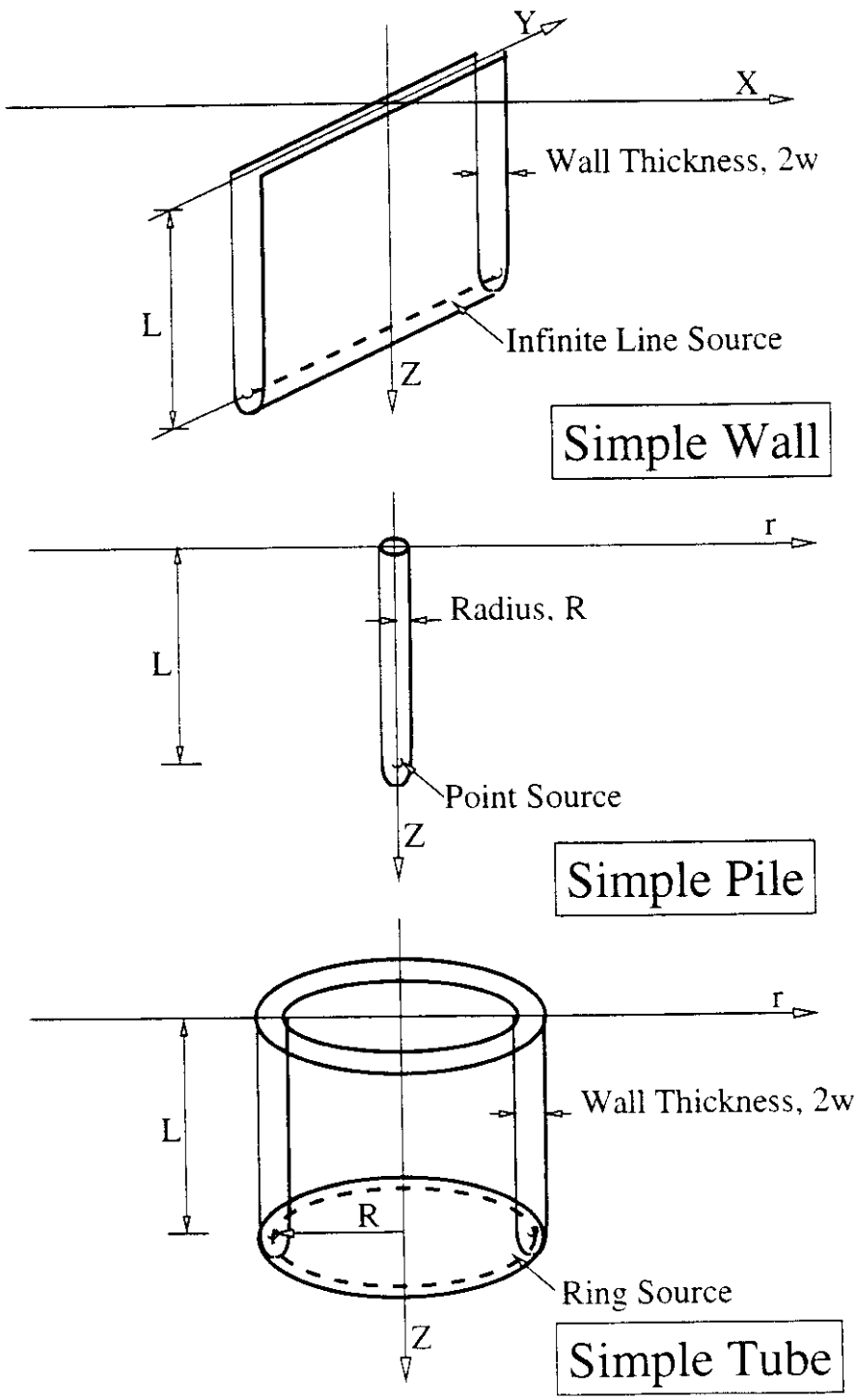

Figure 2.7 Problem Geometry and Notation

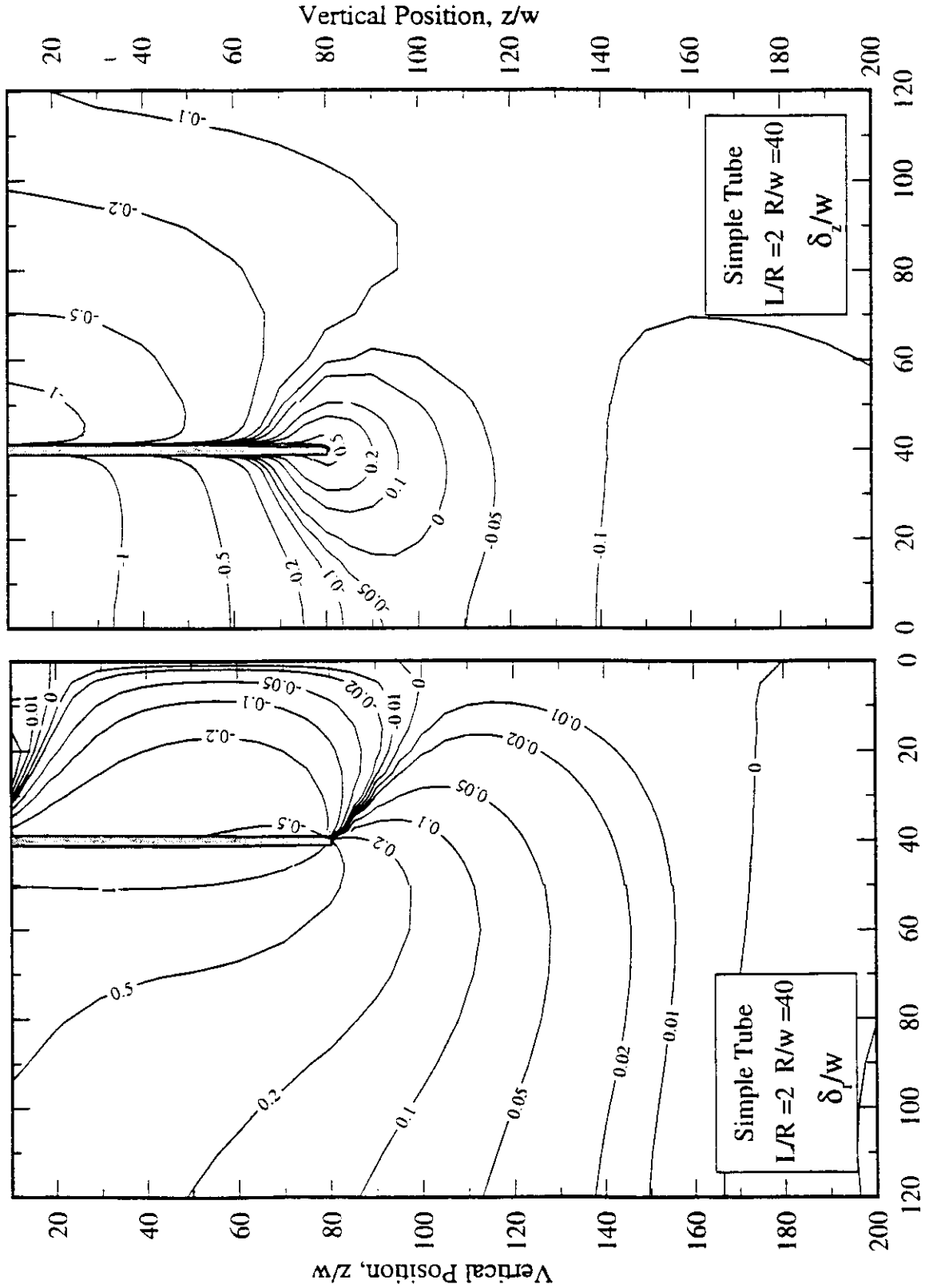

Figure 2.8a. Displacement Contours Around Simple Tube with R/w = 40, at L/R = 2

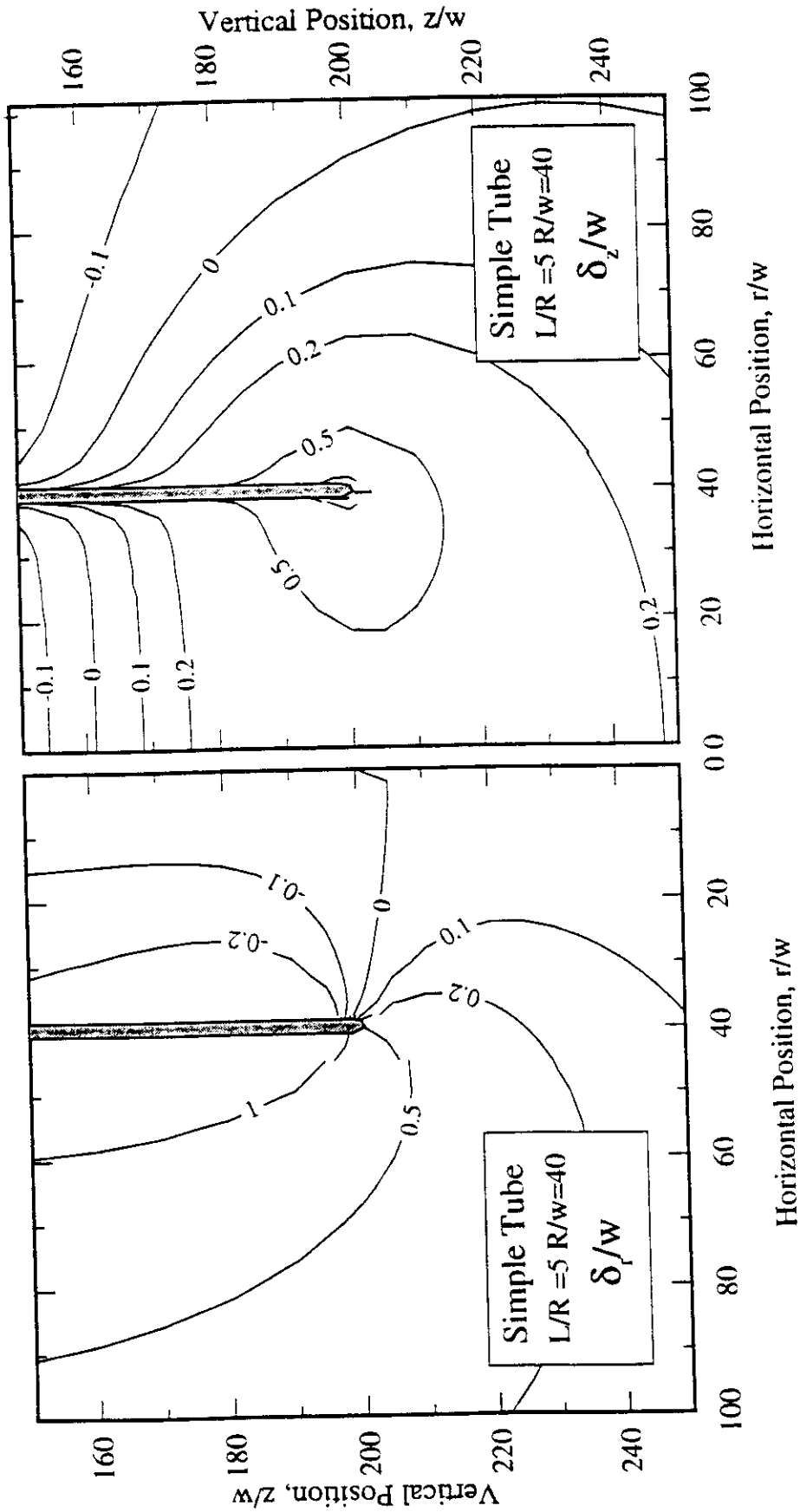

Figure 2.8b. Displacement Contours Around Simple Tube with R/w = 40, at L/R = 5

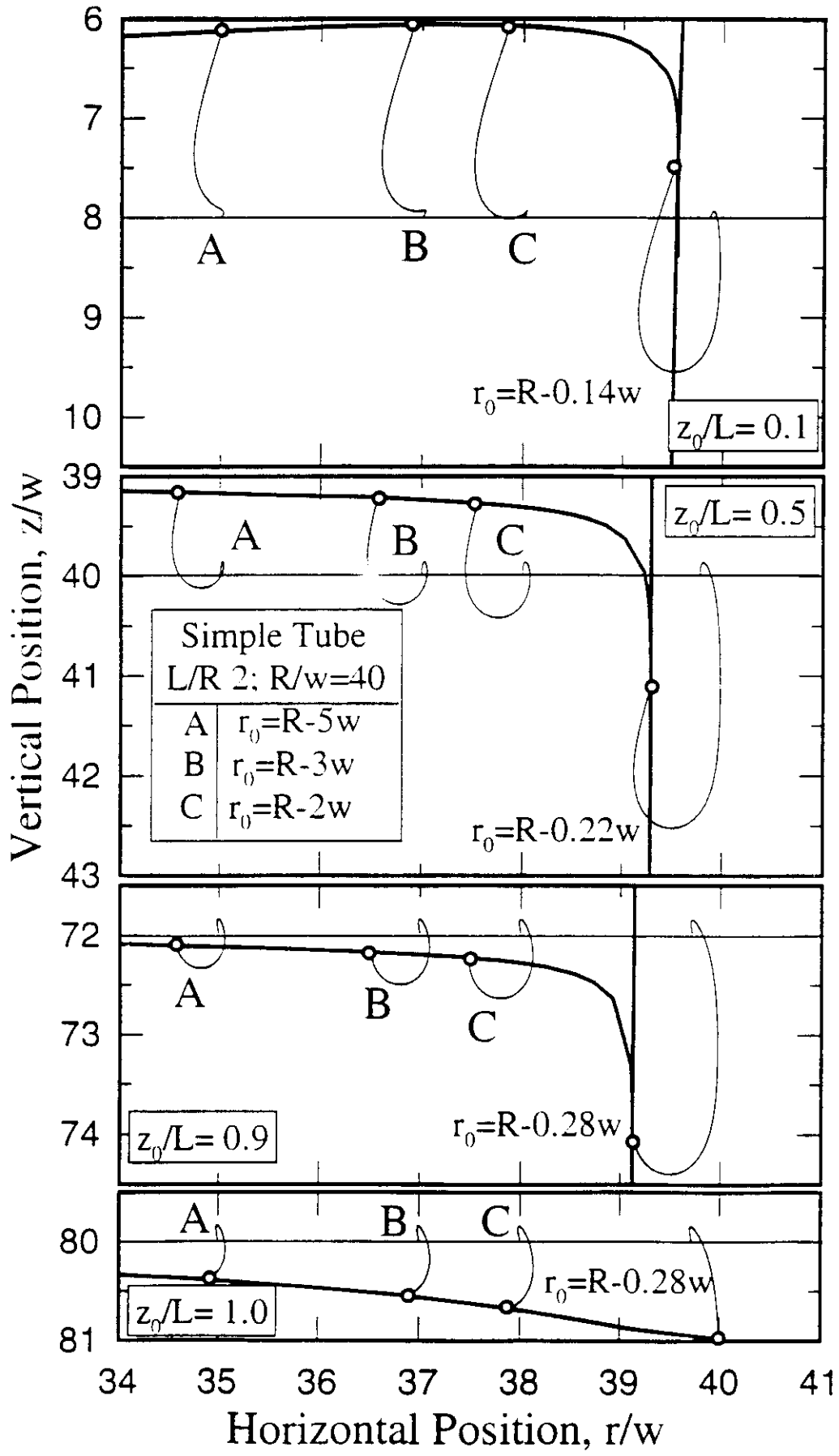

Figure 2.9a. Deformation Paths of Soil Elements Inside Simple Tube with R/w = 40 and L/R = 2

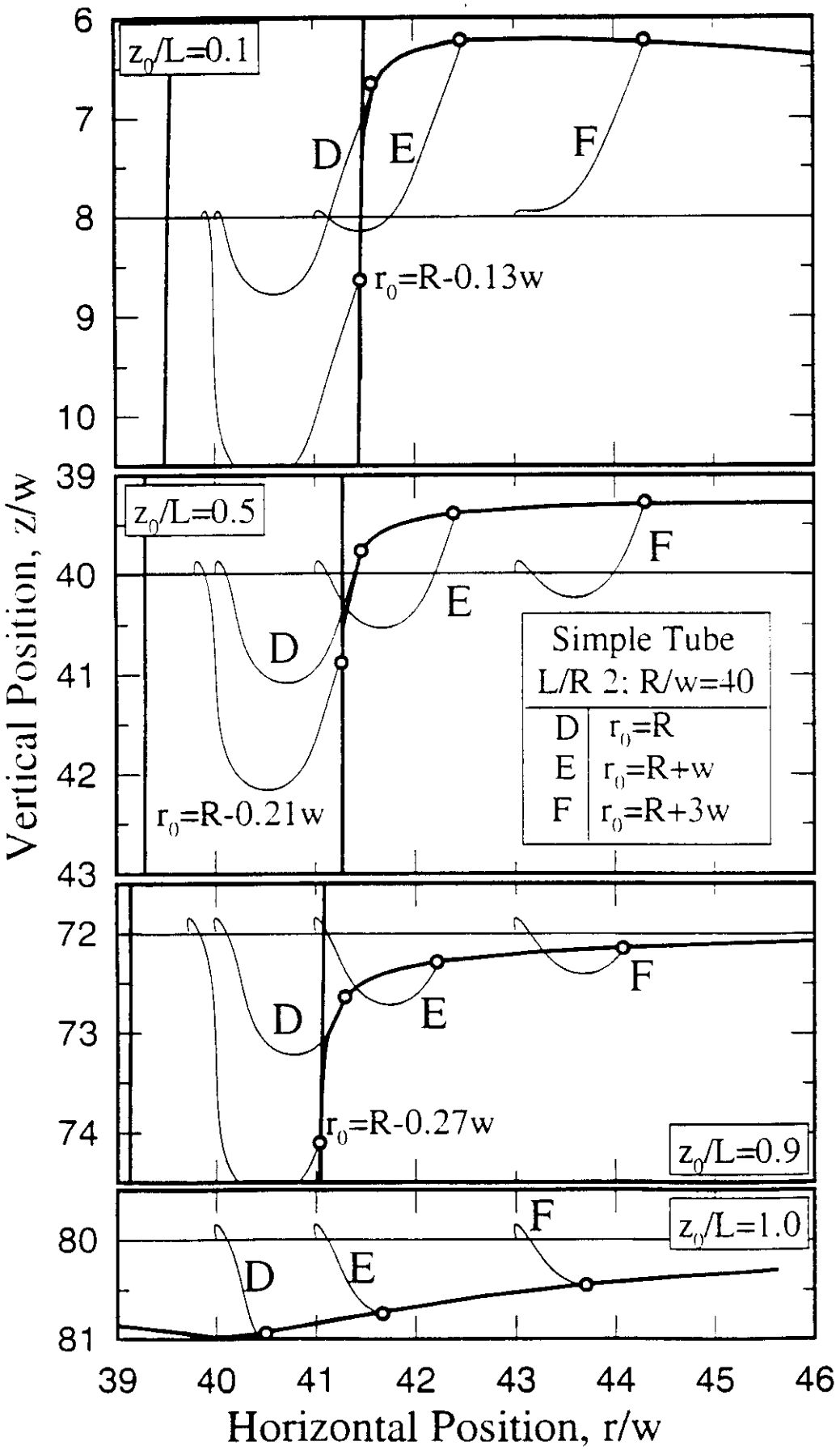

Figure 2.9b. Deformation Paths of Soil Elements Outside Simple Tube with R/w = 40 and L/R = 2

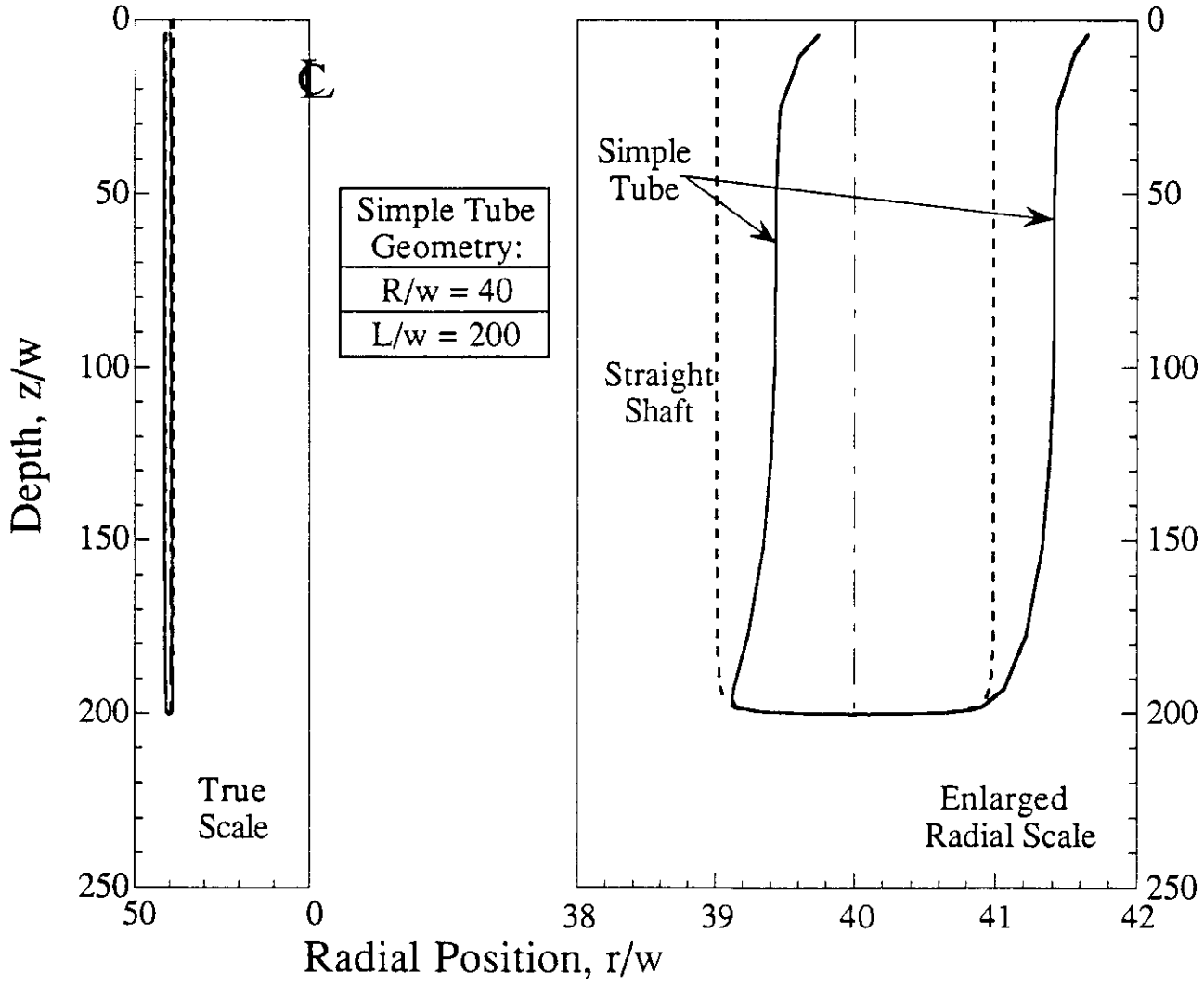

Figure 2.10 Wall Shape of Simple Tube with Aspect Ratio, R/w = 40

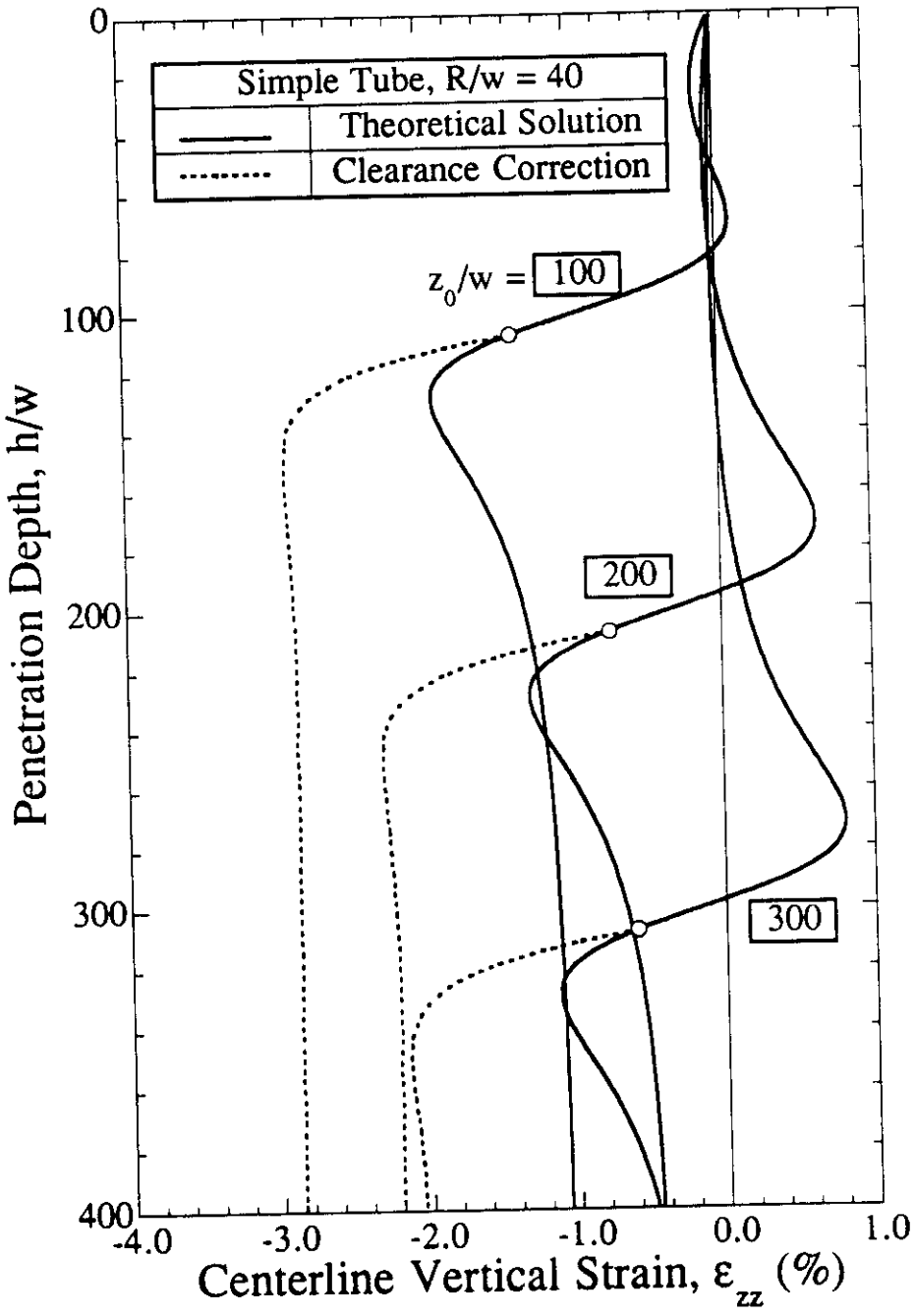

Figure 2.11 Approximate Corrections of Centerline Strains for Simple Tube Geometry

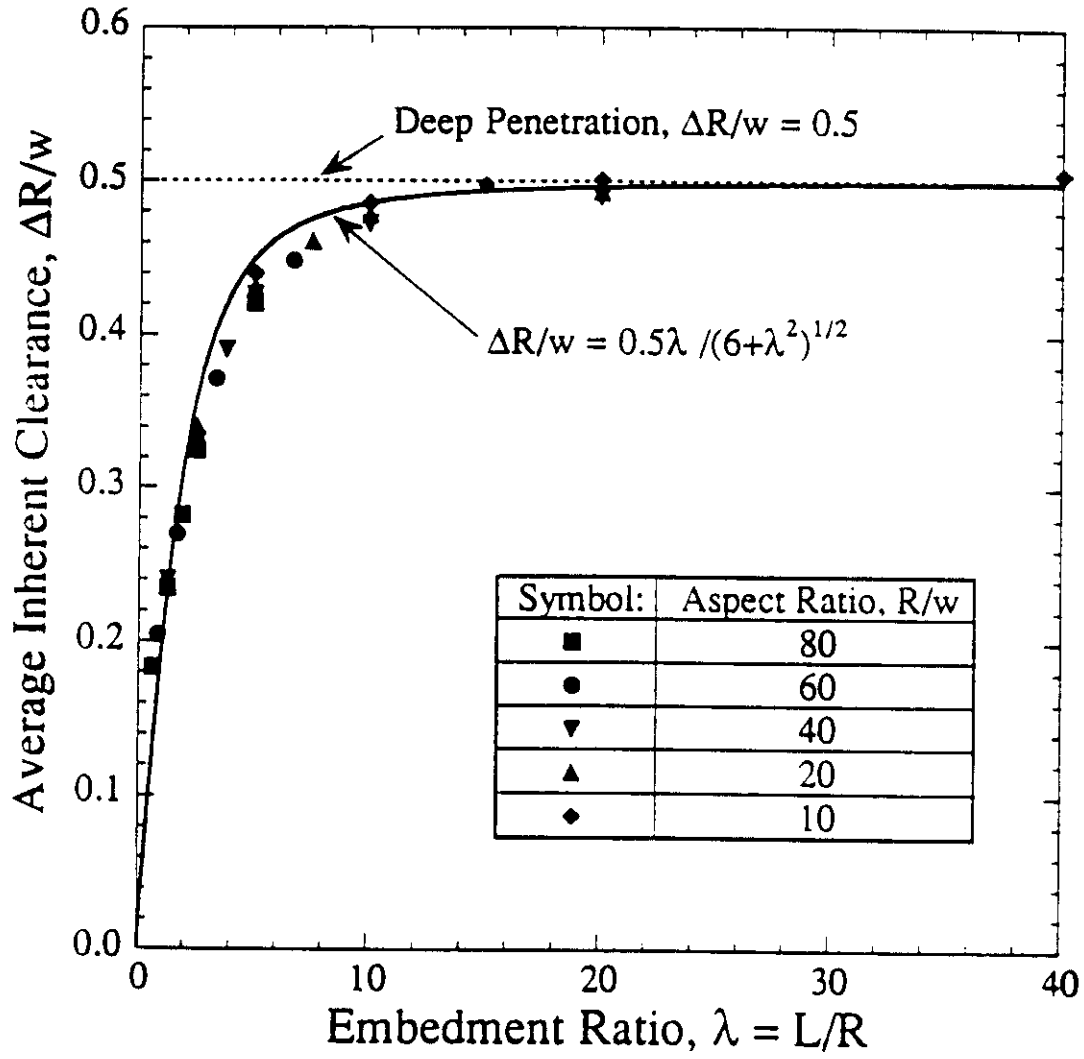

Figure 2.12 Average Clearance for Shallow Penetration of Simple Tubes

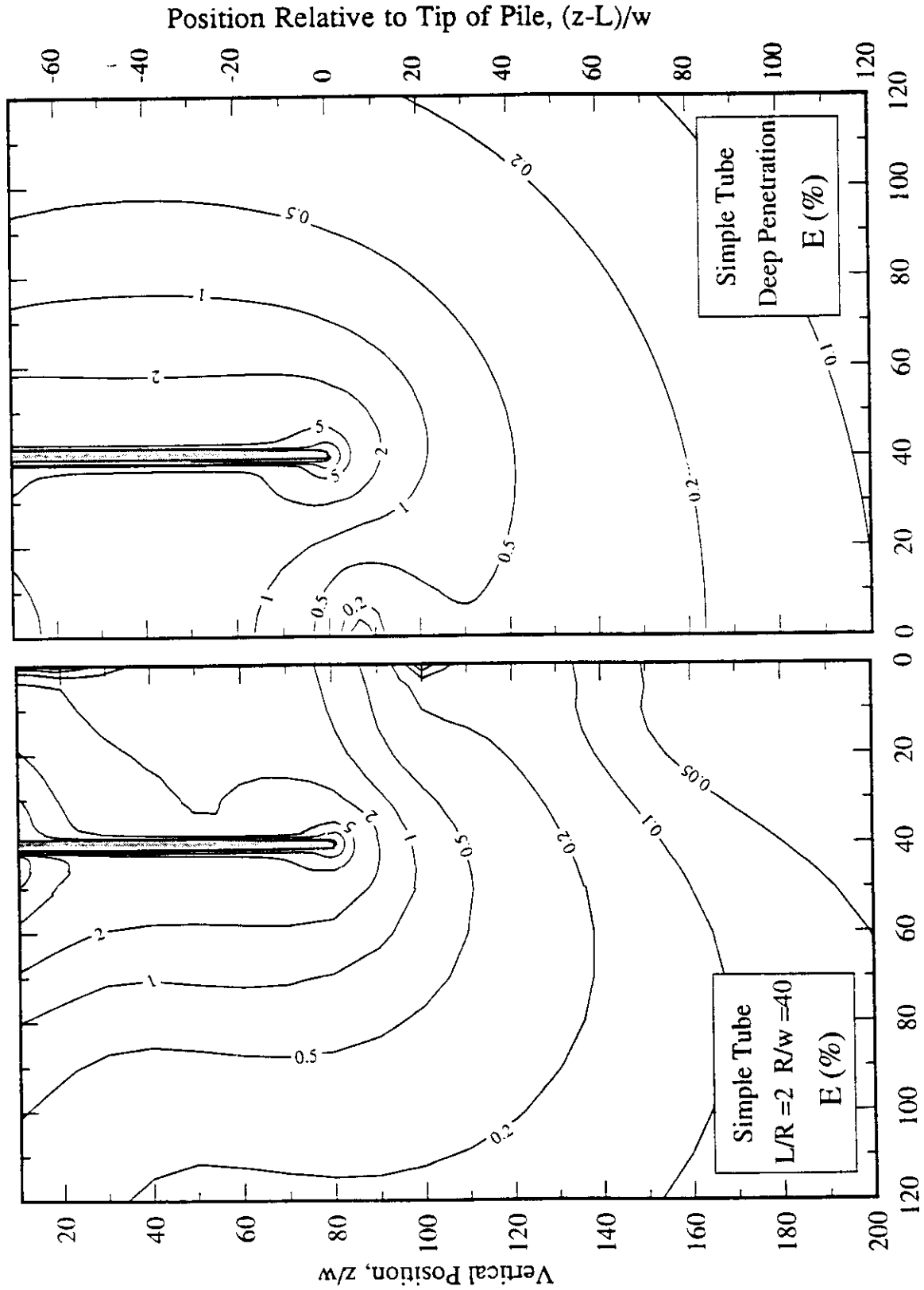

a) L/R=2

b) L/R=∞

Figure 2.13 Contours of Octahedral Shear Strain Around Simple Tube with R/w = 40

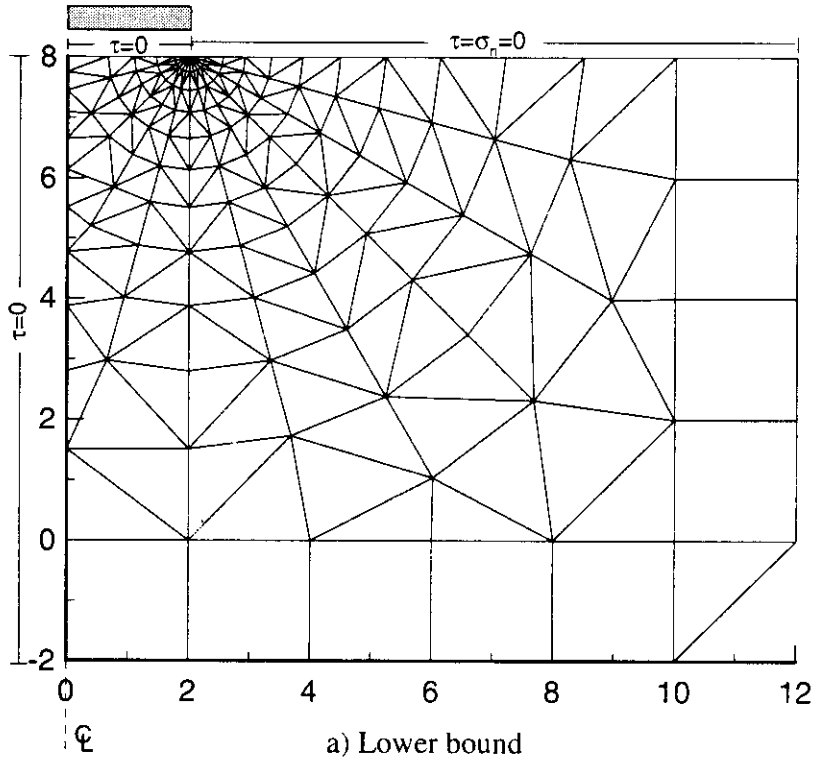

a) Lower bound

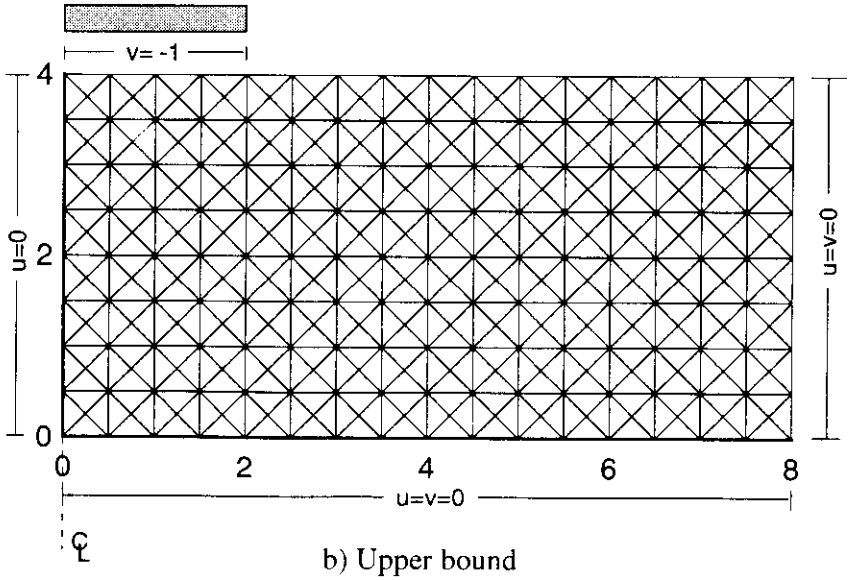

b) Upper bound

Figure 2.16 Typical Meshes Used in Limit Analyses for Vertically Loaded Footing on Clay

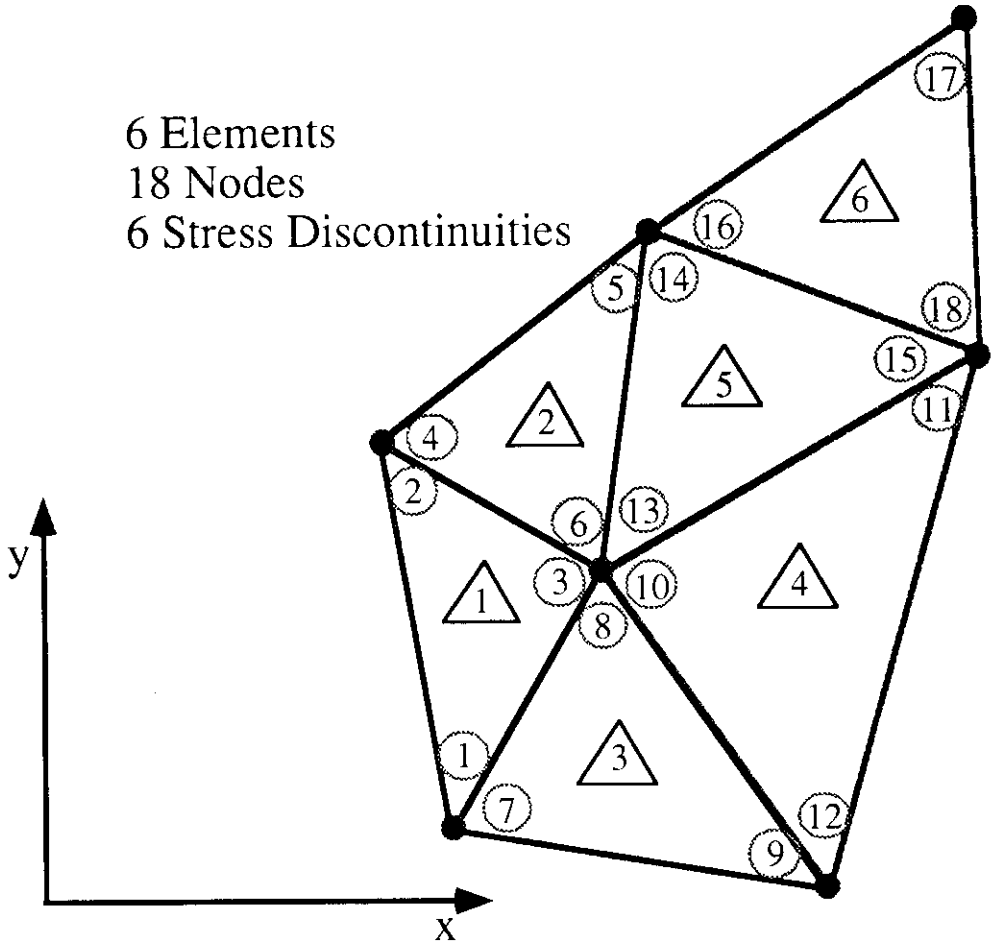

Figure 2.14 Finite Element Discretization for Lower Bound Stress Analysis

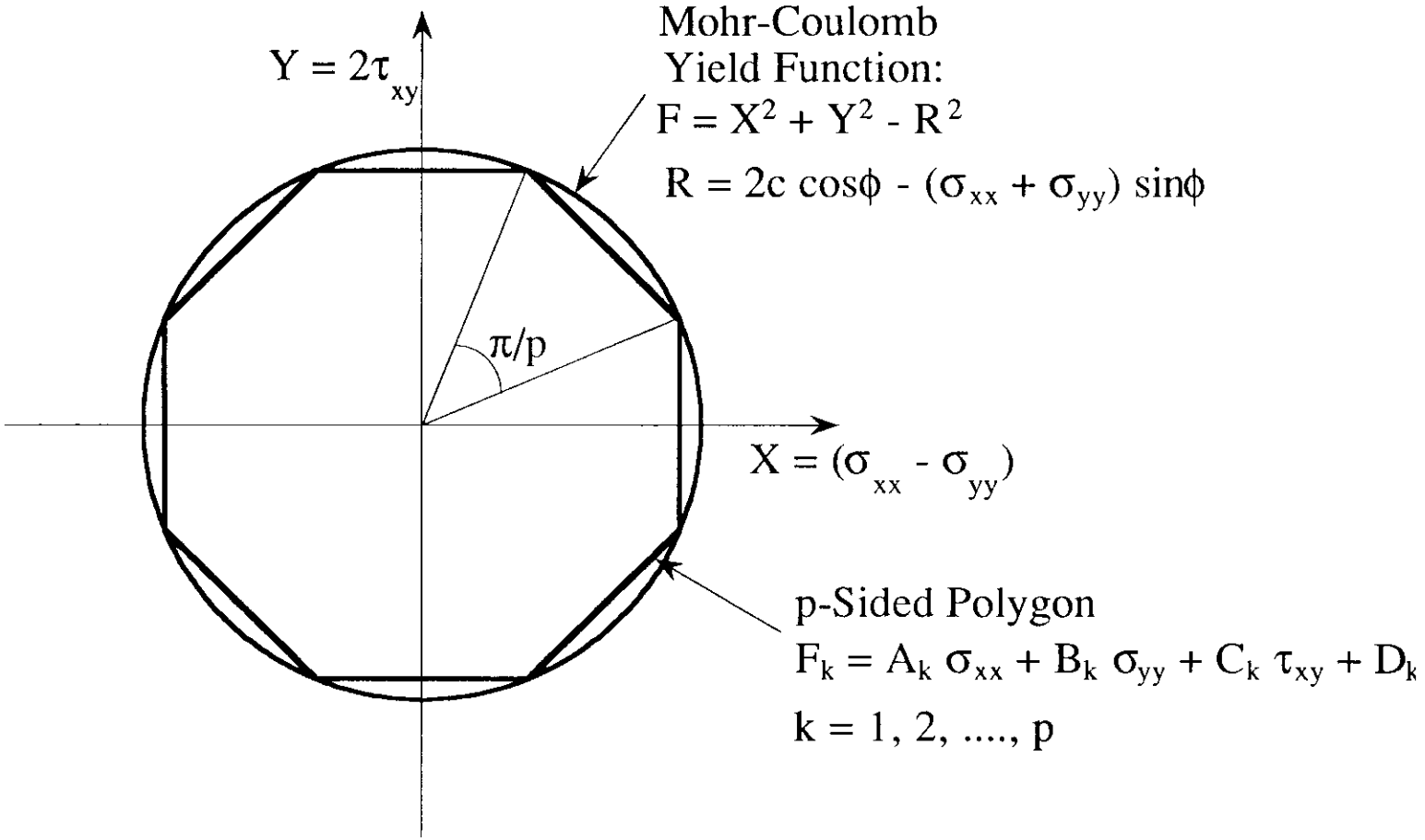

Figure 2.15 Linearization of Mohr-Coulomb Yield Function

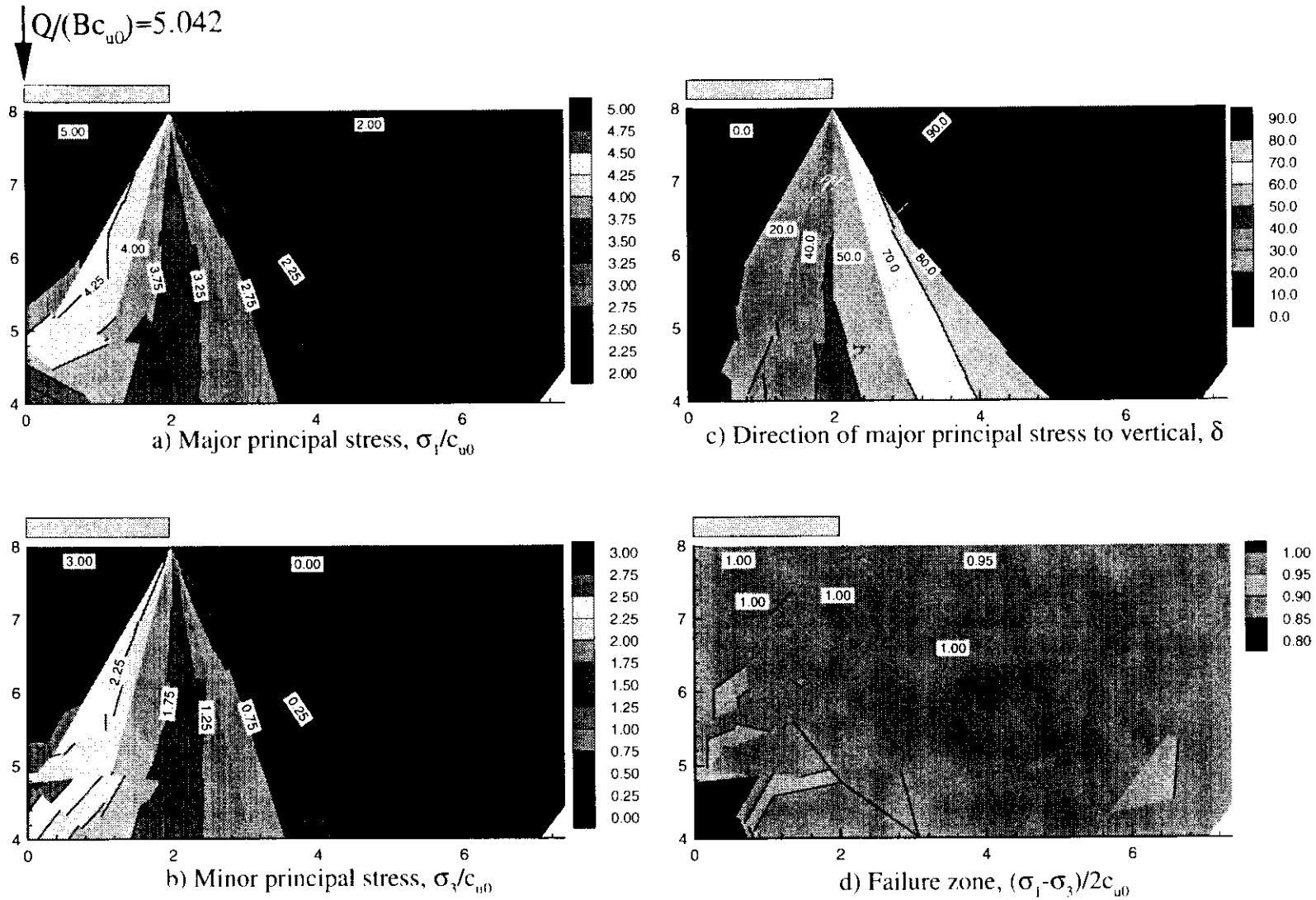

Figure 2.17 Lower Bound Solutions for Vertically Loaded Footing on Deep Homogeneous Clay Layer

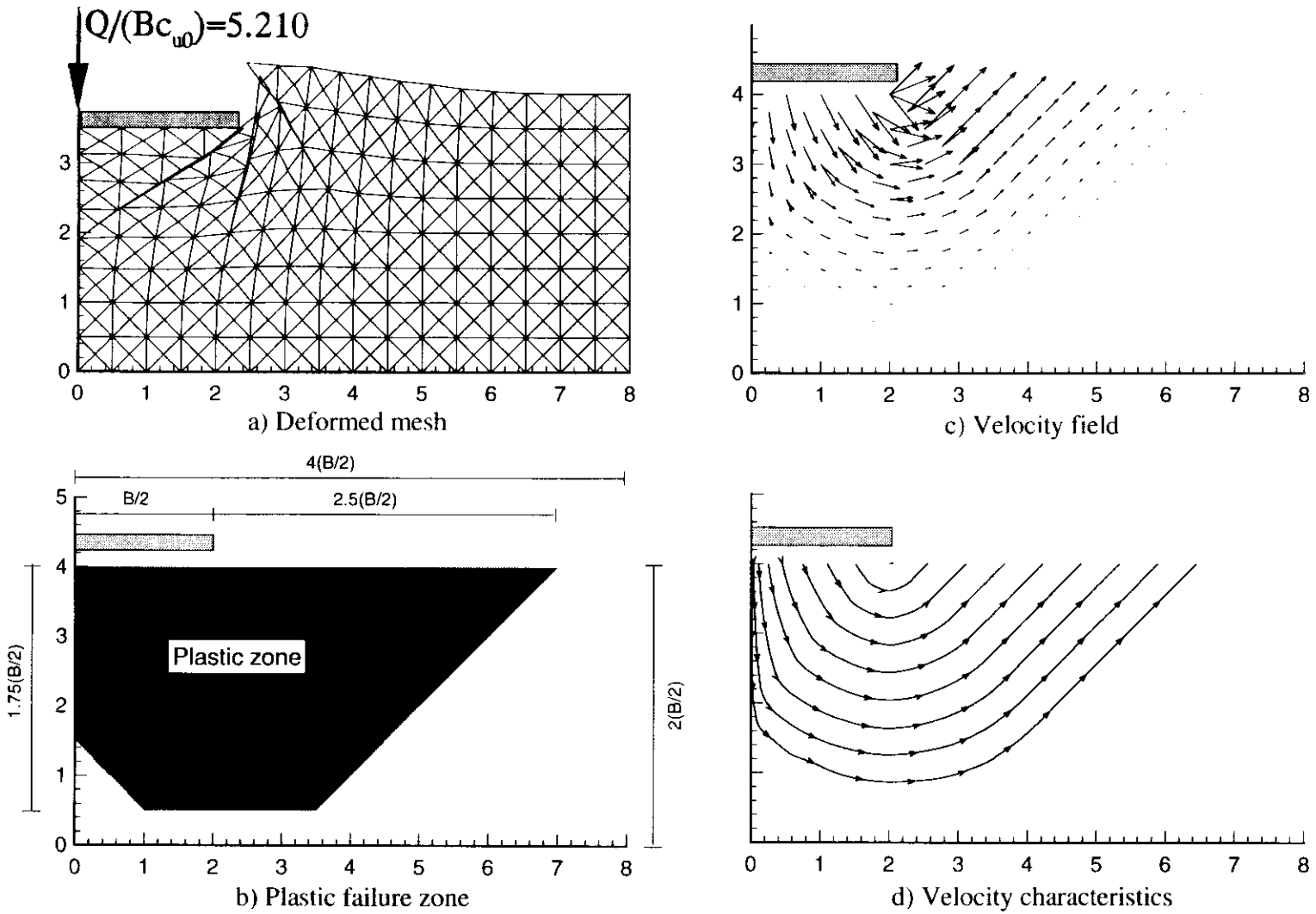

Figure 2.18 Upper Bound Solutions for Vertically Loaded Footing on Deep Homogeneous Clay Layer

7.41 Summary of Force-Deformation Measurements for Sustained Tensile Loading of CET Model Caissons
7.42 Typical Stable Behavior of CET Model Caisson Under Sustained Tensile Loading
7.43 Failure of CET Model Caisson in First Stage Sustained Tensile Load Test
7.44 Failure of CET Model Caisson in Subsequent Sustained Tensile Load Test
7.45 Measurements of Pore Pressure Dissipation During First Stage of Sustained Tensile Loading
7.46 Finite Element Prediction of CET Model Force-Displacement Response in Four-Stage Sustained Tensile Load Test
7.47 Summary of Predicted CET Model Caisson Response in Sustained Tensile Load Tests

3. DESIGN OF CET CELL

This chapter describes the design of the Caisson Element Test (CET) apparatus for simulating the installation, set-up, and axial tensile loading of a miniature caisson in a uniform, saturated 'element' of clay. The CET cell comprises five components, as shown in Figure 3.1: 1) the sealed test chamber, which contains a clay sample with consolidation stresses maintained by air pressure, 2) the model caisson, an unique two-piece design that enables independent control of the caisson wall and cap, 3) the driving system, which controls displacement of the caisson wall and cap and applies total stress on the clay surface, 4) a continuous automated feedback control system that can simulate various stages in the life of a suction caisson, and 5) the instrumentation package, which provides input signals for feedback control and data for test interpretation. Section 2.1 describes each of these components in detail. The samples of resedimented Boston Blue Clay (RBBC) are consolidated one-dimensionally in the test chamber (independent of the CET apparatus) using methods developed previously at MIT. This resedimentation procedure produces a highly uniform CET test sample with known stress history and engineering properties. Section 3.2 summarizes the properties of the RBBC used in the CET experiments. Finally, section 3.3 presents a complete description of the CET test procedures.

3.1 CAISSON ELEMENT TEST CELL

3.1.1 Consolidation Chamber

The basic building block of the CET cell is the consolidation chamber, which is a rigid-walled, stainless steel cylinder attached to a 1.75 cm thick stainless steel baseplate (see Figure 3.2). The cylinder has an inside diameter of D_i = 30 cm, a height of H = 25 cm, and a wall thickness of t = 1 cm. This chamber has been used at MIT since 1980 for the preparation of resedimented Boston Blue Clay (RBBC) samples (Germaine, 1982). For the CET experiments, the original consolidation chamber has been modified to enable penetration of the model caisson into a consolidated clay sample and to include additional instrumentation.

Figure 3.2 shows a schematic cross-section of the original chamber. During consolidation, the top of the clay sample is loaded incrementally through a rigid cap (and attached piston), which is sealed against the chamber wall by a lubricated O-ring. Movements of the piston assembly are guided by a stacked linear ball bearing assembly that minimizes friction. Pore water is free to drain through a 0.5 cm thick porous plastic disc attached to the top cap and through a 0.85 cm thick porous stone that fits on the baseplate. The plastic disc is secured to the top cap with screws in order to facilitate cleaning procedures. The porous stone, which is made of vitrified aluminum oxide (AlO_2) with an average grain size diameter of 120 μm and an induced porosity of 45%, simply lies in a recess within the baseplate. To prevent the migration

of soil particles and porous plate penetration into the clay surface during consolidation, filter paper (0.014 cm thick) separates the clay from the porous disc at the top and the porous stone at the bottom.

Two major modifications were made to the consolidation chamber in order to conform to the requirements of the CET experiments. Figure 3.3 shows additional access ports that were machined into the chamber sidewalls and baseplate to allow for installation of pressure transducers. Eight ports were bored into the sidewalls at four different vertical locations for total stress or pore pressure transducers. Similarly, nine access ports were machined through the baseplate and porous disk to allow installation of miniature pore pressure probes through the base and into the clay sample. These sidewall transducers and baseplate probes are described further in section 3.1.5.

The second major modification was a new sealed top cover and air-pressurized cavity for the model caisson experiments (see Figure 3.4). The main purpose of this design is to allow controlled caisson installation while maintaining the total vertical stress on the consolidated clay sample. The model caisson and soil sample are isolated from the pressurized air cavity by a cylindrical slip tube assembly, which can be divided into four parts: the drainage filter, rubber membrane, outer membrane slip ring, and inner membrane slip tube. The surface of the clay is covered by two layers of filter material: 1) 0.014 cm thick paper filter, and 2) 0.022 cm thick cloth filter. The paper filter allows vertical drainage of pore water while the cloth filter allows both vertical and lateral drainage. A 0.03 cm thick rubber membrane covers the filter and separates the saturated soil sample from the pressurized air cavity. Hence, the air pressure provides a total stress on the surface of the soil sample. The outside edge of the rubber membrane is sealed with RTV (rubber adhesive) to an aluminum slip ring, which is sealed to the chamber sidewall by two "X-rings" that allow the ring to slide up and down in response to soil deformations. The beveled outside bottom edge of the ring (see Figure 3.4) allows pore water to collect and drain freely through hollow tubing, which is connected to the atmosphere. The inside diameter of the rubber membrane is sealed with RTV to an inner slip tube, which is 18 cm tall, has a wall thickness of 0.164 cm, and has an inside diameter of 5.35 cm (see Figure 3.4). The inside diameter narrows to 5.1 cm at the bottom to minimize the clearance between the slip tube and the wall of the model caisson.

A 1.3 cm thick aluminum cover plate encloses the pressure cavity and has one central entry port for the inner membrane slip tube and caisson. The inner slip tube is sealed to the cover plate at the entry port location by one O-ring that allows the tube to move freely in response to clay surface deformations. The cover plate also has access ports for applying and monitoring the chamber air pressure, draining the pore fluid, and making LVDT electrical connections.

This elaborate new test chamber cover assembly enables the application of consolidation stresses to the soil, free drainage and non-uniform deformations of the soil surface, and caisson access to the soil. The surface deformations are measured from within the pressure cavity as described in section 3.1.5.

3.1.2 Model Caisson

The centerpiece of the CET apparatus is the model caisson, which comprises two components, an outer caisson wall and an inner caisson cap, as shown in Figure 3.5. Although the prototype caisson cells are monolithic units, the two-piece design for the CET model is used for two reasons. First, it enables the model to simulate installation by underbase suction (as opposed to self-weight penetration). The clay sample is consolidated initially with the wall tip retracted to a position flush with the cap at the surface of the clay, as shown in Figure 3.13. With the caisson in this position, a uniform stress can be applied across the entire surface of the clay sample (i.e., by applying loads to the caisson that balance exactly the applied air pressure). Installation by underbase suction can then be simulated by driving the caisson wall at a constant rate, measuring the force increment picked up by the wall, and applying an equal but opposite force increment on the cap, as described in section 3.3.2.

The second reason for the two-piece caisson design is that the two components can be controlled independently, a feature that allows independent measurement of the cap and wall force contributions[1]. Separate wall and cap data provide important insights into the caisson behavior during successive phases of the CET experiments.

Figure 3.5 illustrates the construction of the model caisson. The caisson wall is a brass Shelby tube with the tapered cutting edge removed, such that the tip is blunt[2]. The tube has an outside diameter of D_O = 5.08 cm and a wall thickness of t = 0.145 cm. The wall is 33 cm tall (although only the bottom 5 cm penetrate the clay sample) and is attached to the drive assembly by four screw bolts, as shown in Figure 3.5. Figure 3.6 shows the caisson cap, a 5.7 cm tall brass cylinder with an outside diameter of 4.65 cm. Pore pressures can be measured at the center of the base of the cap through a ceramic porous stone and pressure transducer assembly (section 3.1.5 gives full details of the instrumentation). The transducer is secured in place by a threaded brass locking ring. The cap is connected to the cap driver by a hollow aluminum rod which screws into the threaded center hole at the top of the cap.

In order to prevent metal to metal contact between the cap and wall, there is an O-ring around the outer perimeter of the cap. Relative displacements between the cap and wall inevitably generate frictional forces at the O-ring seal and hence, create some uncertainty in the

[1] Alternative methods of instrumenting the caisson walls are impractical for such a small model.
[2] In the first test CET1, the tapered edge was left in place.

relative force contributions of the cap and wall. However, this does not influence the total caisson force measurement (see section 4.3 for discussion). Efforts to reduce this source of friction include minimizing the O-ring squeeze and using a liberal amount of lubrication. In addition to the frictional problem, separating the wall and cap introduces an air gap of 0.07 cm between the tip of the wall and the cap at the soil surface. During all phases of the suction caisson test, there is no applied stress on the soil at the surface of this gap. Hence, soil must form an arch across this gap. Section 4.3 evaluates the uncertainty arising from O-ring friction and the effect of soil arching between the wall and cap.

3.1.3 Driving System

The third component of the CET cell is a three part mechanical driving system, which applies the total stress on the clay surface and drives the movements of the caisson wall and cap. Figure 3.7 highlights each of the three driving subsystems within the CET apparatus. Each of these three driving operations acts independently and is controlled automatically by the computer control system, described in section 3.1.4. This section describes the function and design of each of the driving subsystems in detail.

The first driving subsystem applies a vertical total stress on the surface of the clay outside the caisson by using air pressure in the chamber cavity (see Figure 3.8). The air pressure originates from the central geotechnical laboratory air compressor, which maintains a constant source of pressure between 11 and 13 ksc. This pressure is reduced and regulated by a Fairchild precision pressure regulator (Kendall Model 10). For this testing program, the air pressure is reduced to a level no greater than 1 ksc. This regulator is driven by a reduction gear system connected to a velocity-controlled direct current motor made by Electro-Craft Co. (Model E352). The motor has a power supply and feedback controller that operates the motor at a speed proportional to an analog command signal provided by the computer control system (see section 3.1.4).

Figures 3.9 and 3.10 show the subsystems that drive the caisson wall and cap and constitute the entire superstructure rising 1.5 m above the consolidation chamber (see Figure 3.7). To support the caisson wall and caisson cap driving subsystems, four stainless steel threaded rods (1.8 m long by 1.27 cm diameter) are secured with hex nuts to the bottom of the consolidation chamber and rise 1.5 m above the top of the chamber. Even though caisson movements during testing are restricted to less than the clay sample height (which ranges between 12 and 14 cm) the rather tall superstructure is required to allow coaxial placement of both the wall and cap drivers.

The caisson wall driving subsystem is shown separately in Figure 3.9. Analog command signals from the computer control system are sent to an electric motor, which drives a linear ball

screw actuator via a reduction gear box. The actuator, in turn, is attached to a multi-part drivetrain that is rigidly connected to the caisson wall. The electric motor is identical to the one used for the total stress driving subsystem discussed above (Electro-Craft Model E352). The 100:1 reduction gear box reduces the motor speed from a maximum of 7500 rpm to 50 rpm, while increasing the maximum torque from 0.5 to 16.1 kg-cm. To transfer rotational motion from the motor to linear movement necessary to drive the caisson vertically, the gear box is connected to a linear ball screw actuator made by Duff-Norton (Model M28630-8). The actuator rod is connected to the wall drivetrain comprising 1) the wall force transducer (see section 3.1.4), which is fastened to 2) a square plate that is connected by 3) four 1.27 cm diameter stainless steel rods[3] to 4) a circular drive plate, which is secured rigidly to the caisson wall by 5) a cylindrical connector that fits snugly inside the caisson wall. Four threaded hex head bolts, with washers that conform to the caisson wall exterior, fasten the connector to the wall.

Ancillary components to the caisson wall driving subsystem include the support plate and the acuator tension springs. The linear ball screw actuator housing is bolted to the upper support plate, which is secured by hex nuts to the four support rods extending from the consolidation chamber. The dual purpose of this support plate is to maintain the vertical position of the wall drivetrain and actuator and to react against the soil resistance encountered during testing.

The actuator tension spring setup is used solely to keep the actuator worm screw in tension throughout testing, and hence avoid problems associated with system compliance or lashback. Compliance is definitely a problem during the initial phase of pullout, when the travel direction of the worm screw reverses. Without a tension spring, there is a time lag in the load applied by the actuator such that unacceptable relative displacements can develop between the caisson cap and wall (see section 3.3.2). These problems are mitigated by including two springs, which are compressed between the support plate and a rectangular plate attached to the top of the worm screw actuator (see Figure 3.9). In this design, spring compression applies an upward force on the rectangular plate, which, in turn, applies a tension on the worm screw.

The driving system for the caisson cap is shown in Figure 3.10 and functions in the same way as the wall driver. Analog signals are sent from the computer control system to an electric motor, which, drives a (Duff-Norton) linear ball screw actuator via a reduction gear box. The cap drivetrain includes a force transducer and hollow extension rod. The force transducer is located between the worm screw and the extension rod and measures the cap force for computer control feedback and data acquisition. The extension rod is an aluminum tube that screws into the top of the caisson cap, thereby connecting the cap with the transducer. In order to make the connection, the rod must pass through the circular drivetrain plate and inside the caisson wall

[3]This drivetrain rod extension is necessary to accommodate the caisson cap actuator that is located concentric within the rods (see Figure 3.7).

itself (see Figure 3.9). The rod is hollow to allow access of electrical lines to the cap pore pressure transducer (see sections 3.1.2 and 3.1.5). The ball screw actuator housing is mounted on a support plate that is secured to the four threaded rods extending vertically from the chamber. This support plate maintains the cap drivetrain position, provides the necessary reaction force to the cap, and acts as a fixed reference surface for the displacement transducer that measures wall movements (see section 3.1.5). Finally, the cap actuator operates in tension throughout the test using a pair of pre-compressed springs similar to those used for the wall actuator.

3.1.4 Control System

Once the driving system superstructure and model caisson are assembled on top of the consolidation chamber, testing proceeds under automated control. The concept for control of the CET apparatus is based on previous technology that was used first to automate triaxial testing at MIT (Sheahan and Germaine, 1992). This section first explains briefly how the CET cell conforms with existing automation and outlines the feedback control loop, which is the essential component of the automation. This leads to a detailed discussion of the hardware and software components and how they work together to operate the control loop.

There are two philosophical goals behind laboratory automation: 1) flexibility, to allow the widest range of testing capability for a particular device; and 2) simplicity, to enable future modifications to the control system. To attain these goals, the control system (hardware and software) is necessarily modular in nature. Each of the driving systems in the CET apparatus (cell air pressure, caisson cap and wall actuators) is controlled separately, such that the device requires three independent axes of control. And each phase of the caisson element test is controlled by a separate algorithm, such that complex event sequences can be simulated for individual tests without overly sophisticated software. Another modular component consistent with laboratory automation is the instrumentation and data acquisition, which are discussed in section 3.1.5.

The essential ingredient for automation is the feedback control loop for the driving systems of the CET apparatus. The basis for the control loop is a simple proportional gain adjustment algorithm, a procedure wherein the command signal is generated by an analytical expression that compares a transducer signal to a target value. The command signal is specified by the difference between the target and actual values, divided by a gain factor. The gain factor is equal to a rate of change of the control variable to a unit input voltage over a unit of time. This gain factor is commonly referred to as the virtual stiffness of the variable. The vertical stress driving system is controlled by this feedback control loop in all phases of testing and is a good example to illustrate the algorithm. The air pressure transducer measures the chamber air

pressure (e.g., $P_a(m) = 0.74$ [ksc]) and sends the voltage signal to the computer, which then calculates the proper command signal. This signal is equal to the difference between the actual value and the target value (e.g., $P_a(tg) = 0.75$ [ksc]) divided by the air pressure gain factor (e.g., Gain = 0.05 [ksc/volt-sec]). The resulting command signal for one second of time is:

$$\text{Command Signal} = \frac{P_a(m) - P_a(tg)}{\text{Gain}} = \frac{(0.74\text{ksc} - 0.75\text{ksc})}{0.05\text{ksc/volt-sec}} \times \frac{1}{1\text{ sec}} = -0.2\text{volts}$$

Thus, a command signal of -0.20 volts is sent for one second to the motor that drives the air pressure in order to maintain a target air pressure of 0.75 ksc. After the motor stops, the loop repeats. During certain test phases, the other two driving subsystems (caisson wall and cap) are controlled by a feedback loop that uses proportional adjustment and an additional "integration" term to effect better control. These loops will be discussed below in the control system software section. Note that during all phases of testing, command signals are sent to the air pressure system at the rate of one second per control loop, while signals to the caisson wall and cap driving systems are continuous. That is, the caisson wall and cap motors operate continuously, but their command signals are updated during each control loop.

Both the hardware and software components of the control system cooperate in order to conduct the feedback control loop. The hardware includes the computer equipment, electronic signal converters, driver interfaces, and instrumentation. The software consists of the computer programs that generate the signals necessary to operate the driving systems.

3.1.4.1 Control System Hardware

The main function of the control system hardware is to convey electronic information along the digital feedback control loop that operates the three independent driving systems. Figure 3.11 shows a schematic drawing of the control system hardware components. Note that the computer and the electronic signal converters (analog to digital converter and digital to analog converter) are the only hardware components common to all three control axes.

The first hardware component is the primary transducer. For illustrative purposes, let us say the feedback control loop starts at the primary transducer for a particular driving system. This transducer measures a physical quantity that the computer software is attempting to control. For the CET air pressure system, the primary transducer is always the air pressure transducer, while the primary transducer for the wall and cap systems can be either the displacement or force transducer, depending on the phase of the test. Detailed information on the characteristics of these transducers is provided in section 3.1.5.

The output from the primary transducer is sent to an analog-to-digital (A/D) converter, which converts this continuous, variable analog signal into a digital form (number of bits) that the computer can understand. The A/D converter is the heart of a circuit board that is placed in

an expansion slot in the computer. The CET apparatus uses the multi-channel analog-to-digital converter device (MADC) developed by Sheahan (1990) at MIT for computer-automated triaxial testing. A low cost alternative to commercial A/D circuit boards, the MADC was designed specifically to allow a minimum 18 bit resolution (b.r.) during signal conversion from analog to digital. This means that voltage signals from the primary transducers can be converted with a precision of $\pm 3.8 \times 10^{-5}$ volts over a range of 10 volts (voltage resolution = 10 V/$2^{b.r.}$). The key element of the MADC is the Analog Devices AD1170 analog-to-digital converter, which performs the basic function of translating analog signals in volts to digital signals in bit counts.

An IBM-compatible personal computer (PC-AT with an Intel 80286 processor, an expansion slot for the MADC board, and a parallel printer port for the digital-to-analog board) houses the control system software that determines the new command signal to be sent to the driving system to control the test phase (control system software is discussed in this section below). A monochrome monitor is used with the computer to display values of the measured variables during testing and to allow the user to interface with the control software.

The command signal generated by the software then is converted back into an analog signal through a digital-to-analog (D/A) converter board that is located within the computer and is connected to the parallel printer port. The CET apparatus uses a commercial board (12 bit resolution with a 10 volt range) sold by Strawberry Tree Incorporated.

From the D/A card, the analog command signals are sent via an amplifier to the electric motor that drives one of the three independent systems. The driving subsystem then moves the CET cell components according to the command signal received, thus completing the feedback control loop. A new cycle begins once the MADC converts a new analog signal from the primary transducer.

3.1.4.2 Control System Software

The control software consists of three programs that are written in the BASIC programming language: 1) MASTER.BAS allows the user to operate the driving system motors manually and to evaluate the status of each of the primary transducers; 2) SETUP.BAS lets the user input test-specific variables that are passed on to the control program, which is 3) CETEST.BAS. This last program actually controls the test and consists of separate modules that perform the various phases that simulate the event history of a suction caisson including consolidation, suction driving, holding stress, and monotonic pullout. Each of these programs were derived from programs used to control the phases in triaxial testing. Figure 3.12 depicts the interaction among the three programs.

MASTER.BAS is a menu-driven program that allows the user to operate individually the air pressure and caisson wall and cap control motors. Any of the three motors can be operated in

a step-wise or continuous mode. Both the step increment and rotational speed can be varied. In addition, the transducer readings and input voltage can be displayed on the monitor.

SETUP.BAS is a program that generates the data input file of test parameters to be used by the control program CETEST.BAS. In an on-screen format, the user inputs caisson wall and cap dimensions and weights, transducer zero values, and calibration factors.

CETEST.BAS is the test control program and is composed of four separate control modules: CONS, HOLDSTS, SUCDRV, and MONPULL. CETEST.BAS begins by setting up the computer keyboard, analog-to-digital conversion card (MADC), and the three control motors and obtains an initial set of readings for all primary transducers. The user then starts a particular phase of the suction caisson test by choosing one of the four control modules from an on-screen menu. Each of the software modules incorporates a feedback control loop with at least proportional gain adjustment to control one or more of the three system variables: air pressure, cap force or displacement, and wall force or displacement.

CONS is the software module that starts each increment of consolidation on the CET clay specimen. The algorithm applies a user-specified schedule of incremental vertical loads on the clay surface while maintaining zero relative displacement between the caisson cap and wall. Figure 3.13 illustrates the control methodology for the CONS module. The user first decides the amount and time duration for each increment of load. The principal transducers are the chamber air pressure, caisson cap force, and wall displacement transducers (AP, L2, and D1, respectively in Table 3.1). At the start of a load increment, the air pressure and cap load are increased until reaching the target pressure P_a ($= \sigma'_{vc}$) and cap force F_c ($= \sigma'_{vc}A_c$), respectively. Then, the vertical stress across the entire clay surface is maintained for the specified time duration. To maintain constant stress and zero relative displacement, a feedback control loop is placed on the air pressure transducer, the cap force transducer, and the wall displacement transducer. Note that these control loops are identical to those for the HOLDSTS module with minimal wall penetration (< 1cm), as described below. At the end of the specified consolidation time, the loading continues with the next increment. At any time during the CONS module, the user can escape to the menu screen or switch directly to the HOLDSTS option (see Figure 3.12). If the user does not intervene, the computer automatically enters the HOLDSTS module following the end of the last increment.

HOLDSTS is a module that allows simulation of caisson set-up after installation by underbase suction or caisson set-up during sustained tensile axial loading (See Figure 3.14). This algorithm maintains a constant vertical stress over the clay surface (outside the caisson) and a constant total force on the caisson ($F_{TOT} = F_c+F_w$) with zero relative displacement between the cap and wall. Since the total force is kept constant and the wall and cap are "locked" together, the caisson is allowed to deform as a unit while the stresses redistribute following suction driving

or application of tension forces. The constant vertical stress (σ_v) outside the caisson is achieved through feedback control on the air pressure transducer using a simple proportional algorithm. Control signals are sent in 1 second bursts for each control loop. The target value σ_v is obtained through user-input either from the last increment in CONS or the original menu of test phases.

The total force on the caisson is kept constant by feedback control on either the caisson cap or caisson wall, depending on the relative stiffness of the system. If there is minimal wall penetration into the clay (< 1cm), then the primary transducer is the cap force L2 (see Table 3.1), as the cap has a stiffer response than the wall. If the wall has penetrated more than 1 cm, then feedback control is based on the wall force L1, as the wall has a stiffer response than the cap. The target caisson force, F_{TOT}, is specified either through user input (if HOLDSTS was accessed directly from the test menu) or from the last transducer readings from the preceding control module. During each round of the feedback control loop, the actual cap force and wall force values are measured and summed to give the actual total force, F_{TOT}. Then the difference between the actual F_{TOT} and the target F_{TOT} is computed to give an error value, $errF_{TOT}$. This value is then multiplied by a gain factor (a) and added to the command voltage (V_i) that was sent on the previous loop to give the HOLDSTS integration term (HS_{intg}) as follows:

$$HS_{intg} = V_i + a(errF_{TOT})$$

Adding this integration term to a proportional term yields the command signal as follows:

$$V_{i+1} = HS_{intg} + b(errF_{TOT})$$

where b is a gain factor. Thus the feedback control loop for the total caisson force, F_{TOT}, is proportional with an integration term. This term is necessary because the virtual stiffness of both the wall and cap changes throughout the test depending on how deep the wall has penetrated the soil, and such changes must be incorporated into the control loop. The gain factors a and b are obtained through trial and error, as described in section 4.1.

The last control loop in HOLDSTS maintains zero relative displacement between the cap and wall by simple proportional feedback control on the displacement transducer (either D1 or D2) of the caisson component not currently under force control. From the HOLDSTS module, the user can proceed directly to SUCDRV, MONPULL, or the test menu.

SUCDRV maintains σ_v on the clay surface outside the caisson and drives the caisson wall into the clay sample at a constant rate of displacement. The algorithm models installation by underbase suction by applying increments of load to the cap that are equal and opposite to the wall force caused by driving. Figure 3.15 illustrates the control features of SUCDRV. After obtaining the user-specified drive rate and final penetration depth, the computer sends a continuous signal to the caisson wall motor, which drives the wall at a constant rate until reaching the final depth. The total force on the caisson F_{TOT} is maintained constant from the start of driving. As the wall penetrates the soil, the computer uses a simple proportional

feedback loop on F_{TOT}, with continuous adjustment of cap force, F_c. The difference between the actual and target values of F_{TOT} is calculated to give an error value, $errF_{TOT}$. Then, $-errF_{TOT}$ is added to the cap force. Due to the large increase in wall force that occurs at the start of driving, the algorithm simultaneously sends an initial control signal (to reduce load on the cap) and a signal to drive the wall. At any : nt during the driving phase, the user can switch to HOLDSTS or return to the test menu. If the user does not intervene, the computer will drive the wall to the prescribed depth and then automatically switch to HOLDSTS, which maintains the prescribed σ_v (from CONS or the menu) and F_{TOT} (from the last reading in SUCDRV).

In MONPULL, the computer keeps σ_v constant and pulls the caisson wall and cap together at a constant rate (see Figure 3.16). The computer sends a continuous command signal to withdraw the wall at a constant rate until the caisson reaches a specified displacement or total force. As in all the modules, simple proportional feedback control is performed on the air pressure regulator to maintain a constant σ_v on the clay outside the caisson. For zero relative displacement between the wall and cap, feedback control is performed by incorporating a proportional term for the cap displacement rate and both proportional and integral terms for the relative displacement. The relative displacement integral term (RD_{intg}) is first calculated by multiplying the relative displacement error (errD) by a gain factor (a) and adding the resultant to the prior control loop command signal (V_i) as follows:

$$RD_{intg} = V_i + a(errD)$$

The cap command signal then is generated by adding the integration term to two proportional terms. The first proportional term is the relative displacement error (errD) multiplied by a gain factor (b); the second proportional term is the cap velocity error (errCapv) multiplied by a gain factor (c). ErrCapv is the difference between the prescribed wall velocity and the measured cap velocity, which, in turn, is computed by dividing the measured cap displacement by the elapsed time during one control loop. The cap command signal equation is:

$$V_{i+1} = RD_{intg} + b(errD) + c(errCapv)$$

At the start of pullout, the algorithm simultaneously sends a control signal to pull the wall and a separate signal to pull the cap. Thereafter, the feedback control loop maintains zero relative displacement. As in SUCDRV, the user can switch to HOLDSTS or the test menu. Barring user interaction, the computer automatically proceeds to HOLDSTS once the target displacement or total force is reached.

3.1.5 Instrumentation

The fifth and final component of the CET apparatus is the instrumentation package, which is consistent with the automated laboratory testing concept. The measurements are made by a variety of transducers all connected the Central Data Acquisition System in the MIT

Geotechnical Laboratory. The transducers serve a dual purpose. Five of the instruments (chamber air pressure, caisson wall force and displacement, and caisson cap force and displacement - AP, L1, D1, L2, D2, respectively) serve as primary transducers because they provide voltage signals for the feedback control loops (see section 3.1.4), while the remaining instrumentation is used to monitor parameters of interest that affect the performance of the caisson and clay during a caisson element test. This section describes the physical characteristics, function, and location of the instrumentation used in a typical CET experiment. Chapter 4 evaluates the quality of the measurements obtained in the CET test program.

Each of the transducers is connected to the Central Data Acquisition System, which consists of an IBM compatible PC interfaced with an expanded channel Hewlett-Packard HP3497A data acquisition unit. The system is driven by software called EASYDAT. It is capable of monitoring 120 channels throughout the geotechnical laboratory. One advantage of the Central System is that it simplifies the programming requirements of the CET control software. Since the system is task driven and each task can monitor up to 20 channels at user-specified times greater than one second, test measurements can be tailored to each particular task without altering the program or interfering with the CET control. Another advantage is the high degree of measurement precision. The Central System uses a very high integrating analog-to-digital converter with autoranging capability to produce a precision of one microvolt with a range of 1000 volts.

Typical CET tests require less than 20 channels to monitor instrumentation and power input voltage. A 14 transducer instrumentation package used for test CET-10 is illustrated in Figures 3.17 and 3.18. Table 3.1 lists the CET-10 devices, their location, and their capacity and precision when connected to the Central Data Acquisition System.

Figure 3.17 shows the locations of the five primary transducers, which consist of a pressure transducer to measure chamber air pressure (AP), two force transducers to measure caisson wall and cap force (L1, L2), and two LVDTs for wall and cap displacements (D1, D2). As discussed in section 3.1.4, one purpose of these five transducers is to supply input voltages for the feedback control loops. The other purpose, of course, is to provide data for test interpretation. The wall displacement (D1) is measured relative to the fixed support for the cap driving system (see Figure 3.17) and this provides an absolute displacement of the wall relative to the test chamber. The displacement of the cap is measured relative to the wall, as differential displacements are of primary concern, and subtracting two absolute measurements would introduce precision error. As discussed in section 3.1.4, the control software maintains a specific relative displacement of zero in the CONS, HOLDSTS, and MONPULL modules.

Displacements of the clay surface are measured by direct current Linear Voltage Displacement Transducers (LVDT) located within the pressure chamber (S1 - S5 as shown in

Table 3.1, Figure 3.18). Each of these transducers is mounted on a cross arm radiating from a circular frame that is secured to the inside of the chamber wall by four screws, as shown in Figure 3.19. Two of the cross arms have mounting holes located at a radius of 5.2 cm from the chamber center. The remaining cross arms have mounting holes at radii r = 7.7, 9.8, 12.1 cm. In order to obtain displacement data close to the caisson wall, one of the LVDTs mounted at a radius of 5.2 cm has a core with an elbow extension to measure displacement at a radius of 4.2 cm (labeled S1 in Figure 3.19). The moving core of each transducer rests directly on the rubber membrane covering the clay surface.

Pore pressures beneath the caisson cap are measured by a 1.75 ksc capacity Data Instruments pressure transducer (CP, Table 3.1) mounted directly behind a 0.93 cm thick ceramic porous stone with a 1 ksc air entry pressure. As shown in Figure 3.6, the stone is set flush with the cap bottom surface and has a diameter of 2.2 cm. The stone surface area represents 22% of the total cap area. The pressure transducer is secured to the inside of the cap by a threaded brass fitting and O-ring that seals the transducer face approximately 0.01 cm from the back of the stone. Note that the threaded cap hole also provides a rigid connection for the cap drivetrain extension rod. This rod is hollow to provide a conduit for the pressure transducer wiring.

Pore pressures within the soil mass are measured using stainless steel hypodermic needle probes, which were developed iteratively during the course of this research in order to achieve rapid response and reliable measurements. A full description of the probe analysis is provided in Chapter 4. Figure 3.20 shows a cross sectional drawing of the latest generation CET pore pressure probe, which consists of a Kulite pressure transducer, a transducer block, and a stainless steel tube. The tube has an inside diameter of 0.023 cm and has a 0.2 cm long, 20 micron porous stone press-fitted to the tip. The tube is soldered to a stainless steel transducer block to form one monolithic unit. A threaded coupling connects the pressure transducer to the transducer block, and an O-ring on the pressure transducer seals the void space between the porous stone and the transducer. The transducer block is designed to minimize the clearance (0.013 cm) between the transducer face and the block. The probes are inserted into the clay through holes in the chamber baseplate and porous stone. The baseplate has nine ports for pore pressure probes, as shown in Figure 3.21. The probes are held in place by a threaded brass connector that screws into the baseplate and laterally compresses an O-ring surrounding the probe tube. For a typical CET experiment, pore pressures are typically measured at r = 0.0, 1.78 cm inside the caisson wall and at r = 3.18 cm outside the wall[4].

Total lateral stress and pore pressure on the side of the clay sample can be measured by pressure transducers that are secured to the chamber sidewalls. Figure 3.22 shows the

[4]Note that the caisson wall has an outside radius of 2.54 cm.

consolidation chamber sidewall with entry ports for total stress and pore pressure measurement. The chamber has 8 entry ports at different heights along the sidewall. Stresses are measured by a Kulite transducer that threads into a brass connector. This connector screws into the sidewall and seals against the wall with an O-ring. The connector is designed so that, for total stress measurement, the center of the transducer face is flush with the inside of the chamber wall. Due to the curvature of the chamber wall, part of the transducer face protrudes into the chamber space, which may introduce some errors in the measurements. For the pore pressure measurement, the connector is designed with a 0.93 cm thick ceramic porous stone affixed to the end. The total stresses have been measured in 3 tests (CET-1, 2, 6) and no sidewall pore pressure data have been obtained in the current program.

During the course of testing over two years, different model transducers were used to measure force, displacement, and pore pressure. A complete breakdown of the instruments used for each test are given in Table A1 of Appendix A. The locations of the transducers for each test are illustrated in Figures A1 through A14 of Appendix A.

3.2 RESEDIMENTED BOSTON BLUE CLAY

Resedimented Boston Blue Clay (RBBC) is the standard test material used for the experimental program for the following reasons: 1) procedures for manufacturing uniform samples of resedimented BBC are well-established (Germaine, 1982); 2) the engineering properties of RBBC are well-established from previous laboratory tests; 3) there has been extensive analytical research to model the properties of RBBC (e.g., Whittle 1987); and 4) the engineering behavior of RBBC is typical of natural, uncemented clay deposits with similar index properties.

3.2.1 Origin and Processing

Natural Boston Blue Clay (BBC) was deposited in the Boston basin about 12,000 to 14,000 years ago following the Wisconsin glacial period (Kenney 1964). The source material for the current CET test program was obtained in 1992 from the base of an excavation for MIT's Biology Building (Building #68). Approximately 2500 kg of soil was obtained at a depth of about 12 meters, with an overconsolidation ratio ranging from 1.3 to 4.3 (Berman, 1993). The material was softened with tap water and mixed into a thick slurry. Then, the slurry was passed through a #10 US standard sieve to remove all non-natural material, gravel, coarse sand, and large shell fragments. The slurry was oven-dried at 60°C in preparation for grinding. The dried material, which consisted of pieces ranging in size from 1 to 15 cm across, was ground to 95% passing a #100 US sieve by the Sturtevant Company using a roller mill. Finally, the material was manually randomized by two blending operations. The dry powder, now known as Series

IV Boston Blue Clay, is stored in sealed 40 gallon containers[5].

3.2.2 Index Properties

The properties of natural BBC vary widely over the Metropolitan Boston Area even though the basic mineralogy of the clay is the same. Therefore, each time new material is obtained for resedimentation, it is necessary to perform several index and engineering tests to verify that the soil is sufficiently similar to the prior material. Resedimentation of BBC at MIT has produced close to 70 recorded batches of testing material. This has produced an extensive database of material index and engineering properties. Table B.1 in Appendix B lists specific gravity, Atterberg limits, clay fraction, and salt concentration values for RBBC used in research since 1961. To make use of this database and to ensure that the clay was uniform from sample to sample, numerous index and engineering tests were conducted on all samples used for the CET testing program. Table 3.2 lists the index data for the Series IV BBC powder, 2 RBBC batches used for the research of Sinfield (1994), and 14 batches used in this research. This section discusses the uniformity and repeatability of index properties for the RBBC used in the CET test program and compares these properties with results from previous testing programs.

Figure 3.23 shows the grain size distribution for Series IV BBC powder and resedimented BBC (RBBC). The tests on RBBC batches 406-409, 411 were performed on material after the addition of salts and phenol and additional batching operations (see section 3.3 for batching procedure). The distributions show that the soil has a fine fraction (% passing the #200 sieve) greater than 98%. The average clay fraction (% less than 2μm) is 58±1.2%. The fine fraction and clay fraction is slightly higher than the respective data from Series III BBC[6].

Data from Atterberg limit tests on Series IV BBC reveal batch to batch consistency. Figure 3.24a depicts the plastic and liquid limits for BBC powder and batches RBBC 401-411, 413-417. The average plastic limit is w_p = 23.5±1.1%, the average liquid limit is w_L = 46.1± 0.9%, and the average plasticity index is I_p = 22.7±1.2% (see Table 3.2). These data are plotted in a plasticity chart in Figure 3.24b, which confirms that the material is a low plasticity (CL) clay.

Measurements of specific gravity for Series IV RBBC yielded an average value of G_s = 2.81, which is higher than previous research[7], but is within the expected range of illitic clays (G_s = 2.60 to 2.84 for illite, Lambe and Whitman 1968).

Salt content was measured by conductivity and calibrated against a KCL standard. For

---

[5]Previous tests from 1988-1994 used Series III BBC, which was obtained by augering from a depth of 23 meters during construction of a parking garage near Kendall Square in Cambridge, Massachusetts.

[6]Data from Series III BBC (see Figure B.1, Appendix B) indicate a fine fraction of 90-95% and a clay fraction of 46-56%.

[7]Specific gravity for Series I-III BBC ranges from G_s = 2.75 to 2.785 (see Table B.1, Appendix B)

previous research, the salt content varied from 2 to 35 g/l (see Table B.1, Appendix B). For Series IV RBBC, the average salt content was 11.6±1.5 g/l. As described in the batching procedure in section 3.3, salt is added to the powder to make the clay samples.

Organic content by combustion yielded a value of 4.4% for Series IV RBBC. These data are not available for Series I through III material.

3.2.3 Engineering Properties

This section presents a compact summary of the most important engineering properties of normally consolidated resedimented Boston Blue Clay. Compression, consolidation, and flow characteristics are derived from consolidometer tests on BBC Series IV (RBBC 401, 404-411, 413-417). Undrained stress-strain-strength behavior is culled from tests on BBC Series III and include triaxial compression and extension tests (Sheahan, 1991) and direct simple shear tests (Ortega, 1992).

3.2.3.1 Compression, Consolidation, and Flow Properties

Figure 3.25 summarizes the compression, consolidation, and flow properties resulting from the consolidometer tests for the CET test program[8]. As described in the following section 3.3, the consolidometer test in the CET program is the stage wherein the RBBC is consolidated using a rigid cap. In all tests the slurry was loaded incrementally with a load increment ratio of LIR = 1 to a maximum stress of $\sigma'_v = 0.5$ ksc. In four tests (RBBC 401, 404 - 406), the clay was unloaded in two increments to a stress of $\sigma'_v = 0.125$ ksc.

Figure 3.25 shows compression curves (void ratio vs. consolidation stress) for all presentable consolidometer data and tabulates the compression index C_c, coefficient of volume change m_v, vertical hydraulic conductivity k_v, and vertical coefficient of consolidation c_v. Aside from some variation in the void ratio at a particular consolidation stress[9], the consistency of the slope of the compression lines from batch to batch is unmistakable. There is very little scatter in the compression indices; in the stress range from $0.125 < \sigma'_v < 0.25$ ksc the compression index was $C_c = 0.588 \pm 0.046$, while for $0.25 < \sigma'_v < 0.5$ ksc the index was lower at $C_c = 0.525 \pm 0.033$. These values are slightly higher than data ($C_c = 0.557 \pm 0.068$, 0.479 ± 0.064) for the same two respective stress intervals from 6 consolidometer tests on Series III BBC (Seah, 1989). The swelling index, calculated for two stress intervals, $0.125 < \sigma'_v < 0.25$ ksc and $0.25 < \sigma'_v < 0.5$ ksc, averaged $C_s = 0.022$ and 0.010, respectively.[10]

---

[8]Appendix B contains tabulated data for each individual consolidometer test and the calculation method for the consolidation parameters.

[9]Variation in the void ratio is due to uncertainty in the phase relations calculations. See Appendix B.

[10]Although four tests (RBBC401-402, 405-406) incorporated swelling increments, only two (401 and 405) yielded presentable swell data. See Appendix B.

The vertical coefficient of consolidation (c_v) for 5 stress levels from σ'_v = 0.03125 to 0.5 ksc is tabulated in Figure 3.25. At the lowest stress level of σ'_v = 0.03125 ksc, the average value is $c_v = 3.2 \times 10^{-4}$ cm^2/sec. This rises to $c_v = 10.59 \times 10^{-4}$ cm^2/sec at the maximum stress of σ'_v = 0.5 ksc. Both the magnitude of c_v and the trend with stress level is consistent with previous consolidometer tests on Series III BBC (Seah, 1989).

The vertical hydraulic conductivity *decreases* with increasing consolidation stress, as the data in Figure 3.25 suggest. From σ'_v = 0.0625 to 0.125 ksc, the computed hydraulic conductivity averaged $k_v = 47.4 \times 10^{-8}$ cm/sec. This decreased to $k_v = 41.6 \times 10^{-8}$ cm/sec for the stress interval from σ'_v = 0.125 to 0.25 ksc and dropped further to $k_v = 23.7 \times 10^{-8}$ cm/sec for the range from σ'_v = 0.25 to 0.5 ksc. Once again, this behavior is consistent with prior consolidometer testing (Seah, 1989).

3.2.3.2 Undrained Triaxial Compression

Typical behavior for normally consolidated resedimented BBC during undrained triaxial compression is derived from two tests (CTX-11,13) conducted by Sheahan (1991). The test specimens were trimmed from Series III RBBC, K_O-consolidated to a stress of σ'_{vc} = 2.8 ksc, and sheared in triaxial compression at the standard rate of ε_a/t = 0.5%/hr. The average lateral earth pressure coefficient ($K_0 = \sigma'_h/\sigma'_v$) during consolidation beyond a vertical stress of σ'_v = 0.6 ksc was K_0 = 0.47. The undrained shear strength ratio of the normally consolidated RBBC in compression averaged s_{uTC}/σ'_{vc} = 0.32, which was mobilized at an average axial strain of ε_a = 0.15%. The friction angle at peak shear stress and maximum obliquity averaged ϕ'_p = 25.0° and ϕ'_{mo} = 33.4°, respectively. Gradual post-peak strain softening was evident, as the mobilized shear resistance at ε_a = 10% strain was $q_{10\%}/\sigma'_{vc}$ = 0.25, which is nearly 80% of the peak strength (q_{10}/s_{uTC} = 0.78). Measurement of the shear stiffness at very small strains ($\varepsilon_a < 0.01\%$) was hampered by the lack of on-the-specimen strain measurement equipment. The average normalized secant shear modulus measured at ε_a = 0.01% strain was G_{sec}/σ'_{vc} = 457.

Sheahan (1991) also conducted two standard undrained triaxial extension tests (CTX-9,50), wherein the specimen was K_0-consolidated to an average stress of σ'_{vc} = 2.8 ksc and sheared at the standard rate of ε_a/t = 0.5%/hr. As for the compression test, the lateral earth pressure coefficient during consolidation beyond σ'_v = 0.6 ksc was K_0 = 0.47. An average peak normalized strength of s_{uTE}/σ'_{vc} = 0.13 (60% lower than in compression) was reached at an average strain of ε_a = 12.22% (much higher than in compression) and at a friction angle of ϕ'_p = 35.0°. The friction angle at maximum obliquity was ϕ'_{mo} = 35.3°. At an axial strain of ε_a = 0.01%, the normalized secant shear modulus was G_{sec}/σ'_{vc} = 551, which is about 20% higher than in compression.

3.2.3.3 Direct Simple Shear

Three K_O-normally consolidated undrained direct simple shear tests (DSS-222, 228, 233) were performed on Series III RBBC by Ortega (1992). The DSS specimens were consolidated to a stress of σ'_{VC} = 8.0 ksc prior to shearing at an average rate of γ/t = 3.8%/hr. The measured undrained shear strength, s_{uDSS}/σ'_{vc} = 0.20±0.01 ($s_{uDSS} = \tau_{max}$), was mobilized at an average strain of γ = 5.53±0.65 %. Note that the peak normalized strength in DSS is only 62.5% of the strength measured in triaxial compression (s_{uDSS}/s_{uTC} = 0.625), but is 54% higher than the strength found in triaxial extension (s_{uDSS}/s_{uTE} = 1.54). At peak shear stress in the DSS tests, the angle of shear stress obliquity averaged ψ = 20.1±1.2° [$\psi = \tan^{-1}(\tau/\sigma'_v)$]. At large strains ($\gamma \approx$ 25%), the normalized shear stress had dropped to an average of τ/σ'_{VC} = 0.12±0.02, which is 60% of the peak. Measurement of initial shear stiffness is precluded by large system compliance.

3.3 CAISSON TESTING PROCEDURE

The caisson element test procedure comprises the following four separate stages: 1) BBC resedimentation, 2) RBBC consolidation using the rigid top cap, 3) RBBC consolidation in the CET apparatus, and 3) model caisson test event sequences. The test sequence for a model caisson typically includes installation by underbase suction, equilibration (set-up), axial pullout and/or sustained loading. The resedimentation stage takes approximately 16 hours, while RBBC consolidation (stages 2 and 3) requires a minimum of about 6 days. The model caisson testing stage (4) lasts at least one day. Therefore, the total time for one caisson element test from resedimentation to model testing requires at least 8 days. The following describes each of the caisson element test stages in detail.

3.3.1 BBC Resedimentation

The BBC powder is resedimented using the equipment shown in Figure 3.26 (Germaine, 1982). Fifteen kilograms of oven-dried powder is added under vacuum to 15 kg of deaired, distilled, and deionized water to create a soil slurry. Then, about 100 gm of sodium chloride (a flocculant) and 2 ml of phenol (a bacterial growth inhibitor) are added to the slurry. At an initial water content of nearly 100%, these components are combined with mixing blades rotating at approximately 60 rpm in the upper chamber, which is isolated from the lower chamber. After all the components are added, the slurry is mixed at approximately 120 rpm for 30 minutes. Then, the valve between the two chambers is opened, and the slurry is sprayed through the lower free-fall chamber and into the consolidometer. The entire resedimentation process, from equipment set-up to application of the first consolidation load, takes about 16 hours.

3.3.2 RBBC Consolidation Using Rigid Cap

The slurry is consolidated to a maximum vertical stress of σ_v = 0.5 ksc using a rigid piston top cap and incremental loads[11]. After removal of the free fall chamber, the slurry is loaded incrementally in the 30 cm diameter consolidation chamber from 0.03125 ksc to 0.5 ksc at a load increment ratio (LIR) of one. Thus, the loading schedule requires five increments. To allow full primary consolidation and some secondary consolidation, each increment must be applied for about 48 hours. Therefore, the time required to consolidate the clay with the rigid top cap is approximately 10 days. This time can be reduced by allowing little or no secondary consolidation during each increment. In this case the increment duration is between 9 and 20 hours, depending upon the load level, and the rigid top consolidation time is reduced to two days. Throughout this consolidation phase, vertical deformation is measured by a single LVDT located on top of the rigid piston top cap. After the final increment under the rigid top cap, the clay element and chamber are ready to be positioned beneath the CET superstructure.

3.3.3 RBBC Consolidation in CET Apparatus

After consolidating the sample to 0.5 ksc, the rigid top cap is removed and the CET apparatus is connected to the consolidation chamber. The rigid top cap and one layer of filter paper are removed from the clay surface to reveal the second filter paper, which has a center hole for caisson access. A cloth filter with a center access hole then is placed over the paper filter (see Figure 3.4). The rubber membrane and attached (inner and outer) diameter slip rings, are lowered to the surface of the filter paper. The membrane was previously sealed to the rings with RTV, a silicone rubber adhesive sealant. At this point, the soil is completely covered with the exception of the caisson center access hole. Next, the clay surface displacement LVDT bracket is screwed into the chamber inside wall above the soil surface and the LVDTs are fixed in place. The LVDT wiring and top surface drainage tubing are attached to ports in the cover plate, which is lowered over the inside diameter slip ring and bolted to the chamber top. The superstructure, which is composed of the caisson driving system supported by four 1.8 m long by 1.3 cm diameter threaded rods, is lowered through non-threaded holes in the cover plate, chamber top, chamber bottom, and baseplate. The superstructure and chamber are secured together by hex nuts at the top of the cover plate and bottom of the baseplate. The entire CET cell is leveled using the extension feet in the baseplate. Prior to lowering the caisson to the soil, wall force, cap force, and chamber air pressure zeroes are recorded on the Central Data Acquisition System. By manually operating the caisson wall and cap actuator motor controllers, the cap and wall are brought to the soil surface. At this time, pore pressure probes are inserted through the baseplate

[11]The consolidation of the RBBC slurry using a rigid cap is more commonly referred to as a consolidometer test in previous research (Seah 1989, O'Neill 1985).

and bottom porous stone to a desired depth in the clay and secured to the baseplate with brass connectors.

The probes and the caisson cap porous stone are saturated prior to test set-up using a four step process. After oven drying the cap and probes at 35°C to remove residual moisture, the instruments are evacuated under high vacuum (~10mTorr) for at least one day. They then are flooded with distilled, deaired, deionized water and placed in an ultrasonic vibrating bath for one hour to remove any residual air bubbles. This process has proven to be an effective saturation technique, as described in section 4.2.

After specifying the calibration factors, zero readings, caisson weights, and dimensions as inputs for the program SETUP.BAS, reconsolidation can proceed via computer control of the chamber air pressure and caisson cap and wall actuators. The program CETEST.BAS automatically controls consolidation in the CET apparatus (section 3.1.4) according to a prescribed load increment schedule chosen by the test operator. The current test procedure applies an initial load of 0.0625 ksc, and then reconsolidates the sample in five increments, each with a load increment ratio of LIR = 1, into virgin compression range (i.e., $\sigma'_v \geq 0.50$ ksc). At this point, the clay can be consolidated further into the virgin range and tested as a normally consolidated sample, or unloaded and tested as an overconsolidated sample. The CET test program described in this thesis uses samples that are normally consolidated to 0.75 ksc using an LIR = 0.1 (from σ'_v = 0.5-0.75 ksc) to minimize soil extrusion. The maximum load increment is maintained for at least 24 hours prior to the CET event sequence to simulate aging of natural Boston Blue Clay.

3.3.4 Model Caisson Test Events

Once the clay element has been reconsolidated according to the specified stress history, the caisson test event sequence can proceed with caisson penetration, set-up, and axial loading. The test events are initiated by sending control commands to the CETEST.BAS program. Each phase of the event sequence is fully automated, as described in section 3.1.4. At any time during a particular phase, the test operator can interact with the computer, stop the phase, and either proceed to a different phase or end the test. This flexibility allows the operator to custom-design any test sequence.

The simplest event sequence that involves all phases of a suction caisson element test is a suction driving/set-up/pullout test (standard procedure used in tests CET- 1 through CET- 8). In the first phase, the operator selects the suction driving module SUCDRV. Wall penetration rate and target penetration depth comprise the input control for this routine. This program simulates installation by underbase suction by removing load from the caisson cap to balance the force required to penetrate the wall at a constant rate of displacement (to the prescribed depth).

Once the caisson walls reach the required depth, the computer automatically switches to the HOLDSTS module, which maintains a constant total load on the caisson while keeping zero relative displacement between the cap and wall. Zero relative cap/wall displacement allows the caisson to displace freely as a monolithic unit. After monitoring the pore pressures within the clay to ensure complete dissipation, the test operator exits HOLDSTS and selects the monotonic pullout module, MONPULL, from the test menu. Input parameters for this module include the wall displacement (withdrawal) rate and target displacement. Once activated, MONPULL performs the axial pullout test. When the caisson has met the displacement target, the computer transfers control to HOLDSTS to maintain constant total force and zero relative cap/wall displacement. The operator then ends the test by exiting HOLDSTS. Once all test phases are finished, the CET cell superstructure, chamber cover plate, and rubber membrane are removed. At this point the clay surface is examined to note the general surface topography and the existence of any unusual features (such as cracks). Then, the soil plug from within the caisson is removed immediately for water content determination. The clay cake is divided into four layers of equal thickness along the height, and soil (~200 g) from each layer is removed for water content determination. Following this, the rest of the chamber is dismantled, and the remaining clay is stored in sealed plastic containers for index testing (Atterberg limits, grain size, specific gravity).

The caisson testing sequence of the caisson element test just described requires less than one day. More elaborate sequences including sustained tensile loading have been performed in the current test program (CET- 9-14).

ID #	Device	Measurement	Radial Location from Centerline (cm)	Capacity	Precision	Comments
L1	DI Load Cell	Caisson Wall Force	0.0	90.7 kg	0.06 kg	Primary Transducer
L2	DI Load Cell	Caisson Cap Force	0.0	90.7 kg	0.06 kg	" "
D1	TT LVDT	Caisson Wall Displ.	0.0	15.2 cm	0.002 cm	" "
D2	TT LVDT	Caisson Cap Displ.	0.0	15.2 cm	0.002 cm	" "
AP	Tyco Pressure Trans.	Chamber Air Press.	(cover plate)	1.76 ksc	0.0002 ksc	" "
CP	DI Pressure Trans.	Cap Pore Press.	0.0	1.76 ksc	0.0002 ksc	Monitor Transducer
P1	Cooper Pressure Trans.	Clay Pore Pressure	0.0	14.1 ksc	0.01 ksc	" "
P2	Kulite Pressure Trans.	" " "	1.8	1.76 ksc	0.0002 ksc	" "
P3	Kulite Pressure Trans.	" " "	3.2	14.1 ksc	0.02 ksc	" "
S1	HP LVDT	Clay Surface Displ.	4.2	1.9 cm	0.0004 cm	" "
S2	HP LVDT	" " "	5.2	1.9 cm	0.0004 cm	" "
S3	TT LVDT	" " "	7.7	2.3 cm	0.0004 cm	" "
S4	HP LVDT	" " "	9.8	1.9 cm	0.0004 cm	" "
S5	HP LVDT	" " "	12.1	1.9 cm	0.0004 cm	" "

Notes: Precision based on central data acquisition system with allowance for 3 bits of signal noise.
DI = Data Instruments
TT = Trans-Tek
LVDT = Linear Voltage Displacement Transducer
HP = Hewlett-Packard

Table 3.1 Characteristics of Instrumentation used for a Typical Caisson Element Test (CET10)

Year	Researcher	Source Batch	G_s	w_l	w_p	I_p	Clay Frac. <2μm (%)	Organic Content	Salt (g/l)
1994	Zriek	powder	2.78	46.4	22.5	23.9	60.1	4.4 %	
1994	Sinfield	402		46.8	22.4	24.4			
		403		47.2	23.3	23.9			
	this research	powder	2.81						
		401		46.7	21.8	24.9			
		404		47.4	21.9	25.5			10.4
		405		45.2	22.1	23.1			10.0
		406		45.0	22.6	22.4	57.6		12.5
		407		44.6	23.0	21.6	57.8		13.1
		408		44.7	23.9	20.8	58.7		10.1
		409		45.4	24.0	21.4	56.8		13.0
		410		46.6	25.0	21.6			13.4
		411		46.7	24.5	22.2	56.9		10.2
		413		45.5	24.3	21.2			9.7
		414		46.3	24.3	22.0			12.0
		415		46.1	24.7	21.4			10.5
		416		46.7	24.0	22.7			12.9
		417		47.2	24.5	22.7			13.2
		average		46.0 ±0.9	23.6 ±1.1	22.4 ±1.4	57.6 ±0.8		11.6 ±1.5
	average	powder, 401-411, 413-417	2.81	46.1 ±0.9	23.5 ±1.1	22.7 ±1.4	58.0 ±1.2		11.6 ±1.5

Table 3.2 Index Properties of Resedimented Boston Blue Clay Batches and Powder from Series IV Boston Blue Clay

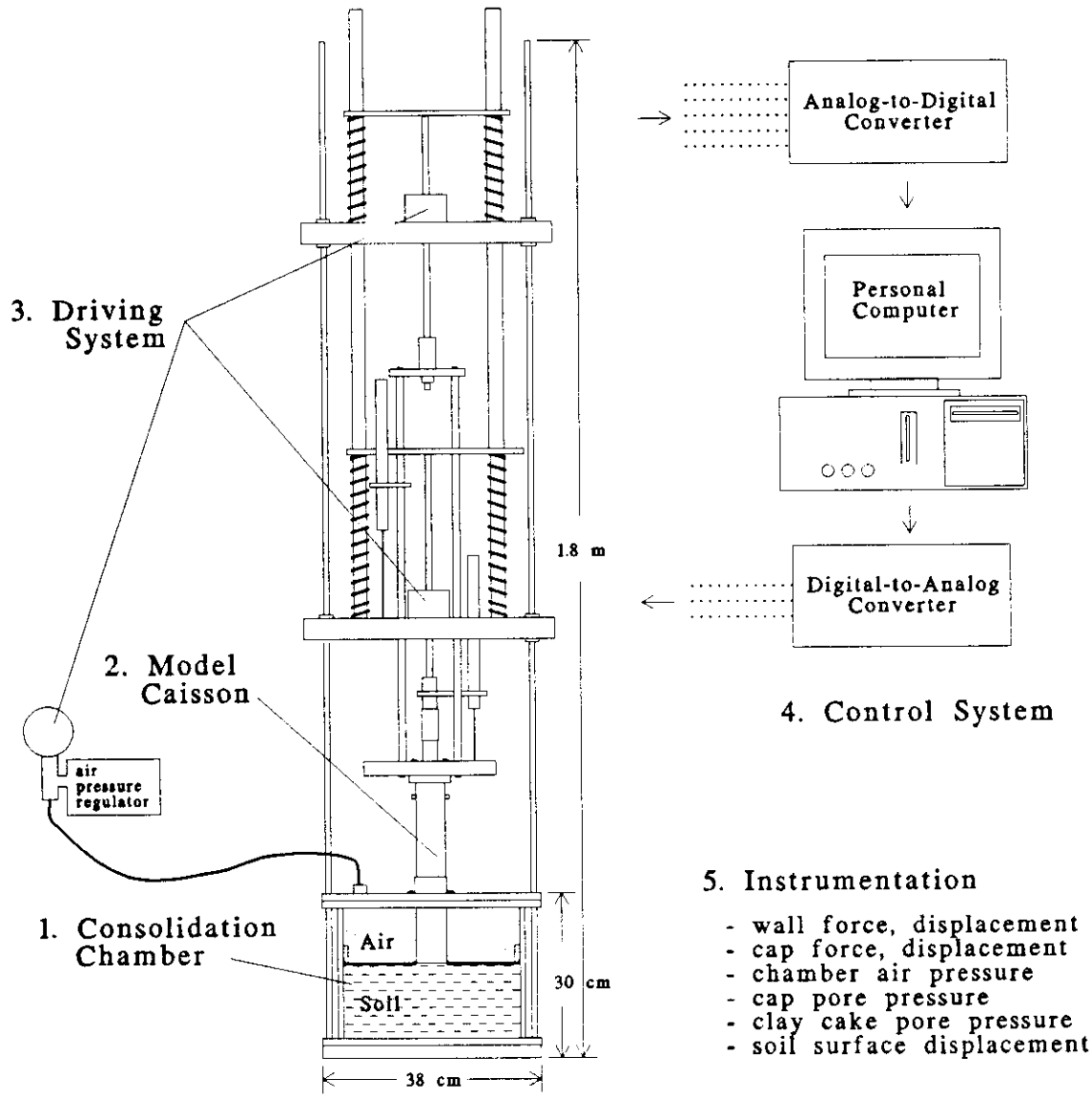

Figure 3.1 Schematic Diagram of the Caisson Element Test Cell Illustrating the Five Main Components

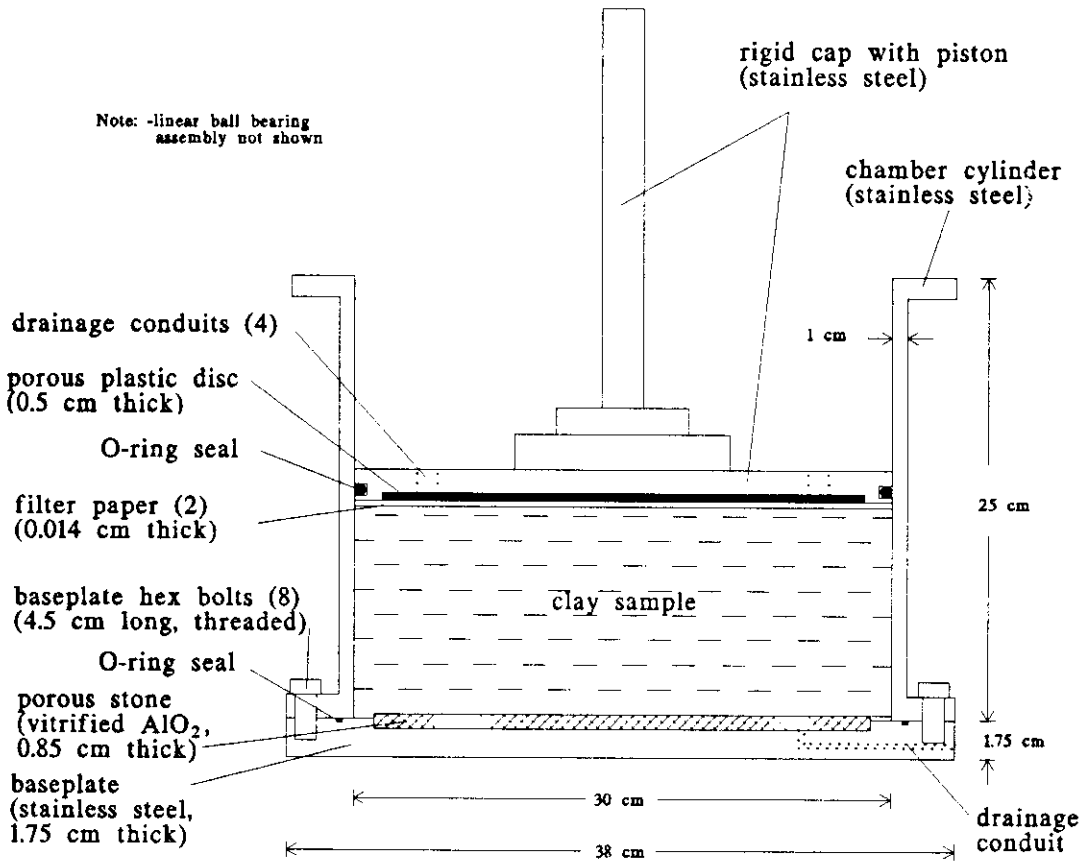

Figure 3.2 Original Chamber for 1-D Consolidation of Clay Samples

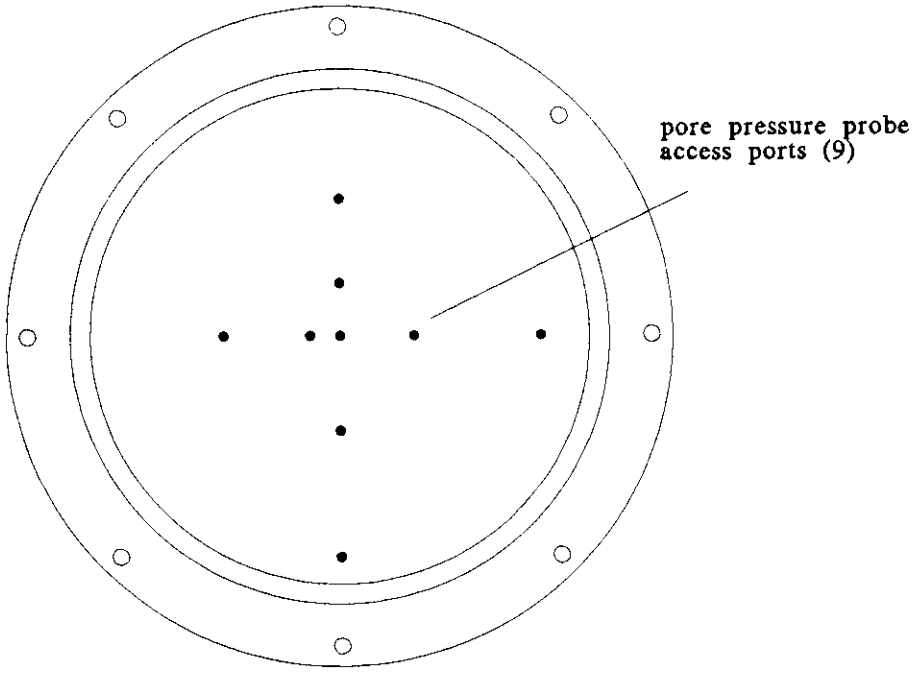

PLAN VIEW

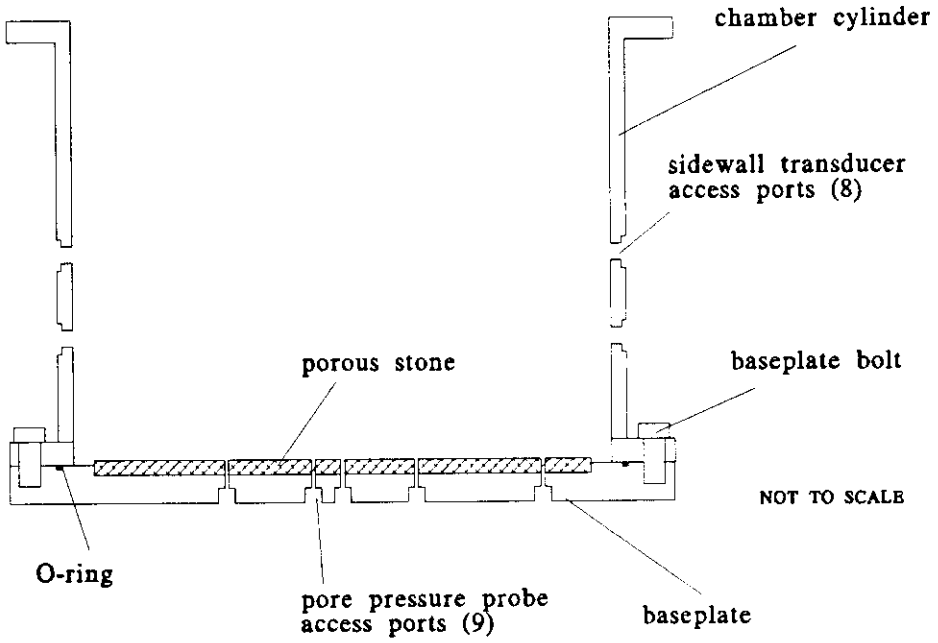

CROSS-SECTIONAL VIEW

Figure 3.3 Modified Consolidation Chamber: Cross Sectional Side and Plan Views

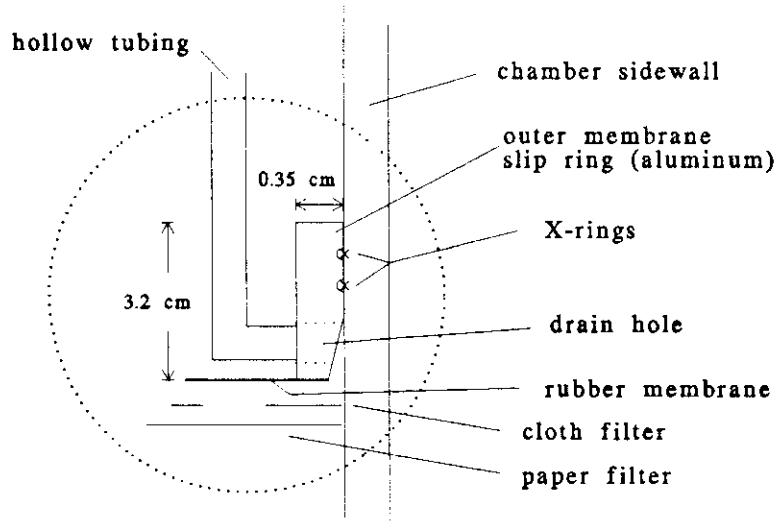

outer membrane slip ring/
surface drainage connection

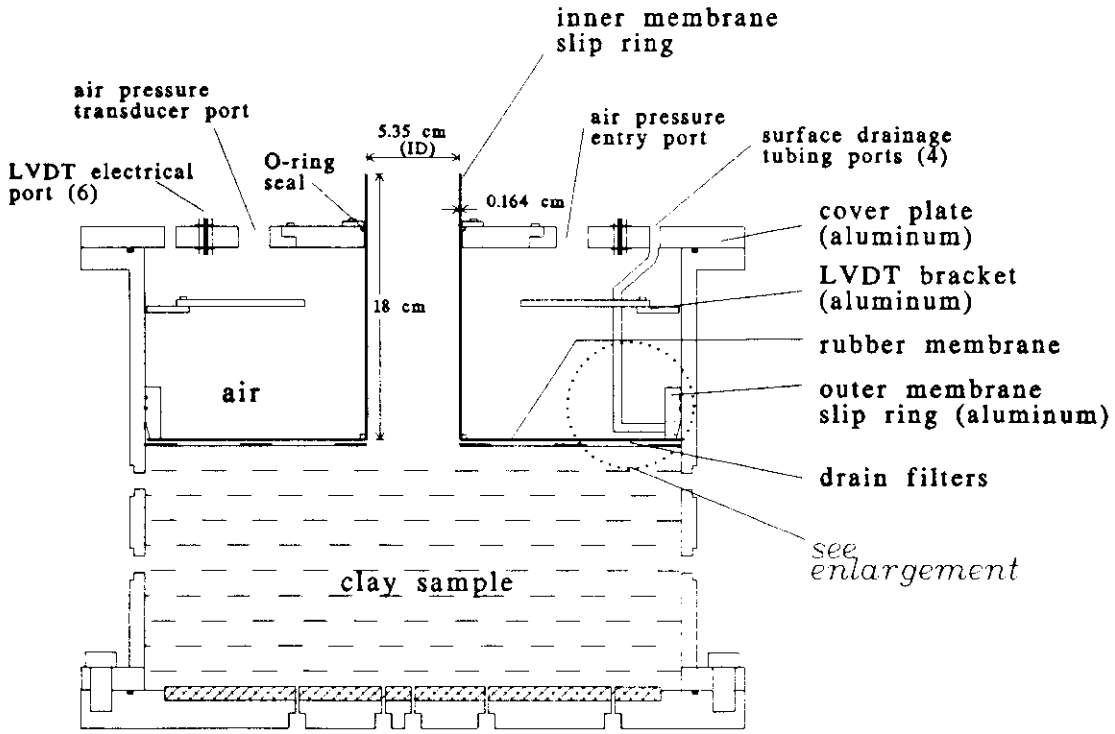

Figure 3.4 New Consolidation Chamber Top Assembly for Caisson Element Experiments

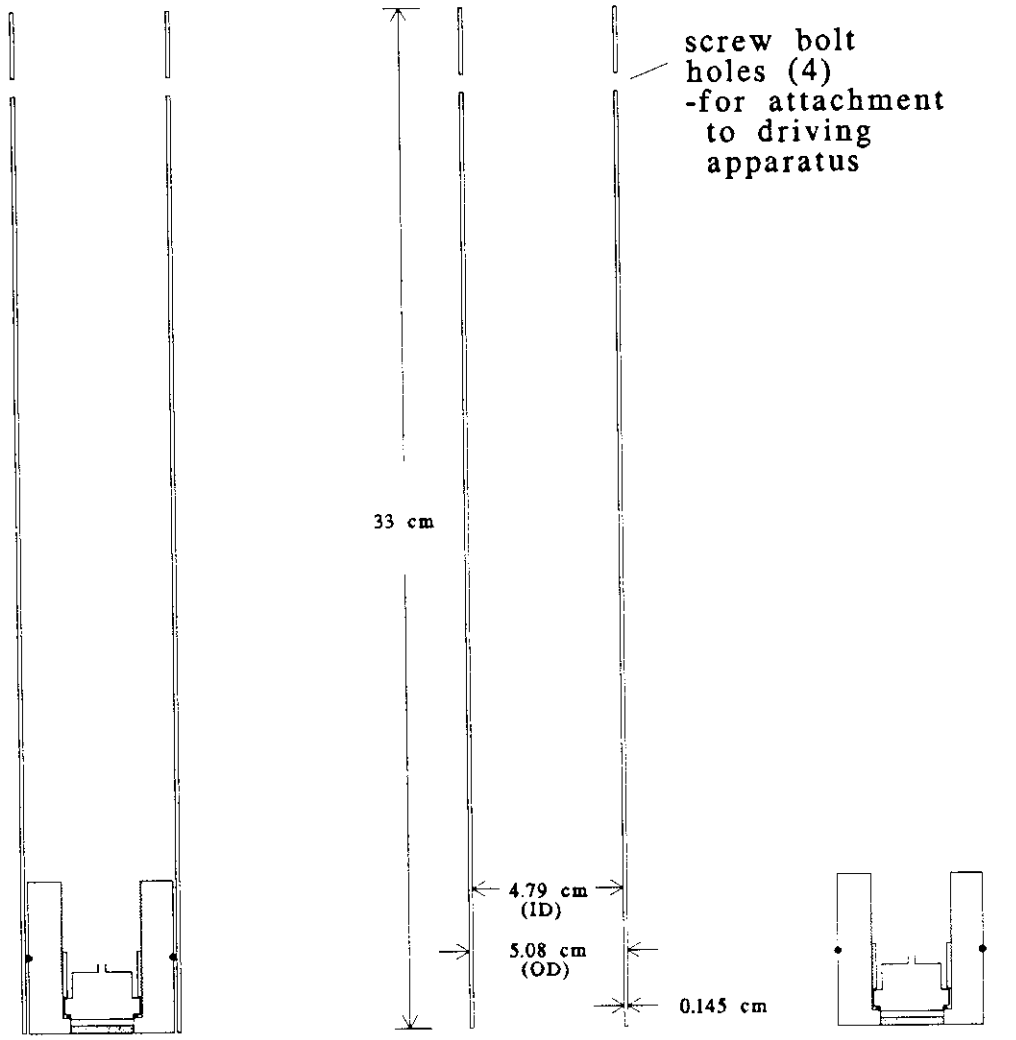

Figure 3.5 Model Caisson: Cross Sectional Side Views of Wall and Cap Components

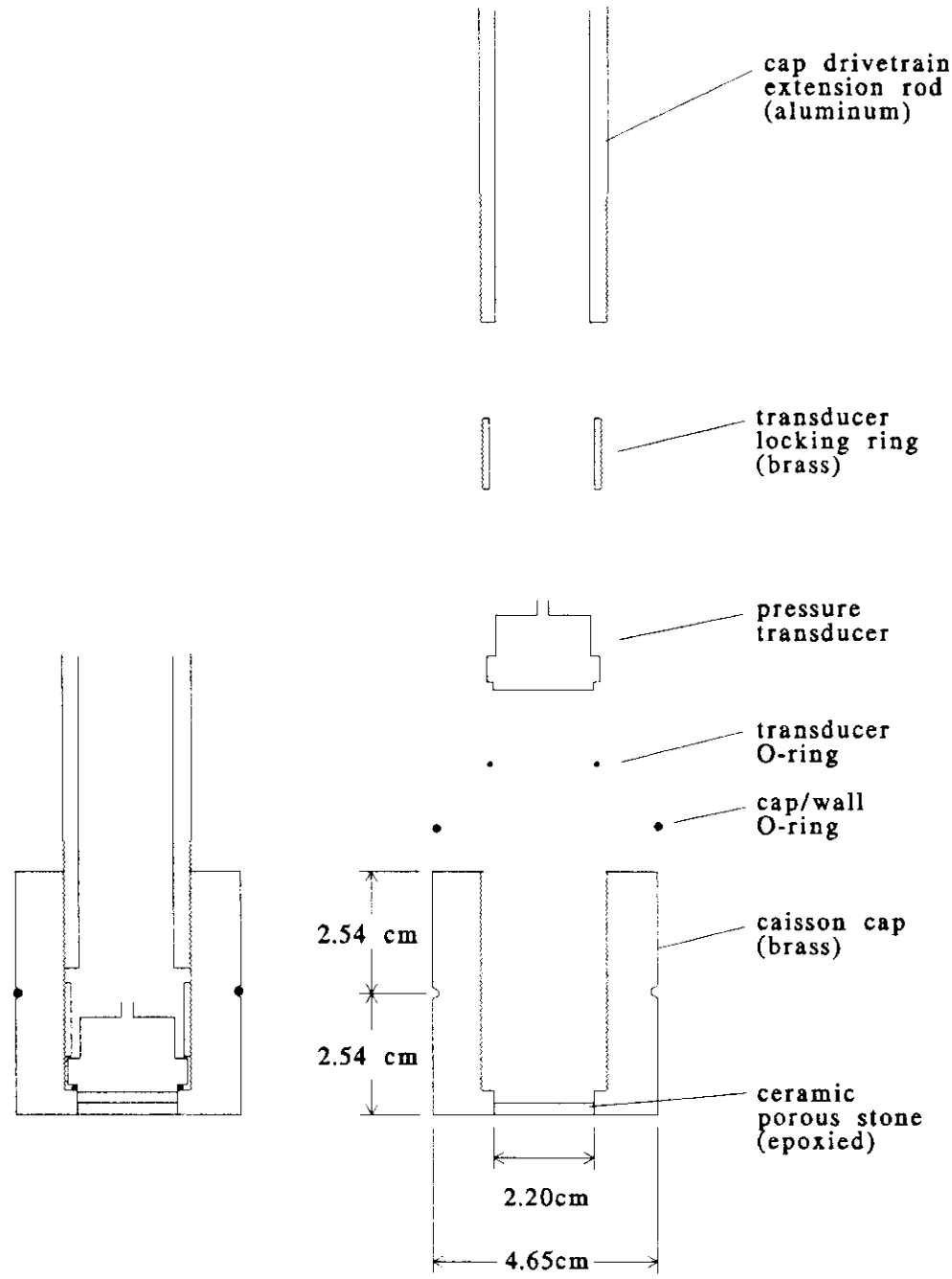

Figure 3.6 Caisson Cap with Pressure Transducer: Cross Sectional Side Views

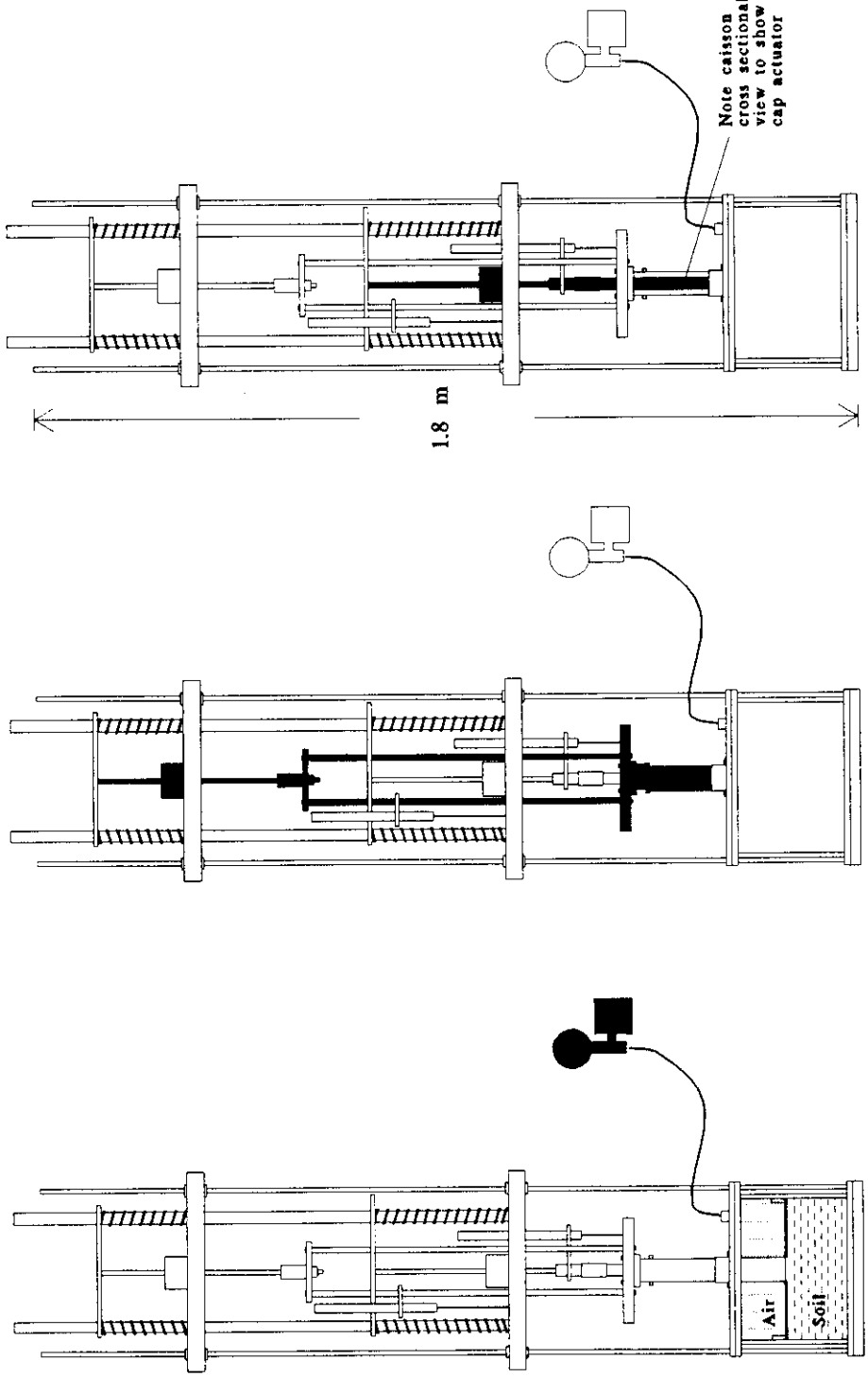

Figure 3.7 Schematic Diagram of the Caisson Element Test Cell with Highlights of the Three Driving Subsystems

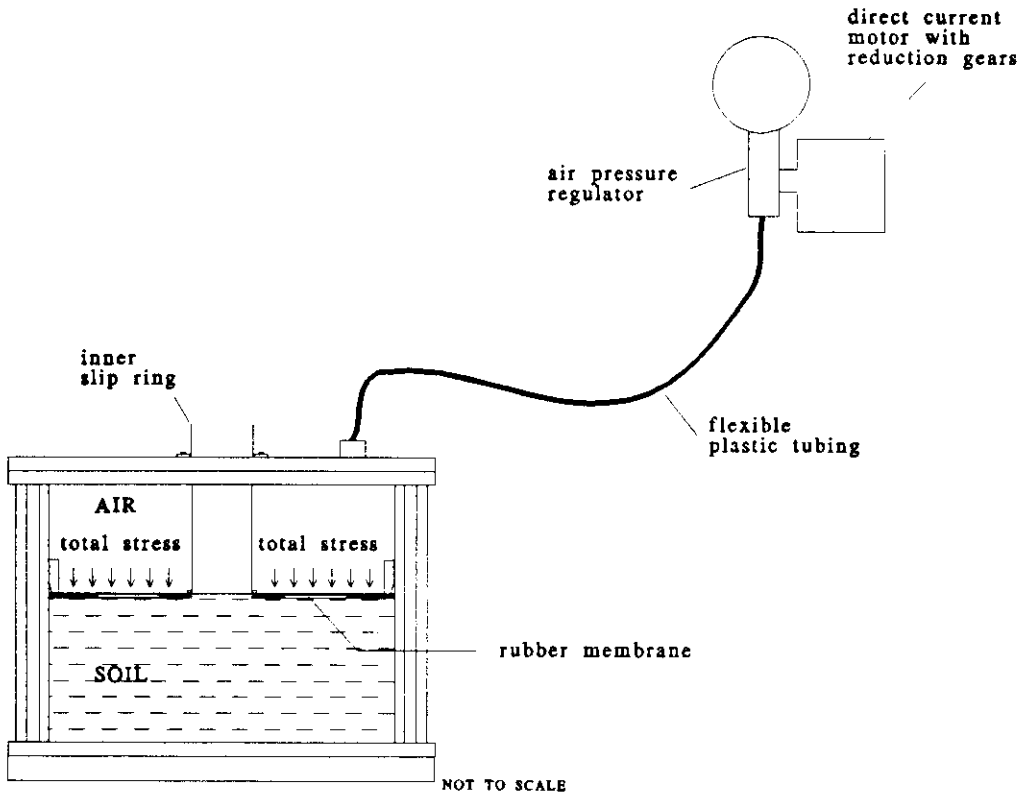

Figure 3.8 Total Stress Driving Subsystem

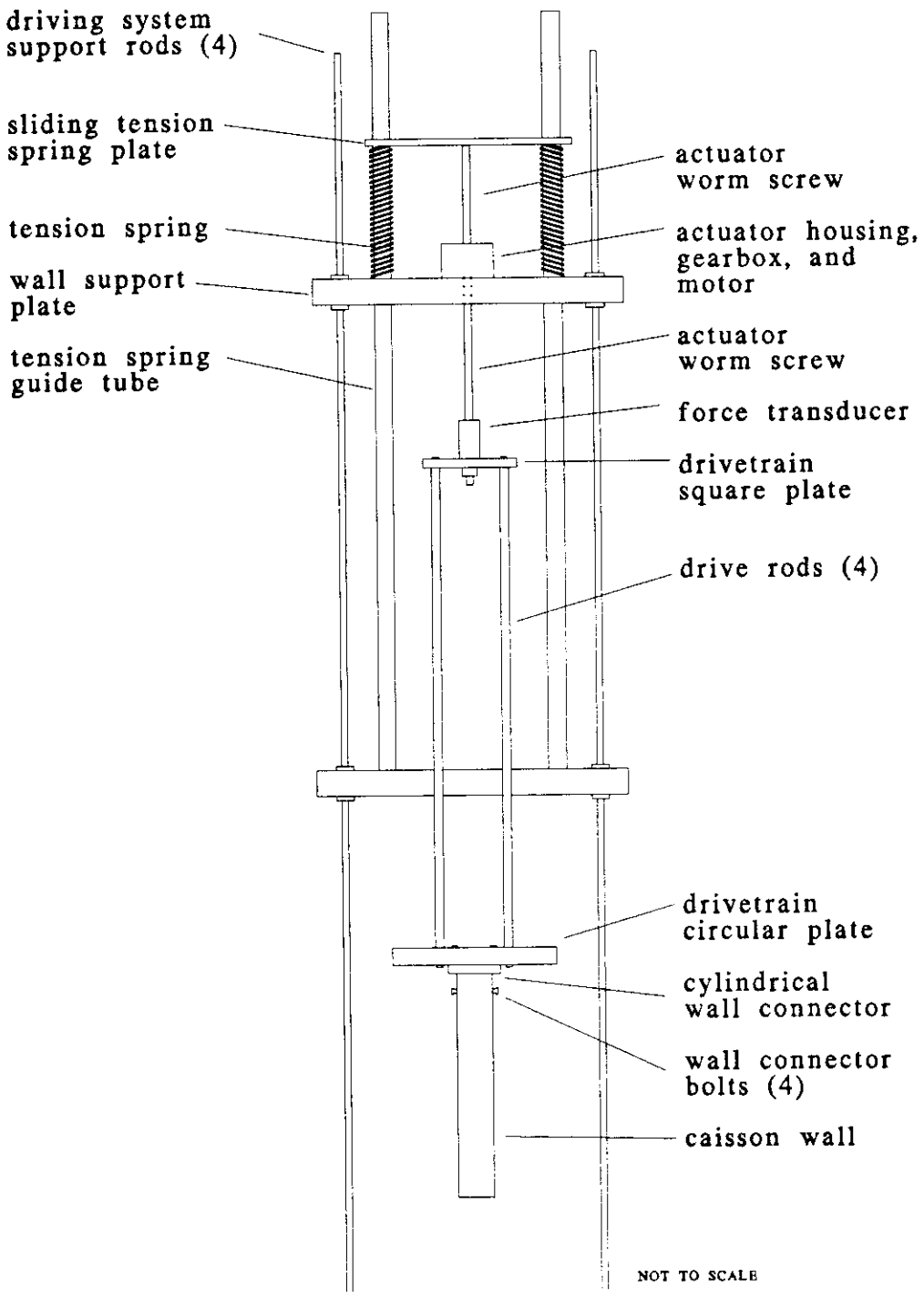

Figure 3.9 Caisson Wall Driving Subsystem

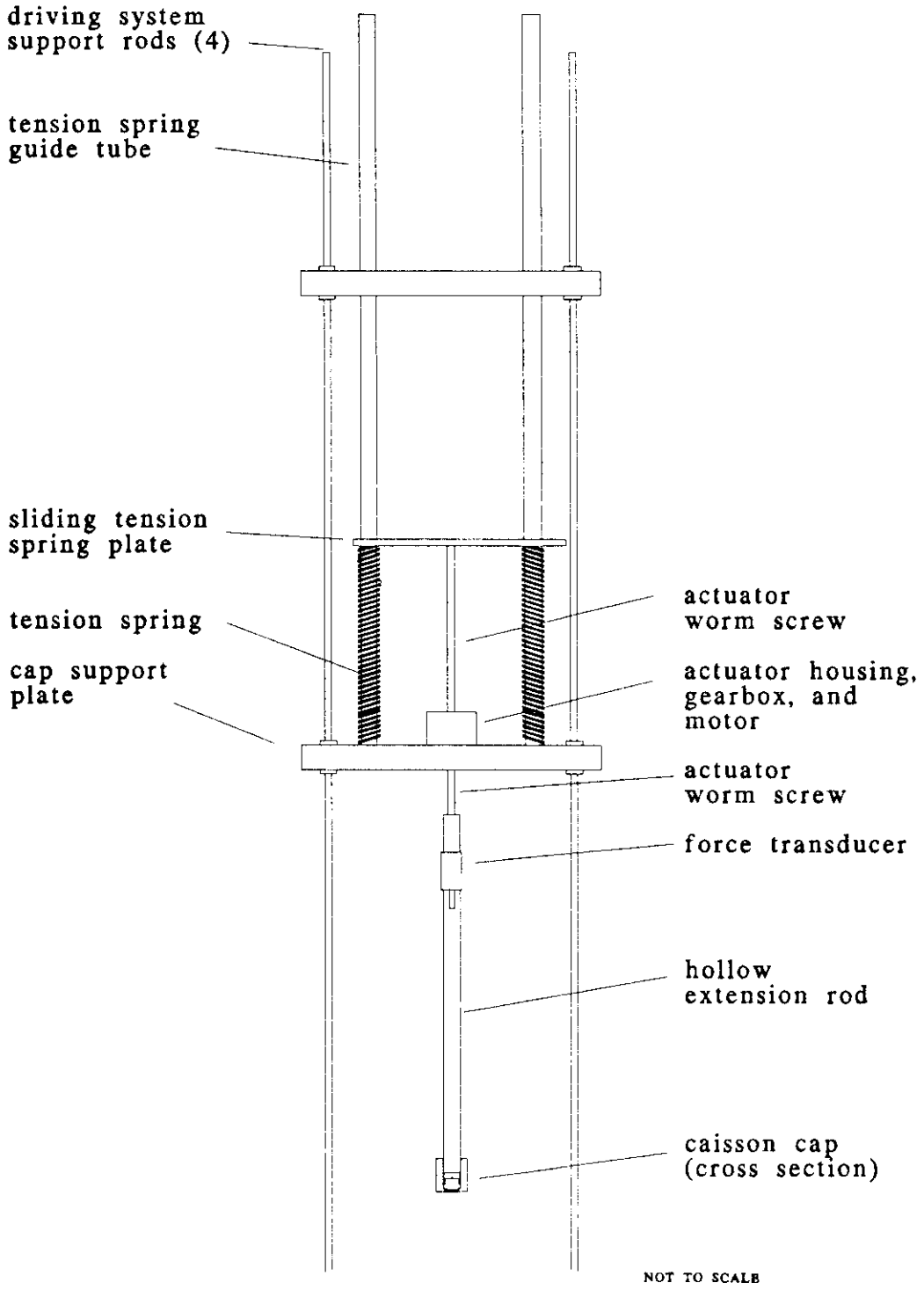

Figure 3.10 Caisson Cap Driving Subsystem

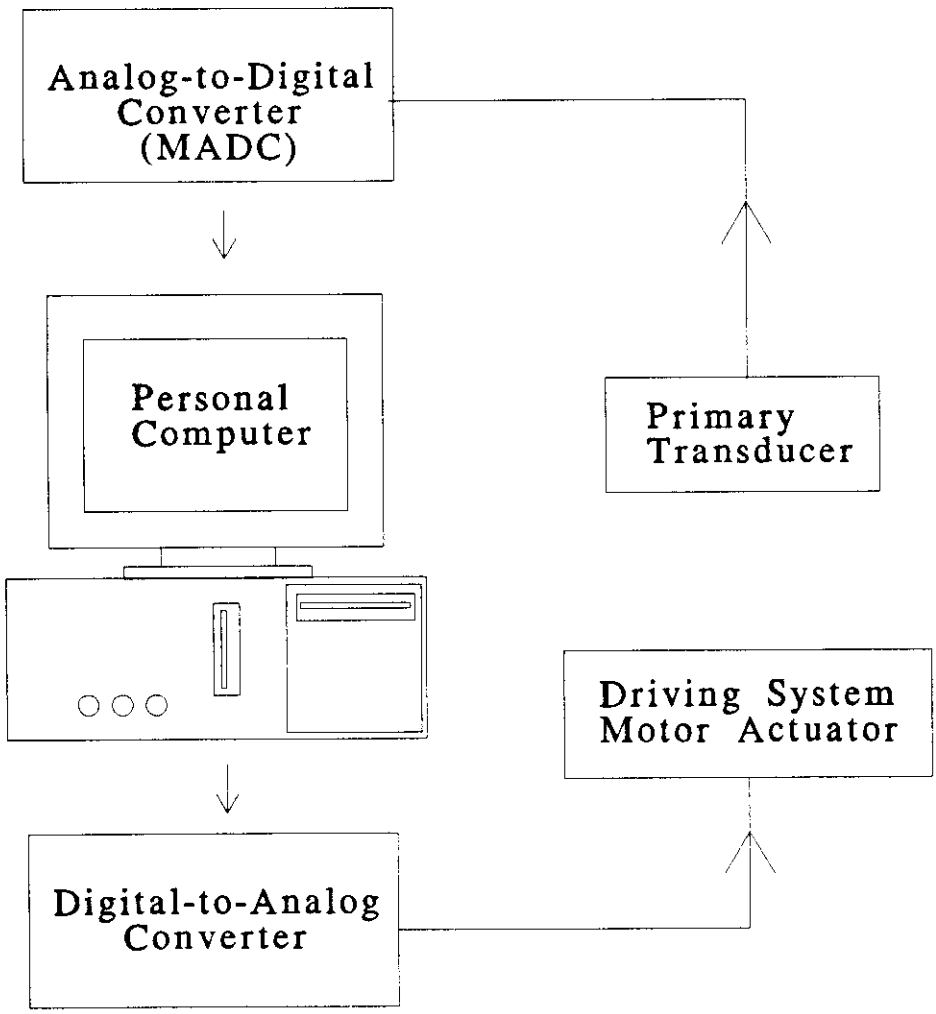

Figure 3.11 Schematic Drawing of the Control System Hardware Components

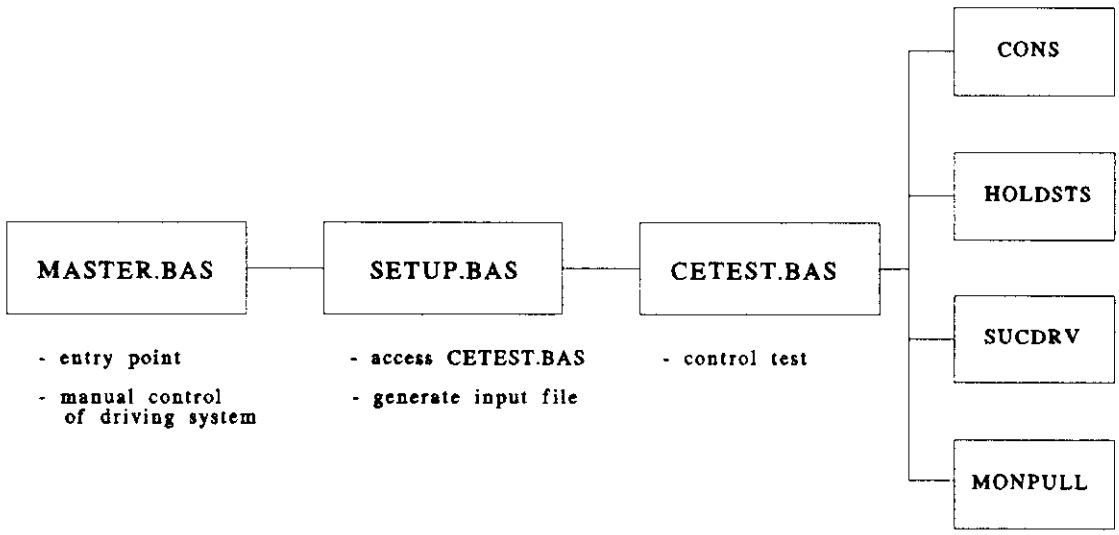

Figure 3.12 Schematic Drawing of the Control System Software Components

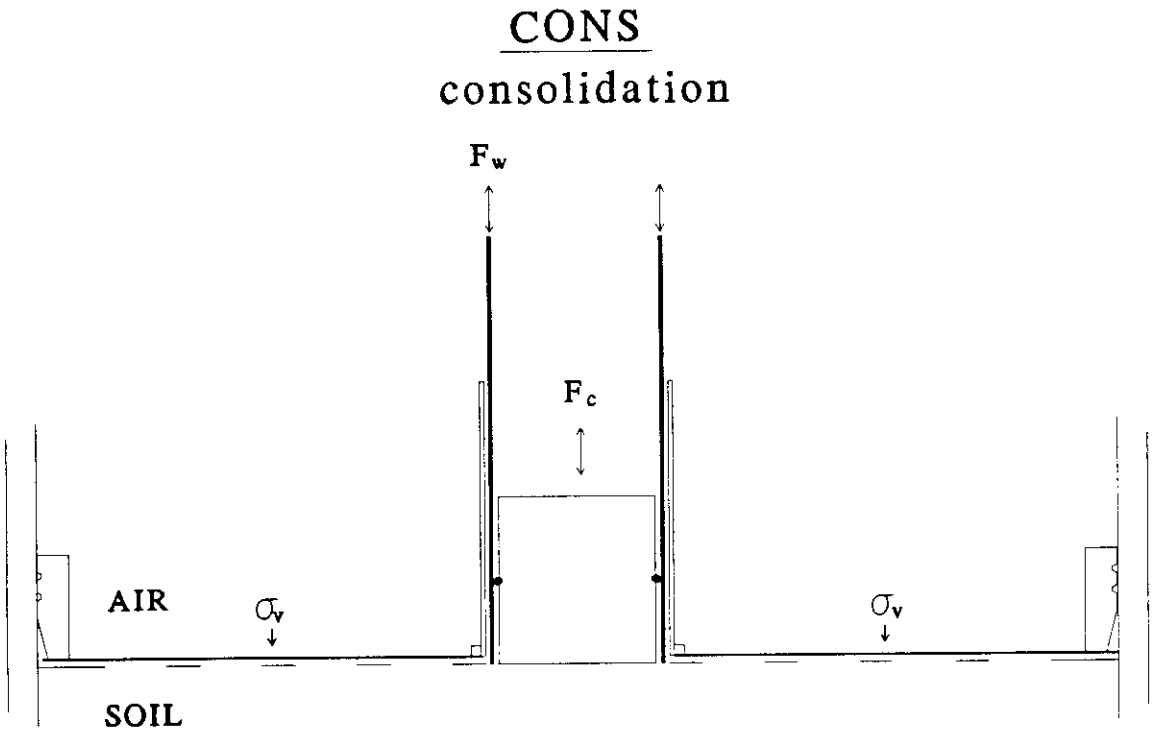

Control Axis	Control Feature
Air Pressure	σ_v = constant
Caisson Wall	$D_w = D_c$
Caisson Cap	$F_c = F_{tot} - F_w$ (F_{tot} = constant)

Legend

F_w = wall force
F_c = cap force
D_w = wall displacement
D_c = cap displacement
σ_v = vertical stress

Figure 3.13 Schematic Drawing of Consolidation Chamber Air/Soil Interface Illustrating the Control Methodology for the CONS Module

HOLDSTS

holding stress:
- equilibration
- sustained load

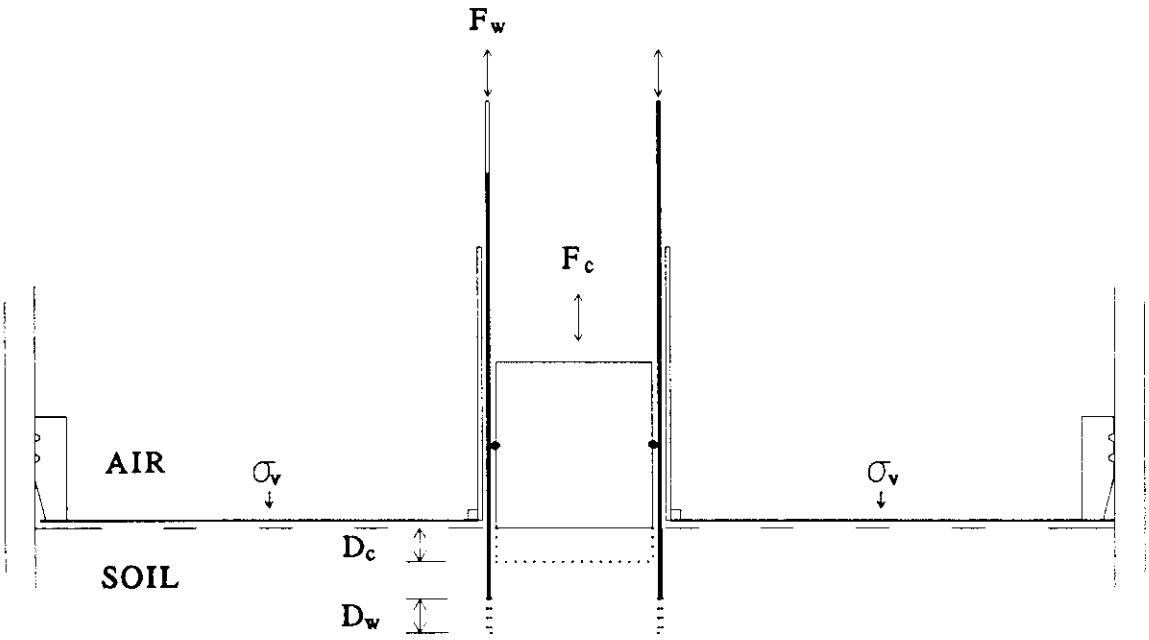

Control Axis	Control Feature	
	wall pen. < 1 cm	wall pen. > 1 cm
Air Pressure	σ_v = constant	σ_v = constant
Caisson Wall	$D_w = D_c$	$D_c = D_w$
Caisson Cap	$F_c = F_{tot} - F_w$ (F_{tot} = constant)	$F_w = F_{tot} - F_c$ (F_{tot} = constant)

Legend

F_w = wall force
F_c = cap force
D_w = wall displacement
D_c = cap displacement
σ_v = vertical stress

Figure 3.14 Schematic Drawing of Consolidation Chamber Air/Soil Interface Illustrating the Control Methodology for the HOLDSTS Module

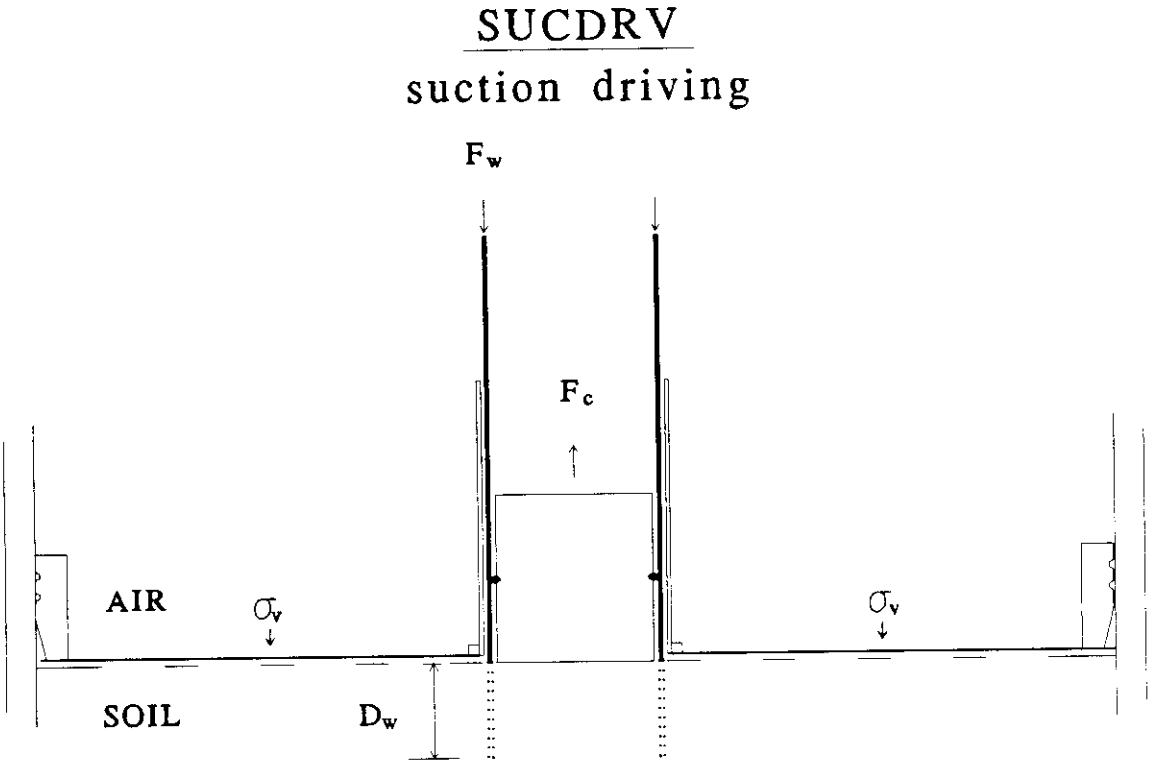

Control Axis	Control Feature
Air Pressure	σ_v = constant
Caisson Wall	$D_w/\Delta t$ = constant
Caisson Cap	$F_c = F_{tot} - F_w$ (F_{tot} = constant)

Legend

F_w = wall force
F_c = cap force
D_w = wall displacement
D_c = cap displacement
σ_v = vertical stress
Δt = elapsed time

Figure 3.15 Schematic Drawing of Consolidation Chamber Air/Soil Interface Illustrating the Control Methodology for the SUCDRV Module

MONPULL

monotonic pullout

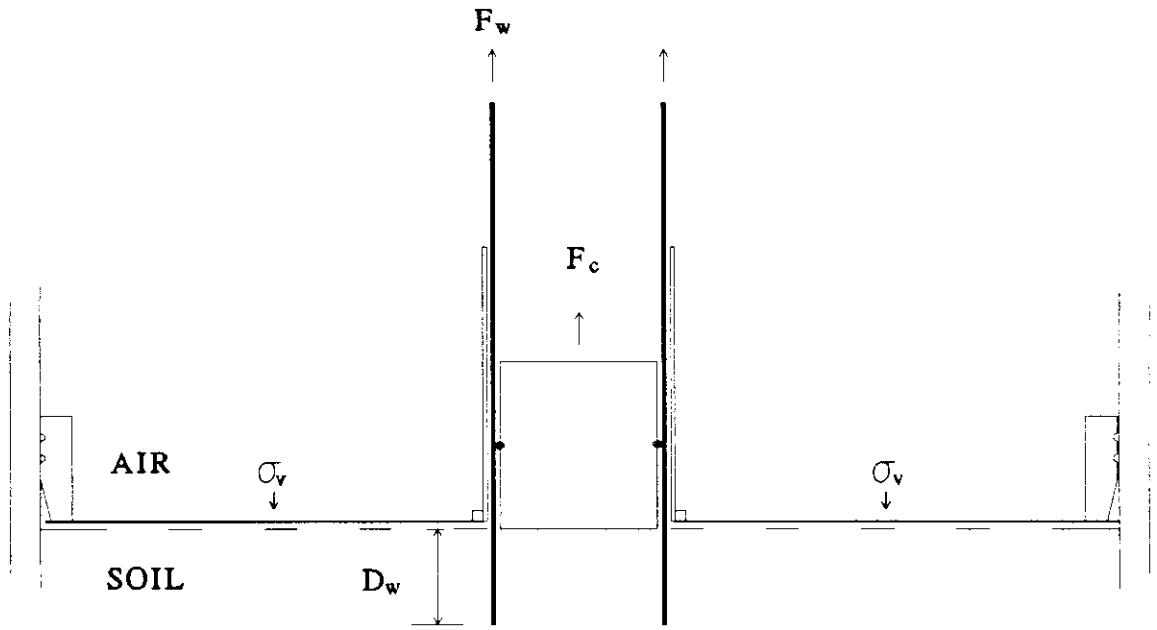

Control Axis	Control Feature
Air Pressure	σ_v = constant
Caisson Wall	$D_w/\Delta t$ = constant
Caisson Cap	$D_c/\Delta t = D_w/\Delta t$

Legend

F_w = wall force
F_c = cap force
D_w = wall displacement
D_c = cap displacement
σ_v = vertical stress
Δt = elapsed time

Figure 3.16 Schematic Drawing of Consolidation Chamber Air/Soil Interface Illustrating the Control Methodology for the MONPULL Module

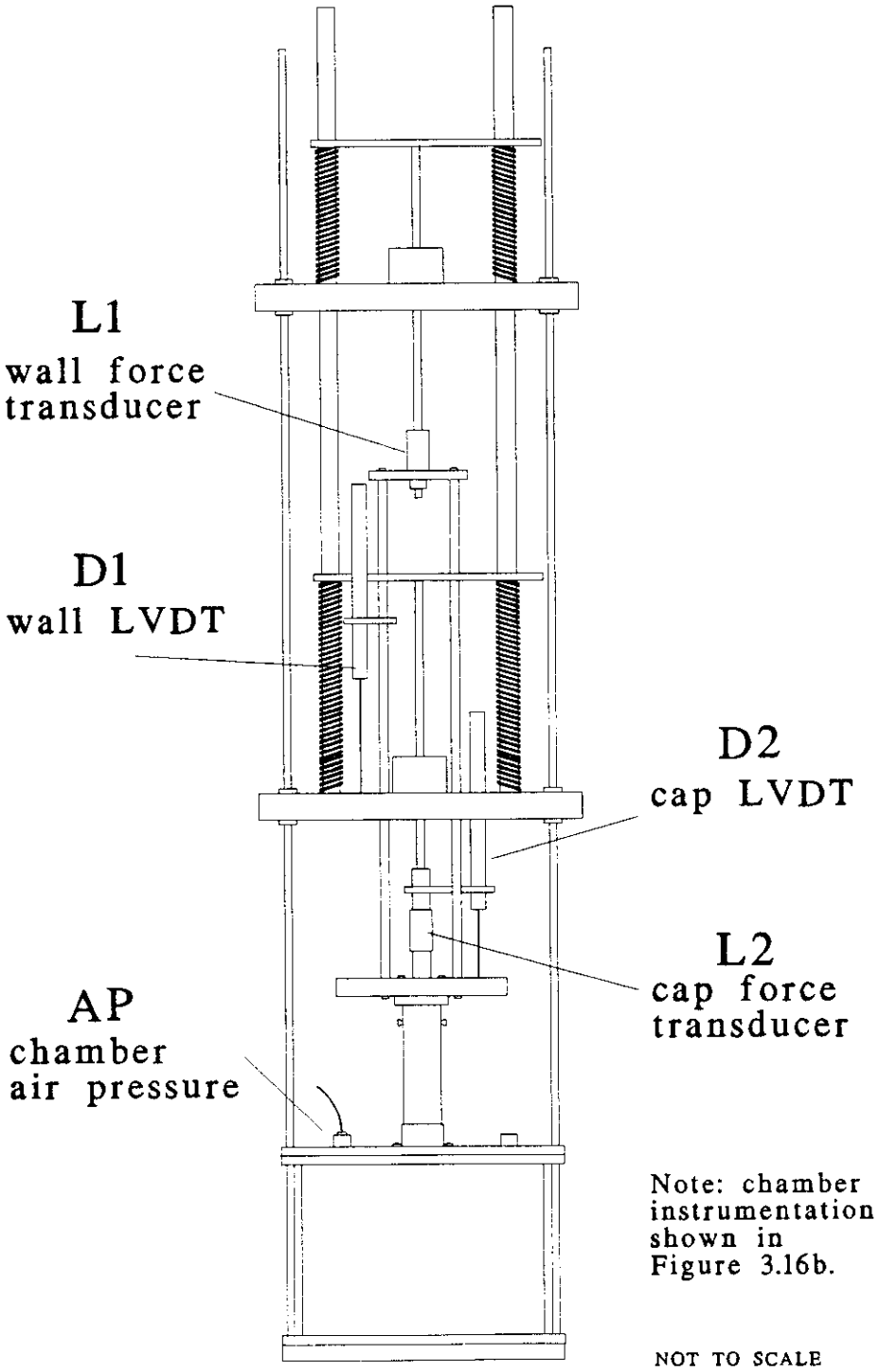

Figure 3.17 Schematic Drawing of CET Cell Showing Typical Instrumentation Package Used for CET Test: Primary Transducers

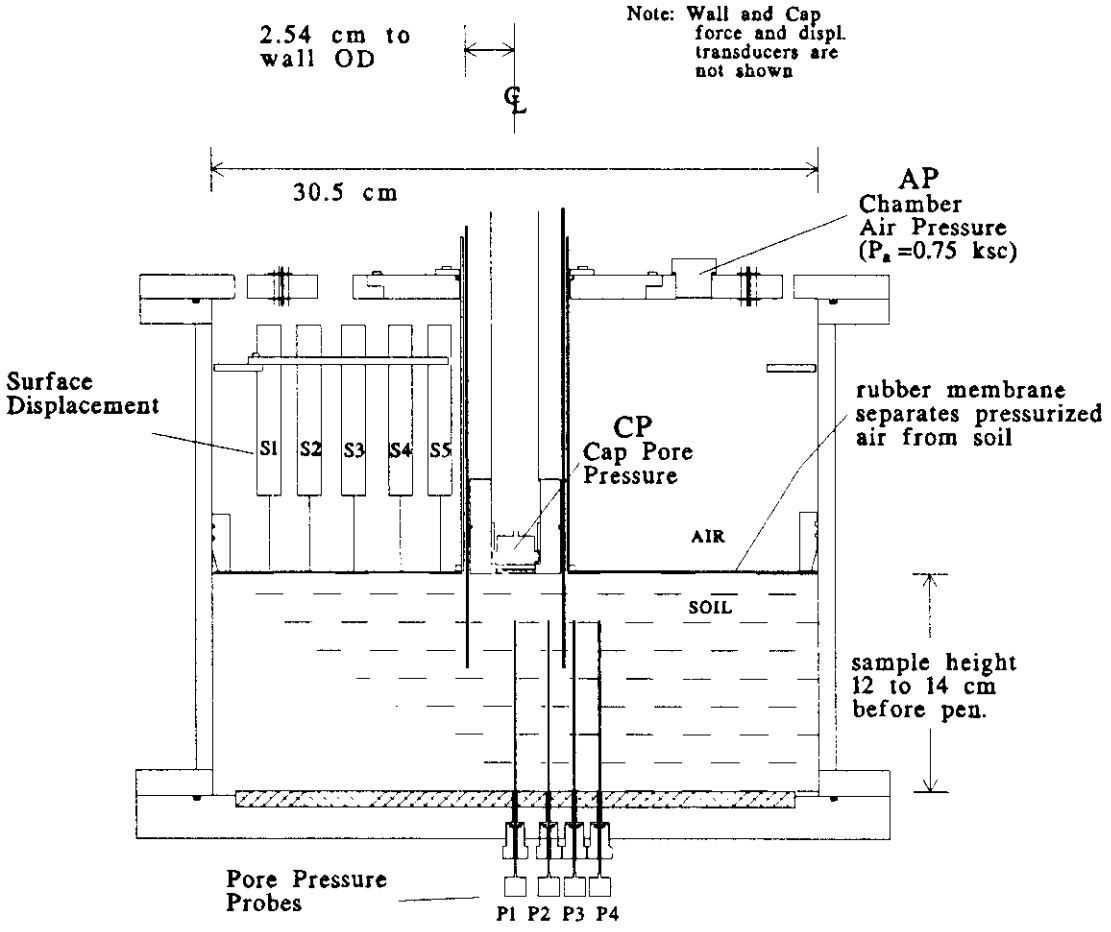

I.D. #	Instrument	Radial Location (cm) from centerline
CP	Cap Pore Pressure	0.00
AP	Chamber Air Pressure	(cover plate)
P1	Pore Pressure Probe	0.00
P2	" " "	1.78
P3	" " "	3.18
P4	" " "	4.45
S1	Surface Displacement	4.2
S2	" "	5.2
S3	" "	7.7
S4	" "	9.8
S5	" "	12.1

Figure 3.18 Consolidation Chamber Cross Sectional Side View Showing Typical Instrumentation Package Used for CET Test: Chamber Transducers for CET 10

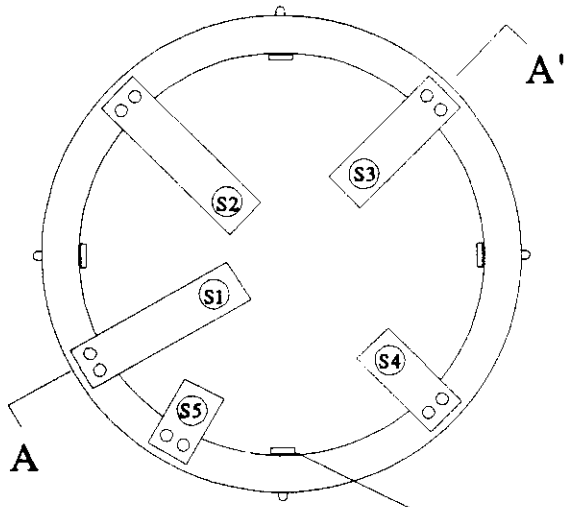

LVDT	Radius (cm) from centerline
S1	5.2 (4.2)
S2	5.2
S3	7.7
S4	9.8
S5	12.1

Note: LVDT at S1 measures at radius of 4.2 cm using elbow extension

Top View
(LVDT bracket only)

bracket screw

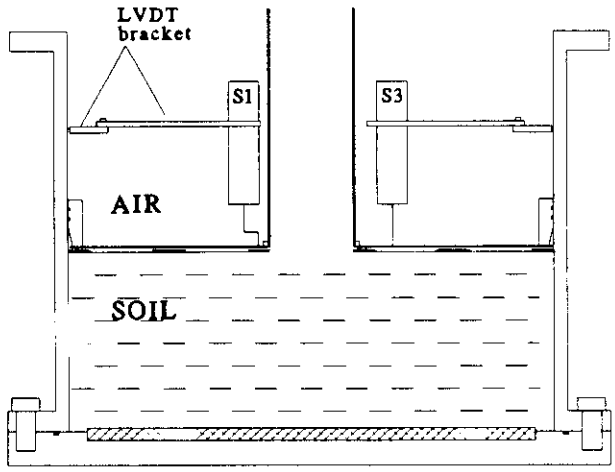

NOT TO SCALE

Cross Sectional Side View
A - A'

Figure 3.19 Consolidation Chamber Cross Section Showing Side and Top Views of Clay Surface LVDTs with Mounting Bracket

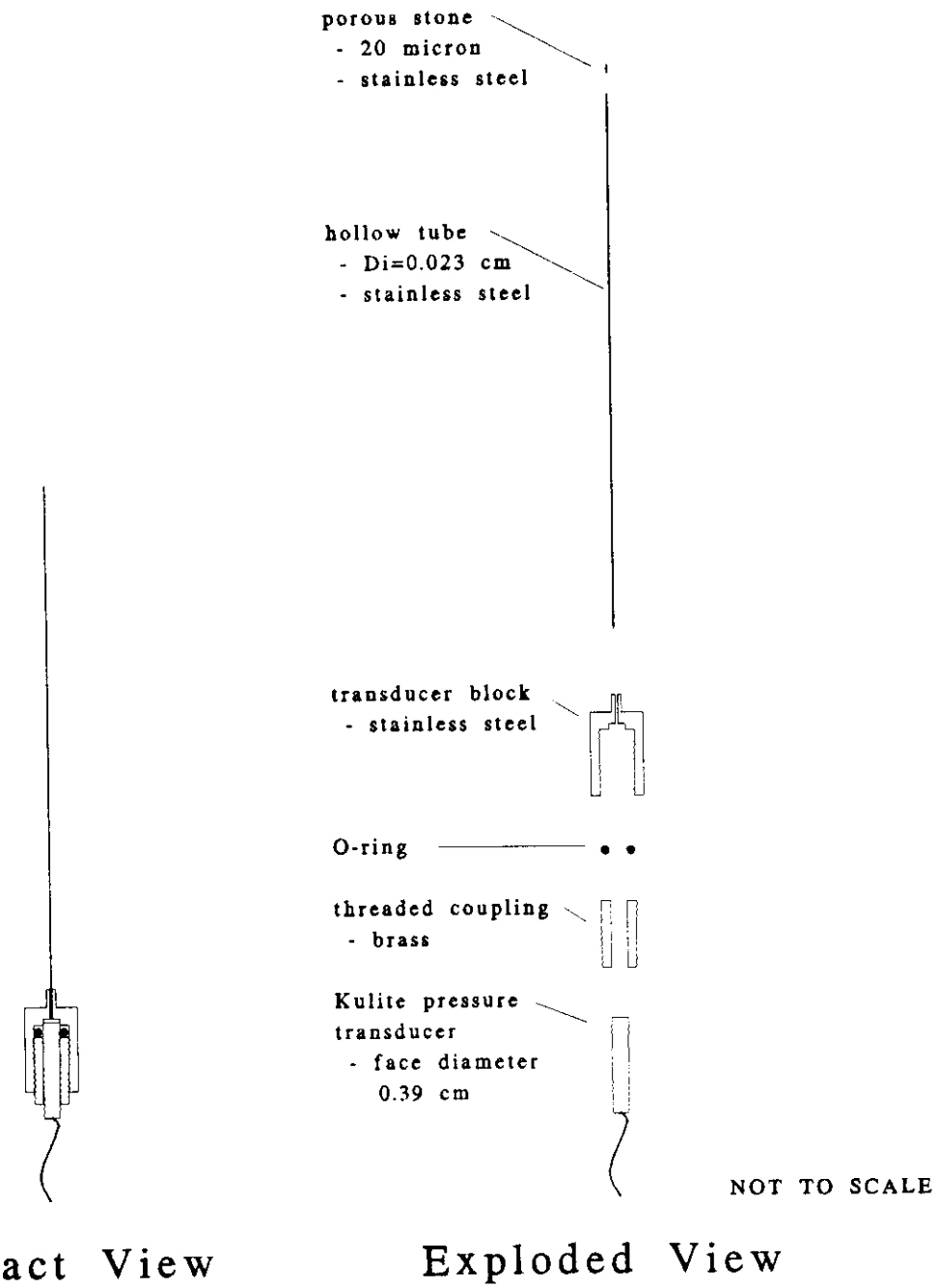

Figure 3.20 Pore Pressure Probe with Kulite Transducer: Cross Sectional Views

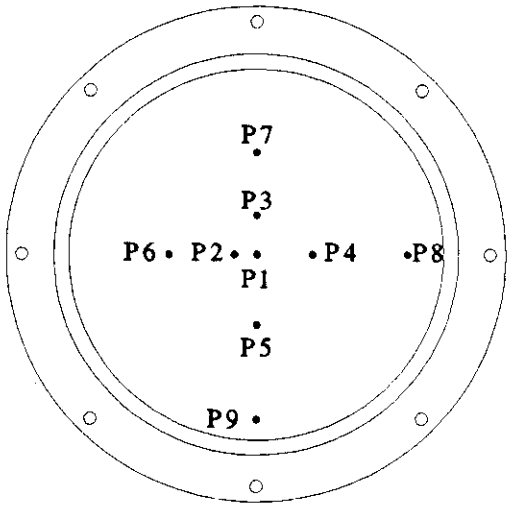

Probe Port #	Radius (cm) from centerline
P1	0.00
P2	1.78
P3	3.18
P4	4.45
P5	5.72
P6	6.99
P7	8.26
P8	12.07
P9	13.34

PLAN VIEW

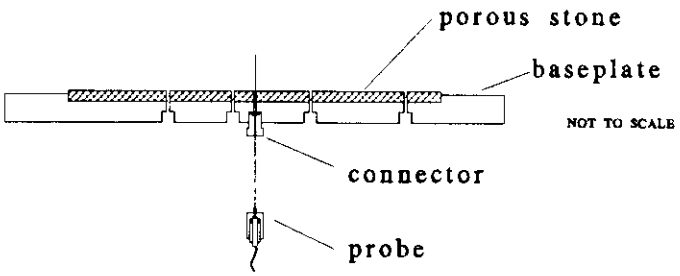

CROSS SECTIONAL SIDE VIEW

Figure 3.21 Consolidation Chamber Baseplate Showing Radial Location of Pore Pressure Probe Ports and a Probe in Place: Cross Sectional Side and Top Views

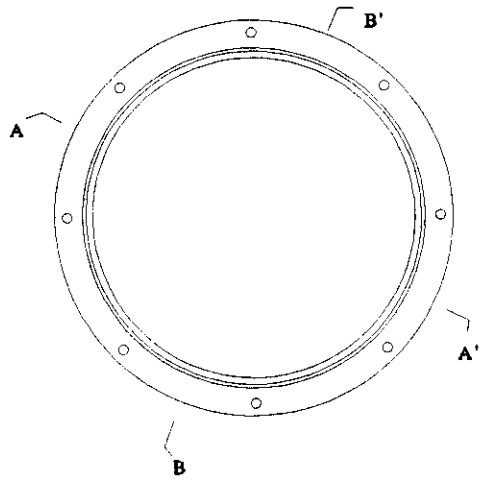

TOP VIEW

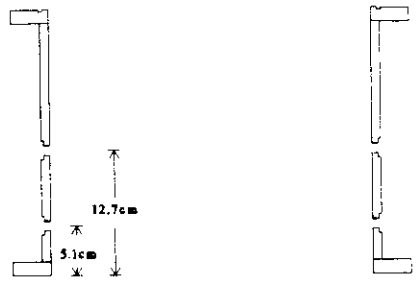

CROSS SECTIONAL SIDE VIEW
BB'

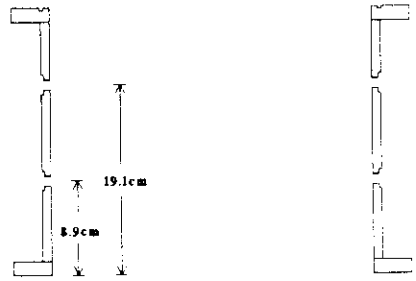

CROSS SECTIONAL SIDE VIEW
AA'

Figure 3.22 Consolidation Chamber Sidewalls Showing Location of Total Stress and Pore Pressure Ports: Cross Sectional Side and Top Views

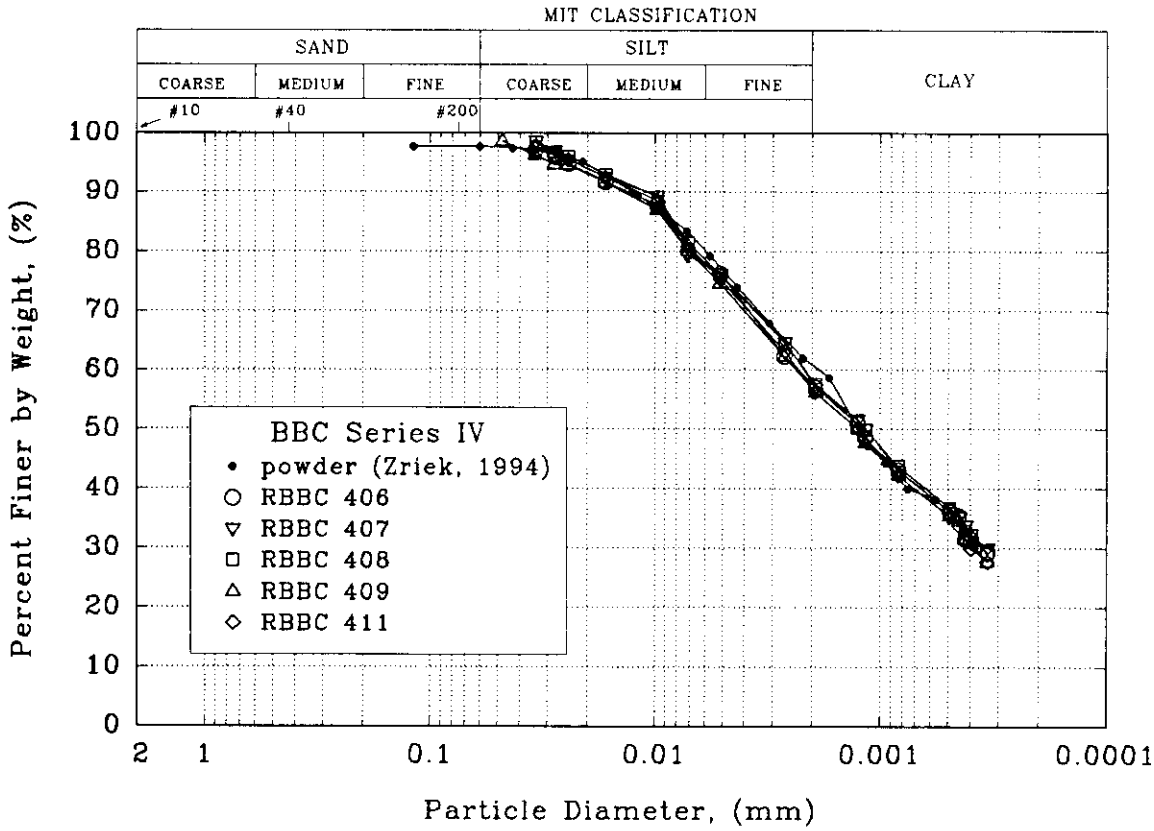

Figure 3.23 Grain Size Distribution of Series IV Boston Blue Clay

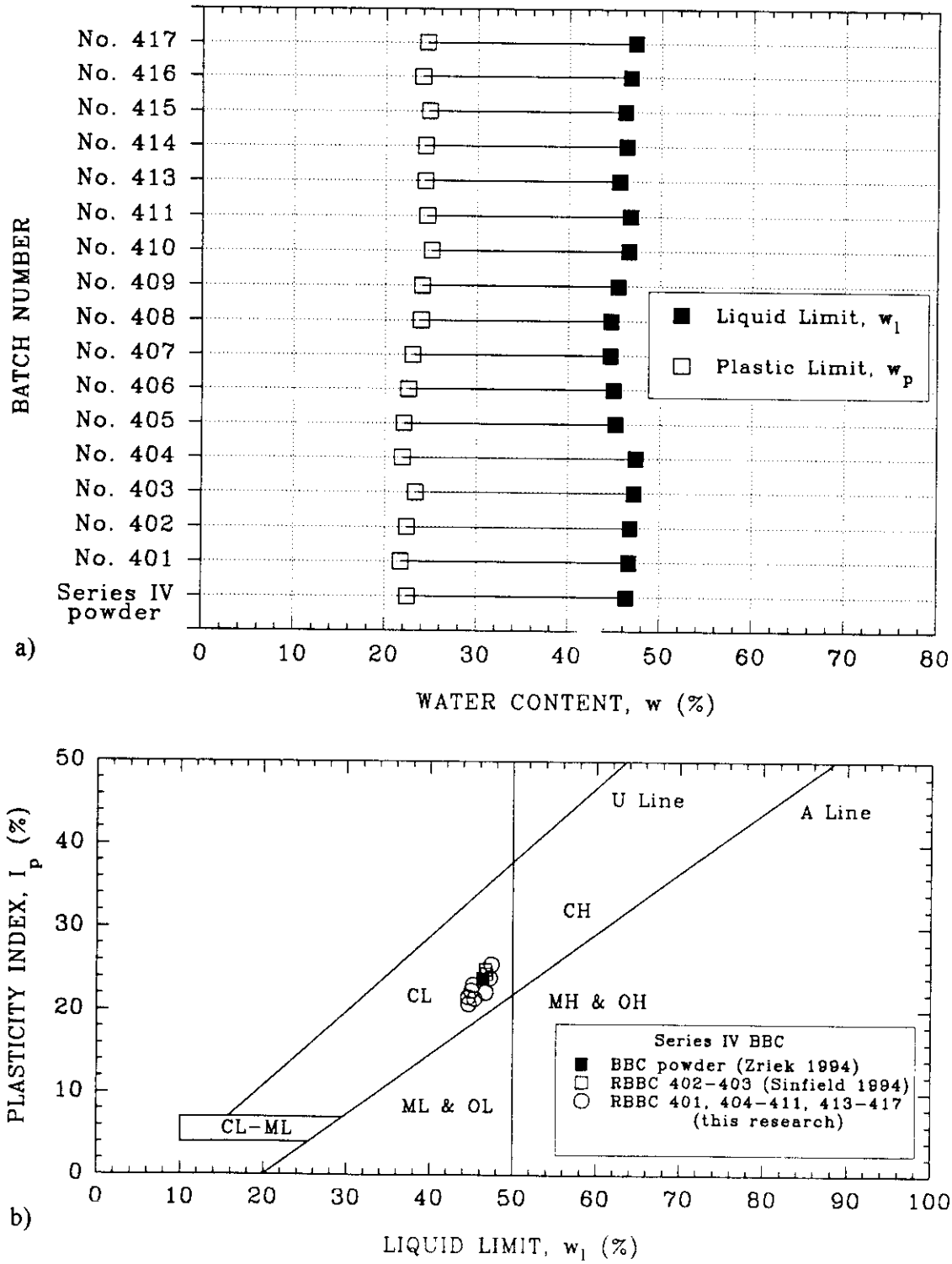

Figure 3.24 Atterberg Limits for Series IV Boston Blue Clay
a) Plastic and Liquid Limits for BBC IV Powder and RBBC 401-411, 413-417
b) Plasticity Chart with Data from Series IV BBC

Consolidation with Rigid Cap
Compression, Flow, and Consolidation
Average Values

Stress Interval (ksc)	n	C_c	m_v (cm^2/kg)	k_v ($\times 10^{-8}$ cm/s)
0.0625 - 0.125	7	0.571 ± 0.086	0.824 ± 0.222	47.4 ± 14.6
0.125 - 0.25	9	0.588 ± 0.046	0.502 ± 0.065	41.6 ± 14.5
0.25 - 0.5	11	0.525 ± 0.033	0.230 ± 0.031	23.7 ± 3.5

Stress Level (ksc)	n	c_v ($\times 10^{-4}$ cm^2/s)
0.03125	6	3.27 ± 0.59
0.0625	7	4.18 ± 1.07
0.125	8	6.51 ± 2.28
0.25	11	8.80 ± 2.85
0.5	12	10.59 ± 1.94

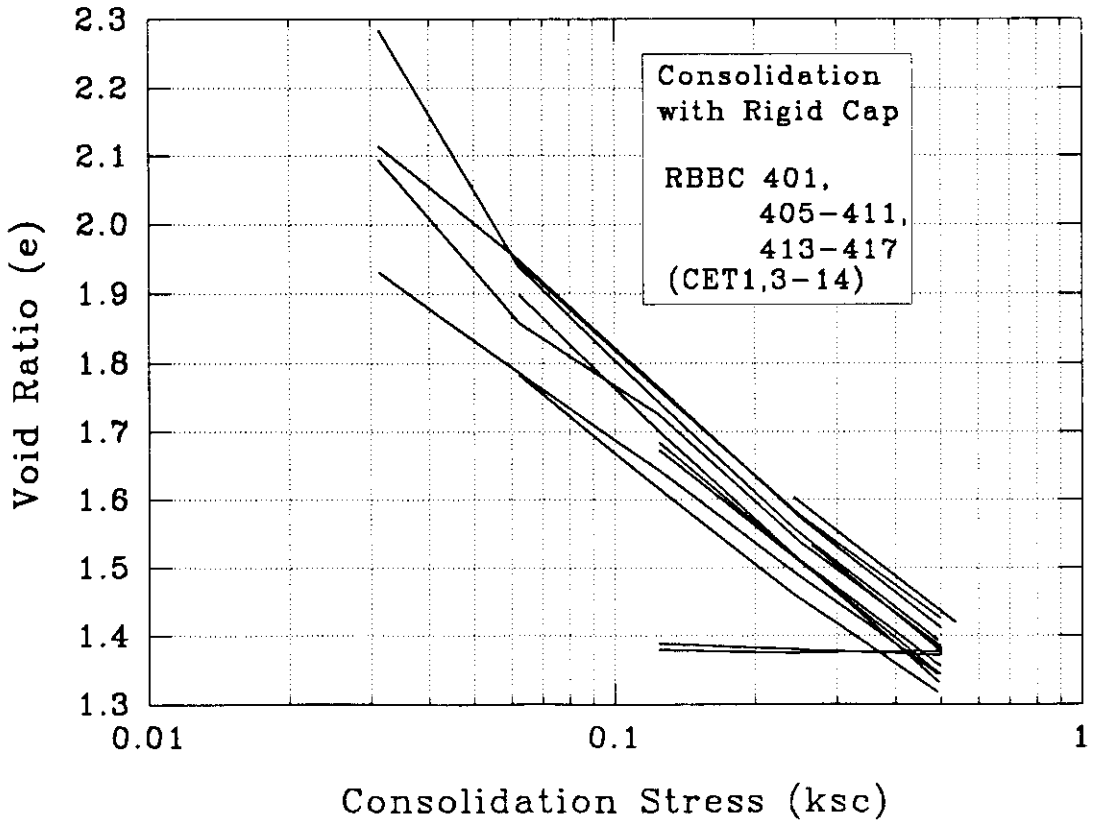

Figure 3.25 RBBC Consolidation with Rigid Cap: Compression, Consolidation, and Flow Characteristics

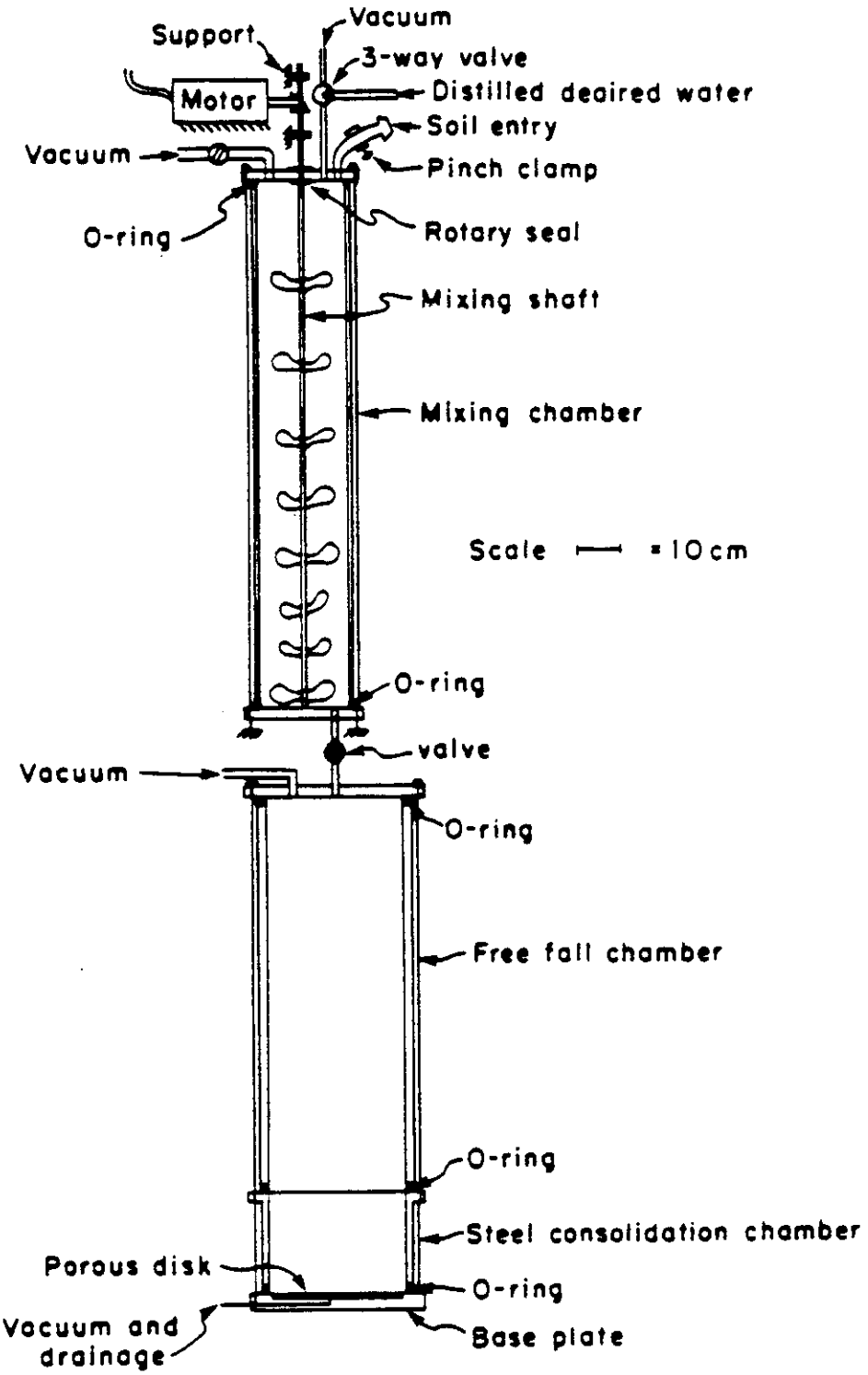

Figure 3.26 Schematic Diagram of the Resedimentation Equipment for Boston Blue Clay (from Germaine 1982)

4. EVALUATION OF CET CELL

This chapter evaluates the limitations of the Caisson Element Test (CET) apparatus in terms of its ability to: 1) simulate the installation, set-up, and axial tensile loading of suction caissons, and 2) measure the behavior of the model caisson and the test soil during the simulation. Results from the initial test (CET-1) revealed numerous limitations that were corrected for subsequent tests. Section 4.1 chronicles the CET cell development throughout the testing program, from CET-1 through CET-14. (Chapter 3 fully describes the CET apparatus in its final form, prior to tests CET-13 and 14.) Sections 4.2 through 4.6 evaluate the extant limitations of each of the five components of the CET cell: consolidation chamber, model caisson, driving system, control system, and instrumentation.

4.1 EQUIPMENT DEVELOPMENT CHRONOLOGY

During the first year of suction caisson research at MIT, from September 1992 to September 1993, the original CET apparatus was designed, fabricated, and proof tested (Whittle & Germaine, 1993). Data from the first test CET-1, conducted in early September 1993, illuminated many of the limitations of the apparatus in simulating suction caisson installation and loading. In order to eliminate, or at least lessen, these deficiencies, significant modifications were made to the CET cell. Subsequent tests revealed other persistent problems, which were solved by further equipment changes. Table 4.1 lists the test date[1] for all 14 CET tests in the testing program and the equipment modifications that were made to the CET apparatus in between tests. Note that the improvements are categorized according to the five components of the CET cell.

4.1.1 Cylindrical Slip Ring Assembly Modifications

Modifications to the slip ring assembly that covers the clay cake in the consolidation chamber fall into one of three categories: air leak prevention, surface drainage improvement, and caisson/slip ring separation. Air leakage from the pressurized cavity through the slip ring/rubber membrane cover and into the test soil was a chronic problem for tests CET-1 through CET-6, as evidenced by visual and audible observation. Several attempts were made to stop the leaks including adding more rubber adhesive (RTV) to bond the membrane and slip rings, drilling air leak relief ports in the outer slip ring, and re-machining the outer slip ring to allow better contact with the rubber membrane and more O-ring friction between the outer slip ring and the inner chamber wall. As listed in Table 4.1, these modifications followed tests CET-2, 3 and lessened

[1]The test date is the first day of model caisson test events, as described in section 3.3.4.

the air leak problem. However, air leakage was eliminated following CET-6 by replacing the outer slip ring O-ring seals with "X-rings". As shown in Figure 4.1, the X-ring seals the outer ring to the inner chamber with two points of contact thus doubling the protection against pressurized air penetrating the seal, while still allowing the slip ring/membrane assembly to move vertically.

The first surface drainage improvement, which followed CET-1, was placement of a cloth filter over the original paper filter on top of the clay cake in order to encourage radial fluid flow toward the outer ring collection point (see Figure 4.2). Attempts were made to increase surface drainage flow after CET-3 by drilling two more drain ports in the outer slip ring, and after CET-6 by widening the drainage tubing leading from the outer slip ring to the atmosphere via the cover plate. Unfortunately, these modifications did little to improve top drainage; this topic is discussed further in section 4.2.2, which evaluates the slip ring assembly as a whole unit.

The final consolidation chamber modifications involved the inner slip ring, which is sealed to the rubber membrane. This ring moves vertically through a port in the cover plate and separates the model caisson from the pressurized air cavity (see Figure 4.3). During model installation in CET-2, the model caisson caught the inside lip of the inner slip ring and dragged the ring into the clay cake. This destroyed the slip ring/rubber membrane connection and severely disturbed the clay cake, and the test was abandoned. To prevent a future occurrence of this, the inside lip of the inner slip ring was tapered, as shown in Figure 4.3. During installation in CET-7, the caisson wall was in contact with the inside wall of the inner slip ring, a condition which added approximately 5 kg of force to the wall. For tests CET-8 through CET-14, this problem was solved by placing thin (~0.5 mm thick) shims between the caisson wall and the inside wall of the inner slip ring *prior* to installation in order to maintain proper caisson alignment. The shims were removed before the start of caisson wall penetration.

4.1.2 Model Caisson Improvements

Figure 4.4 shows the two improvements made to the model caisson: removal of the taper at the wall tip and reduction of the O-ring friction between the cap and wall. The original caisson wall was a standard 1" diameter Shelby tube with a tapered tip. Following CET-1, the taper was removed to create a blunt end, which better simulates prototype caisson wall tips. After CET-2, the O-ring groove on the caisson cap was deepened in order to reduce the O-ring "squeeze" between the cap and wall, which in turn dropped the cap/wall friction from ±5 kg to ± 1 kg. The subject of cap/wall friction is discussed further in section 4.3.2.

4.1.3 Driving System Modifications

Section 3.1.3 described the driving system, which is composed of the total force, cap, and wall driving subsystems. The most serious mechanical problem during CET-1 was the limitation on the stroke of the cap actuator during the pullout phase. The original design used a pressure-volume controller to supply oil to an hydraulic actuator. This system was completely replaced by a ball screw actuator, identical to the control mechanism for the caisson wall.

Following CET-5, tighter control over caisson forces and displacements were achieved by two modifications to the driving systems. First, to allow the actuator to respond to very small control signals from the computer, the gear reduction between the electric dc motor and the linear ball screw actuator was increased by a factor of ten. In addition, to remove the actuator compliance (or lashback) arising from changes in direction of the worm screw, compression springs were added to both the wall and cap drive systems to maintain a constant upward force on the worm screw throughout all phases of testing (refer to Figures 3.9 and 3.10).

4.1.4 Control Software Changes

Numerous modifications were made to the control software modules (SUCDRV, HOLDSTS, MONPULL) during the course of the testing program in order to maintain complete control over cap and wall force and displacement. The final software system was described fully in section 3.1.4. SUCDRV, which is used to control the driving system during caisson installation with underbase suction, underwent serious modification early in the testing program. In CET-1, the algorithm was unable to match the reduction in the cap force to the increase in wall force. The original control algorithm used feedback control on the total force F_{TOT} to compute the required amount of cap force reduction. The control signals for the cap actuator were sent for a fixed time interval of 1 second in each loop, which was found to be ineffective. For CET-3, the system used feedback control on the total force F_{TOT} and the rate of change in wall force (F_w/t), with continuous adjustment of the cap force F_c. These modifications reduced fluctuations in total force F_{TOT} during installation from ±39 kg in CET-1 to ±5 kg in CET-3. Further proof testing showed feedback control on the rate of wall force (F_w/t) was unnecessary. Hence, for all tests beyond CET-3, the algorithm uses feedback control on the total force F_{TOT} with continuous adjustment of the cap force F_c, as described in section 3.1.4.

HOLDSTS controls the equilibrium (setup) and sustained tensile load phases, both of which are simulated by maintaining a constant total force on the caisson and zero relative displacement between the cap and wall. The original algorithm was not able to hold a constant total force on the caisson. The algorithm in CET-1 used feedback control on the cap force and wall displacement to set a constant total caisson force F_{TOT}, and zero relative displacement between cap and wall. The control signals for the cap and wall actuators were sent for fixed time

intervals of 1 second in each loop. However, friction between the cap and the wall caused unacceptably large total force fluctuations, $\Delta F_{TOT} = \pm 20$ kg. This problem was solved in CET-3 by reducing the cap/wall friction (using a lower O-ring squeeze between the cap and wall, as described in section 4.1.2), using feedback control on the total caisson force, and providing a keyboard "toggle" to allow manual adjustment of the cap force gain factor during testing. These modifications reduced fluctuations of total force to within $\Delta F_{TOT} = \pm 1.0$ kg. Following CET-5, the HOLDSTS module was streamlined by providing continuous control of the wall and cap actuators, keyboard toggles for all gain factors, and a "stiffness trigger" to allocate force control over the stiffer component of the cap/wall system. As described in section 3.1.4, the total force on the caisson is kept constant by feedback control on either the caisson cap or wall, depending on the relative stiffness of the system. For minimal wall penetration into the clay (<1 cm), the primary transducer is the cap force, as the cap has a stiffer response than the wall. If the wall has penetrated more than 1 cm, the feedback control is based on the wall force. The final improvement to HOLDSTS came following CET-9. In order to maintain zero relative displacement control during sustained tensile loading, an integration term was added to the original proportional term for the command signal (see section 3.1.4).

Major modifications were made to the pullout algorithm, MONPULL. During CET-3, constant control signals were sent to the cap and wall driving systems to withdraw the caisson at a constant predetermined rate. These signals were calculated based on the stiffness of each actuator, which was determined during proof testing, and were not changed throughout pullout. Due to the difference in actuator stiffness between proof testing and actual test conditions, the caisson wall and cap were not pulled at identical rates and a relative displacement developed. This problem was reduced significantly in tests CET-4, 5 by performing feedback control using a proportional term for the cap displacement rate and both proportional and integral terms for the relative displacement. While the target relative displacement is 0.001 cm, this modification improved the relative displacement during the first 0.01 cm of pullout from 0.1 cm in CET-3 to 0.01 cm in tests CET-4 and 5. With the addition of compression springs to reduce actuator compliance (see section 4.1.3), the relative displacement during the first 0.01 cm of pullout was reduced to less than 0.003 cm in CET-6.

4.1.5 Instrumentation Improvement

Inadequate time response and total stress sensitivity of the stainless steel probes used to measure pore pressures within the clay necessitated several probe modifications following CET-1. Figure 4.5 shows the probes used for CET-1 through CET-5. The probes did not respond as expected during the pullout phase of CET-1. This behavior may have been associated with soil forming a plug at the tip of the needle (and, hence, causing the probe to act as a total stress

sensor). Better response during CET-3 was achieved by crimping the tip of the probe, such that the aperture diameter decreased from 0.023 cm to 0.011 cm. During CET-4, it was discovered that the Motorola transducers attached to the bottom of the needle probes were incompatible with liquid fluids; long term fluid contact caused unstable voltage output due to diffusion of water through the gelatin seal used to protect the electronics. For CET-5 the probes were redesigned to fit much larger, water-compatible transducers (Data Instruments). These showed excellent response when tested in water, but when placed in clay, the probes responded very sluggishly. As described in section 4.6.2, the poor response of the probes in CET-5 prompted a lengthy theoretical and experimental study of the design of pore pressure probes. For CET-6, 20 micron porous stones were press-fitted within the 0.023 cm diameter probe tip to prevent soil plugging and one Data Instruments transducer was replaced with a less compliant Cooper transducer. Research involving testing the probes in triaxial clay specimens revealed that the Cooper probe responded 70 times faster than the Data Instruments probe. Following CET-6, the remaining two Data Instruments transducers were replaced with Kulite transducers. The Kulite transducers responded 140 times faster than the Data Instruments transducers.

Sluggish response of the cap pore pressure sensor in CET-1 was attributed to inadequate saturation of the pore pressure stone, while the pressure transducer failed during equipment setup in CET-3. For CET-4 through CET-14, good pore pressure response was achieved by fitting the cap with a new Data Instruments transducer and using a reliable pore pressure stone saturation technique (see section 3.3.3).

The final instrumentation improvement was the addition of a fifth clay surface displacement transducer prior to CET-4. As discussed in section 3.1.5, an elbow extension on the LVDT core at the fifth radial location enabled measurements close to the caisson wall (r = 4.2 cm).

This section focused on the development of the caisson element test (CET) apparatus throughout the testing program. In the following sections, 4.2-4.6, the CET cell is evaluated as it exists following all of the improvements discussed above in section 4.1.

4.2 CONSOLIDATION CHAMBER

Evaluation of the CET cell begins with the consolidation chamber, which has two main areas of concern: 1) the effect of the rigid wall boundary during installation, set-up, and axial tensile loading, and 2) the ability of the cylindrical slip ring assembly to prevent air leaks, encourage surface drainage, and allow caisson passage.

4.2.1 Boundary Total Stress

Ideally, the rigid-walled cylindrical chamber that contains the clay cake should be large enough so that penetration and pullout behavior of the model caisson is not affected by the proximity of the rigid boundary. Measurements of total stress on the chamber sidewall during CET-6 indicate that the model caisson events in the clay cake did cause total stress changes at the boundary. Figure 4.6 shows a cross section of the consolidation chamber for CET-6 with the total stress transducer on the rigid boundary. Note that the total stress[2] was measured on the sidewall approximately 11.7 cm above the rigid porous bottom plate and 2 cm below the clay cake surface prior to caisson installation.

Figure 4.7 shows the horizontal total stress record for all five phases of CET-6: suction installation, post-installation equilibration, monotonic pullout 1, re-equilibration, and monotonic pullout 2. Prior to installation, the horizontal total force is σ_h = 0.27 ksc[3]. After the caisson wall has penetrated z_w = 5.1 cm, the total force increases slightly by $\Delta\sigma_h$ = 0.025 ksc to reach σ_h = 0.295 ksc. During the subsequent equilibration phase, the horizontal total force falls back to approximately σ_h = 0.26 ksc. This suggests that the slight total force buildup during penetration is due to a positive change in excess pore pressure, which dissipates during equilibration at this boundary location. It is important to note that the 'cycling' pattern measured by the total force sensor (approximately 3.5 cycles per 1cm during penetration) is caused by the cycling air pressure, which is applied to the surface of the clay cake. In Figure 4.8, which presents the air pressure record for all five phases of CET-6, it is apparent that although cycling exists throughout the test, cyclic magnitude is small (P_a = 0.75±0.02 ksc).

During both phases of monotonic pullout, the horizontal total force decreases by approximately $\Delta\sigma_h$ = -0.04 (from σ_h = 0.265 to 0.225 ksc during pullout 1 and from σ_h = 0.25 to 0.21 ksc during pullout 2). During the intervening re-equilibration phase, the total force rises to nearly σ_h = 0.34 ksc before falling to σ_h = 0.25 ksc. As with installation, this behavior suggests that pullout and the initial portion of re-equilibration induce at the chamber sidewall a slight excess pore pressure, which dissipates by the end of re-equilibration.

A comparison of the total stress decrease $\Delta\sigma_h$ = -0.04 ksc) with the induced excess pore pressure within the soil plug (Δu < -0.4 ksc, see Figures 5.71, 5.144) shows that the total stress

---

[2]Total stress was also measured in CET-1 and 2, but severe problems during these tests preclude a presentation of total stress measurements (see section 5.1).

[3]Assuming there is no excess pore pressure and the clay cake has a uniform vertical effective stress prior to installation, then the horizontal effective stress is σ'_h = 0.27 ksc and the vertical effective stress is σ'_v = 0.75 ksc, which yields a lateral stress ratio of K = 0.36.

decrease is less than 10% of induced negative excess pore pressure within the caisson[4].

4.2.2 Cylindrical Slip Ring Assembly

The slip ring assembly is comprised of a drainage filter, rubber membrane, inner membrane slip tube, and outer membrane slip ring (see section 3.1.1). Evaluation of this assembly centers on its ability to maintain total stress without air leaks, allow clay surface drainage, and permit caisson passage.

Air leaking from the pressurized chamber cavity through the slip ring assembly prevents the complete dissipation of positive excess pore pressure within the clay cake, de-saturates the clay cake, and potentially dries out the clay cake surface. Hence, constant vigilance was necessary throughout the testing program. Air leaks were detected in tests CET-1 through CET-6 by a combination of one or more of the following signs: slight rise in clay cake pore pressure[5], audible bubbling noise emitting from the annulus between the inner slip tube and caisson wall, and visible air bubbles emanating from the surface drainage collected in the slip tube/caisson wall annulus and from the drainage port connected to the clay cake bottom. Figure 4.9 shows the air leak path, which starts from the pressurized chamber, and penetrates through the slip ring assembly at the following locations: a) between the side of the outer slip ring and the chamber sidewall, b) between the rubber membrane and the bottom of the outer slip ring, and c) between the rubber membrane and the bottom of the inner slip ring. Once the air has penetrated the slip ring assembly, the air travels radially beneath the rubber membrane to the annulus between the inner slip ring and the caisson wall. The air then rises vertically in the annulus and into the atmosphere. As described in section 4.1.1, modifications to the slip ring assembly blocked these air leak routes; tests CET-7 through CET-14 showed no overt signs of air leakage.

The slip ring assembly was designed to permit free drainage through the surface of the clay cake. Analysis of the consolidation results from the first test CET-1 revealed that the drainage rate through the slip ring assembly was slower than the drainage rate through the rigid top cap used in standard RBBC consolidation (Whittle and Germaine, 1993). Attempts to improve the drainage through modification of the slip ring assembly following tests CET-3 and 6 (see section 4.1.1) proved futile. Figure 4.10 shows the time curves (vertical strain vs. log time) for consolidation in the CET apparatus during the load increment from σ'_v = 0.67 to 0.73 ksc for

---

[4]A comparison of boundary total stress versus near-caisson excess pore pressure during installation is precluded by the countering effects of cap suction and wall penetration.

[5]The pore pressure rise due to air leaks never exceeded Δu = 0.05 ksc.

tests CET-3-14[6]. An increase in the rate of compression would reflect improved drainage, but Figure 4.10 clearly shows that the compression rate is quite variable and did not increase following slip ring assembly improvements (e.g., at a vertical strain of $\varepsilon_v = 0.3\%$, the elapsed time ranges from $\Delta t = 50$ to 800 minutes). The drainage rate variability indicates that there are other obstacles preventing free surface drainage. Note that the only serious consequence of slower drainage rates is increased consolidation times.

The last slip ring assembly function subject to evaluation is the ability of the assembly to allow vertical passage of the caisson wall into the clay cake. As shown in Figure 4.3, the inner slip ring provides the caisson wall with central vertical access to the surface of the clay cake while acting as a barrier to the pressurized air cavity. The upper 17.5 cm of the slip ring has an inside diameter of 5.35 cm to allow easy caisson access during CET apparatus setup. However, over the bottom 0.5 cm, the inner diameter narrows from 5.35 to 5.1 cm in order to minimize the annular clearance (0.01 cm) between the slip ring and the caisson wall. Throughout caisson testing, the clay surface at this annular gap is exposed to the atmosphere and must rely on soil arching for stability. It is likely that during the testing phases, some soil may extrude into the annular gap between the wall and ring and henceforth introduce a frictional component to the wall force. The subjects of soil arching and wall/ring friction are discussed further in the next section (4.3). As mentioned in section 3.1.1, inner slip ring allowed adequate caisson passage in all tests except two. During penetration in CET-2, the wall caught the inner lip at the bottom of the ring and destroyed the slip ring/membrane connection; the inside bottom lip of the inner lip ring was tapered for all subsequent tests (see Figure 4.3). In CET-7, the caisson wall was not concentric within the inner ring, but was in contact with the inside bottom edge of the ring; in the tests following CET-7, shims were used to ensure concentric wall placement prior to installation.

4.3 MODEL CAISSON

The unique design of the two-component model caisson and its position relative to the inner slip ring leads to two major areas of concern: 1) the stability of the soil surface through soil arching between the cap and wall and between the wall and the inner slip ring, and 2) friction arising between the wall and inner slip ring and between the cap and wall.

4.3.1 Clay Surface Stability Through Soil Arching

Figure 4.11 shows the clay cake surface with the slip ring assembly and model caisson in

---

[6]During consolidation in the CET apparatus, a very low load increment ratio (LIR = $\Delta\sigma_v/\sigma_i = 0.1$) was used to prevent soil extrusion, and little or no secondary compression was allowed in order to expedite testing (see section 3.3.3)

position just prior to the penetration phase. There is an annular gap of 0.07 cm between the cap and wall and an annular gap of 0.01 cm between the wall and inner slip ring. Since the clay surface in these two gaps remains uncovered throughout model caisson testing, the surface stability must be maintained through soil arching. During the consolidation phase of the test, the slip ring assembly and model caisson apply a compressive total stress of σ_v = 0.75 ksc to the clay cake. Because of consolidation, the soil beneath the slip ring assembly, wall tip, and cap compresses in response to this load, but the soil directly beneath the annular gap is not contained and tends to yield upward. Hence, there is relative movement between the two soil masses. Excessive upward movement of the annular gap soil is opposed by shearing resistance in the zone of contact between the two moving soil masses. This leads to a transfer of pressure from the limited zone of upward yielding soil mass to the much larger zone of compressing soil. This transfer of pressure from the upward-yielding soil to the downward-yielding soil on either side is called the *arching effect* because the soil *arches* over the annular gap soil[7]. Stability of the annular gaps during other phases of the test (penetration, sustained load, monotonic pullout) also can be explained by the soil arching concept.

From visual observations made during and after testing, annular gap stability was only a problem for test CET-1. During consolidation in the CET apparatus, load was applied using a load increment ratio of LIR = 1. Excessive soil extrusion between the wall and inner slip ring (~0.6cm) and between the wall and cap (2cm) proved that the load increment ratio was excessively large as the clay cake was consolidated into the virgin compression zone (σ'_v = 0.5 to 1.00ksc). Thereafter, for tests CET-2-14, the load increment ratio was lowered to LIR = 0.1. In these tests there was no soil extrusion between the wall and inner slip ring and only minimal extrusion (1-3 mm) between the wall and cap.

4.3.2 External and Internal Model Caisson Friction

During the model caisson test events, the proximity of the inner slip ring to the caisson wall and the connection between the cap and wall lead to frictional force contributions to the wall and cap force records. Figure 4.12 shows the clay cake surface prior to penetration in order to illustrate the four locations where friction arises: 1) metal-to-metal contact between the inner slip ring and the caisson wall, 2) extruded soil between the inner slip ring and the caisson wall, 3) extruded soil between the cap and wall, and 4) O-ring connection between the cap and wall. The first two sources of friction are 'external' and contribute force to both the wall and total force records. For CET- 3-14, visual inspection of the inner slip ring following the conclusion of each test verified that no soil had extruded between the inner slip ring and caisson walls; this source of

---

[7]This is an extension of the "soil arching" phenomenon defined by Terzaghi (1943).

external friction was considered insignificant. However, as mentioned in section 5.2.1, wall force records during wall penetration indicate the likelihood of metal-to-metal contact between the caisson wall and inner slip ring in tests CET-7 and 10. In these two tests, this external source of friction contributed 4-5 kg of friction to the wall force (see Figure 5.6).

The last two sources of friction are 'internal' and do not affect the total force. Internal friction contributes force to the wall force signature, which is balanced by an equal but opposite contribution to the cap force. The only caisson testing phases that are seriously affected by internal friction are: 1) consolidation, wherein soil may extrude between the cap and wall as the clay is loaded into the virgin stress range, and 2) caisson installation, during which the wall moves at a constant rate past the cap. Visual inspection of the model caisson following tests CET-3-14 revealed approximately 1 to 3 mm of extruded clay between the cap and wall. This amount of extruded clay contributes between 0.2 and 0.7 kg of friction to the wall and cap when the two components are in relative motion[8]. Following CET-2, proof testing revealed that the O-ring connecting the wall and cap contributed ±1 kg of internal friction[9]. The two sources of internal friction combine to contribute as much as ±1.7 kg to the wall and cap force records. As discussed in section 5.2.1, internal friction is the most likely cause of the 'transition zone' behavior during caisson installation.

4.4 DRIVING SYSTEM

Evaluation of the driving system centers on the ability of the mechanical driving subsystems (chamber air pressure, wall drive, cap drive) to respond to control signals sent by the computer. In these three driving subsystems, there is a certain amount of compliance, which delays the mechanical system response. As mentioned in section 4.1.3, compression springs maintained tension in the wall and cap ball screw actuators, and this eliminated much of the compliance in these two driving systems. Because the test material, normally consolidated RBBC, is a soft clay, exact determination of the small amount of remaining compliance was not necessary[10]. The total stress driving system had the relatively simple task of maintaining a constant air pressure in the chamber throughout testing; compliance in this system was insignificant and ultimately tempered by the total stress control algorithm, which is evaluated in the next section.

---

[8]The extruded soil resistance was computed by assuming an undrained strength ratio of K_o-normally consolidated RBBC in direct simple shear, $s_{uDSS}/\sigma'_{vc} = 0.2$ (Ladd 1991).

[9]Prior to CET3, the O-ring connection contributed as much as ±5 kg of internal friction (see section 4.1.2).

[10]Determination of compliance magnitude would be necessary for a stiff test material, such as highly overconsolidated RBBC.

4.5 CONTROL SYSTEM

The control system uses the four software algorithms[11] described in section 3.1.4, to manage the caisson test event sequence. This section presents quantitative evidence of the effectiveness of the algorithms in maintaining: 1) constant total stress on the clay surface throughout testing, 2) constant total force on the caisson during suction installation, 3) constant total force and zero relative displacement during equilibration and sustained loading, and 4) constant rate c: n withdrawal during monotonic pullout.

4.5.1 Constant Total Stress

For CET-2 through 14, the control system was able to maintain a constant total stress (air pressure) of $\sigma'_{vc} = 0.75 \pm 0.04$ ksc on the surface of the clay cake. As an example of a typical total stress record, Figure 4.13 shows the air pressure versus log of time for the installation, equilibration, and pullout phases of CET-8. Note that, with the exception of the initial portion of installation and pullout[12], the air pressure was maintained to within ±0.04 ksc of the target stress of $\sigma'_{vc} = 0.75$ ksc; this variation was acceptable for this testing program.

4.5.2 Constant Total Force During Installation by Underbase Suction

During suction driving, the wall penetrates at a constant rate, while increments of load are removed from the cap to balance load increments picked up by the wall. Hence, the total force ($F_{TOT} = F_w + F_c$) is maintained constant. Figures 5.4 and 5.5, which are discussed in section 5.2.1, depict the total force versus wall tip penetration for tests CET-3-12. With the exception of CET-3[13], the total force was held constant at or within 2 kg of the target value of $F_{TOT} = 15.2$ kg. This small variation, which can be traced to slight target adjustments in the control algorithm, indicates very good control.

4.5.3 Constant Total Force During Equilibration and Sustained Load

During the equilibration and sustained load phases of caisson testing, the control features are identical: a constant total force is maintained with zero relative displacement between the cap and wall. Measurements during equilibration for tests CET-4 through 14 indicate that within 3 minutes of the start of set-up, the total force reached the target of $F_{TOT} = 15.2$ kg and maintained this level to within ±0.3 kg for the remainder of equilibration (see Figure 5.40).

---

[11]CONS, HOLDSTS, SUCDRV, MONPULL

[12]Air pressure drifts slightly during the transition from one module to the next.

[13]Significant SUCDRV algorithm improvements were made following CET3 (see section 4.1.4)

Likewise for the sustained load tests (CET-9-14), the target tensile load levels, which ranged from F_{TOT} = -2.2 to -12.9 kg, were held to within ±0.3 kg (see Figures 5.93-5.98).

Zero relative displacement control was excellent for both equilibration and sustained load phases. Cap and wall displacement measurements indicated that the relative displacement was no more than ±0.0015 cm. However, because these phases usually required at least 24 hours to completion, electrical power surges occasionally disrupted the otherwise tight displacement control[14].

4.5.4 Constant Rate Withdrawal During Monotonic Pullout

The key measurement to evaluate the effectiveness of constant rate withdrawal during monotonic pullout is relative displacement between the cap and wall. As described in section 3.1.4, during pullout the control algorithm sends a constant signal to move the wall at a constant rate and continually controls the cap rate to match the wall rate; ideally, there should be no relative displacement between the cap and wall, as the caisson moves upward as one monolithic unit. Following extensive driving and control system improvements (see section 4.1.3 and 4.1.4), measurements revealed that the relative displacement was less than ±0.003 cm for tests CET-6-14. Considering the relatively high stiffness of the caisson/soil system at the start of pullout[15], this low relative displacement represents excellent control.

4.6 INSTRUMENTATION

For each caisson element test, an array of up to 14 measuring devices collected data. Five 'primary transducers' (chamber air pressure, caisson wall force and displacement, and caisson cap force and displacement) served a dual purpose by providing data for the control system and for test interpretation, while the remaining sensors (cap pore pressure, clay cake pore pressure, and clay cake surface displacement) monitored parameters of interest that affect the caisson and clay performance during a caisson element test. All instrumentation was checked to ensure proper resolution and precision for the testing program[16]. In addition, each sensor was calibrated for accuracy. Section 3.1.5 described the physical characteristics, function, and location of this instrumentation. This section briefly evaluates the accuracy of the instrumentation. Section 4.6.1 covers the primary sensors and the clay surface LVDTs, section

---

[14]Electrical surges during some tests caused a relative displacement of no more than ±0.01 cm, after which excellent relative displacement control resumed.

[15]Figure 5.60 plots the total force vs. wall tip displacement during early pullout.

[16]Table 3.1 lists the instrumentation location, capacity, and precision for a typical caisson element test (CET10).

4.6.2 evaluates the pore pressure probes, and section 4.6.3 discusses the cap pore pressure sensor.

4.6.1 Primary Transducers and Clay Surface LVDTs

The accuracy of the caisson force and displacement transducer measurements is largely dependent upon the compliance of the cap and wall drivetrains. As described in section 3.1.3, the wall drivetrain comprises the ball screw actuator, the wall force transducer, an aluminum square plate, four steel rods, an aluminum circular drive plate, an aluminum cylindrical connector, and then the caisson wall itself (see Figure 3.9). Under a compressive load, all of these components will compress. The compliance is the amount of drivetrain compression for a given increment of compressive load (or the amount of extension for a given tensile load increment). This compliance introduces a bias in the wall force and displacement measurements during the various phases of model caisson testing. But because the test material (normally consolidated RBBC) was soft relative to the drivetrain compliance, this measurement bias remained insignificant. Compliance also is inherent to the cap drivetrain, but like the wall drivetrain, the measurement bias is very small. The fifth primary transducer, the chamber air pressure sensor, is located in the plate covering the consolidation chamber, directly measures chamber pressure, and, therefore, does not suffer any loss of accuracy.

The clay surface LVDTs have moving cores that rest directly on the rubber membrane, which covers two thin filters that overlie the soil surface (see section 3.1.1). Because the rubber membrane and filter system have a very thin combined thickness (< 0.07 cm), compliance is not a problem, and, therefore, the surface displacement measurement accuracy is not seriously compromised.

4.6.2 Pore Pressure Measuring Devices

As described in section 4.1.5, following CET-5, the pore pressure probes were redesigned to fit water-compatible transducers (Data Instruments) and showed excellent time response when tested in water. Experiments were then performed with the probe penetrated into a triaxial specimen. Measurements in a free-draining fine sand showed that the probe was insensitive to changes in total stress. However, when placed in clay, the probe responded sluggishly. This prompted a major theoretical and experimental study of the design of pore pressure probes to understand the factors that contribute to probe response and to determine exactly what type of probe would be required to accurately measure pore pressure changes during a caisson element test. The physical characteristics of the latest generation CET pore pressure probe, which consists of a Kulite pressure transducer, a transducer block, and a stainless steel tube, were presented in section 3.1.5. The time response study evaluated three different transducers with different transducer face diameters and deflections (Data Instruments, Cooper, and Kulite

transducers). Table 4.2 lists the physical characteristics for each of these sensors.

Probe Response in Water

To gauge the effectiveness of the saturation procedure and to obtain values for comparison with the probe response in soil, the probe response in water was investigated first. A theoretical time response equation was developed for a saturated pore pressure probe subjected to a unit step pressure increase by Henderson (1994):

$$\frac{Po}{Pa} = (1 - e^{-bt}) \quad ; \quad b = \frac{kA}{\gamma_w LM} \tag{4.1}$$

where: P_O = probe output pressure

P_a = applied pressure

t = time

k = probe tip hydraulic conductivity

A = probe tip cross-sectional area

γ_w = unit weight of water

L = probe tip length

M = probe system compliance

This equation was used to calculate the time response of the three different probes used in this study. Figure 4.14 shows the theoretical time response in terms of pressure normalized by the step increase versus time. The Kulite has the fastest predicted response, registering 95% of the applied pressure within 0.0008 sec. The Cooper registers 95% within 0.004 sec., while the Data Instruments registers 95% within 0.17 sec. All the variables in the response equation are equal for the three transducers except M, the probe compliance. The greatest contribution to probe compliance is the transducer face compliance, which is due to the face deflection in response to a pressure change. The predictions show that the probe with the slowest response (Data Instruments) also has the greatest face deflection (see Table 4.2). Given equal probe geometries, the only factor other than compliance that could cause variation among the different probes is the hydraulic conductivity of the porous stone in the tip. The response time for each probe in water was measured by placing the probe into a sealed chamber of water, applying a step increase of pressure to the chamber water, and recording the pressure increase in the probe. Table 4.3 shows that the measured response times are slower than the calculated response times. Note that the Kulite and Cooper probes had response times that were quicker than the data acquisition system was able to record for a monotonic increase in chamber pressure. Therefore, a cyclic pressure was applied to these probes and the response time was based on the phase lag between the applied and measured cyclic pressures. Rigorous comparisons are only possible for

the Data Instruments probe and they show that the measured response is about twice as slow as the computed value. The shape of the measured response curve is similar to the calculated response curve, suggesting that the theoretical equation is reasonably accurate.

Probe Response in Soil

In order to validate the accuracy of pore pressure probe measurements during a CET test, it was necessary to test the probe response in soil under controlled conditions. A theoretical model was developed to calculate the response time of a probe inserted into the middle of a triaxial specimen of clay, which is then subjected to a hydrostatic stress increase. Based on closed form solutions for pore pressure probes with rigid spherical porous stones at the tip in an elastic soil (DeJosselin De Jong 1953; Gibson 1963; Kutter 1990), an equation was developed to model the three probes used in the water response tests. The calculated response for each of the probes is presented in Figure 4.15 for a given soil hydraulic conductivity, $k = 1 \times 10^{-7}$ cm/s. As for the response in water, the results show that for the given soil parameters, as the probe compliance increases, response time increases. The calculated response times at 95% of the applied pressure for the Kulite, Cooper, and Data Instruments probes are 1 sec, 5.1 sec., and 212 sec., respectively. Note that the Kulite, which is the least compliant, has the quickest response. Most importantly, though, the calculated probe response time in soil is more than three orders of magnitude larger than the response time in water. The effect of varying hydraulic conductivity on the Kulite response is shown in Figure 4.16. It is clear that the response time is proportional to clay hydraulic conductivity.

The measured response in clay was conducted as follows. The probe was inserted into a triaxial clay specimen, which was then hydrostatically consolidated to an effective stress of 0.75 ksc. Lastly, an increment of hydrostatic pressure was applied and the pore pressure response was measured in the probe and in the top of the specimen. Figure 4.17 shows the response time of all three probes. Note that the measured pressure increment never equals the applied increment (i.e., the normalized pressure never reaches 1), which is most likely due to system and soil compliance. The results confirm the theoretical predictions that the more compliant the probe, the slower the response. Note that the Kulite, Cooper, and Data Instruments probes measured 95% of the applied pressure within 5, 10, and 710 seconds, respectively. These response times are higher than the theoretical values (1, 5.1, and 212 seconds, respectively) by approximately the same ratio (see Table 4.3). Once again, the shape of the theoretical and measured curves are nearly the same. The difference in magnitude is likely due to uncertainty in soil parameters, namely soil hydraulic conductivity.

The results of this probe response study indicate that for the rates of caisson movement during the installation ($z_w/t = 0.005$ cm/s) and pullout ($z_w = -0.0005$ cm/s) phases of the CET

program, the Kulite and Cooper probes are sufficiently accurate, while the Data Instruments probe does not respond quickly enough to register accurate changes in pore pressure[17].

4.6.3 Cap Pore Pressure Sensor

There are three factors affecting the accuracy of pore pressure measurements directly beneath the caisson cap: 1) limited areal extent of sensor coverage, 2) susceptibility to cavitation, and 3) time response. As described in section 3.1.5, pore pressure beneath the cap is measured by a Data Instruments pressure transducer mounted directly behind a 0.93 cm thick ceramic porous stone with a porosity of 45% and a 1 ksc air entry pressure. The stone is set flush with the cap bottom surface, has a diameter of 2.2 cm, and represents 22% of the total cap area (see Figure 3.6). The fact that the stone *does not* cover the entire cap surface area introduces inaccuracy into the pore pressure measurement. Because the cap is rigid, the stress field directly beneath the cap will be nonuniform during the various phases of model caisson testing. Strictly speaking, therefore, pore pressure data measured by the cap sensor applies only to the zone directly beneath the porous stone and *not* under the entire cap surface.

Data indicated that cavitation occurred directly beneath the cap during installation by underbase suction in CET-1 and during monotonic pullout in CET-8. In CET-1, the pore fluid cavitated due to the large total stress (σ_v = 1.0 ksc) imposed on the clay cake[18]. In CET-8, it is suspected that the soil separated along the outside edge of the cap during later stages of pullout. This would reduce the soil/cap contact area and increase the tensile stress on the cap. A large enough increase in tensile stress on the center of the cap could cause the pore fluid to cavitate. A small amount of air trapped between the wall and cap could have encouraged soil separation at the outer edges of the cap. Hence for tests CET- 9-14, the cap/wall annular space was packed with lubricant to eliminate the air space. No cavitation was detected in these tests.

The final area of concern for the cap pore pressure sensor is its time response. Using the equations developed for the pore pressure probes described in section 4.6.2, the theoretical time response was calculated for the cap sensor in both water and soil (see Figure 4.18 and Table 4.3). When subjected to a step increase in stress in water, the cap sensor registers 95% of the applied stress within 0.32 seconds. Note that this is nearly twice as slow as the Data Instruments (D.I.) probe because the cap sensor has a porous stone with a different geometry and a lower hydraulic conductivity. However, in soil with a hydraulic conductivity of k = 1.4×10^{-7} cm/s, the theory predicts that the cap will measure 95% of the applied stress within 5.3 seconds, which is 36 times

---

[17]Only pore pressure data from Kulite and Cooper probes are presented in Chapter 5 (see section 5.1).

[18]A total stress of σ_v = 0.75 ksc was used in all subsequent tests.

faster than the D.I. probe. Even though the cap sensor and the D.I. probe both use a Data Instruments transducer, the cap sensor has a much quicker predicted response in soil because the porous stone has a much larger diameter ($D_{cap\ stone}$ = 2.2 cm, $D_{probe\ tip}$ = 0.058 cm), which allows a much larger pore fluid flow rate in response to a pressure change. As with the Kulite and Cooper pore pressure probes, the cap sensor time response is deemed rapid enough for the caisson movement rates encountered in the CET testing program.

Date	Test	CET Apparatus Component					Modification
		1	2	3	4	5	
		X	X	X	X	X	Original CET apparatus development
9-10-93	CET 1						
		X					Added cloth filter for radial surface drainage
			X				Removed taper to create blunt-tipped model
				X			Replaced hydraulic cap actuator with ball screw actuator for cap driving system
					X		Improved cap force control during HOLDSTS
						X	Crimped tips of pore pressure probe needles
2-22-94	CET 2						
		X					Tapered inside wall of inner slip ring
		X					Increased rubber adhesive to slip ring/rubber membrane connection to thwart air leaks
			X				Decreased O-ring squeeze between cap and wall
					X		Incorporated keyboard toggle to adjust cap force gain during HOLDSTS
					X		Improved cap force control during SUCDRV: initial control signal, feedback on wall force change and total force error
3-16-94	CET 3						
		X					Drilled two additional drain ports in outer slip ring to increase fluid flow
		X					Drilled two air leak relief ports in outer slip ring
		X					Re-machined slip ring assembly to prevent air leaks
					X		Improved cap control during MONPULL
					X		Improved cap control during SUCDRV
						X	Machined cap to fit Data Instruments transducer
						X	Added fifth radial position to LVDT bracket

CET Apparatus Component Key

1. Consolidation Chamber
2. Model Caisson
3. Driving System
4. Control System
5. Instrumentation

Table 4.1 CET Equipment Modification Chronology

Date	Test	CET Apparatus Component					Modification
		1	2	3	4	5	
7-26-94	CET 4						
						X	Fitted pore pressure probes with liquid-compatible Data Instruments transducers
8-18-94	CET 5						
				X			Machined new gears for cap and wall reduction gear box
				X			Incorporated tension springs for wall and cap actuators
					X		Improved HOLDSTS: continuous caisson control, keyboard toggles for all gain factors, relative cap/wall stiffness trigger
						X	Improved pore pressure probes: porous filter tips, replaced one Data Instruments with Cooper transducer
3-5-95	CET 6						
		X					Widened drain tubing diameter
		X					Replaced outer slip ring O-rings with X-rings
						X	Improved pore pressure probes: replaced two Data Instruments with Kulite transducers, researched probe response
6-7-95	CET 7						
		X					Incorporated shims to separate inside wall of slip ring from caisson wall
6-26-95	CET 8						
7-31-95	CET 9						
					X		Improved cap and wall control in HOLDSTS
8-28-95	CET 10						
9-19-95	CET 11						
10-23-95	CET 12						
						X	Added pore pressure probe with Kulite transducer
11-30-95	CET 13						
12-16-95	CET 14						

CET Apparatus Component Key

1. Consolidation Chamber
2. Model Caisson
3. Driving System
4. Control System
5. Instrumentation

Table 4.1 (cont.) CET Equipment Modification Chronology

Transducer Diaphragm	Kulite	Cooper	Data Instruments
diameter, cm	0.39	0.55	1.59
area, cm^2	0.12	0.24	1.98
thickness, cm	0.016	0.013	0.042
*deflection $cm^5 p_a(t)/N$	1.68×10^{-6}	8.92×10^{-6}	3.72×10^{-4}

*$p_a(t)$ = applied pressure

Table 4.2 Important Physical Characteristics of the Three Probe Transducers

*t_{95}, seconds	Pore Pressure Probes			Cap Sensor
	Kulite	Cooper	Data Instruments	
Theoretical in water	0.0008	0.004	0.17	0.32
Measured in water	<0.05**	<0.1**	0.6	†
Theoretical in soil ($k = 1.4 \times 10^{-7}$ cm/s)	1.0	5.1	212	5.6
Measured in soil	4	10	710	†

*t_{95}= time required for probe to reach 95% of applied pressure
**applied cyclic pressure and recorded phase lag
†cap sensor time response not measured

Table 4.3 Time Response to Applied Pressure of Pore Pressure Probes and Cap Sensor in Water and Soil: Theoretical vs. Measured Values

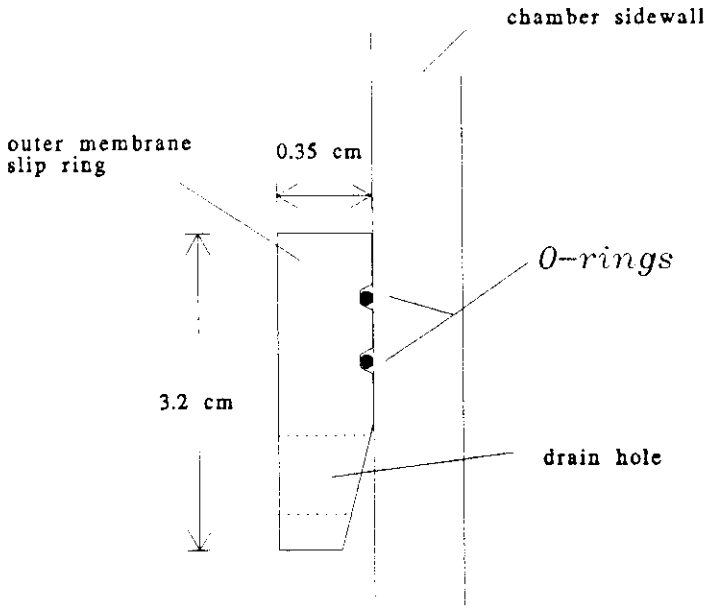

CET 1-6

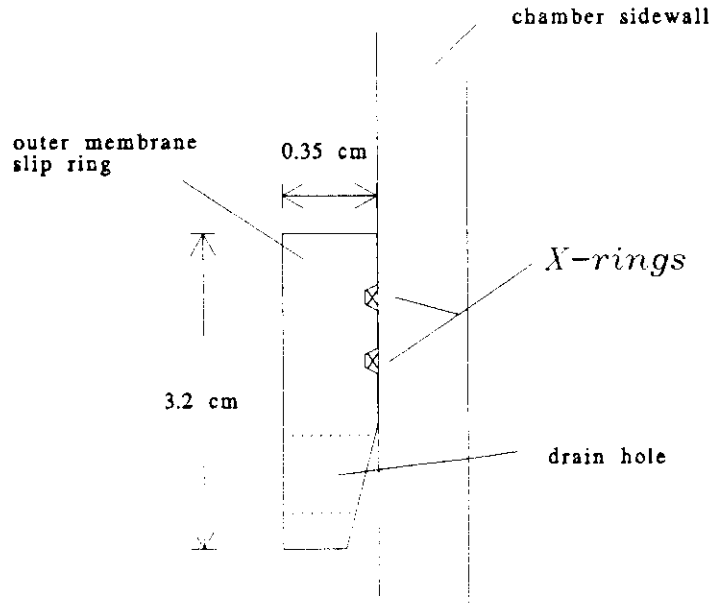

CET 7-14

Figure 4.1 Slip Ring Assembly Modification: Replacement of O-rings with X-rings in Outer Slip Ring to Prevent Air Leaks

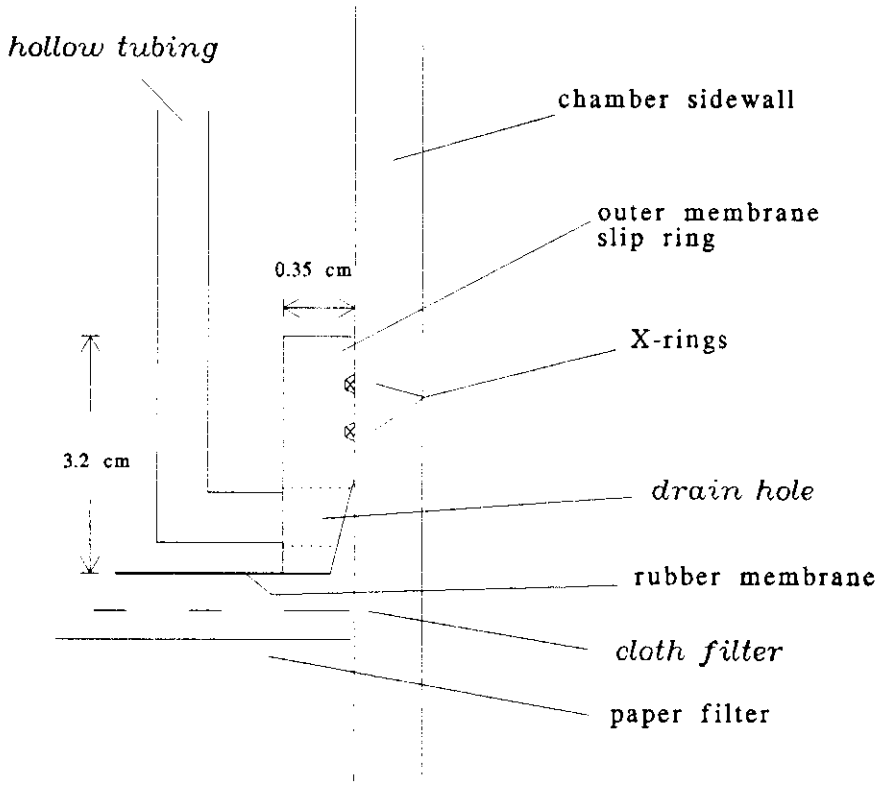

Surface Drainage Improvements

1. Added cloth filter (after CET1)
2. Increased drain ports from 2 to 4 (after CET3)
3. Widened drainage tubing (after CET6)

Figure 4.2 Slip Ring Assembly Modification: Three Surface Drainage Improvements

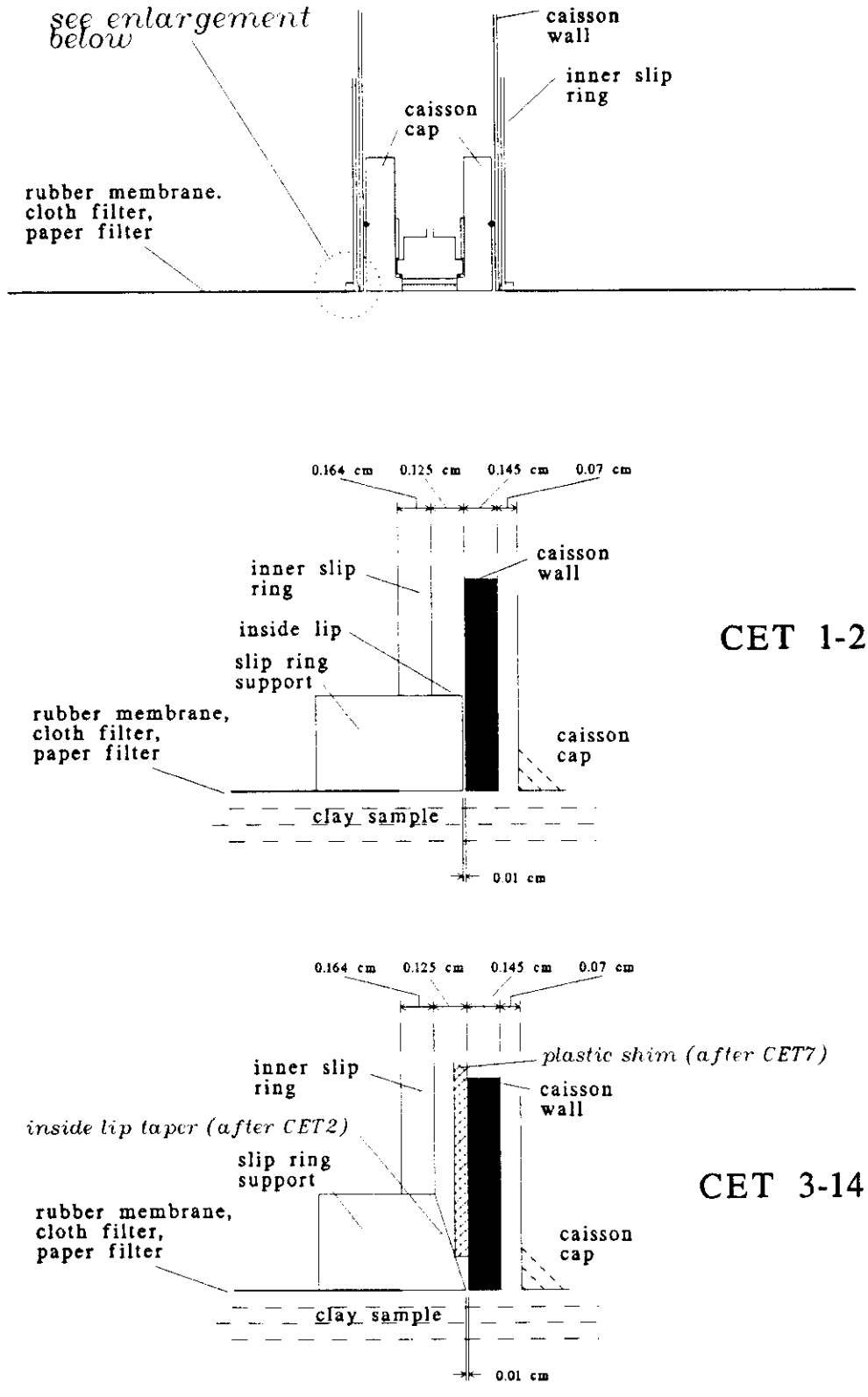

Figure 4.3 Slip Ring Assembly Modification: Two Modifications to Improve Caisson Wall Passage

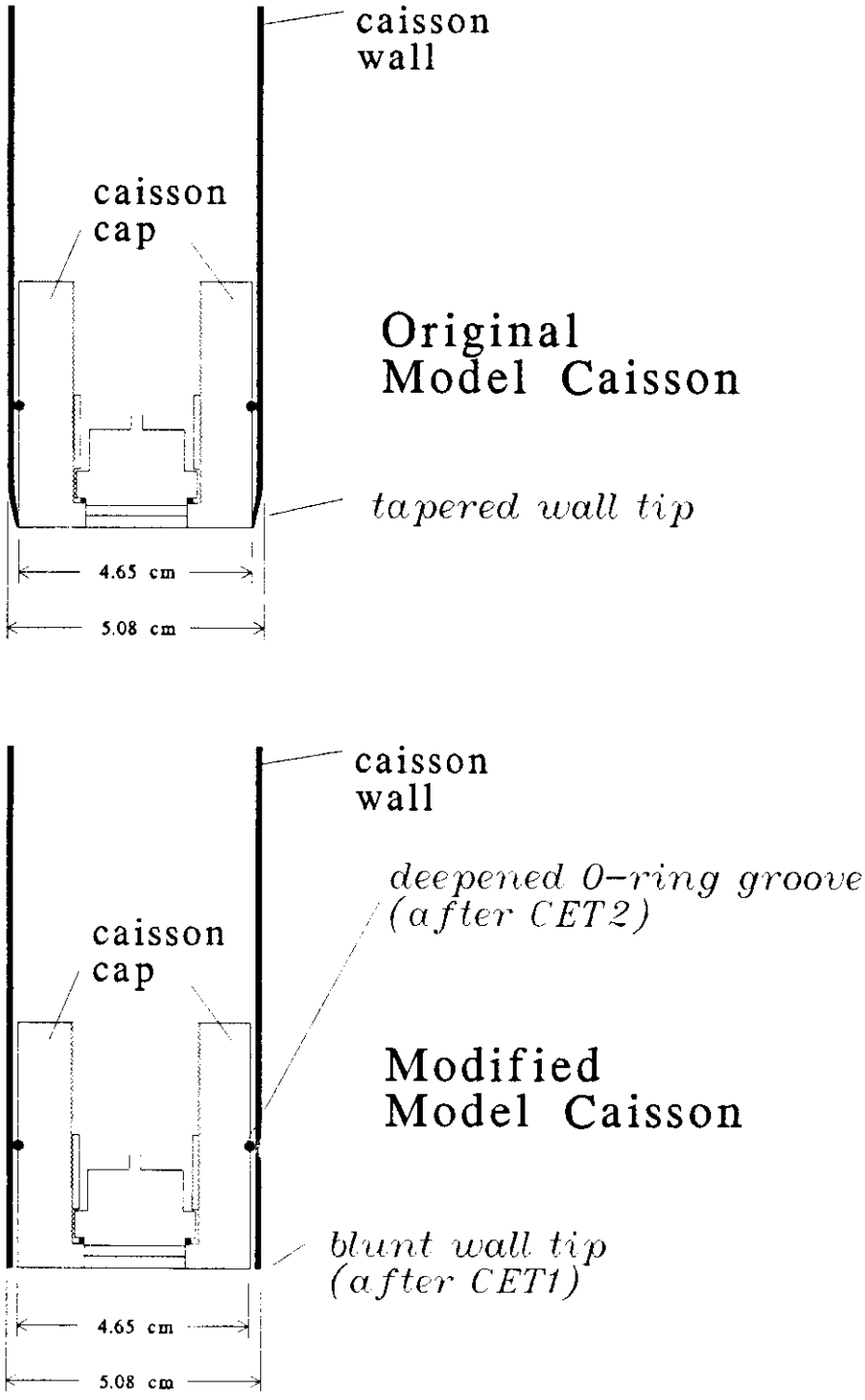

Figure 4.4 Two Model Caisson Modifications

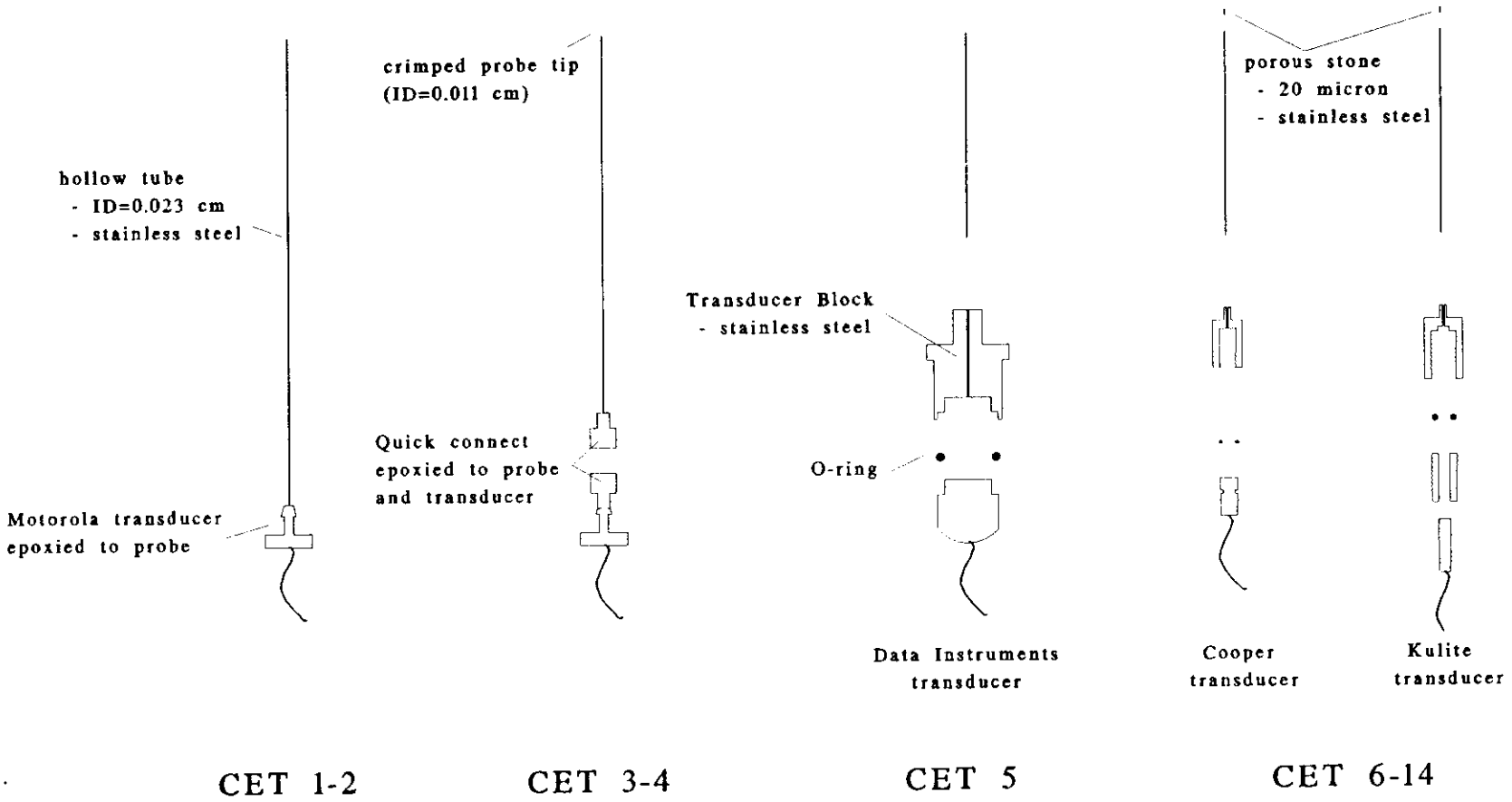

Figure 4.5 Pore Pressure Probe Development: Five Different Probes

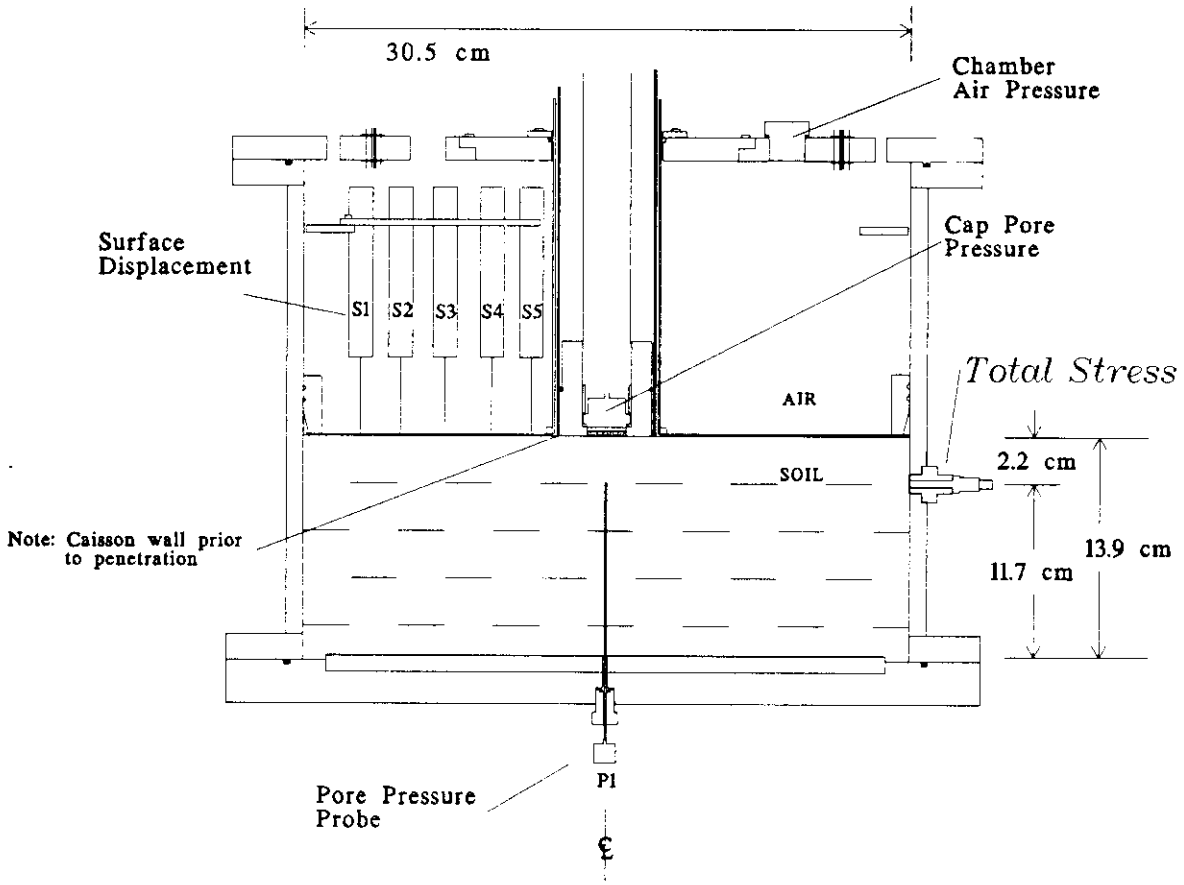

Figure 4.6 Cross-section of the Consolidation Chamber for CET6 Showing Instrumentation, Including Horizontal Total Stress Transducer

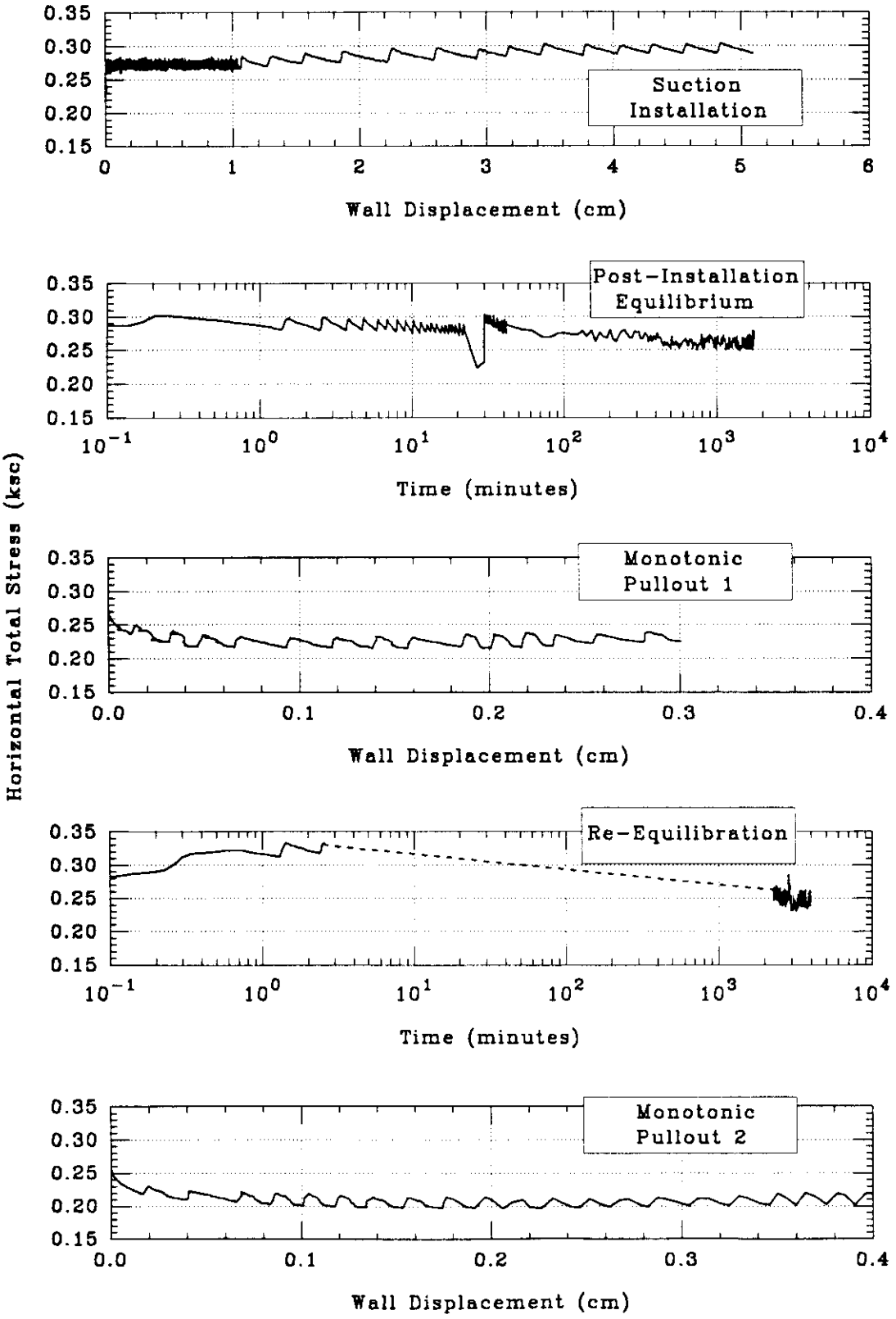

Figure 4.7 Horizontal Total Stress Record for Five Test Phases of CET6

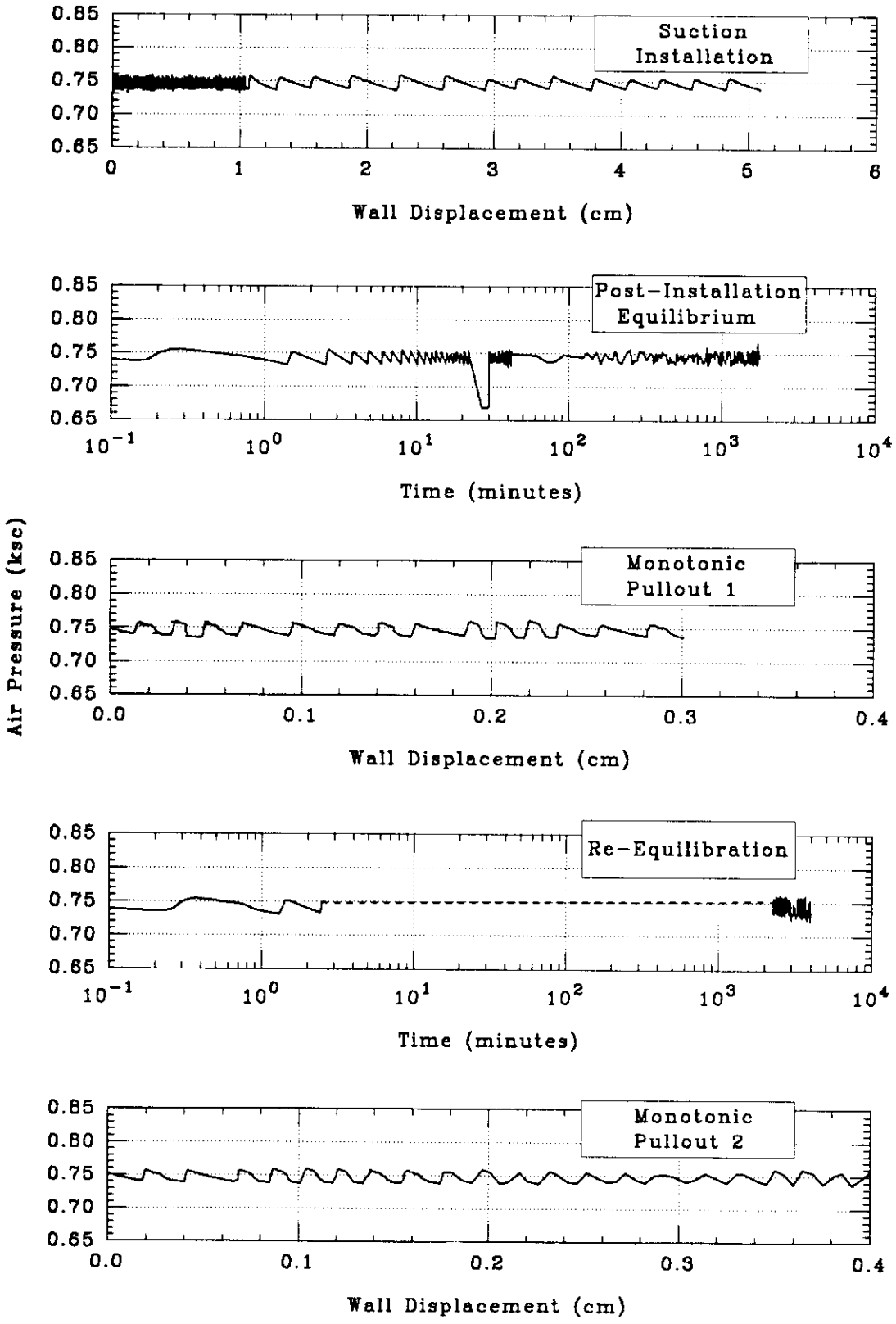

Figure 4.8 Chamber Air Pressure Record for Five Test Phases of CET6

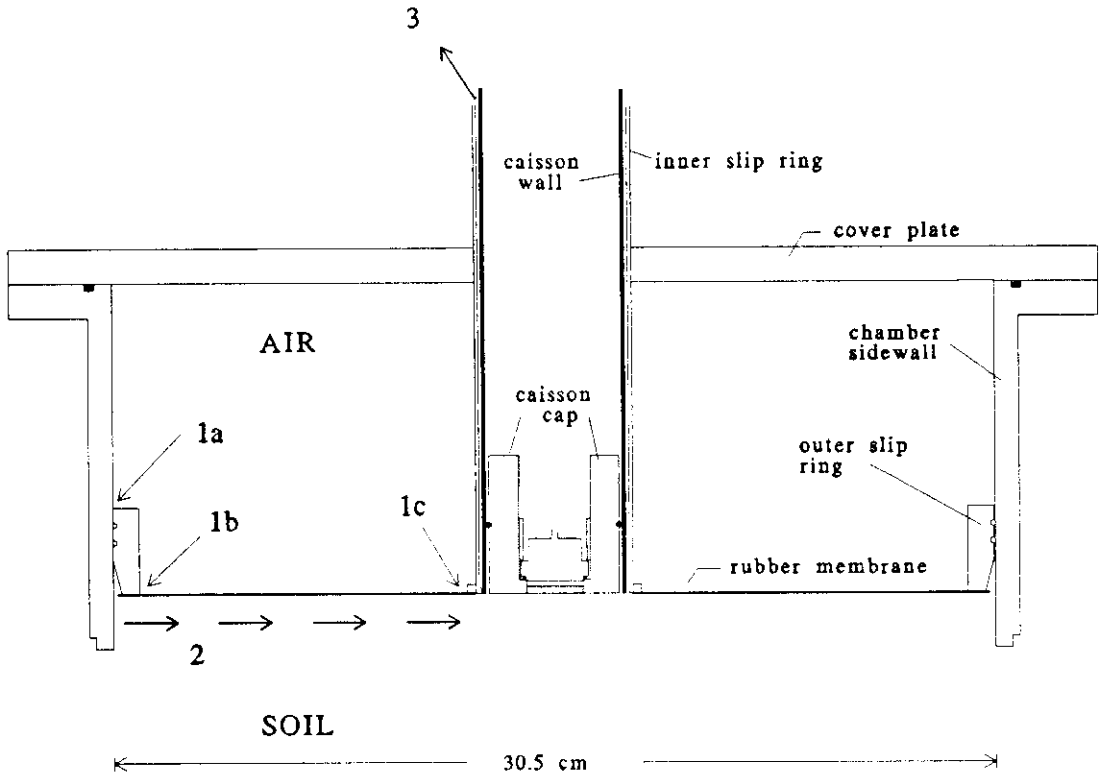

Slip Ring Assembly
Air Leak Path

1) From air chamber
   a) outer ring/sidewall
   b) outer ring/membrane
   c) inner ring/membrane
2) Beneath rubber membrane
3) Between inner ring and caisson wall
   to atmosphere

Figure 4.9 Air Leak Path Through Cylindrical Slip Ring Assembly

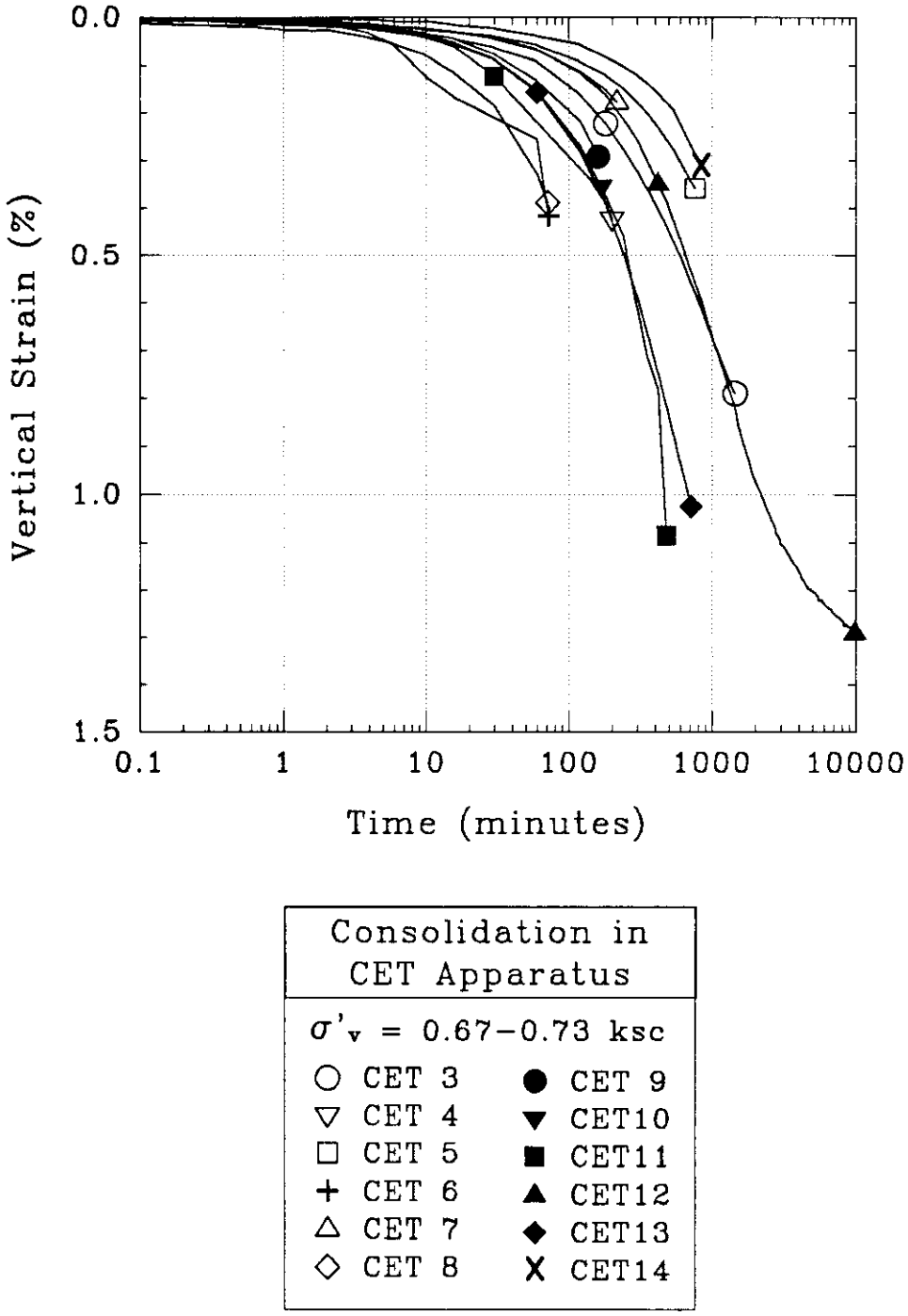

Figure 4.10 Time Curves (vertical strain vs. log time) for Consolidation in CET Apparatus During Load Increment from σ'_v=0.67 to 0.73 ksc for tests CET 3-14.

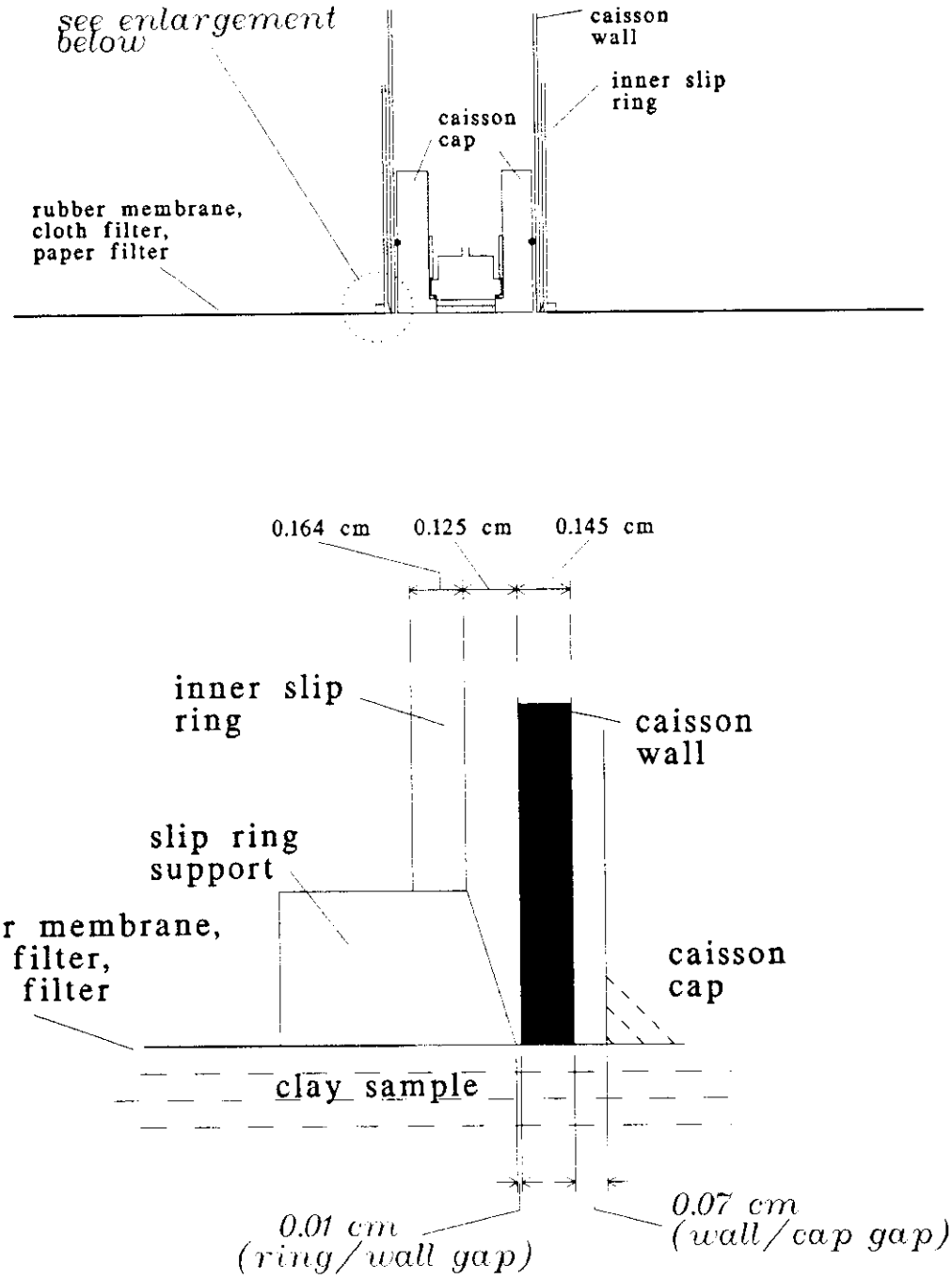

Figure 4.11 Slip Ring Assembly and Model Caisson in Position Prior to Wall Installation to Illustrate Annular Gaps Between Slip Ring and Wall and Between Wall and Cap.

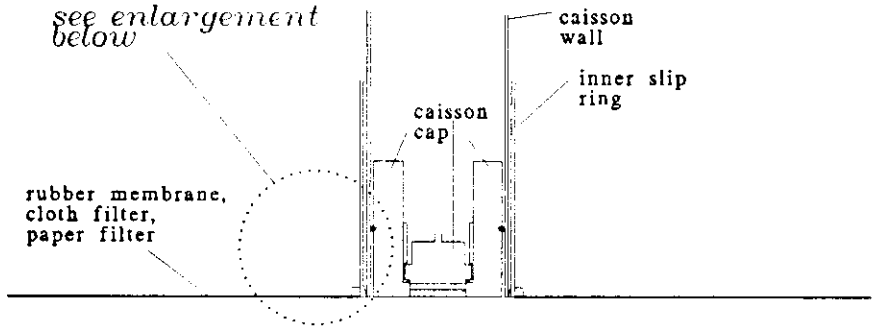

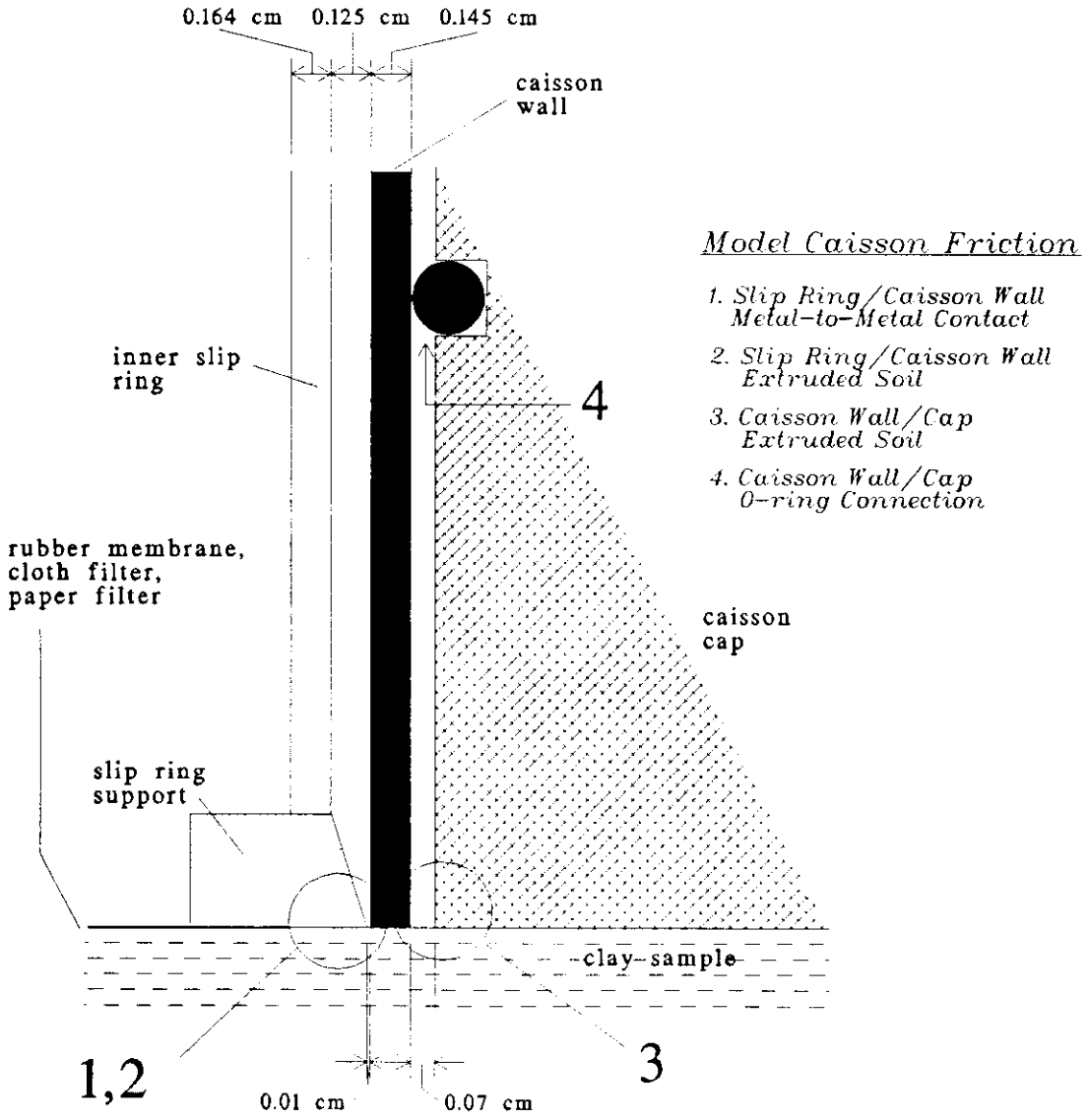

Figure 4.12 Slip Ring Assembly and Model Caisson in Position Prior to Wall Installation to Illustrate Four Locations of Model Caisson Friction

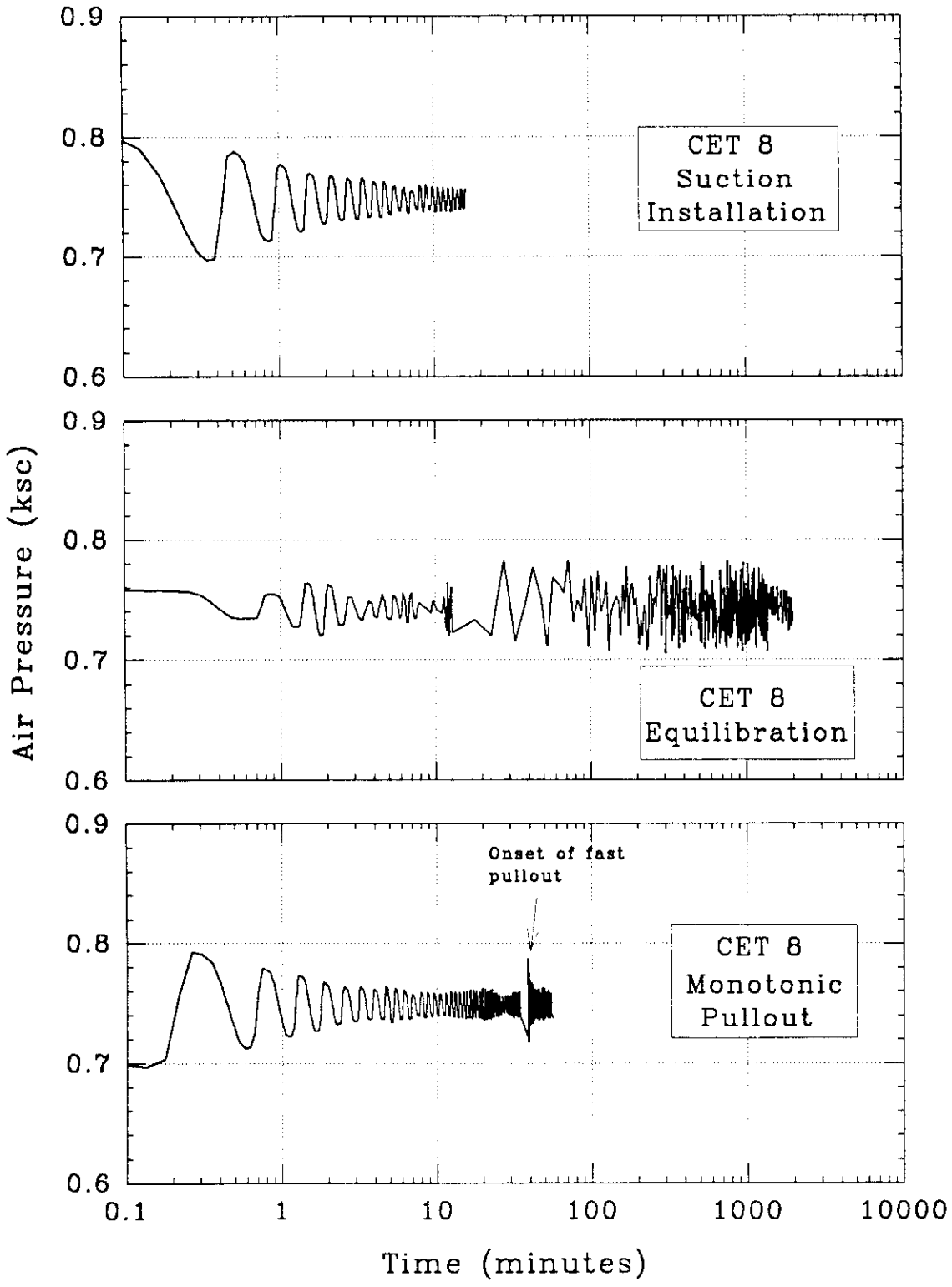

Figure 4.13 Chamber Air Pressure versus Log Time for Suction Installation, Equilibration, and Monotonic Pullout for CET8

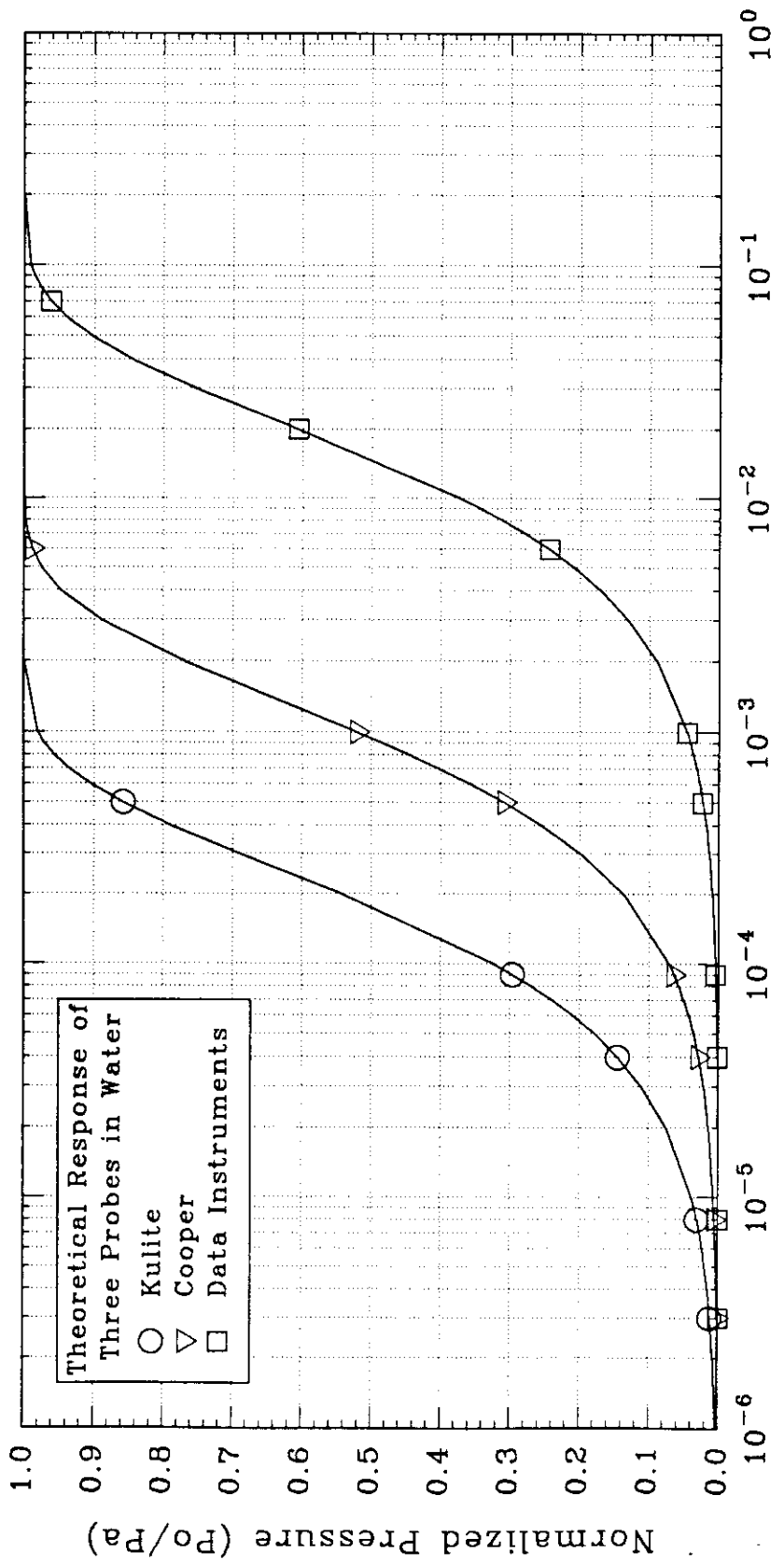

Figure 4.14 Theoretical Time Response of Three Pore Pressure Probes in Water

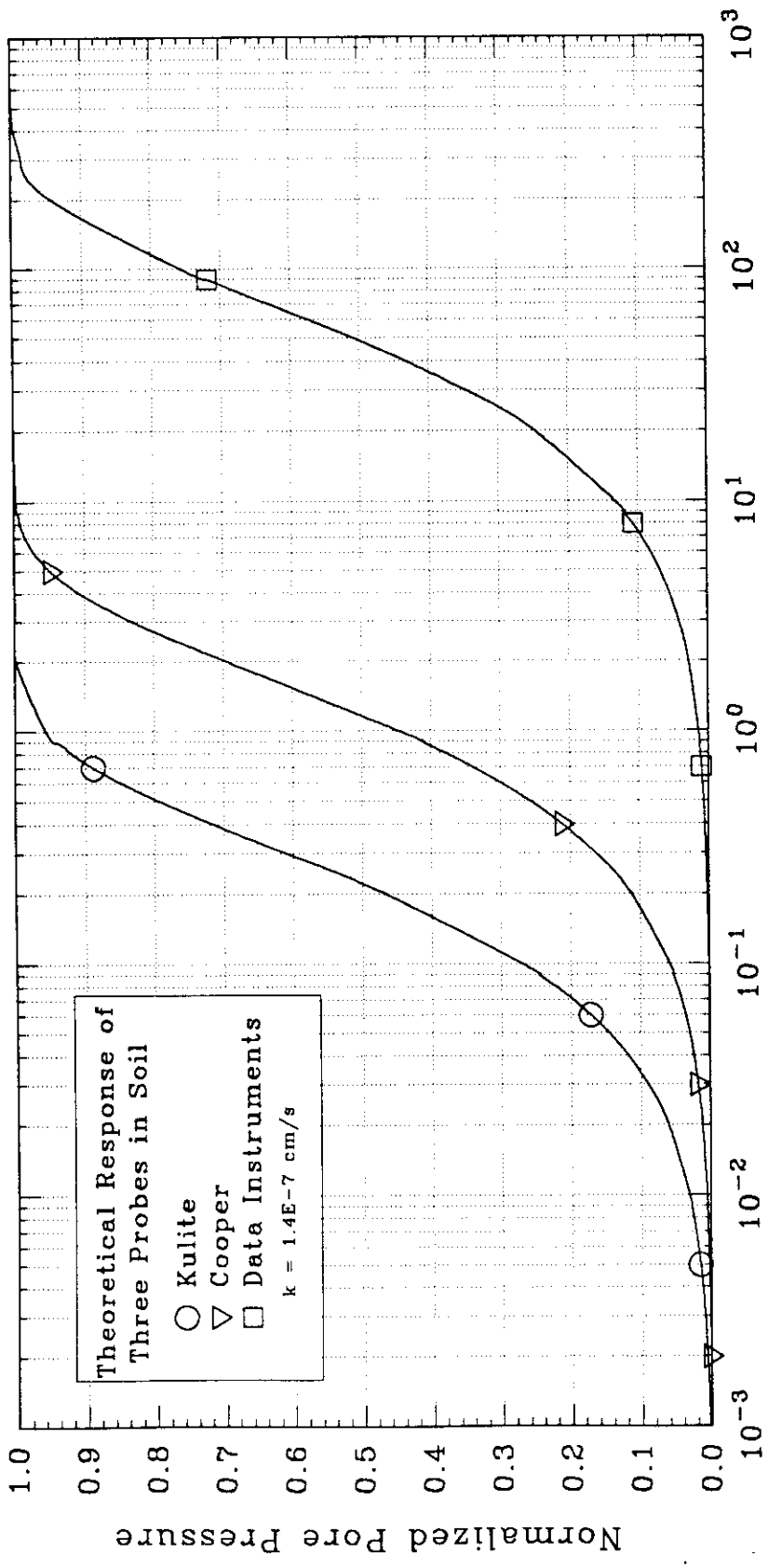

Figure 4.15 Theoretical Time Response of Three Pore Pressure Probes Inserted into a Triaxial Specimen of Clay

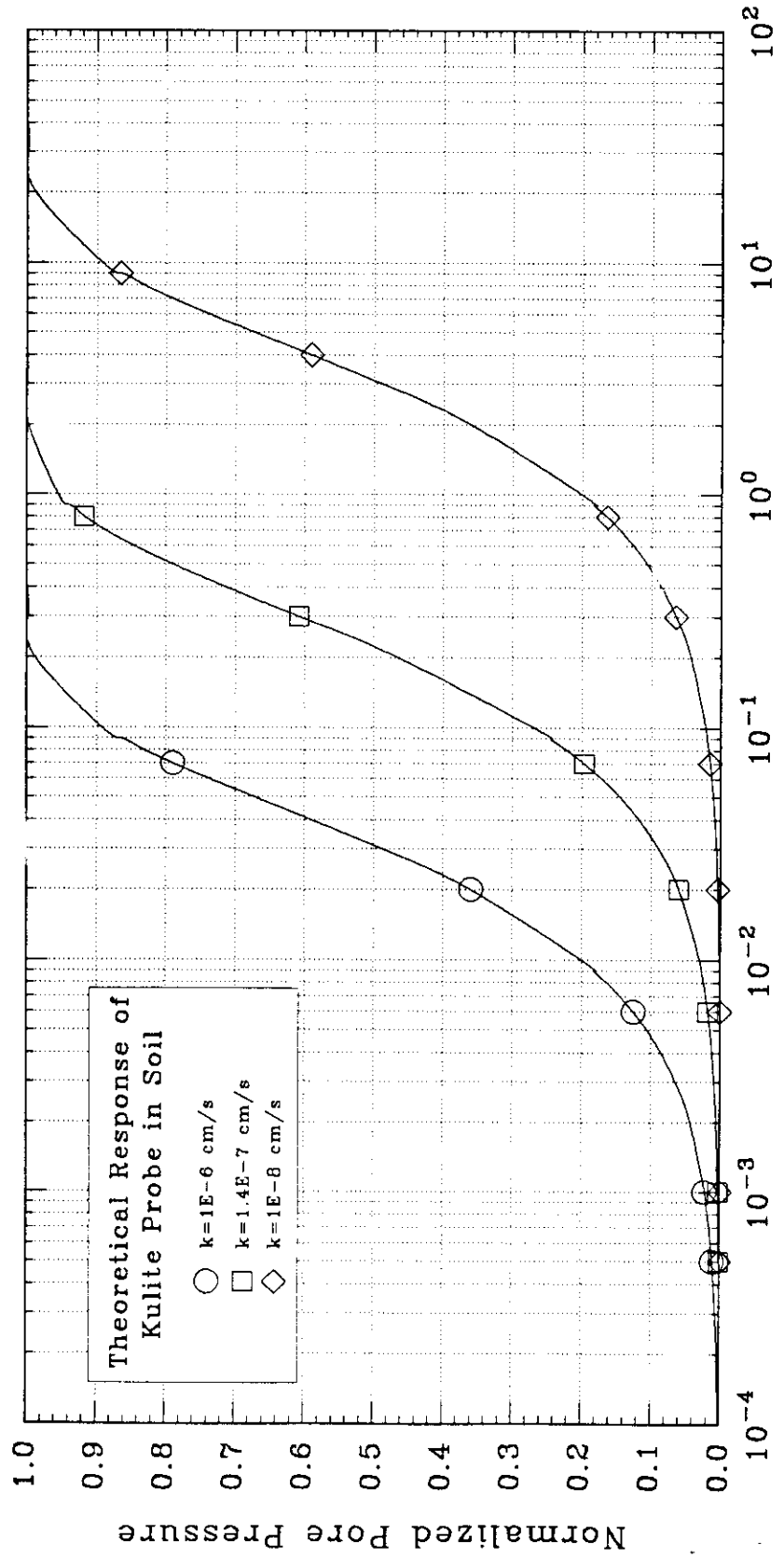

Figure 4.16 Theoretical Time Response of Kulite Probe Inserted into a Triaxial Specimen of Clay at Three Different Soil Hydraulic Conductivities

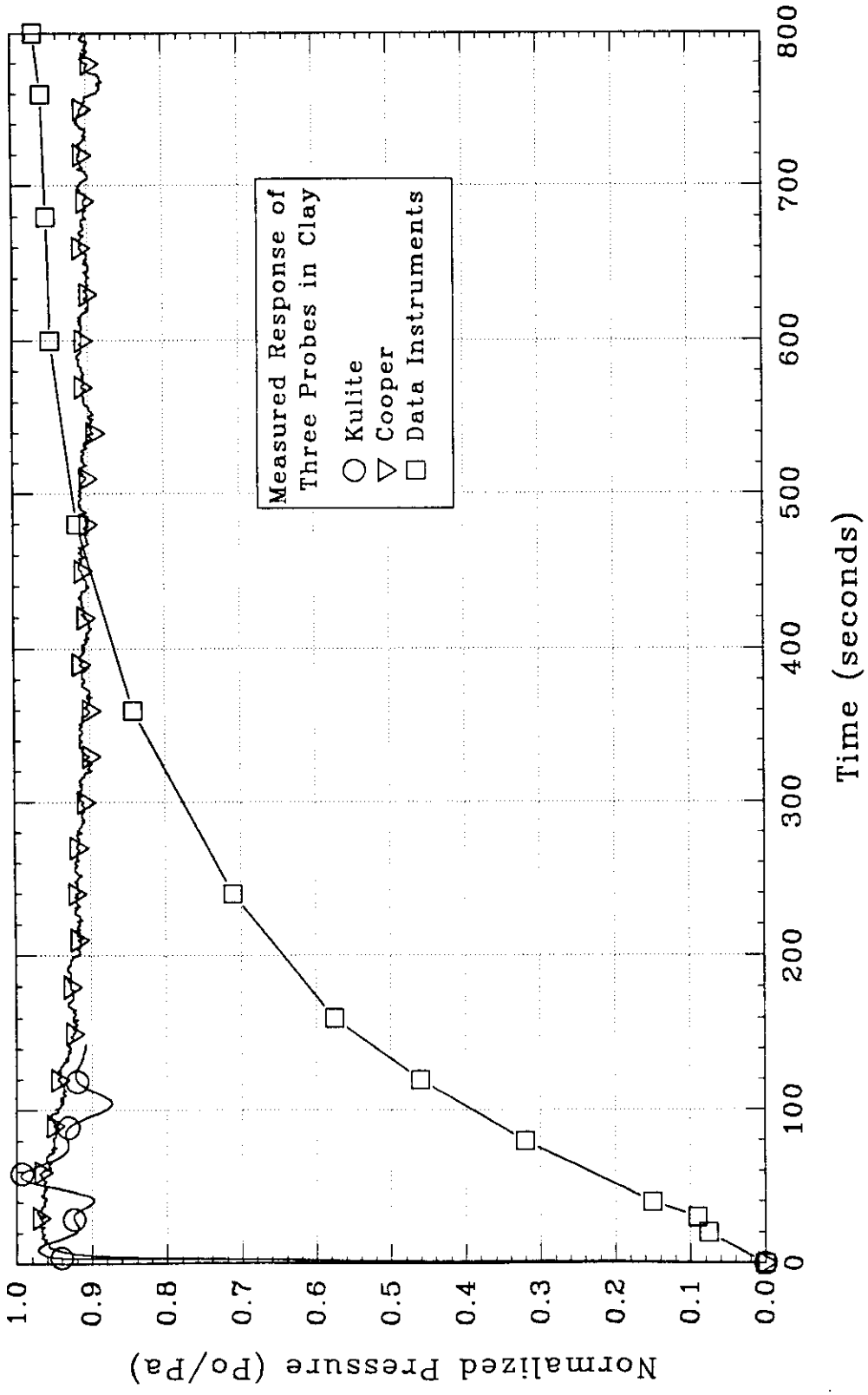

Figure 4.17 Measured Time Response of Three Probes Inserted into a Triaxial Specimen of Clay

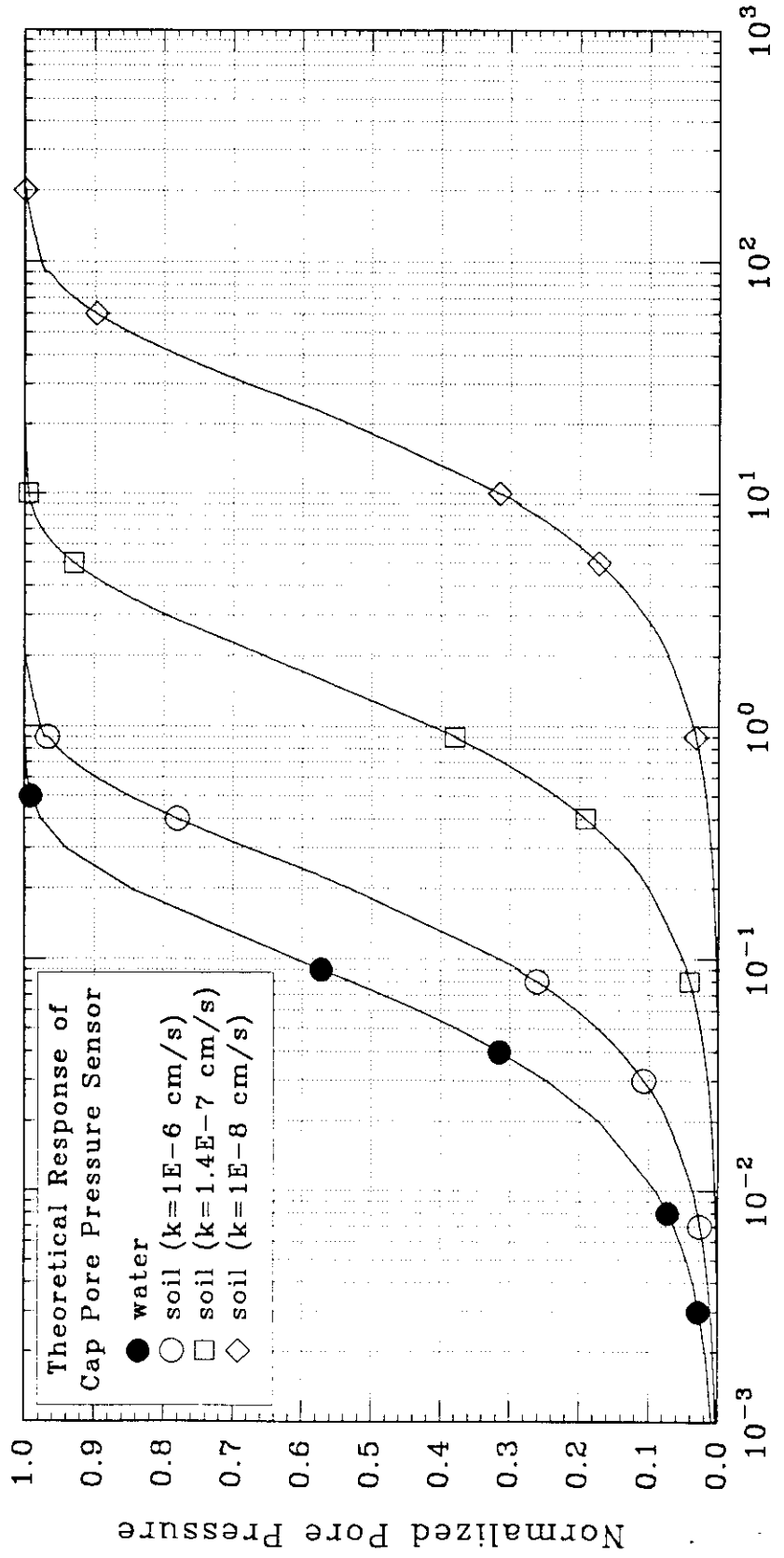

Figure 4.18 Theoretical Time Response of Cap Sensor in Water and Soil

5. RESULTS OF CET CELL EXPERIMENTS

This chapter describes the results of the testing program using the Caisson Element Test (CET) apparatus. The main objectives of the testing were to gain insight into the installation, set-up, and axial tensile loading of a suction caisson and to provide experimental data for comparison with analytical investigations. The tests were conducted in the CET cell, which simulates suction caisson behavior by using a miniature caisson installed in a uniform, saturated 'element' of clay (for a full description of the CET cell, see Chapter 3). The test program consisted of 14 tests and has yielded a tremendous amount of data regarding caisson performance. Most of the data from the test program is presented in this chapter in the form of compilation plots to exhibit characteristics of caisson behavior. Section 5.1 presents the testing program philosophy and a summary of the individual test geometry, instrumentation package, loading schedule, and quality assessment. Then, sections 5.2 through 5.8 describe the basic characteristics that were measured during installation, equilibration, monotonic pullout, and sustained loading. In each of these sections, the discussion focuses on force-displacement relations for the caisson and pore pressure and surface displacement of the surrounding clay mass.

5.1 THE TESTING PROGRAM

5.1.1 Program Objectives

The two main objectives of this testing program are to gain insight into fundamental suction caisson behavior and provide data for comparisons with analytical prediction. In order to achieve these goals, the tests were designed to illuminate the following principal parameters:

1. Penetration resistance for a caisson installed by underbase suction
2. Timeframe for the equilibration of pore pressures after installation
3. Caisson displacement during the equilibration phase
4. Ultimate pullout capacity and wall friction contribution for monotonic axial tensile loading
5. Timeframe for release of underbase suction and caisson displacement during sustained tensile loading
6. Effect of installation disturbance on tensile load capacity of the caisson

Other parameters considered in the tests include the penetration rate, the rate of tensile load application, and the effect of reconsolidation on pullout capacity.

5.1.2 Test Geometry and Instrumentation

The model caisson and clay sample geometry were similar for all tests. Figure 5.1 shows a schematic cross section of the model caisson fully installed in a clay element. Table 5.1 lists

the dimensions of the model caisson and clay cake for each of the 14 tests. The caisson is a two-component cylindrical model, comprising an outer caisson wall and an inner caisson cap. The wall is blunt-tipped with an outside diameter of D_o = 5.08 cm and a wall thickness of t = 0.145 cm to give a diameter to thickness ratio of $D_o/t = 35$[1]. The caisson for each test penetrated L = 5.08 cm into the clay element to give a embedment to diameter ratio of $L/D_o = 1$. The clay element has a diameter of 30.5 cm and a pre-installation height that ranges from H_c = 2.1 to 14.3 cm with an average $\overline{H}_c$ = 13.2 cm.

The instrumentation package for each test includes between 12 and 15 transducers (Table 5.1). All tests include the five primary transducers, which measure the caisson wall and cap force (F_w and F_c) and displacement (d_w and d_c, respectively) and consolidation chamber air pressure (P_a). Section 3.1.4 explains the role of the primary transducers in the automated feedback control loop for the CET tests. The remaining transducers include a pressure transducer in the cap to measure pore pressure in the soil beneath the cap, pressure transducers to measure pore pressure in the clay cake and total stress along the chamber wall, and displacement transducers to measure clay surface displacement (Figure 5.1, Table 5.1). Most of the pore pressure probes were located in the clay at a depth of approximately 2.5 cm below the clay surface with radial locations shown in Figure 5.1. This geometry provides pore pressure data inside and outside the caisson walls during and after caisson penetration. In two tests (CET-13, 14) pore pressures were measured near the base of the clay sample, and in three other tests (CET-1, 2, 6) total stress was measured on the sidewall of the chamber (Fig. 5.1). A series of displacement transducers measure the vertical displacements of the clay surface (Fig. 5.1). Section 5.1.4 reviews the quality of these data before proceeding to present reliable results from the CET tests.

5.1.3 Test Loading Schedule

The load history for each test can be divided into a series of driving, equilibration, and tensile loading stages. Table 5.2 lists the phases of each test and includes the elapsed time, imposed loads, and imposed displacements, where appropriate. The chronology of each test is shown schematically by caisson force and wall tip displacement timelines in Figure 5.2. Each timeline depicts the record of the total caisson force F_{TOT} (positive in compression) and caisson displacement throughout the test. Note that the displacement during driving refers only to the wall displacement, while displacement thereafter refers to entire caisson movements. In each test the clay element was consolidated into the virgin compression range to a consolidation stress

[1]The model for CET1 had a tapered tip geometry, but because of test control problems, the results are not reported.

of $\sigma'_{vc} = 0.75$ ksc with the caisson wall tip flush with the caisson cap at the surface of the clay[2]. In all tests except CET-2, this consolidation phase was held for at least 24 hours prior to penetration.

In the majority of tests (CET-1-12), installation by underbase suction (SD, Figure 5.2) was simulated by penetrating the wall into the clay at a constant displacement rate while maintaining a constant total force on the caisson (see timelines in Fig. 5.2). In order to simulate underbase suction, net increases in the wall force are balanced by equal and opposite load increments applied to the cap. The wall was penetrated to a final depth, L = 5.08 cm, at a rate of 0.3cm/min (CET-1-5, 7-12). A much slower penetration rate was used initially in test CET-6; the wall was penetrated to a depth of L = 1.05 cm at a rate of 0.01 cm/min (the remaining penetration was performed at the standard rate, as shown in Table 5.2).

In order to study the effects of installation disturbance by underbase suction, tests CET-13 and 14 used different penetration control schemes. In CET-13, the cap force was held constant as the wall penetrated the clay (comparable to an open-ended pile). In CET-14, zero cap displacement was attempted during wall penetration. Due to control problems (see section 5.1.4), the cap displaced slightly. Nevertheless, an unique installation disturbance was established for comparison with suction installation. Figure 5.2 shows variations in the total force during installation for both CET-13 and 14.

Following the penetration phase in all tests, the caisson was allowed to equilibrate (EQ1, Fig. 5.2) for at least 18 hours prior to tensile loading. During the equilibration phase, a constant total force of $F_{TOT} = 15.2$ kg was maintained on the caisson, allowing no relative displacement between the cap and wall. Figure 5.2 indicates that the caisson tended to settle slightly during this period.

After the first set-up phase, a variety of tensile loading schemes were applied. These can be classified into two categories: monotonic pullout (MP) to failure and sustained loading (SL), as shown in Figure 5.2. Six tests were pulled monotonically to failure, while six were subject to a sustained load following the first equilibration period.

In three tests (CET-3, 4, 8) the caisson was withdrawn at a rate of 0.03cm/min beyond peak tensile load and then was pulled at a rate of 0.3cm/min until complete extraction. In tests CET-5, 6, and 7, the caisson was pulled at 0.03cm/min until just after peak load, whereupon the caisson was re-equilibrated in the clay with a compressive force of $F_{TOT} = 15.2$ kg for more than a day. After reconsolidation in these tests, the caisson was then pulled again at a rate of 0.03cm/min. Figure 5.2 shows the timelines for these two types of monotonic pullout tests.

For the sustained loading test, CET-9, the caisson was withdrawn at a rate of 0.03cm/min

[2]A total force of $F_{tot}=15.2$ kg$(=A_{tot}\sigma'_{vc})$ was applied to the caisson to ensure constant contact pressure across the surface of the clay sample.

until reaching a tensile load of F_{TOT} = -2.2 kg, which was held for 13.4 hours. Then, the caisson was loaded monotonically to failure at 0.03cm/min. For tests CET-10-14, the caisson was pulled at 0.03cm/min to a predetermined tensile load level and held at this load until either the caisson began to fail or more than 24 hours had passed. whichever came first. If no failure occurred, then an increment of tensile load was applied and maintained for up to 24 hours. The process was repeated until failure, whereupon the test was either ended (CET-10,11) or the caisson was re-equilibrated (CET-12-14). After the post-loading set-up in CET-12-14, the model was pulled a second time.

5.1.4 Test Quality Assessment

Before presenting test results, it is important to discuss the quality of the data in order to clarify certain perturbations in the results that are due to control or instrumentation errors. This quality assessment ensures the integrity of comparisons made in the presentation and analysis of the test results. In order to assess the test quality, a system was developed to rate the quality of control in each of the test phases and the accuracy of the instrumentation. Table 5.3 lists the rating for the control and instrumentation for each phase in all of the 14 tests using a scale from 1 (good) to 4 (unusable). Table 5.4 lists the guidelines used to grade the control and instrumentation aspects of the tests. In terms of test control, the grade represents how well the automated feedback control was able to maintain the target force or displacement for that particular test phase. (Note that the accuracy benchmark for test control and instrumentation was outlined in the evaluation of controls and instrumentation in Chapter 4.) Most of the data for test phases and instrumentation that received ratings of 1, 2, or 3 are included in the results and analysis that are presented. In order to present clearly the results of several tests in one plot, small data perturbations that do not reflect true soil behavior have been "smoothed" out using a data averaging process. Data that received a rating of "4" are considered unusable and are *not* presented in this thesis.

As listed in Table 5.3, the control for tests CET-1 and 2 received a "4" rating and therefore are omitted from this thesis. In CET-1 proper testing was hampered by severe control problems in each phase of testing, while CET-2 was aborted after the caisson caught and dragged the inner membrane slip tube into the clay cake (see section 4.1). The control for the remaining tests were rated above "4" and are included in the presentation. In general, the quality improved with each successive test, so that most of the data in the later tests were considered either fair or good.

The quality of the instrumentation data also progressed with successive tests. In the early tests, the cap and particularly the probe pore pressure instruments were undergoing intense research development, and hence much of the data were not worth reporting. Later in the testing,

the probes became much more accurate and responsive. Note that a few surface displacement transducers became stuck or were beyond the linear range during testing and therefore became unreliable.

5.2 SUCTION INSTALLATION

This section presents the results of installation by underbase suction in 9 tests (CET-3-5, 7-12). Following clay cake consolidation at σ'_v = 0.75 ksc for a period of at least 24 hours, the caisson wall penetrated the soil at a rate of 0.3 cm/min to a depth of L = 5.1 cm to give an embedment depth to diameter ratio of L/D_o = 1. During driving, the cap force was reduced to offset the increase in force needed to drive the wall. Only the basic measured characteristics including caisson forces, soil pore pressures, and clay surface displacement, will be shown.

5.2.1 Caisson Force Distribution

In order to illustrate typical caisson force behavior during suction installation, Figure 5.3 shows the caisson wall, cap, and total ($F_{TOT} = F_w+F_c$) forces as a function of penetration depth for CET-9, which was chosen for the quality of its test control and instrumentation data. The total force remains constant at F_{TOT} = 15.5 kg, which is just 0.3 kg above the design value of F_{TOT} = 15.2 kg (= $A_c\sigma'_{vc}$, where A_c is the total cross-sectional area of the caisson). The wall force rises sharply from $F_w \approx$ -0.7 kg to $F_w \approx$ 13 kg during the first 0.3cm of penetration and increases linearly with depth at a rate of 1.3 kg/cm from approximately z_w = 0.8 cm to the end of penetration at z_w = 5.1 cm. There is a transition zone from z_w = 0.3 to 0.8 cm where the wall force drops 1.5 kg and then remains essentially constant. The caisson cap shows the inverse response with a sharp drop from $F_c \approx$ 16 to 2.5 kg at z_w = 0.3 cm, a transition phase from z_w = 0.3 to 0.8 cm, and a linear decrease to $F_c \approx$ -2.5 kg.

5.2.1.1 Total Force

The caisson force behavior exhibited in CET-9 is similar to that in the suction installation phase in the remaining eight tests (CET-3-5, 7-8, 10-12). It is important now to establish the individual caisson force trends during suction penetration for all nine tests. Figures 5.4 and 5.5 show the total force versus wall tip penetration for these nine tests at two different scales. It is clear that the total force is constant at, or within 2 kg above, the design value of F_{TOT} =15.2 kg. Note that the total force for CET-3 exhibits greater fluctuations about a constant value than the rest because the software control module was still in the early stages of development (see section 4.1).

5.2.1.2 Wall Force

There appears to be no correlation between the amount of total force deviation above the design value of 15.2 kg and the wall force behavior. Figure 5.6 depicts the wall force versus wall tip penetration for eight tests. Note that while the total force for CET-8 is approximately 2 kg larger than in CET-9, the wall force records are nearly identical. It is not surprising that variations in the total force do not affect the wall force because the wall follows a prescribed penetration rate independent of the total force, as explained in section 3.1.4.

Further inspection of Figure 5.6 reveals three zones of wall force penetration behavior: initial, transition, and deep penetration. Initial, or early, penetration is characterized by a sharp increase in wall force of at least 10 kg during the first few tenths of a centimeter (wall thickness is 0.145 cm), with the force increasing at a decreasing rate. During deep penetration, the wall force increases linearly with depth at a rate of approximately 1.5 kg/cm starting from a depth of between z_w = 0.8 and 1.8 cm and lasting until the end of penetration at z_w = 5.1 cm. In between the initial and deep penetration is the transition zone. The wall force behavior during this zone and the extent of this zone varies from test to test and is largely a result of friction between the caisson wall anc cap components.

Before discussing each of the three penetration zones in detail, it is helpful to review caisson component friction, which accounts for the variation in initial and deep penetration wall force behavior and may account for much of the wall force behavior during the transition zone. As stated in section 4.3.2, caisson intercomponent friction can arise from four different sources: 1) metal-to-metal contact between the caisson wall and chamber inner slip ring, 2) extruded soil between the wall and inner slip ring, 3) extruded soil between the caisson wall and cap, and 4) the O-ring separating the wall and cap. The locations of these four sources of friction are illustrated in Figure 4.12. During penetration all sources of friction potentially can contribute a compressive component to the wall force.

The initial and transition penetration zones for the nine suction installation tests (CET-3-5, 7-12) are represented clearly in Figure 5.7, which shows the wall force for the first two centimeters of penetration. Ideally, at the start of penetration (z_w = 0 cm), the caisson wall should apply a force of F_w = 1.7 kg (= $\sigma'_{vc}A_w$) to the surface of the clay. However, it is likely that soil extruded between the caisson components during the consolidation process prior to penetration, and this soil introduced tensile or compressive components of force to the caisson wall. As a result, the initial wall force ranges from F_w = -1.2 to 5 kg and is within ±3.3 kg of the ideal initial force. Initial penetration is characterized by a stiff wall response. During the first z_w = 0.2 cm of penetration in 7 of 9 tests, the wall force increases by more than 10 kg. In order to compare the initial stiffness among the tests, a "penetration modulus" can be defined by dividing the wall force increment by the initial penetration depth ($M_w = \Delta F_w/\Delta z_w$). The moduli for penetration depths of z_w = 0.05, 0.1, and 0.2 are listed in Table 5.5. In most tests the modulus

decreases with increasing penetration, as the wall approaches the transition zone. Note that the initial stiffness for tests CET-5, 10-12 was lower than the remaining tests, particularly at depths of $z_w = 0.05$ and 0.1cm. In these four tests, it is possible that the soil surface was disturbed by a premature wall penetration during the final consolidation stage prior to penetration. In CET-10 a power shutdown led to a wall penetration of 0.4 cm, and in CET-12 a displacement transducer malfunction caused a wall penetration of 0.3 cm. In both tests, the wall was repositioned to be flush with the cap before consolidation continued. By a penetration depth of $z_w = 0.2$ cm, the moduli for the tests with potentially disturbed surfaces have approached the moduli for the remaining tests, as listed in Table 5.5. The end of the initial penetration zone is not clear, as various intercomponent frictional forces and perhaps soil surface effects combine to create a transition zone between initial and deep penetration. However, it will be shown in the subsequent discussion regarding the most representative and "best estimate" of wall force behavior, that a depth, $z_w = 0.2$ cm (i.e., approximately equal to the wall thickness), is a reasonable endpoint for the initial penetration zone.

The transition zone of wall penetration is defined by a "hump-shaped" rise and fall in wall force, with a local maximum wall force at a penetration depth of between $z_w = 0.3$ and 1.0 cm, as shown in Figure 5.7. The end of the transition zone, at a depth ranging from $z_w = 0.8$ to 1.8 cm, occurs when the incremental penetration modulus becomes constant (i.e., linear variation of F_w with z_w). The transition zone peak and final wall force values and depths are listed in Table 5.5. To illustrate the size and extent of the transition "hump", consider CET-9 in Figure 5.7. The wall force peaks at $F_w = 12.9$ kg at a depth of $z_w = 0.4$ cm and falls to a value of $F_w = 11.5$ kg at a depth of $z_w = 0.8$ cm to mark the end of the transition zone and the start of deep penetration. In general, the transition is probably caused by the build-up and subsequent release of intercomponent friction contributed by one or more of the sources mentioned above (see Figure 4.12). As the wall passes by the cap during early penetration, friction builds up between the O-ring and the wall and between the extruded soil and the wall until reaching a maximum contributing value, which is depicted as the peak of the transition "hump". Following this, the friction contribution drops due to a combination of one or more of the following events: 1) O-ring friction drops to a residual value, 2) the cap, which rises during wall penetration, releases the friction caused by the soil extruded between the cap and wall, 3) the wall drags down the extruded soil between the wall and inner slip ring, thus reducing this frictional source. Once a residual friction value is reached, deep penetration can be characterized by a linear relation between wall force and penetration depth. Variations in the frictional contributions from test to test are reflected in variations in the size and extent of the "hump". Note that in CET-12, no "hump" exists, which suggests the lack of a transition zone. In test CET-4, the transition zone is denoted by two "humps", the first peaking at $z_w = 0.3$ cm and the second peaking at $z_w = 0.6$ cm.

The remaining tests display fairly recognizable transition zones.

Following the initial and transition zones, the wall enters a deep penetration zone, where the wall force increases at a constant rate with depth. Figure 5.8 shows the wall force versus depth for the deep penetration zone in tests CET-3-5, 7-12. Due to variations in the extent of the transition behavior, the onset of deep penetration ranges from z_w = 0.8 to 1.8 cm. In order to compare the linear increase in force among tests, a first-order regression was performed on the wall force vs. penetration data in the deep penetration zone for each test. The starting depth and regression coefficients for each test are listed in Table 5.5. For all tests, the slope of the secant deep penetration modulus ranges from $M_w = F_w/z_w$ = 1.11 to 2.04 kg/cm with an average value of M_w = 1.47 kg/cm.

Of the nine tests depicted in Figure 5.8, four of them (CET-3, 5, 7, 10) reveal deep penetration behavior that is significantly different from the remaining five tests. The deep penetration modulus for CET-3, M_w = 2.04, is 39% higher than the average and 27% higher than the next highest slope (CET-7). This is probably due to a build-up of friction from the O-ring separating the wall and cap. As noted in section 4.1.2, the O-ring "squeeze", and hence friction, was quite high for tests CET-1-3. For the remaining tests, this O-ring "squeeze" was lessened significantly. In CET-5, the slope is M_w = 1.11 kg/cm, which is 26% lower than the average due to an unusually low slope during the initial 1.2 cm of deep penetration. The most likely cause is continued drop-off in intercomponent friction from the transition zone. Both CET-7 and CET-10 show a deep penetration zone with much higher starting and final wall force values relative to the remaining tests. This indicates that the residual intercomponent friction contribution at the end of the transition zone was much higher than the other tests. It is possible that in these two tests, the wall had continuous metal-to-metal contact with the inner chamber slip ring. Neglecting these outliers, the slope of the regression line ranges from M_w = 1.29 to 1.60 kg/cm with an average value of M_w = 1.45 kg/cm.

Combining the most reliable wall force data for the initial and deep penetration zones facilitates the interpretation of the overall behavior of the caisson wall force during suction driving. Figure 5.9 shows the most representative wall force data for both the initial and deep penetration zones. For initial penetration, only two tests (CET-8-9) are depicted. These are the only tests that did not show possible evidence of surface disturbance, which led to decreased initial penetration "moduli", and also did not suffer from excessive intercomponent friction, as revealed in the transition and deep penetration zones. For both tests, the endpoint was chosen to coincide with the extension of the deep penetration regression line for that particular test. For deep penetration, five tests (CET-4, 8-9, 11-12) showed consistently linear behavior without excessive intercomponent friction. The transition zone is not shown for any plot in Figure 5.9 because it is assumed that the wall force behavior in this zone is the result of caisson

intercomponent friction and not strictly the caisson-soil interaction. In order to show continuity between the initial and deep zones, dotted lines extend from a depth of $z_w = 0.2$ cm to the depth at which deep penetration begins for each of the five tests. These dotted lines are simply an extension of the regression lines that were calculated and listed in Table 5.5 for each test. Hence, deep penetration is assumed to begin immediately following the initial penetration depicted. The penetration data presented in Figure 5.9 clearly shows the distinct nature of the wall force behavior during shallow and deep penetration. Without the masking effect of caisson intercomponent friction, the wall force shows a very stiff response (M_w>55 kg/cm) during the first $z_w = 0.2$ cm of penetration. This is followed immediately by a linear increase in force with depth at an average rate of $M_w = 1.45$ kg/cm for the remainder of penetration. The variation in magnitude of the slope of deep penetration reflects the variable contributions of normal residual intercomponent friction and the minor differences in soil resistance from test to test.

The measured behavior for suction installation presented in Figure 5.9 can be simplified by assuming that the wall force is bi-linear. Figure 5.10 shows the initial and deep zones represented by two linear ranges. Starting at $F_w = 1.7$ kg (= $\sigma'_{vc}A_w$), the wall force increases linearly to a depth of $z_w = 0.2$ cm. This depth was chosen because it is the endpoint for initial penetration in CET-8, which had the least amount of intercomponent friction (see Figs. 5.7 and 5.9). At this depth the wall force coordinate, which ranges from F_w = 10.4 to 11.05 kg, represents the intersection of the initial zone line and the deep zone regression lines that were presented in Figure 5.9. Deep penetration, represented by the dashed lines, begins at $z_w = 0.2$ cm and ends at $z_w = 5.1$ cm. The lower boundary starts at $F_w = 10.4$ kg and rises at a rate of $M_w = \Delta F_w/\Delta z_w = 1.29$ kg/cm, which is the lowest slope of the regression lines calculated for the deep penetration records. Starting at $F_w = 11.05$ kg, the upper boundary rises at the highest slope, $F_w/z_w = 1.60$ kg/cm. The wall force at the end of penetration ranges from F_w = 16.7 to 18.9 kg. Admittedly, this bi-linear model of wall force during penetration is only a "best estimate" of the true behavior. While the model neglects much of the intercomponent friction that clouds the true wall force signature, particularly at penetration depths within the transition zone from $z_w = 0.8$ to 1.8 cm, it is based on measured data in the initial and deep zones (see Fig. 5.9) that does incorporate some friction. Nevertheless, this model is an important representation of wall force installation behavior, upon which interpretations regarding caisson wall bearing capacity and adhesion are based in Chapter 6.

5.2.1.3 Cap Force

During suction driving, the cap force is controlled as the difference between the measured wall force and the preset total force ($F_c = F_{TOT} - F_w$). The cap force behavior, therefore, should be equal but opposite to the wall force behavior. Figure 5.11 shows the cap force versus wall tip

penetration for nine tests (CET-3-5, 7-12). The cap force behavior is defined by the same three wall penetration zones that were described above in the discussion of wall force behavior. During the initial penetration zone from $z_w = 0.0$ cm to approximately $z_w = 0.2$ cm, the cap force drops sharply by more than $\Delta F_c = 10$ kg at a decreasing rate with depth. During the "hump-shaped" transition zone, which starts from approximately $z_w = 0.2$ cm, the cap force continues dropping un[illegible] reaching a local minimum before rising toward the end of the transition, which occurs at depths ranging from $z_w = 0.8$ to 1.8 cm. In Figure 5.11, the individual test "hump" minima are identified by symbols except for CET-10, which did not exhibit a transition zone. Following the transition zone, the cap force drops at a constant rate with depth until the end of penetration at $z_w = 5.1$ cm. At this depth the cap force has decreased to tensile values between $F_c = 0.0$ and -7.0 kg. Table 5.5 lists the cap force and depth coordinates for the three penetration zones for each test.

Using the criterion outlined for the wall force, the most representative cap force behavior for both the initial and deep penetration zones is depicted in Figure 5.12. For the initial zone, only those tests not suffering from excessive intercomponent friction or soil surface disturbance are shown (CET-8-9). For deep penetration, the five tests that do not exhibit excessive friction are shown (CET-4, 8-9, 11-12). Continuity between the initial and deep penetration zones is not illustrated by extending deep penetration regression lines because of the effect of variations in the total force. Unlike the wall force, the cap force trend *is* affected by variations in the total force from the design value of $F_{TOT} = 15.2$ kg. This effect can be seen by comparing tests CET-8 and CET-9. In CET-8, the total force was approximately 2 kg too high at $F_{TOT} = 17.2$ kg. In CET-9, the total force was much closer to design at $F_{TOT} = 15.4$ kg. The wall force in these two tests is nearly identical during deep penetration as depicted in Figure 5.9, but the cap force for CET-8 is approximately 1.8 kg higher than that for CET-9 during deep penetration. Despite the effect of total force, the general cap force behavior during initial and deep penetration is shown clearly by Figure 5.12. The cap responds stiffly ($\Delta F_c/\Delta z_w = -55$ kg/cm) during the first $z_w = 0.2$ cm of penetration. First order regression analyses on the deep penetration cap force behavior indicates an average cap modulus $M_c = \Delta F_c/\Delta z_w = -1.5$ kg/cm.

5.2.2 Pore Pressure Generation Beneath Cap

At the start of suction penetration, there is no excess pore pressure beneath the caisson cap. Measurements of excess pore pressure generated beneath the cap during driving for 8 tests (CET-4-7, 8-12) are shown in Figure 5.13. The first $z_w = 2$ cm of penetration are shown in Figure 5.14 for clarification. Note that no record is shown for CET-3 due to poor transducer response (see section 5.1.4). Aside from variations in magnitude, the figure shows remarkable uniformity in the general pore pressure behavior throughout penetration. After an initial drop

ranging from Δu = -0.05 to -0.26 ksc during the first z_w = 0.2 cm of driving, positive excess pore pressures are generated during the transition zone at a decreasing rate until reaching a peak at a depth that ranges from z_w = 1.0 to 2.4 cm. During deep penetration, the excess pore pressure drops at a constant rate, reaching values between Δu = +0.04 to -0.27 ksc at the end of penetration (z_w = 5.1 cm). The variations in magnitude of pore pressure can be traced to differences in cap force magnitude which, as noted above, were due to variations in total force and intercomponent friction from test to test. Note that in CET-10, the excess pore pressure does not rise significantly after the initial drop, but instead descends from Δu = -0.04 ksc at z_w = 0.4 cm to Δu = -0.27 ksc by the end of penetration. This lack of intermittent cap pore pressure rise in CET-10 is due directly to the lack of a transition penetration zone for the wall and cap force, as shown in Figures 5.6 and 5.11, respectively. A notable cap pore pressure feature visible in all tests but CET-10 in Figure 5.13 is that the end of the transition zone is at a greater depth than the transition end in wall force or cap force. For example, consider test CET-11. Excess pore pressure reaches a peak of Δu = 0.16 ksc at z_w = 1.4 cm, which is the end of transition and the beginning of deep penetration. However, the end of transition for both wall and cap force is at the shallower depth of z_w = 0.6 cm (see Figs. 5.6 and 5.11). It is likely that the linear decrease in excess pore pressure beneath the cap starts later than the linear decrease in cap force because of positive pore pressures generated by the penetrating wall.

5.2.3 Cap Displacement

Figure 5.15 shows the caisson cap displacement versus wall tip penetration for 9 tests (CET-3-5, 7-12) during suction driving. The cap rises at a nonlinear rate throughout penetration and reaches z_c = 0.55 to 0.98 cm by the end of wall penetration. Although there is considerable scatter among the 9 tests, scrutiny of the shape of the cap rise curves reveals two general patterns. In the first pattern, which is followed by tests CET-3, 5, 7, and 12, the cap rises at a gradually increasing rate until a wall depth ranging from z_w = 3.5 to 4.6 cm, whereupon the cap rise rate decreases with continued wall penetration until the end. These tests show the largest upward movements of the cap, z_c = 0.78 to 0.98 cm. In the second pattern, followed by CET- 8-10, the cap initially rises at a gradually increasing rate that is greater than in the first pattern. However, the cap reaches a peak rate at a shallower depth range (z_w = 1.8 to 2.2 cm) and then rises at a continually decreasing rate until reaching a total rise of between z_c = 0.54 to 0.64 cm by the end of wall penetration. Tests CET-4 and 11 do not fit either pattern. In CET-4 the cap rises very swiftly, but then actually begins dropping until the wall has penetrated z_w = 3 cm, whereupon the cap rises rapidly to a final height of z_c = 0.56 cm. In test CET-11, the cap begins to rise gradually according to pattern 1, but continues to rise at a linear rate beginning at a wall depth of z_w = 2 cm to reach a final rise of z_c = 0.56 cm by the end.

Comparisons between the cap displacement curves and cap force, wall force, and cap excess pore pressure behavior have not yielded an explanation for either the two general patterns of cap rise or the two aberrational patterns (CET-4, 11). Complicating the interpretation of the cap rise patterns is the combination of many interacting factors including intercomponent friction, variation in total force, and the possibility of separation of the cap from the soil surface. This latter factor is explored more fully in Chapter 6.

5.2.4 Pore Pressure Generation in Soil Mass

The generation of excess pore pressure within the clay cake during the suction driving phase was measured by needle probes. As shown in Figure 5.1, the probe tips were located at a depth of approximately 2 to 2.5 cm below the clay surface and at three radial locations from the caisson centerline: r = 0.0, 1.8, and 3.2 cm (P1, P2, and P3, respectively). Probes P1 and P2 measure pore pressures within the soil plug inside the caisson wall, while the third probe (P3), was located outside the wall during penetration. The overall behavior of the clay mass pore pressures is influenced by both the actions of the advancing caisson wall and the retreating cap.

The centerline pore pressure behavior, as measured by probe P1, is shown in Figure 5.16, which plots excess pore pressure versus wall tip penetration for 5 tests (CET-7, 9-12). Note that the probe tip depth is marked with a horizontal dashed line for each test. For the first z_w = 3.5 cm of penetration, the pore pressure record for four of the tests (CET-7, 9, 11-12) is similar in shape but muted in magnitude when compared to the pore pressure record beneath the cap (see Fig. 5.13). During the first z_w = 0.3 cm of penetration, the pressure drops slightly (Δu = -0.005 to -0.07 ksc) in response to the immediate tension applied to the cap. In CET-9, 11, and 12, the pressure then gradually rises to maximum excess values ranging from Δu = 0.04 to 0.06 ksc as the caisson wall approaches the depth of the probe tip. The maximum pressure during this range occurs when the wall is approximately 0.4 cm above the probe tip. Test CET-7 does not show this gentle rise due to a slightly sluggish probe response (see Table 5.3a) and to a greater than average tensile force applied to the cap (see Fig. 5.11). After reaching the local maximum excess pore pressure in CET-9, 11, and 12, and just after the wall passes the probe in CET-7, the pore pressure begins a steady decline as the retreating cap exerts greater tension on the soil plug. This decline continues to the end for CET-7 and 12. In CET-9 and 11, the pore pressure drops until the wall reaches z_w = 3.4 to 3.6 cm, after which the pressure rises for the remainder of penetration. Note that at the end of penetration (z_w = 5.1 cm), the magnitude of centerline pore pressure for each test is within Δu = 0.1 ksc of the value measured beneath the cap (see Fig. 5.13).

The behavior of the centerline excess pore pressure for CET-10 deviates from the remaining four tests because of different cap behavior. After dropping initially to Δu = -0.04

ksc, the pore pressure declines sharply as the wall advances from z_w = 1 to 2.6 cm. This drop is consistent with the drop in cap force and cap pore pressure (see Figs. 5.11, 5.13). Yet, after reaching a minimum of Δu = -0.26 ksc, the pore pressure rises to a local peak of Δu = -0.12 ksc at z_w = 4.2 cm and then falls to Δu = -0.18 ksc by the end of penetration. This pore pressure rise and fall during the second half of penetration could be directly related to the slight rise and fall in cap force, as shown in Figure 5.11.

Probe P2 measured the excess pore pressure of the soil plug at a radial distance of 0.6 cm from the inside of the wall. The pore pressure records for four tests (CET-7-10) are shown in Figure 5.16. Two patterns of behavior are plainly visible. In CET-7 and 10, after a slight initial drop, the excess pore pressure declines linearly from near-zero values at z_w = 1 cm to a value ranging from Δu = -0.19 to -0.26 ksc by the end of penetration. The wall has no significant effect on the pore pressure in these tests because of the dominating effect of the tensile stress applied by the cap (see Fig. 5.11), which is a direct result of the higher than average wall force magnitude (see Fig. 5.6). Recall from section 5.2.1 that in these two tests, there possibly was metal-to-metal contact between the wall and inner slip ring, which would contribute friction to the wall force signature. In contrast, both the wall and cap contribute to the shape of the curves for CET-8 and 9. In these tests, the excess pore pressure increases to a peak of between Δu = 0.2 to 0.25 ksc by the time the wall has passed the probe tips and has reached a depth of z_w = 3.2 to 3.5 cm. The effect of the decrease in cap force then causes the pore pressure to drop to values of Δu = 0.06 to 0.08 ksc by the end of penetration.

Excess pore pressure behavior at a radial distance of 0.6 cm *outside* the wall indicates some influence from the passing wall and little, if any, influence from the retreating cap. Figure 5.16 shows the excess pore pressure record as measured by probe P3 for four tests (CET-7-8, 12). In the most representative tests, CET-7-8, the pore pressure rises at a decreasing rate until reaching a peak of between Δu = 0.14 to 0.16 ksc at a wall depth of z_w = 2.0 to 2.1 cm. At this point, the wall is just 0.4 cm above the probe tip depth. With continued penetration, the pressure dissipates toward zero. During the final z_w = 1.5 cm of penetration for CET-7, the pressure behavior is clouded by probe response instability (see Table 5.3a). Slow response masks the pore pressure behavior in CET-12, but it is clear that suction driving generates only slightly positive pore pressures. In this test, excess pore pressure rises very slowly to a peak of Δu = 0.05 ksc at a wall depth of z_w = 4 cm and declines slightly toward the end of driving.

The magnitude of excess pore pressure beneath the cap and at the three locations within the soil mass (P1, P2, and P3) generated during installation by underbase suction never exceeded Δu = ±0.3 ksc. Much larger pore pressures (Δu>-0.5 ksc) are generated during the monotonic pullout phases, as described in sections 5.5 and 5.8.

5.2.5 Soil Surface Displacement

The vertical displacement of the clay surface exterior to the caisson was measured by up to five transducers located within the CET chamber at various radial distances from the caisson wall (see Fig. 5.1). There are three general characteristics of clay surface settlement during suction penetration: 1) the clay surface generally depresses at a rate that increases with increasing wall penetration, 2) the magnitude of settlement decreases with increasing radial distance from the caisson wall, and 3) the overall magnitude of settlement is small relative to the wall penetration depth. These three settlement characteristics are illustrated by Figure 5.17, which plots the clay surface displacement versus wall tip penetration for CET-8. At a radial distance from the wall of r_w = 1.7 cm, the surface has compressed -0.004 cm by the end of penetration. Note that this value is less than 0.1% of the final wall depth, z_w = 5.1 cm. A short distance further from the wall, the settlement drops dramatically to -0.0005 cm at r_w = 2.7 cm. By a radial distance of r_w = 7.3 cm, the depression is nearly immeasureable.

Clay surface settlement records for all tests are displayed in Figure 5.18, which shows the displacement at a specific radial distance for several tests. In general this figure shows that, allowing for some scatter in settlement magnitude from test to test, the clay surface settlement behavior is consistent with that described above for CET-8. However, at the three closest radial locations, r_w = 1.7, 2.7, 5.3 cm, many of the tests indicate that the surface heaves slightly (<0.001 cm) prior to settlement. Moreover, the wall penetration depth at which peak heave occurs increases with increasing radial distance from the caisson wall. To illustrate this last point, consider the peak heave points for the first three radial distances (S1, S2, S3) in Figure 5.18. At a radial distance of r_w = 1.7 cm, peak heave occurs at a wall depth that ranges from z_w = 0.4 to 1.3 cm. At r_w = 2.7 cm, peak heave happens at a wall depth ranging from z_w = 0.5 to 2.8 cm. Finally, at a distance of r_w = 5.3 cm, the peak heave occurs at a corresponding wall depth that ranges from z_w = 2.3 to 3.2 cm. Note that at the furthest radial locations, r_w = 7.3 and 9.6 cm, there is no evidence of soil heave.

The soil settlement records displayed in Figure 5.18 represent the most reliable soil surface behavior for the suction penetration phase of testing. Important links between the movement of the outer soil surface, the soil displaced by the penetrating wall, and the soil plug rising beneath the cap are explored in Chapter 6.

5.3 OTHER INSTALLATION METHODS

In three caisson element tests, the caisson was installed using a method that differed from the standard underbase suction described in section 5.2. Recall that during suction driving, the wall penetrates the soil at a constant rate, while force is removed from the cap to offset increases in the wall force. Throughout driving, therefore, the total force ($F_{TOT} = F_w + F_c$) is held

constant. In test CET-6, the caisson was installed using the same algorithm, but using a much slower penetration rate (z_w/t = 0.03 cm/min) over the first z_w = 1 cm. The wall penetrated the final z_w = 4.1 cm at the standard rate (z_w/t = 0.3 cm/min). For CET-13, the cap force was held constant (F_c = 14 kg) and the wall was driven at the standard rate. This simulation corresponds to installation of an open-ended pile. Finally, test CET-14 targeted zero cap displacement during installation. Poor control of the cap displacement in CET-14 led to cap movements up to z_c = 0.22 cm (see Fig. 5.23). In this section the results of these three tests are compared to the standard results from suction driving. Later sections illustrate that the different installation methods have little effect on subsequent equilibration and caisson pullout behavior.

5.3.1 CET-6: Partial Slow Rate Suction Installation

The slow initial penetration rate in CET-6 (z_w/t = 0.03 cm/min over first z_w = 1 cm) was the result of an incorrect rate input parameter. The results from this two phase installation test indicate that: 1) the overall caisson force results do not differ significantly from the standard tests, but 2) the minor change in installation rate *does* affect the cap movements and pore water pressure.

The caisson force behavior was relatively unaffected by the slow rate installation phase. The total force versus wall tip penetration for CET-6 is shown in Figure 5.19. Throughout suction driving the total force for CET-6 remains constant at a value just above the design force of F_{TOT} =15.2 kg. During the slow drive rate in the first z_w = 1.05 cm of penetration, the total force is F_{TOT} = 15.5 kg. This rises to an average of F_{TOT} = 16 kg for the remainder of penetration, which occurs at the standard rate. These values of total force are within the range observed for the 9 standard suction driving tests presented in Figures 5.4 and 5.5. The wall force behaves like a standard suction installation test (see Fig. 5.20). The initial penetration 'modulus', defined as the increase in wall force divided by the penetration increment ($M_w = \Delta F_w/\Delta z_w$ = 180 kg/cm) is similar to those suction driving tests that did not suffer from a potentially disturbed soil surface (see Table 5.5). The definition of a transition zone is unclear in CET-6 because the slow rate driving phase ends early at a depth of z_w = 1.05 cm. However, a transition is apparent during the subsequent standard penetration as the wall force falls from F_w = 16 kg to approximately F_w = 14 kg from z_w = 1.05 to 2.1 cm. Deep penetration behavior is consistent with the tests reported in section 5.2.1, as the wall force increases at a constant rate of M_w = 1.67 kg/cm to reach F_w = 19 kg by the end of driving. Figure 5.21 depicts the cap force versus wall tip penetration and reveals that the slow rate of driving during the first z_w = 1.05 cm did not have any significant effect on the cap force behavior. As for the standard rate suction driving tests displayed in Figure 5.11 the cap force drops swiftly by more than ΔF_c = -10 kg during the first z_w = 0.2 cm of wall penetration. During deep penetration from z_w = 2.4 to 5.1 cm, the cap force

declines at a constant rate until reaching a final tensile value of F_c = -2.5 kg.

Figure 5.22 shows the excess pore pressure measured beneath the cap versus wall tip penetration. Very little positive excess pore pressure was generated during the two phases of suction driving in CET-6. Unlike the standard rate suction installation tests portrayed in Figure 5.13, the slow rate of driving during the first z_w = 1.05 cm allows significant partial drainage of pore fluid in the vicinity of the caisson. As a result, only a small excess pore pressure of Δu = 0.05 ksc is registered after the wall has penetrated z_w = 0.05 cm. For the remainder of slow penetration, this excess starts to decline due to both dissipation and a slight decrease in cap stress. During the standard rate penetration from z_w = 1.05 to 5.1 cm, pressure barely builds to Δ u = 0.1 ksc before falling to a slightly negative value of Δu = -0.02 ksc by the end as the cap slowly acquires a tensile stress.

Figure 5.23 shows the pore pressure generated by the centerline probe P1 in this two-phase suction driving test. Only very slight positive pore pressures (Δu = 0.04 ksc) are generated during the slow phase, and somewhat higher positive pore pressures (Δu = 0.12 ksc) are generated during the standard rate phase. Note that the slow rate of penetration prevented the development of negative excess pore pressures, an occurrence common to all standard rate tests (see Fig. 5.16).

There is a large difference in cap movements between the two-phase test CET-6 and the standard rate tests, as described in section 5.2.3. As shown in Figure 5.24, the cap in CET-6 nudges upward by only z_c = 0.02 cm for the first z_w = 0.5 cm of penetration in order to develop the tension necessary to offset the wall force increase. This initial behavior is also apparent in standard rate suction driving tests, as shown in Figure 5.15. However, the cap in the standard tests continues to rise, whereas the cap in CET-6 *drops* to its original position by the end of slow penetration at z_w = 1.05 cm. This behavior may be related to the combination of dissipating pore pressure beneath the cap and the potential for tensile forces due to friction in the O-ring between the cap and wall. During the standard rate driving of CET-6, the cap rises at a rate that generally increases with increasing wall penetration. Due to the slow initial wall penetration, the final cap rise is low at z_c = 0.37 cm. This value is lower than the cap rise in all standard rate tests, which displayed a cap rise ranging from z_c = 0.55 to 0.98 cm.

Due to the slow initial rate of penetration during the first z_w = 1.05 cm in CET-6, the soil surface compresses a small amount (-0.001 to -0.005 cm depending on the radial distance from the wall), as shown in Figure 5.25. This is in contrast to the initial near-wall soil heave exhibited in standard rate suction installation tests (see Fig. 5.18). However, during the standard rate portion of CET-6, from z_w = 1.05 to 5.1 cm, the soil surface displaces in a fashion similar to that for standard rate tests discussed in section 5.2.5. Near the caisson wall at r_w = 2.7 cm the soil heaves approximately 0.001 cm until z_w = 3.7 cm, whereupon it compresses to the end of

penetration. Similar behavior is apparent at greater distances from the wall until arriving at a radius of r_w = 9.6 cm, where the soil surface remains steady throughout standard rate penetration.

5.3.2 CET-13, 14: Fixed Cap Force, Cap Displacement Installation

In both CET-13 and CET-14, the wall was driven at the standard rate of z_w/t = 0.3 cm/min. In test CET-13, the cap force was held constant at F_c = 14 kg, while in test CET-14, the algorithm attempted to maintain zero cap displacement. These two tests are discussed together because installation is achieved by supplying additional force to the system.

Figure 5.19 shows that the total force recorded in CET-13 and 14 is significantly higher than in the standard rate suction installation tests. The total force signature for CET-13 reflects that for the wall force and reaches F_{TOT} =37.6 kg by the end of driving. This value is more than double the total force measured for suction driving tests. The total force in CET-14 varies widely during the first 0.3 cm of penetration. However, o· · the cap displacement is under control ($\Delta z_c = 0$), the total force rises rapidly and is similar in magnitude (F_{TOT} =34.5 kg) to that measured in CET-13.

As shown in Figure 5.20, which depicts wall force versus wall tip penetration, the wall force for CET-13 behaved very much like a caisson wall with intercomponent friction in a standard suction driving test, but without a "hump"-shaped transition zone. During the initial zone, the wall responds stiffly, acquiring approximately ΔF_w = 10.5 kg during the first z_w = 0.2 cm of penetration. Thereafter, the wall force continues increasing at a decreasing rate until a depth of z_w = 0.5 cm, whereupon the wall force increases at an average constant rate of $M_w = \Delta F_w/\Delta z_w$ =2.2 kg/cm until reaching a final value of F_w = 23.5 kg. The high rate of force pickup during deep penetration suggests a high friction contribution arising from sources described in section 5.2.1. Similar wall force behavior was shown in the standard suction driving test CET-10, which is illustrated in Figure 5.6. The wall force behavior in CET-14 is unclear during the initial and transition stages due to poor cap control, but, like CET-13, it is similar in overall shape to standard suction driving wall behavior. Examination of Figure 5.20 reveals a stiff initial wall response, as the force increases from F_w = 2 to 11.2 kg during the initial z_w = 0.02 cm of penetration. Uncontrolled movements in the cap from z_w = 0.02 to 1.4 cm created sudden friction contributions arising from the O-ring connecting the cap and wall. Thereafter, from z_w = 1.4 to 5.1 cm, the wall force rises at a constant rate of approximately M_w = 1.3 kg/cm, which is just below the average and within the range of rates recorded for suction driving tests (see Table 5.5)

The cap force was controlled to be constant at F_c = 14 kg throughout wall penetration in CET-13, as Figure 5.27 shows. In contrast, for CET-14 zero cap displacement was attempted. The cap force record for this test shows the significant effect of small uncontrolled cap

movements, which are plotted versus wall tip penetration in Figure 5.29. In response to a small cap penetration of z_c = -0.22 cm, the cap force shoots to nearly F_c = 32 kg. As the cap is brought back to zero displacement, the cap force drops to tensile values before rising for the remainder of wall penetration to a final value of F_c = 18 kg.

In general, large positive excess pore pressures are generated in the soil plug created by the penetrating caisson and in the soil mass external to the caisson. Figure 5.22 shows the development of excess pore pressure measured beneath the cap. Although the cap force remains constant throughout penetration, large excess pore pressures (Δu = 0.6 ksc) developed during the initial 1 cm of penetration. Thereafter during deep penetration, the pressure slowly rose to Δu = 0.68 ksc by the end. This pore pressure behavior is a result of pore pressure generated by the wall penetration and by displacements of the caisson cap (see below). The pore pressure generation beneath a fixed cap is obscured by small cap movements that occurred during CET-14. As shown in Figure 5.24, the cap dropped z_c = -0.22 cm during the first z_w = 0.5 cm . This caused the excess pore pressure to rise to Δu = 0.9 ksc, but stabilization of the cap dropped the pressure to Δu = -0.25 ksc. With the cap position held approximately constant for the remainder of penetration, displaced soil from the continued wall penetration caused the excess pore pressure to climb to Δu = 0.98 ksc by the end of driving.

Only one pore pressure probe in test CET-13 was considered reliable (adequately responsive), while all four probes performed well in CET-14 (see Table 5.3). Figure 5.23, which shows the excess pore pressure in the soil mass vs. wall tip penetration, clearly indicates that the large total force applied to the system in these two tests raised the soil mass pore pressure to values larger than any recorded outside the wall for any test with underbase suction installation. In CET-13, wherein the cap force was held constant, the probe was located at a distance from the outside of the caisson wall of r_w = 1.9 cm. As the wall approaches the probe tip depth, a large excess positive pore pressure is generated, leveling out at Δu = 0.3 ksc when the wall is 0.5 cm above the tip depth. This excess pressure is maintained as the wall passes the tip depth, and begins to slowly decline once the wall has penetrated approximately 0.6 cm beyond the probe depth. At the end of penetration, there is still an excess pressure of Δu = 0.25 ksc at this location.

Probes P2 through P4 in CET-14 measured pressure at a depth of 2.9 cm and were spaced radially from centerline at r = 1.8, 3.2, and 4.45 cm, respectively. Probes P2 and P3 both recorded pore pressure behavior similar to that beneath the cap. Figure 5.23 shows the pore pressure generated at a distance of 0.5 cm (P2) from the inside wall for CET-14. Except for the magnitude of initial peaks and valleys, this curve mimics that for the pore pressure beneath the cap. In fact, the excess pore pressure from a wall penetration of z_w = 1.5 to the end is nearly identical, indicating that the entire soil plug created within the caisson is experiencing the same pore pressure generation pattern. Just outside the caisson at a distance from the wall of r_w = 0.6

cm, P3 also measures a similar pattern. However, as the wall approaches to within 0.3 cm of P3's tip depth, the increasing excess pressure peaks and begins slowly falling. As the wall passes the tip, the excess pore pressure slowly continues falling and reaches $\Delta u = 0.5$ ksc, which is half the value measured within the soil plug. Probe P4, which was located $r_w = 1.91$ cm from the caisson wall, only measured a gradual increase in excess pore pressure, reaching $\Delta u = 0.35$ ksc by the end of penetration.

At 2 cm above the clay bottom, probe P1 in CET-14 measures a gradually rising excess pore pressure that reaches $\Delta u = 0.25$ ksc by the end of penetration when the wall is approximately 7 cm above the probe tip. Note that the positive and negative swings in pore pressure so apparent at the surface location just beneath the cap (see Fig. 5.22) are not reflected at all at the clay bottom. However, at the end of driving, the combined effect of the cap movements and the wall penetration was enough to raise the pressure to a value of $\Delta u = 0.25$ ksc, which is larger than any soil mass pore pressure recorded for any of the test suction installation tests.

Cap displacements during wall penetration are shown in Figure 5.24. The cap in CET-13, which has a controlled constant cap force of $F_c = 14$ kg, initially moves downward by $z_c = -0.06$ cm during the initial $z_w = 1.2$ cm of penetration. This movement implies partially plugged penetration, which is probably a result of the constant stress distribution on the rigid cap. As the wall initially penetrates and picks up load, the inside surface of the caisson becomes highly stressed, which could possibly cause more soil to displace toward the outside. For the remainder of penetration, the cap movement is similar to pattern 2 exhibited by CET-8-10, as described in section 5.2.2. From $z_w = 1.2$ to 3.2 cm, the cap rises at an increasing rate, but thereafter it rises at a decreasing rate until reaching a final rise of $z_c = 0.52$ cm, which is just below the range for standard rate tests. The goal of caisson installation in CET-14 was to maintain zero cap displacement, but as Figure 5.29 shows, problems with control led to some cap movements. The cap drop of $z_c = -0.22$ cm at a wall penetration of $z_w = 0.5$ cm and the slight cap rise of $z_c = 0.06$ cm at $z_w = 3.2$ cm severely affected the cap force, total force, and pore pressure behavior throughout penetration, as noted before. However, the change in cap directions only lightly affected the wall force behavior, which was similar in overall shape and magnitude to the most representative standard suction driving tests.

In response to the fixed cap force in CET-13, the soil surface heaves between 0.003 to 0.0075 cm, depending on the radial location. Figure 5.25 shows that at locations closer to caisson wall, $r_w = 1.7$ and 2.7 cm, the surface heaves initially and then compresses toward the end of wall penetration. The heaving is caused by the movement of soil displaced by the dropping cap, while the compression is in response to the soil volume moving up with the cap (cap movements were shown in Fig. 5.24). At the farther radial locations, $r_w = 5.2$, 7.3, and 9.6

cm, the surface heaves less, but the heaving continues right to the end of wall penetration without any compression. Note that the peak heave at both r_w = 1.7 and 2.7 cm is approximately 0.0075 cm, which is 5 times greater than the peak heave of 0.0015 cm recorded for standard rate suction tests (see S2 for CET-5 in Fig. 5.18), but this magnitude is still quite small (~5% of wall thickness). As for the caisson force and soil pore pressure records, the soil displacement record for CET-14 is a product of the unplanned cap deviations from zero-displacement control. Responding to compression and uplift cycle of the cap during the first z_w = 1.5 cm of wall penetration, the soil surface first heaves then compresses, as shown in Figure 5.25. After the cap is stabilized, the soil surface undergoes tremendous heave, as the wall-displaced soil has nowhere to go but outside the walls. At a distance of r_w = 2.7 cm, the soil initially heaves 0.013 cm, compresses to -0.002, and then reaches a final heave value of 0.021 cm (14.4% of wall thickness). At each radial location beyond r_w = 2.7 cm this pattern is exhibited, with the magnitude diminishing with increasing distance from the wall. Note that at the closest radial location, r_w = 1.7 cm, the initial heave and compression is larger than that at r_w = 2.7 cm, but the final heave is only 0.012 cm. This suggests that by the end of penetration, the soil surface topography incorporates a "bulge" that peaks at a radial distance located between r_w = 1.7 and 5.2 cm.

5.4 EQUILIBRATION

Immediately following installation for all tests, the caisson was allowed to equilibrate with the surrounding soil for at least 18 hours (Table 5.2). The basic behavior of the caisson forces, caisson settlement, soil pore pressure, and soil compression are presented in this section[3]. During the set-up phase, the total force on the caisson F_{TOT} (= F_w+F_c) was held constant at F_{TOT} =15.2 kg (= $\sigma'_{vc}A_{tot}$), while allowing zero relative displacement between the cap and wall.

5.4.1 Caisson Force Distribution

Typical caisson force behavior during equilibration is illustrated in Figure 5.26, which plots the caisson wall, cap, and total forces as a function of time (log scale) for CET-9, which was chosen for the quality of its test control and instrumentation data (Table 5.3b). The total force remains constant at F_{TOT} = 15.1 kg, which is just 0.1 kg below the design value of F_{TOT} =15.2 kg (= $A_c\sigma'_{vc}$). Redistribution of the wall and cap forces is rapid. After reaching a peak wall force of F_w = 17 kg by the end of penetration, the wall sheds 3 kg within 2 minutes and maintains a range of F_w = 14 to 15 kg for the remainder of set-up. Similarly, the cap, which holds a tensile load of F_c = -1.5 kg at the end of installation, acquires 2.5 kg of compressive load

[3]Electrical power fluctuations marred otherwise excellent equilibration behavior in CET4, 5, and 10, and most results from these tests are not presented.

in 2 minutes and holds a slightly positive load of between F_c = 0-1 kg for over 33 hours. As discussed in section 4.5, the minor force fluctuations observed beyond 2 minutes probably are due to intercomponent friction. The caisson force distribution pattern exhibited by CET-9 is similar to the pattern in every test. The remainder of this section examines this similarity by focusing on each caisson force component, starting with total force.

5.4.1.1 Total Force

Figure 5.27 shows the total force versus log of time for 6 standard suction driving tests (CET-3, 7-9, 11-12) and two non-standard tests (CET-13, 14) during the equilibration phase. Note that for both the suction driving and equilibration phases, the design total force was F_{TOT} =15.2 kg. As explained in section 4.5.1, small differences in the control program led to some variation in total force during driving. This variation is visible at the start of set-up, at which point the total force varies from F_{TOT} =15.2 to 17.2 kg. Within 3 minutes of the start of set-up, however, the total force for all tests reaches the design value of F_{TOT} =15.2 ±0.3 kg. For CET-13, in which the caisson was driven with a constant cap force, the total force at the end of penetration was F_{TOT} =33.6 kg. Within 2 minutes of the start of set-up, the design value of total force had been established. In CET-14 the cap position was fixed during penetration and this led to a final total force of F_{TOT} =37.6 kg. Because no data was recorded during the first 5 minutes of set-up, the dashed line in Figure 5.40 shows the total force dropping to the design value within 5 minutes of the start of set-up. It is likely that the design total force of F_{TOT} =15.2 kg would have been established within 3 minutes, as it was for the other tests.

5.4.1.2 Wall Force

The wall force measurements during set-up exhibit a quick redistribution of force from the end of penetration, but with a bit more scatter in equilibrium force from test to test compared to the total force records. Figure 5.27 shows the wall force versus log of time for CET-3, 7-9, and 11-14. The wall force for the six standard rate suction driving tests (CET-3, 7-9, 11-12) starts at a value ranging from F_w = 17 to 22.5 kg and falls in 3 minutes to a range of F_w = 13.5 to 16.5 kg, which is then held with a few minor deviations until the end of equilibration. The variation in force among the tests can be attributed to the different values of contributing intercomponent friction, which was described in section 5.2.1. In CET-13 the wall force starts high at F_w = 23.5 kg, drops to F_w = 3 kg in 30 seconds, and then slowly builds to a value of approximately F_w = 14 kg by the end of equilibration. The wall force drop to F_w = 3 kg and subsequent build-up to equilibrium value was caused by control program overcompensation: the wall was lifted a bit too much as the control program attempted to reduce the high final penetration total force (F_{TOT} = 33.6 kg) to the set-up design value (F_{TOT} = 15.2 kg). Similar

overcompensation caused the wall force in CET-14 to drop first from F_w = 15.9 kg to 3.5 kg in 5 minutes before slowly building up to approximately F_w = 10.5 kg by the end of set-up. Because of the lack of recorded data before 5 minutes, it is possible that the wall force reached a value lower than F_w = 3.5 kg within 5 minutes of the start of set-up. Note that the shape of the wall force curve in CET-14 indicates that the wall may still be accumulating force at the end of 24.9 hours. Given more set-up time, it is conceivable that the wall force may reach the equilibration range of F_w = 13.5 to 16.5 kg.

5.4.1.3 Cap Force

Because the total force is held constant during set-up, the cap force behavior is a nearly perfect reflection of the wall force record. As Figure 5.27 shows, the initial tensile cap force ranges from F_c = -6 kg to 0.2 kg for the suction driving tests (CET-3, 7-9, 11-12). Within 3 minutes the cap has shed most of its force. For the remainder of set-up, the cap force ranges from F_c = -0.5 to 1.5 kg with a few small deviations. In CET-13 and 14 the cap force at the end of penetration is high at F_c = 14 and 17.8 kg, respectively. Due to the time required to dissipate the large installation pore pressures, the compressive cap force in these tests slowly declines. By the end of equilibration, it appears that the cap force in CET-13 has reached an equilibrium value of F_c = 2 kg. However, in CET-14 the cap force would probably continue dropping if allotted more set-up time.

From the evaluation of force components during post-installation equilibration in suction driving tests, it is clear that the cap quickly sheds any residual tensile force from installation and carries very little load for the remainder of set-up. The wall force balances the cap behavior and carries nearly all of the total caisson force for the rest of equilibration. For tests wherein the caisson was installed using non-suction methods, the longer dissipation of much greater installation pore pressures delays the redistribution of cap and wall forces; by the end of equilibration the wall carries most of the load and the cap retains a small (~2-5 kg) compressive load.

5.4.2 Pore Pressure Dissipation

The pore pressure pattern measured beneath the cap and in the soil mass generally reflects the redistribution of the caisson forces during the set-up stage. Figure 5.28 plots the excess pore pressure beneath the cap that was generated during installation for 6 suction driving tests (CET-4, 7-9, 11) and 2 non-suction tests (CET-13-14). Pressure for the suction driving tests starts at low positive or negative values (Δu = 0.04 to -0.21 ksc) due to the low positive or tensile stress on the cap at the end of suction driving (see Figures 5.14, 5.15). As the cap force rises during the first 3 minutes of equilibration, the pore pressure in these tests rises to a range Δu =

0.02-0.08 ksc. Beyond 3 minutes the cap force is constant, and complete dissipation of the small excess pore pressures occurs in approximately 16 hours. The excess pore pressure in tests CET-13 and 14 responds immediately to the pre-set change in total force F_{TOT}. For CET-13 the pre-set value, F_{TOT} =15.2 kg, was achieved within approximately 3 minutes and is accompanied by a pore pressure drop beneath the cap from Δu = 0.68 ksc to 0.3 ksc. Thereafter, as the loads on the cap and wall redistribute, these remaining excess pressures dissipate in approximately 16 hours. The excess pore pressure record in CET-14 also reflects the unloading of the caisson (t<5 minutes) and then the dissipation accompanied by stress redistribution within 16 hours.

The same dissipation trends are evident in excess pore pressure measurements within the soil mass. Figure 5.28 shows the excess pore pressure versus time (log scale) for probes P1, P2, P3, and P4 located at radial distances from centerline of 0.0, 1.8, 3.2, and 4.45 cm, respectively[4]. This probe measured pressure 2 cm above the clay bottom. The behavior of the pore pressure within the soil plug inside the caisson, as measured by P1 and P2, is very similar to the dissipation of pore pressure beneath the cap, which was discussed above. As shown in Figures 5.28, the soil plug excess pore pressure rises during the first 3 minutes of set-up to a slightly positive range between Δu = 0.07 to 0.14 ksc in response to cap force equilibration. Thereafter, the excess pore pressure dissipates completely by approximately 16 hours (1000 minutes). The excess pressure at the end of set-up is not exactly zero but is approximately $\Delta u = 0.00 \pm 0.05$ ksc due to temperature and barometric pressure variations occurring throughout the approximately 24 hours of set-up. Note in Figure 5.28 that the pore pressure measured at the clay bottom in CET-14 remains steady at approximately Δu = 0.22 ksc until 30 minutes into set-up, whereupon it drops rapidly for 10 minutes and then slowly dissipates for the remainder of set-up. This sudden drop is due to the evacuation of soil that had been blocking the chamber bottom drainage line. At the probe P3 location just outside the caisson at a radius of r = 3.2 cm, the excess pore pressure dissipation behavior is identical to that for soil plug inside the caisson except for the initial 3 minutes for the suction installation tests. The redistribution of the tensile cap force during initial set-up does not affect the fluid pressure in the soil mass exterior to the caisson, as the excess pore pressure at the probe P3 location begins dissipating within only a few seconds of the start of set-up. Measurement of pore pressure at the furthest location by P4 (r = 4.45 cm) was only available for the non-suction installation tests, CET-13 and 14. Figure 5.28 shows that the excess pressure dissipates completely within 10 hours for CET-13 and to a negligible value by the end of set-up in CET-14[5].

---

[4]All probes were located at a depth of between 2.0 and 2.9 cm below the surface of the clay prior to installation except for probe P1 in CET14.

[5]The excess pore pressure at the end of set-up in CET14 is Δu<0 due to a slightly inaccurate zero reading at the start of installation.

5.4.3 Caisson Displacement

During equilibration, the model caisson displaces as a monolithic unit. This is achieved by controlling the cap to follow the wall displacement (section 3.1.4). Figure 5.29 shows the typical displacement pattern for CET-8 including the displacements of the wall and cap, and the relative displacement of the wall and cap. The caisson wall and cap settle at an increasing log rate until reaching approximately -0.015 cm after 70 minutes. For the remainder of set-up, the caisson settles at a constant log-linear rate of approximately -0.035 cm per log time cycle until reaching a final settlement of just over -0.07 cm. Note that in this test, the wall displaces downward nearly -0.002 cm relative to the cap during the first 10 minutes. Figure 5.30 shows the wall and cap displacement, respectively, for the other reliable tests. The overall trend is clear. The caisson settlement log rate increases until reaching a certain point in time, after which the settlement rate is approximately log-linear. The rate of log linear settlement varies from test to test. This variation is probably a result of drainage condition differences from test to test because the effectiveness of the clay surface drainage varied. The final settlement varied from -0.021 to -0.092 cm (i.e., approximately 10-65% of the wall thickness). Note that differences between the cap and wall displacement for a particular test indicates a relative displacement at some point during set-up that usually was due to electrical control disturbances. The caisson in test CET-13 heaves by approximately 0.012 cm due to unloading of the caisson ($t<3$ minutes) and then undergoes a net settlement of -0.04 cm as the pore pressures equilibrate.

The caisson settlement behavior for CET-14 is depicted separately in Figure 5.31. Settlement appears to proceed much like the other tests until 30 minutes into set-up, whereupon the settlement rate abruptly increases and leads to a higher than normal final settlement of approximately -0.25 cm. This is due directly to the evacuation of a soil plug in the chamber bottom drainage line, an action that caused the abrupt increased dissipation of excess pore pressure near the clay bottom (see section 5.4.2).

The caisson settlement exhibits a pattern that is very similar to one-dimensional compression. In Chapter 6, comparisons are made between these caisson settlements and one-dimensional compression data for Resedimented Boston Blue Clay (RBBC).

5.4.4 Soil Surface Settlement

The settlement of the soil surface outside of the caisson follows the same pattern as the caisson. However the magnitude of settlement generally decreases with increasing distance from the caisson. Figure 5.32 shows the soil surface settlement versus log of time at five radial locations in CET-8 during post-installation equilibration. The soil surface settles at an increasing log rate until between 5 to 8 hours have elapsed, after which settlement continues at a linear rate

with log time. Note that up to the constant log linear settlement zone, the settlement rate decreases with increasing radial distance from the caisson, ranging from -0.035 cm at S1 to -0.013 cm at S5. The surface settlement for the remaining reliable tests is shown in Figure 5.33. As for the caisson settlement, the variation in settlement rates among the tests can be attributed to variations in the effectiveness of pore fluid drainage. Although there are some exceptions, in general the settlement decreases with increasing distance from the caisson wall. At a radius of r_w = 1.7 cm, the settlement varies from -0.027 to -0.083 cm, decreasing to a range between -0.002 and -0.057 cm at r_w = 9.6 cm.

As for the caisson displacement, the soil surface settlement in CET-14 was affected greatly by the increased drainage approximately 30 minutes after the start of set-up. As shown in Figure 5.58, the final surface settlement ranges from -0.253 to -0.3, which is 3 to 10 times (depending on radial location) greater than the settlement in other tests.

As for the caisson settlement, comparisons are made in Chapter 6 between the soil surface settlement record and the one-dimensional compression pattern for RBBC.

5.5 MONOTONIC PULLOUT 1

The results of the initial monotonic pullout phase in 11 tests (CET-3-6, 8-14)[6] are presented in this section. After the caisson had settled and the installation pore pressures had dissipated during the equilibration phase, the caisson was withdrawn from the soil at a rate v_w = 0.03 cm/min while maintaining zero relative displacement between the cap and wall. In five tests (CET-3-6, 8) the caisson was pulled for at least δ_w = 0.3 cm[7] in order to measure tensile capacity. Thereafter the caisson was either pulled at a rate of v_w = 0.3 cm/min. until complete extraction (CET-3, 4, and 8) or was re-equilibrated within the soil (CET-5-6). For the last six tests (CET-9-14), the caisson was pulled to a specific tensile load level in order to investigate the effects of sustained tension. The total displacements in these tests are less than 0.01 cm.

5.5.1 Caisson Force Distribution

Figures 5.35a,b shows relative contributions of the caisson force components (F_w, F_c, and F_{TOT}) as a function of wall displacement (at two scales) during monotonic tensile loading in CET-8. The caisson exhibits a very stiff initial load-displacement response (Fig. 5.35a); an applied tensile load of ΔF_{TOT} =30 kg was required to displace the wall by 0.02 cm (i.e., F_{TOT} =-15 kg in tension at δ_w = 0.02 cm). The caisson response is dominated initially by the behavior of the wall, which carried an applied load of ΔF_w = 24.5 kg in the same displacement range ($\Delta F_w/\Delta F_{TOT}$ = 82%), and reached a tensile force F_w = -11 kg at δ_w = 0.02 cm. In contrast, the

[6]Results for CET7 are not shown due to excessive inner slip ring/caisson wall friction (see section 5.2.1).
[7]0.3 cm = 2w, where w is the caisson wall thickness.

measurements show a very abrupt change in cap force (ΔF_c = 5 kg), which then remains constant in the range 0.001 to 0.02 cm, and accounts for only 20% of the total tensile load on the caisson at δ_w = 0.02 cm. The enlarged displacement scale shows that δ_w = 0.02 cm corresponds to a yield point in the system response. Further displacement causes tensile hardening response of both the cap and wall forces, such that the maximum resistance of both components and the total caisson occurs at a displacement $\delta_w \approx 0.2$ cm. As shown in Figure 5.35b, in CET-8 at a displacement δ_w =0.23 cm, the caisson has a tensile load capacity F_{TOT} =-22.4 kg, to which the cap force contributes 40% (F_c = -8.9 kg) and the wall force 60% (F_w = -13.5 kg). With a couple of exceptions, the monotonic pullout force behavior exhibited by CET-8 is typical of all tests.

5.5.1.1 Total Force

Figure 5.36a shows the total force versus wall displacement for six tests (CET-3-6, 8). The overall response is very similar to that outlined above for CET-8. In all cases, the caisson exhibits a very stiff initial response, reaching a tensile force F_{TOT} = -7 to -12.5 kg within a displacement δ_w = 0.01-0.02 cm. There is a well-defined yield point at δ_w =0.01-0.02 cm, after which the the caisson continues to pick up additional tensile load, but at a rapidly decreasing rate. The maximum caisson capacity ranges from F_{TOT} = -17.6 to -23.95 kg and occurs at δ_w = 0.17 to 0.3 cm. There is only slight post-peak softening of the resistance for displacements up to δ_w = 0.4 cm. The total capacity in CET-3 is slightly lower than the other tests by about 3 kg. Control problems caused the cap to move more slowly than the wall after a displacement of approximately δ_w = 0.01 cm, and thus the cap was not able to mobilize as much tension as the other tests (see Fig. 5.36c). If the data from test CET-3 is neglected, the total force behavior appears very consistent. The average caisson capacity for the remaining 4 tests is F_{TOT} = -22.8 ± 0.7 kg and occurs at a displacement δ_w = 0.25±0.03 cm.

The total force record during early withdrawal is particularly consistent. Figure 5.37 plots the caisson force components in 8 tests (CET-6, 8-14) for δ_w = 0-0.02 cm. Note that CET-3, 4, and 5 are not included because they were hampered by relative displacement control problems during early withdrawal (see section 4.1.4). Starting from an equilibrium compressive force that ranges from F_{TOT} = 14.1 to 15.6 kg, the caisson in all tests responds very stiffly to axial withdrawal.[8] The initial stiffness ranges from $M_{tot} = \Delta F_{TOT}/\Delta\delta_w$ =9000-5000 kg/cm.

5.5.1.2 Wall Force

[8]In the sustained load tests (CET9-14), the total force record ends at $\delta_w \leq 0.003$ cm of displacement, but it is clear that total force for these tests was rising according to a trend similar to that for CET 6 and 8, which show a total force increasing at a decreasing rate.

Individual wall force versus wall displacement records for the 5 capacity tests (CET-3-6, 8) are shown in Figure 5.36b. The wall initially reacts stiffly and carries a tensile load F_w = -3 to -12 kg at the yield displacement δ_w = 0.01-0.02 cm. The maximum wall resistance ranges F_w = -12 to -14 kg (neglecting one outlier test CET-4) and is mobilized at a displacement range δ_w = 0.15-0.25 cm, which is similar to the range of mobilization for the maximum caisson capacity (δ_w = 0.17-0.3 cm). In CET-4 the wall force exhibits an uncharacteristic cycling pattern that is caused by changing frictional conditions between the caisson wall and cap (see Figs. 5.36b,c). Note that the cap force for this test shows a complementary cycle (see Fig. 5.62). The total force in CET-4 is unaffected by the inter-component friction, as shown in Figure 5.36a. If the percentage wall force contribution is calculated for each of the 3 tests that had representative cap and wall force behavior (CET-5, 6, and 8), the wall contributes an average of 58% of the total capacity.

Figure 5.37 shows the initial wall response (δ_w = 0.0 to 0.02 cm) for 8 tests (CET-6, 8-14). The initial compressive forces range (at equilibrium) from F_w = 9.7 to 16.35 kg, and the data reveal an initial wall stiffness in the range, $M_w = \Delta F_w/\Delta\delta_w$ = 3300-2600 kg/cm, which is significantly lower than that of the overall caisson. Even though tests CET-9-14 were interrupted at small displacements ($\delta_w \leq$ 0.007 cm), their trend is clearly within the limits set by the capacity tests, CET-6 and 8.

5.5.1.3 Cap Force

Figure 5.36c shows the cap force records for CET-3-6, 8, which contains a subset of reliable tests CET-5-6, 8. In these more reliable tests, the cap carries almost no load at initial equilibrium, but mobilizes F_c = -4 to -7 kg of tension within δ_w = 0.001 cm (i.e., almost instantaneously), and then slowly accumulates ΔF_c = -3.5 to -5 kg as the displacement mobilizes peak capacity at δ_w = 0.2 cm. The maximum cap force almost coincides with the displacement necessary to mobilize total caisson capacity. Control problems beset the cap force data in tests CET-3-5, causing a characteristic delay in the initial force mobilization (at δ_w<0.02 cm). In test CET-3, the cap withdrew at a slower rate than the wall, and this rendered the cap force record non-representative. In CET-4, the cycling behavior evident in the cap force was due to changing friction between the caisson cap and wall, as discussed for the wall force record above. Considering just the representative tests CET-5-6, 8 the average cap force at the moment of total capacity was F_c = -9.7±1.4 kg.[9] Based on those tests that had both representative cap and wall behavior (CET-5, 6, and 8), the cap force contributes an average of 42% to the total capacity.

Figure 5.37 focuses on the initial cap behavior (δ_w = 0.0 to 0.02 cm) behavior for 8 tests

[9]50% of the peak cap level is mobilized almost instantaneously at $\delta_w \leq$ 0.001 cm.

(CET-6, 8-14). These data suggest that the cap exhibits a very stiff initial response, $M_w = \Delta F_c/\Delta \delta_w =$ 6400-2500 kg/cm with a well-defined yield point at $\delta_w = 0.003$ cm.

5.5.1.4 Best Estimate of Component Force Behavior

In order to interpret the behavior of the caisson force components during monotonic pullout, a "best estimate" of the total, wall, and cap force behavior was developed. Figures 5.38a,b,c depict the most representative total, wall, and cap force records at both small displacements, δ_w = 0.0-0.02 cm, and for displacments up to peak resistance (δ_w = 0.0-0.4 cm). The initial small displacements show clearly the yield points for the cap (δ_w = 0.003 cm) and wall (δ_w = 0.02 cm) components. For example, the cap force behavior is derived from measurements in tests CET-14, CET-11, and CET-6. The best estimate of caisson capacity ranges from a low, F_{TOT} = -22.2 kg at $\delta_w = 0.257$, to a high, F_{TOT} = -23.8 kg at $\delta_w =$ 0.237 cm, with an average F_{TOT} = -23 kg at $\delta_w =$ 0.25 cm. At this displacement, the best estimate of wall force ranges from $F_w =$ -11.4 to -14.9 kg (50-65% of total), while the cap ranges from $F_c =$ -9 to -11.8 kg (40-51% of total).

5.5.1.5 Fast Rate Monotonic Pullout

In tests CET-3, 4, and 8, the caisson was loaded monotonically to beyond peak resistance at a rate of v_w = -0.03 cm/min. Thereafter, the rate of loading was increased to v_w = -0.3 cm/min until complete caisson extraction (i.e., δ_w = 5.1 cm). Figures 5.39a,b,c show the total, wall, and cap force behavior, respectively, for both the slow and fast pullout phases for these three tests. In each case, the applied forces relax as the load rate is adjusted (because the control program was manually stopped and restarted). Note also that after the end of slow pullout in test CET-4, the caisson continued to displace an additional 0.15 cm due to a small sustained tensile load. At $\delta_w = 0.3$ cm in CET-3, the total force is F_{TOT} =-18 kg, which relaxes to F_{TOT} =-17 kg. Loading at the higher displacement rate causes a very soft response such that after $\Delta\delta_w$ = 0.1 cm, the total force reaches nearly F_{TOT} =-25 kg, an increase of ΔF_{TOT} =-7 kg over the peak resistance for slower loading. The total force in CET-4 and 8 increased by approximately ΔF_{TOT} =-3 kg over their total force values at the end of slow pullout. Due to control problems during the slow pullout in CET-3 and 4 mentioned above, the magnitude of the increased capacity resulting from the faster pullout cannot be compared from test to test. However, the shape of the fast rate total force curve appears similar in all three tests. In all caissons, peak resistance occurs within 0.1 cm displacement at the higher imposed velocity, after which the total force decreases at a constant rate until reaching approximately δ_w = 4 cm, at which time the remaining tensile force is shed rapidly.

As shown in Figures 5.39b, c, the wall and cap force records during the fast rate pullout

do not show any consistent trends. In CET-3, the wall force only rises ΔF_w = -1 kg above the final slow rate value before dropping at a constant rate for the remainder of pullout. Most of the rate sensitivity is due to the behavior of the cap force, which increases by approximately ΔF_c = -8 kg within $\Delta\delta_w$ = 0.1 cm at the higher displacement rate. In both CET-4 and 8, the wall and cap records are affected by intercomponent friction, but appear to contribute equally to the total caisson force throughout fast rate pullout. Further insight into the rate effects on caisson forces are discussed in section 5.8, which covers the second round of monotonic pullout tests.

5.5.2 Pore Pressure Generation

Monotonic pullout of the caisson generates large negative excess pore pressure in the soil plug within the caisson. Figure 5.40 plots the excess pore pressure measured beneath the cap versus the wall displacement for two tests in which the caisson was displaced to its capacity (CET-5-6) and six additional tests in which only small displacements were imposed (CET-9-14). The underbase excess pore pressure matches very closely the average basal stress due to the cap load, $\overline{\sigma_b}$. In 7 tests (CET-5, 9-14) between Δu = -0.2 and -0.4 ksc is generated at the cap yield displacement δ_w = 0.003 cm. With continued displacements, more (negative) excess pressure is generated, reaching a peak at $\delta_w \approx 0.2$ cm, where the cap force is also mobilized (see Fig. 5.36c). The maximum excess pore pressures for CET-5 and 6 are Δu = -0.5 and -0.46, respectively. The variation in magnitude can be attributed to variations in the mobilized cap load (see Fig. 5.36c). Friction between the cap and wall caused the cycling pore pressure measurement in CET-7, but the overall trend of large excess negative pressure generation is consistent with the trends for CET-5 and 6.

Figure 5.41a shows that the pore pressures measured by probe P1, located approximately 2 to 3 cm above the wall tip on the centerline of the caisson (see Table 5.1), are very similar to those measured below the cap. In CET-5, P1 was located at the centerline, but at a depth above the wall tip of approximately 1 cm.[10] The records from 7 tests (CET-5-6, 9-12, 14) show that large negative excess pressures (Δu = -0.42 to -0.5 ksc) are mobilized within the soil plug at full caisson resistance (δ_w = 0.2-0.3 cm). During the initial phase of the tests (δ_w = 0-0.02 cm), much greater negative pore pressures are generated for tests CET-9-12 than for CET-6. There is no apparent explanation for this discrepancy. Note that practically no excess pore pressure is generated at the base of the clay cake, as evidenced by the probe response in CET-14.

The probes P2 measure pore pressure at the same depth as P1, but at a radius r = 1.8 cm (i.e., 0.6 cm from the inside caisson wall). Figure 5.41b presents the P2 excess pore pressure record for six tests (CET-4, 8-10, 13-14). The results show large negative excess pore pressures:

[10]Note that P1 in CET14 was located approximately 2 cm above the clay cake bottom and 6 cm below the caisson wall tip.

Δu = -0.25 and -0.4 ksc generated at δ_w = 0.003 cm. However, as the caisson displacements continue, the P2 excess pore pressure become significantly higher than those measured at other locations within the plug (see Figs. 5.40, 5.41a), reaching a peak value, Δu = -0.68 ksc, at δ_w = 0.21 cm for CET-8. With continued loading of the caisson, the P2 pore pressure decreases slightly.

Completely different pore pressure behavior is measured in the soil mass outside the caisson. Figures 5.41c, d show the pore pressure records for probes P3 and P4, respectively, both of which were located at the same depth as P1 and P2, but at radii r = 3.2 cm (i.e., 0.66 cm from the outside wall) and r = 4.45 cm, respectively. The P3 probe measurements at small displacements $\delta_w \leq 0.003$ cm show a wide variation in response. In tests CET-9-11, the P3 measurements follow closely the pore pressure measurement inside the caisson (Δu = -0.2 to -0.4 ksc, see Figs. 5.40, 5.41a, b), while much smaller negative pressures occur in tests CET-8, 14. In test CET-8, the P3 pore pressure stabilizes at Δu = 0.1 ksc by δ_w = 0.02 cm and decreases with continued caisson extraction. By the time the caisson capacity is fully mobilized at δ_w = 0.2 cm, P3 pore pressure has reached Δu = -0.1 ksc. There is minimal data available from probe P4 (tests CET-13,14 only). Figure 5.41d is included for completeness only.

5.5.2.1 Fast Rate Monotonic Pullout

There is very limited pore pressure data for the three pullout tests at the higher displacement rate v_w = -0.3 cm/min. However, a significant rate effect can be seen in these data. Figure 5.42a shows the excess pore pressure measured by probe P2 inside the caisson for CET-8. The relaxation of total stress that occurs as the displacement rate is adjusted causes a significant change in the P2 pore pressure (from Δu = -0.44 to -0.21 ksc). Loading at the higher displacement rate causes the P2 pore pressure to rise rapidly to a peak value which is -0.15 lower than that observed at the end of the previous phase. For the remainder of pullout, the negative excess pressure declines at a constant rate.

The only record of fast pullout rate pore pressure behavior in the soil mass outside the caisson was measured by probe P3 (r = 3.2 cm) in CET-8 (see Fig. 5.42). Fast rate pullout generates no significant pore pressures at this location until reaching a displacement of $\delta_w \approx 2.05$ cm, whereupon negative excess pore pressure is generated as the wall tip rises past the probe tip. After reaching a maximum negative pressure of Δu = -0.18 ksc by a pullout distance of z_w = 3.3 cm, the negative excess pore pressure declines.

5.5.3 Soil Surface Displacement

Data from the five soil surface displacement transducers (S1-S5, Fig. 5.2) indicate a consistent pattern of surface movement during monotonic pullout from test to test. Figure 5.43

shows the surface displacement at five radial locations during wall displacement, δ_w = 0-0.4 cm, for CET-8. This figure illustrates the following characteristics of soil surface displacement during monotonic pullout that are common to all tests: 1) soil surface movements are small, less than 0.015 cm (δ_s/δ_w<4%) even close to the wall (S1, S2), 2) the soil surface close to the wall (S1, S2) heaves during the initial phase of loading, δ_w<0.1-0.15 cm, 3) at radial distances farther from the wall (S3, S4, S5) settlements increase monotonically with pullout displacement of the caisson, and 4) the magnitude of surface settlements decreases with radial distance.

Figure 5.44 shows the soil surface displacement at five radial locations versus wall displacement during monotonic pullout for 4 tests (CET-4-6, 8). The data from S1, S2, and S3 show some significant scatter, but very consistent trends as discussed above for CET-8. The surface heave (0.001-0.002 cm) measured by S1 is slightly larger than that at S2 (0.001 cm), but both transducers measure similar settlements as the caisson reaches full capacity at δ_w = 0.2-0.3 cm (δ_s = -0.008 to -0.002 cm for S1 and S2). The settlement rates for S1 and S2 are also very similar: $\Delta\delta_s/\Delta\delta_w$ = -0.006 to -0.007 cm/cm for both S1 and S2. The records for S3, S4, and S5 show settlements increasing approximately linearly with wall displacements at rates of $\Delta\delta_s/\Delta\delta_w$= 0.003, 0.0018, 0.001 cm/cm, respectively.

5.5.3.1 Fast Rate Monotonic Pullout

The soil surface displacement during both slow and fast rate withdrawal in tests CET-4, 8, as measured by S1-S5, are shown in Figure 5.45. The surface settlement patterns do not reveal any particular rate effect. Instead, the dramatic settlement near the caisson wall (≈-0.2 cm at δ_w = 2 cm for S1 and S2) indicate that the soil mass at these near-wall locations is clearly participating in the general failure as the caisson moves at the faster rate, v_w = 0.3 cm/min. In contrast, the soil surface at distant locations (S4,S5) ceases to settle significantly as the caisson is withdrawn at the fast rate beyond δ_w = 1 cm, thereby indicating that the soil mass at these locations is not part of the general failure mechanism.

5.6 SUSTAINED LOAD

This section presents the results of the sustained load phase for six tests that can be divided into two main groups: 1) single sustained load level (CET-9, 10) and 2) step sequence of sustained loads (CET-11-14). In the single sustained load tests, the caisson was pulled at a constant displacement rate to a specified tensile force (F_{TOT}), which was then held constant until a either the pore pressures equilibrated or the soil system developed a failure mechanism. In CET-9 the caisson was allowed to equilibrate at F_{TOT} = -2.2 kg over a period of approximately 10 hours, after which the caisson was pulled immediately to failure at v_w = 0.03 cm/min. In CET-10 a failure mechanism developed at F_{TOT} = -11.4 kg.

In the step sequence of sustained load tests, the tensile loads were maintained for 24 hours before applying an additional increment of tensile load (typically ΔF_{TOT} = -2kg). This process was repeated until a failure mechanism developed during sustained loading. In three of these tests (CET-12-14), further caisson testing events were carried out after failure under sustained loading (see sections 5.7,5.8). The specific loading schedule for individual tests are listed in Table 5.2. The total force and displacement timelines are illustrated in Figure 5.2.

The caisson and soil response during sustained loading phases are reported as a function of time after load application (on a log scale)[11]. The time frame for load increment application is very short.

5.6.1 Caisson Force Distribution

Figure 5.46 shows the total, wall, and cap forces versus (the log of) time for tests CET-9 and 10, with single sustained tensile load stages F_{TOT} = -2.2kg and -11.4kg, respectively. In the first minute, the wall and cap adjust to the applied load, after which there is a progressive transfer of load to the wall of the caisson in both tests. In test CET-9 the wall initially carries a small compressive force of F_w = 11 kg and acquires a tensile load of F_w = -3.6 kg within 8 hours. The cap, meanwhile, sheds its initial tensile load of F_c = -3 kg and carries a small compressive load, F_c = 1.4 kg, after 8 hours. During the final 5 hours of sustained load, the caisson load redistributes slightly, as the cap loses its compressive load and the wall sheds 1 kg of tension. In test CET-10, 73% of the applied total tensile load (F_{TOT} = -11.4 kg) is initially (at 1 minute) carried by the cap (F_c = -8.3 kg while F_w = -3.1 kg). The cap force decreases by 5 kg within 40 minutes, but the cap is unable to shed the remaining tensile load F_c = -3.5±0.5kg (30% of the total tension). This behavior indicates a failure mechanism, which is witnessed by the displacement and pore pressure responses (Figs. 5.51 and 5.56). The wall increases its share of tensile load from F_w = -3.1 kg to -7.9 kg during the first 40 minutes of sustained loading and maintains nearly -8 kg of tension for the rest of the test.

In tests CET-11-14, at least 3 increments of sustained load were required before the caisson begin to fail. Figures 5.47-5.50 show the total, wall, and cap force versus log of time for the sustained load increments in these tests. Each individual figure shows all increments of sustained load for one particular test. During the first tensile load increment (SL1, Figs. 5.47-5.50) in each of these multiple step tests, the cap and wall force redistribution pattern is similar to that described above for CET-9. The cap initially carries all of the tensile load, but then sheds most of this tension within 1 hour. Meanwhile, the wall initially carries little or no tension, but gradually absorbs all the tensile load that the cap relinquishes. For subsequent load increments

[11]In each case the log time axes start at t=0.1 minutes (6 seconds).

(SL2-6), the wall immediately carries most of the additional tensile load with almost no change in the cap force. For load increments that cause failure, small tensile cap forces can develop (e.g., SL4 in CET-11, Fig. 5.47) as pore pressures develop within the soil plug due to displacement of the caisson. Consider test CET-13 as depicted in Figure 5.49. During the first increment of sustained total load (SL1), F_{TOT} = -6.9kg, the cap initially carries all of the tension, but then drops all tensile load within 20 minutes and accepts a slightly compressive load of $F_c \approx 1$ kg for the remainder of the increment. For each of the five subsequent total tensile load increments, the cap load remains compressive between F_c = 1 and 2 kg as the wall accepts increasingly higher tensile load. After approximately 3.5 hours (210 minutes) of the sixth and final sustained load increment (SL6; F_{TOT} = -12.9 kg), tensile cap forces begin to develop as the caisson pulls out of the soil (compare Figs. 5.49 and 5.54). Similar caisson component load behavior is found in the remaining sustained load tests (CET-11-12, 14). The only significant difference among these tests is the total tensile load level at which the caisson begins to fail.

5.6.2 Caisson Displacement

Figures 5.51-5.55 plot the wall and cap displacement versus time (log scale) for each level of sustained tensile load[12]. Figure 5.51 compares the displacement response for tests CET-9 and 10. In CET-9, the caisson reaches an equilibrium displacement, $\Delta\delta_w$ = 0.012 cm in approximately 100 minutes. In constrast, the displacement rate in test CET-10 increases continuously with time, reaching δ_w = 0.2 cm in 80 minutes, and thus indicating a well-defined failure in sustained loading. During the first load step in tests CET-11-14, the displacement pattern is similar to that in CET-9, reaching a stable displacement δ_w<0.02 cm for CET-11 (F_{TOT} =-2.9 kg) and δ_w = 0.02 to 0.03 cm for CET-12-14 (F_{TOT} = -6.9 kg) within approximately 200 minutes. Thereafter, the intermediate (pre-failure load increments cause smaller caisson displacements (δ_w<0.02 cm). In all of these steps, the displacement rate decreases with log time for the period up to t = 1000 minutes.

Caisson failure is identified by a caisson displacement rate that increases with increasing time. Failure does not occur at the same level of tensile load nor does it occur at the same time following the initiation of a particular load increment. The lowest level of tensile load at which failure occurs is F_{TOT} = -8.9 kg in CET-11 (Fig. 5.52), wherein the caisson withdrew 0.1 cm within 3.3 hours (200 minutes). In CET-12 the caisson failed at F_{TOT} = -9.9 kg, reaching a displacement δ_w = 0.1 cm within 25 hours (see Fig. 5.53). Higher tensile loads were required to fail the caisson in CET-13 and 14. At a load of F_{TOT} = -12.9 kg in CET-13, the caisson pulled out at an increasing rate with the log of time and reached 0.1 cm by 6.7 hours (400 minutes). In

[12]The cap and wall displacement are nearly identical as the caisson is controlled to move as a single unit.

CET-14 a load of F_{TOT} = -10.9 kg was required to fail the caisson, which lifted 0.1 cm within 11.7 hours (700 minutes). The higher failure loads in CET-13 and 14 could be attributed to the different methods of caisson installation. This result is explored further in Chapter 6.

5.6.3 Excess Pore Pressure

Measurement of pore pressure in the soil both within and outside of the caisson indicate four pore pressure characteristics during sustained loading: 1) negative pore pressure generated during the brief monotonic pullout stage dissipates within 100 minutes of the initial sustained loading phase unless the caisson fails during the first stage, 2) subsequent sustained load stages do not generate significant excess pore pressure in the soil plug within the caisson unless the caisson cap carries a tensile load, 3) intermediate sustained load stages do not generate significant excess pore pressures in the soil exterior to the caisson, and 4) for sustained loading to failure, increasing tensile force on the cap generates increasing negative excess pore pressure in the soil plug. The excess pore pressure record for tests CET-9 through CET-14 are shown in Figures 5.56 through 5.60. Each figure plots the excess pore pressure beneath the cap or within the soil mass at a radius from centerline of r = 0, 1.8, 3.2, or 4.45 cm. The depth of the probes that measure the pressure at the radial locations ranges from 2 to 3 cm above the caisson wall tip (see Table 5.1).

The dissipation of negative excess pore pressure generated during initial pullout is illustrated best by Figure 5.56, which shows the pore pressures beneath the cap and those measured by probes P1, P2, and P3 for CET-9 and 10. In CET-9, the initial negative excess pore pressure Δu = -0.2 ksc fully dissipated within 40 minutes, with small positive pore pressures (Δu = 0.02 to 0.04 ksc) remaining up to 800 minutes. Within the soil plug, P1 and P2 measured similar initial values, Δu = -0.15 to -0.2 ksc, which also dissipates to zero values over 40 minutes. In CET-10, the higher tensile load causes much larger initial pore pressure inside the caisson (Δu = -0.52 to -0.57 ksc); these dissipate to Δu = -0.2 to -0.24 ksc in 100 minutes. Thereafter, the plug pore pressures remain constant, as the mechanisms of dissipation and generation (due to caisson displacement) become balanced and the caisson fails.

Dissipation of negative excess pore pressures during the initial step of the staged loading tests (CET-11-14) are very similar to results described for CET-9 (see Figs. 5.57-5.60). During the intermediate load stages, no significant pore pressure is generated within the caisson soil plug unless the cap acquires tensile load. The pore pressure record for CET-13, as shown in Figure 5.59, illustrates this behavior. Pore pressure data recorded beneath the cap and by probe P2 (r = 1.8 cm) indicate that sustained load stages SL2 (F_{TOT} = -8.9 kg) through SL6 (F_{TOT} = -12.9 kg) generally do not generate substantial pore pressure within the soil plug. During stage SL2 a small amount of negative excess pressure, Δu = -0.13 ksc, is initially generated as the tensile load

increases from F_{TOT} = -6.9 to -8.9 kg. However, this pressure dissipates within several minutes as the cap tension is redistributed to the wall. During the final stage (SL6, F_{TOT} = -12.9 kg), negative excess pore pressure begins building as the caisson fails and tensile loads are carried by the cap. The general lack of pore pressure generation during intermediate stages of sustained loading is also apparent in CET-11,12, and 14 (see Figs. 5.58-5.60).

Probes P3 and P4 measured pore pressure outside the caisson. Presentable data at these locations were available in tests CET-9, 12-14, as shown in Figures 5.56, 5.58-5.60. It is clear upon examination of the data that monotonic pullout and all subsequent stages of sustained load do not generate significant excess pore pressure within the soil mass exterior to the caisson.

The fourth and final characteristic common to all tests that failed during sustained loading is the generation of negative excess pore pressure in the soil plug as the caisson fails. Figures 5.57-5.59 show this telltale sign of failure for tests CET- -13, respectively. Note that the amount of generated negative excess pore pressure is small (Δu = -0.04 to -0.06 ksc), and the generation occurs during the last several hours of the failure stage as the cap acquires tensile load due to the increasingly rapid caisson rise. As shown in Figure 5.60, this pore pressure generation in CET-14 is almost undetectable perhaps because the caisson was stopped before the caisson accelerated as rapidly as the caisson in the other tests.

5.6.4 Soil Surface Displacement

With the exception of the sustained load stage during which caisson failure occurs, the characteristic movement of the soil surface during sustained load appears to be very subtle. However, four surface movement trends can be identified. Figures 5.61 through 5.65 illustrate the clay surface displacement during all sustained load stages for tests CET-9 through 14. Each figure plots the surface displacement versus the log of time for one or more radial locations for all the sustained load phases of a particular test. Although measurements were made at five radial locations from the wall in all tests, poor instrument performance prevented the inclusion of some data in two tests, CET-11 and 12 (see Table 5.3).

The first trend common to most tests occurs during the initial tensile load increment. Due to the caisson displacement, the soil surface near the caisson wall tends to heave slightly upon load application, and later settles as the tensile load transfers to the wall of the caisson. This small heave was measured only at three radial locations nearest the wall (r_w = 1.7, 2.7, and 5.2 cm), and the amount of heave varied from test to test. Figure 5.61 shows that in CET-9, the soil at r_w = 2.7 cm, as measured by S2, heaves nearly 0.002 cm within 1 hour of the start of sustained load before compressing to almost -0.003 cm by the end of the 18 hour period. In addition, an almost negligible amount of heave (less than 0.001 cm) is measured at r_w = 1.7 and 5.2 cm. At r_w = 1.7 cm in CET-10, the soil heaves 0.002 cm but then rapidly compresses as the

caisson fails under the large initial tensile load of F_{TOT} =-11.4 kg. Similar amounts of soil heave were detected in tests CET-12, 13, and 14, as shown in Figures 5.63-5.65, respectively.

For intermediate load stages, there is a net surface settlement at all points, with slightly larger settlements occuring further away from the caisson wall. Figure 5.65 clearly shows this trend for CET-14. At the end (20.8 hours) of the first load stage, (SL1, F_{TOT} =-6.9 kg), the soil surface at S1 (r_w = 1.7 cm) settles δ_s = -0.015 cm. which increases to δ_w =-0.048 cm for S5 (r_w = 9.6 cm). This trend is also apparent in tests CET-9, 11-13.

The third surface displacement trend appears in CET-12 through 14. For intermediate sustained load stages, the surface settlement at one particular radial distance decreases with each successive sustained load increment. Consider the settlement at S3 (r_w = 5.2 cm) in CET-14, as shown in Figure 5.65. The compression after 16.7 hours (1000 minutes) of the second load increment (SL2, F_{TOT} =-8.9 kg) is -0.01 cm. At the same elapsed time for the third increment (SL3, F_{TOT} =-9.9 kg), the settlement is only δ_s = -0.005 cm, and for the fourth increment (SL4, F_{TOT} =-10.9 kg), δ_s<-0.004 cm. This trend appears at all radial locations in CET-12 through 14. However, Figure 5.62 shows the opposite trend in CET-11, where after 16.7 hours, SL2 (F_{TOT} =-4.9 kg) causes a surface settlement of δ_s = -0.002 cm at S3 (r_w = 5.3 cm). At the same time during the third increment (SL3, F_{TOT} =-6.9 kg), the settlement is δ_s>-0.004 cm. Although there is no clear explanation for this trend reversal, the lower level of sustained tensile loading in CET-11 could be a factor. The last trend concerns the soil surface behavior for sustained loads that cause failure. If the caisson is allowed to reach large uplift displacement values (e.g., CET-10 and 11), then the soil surface compression increases dramatically, especially at points near the caisson. The data also show that the surface compression decreases with increasing radial distance from the wall as soil nearer to the wall is more readily drawn downward and into the base of the caisson during uplift. This trend is shown clearly in Figure 5.62, which depicts surface movements at five radial locations during sustained loading for CET-11. The sustained load stage ended after 30.8 hours (1847 minutes), at which time the soil surface had settled -0.14 cm at S1, decreasing to -0.007 cm at S5.

5.7 RE-EQUILIBRATION

This section describes measurements of re-equilibration behavior for five tests (CET- 5-6, 12-14), which were previously loaded to failure (i.e., to the point of maximum tensile resistance). The caisson was re-equilibrated in the clay for at least 24 hours. In 2 tests, CET-5-6, the caisson capacity was mobilized by monotonic tensile loading (approximately undrained) with $\delta_w \approx 0.3$ cm (see Fig. 5.36). In tests CET-12-14, the caisson was failed under sustained tensile loading prior to re-equilibration.

During the re-equilibration phase, a constant total force F_{TOT} =15.2 kg (i.e., no net load

compared to initial conditions) is applied to the caisson with zero relative displacement between the cap and wall. In all cases the re-equilibration phase lasts fro at least 24 hours. The data are presented in a format similar to section 5.4, as a function of time after the end of tensile loading (log scale). Active control of the system typically occurs within 5 seconds after the end of tensile loading[13].

5.7.1 Caisson Force Distribution

Figure 5.66 shows the total, wall, and cap force components during re-equilibration. By the end of this phase, the wall carries more than 90% (F_w = 12.5-14 kg) of the total caisson load, while the cap force accounts from only 1-3 kg. This result is similar to observations of the original (post-installation) caisson equilibration. However, because both the cap and wall begin this phase with large tensile loads, the timeframe required for cap and wall forces to redistribute is longer than that during post-installation equilibrium.

Figure 5.66 shows that up to 10 minutes is required to unload the caisson and restore the equilibrium condition, F_{TOT} =15.2±0.3 kg. This is 7 minutes longer than the time required for the total force to reach equilibrium in post-installation set-up (see section 5.3.1, Fig. 5.27). More time is required for re-equilibration because the target total force is more than 15 kg greater than that at the end of tensile loading, whereas the target F_{TOT} in the first equilibrium is identical to that throughout installation for most tests (i.e., F_{TOT} =15.2 kg for CET-5-6, 12).

The wall force initially rises to between F_w = 12-15 kg before dropping to a range, F_w = 7-10 kg (see Fig. 5.66). This 'overshoot' behavior is due to intercomponent friction between the wall and cap. In order to attain a total load of F_{TOT} =15.2 kg, the control algorithm first drives the wall, which causes the wall force to increase. To maintain the zero relative displacement condition, the cap follows the wall, and thus the cap force increases, but intercomponent friction causes the wall force to drop. Thereafter, wall force increases throughout re-equilibration, reaching approximately $F_w \approx$ 14 kg (or 92% of the total load) at an elapsed time of 8.3 hours (500 minutes). After this point, intercomponent friction causes the wall force to vary ±2 kg[14]. The timeframe for re-distribution of the wall force (400-500 minutes) is much longer than that measured for equilibration following installation by underbase suction (3 minutes), but is comparable to tests CET-13 and 14, where there was a large change in the net force at the end of penetration (see Fig. 5.19).

Within the first minute of re-equilibration for CET-6, 12-14, the cap force rises to a

[13]Data were not recorded between 2.2 and 200 minutes for CET6; the missing portion is represented by a dashed line in the figures.

[14]The wall force behavior in CET6 between t=2.2 and 2200 minutes is interpolated, but generally indicates a pattern similar to the other four tests.

compressive value that ranges from F_c = 4 to 7.5 kg, as shown in Figure 5.66. For the next 500 minutes, the cap sheds most of this load to reach an equilibrium value, F_c = 1±1 kg. Intercomponent friction causes the cap force to fluctuate ±2 kg for the remainder of re-equilibration. In CET-5 the cap force inexcplicably creeps up slowly to F_c = 1.5 kg within the first 10 minutes and drops gradually to F_c = 0.5 kg by the end of the set-up phase The timeframe for cap force re-equilibration is similar to that measured during the post-installation of tests CET-13 and 14.

5.7.2 Pore Pressure Dissipation

The pore pressure measured beneath the cap and within the soil plug (i.e., probes P1 and P2) during re-equilibration reflect changes in the cap force. Much smaller changes in pore pressure occur in the soil mass outside the caisson. Figure 5.67 shows the excess pore pressure beneath the cap versus log of time for the five tests that incorporated a re-equilibration phase (CET-5-6, 12-14). The excess pore pressure at the start of re-equilibration for tests CET-5-6 are in the range Δu = -0.25 to -0.45 ksc, which reflects the large negative pore pressure generation that occurred in the preceding monotonic tensile load test. In contrast, tests CET-12-14 start out with nearly zero (± 0.1 ksc) excess pore pressure, as the preceding sustained tensile load stage was a fully drained process[15]. Complete dissipation of excess pore pressure occurs within 500 minutes. In all cases, Δu = ±0.1 ksc by the end of re-equilibration.

Figure 5.67 shows the excess pore pressure versus log of time for probes P1 and P2 within the soil plug. Most of these probes were located at a depth of approximately 2.5 cm above the wall tip, except in CET-5 where P1 and P2 are at the wall tip elevation, and in CET-14 where P1 is located 6 cm below the caisson. In general, the pore pressure measured by P1 and P2 follow very closely the magnitude and dissipation behavior measured beneath the cap; full dissipation occurs within 500 minutes.

Probes P3 and P4 were located outside the caisson at radial distances r = 3.2 and 4.45 cm, respectively. As shown in Figure 5.67, these probes measured a muted pore pressure response with initial excess pore pressure, Δu = 0.1-0.26 ksc at P3 and Δu≈0.08 ksc at P4. After several hours, the excess pressure has dissipated toward zero. Note that the slight positive pressure at the end of set-up in CET-12 may be due to the effect of temperature and barometric variation.

5.7.3 Caisson Displacement

The preceding loading history has a major effect on the settlement measured during re-equilbiration. Figure 5.68 plots the wall and cap settlement, respectively, versus the log of time

[15]In these tests, the preceding sustained load event only generated significant pore water pressure at failure.

in minutes. As mentioned in section 5.7.1, the large difference in total force between the end of the tensile load stage (F_{TOT} =-2 to -22 kg) and the target total force for re-equilibration (F_{TOT} =15.2 kg) affected the zero relative displacement condition during the first ten minutes. The control program drove the wall ahead of the cap in order to attain the total force target, F_{TOT} =15.2 kg (see Fig. 5.68). By the end of the re-equilibration phase, the caisson has settled an amount that ranges from -0.14 to -0.37 cm, which is much larger than displacements observed in post-installation equilibration (~-0.1 cm, see section 5.4.4).

There is a distinct difference between the settlement curves for the caissons that re-equilibrated after monotonic tensile loading (CET-5-6) and those that followed sustained loading (CET-12-14). After approximately 10 minutes have elapsed in CET-5-6, the caisson settles at a nearly log-linear rate that ranges from 0.06 to 0.07 cm per log cycle of time. Note that this rate is approximately double the log-linear caisson settlement rate during the post-installation phase. In CET-12-14, the caisson rapidly settles an amount that is approximately equal to the upward displacements of the caisson achieved during the preceding sustained load stage. The pullout displacements measured during the previous stages of sustained loading were 0.2, 0.41, and 0.16 cm for CET-12, 13, and 14, respectively. As shown in Figure 5.68, the caisson settlement during the rapid settlement stage for these tests was 0.19, 0.35, and 0.14 cm, respectively. Beyond the rapid drop stage, the caisson settles at a log-linear rate of approximately 0.02 cm per log time cycle.

5.7.4 Soil Surface Displacement

Figure 5.69 plots the surface compression for the five re-equilibration tests (CET-5-6, 12-14). The figure shows the settlement for several tests at a specific radial distance from the wall, r_w. Soil compression was much larger in the tests where re-equilibration followed monotonic pullout (CET-5-6) than in those following sustained loading (CET-12-14). For example, S1 measures settlement -0.11 to -0.12 cm for CET-5 after 1000 minutes, but only -0.02 cm in tests CET-13,14. This difference in soil surface compression between the monotonic pullout tests and the sustained load tests is apparent at each of the five radial locations.

As expected, the settlement magnitude decreases with increasing radial distance from the caisson. For test CET-5, the compression after 1000 minutes decreases from a range of -0.11 to -0.12 cm at S1 (r_w = 1.7 cm) to -0.015 to -0.03 cm at S5 (r_w = 9.6 cm). For CET-13 and 14, the corresponding ranges are -0.02 cm at S1 to less than -0.005 cm at S5.

5.8 MONOTONIC PULLOUT 2

This section presents the results of a second series of tensile monotonic pullout tests performed after re-equilibration in CET-5-6, 12-14 and immediately following the final

increment of sustained load in CET-9. In each test the caisson loading was performed at a constant displacement rate v_w = -0.03 cm/min, allowing no relative displacement between the cap and wall. In all six tests the caisson was pulled to a displacement of at least δ_w = 0.3 cm in order to determine the total capacity. After establishing the caisson capacity, three tests (CET-12-14) were loaded to large displacement at a faster rate of v_w = 0.3 cm/min until complete extraction. The following discussion focuses on the similarities and differences in the caisson response measured in the first (section 5.5) and second phases of monotonic loading.

5.8. Caisson Force Distribution

Measurements of the caisson forces during the second pullout phase indicate that re-equilibration of the caisson increased the wall resistance, but did not affect the cap resistance. Hence, the caisson capacity is greater during the second pullout phase than during the initial pullout. For test CET-9, where the caisson did not re-equilibrate, the wall resistance and caisson capacity during the second pullout was slightly *lower* than the average values during initial pullout. For all five re-equilibrated tests, the initial stiffness of the caisson and wall force are higher in the second monotonic test than in the first. The following discussion compares the total, wall, and cap forces during the second monotonic pullout series (#2) with the 'best estimate' of caisson response from the first test series (#1, section 5.5.1).

5.8.1.1 Total Force

Figure 5.70 plot the total, wall, and cap forces versus the wall tip displacement for 6 tests (CET-5-6, 9, 12-14) at a displacement scale from δ_w = 0.0 to 0.4 cm, while the small displacement response (δ_w = 0.00 to 0.02 cm) is shown in Figure 5.71. The results of series #2 tests can be subdivided into 3 groups: 1) CET-5 and 6, which were re-equilibrated after being loaded to failure in an (undrained) monotonic mode, 2) CET-12-14, which were re-equilibrated after failure under long-term sustained tensile loads, and 3) CET-9, which corresponds to reloading with no re-equilibration.

In the series #2 test, CET-5,6 mobilize a maximum capacity F_{TOT} =-25 to -27 kg at a displacement δ_w = 0.25 cm, and show no well-defined yield point in the load-deformation response. In the second group of tests, CET-12-14, the series #2 data show maximum caisson resistance, F_{TOT} =-25 to -29 kg at δ_w = 0.1-0.15 cm, and a well-defined yield point at δ_w= 0.02 cm. They have a much higher pre-yield stiffness than CET-5, 6. Comprising the last test group, CET-9 reaches a maximum caisson resistance F_{TOT} =-21 kg at δ_w = 0.1 cm, with a very stiff initial response and yield at δ_w = 0.02 cm.

Comparison of these results with previous monotonic test data (Fig. 5.36-5.37) reveals that all of the re-equilibrated caissons have tensile load capacities 20-25% higher than in series

#1 (F_{TOT} =-22 to -24 kg). The initial stiffness and yield displacement in CET-12-14 are comparable to series #1 behavior, but the CET-5 and 6 data have *lower* stiffness compared to previous performance. Test CET-9 has a lower stiffness and capacity than that measured in series #1.

5.8.1.2 Wall Force

Figure 5.70 shows the wall force behavior for tests CET-5-6, 9, 12-14. It is more difficult to discern major trends among these data than were seen in the total force plots. However, the wall force in CET-9 is notably lower than those from all 5 tests where re-equilibrium occurred. The initial wall response for the re-equilibrated tests is very similar to the response observed in the series #1 pullout. At the point of peak total load during pullout #2, the wall force from the five re-equilibrated tests averages F_w = -17.3±1.6 kg, which corresponds to 63% of the average peak tensile load, F_{TOT} =-27.3 kg. This result confirms a small but pervasive increase in wall capacity achieved in the series #2 tests.

The wall resistance in test CET-9, F_w = -11.3 kg at δ_w = 0.18 cm (maximum caisson resistance), corresponds to 65% of the average wall force for the re-equilibrated tests.

5.8.1.3 Cap Force

In contrast to the wall in the re-equilibrated tests, the cap does *not* mobilize more capacity during the second pullout. The cap force versus wall tip displacement is plotted in Figures 5.70 and 5.71. The initial cap stiffness is very similar to behavior measured in the series #1 tests. At maximum caisson resistance, the cap force for all five re-equilibrated series #2 tests averages F_c = -10.0±2.1 kg, which compares very closely with the average value F_c = 10.4 kg, quoted from series #1. The resulting cap force contribution corresponds to 37% of the series #2 pullout capacity.

The cap response in CET-9 is very similar to the other series #2 tests. At maximum capacity, the cap force is F_c = -9.60 kg, which is within the range exhibited by the re-equilibration tests. However, due to the low wall force of F_w = -11.3 kg, the cap force contribution to the total capacity is 46%, which is similar to the series #1 behavior.

5.8.1.4 Fast Rate Monotonic Pullout 2

After the caisson was pulled to capacity at v_w = -0.03 cm/min, tests CET-12-14 continued loading up to complete extraction at a faster rate, v_w = -0.3 cm/min. The general caisson force behavior is very similar to series #1 tests with a similar load sequence (section 5.5.1). Figure 5.72 shows the total, wall, and cap forces versus wall tip displacement for both rates of pullout. The caisson relaxes during the interval between the two loading phases as the control program is

stopped and restarted manually. As shown in Figure 5.72, the total force relaxation ranges from ΔF_{TOT} =3 to 7 kg. After incremental displacements of $\Delta\delta_w$ =0.18 to 0.22 cm at the fast displacement rate, the caisson has mobilized a tensile load that is ΔF_{TOT} =-2 to -3 kg higher the total tensile load at the end of slow pullout. This tensile load increase between slow and fast pullout is similar in magnitude to that during series #1 tests. After reaching peak load, the total tensile load declines at an approximate rate of F_{TOT}/δ_w =5 kg/cm, which also is similar to the rate of decline in series #1.

The wall and cap force records (Fig. 5.72) indicate that the increased capacity during fast rate pullout can be attributed to an increased cap contribution. The wall force in both CET-12 and 14 does not increase significantly at the start of the faster pullout, but instead continues following the trend of declining tensile load established during the slow pullout. In test CET-13, the wall force initially does jump ΔF_w = -3 kg above the tensile wall load at the end of slow pullout, but sheds load at a slightly quicker rate than the other two tests for the remainder of pullout. In Fig. 5.72 all three tests show an increase in cap tensile load due to increased displacement rate. The cap tensile load increase at the start of fast pullout ranges from ΔF_c = -2 to -6 kg above the tensile load at the end of slow pullout. However, relatively large incremental displacements ($\Delta\delta_w$ =0.4 to 1.1 cm) are necessary to mobilize this increased cap tensile load.

5.8.2 Pore Pressure Generation

Figure 5.73 plots the excess pore pressure beneath the cap versus wall tip displacement for the series #2 monotonic pullout tests. Due to the stiff cap response, large negative excess pore pressures are generated at very small displacements. At δ_w = 0.003 cm, the excess pressure ranges from Δu = -0.14 to -0.5 ksc, a range that is similar to behavior measured in series #1 tests. Note that for the three sustained load tests CET-12-14, the peak negative excess pore pressure (Δu = -0.5 to -0.78 ksc) is mobilized rapidly at δ_w<0.04 cm. In CET-5-6 and CET-9, much larger caisson displacements are necessary to mobilize the peak negative excess pore pressure (δ_w<0.3-0.4 cm in CET-5, 6).

Figure 5.74 shows the excess pore pressure versus wall displacement for probe P1 in 5 tests (CET-5, 6, 9, 12, 14). In CET-5, 6, 9, and 12, the record shows that the magnitude of peak negative pore pressure is similar to that for the pressure beneath the cap. Note that pullout does generate a measurable amount ($\Delta u \approx$-0.1 ksc) of negative pore pressure near the bottom of the clay, as measured by P1 in CET-14.

Although only two records of pore pressure are available for probe P2 (located within the caisson walls at r = 1.8 cm), the pattern generated is similar to that revealed in pullout #1. The data for CET-9 and 14 (Fig. 5.74) show larger negative excess pore pressures than those measured below the base or at P1. In CET-14, at δ_w = 0.022 cm, the excess pressure reaches a

peak, Δu = -0.9 ksc, which is -0.12 ksc greater than the peak reached beneath the cap (Δu = -0.78 ksc). For CET-9, the caisson must displace $\delta_w = 0.15$ cm before reaching a peak pressure of Δu = -0.68 ksc, which is -0.17 ksc greater than the peak attained below the cap (Δu = -0.51 ksc).

Very small excess pore pressures are generated during the series #2 tests in the soil outside the caisson walls. Figure 5.74 shows the limited data available for probes P3 and P4. At the final caisson displacement (δ_w = 0.4 cm), both probes measure approximately Δu = -0.1 ksc of excess pore pressure.

5.8.1.2 Fast Rate Monotonic Pullout #2

Enough data was collected to show that there is a significant load rate effect on pore pressure development within the soil plug. Figure 5.75 shows the excess pore pressure measured beneath the cap for both pullout rates in tests CET-12-14. During the time interval between the end of slow pullout and the start of fast pullout, the excess pressure reduces due to relaxation of the applied force. Within $\Delta\delta_w = 0.5$ cm of restarting pullout, the negative excess pore pressure jumps -0.2 to -0.25 ksc below the value at the end of slow pullout. Thereafter, the excess pressure reduces at a constant rate with wall displacement. Similar pore pressure behavior is measured by the P1 probes (Fig. 5.76); by the time the caisson has withdrawn δ_w = 1 cm, the large negative excess pore pressure generated during the initial 0.1 cm of pullout has dissipated 114to approximately Δu = -0.37 ksc. Fast pullout induces the excess pore pressure to jump back to nearly Δu = -0.5 ksc before it begins dissipating at a constant rate. Note in this figure that fast pullout has little effect on the pore pressure at the bottom of the clay, as measured by P1 in CET-14. The excess pore pressure at this location never rises more than Δu = -0.14 ksc during the first 1 cm of fast pullout before dropping back to negligible values. At the soil plug location r_w = 0.6 cm from the inside caisson wall, probe P2 measures a pore pressure pattern consistent with the other soil plug patterns measured beneath the cap and by P1. Figure 5.76 shows the excess pore pressure measured by P2 in CET-14 for both pullout rates. After only 0.1cm of fast withdrawal, the negative excess pressure rises to Δu = -86 ksc, which is -0.26 ksc higher than the value at the end of slow pullout.

Figure 5.76 plots the excess pore pressure measured outside the caisson in CET-14 by probes P3 and P4. At the farther location r_w = 1.91 cm from the exterior caisson wall, probe P4 measures no rate effect on pore pressure, as the slight amount of negative excess pressure generated during slow pullout continues dissipating to negligible values. Closer to the wall, probe P3 (r = 3.2 cm) reveals very interesting pore pressure behavior, as shown in Figure 5.76. At the onset of fast pullout, *positive* excess pore pressure is generated, so that by a caisson displacement of δ_w = 1.77 cm, the excess pore pressure is Δu = 0.16 ksc. Then, as the caisson wall passes the depth at which probe P3 is located (approximately 2 cm above the wall tip prior

to slow pullout), large negative excess pore pressure is generated and reaches a peak of nearly Δu = -0.6 cm at a caisson displacement of δ_w = 3 cm. With further displacement the negative excess pore pressure dissipates until reaching zero by the end of extraction.

5.8.3 Soil Surface Displacement

The soil surface displacement patterns measured during the series #2 pullout tests are nearly identical to those for series #1 (compare Figs. 5.77 and 5.44). Figures 5.77 illustrates these four trends for series #2 tests. Each figure plots the surface displacement versus wall displacement at a specific radial distance r_w for several tests. Figure 5.78 shows the soil movement for the wall pullout from z_w = 0 to 0.4 cm. Note that the one test (CET-9) that did not incorporate a re-equilibration phase exhibited the same soil surface displacement characteristics as the re-equilibration tests except for trend #1; the soil surface near the caisson wall at r_w = 1.7 cm did not heave significantly.

Figure 5.78 shows that the soil surface at r_w = 1.7 and 2.7 cm in all tests except CET-9 heaves at a rate that decreases with increasing radial distance from the wall during early pullout. At z_w = 0.02 cm the soil heave near the wall (r_w = 1.7 cm) ranges from 0.0005 to 0.0022 cm, while the soil heave a short distance farther out (r_w = 2.7 cm) is smaller, ranging from 0.0006 to 0.0011 cm. At locations beyond r_w = 2.7 cm, the soil compresses during early pullout by an amount that increases with increasing radial distance from the wall. At r_w = 5.3 cm the soil compresses between 0 and -0.0004 cm. At r_w = 7.3 cm the compression is just a bit more, ranging from -0.0003 to -0.0005 cm. Even more displacement occurs at r_w = 9.6 cm, where the soil compresses ranges from -0.0006 to -0.0007 cm.

The increasing rate of compression with continued pullout at radial distances of r_w = 1.7 and 2.7 cm is apparent only in a few tests, in Figure 5.78. Consider the soil displacement at r_w = 2.7 cm for CET-6. From z_w = 0.1 to 0.2 cm, the soil compressed -0.0031 cm, while from z_w = 0.2 to 0.3 cm, the soil compressed -0.0041 cm. Near the end of pullout, from z_w = 0.3 to 0.4 cm, the soil surface compression increases to -0.0048 cm.

The fourth soil compression characteristic, that for radial locations beyond r_w = 2.7 cm the compression rate decreases with increasing radial distance. At a pullout distance of z_w = 0.2 cm, the soil compression range decreases from -0.0036 to -0.0067 cm at r_w = 5.3 cm to -0.0015 to -0.0041 cm at r_w = 7.3 cm. At the farthest location, r_w = 9.6 cm, the range has dropped to -0.0025 to -0.0031 cm.

5.8.3.1 Fast Rate Monotonic Pullout #2

As for the slow rate surface displacement, the fast pullout rate surface displacement characteristics during pullout #2 are very similar to those for pullout #1, which were discussed in

section 5.5.3. Namely, the only surface movement trend common to both slow and fast pullout is that compression generally decreases with increasing radial distance from the caisson wall. Figure 5.78 also plots the surface displacement at both slow and fast pullout rates at the five radial locations. Near the wall at r_w = 1.7 and 2.7 cm, the compression records are similar in shape and magnitude. At the onset of fast pullout, the soil does not heave, but instead continues compressing at an increasing rate. Note that in CET-12, the surface at r_w = 1.7 cm stops compressing at a pullout of z_w = 3.5 cm and heaves for the remainder of pullout to reach a final absolute compression of -0.24 cm. At r_w = 2.7 cm in CET-12, the surface stops compressing after reaching -0.41 cm at a pullout of z_w = 3.7 cm. This near-wall behavior is similar to that of CET-4 during pullout #1 and could suggest that during the final 1cm of pullout, soil is adhering to the outer surface of the caisson wall, which would cause soil surface to heave. In CET-13 and 14, the soil surface near the wall compresses throughout fast rate pullout. At the farther radial locations, r_w = 5.3, 7.3, and 9.6 cm, fast rate pullout does not alter the pattern of surface compression set by the slow rate. Not only is the compression small relative to the near wall surface compression, but the magnitude decreases with increasing radial distance. At r_w = 5.3 cm, the final soil compression ranges from -0.08 to -0.15 cm. This range decreases to -0.01 to -0.03 cm at r_w = 7.3 cm. Finally, at r_w = 9.6 cm the compression is less than -0.01 cm.

Common Geometry

Clay Cake Diameter = 30.5cm
Clay Cake Height = 12.1-14.3cm
Caisson Outside Diameter = 5.08cm
Caisson Wall Thickness = 0.145cm
Caisson Penetration = 5.08cm

Common Instrumentation

Caisson Wall Force, L1
Caisson Cap Force, L2
Caisson Wall Displacement, D1
Caisson Cap Displacement, D2
Chamber Air Pressure, AP
Caisson Cap Pore Pressure, CP

Clay Height and Other Instrumentation

Test	Clay Height H_c (cm)	Pore Pressure Probes						Surface Displacement LVDTs					Total Stress σ_H
		d1 cm	d2 cm	P1	P2	P3	P4	S1	S2	S3	S4	S5	
CET1	12.4	5.3	7.1	X	X	X	-	-	X	X	X	-	X
CET2	12.8	5.4	7.4	X	X	X	-	-	X	X	X	-	X
CET3	12.1	4.9	7.2	X	X	X	-	-	X	X	X	X	-
CET4	14.3	5.8	8.5	X	X	-	X	X	X	X	X	-	-
CET5	13.5	4.0	9.5	X	X	X	-	X	X	X	X	X	-
CET6	13.9	2.2	11.7	X	-	-	-	X	X	X	X	X	X
CET7	12.9	2.5	10.4	X	X	X	-	X	X	X	X	X	-
CET8	13.3	2.4	10.9	X	X	X	-	X	X	X	X	X	-
CET9	13.4	2.5	10.8	X	X	X	-	X	X	X	X	X	-
CET10	13.6	2.3	11.2	X	X	X	-	X	X	X	X	X	-
CET11	12.9	2.0	10.9	X	X	X	-	X	X	X	X	X	-
CET12	13.7	2.5	11.2	X	X	X	-	X	X	X	X	X	-
CET13	12.7	2.5	10.2	X*	X	X	X	X	X	X	X	X	-
CET14	14.0	2.9	11.1	X*	X	X	X	X	X	X	X	X	-

Notes: H_c = clay height prior to driving
σ_H = total stress transducer along chamber sidewall in CET1,2,6
d1 = depth from clay surface prior to driving
d2 = height from clay bottom prior to driving
X = transducer in use for test
X* = these probes located 2cm above clay bottom

Table 5.1 Individual Test Geometry and Instrumentation

Test	Consol. at 0.75ksc	Suction Driving	Equil. 1 15.2 kg	Monotonic Pullout 1	Sustained Loading	Equil. 2 15.2 kg	Monotonic Pullout 2
CET1*	56 hr	0.3cm/min L=5.1cm	26 hr	0.3cm/min out	-	-	-
CET2†	17 hr	0.3cm/min L=3.8cm	-	-	-	-	-
CET3	24 hr	0.3cm/min L=5.1cm	24 hr	0.03cm/min L=0.3cm 0.3cm/min, out	-	-	-
CET4	28 hr	0.3cm/min L=5.1cm	18 hr	0.03cm/min L=0.3cm 0.3cm/min, out	-	-	-
CET5	48 hr	0.3cm/min L=5.1cm	24 hr	0.03cm/min L=0.3cm	-	67 hr	0.03cm/min L=0.3cm
CET6	25.5 hr	0.01cm/min L=1.05cm 0.3cm/min L=5.1cm	30 hr	0.03cm/min L=0.3cm	-	66.6 hr	0.03cm/min L=0.4cm
CET7	24.9 hr	0.3cm/min L=5.1cm	25.6 hr	0.03cm/min L=0.3cm	-	24.1 hr	0.03cm/min, L=0.3cm 0.3cm/min out
CET8	25.8 hr	0.3cm/min L=5.1cm	33.3 hr	0.03cm/min L=1.1cm 0.3cm/min, out	-	-	-
CET9	24.4 hr	0.3cm/min L=5.1cm	34.2 hr	0.01cm/min L=0.0026cm	-2.2kg, 13.4hr	-	0.03cm/min L=1.24cm
CET10	69 hr	0.3cm/min L=5.1cm	41.7 hr	0.02cm/min L=0.0073cm	-11.4kg, 15hr	-	-

*σ_v'=1.0 ksc
†CET2 aborted during driving (see section 5.1.4)

Table 5.2 Individual Test Loading Phases

Test	Consol. at 0.75ksc	Suction Driving	Equil. 1 15.2 kg	Monotonic Pullout 1	Sustained Loading	Equil. 2 15.2 kg	Monotonic Pullout 2
CET11	24 hr	0.3cm/min L=5.1cm	24.2 hr	0.03cm/min L=0.0032cm	-2.9kg, 24.5hr -4.9kg, 23.9hr -6.9kg, 26.9hr -8.9kg, 30.5hr end	-	-
CET12	24 hr	0.3cm/min L=5.1cm	24.3 hr	0.01cm/min L=0.0027cm	-6.9kg, 25.2hr -8.9kg, 120.5hr -9.9kg, 27hr	24.1 hr	0.03cm/min L=1cm 0.3cm/min, out
CET13	27.2 hr	*0.24cm/min L=5.1cm	25.7 hr	0.02cm/min L=0.0048cm	-6.9kg, 26.3hr -8.9kg, 24.5hr -9.9kg, 24.1hr -10.9kg, 25hr -11.9kg, 24.1hr -12.9kg, 14.1hr	25.7 hr	0.03cm/min L=1cm 0.24cm/min, out
CET14	26.4 hr	**0.25cm/min L=5.1cm	24.9 hr	0.02cm/min L=0.0058cm	-6.9kg, 20.8hr -8.9kg, 21.8hr -9.9kg, 23.1hr -10.9kg, 25 hr	153.8 hr	0.03cm/min L=0.6cm 0.24cm/min, out

* CET13 drove with constant cap force
** CET14 drove with zero cap displacement

Table 5.2 Individual Test Loading Phases (cont.)

CET Test	1	2	3	4	5	6	7	8	9	10	11	12	13	14
Control														
Installation	4	4	3	2	3	3	3	1	1	3	2	2	1	3
Equilibration 1	4	-	1	3	3	2	1	2	1	3	3	1	3	3
Monotonic Pullout 1	4	-	3	3	2	1	3	1	1	1	2	1	2	1
Sustained Loading	-	-	-	-	-	-	-	-	2	1	2	2	2	1
Equilibration 2	-	-	-	-	1	2	2	-	-	-	-	2	1	1
Monotonic Pullout 2	-	-	-	-	2	1	1	3	1	-	-	2	2	1
Instrumentation for Installation														
Cap Pore Pressure	4	-	4	1	1	1	1	3	1	1	1	1	1	1
Pore Pressure Probe 1	4	-	4	4	4	1	2	4	1	1	1	1	4	1
Pore Pressure Probe 2	4	-	4	4	4	-	1	1	1	2	4	4	3	1
Pore Pressure Probe 3	4	-	4	-	4	-	2	1	4	3	4	2	4	1
Pore Pressure Probe 4	-	-	-	4	-	-	-	-	-	-	-	-	1	1
Horizontal Total Stress	2	-	-	-	-	1	-	-	-	-	-	-	-	-
Surface Displacement 1	-	-	-	1	1	4	1	1	1	1	4	4	1	1
Surface Displacement 2	1	-	1	1	1	1	1	1	1	1	1	1	1	1
Surface Displacement 3	4	-	1	1	4	1	4	1	1	1	1	1	1	1
Surface Displacement 4	4	-	1	4	4	1	1	1	1	1	4	1	1	1
Surface Displacement 5	-	-	1	-	4	1	4	1	1	1	1	4	1	1

KEY
1 = good
2 = fair
3 = poor
4 = unusable

Table 5.3 Quality Assessment for Individual Test Control and Instrumentation
a) Test Control, Installation Phase Instrumentation

CET Test	1	2	3	4	5	6	7	8	9	10	11	12	13	14
Instrumentation for Equilibration 1														
Cap Pore Pressure	4	-	4	3	3	3	1	1	1	3	1	1	1	1
Pore Pressure Probe 1	4	-	4	4	4	2	4	4	1	3	1	1	4	4
Pore Pressure Probe 2	4	-	4	4	4	-	1	1	1	3	4	4	3	1
Pore Pressure Probe 3	4	-	4	-	4	-	1	3	2	3	3	2	3	1
Pore Pressure Probe 4	-	-	-	4	-	-	-	-	-	-	-	-	1	1
Horizontal Total Stress	2	-	-	-	-	1	-	-	-	-	-	-	-	-
Surface Displacement 1	-	-	-	1	1	1	1	1	1	4	1	4	1	1
Surface Displacement 2	1	-	1	1	1	1	1	1	1	4	1	1	1	1
Surface Displacement 3	4	-	1	1	4	1	1	1	1	1	1	1	1	1
Surface Displacement 4	4	-	1	4	4	1	1	1	1	1	1	1	1	1
Surface Displacement 5	-	-	1	-	1	1	1	1	1	1	1	1	1	1
Instrumentation for Monotonic Pullout 1														
Cap Pore Pressure	4	-	4	3	1	1	1	4	1	1	1	1	1	1
Pore Pressure Probe 1	4	-	4	4	2	1	2	4	1	1	1	1	4	1
Pore Pressure Probe 2	4	-	4	3	4	-	1	1	1	2	4	4	3	1
Pore Pressure Probe 3	4	-	4	-	4	-	1	1	1	3	3	2	4	1
Pore Pressure Probe 4	-	-	-	4	-	-	-	-	-	-	-	-	1	1
Horizontal Total Stress	2	-	-	-	-	1	-	-	-	-	-	-	-	-
Surface Displacement 1	-	-	-	1	1	4	1	1	1	1	1	4	1	1
Surface Displacement 2	1	-	1	1	1	1	1	1	1	1	1	1	1	1
Surface Displacement 3	4	-	1	1	2	1	2	1	1	1	1	1	1	1
Surface Displacement 4	4	-	1	4	4	1	4	1	1	1	4	1	1	1
Surface Displacement 5	-	-	1	-	2	1	3	1	1	4	1	2	1	1

KEY
1 = good
2 = fair
3 = poor
4 = unusable

Table 5.3 Quality Assessment for Individual Test Control and Instrumentation
b) Equilibration and Monotonic Pullout 1 Phase Instrumentation

CET Test	1	2	3	4	5	6	7	8	9	10	11	12	13	14

Instrumentation for Sustained Loading

Cap Pore Pressure	-	-	-	-	-	-	-	-	1	1	1	1	1	1
Pore Pressure Probe 1	-	-	-	-	-	-	-	-	1	1	1	1	4	1
Pore Pressure Probe 2	-	-	-	-	-	-	-	-	1	2	4	4	3	1
Pore Pressure Probe 3	-	-	-	-	-	-	-	-	1	3	3	2	4	1
Pore Pressure Probe 4	-	-	-	-	-	-	-	-	-	-	-	-	1	1
Horizontal Total Stress	-	-	-	-	-	-	-	-	-	-	-	-	-	-
Surface Displacement 1	-	-	-	-	-	-	-	-	1	1	1*	4	1	1
Surface Displacement 2	-	-	-	-	-	-	-	-	1	1	1	1	1	1
Surface Displacement 3	-	-	-	-	-	-	-	-	1	1	1	1	1	1
Surface Displacement 4	-	-	-	-	-	-	-	-	1	1	1*	1	1	1
Surface Displacement 5	-	-	-	-	-	-	-	-	1	1	1	2	1	1

Instrumentation for Re-Equilibration

Cap Pore Pressure	-	-	-	-	1	1	1	-	-	-	-	1	1	1
Pore Pressure Probe 1	-	-	-	-	2	1	2	-	-	-	-	1	4	1
Pore Pressure Probe 2	-	-	-	-	4	-	1	-	-	-	-	4	3	1
Pore Pressure Probe 3	-	-	-	-	4	-	1	-	-	-	-	4	4	1
Pore Pressure Probe 4	-	-	-	-	-	-	-	-	-	-	-	-	4	1
Horizontal Total Stress	-	-	-	-	-	1	-	-	-	-	-	-	-	-
Surface Displacement 1	-	-	-	-	1	4	1	-	-	-	-	4	1	1
Surface Displacement 2	-	-	-	-	1	1	1	-	-	-	-	1	1	1
Surface Displacement 3	-	-	-	-	1	1	1	-	-	-	-	1	1	1
Surface Displacement 4	-	-	-	-	4	1	1	-	-	-	-	1	1	1
Surface Displacement 5	-	-	-	-	1	1	1	-	-	-	-	4	1	1

*unusable in sustained load stage 1

KEY
1 = good
2 = fair
3 = poor
4 = unusable

Table 5.3 Quality Assessment for Individual Test Control and Instrumentation
c) Sustained Load and Re-Equilibration Phase Instrumentation

CET Test	1	2	3	4	5	6	7	8	9	10	11	12	13	14
Instrumentation for Monotonic Pullout 2														
Cap Pore Pressure	-	-	-	-	1	1	1	-	1	-	-	1	1	1
Pore Pressure Probe 1	-	-	-	-	2	1	2	-	1	-	-	1	4	1
Pore Pressure Probe 2	-	-	-	-	4	-	1	-	1	-	-	4	3	1
Pore Pressure Probe 3	-	-	-	-	4	-	1	-	1	-	-	4	4	1
Pore Pressure Probe 4	-	-	-	-	-	-	-	-	-	-	-	-	4	1
Horizontal Total Stress	-	-	-	-	-	1	-	-	-	-	-	-	-	-
Surface Displacement 1	-	-	-	-	1	4	1	-	1	-	-	4	1	1
Surface Displacement 2	-	-	-	-	1	1	1	-	1	-	-	1	1	1
Surface Displacement 3	-	-	-	-	1	1	1	-	1	-	-	1	1	1
Surface Displacement 4	-	-	-	-	4	1	1	-	1	-	-	1	1	1
Surface Displacement 5	-	-	-	-	1	1	1	-	1	-	-	4	1	1

KEY
1 = good
2 = fair
3 = poor
4 = unusable

Table 5.3 Quality Assessment for Individual Test Control and Instrumentation
d) Monotonic Pullout 2 Phase Instrumentation

Rating Key
1 = good
2 = fair
3 = poor
4 = unusable

Test Control Guideline

Installation:	1 - F_{tot} = ±1kg
	2 - F_{tot} = ±3kg
	3 - F_{tot} = >3kg
	4 - F_{tot} = no control
Equilibration/Sustained Loading:	1 - Relcapd = ±0.001cm
	2 - Relcapd = ±0.01cm
	3 - Relcapd = >0.01cm
	4 - Relcapd = no control
Monotonic Pullout:	1 - Relcapd = ±0.003cm
	2 - Relcapd = ±0.01cm
	3 - Relcapd = >0.01cm
	4 - Relcapd = no control

Instrumentation Data Guideline

Pore Pressure Probe:	1 - good response
	2 - fair response
	3 - poor response
	4 - no response
Surface Displacement LVDT:	1 - in linear calibrated range
	2,3 - in range, but unstable
	4 - stuck or out of range

*F_{tot} = total force on caisson
**Relcapd = relative displacement between cap and wall

Table 5.4 Guidelines for Quality Assessment Code

Initial Penetration Zone

CET Test	Start				End				Penetration Modulus $M_w=\Delta F_w/\Delta z_w$		
	Wall Pen. (cm)	Wall Force (kg)	Cap Force (kg)	Total Force (kg)	Wall Pen. (cm)	Wall Force (kg)	Cap Force (kg)	Total Force (kg)	z_w = 0.05 cm (kg/cm)	z_w= 0.1 cm (kg/cm)	z_w = 0.2 cm (kg/cm)
3	0	3.35	7.42	10.77	0.2	14.75	3.01	17.76	163	92.5	57
4	0	0.22	15.14	15.35	0.2	12.49	3.40	15.89	54	65	61.5
5	0	1.62	13.78	15.40	0.2	13.30	2.92	16.22	196	104	58
6	0	0.19	14.72	14.90	0.2	12.55	2.72	15.27	180	106	61.5
7	0	5.04	10.25	15.29	0.2	18.06	-1.11	16.95	166	111	65.5
8	0	-1.17	17.74	16.57	0.2	10.87	6.22	17.08	200	112	60.5
9	0	-0.70	15.89	15.19	0.2	12.21	3.52	15.72	202	115	63.5
10	0	0.88	14.68	15.56	0.2	11.22	3.20	14.41	86	69	51.5
11	0	1.10	14.07	15.17	0.2	10.14	5.49	15.63	28	40	44.5
12	0	0.54	14.89	15.43	0.2	6.61	10.51	17.12	54	33	30
13	0	1.27	14.30	15.57	0.2	11.80	13.73	25.52	180	87	52
14	0	1.99	12.90	14.89	0.2	10.66	24.73	35.39	122	86	-

Transition Penetration Zone

CET Test	Start				Peak Wall Force (Local Peak)				End			
	Wall Pen. (cm)	Wall Force (kg)	Cap Force (kg)	Total Force (kg)	Wall Pen. (cm)	Wall Force (kg)	Cap Force (kg)	Total Force (kg)	Wall Pen. (cm)	Wall Force (kg)	Cap Force (kg)	Total Force (kg)
3	0.2	14.75	3.01	17.76	0.41	16.58	2.05	18.63	0.83	11.33	2.47	13.80
4	0.2	12.49	3.40	15.89	0.27	13.77	2.52	16.29	1.62	13.17	2.84	16.01
5	0.2	13.30	2.92	16.22	0.32	14.13	2.57	16.70	0.48	13.58	2.54	16.12
6	0.2	12.55	2.72	15.27	-	-	-	-	2.40	14.36	2.71	16.07
7	0.2	18.06	-1.11	16.95	0.35	19.36	-2.44	16.93	0.98	16.31	-0.12	16.19
8	0.2	10.87	6.22	17.08	1.02	12.28	4.93	17.16	1.19	12.05	5.07	17.11
9	0.2	12.21	3.52	15.72	0.38	12.93	2.78	15.71	0.80	11.41	3.86	15.27
10	0.2	11.22	3.20	14.41	-	-	-	-	0.90	16.86	-1.59	15.27
11	0.2	10.14	5.49	15.63	0.44	11.98	3.48	15.45	0.59	11.30	3.70	15.00
12	0.2	6.61	10.51	17.12	0.63	17.60	-2.26	15.33	1.83	14.06	1.01	15.07
13	0.2	11.80	13.73	25.52	-	-	-	-	0.44	13.00	13.77	26.76
14	0.2	10.66	24.73	35.39	-	-	-	-	1.40	11.38	-4.12	7.26

Note: No obvious local peak in CET6, 10, 13, and 14

Table 5.5a Caisson Force Characteristics During Installation: Initial and Transition Zones

Deep Penetration Zone

CET Test	Start				End				Wall Force Regression		
	Wall Pen. (cm)	Wall Force (kg)	Cap Force (kg)	Total Force (kg)	Wall Pen. (cm)	Wall Force (kg)	Cap Force (kg)	Total Force (kg)	Slope (kg/cm)	Force intercept (kg)	R^2
3	0.83	11.33	2.47	13.80	5.08	19.87	-3.82	16.04	2.04	9.71	0.998
4	1.62	13.17	2.84	16.01	5.09	18.27	-0.55	17.72	1.46	10.74	0.998
5	0.48	13.58	2.54	16.12	5.10	18.57	-0.96	17.61	1.11	12.75	0.983
6	2.40	14.36	2.71	16.07	5.09	18.76	-2.40	16.36	1.70	10.03	0.995
7	0.98	16.31	-0.12	16.19	5.08	22.55	-6.00	16.55	1.61	14.22	0.994
8	1.19	12.05	5.07	17.11	5.08	17.15	0.18	17.34	1.29	10.46	0.995
9	0.80	11.41	3.86	15.27	5.08	17.02	-1.54	15.47	1.35	10.14	0.997
10	0.90	16.86	-1.59	15.27	5.09	22.05	-6.87	15.18	1.19	15.55	0.960
11	0.59	11.30	3.70	15.00	5.13	18.14	-2.68	15.46	1.55	10.49	0.997
12	1.83	14.06	1.01	15.07	5.09	18.66	-3.42	15.23	1.60	10.14	0.956
13	0.44	13.00	13.77	26.76	5.09	23.63	13.99	37.62	2.13	12.30	0.998
14	1.40	11.38	-4.12	7.26	5.07	15.89	17.79	33.68	1.18	10.14	0.992

Table 5.5b Caisson Force Characteristics During Installation: Deep Zone

Monotonic Pullout 1: 0.03 cm/min

CET Test	Start				Peak Total Force				End			
	Wall Pull (cm)	Wall Force (kg)	Cap Force (kg)	Total Force (kg)	Wall Pull (cm)	Wall Force (kg)	Cap Force (kg)	Total Force (kg)	Wall Pull (cm)	Wall Force (kg)	Cap Force (kg)	Total Force (kg)
3	0	13.40	-2.70	10.70	0.172	-12.7	-6.58	-19.3	0.303	-12.5	-6.19	-18.7
4	0	9.38	2.04	11.42	0.227	-14.3	-8.41	-22.7	0.300	-12.1	-10.2	-22.3
5	0	9.10	2.45	11.55	0.235	-15.2	-8.75	-24.0	0.240	-15.0	-8.71	-23.7
6	0	16.35	-0.93	15.43	0.300	-11.0	-11.3	-22.3	0.301	-10.2	-11.2	-21.4
7	0	14.78	0.62	15.40	0.187	-7.04	-10.6	-17.6	0.303	-5.87	-11.2	-17.0
8	0	13.57	1.74	15.31	0.234	-13.5	-8.9	-22.4	1.077	-10.9	-7.77	-18.6
9	0	13.66	1.01	14.67	-	-	-	-	0.003	1.42	-3.65	-2.23
10	0	11.44	3.81	15.25	-	-	-	-	0.007	-2.50	-8.79	-11.3
11	0	15.55	-0.38	15.17	-	-	-	-	0.003	5.39	-8.88	-3.49
12	0	13.42	2.13	15.55	-	-	-	-	0.003	1.29	-7.91	-6.62
13	0	13.75	1.46	15.21	-	-	-	-	0.005	-2.02	-5.35	-7.37
14	0	9.69	4.44	14.13	-	-	-	-	0.006	-2.60	-4.25	-6.85
Monotonic Pullout 1: 0.3 cm/min												
3	0.313	-11.1	-5.44	-16.5	0.464	-12.9	-12.2	-25.2	4.37	2.00	-1.93	0.07
4	0.544	-10.2	-9.12	-19.3	0.693	-13.4	-11.3	-24.7	4.35	2.52	-2.17	0.35
8	1.079	-4.00	-6.50	-10.5	1.179	-11.4	-10.0	-21.4	4.32	1.40	-1.66	-0.26

Monotonic Pullout 2: 0.03 cm/min

CET Test	Start				Peak Total Force				End			
	Wall Pull (cm)	Wall Force (kg)	Cap Force (kg)	Total Force (kg)	Wall Pull (cm)	Wall Force (kg)	Cap Force (kg)	Total Force (kg)	Wall Pull (cm)	Wall Force (kg)	Cap Force (kg)	Total Force (kg)
5	0	16.26	1.68	17.94	0.275	-18.5	-9.52	-28.0	0.295	-17.7	-10.4	-28.1
6	0	14.09	1.12	15.21	0.325	-15.2	-10.1	-25.2	0.411	-14.8	-10.4	-25.2
7	0	14.79	0.43	15.22	0.199	-10.8	-9.41	-20.0	0.351	-8.90	-10.5	-19.4
9	0	-2.84	0.13	-2.72	0.181	-11.3	-9.60	-20.9	1.246	-10.2	-3.67	-13.8
12	0	12.23	3.22	15.45	0.108	-16.6	-9.18	-25.8	1.014	-13.1	-3.70	-16.9
13	0	14.5	0.45	15.35	0.260	-19.4	-7.81	-27.2	1.003	-14.6	-8.20	-22.8
14	0	14.06	1.11	15.17	0.224	-16.9	-13.7	-30.5	0.650	-16.1	-10.6	-26.7
Monotonic Pullout 2: 0.3 cm/min												
7	0.609	-8.80	-4.82	-13.6	0.810	-8.26	-12.9	-21.1	3.51	4.39	-1.73	2.66
12	1.021	-12.1	-0.81	-12.9	1.208	-15.1	-5.15	-20.2	4.61	-0.16	0.13	-0.03
13	1.005	-14.9	-5.21	-20.0	1.225	-17.5	-7.85	-25.4	4.40	1.76	-2.11	-0.35
14	0.652	-13.1	-5.92	-18.9	0.832	-14.6	-15.5	-30.1	4.47	1.96	-2.14	-0.18

Table 5.6 Caisson Force Characteristics During Monotonic Pullout 1 and 2

I.D. #	Instrument	Radial Location (cm) from centerline
CP	Cap Pore Pressure	0.00
AP	Chamber Air Pressure	(cover plate)
P1	Pore Pressure Probe	0.00
P2	" " "	1.78
P3	" " "	3.18
P4	" " "	4.45
S1	Surface Displacement	4.2
S2	" "	5.2
S3	" "	7.7
S4	" "	9.8
S5	" "	12.1
σ_H	Total Stress	(chamber sidewall)

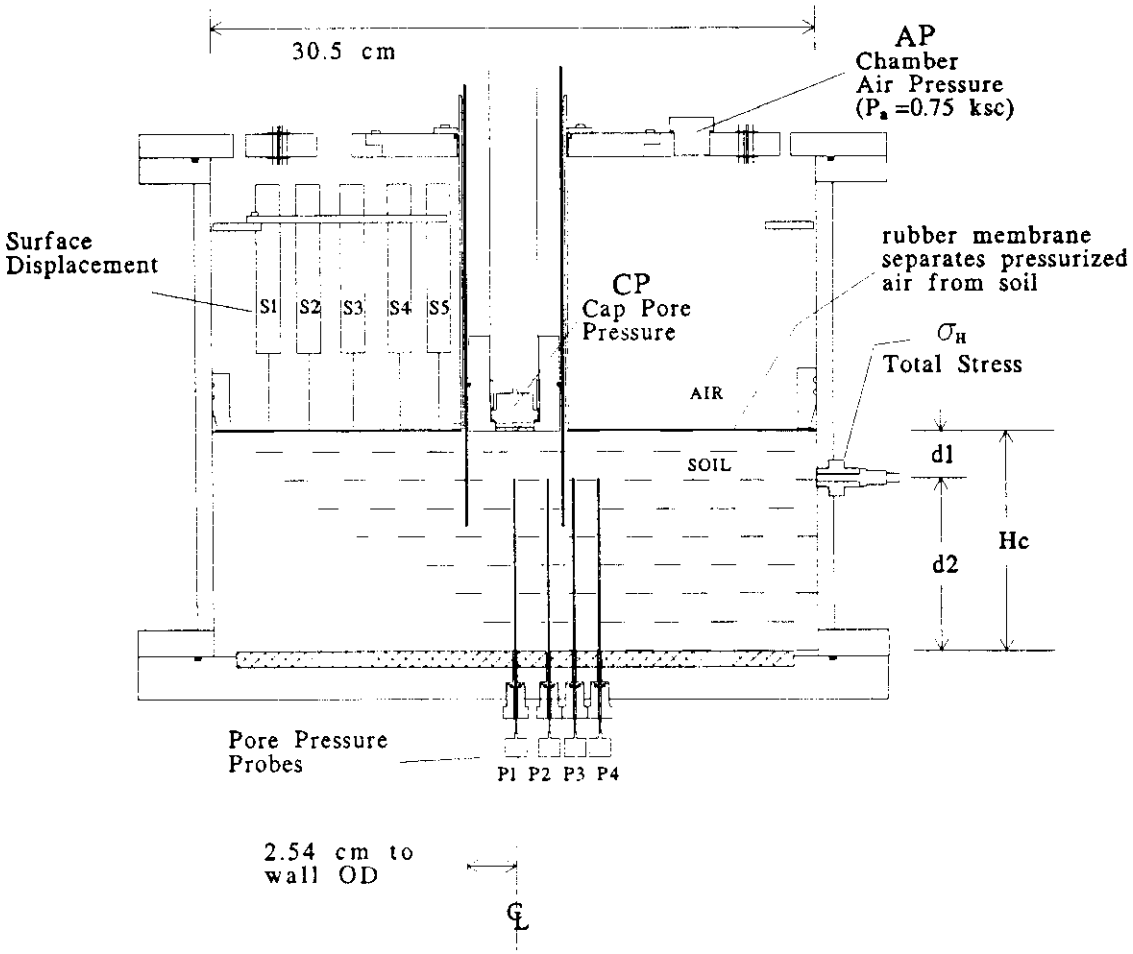

Figure 5.1 Schematic Cross Section of CET Chamber with Caisson Fully Penetrated to Illustrate Test Geometry and Instrumentation

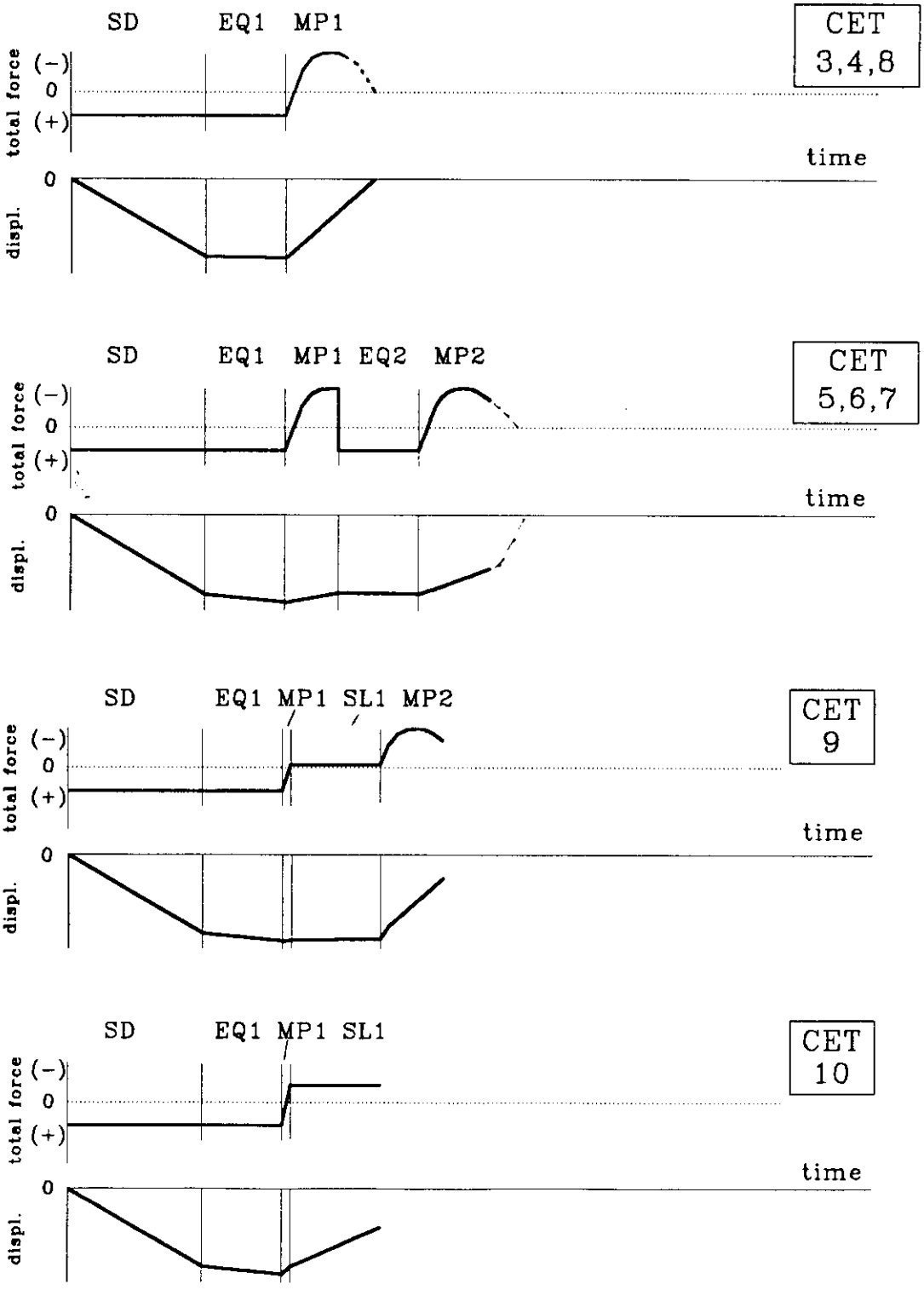

Figure 5.2a Individual Test Force and Displacement Timelines for CET3-10

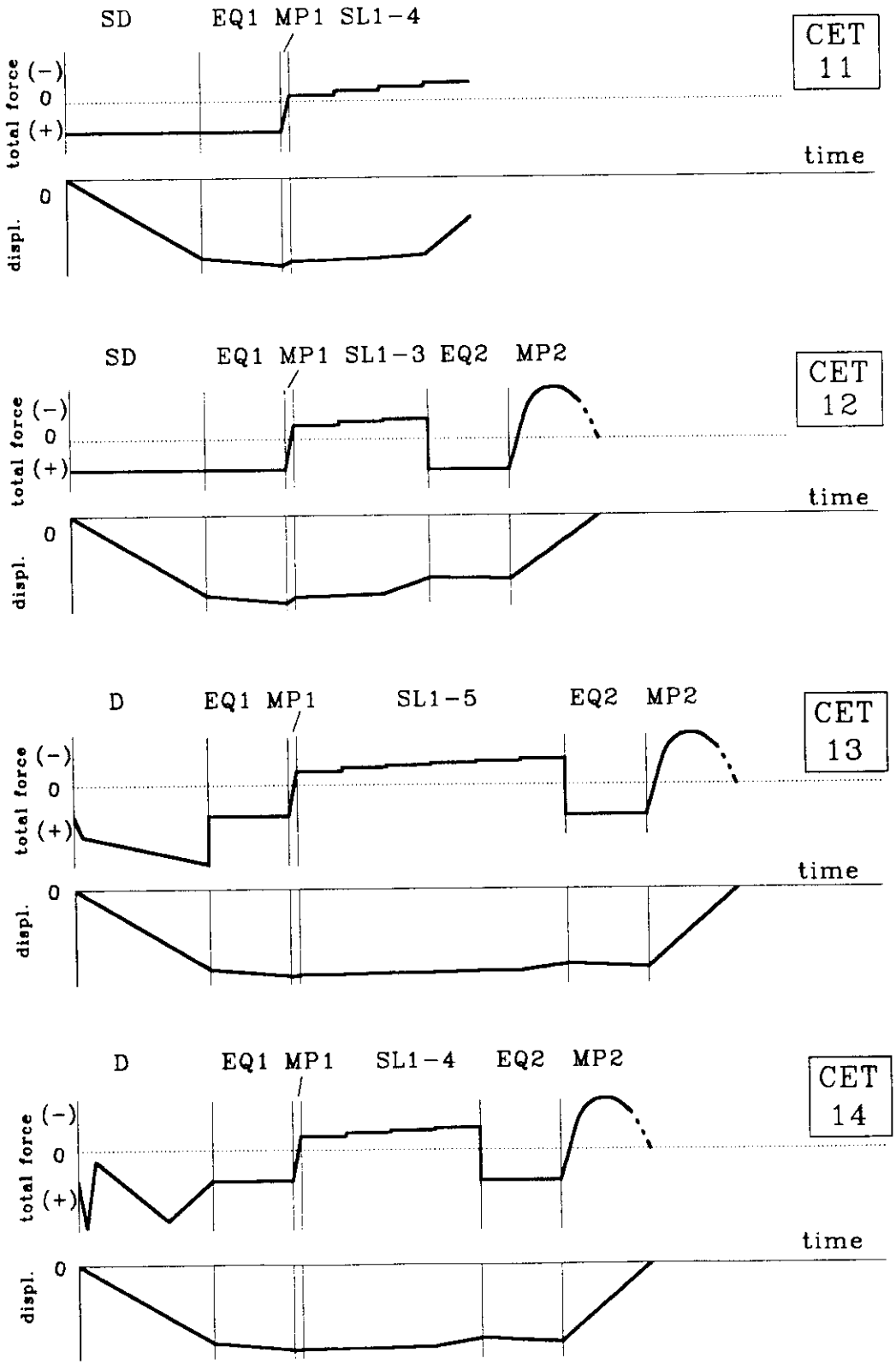

Figure 5.2b Individual Test Force and Displacement Timelines for CET11-14

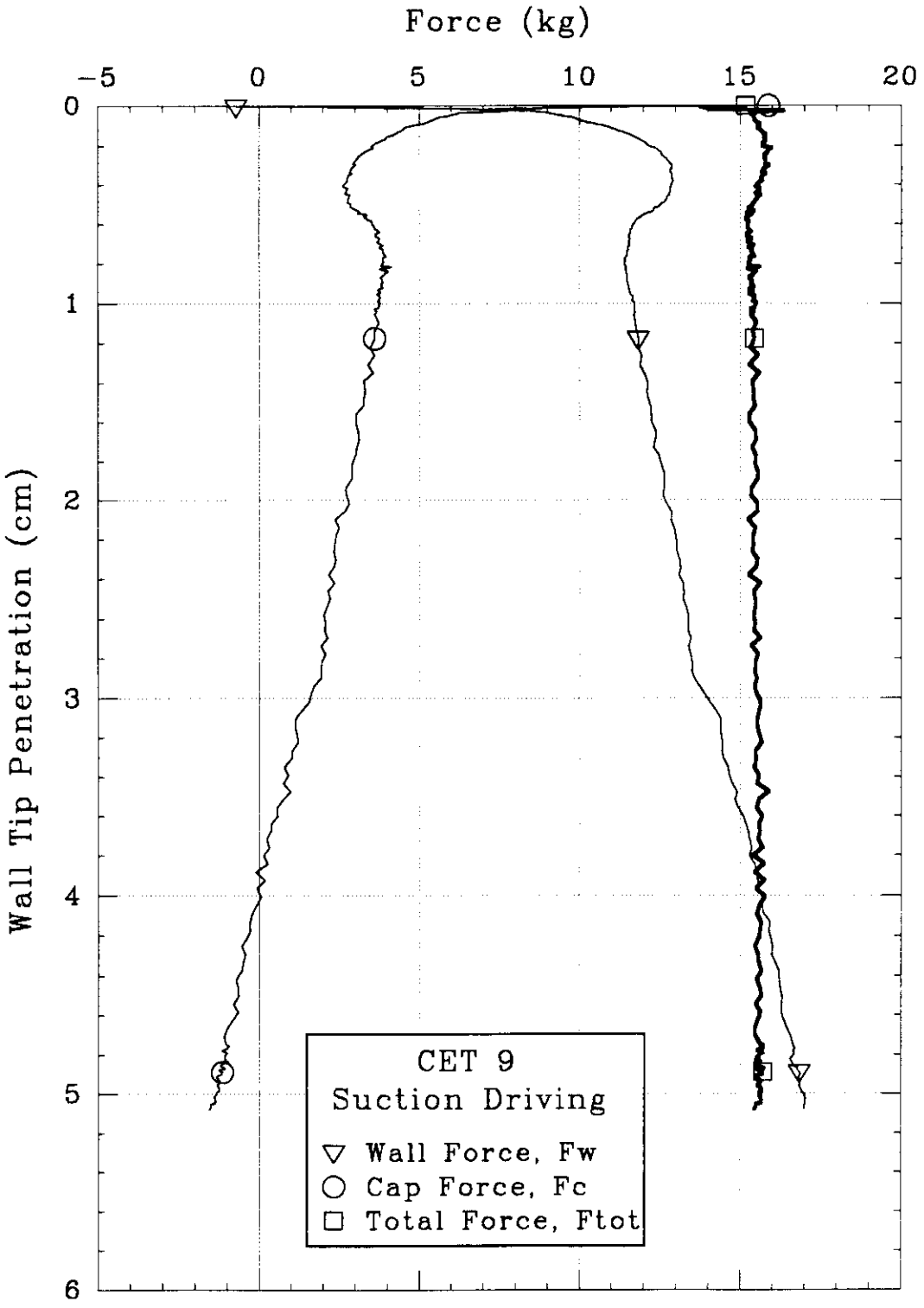

Figure 5.3 Measured Forces on Caisson Components During Suction Driving in CET9

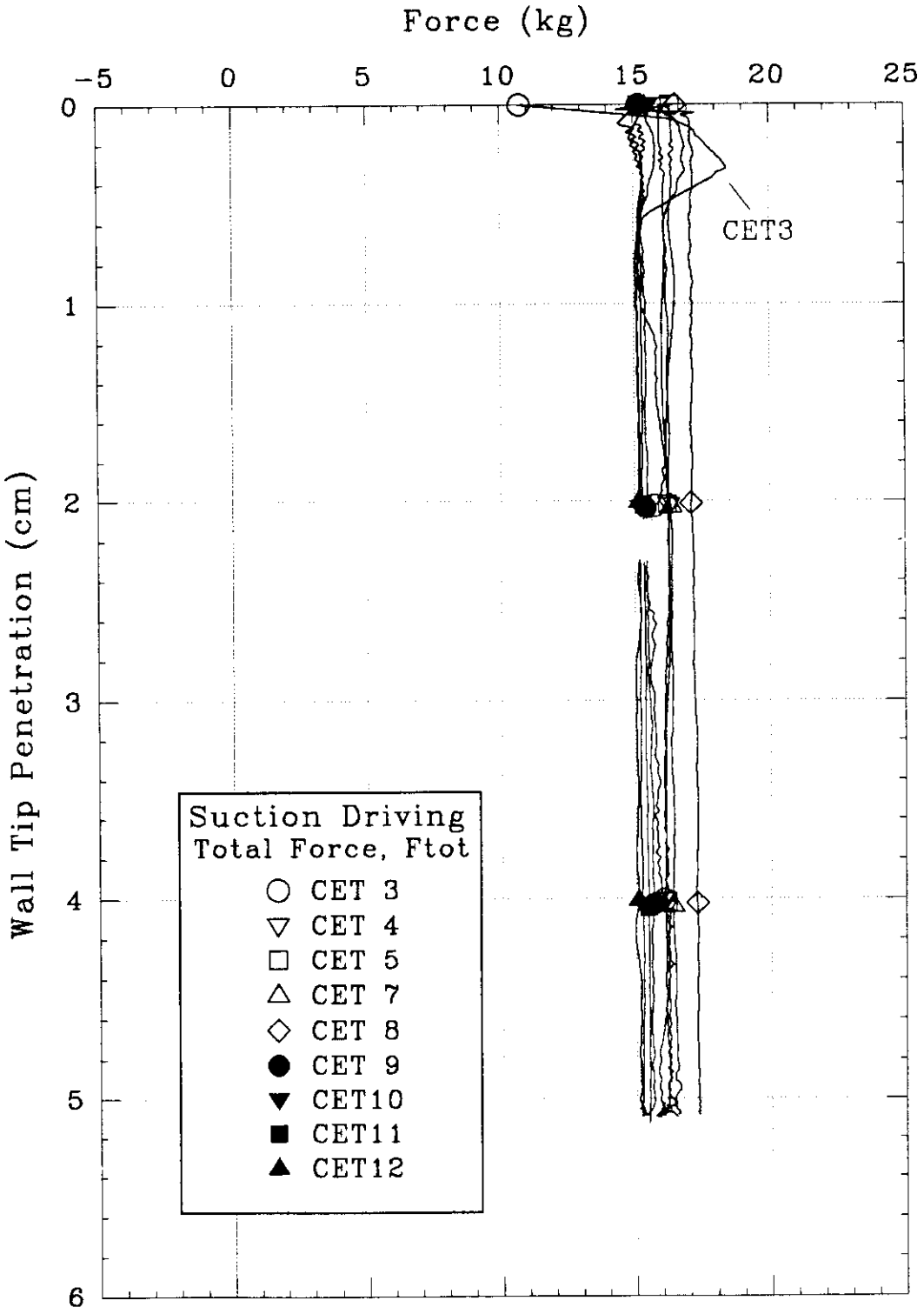

Figure 5.4 Measured Total Force on Caisson During Suction Driving for CET3-5, 7-12 at Large Scale (-5 to 25 kg)

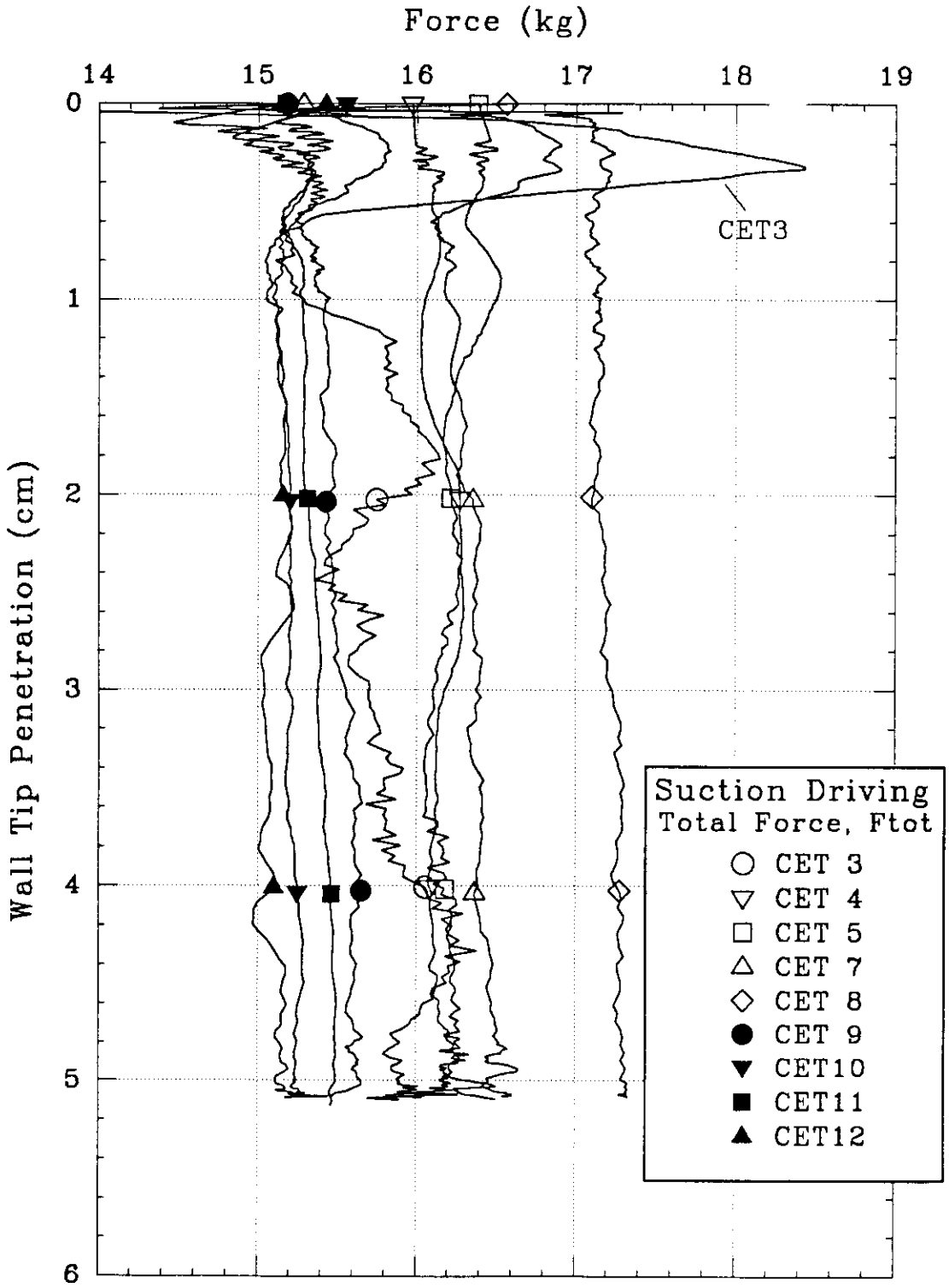

Figure 5.5 Measured Total Force on Caisson During Suction Driving for CET3-5, 7-12 at Small Scale (14 to 19 kg)

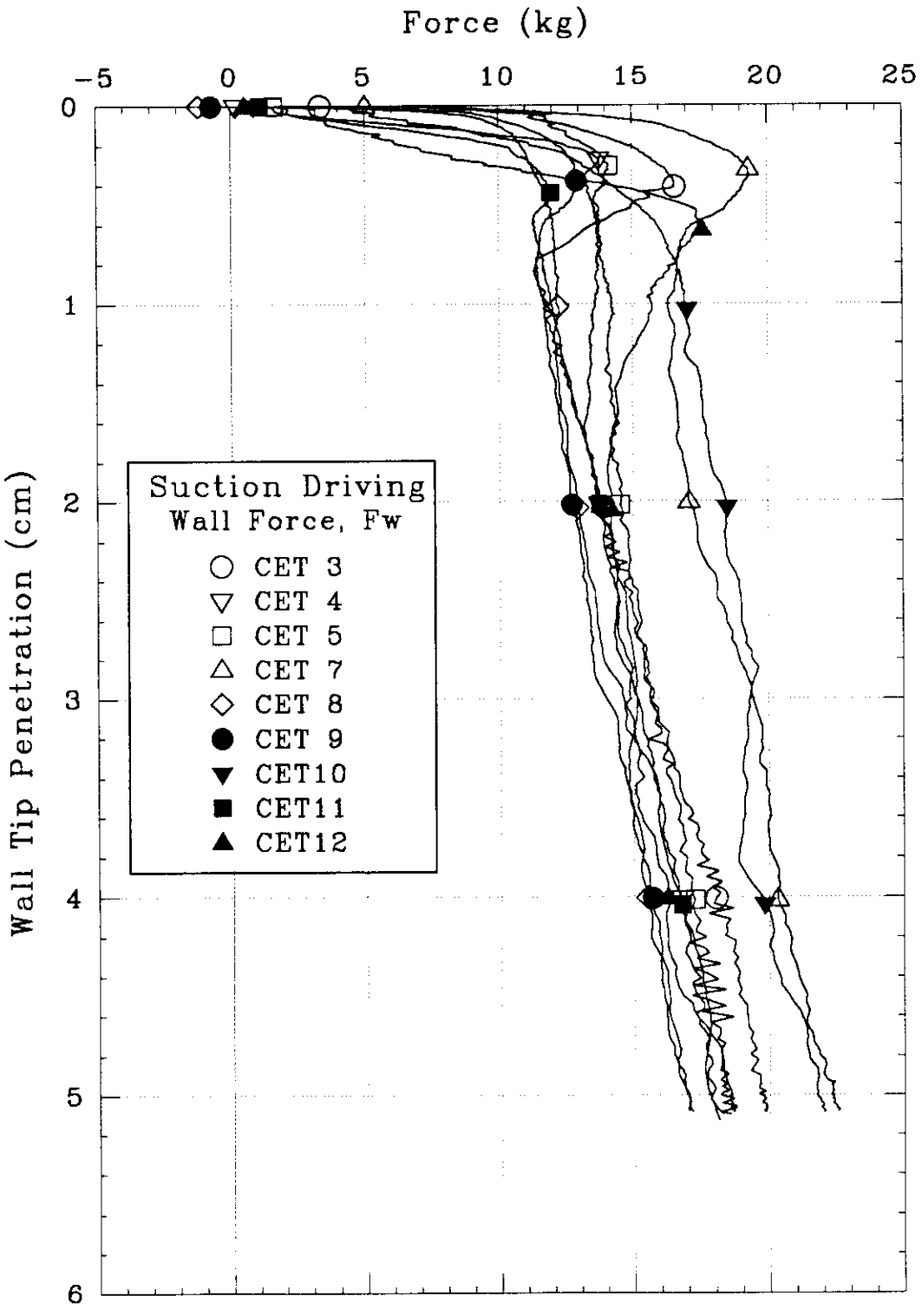

Figure 5.6 Measured Wall Force Component During Suction Driving for CET3-5, 7-12

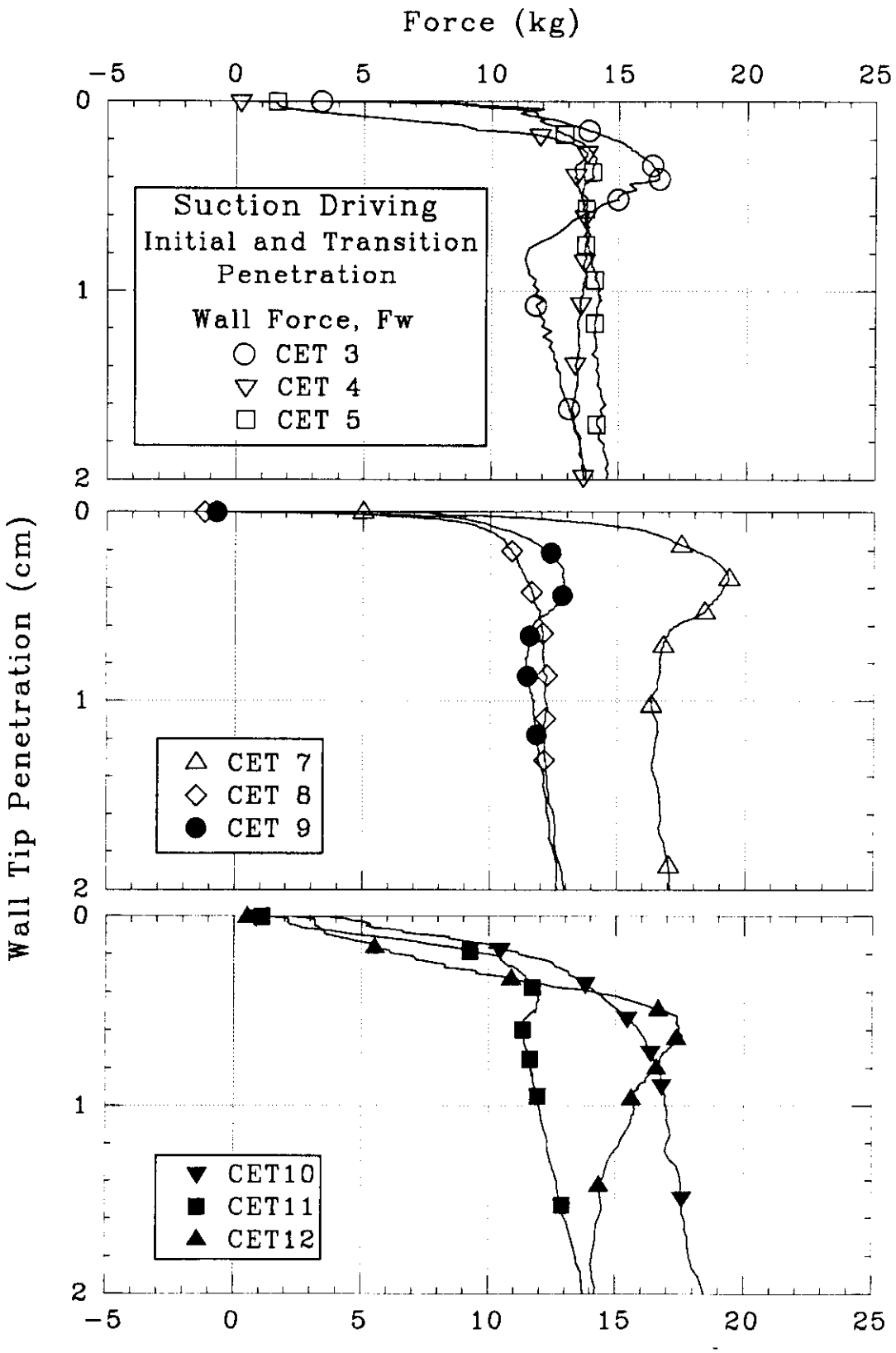

Figure 5.7 Measured Wall Force Component During Suction Driving for CET3-5, 7-12: Initial and Transition Zones

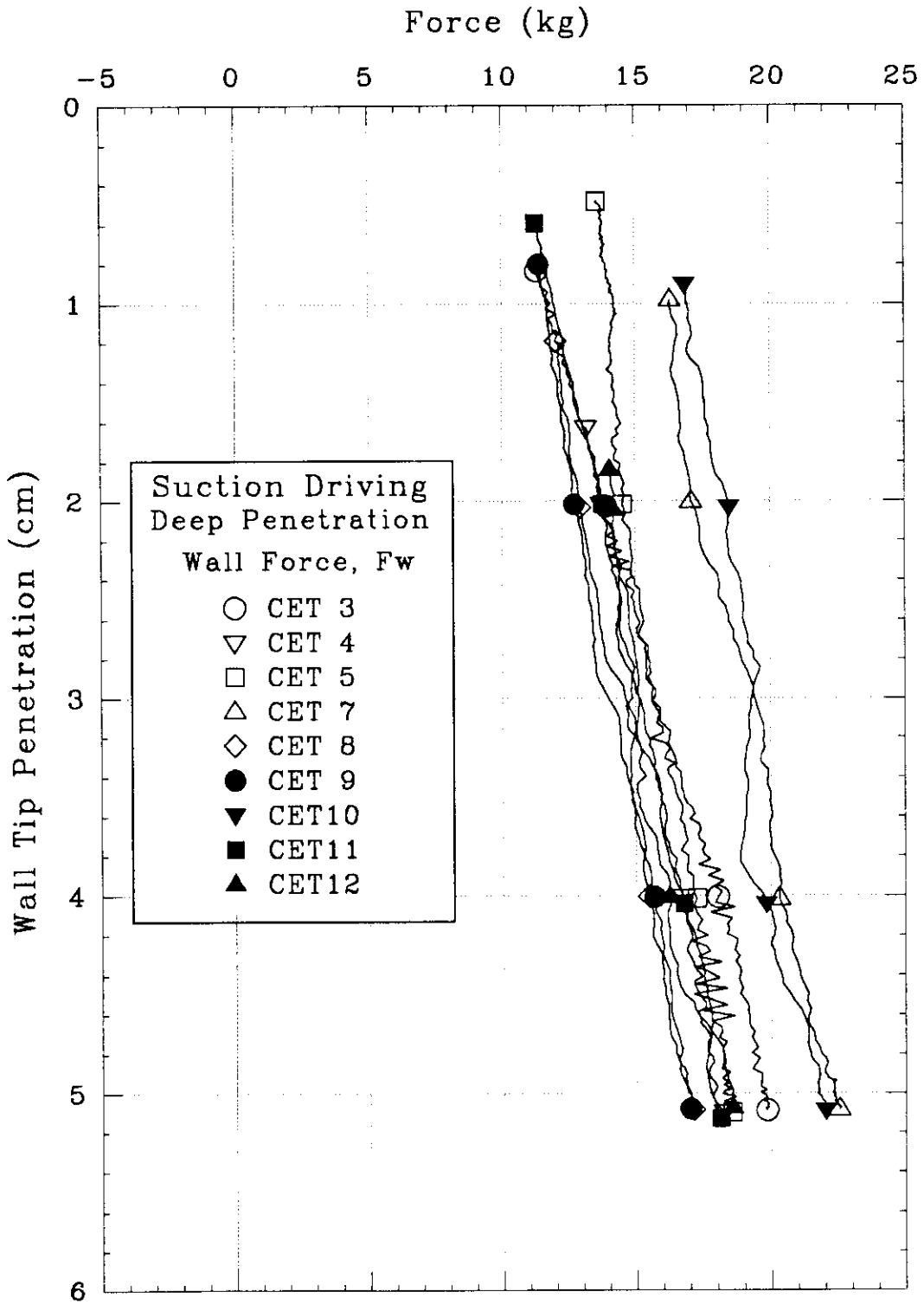

Figure 5.8 Measured Wall Force Component During Suction Driving for CET3-5, 7-12: Deep Zone

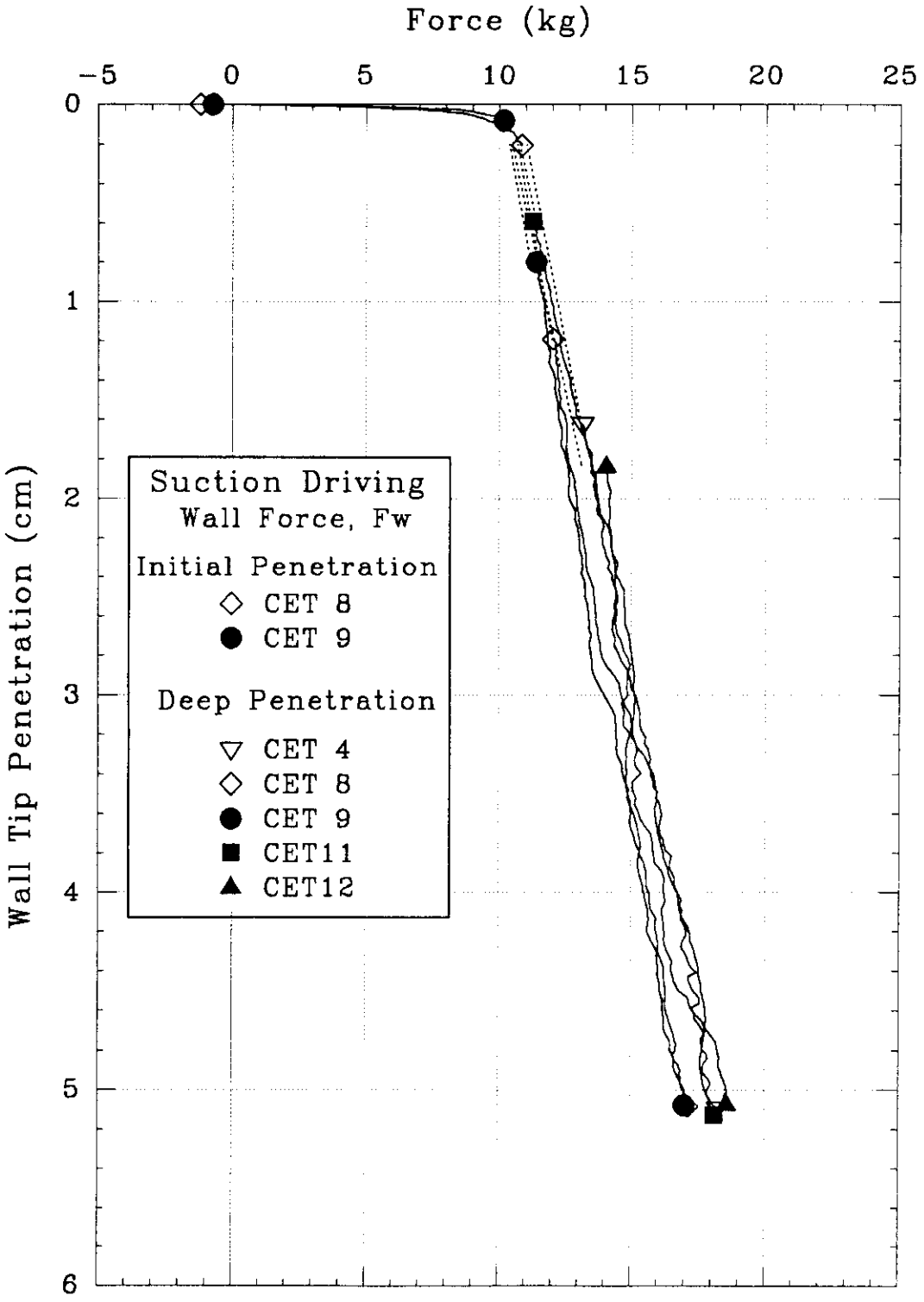

Figure 5.9 Most Representative Measured Wall Force During Initial and Deep Penetration of Suction Driving

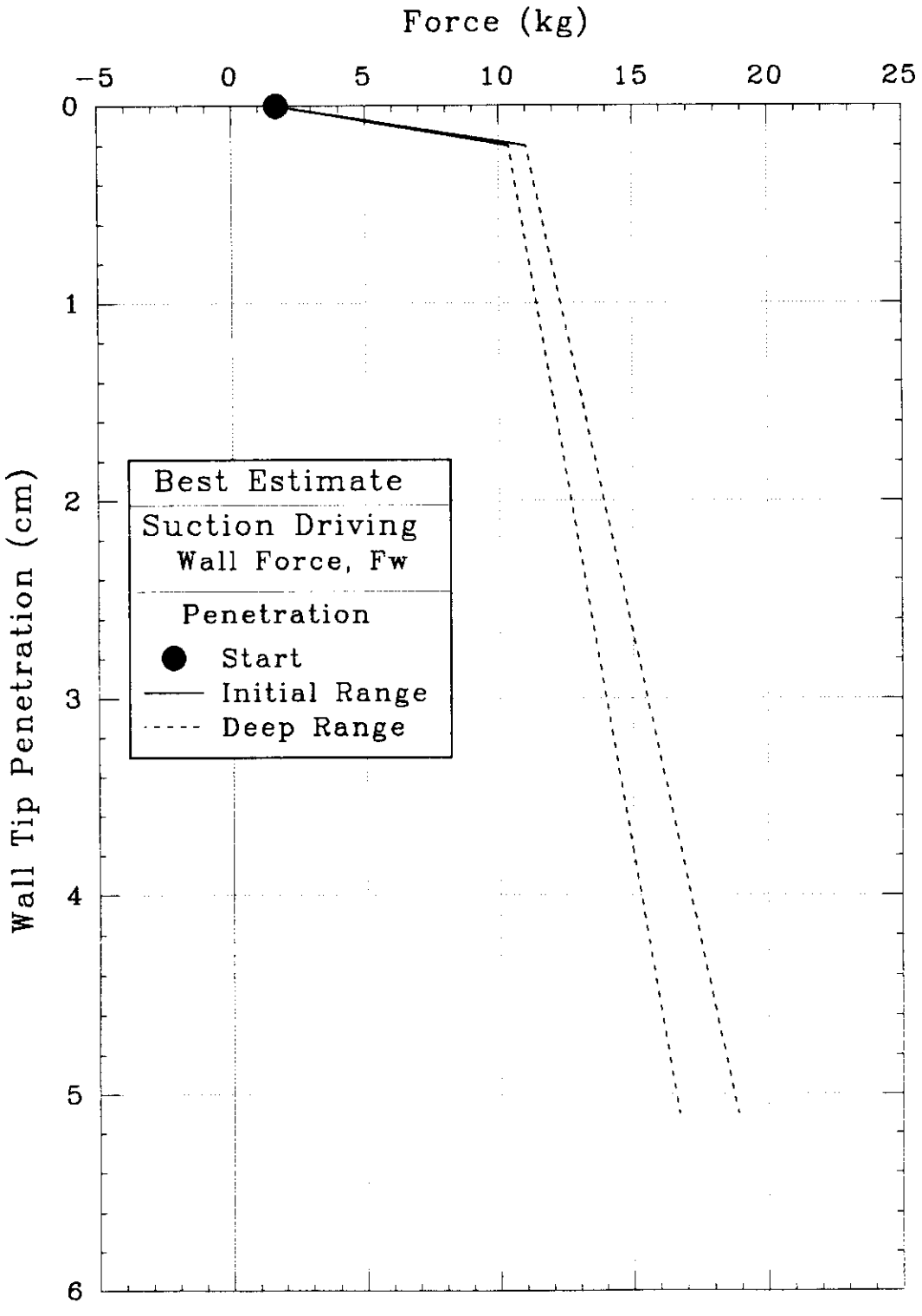

Figure 5.10 Best Estimate of Wall Force versus Wall Tip Penetration During Suction Driving

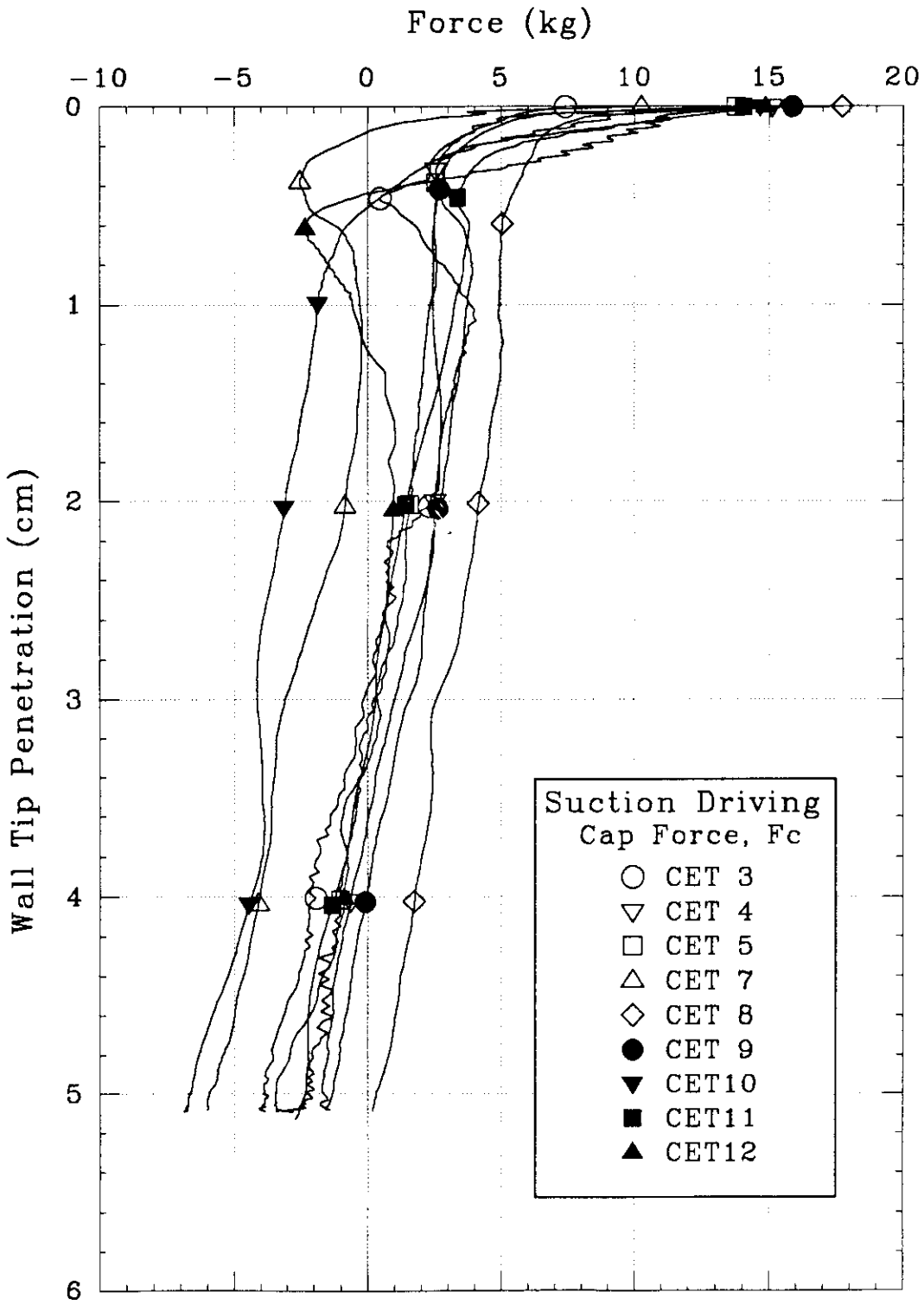

Figure 5.11 Measured Cap Force Component During Suction Driving for CET3-5, 7-12

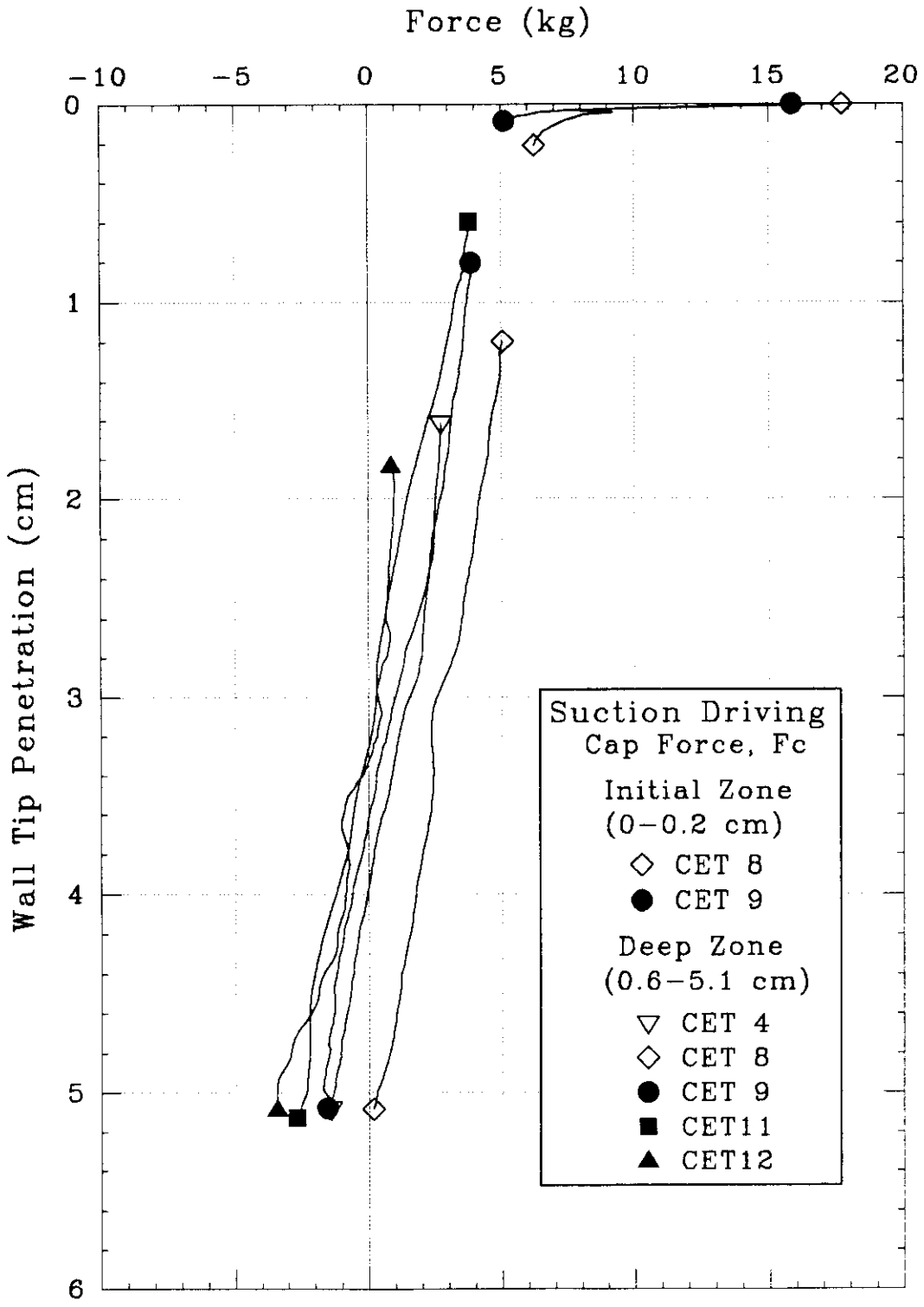

Figure 5.12 Measured Cap Force Component During Suction Driving for CET3-5, 7-12: Initial and Deep Zones

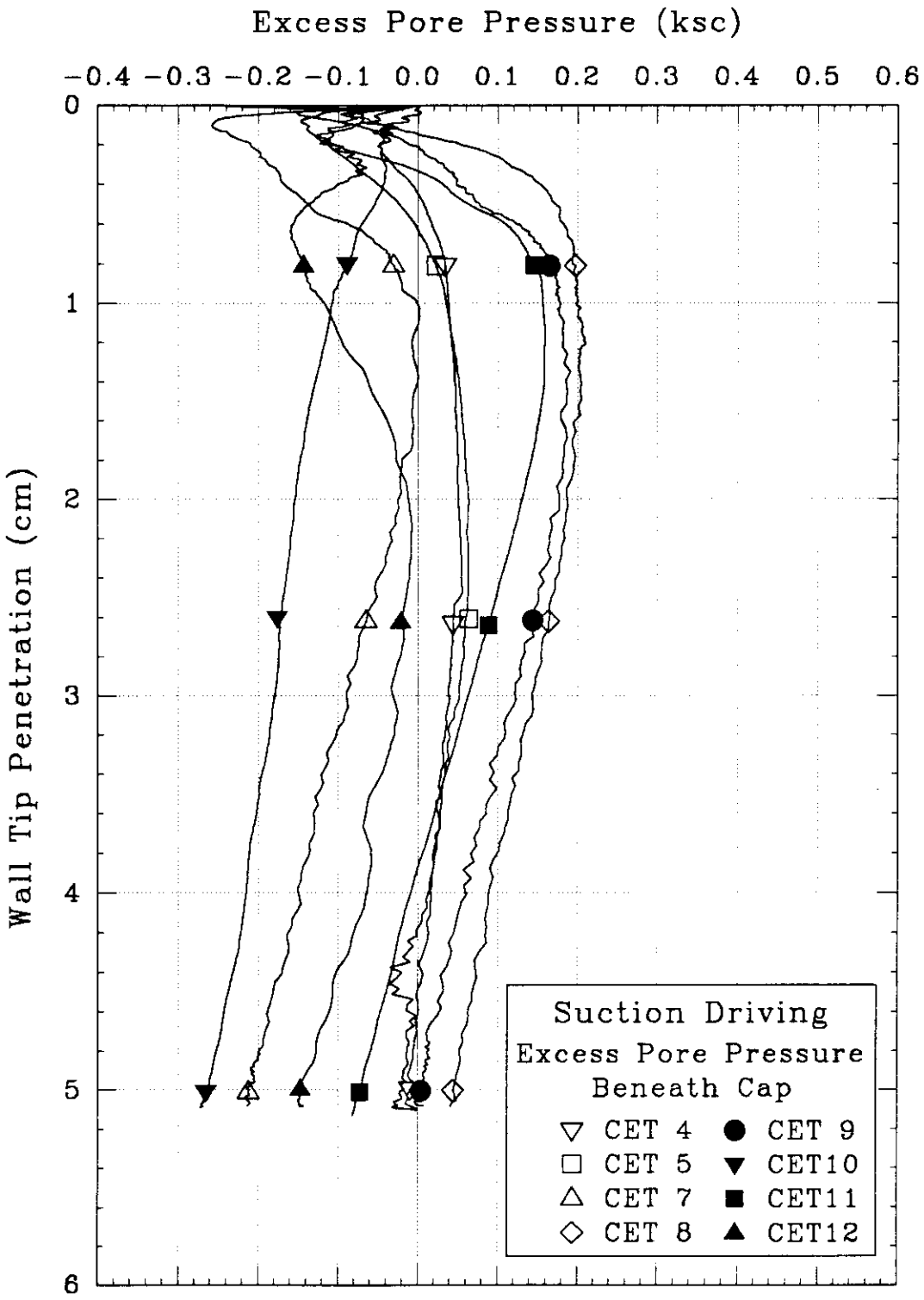

Figure 5.13 Measured Excess Pore Pressure Beneath Cap During Suction Driving for CET4-5,7-12

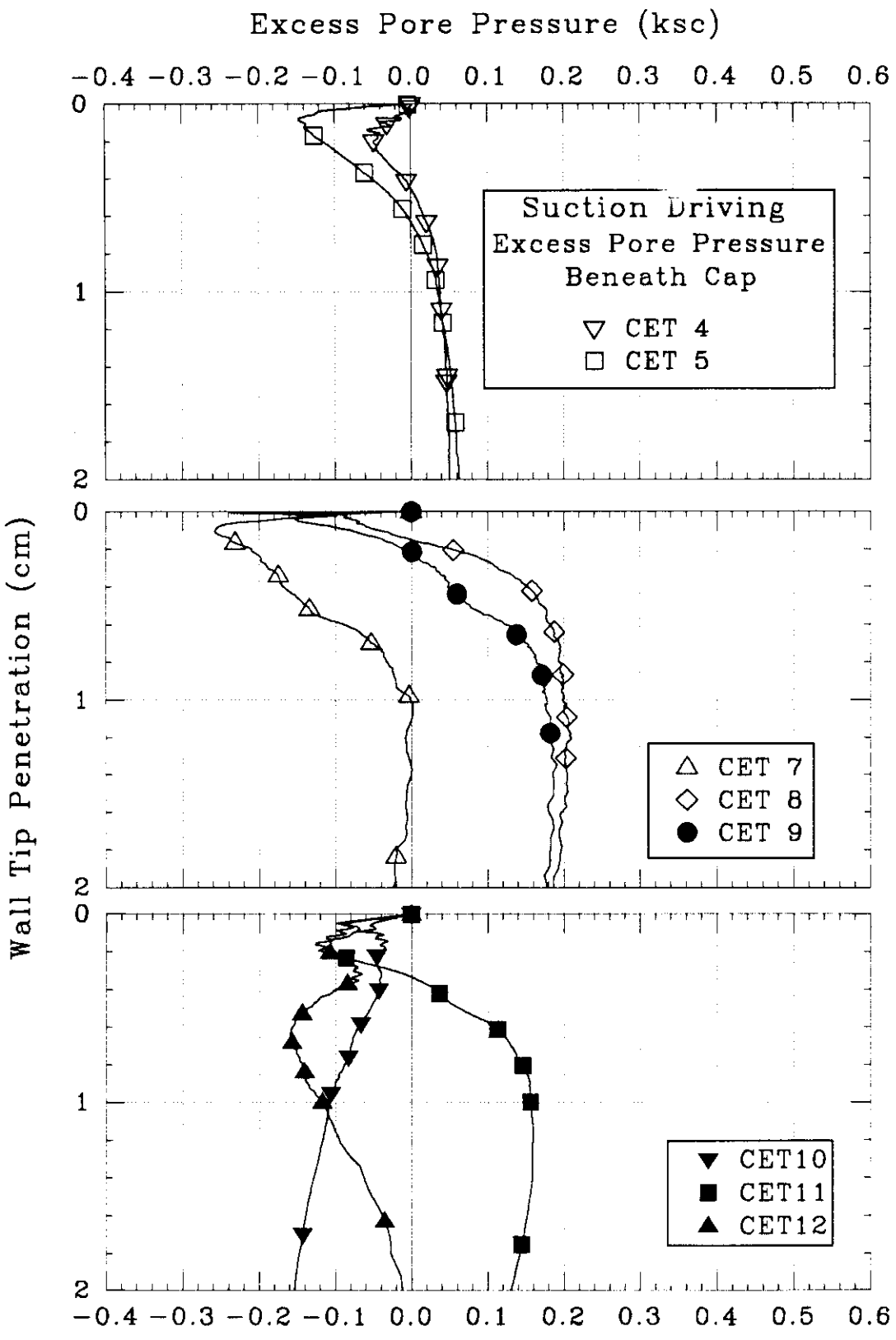

Figure 5.14 Measured Excess Pore Pressure Beneath Cap During Suction Driving for CET4-5, 7-12: Initial and Transition Zones

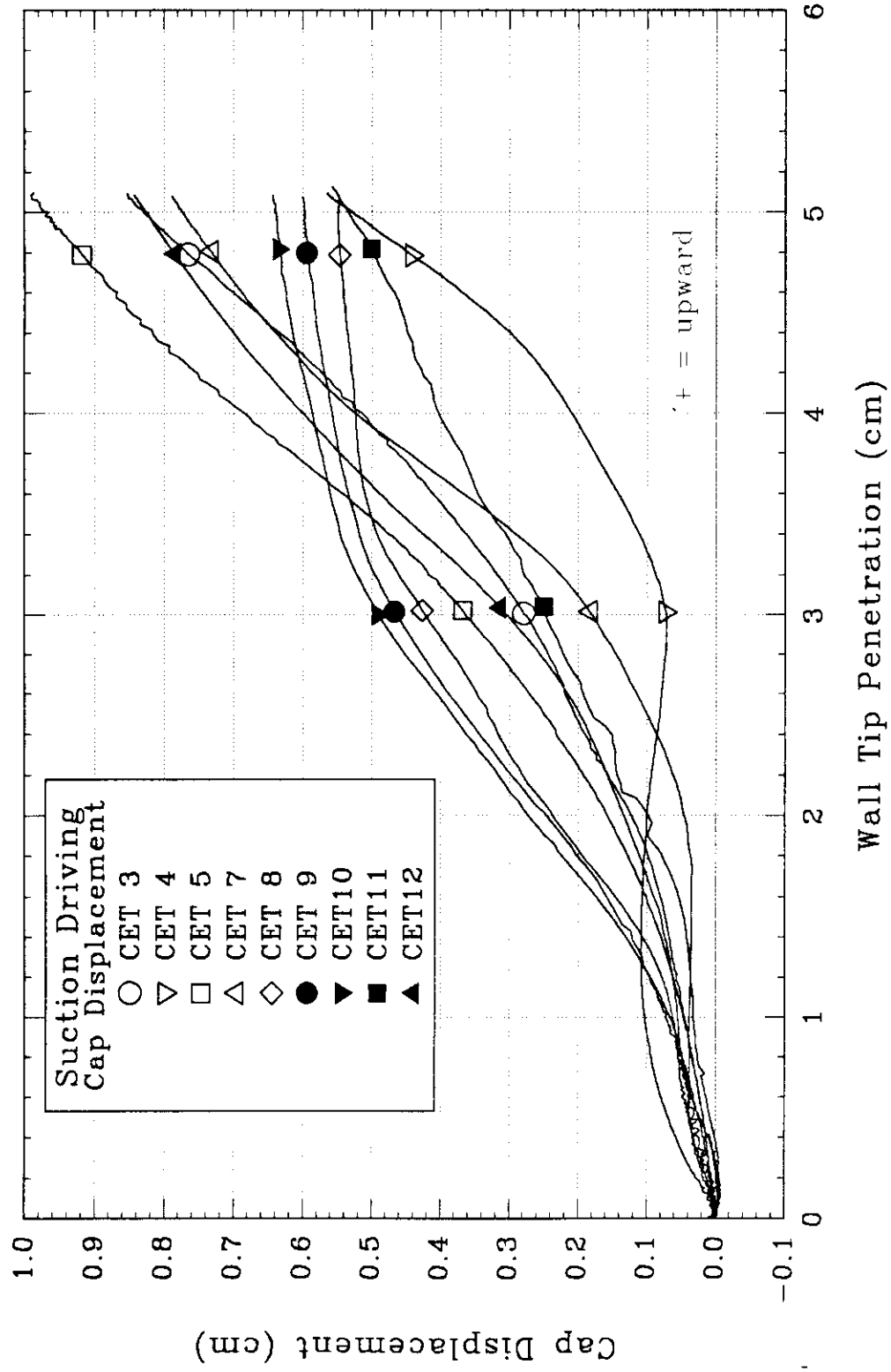

Figure 5.15 Measured Cap Displacement During Suction Driving for CET3-5,7-12

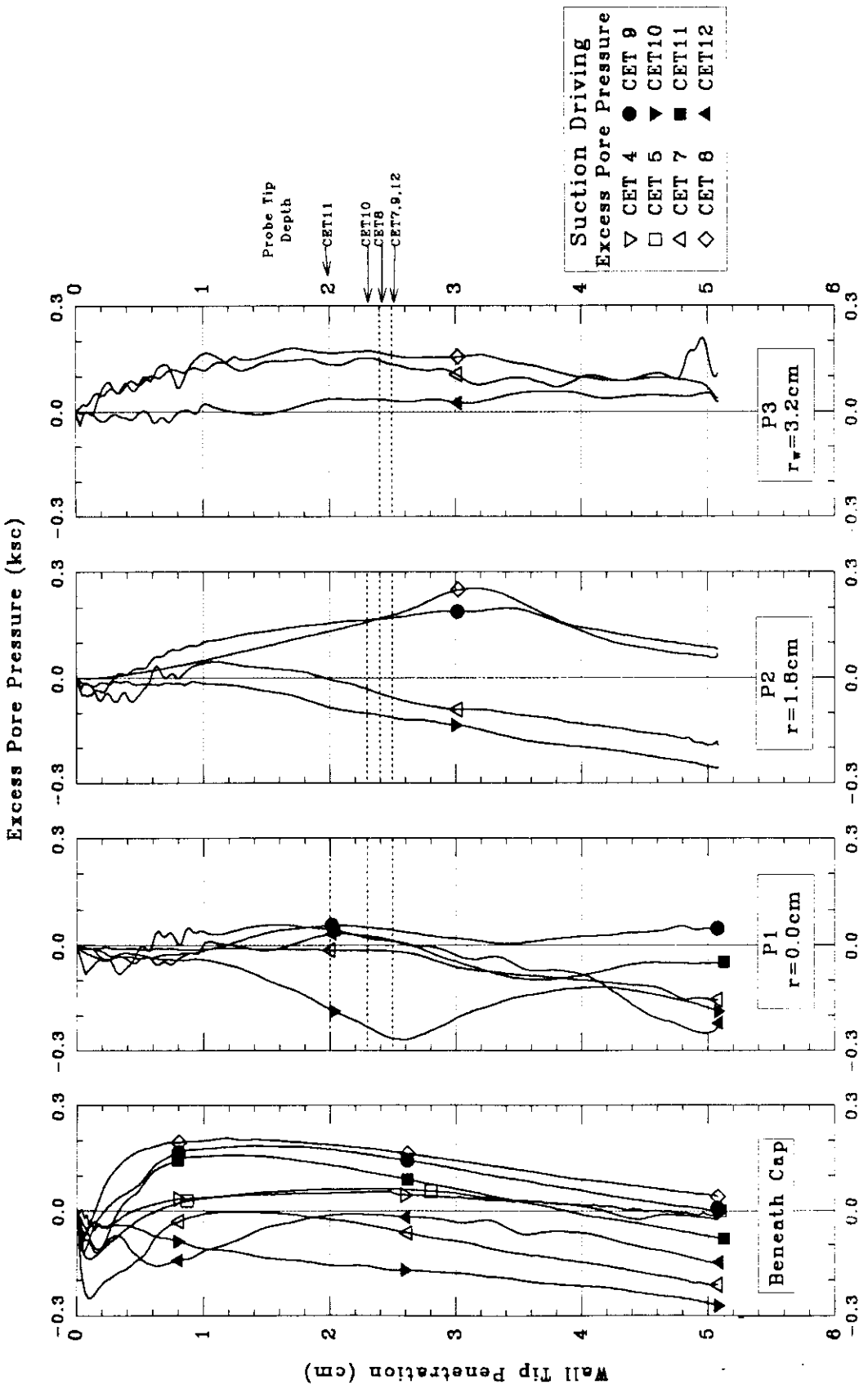

Figure 5.16 Measured Excess Pore Pressure Beneath Cap and by Probes P1, P2, and P3 During Suction Driving for CET7-12

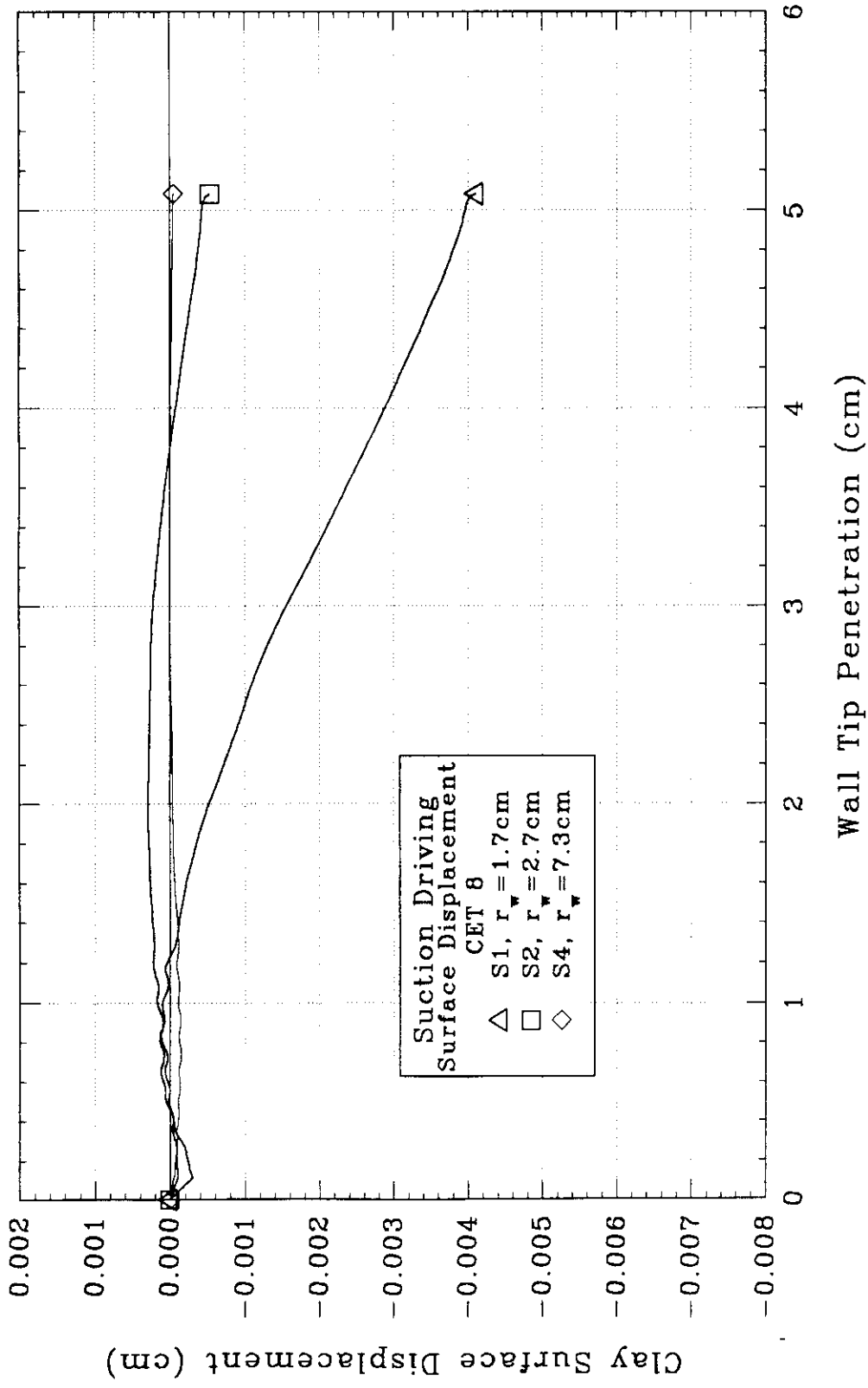

Figure 5.17 Measured Soil Surface Displacement at Three Radial Locations During Suction Driving for CET8

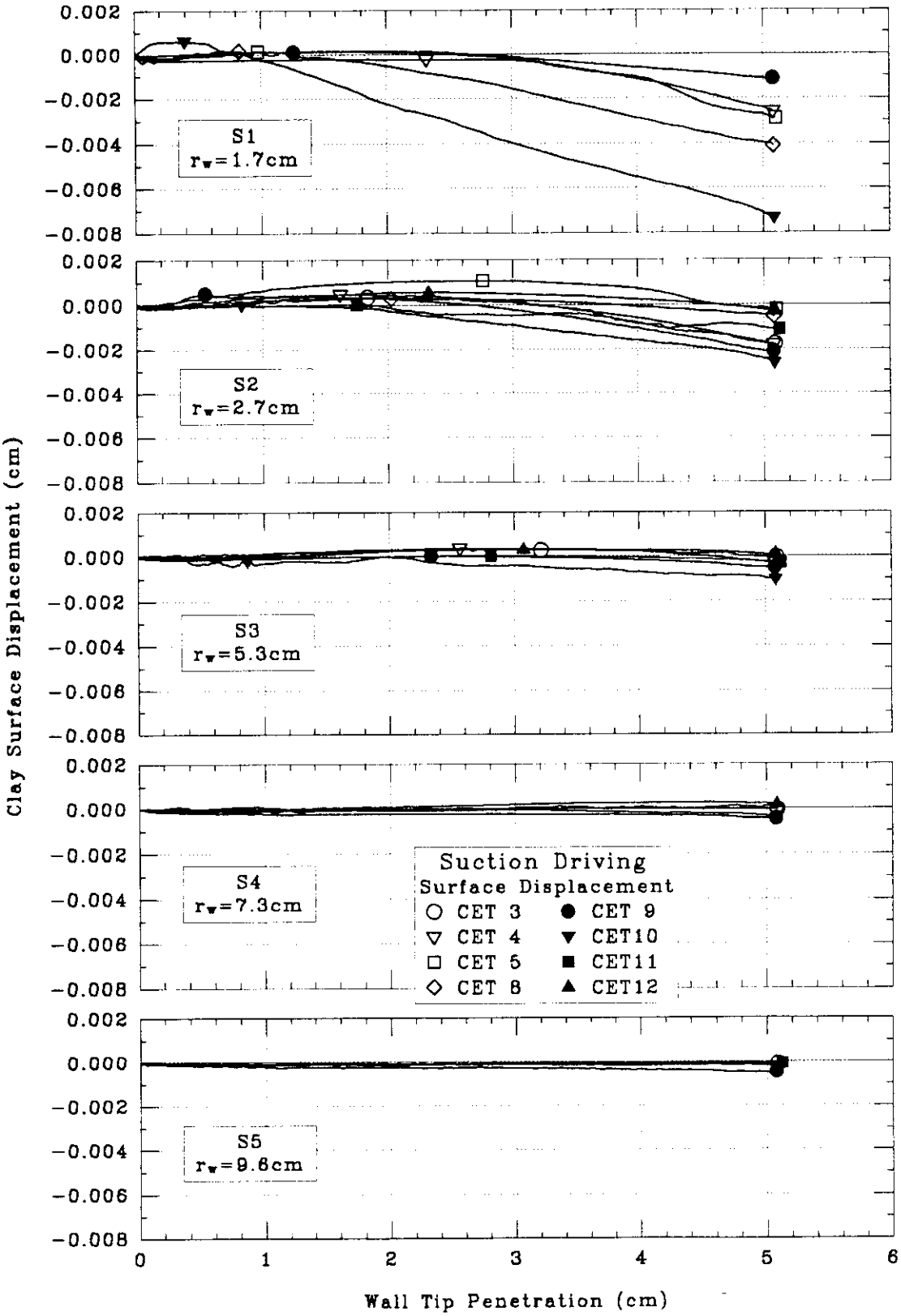

Figure 5.18 Measured Soil Surface Displacement by S1-S5 During Suction Driving for CET3-5,8-10

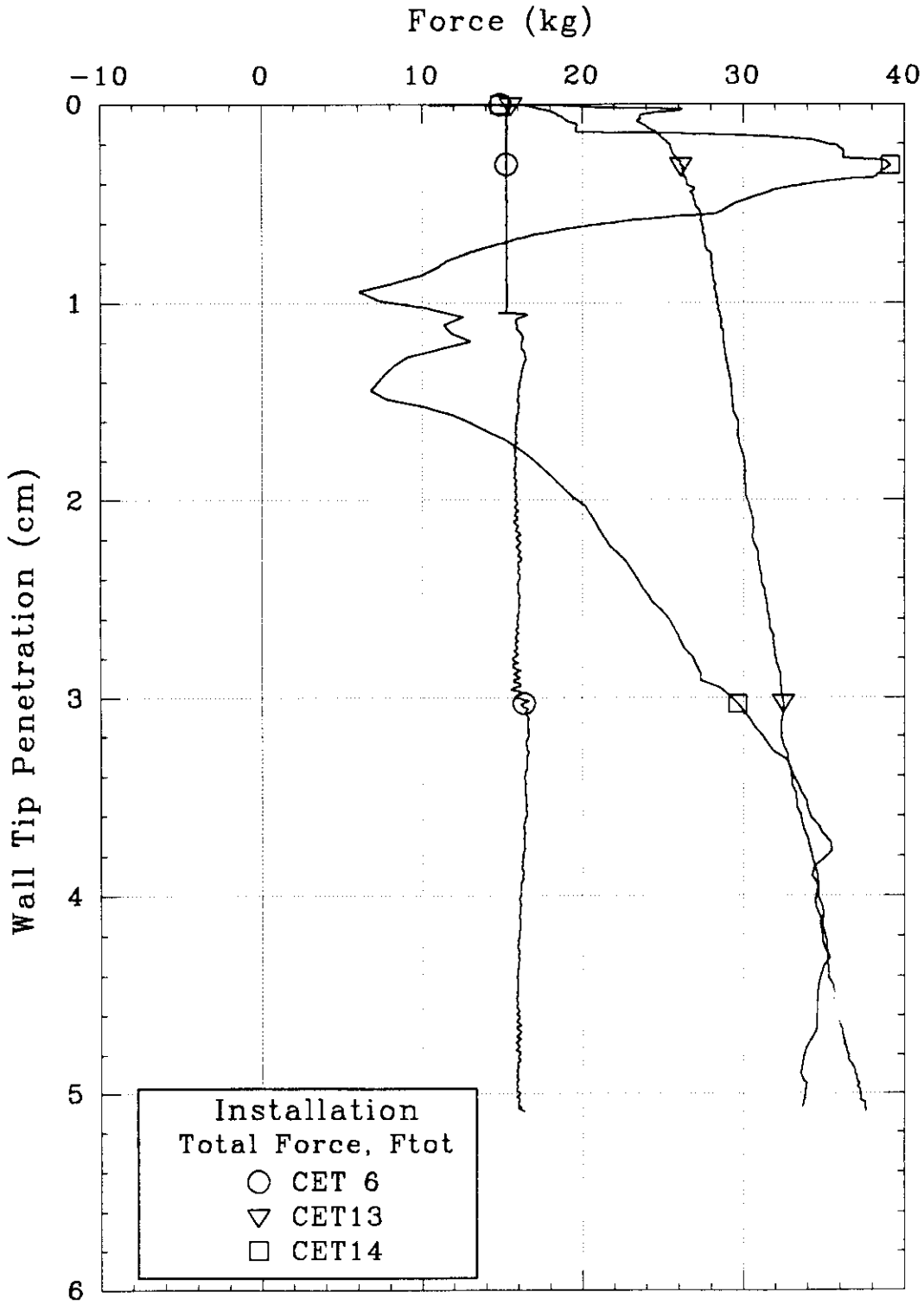

Figure 5.19 Measured Total Force on Caisson During Installation for CET6,13,14

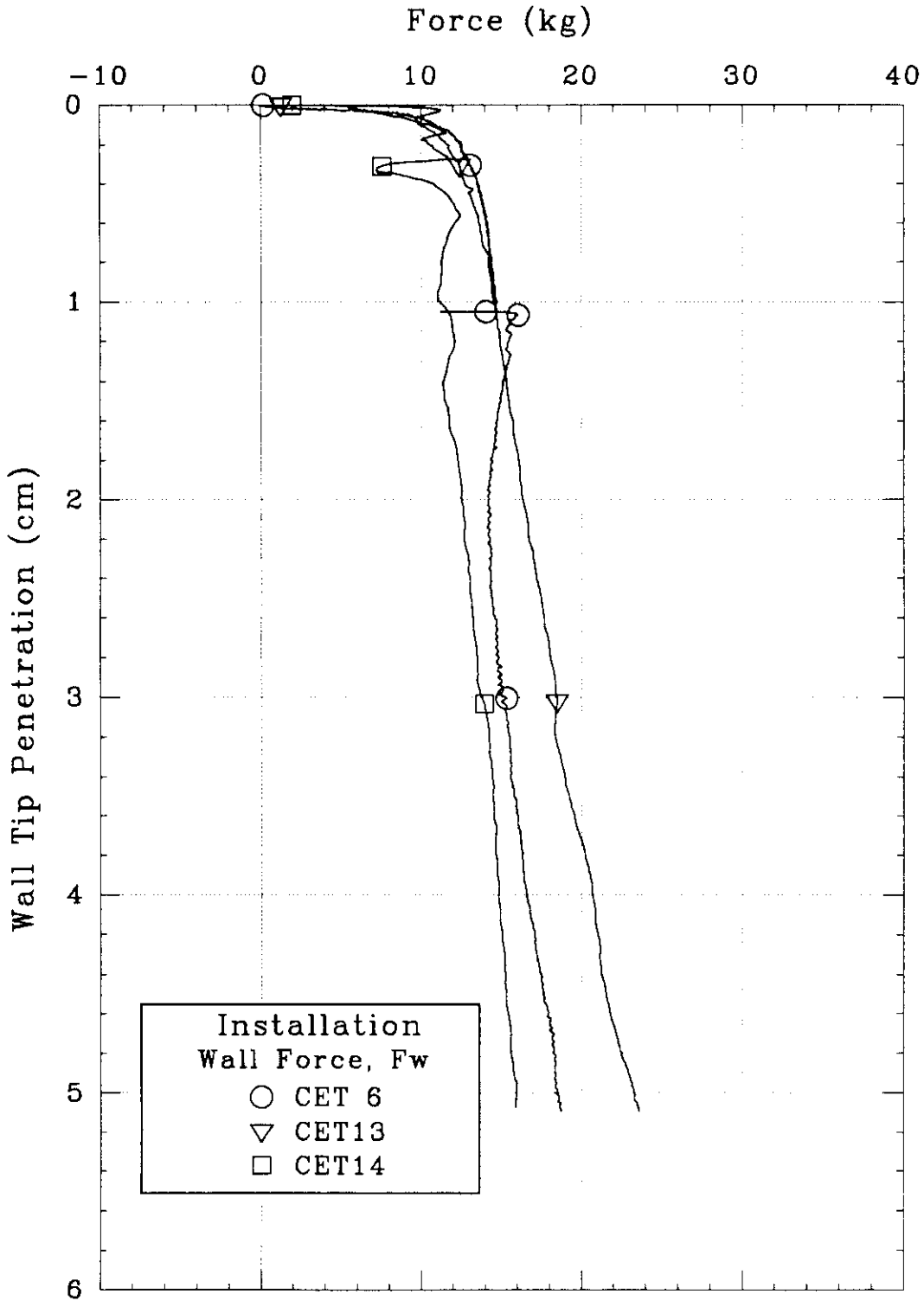

Figure 5.20 Measured Wall Force Component During Installation for CET6,13,14

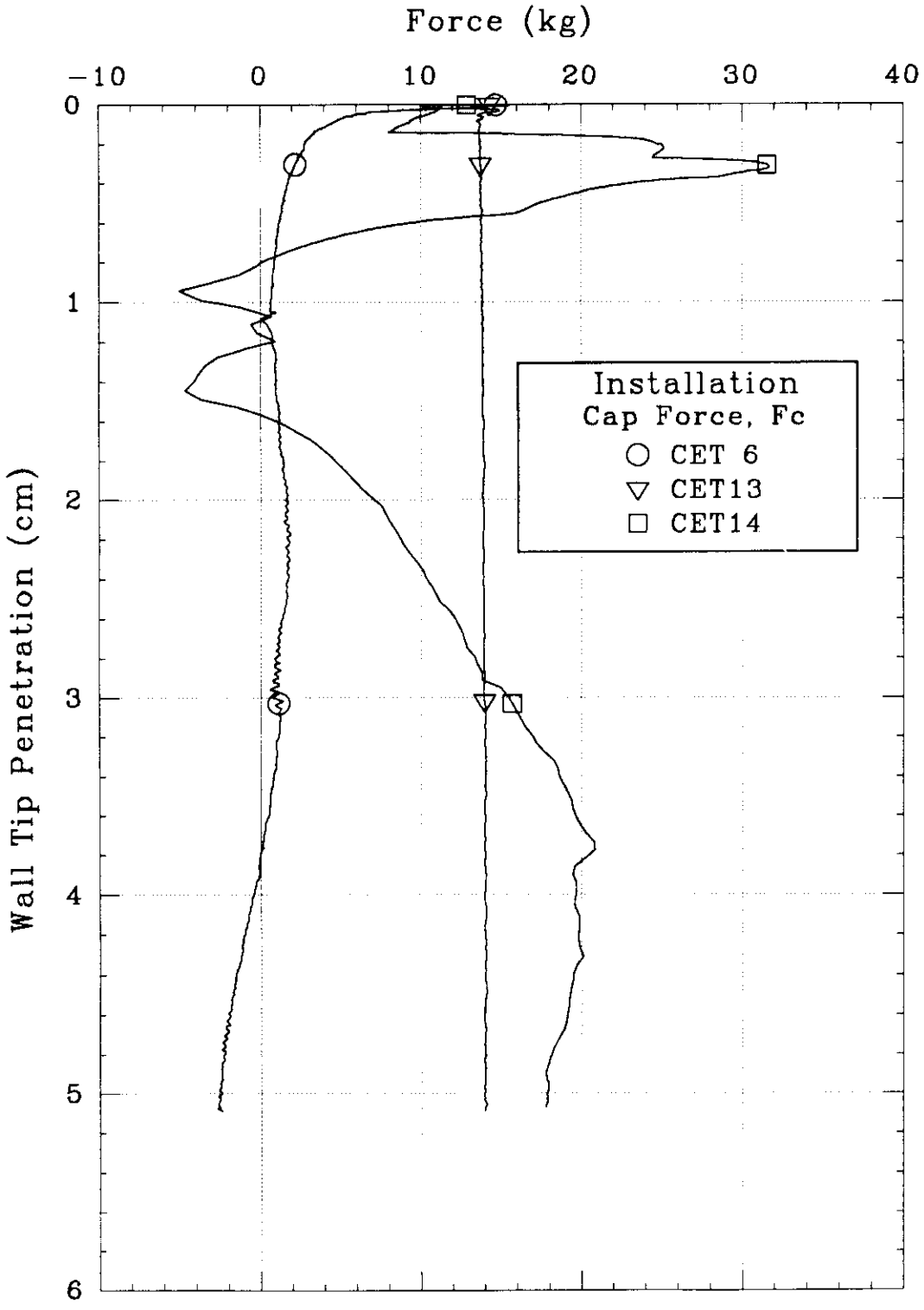

Figure 5.21 Measured Cap Force Component During Installation for CET6,13,14

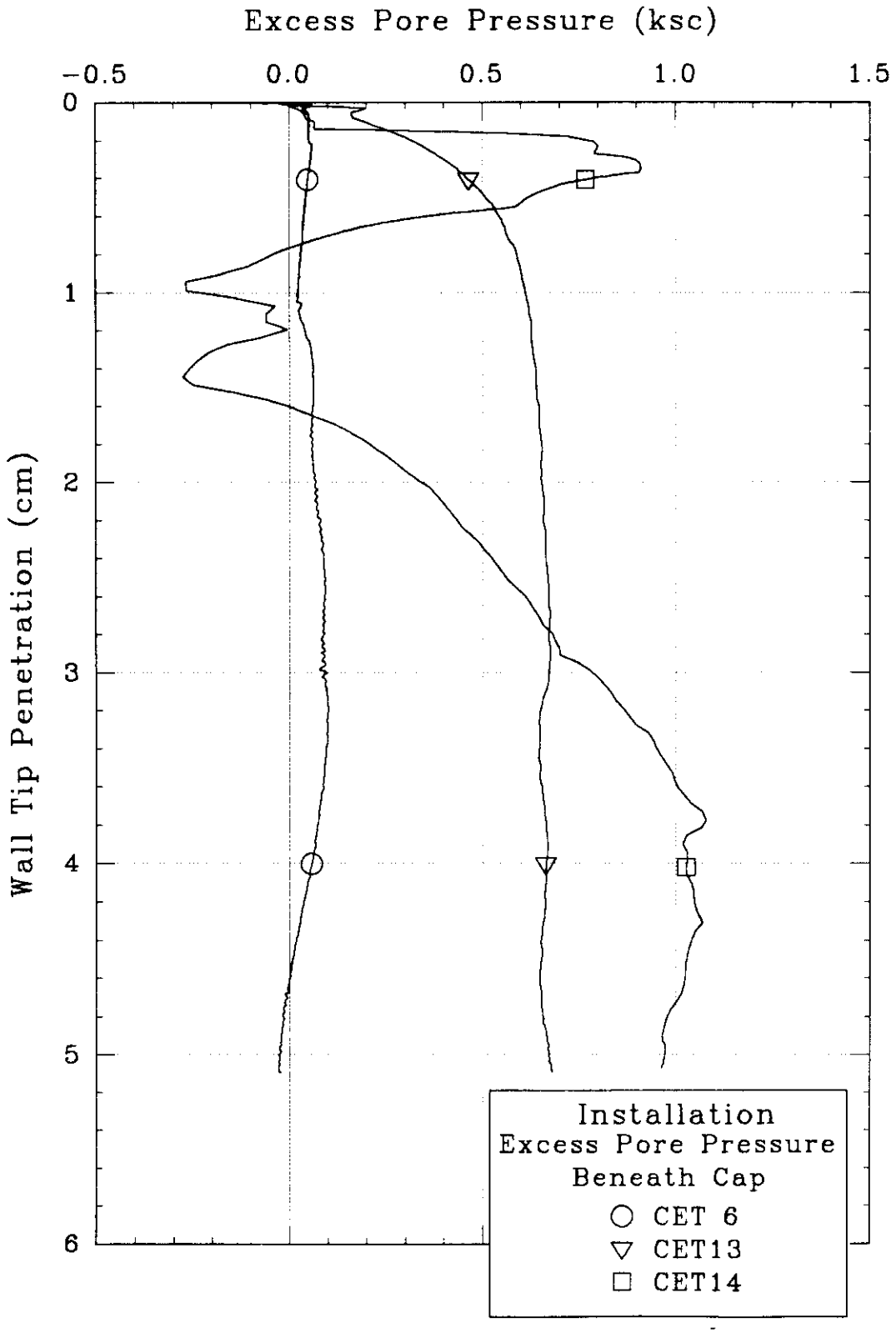

Figure 5.22 Measured Excess Pore Pressure Beneath Cap During Installation for CET6,13,14

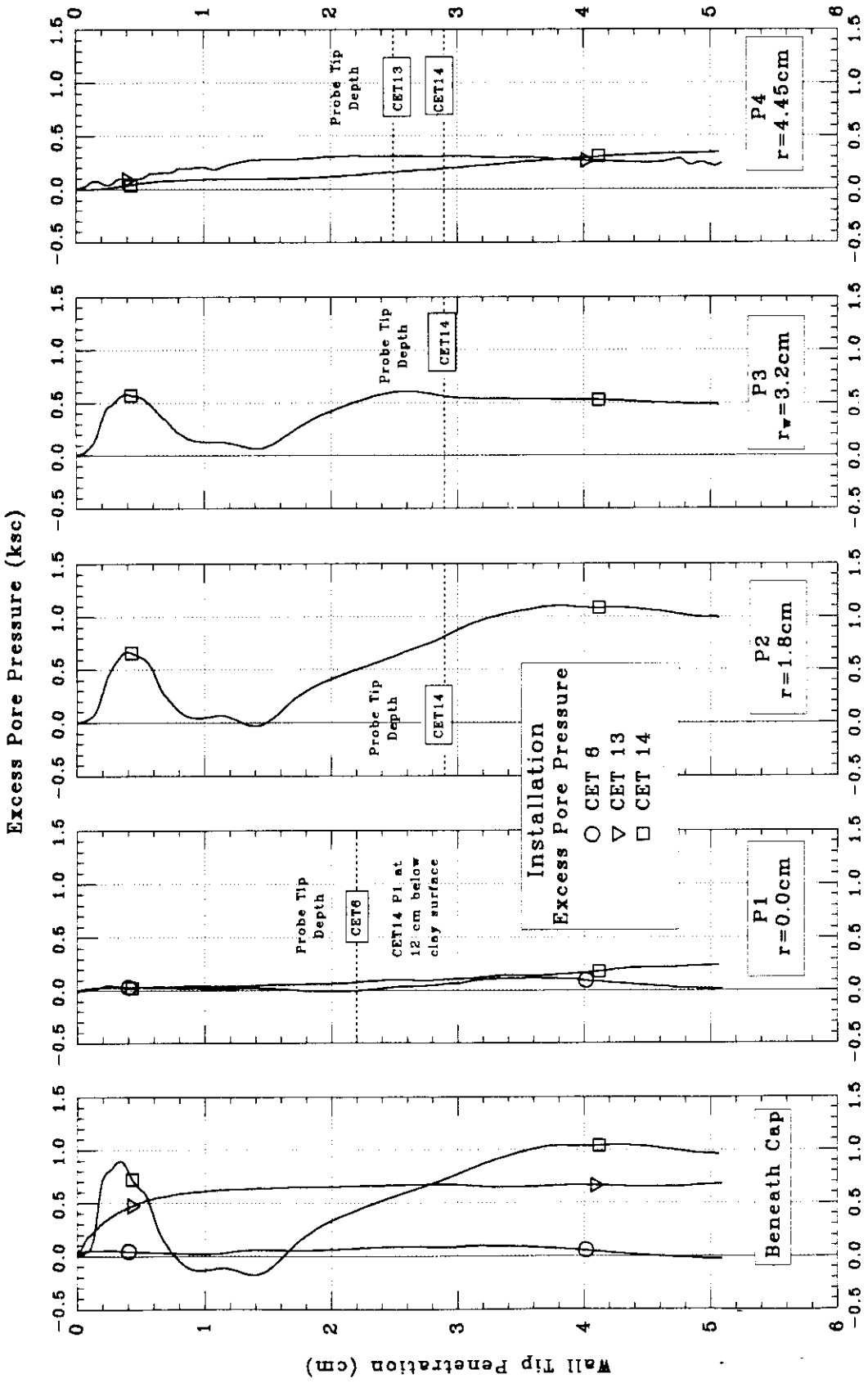

Figure 5.23 Measured Excess Pore Pressure Beneath Cap and by P1-P4 During Installation for CET6,13,14

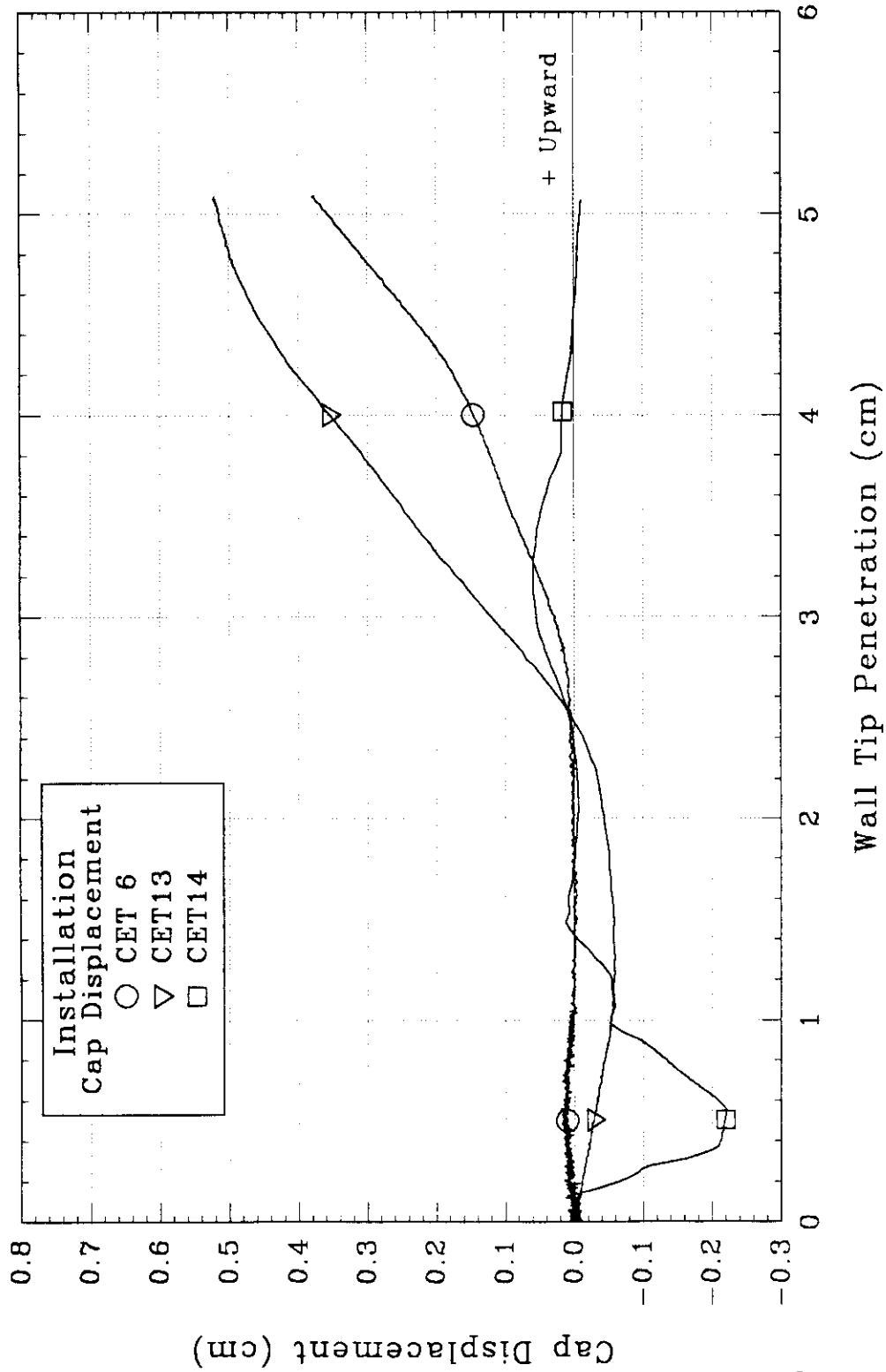

Figure 5.24 Measured Cap Displacement During Installation for CET6,13,14

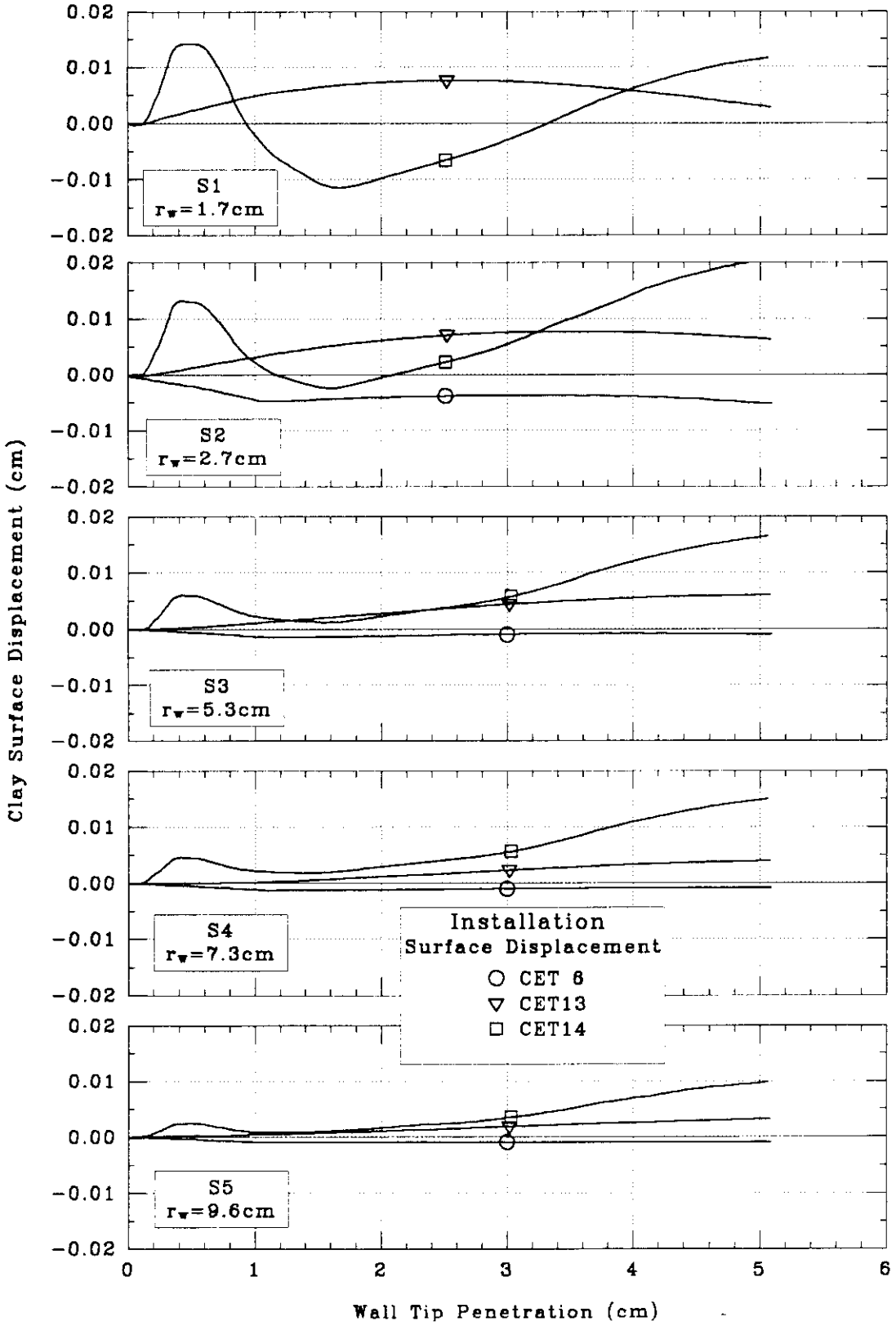

Figure 5.25 Measured Soil Surface Displacement by S1-S5 During Installation for CET6,13,14

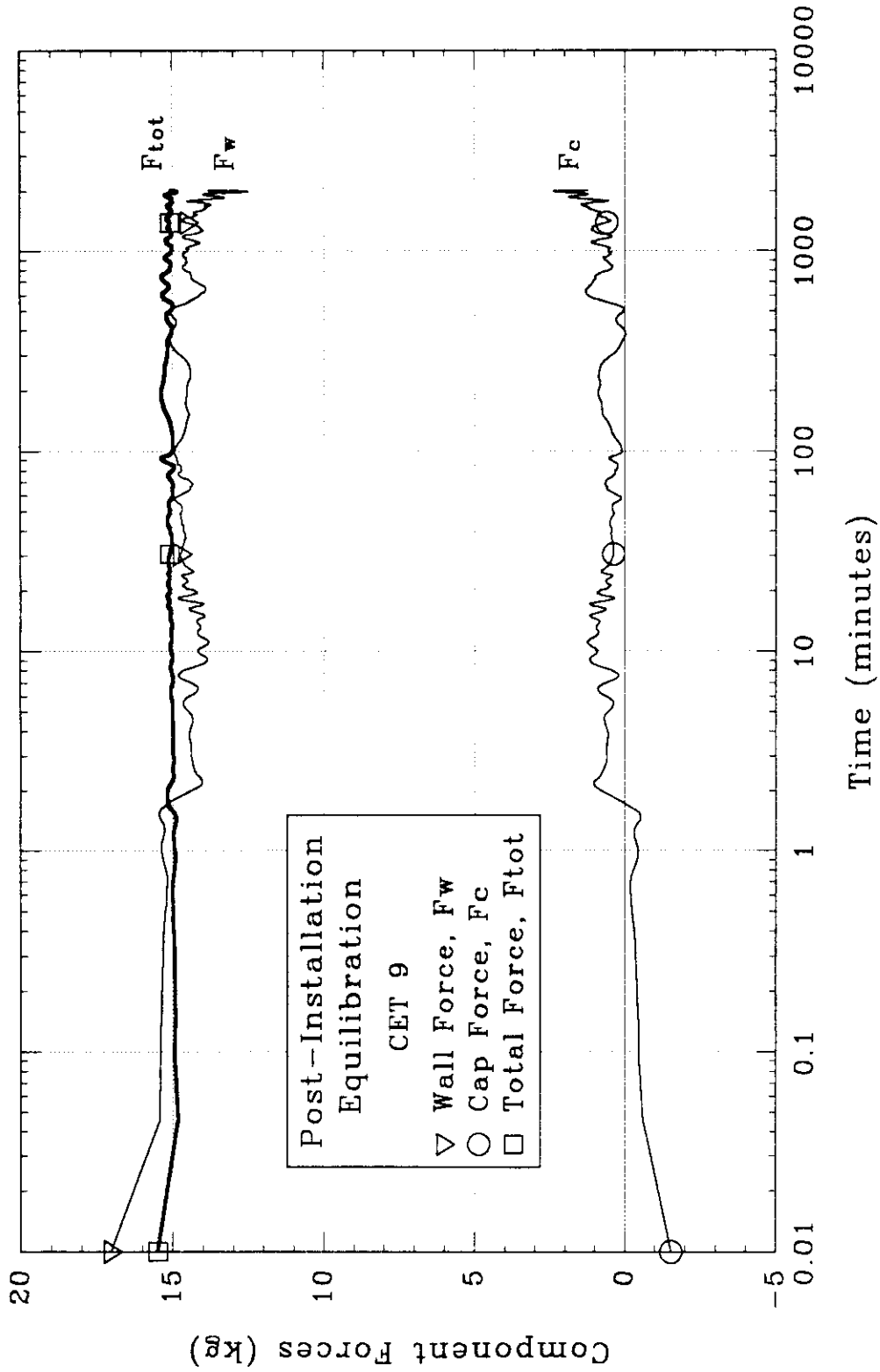

Figure 5.26 Measured Forces on Caisson Components During Post-Installation Equilibration in CET9

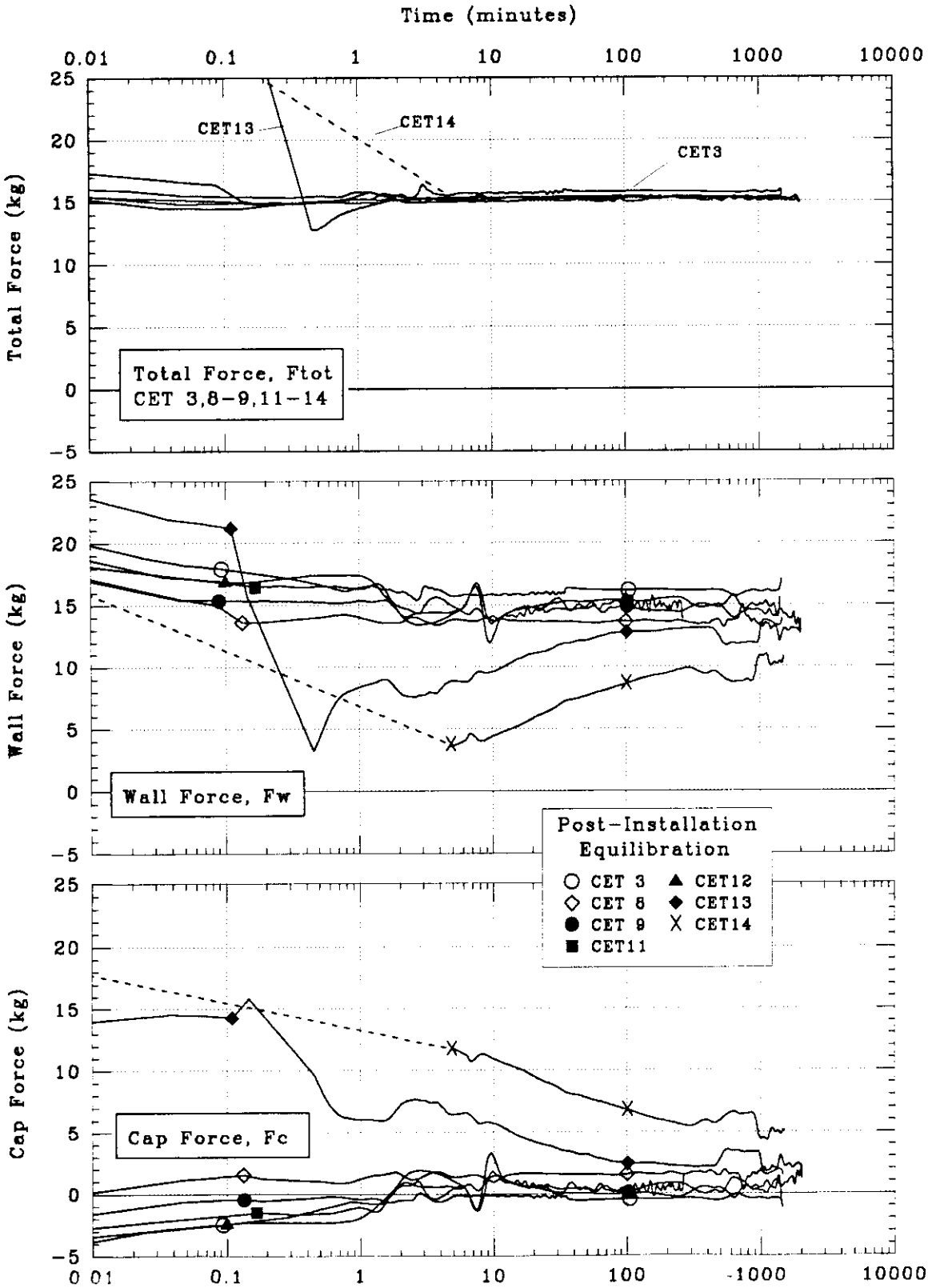

Figure 5.27 Measured Total, Wall, and Cap Force on Caisson During Post-Installation Equilibration for CET3,8-9,11-14

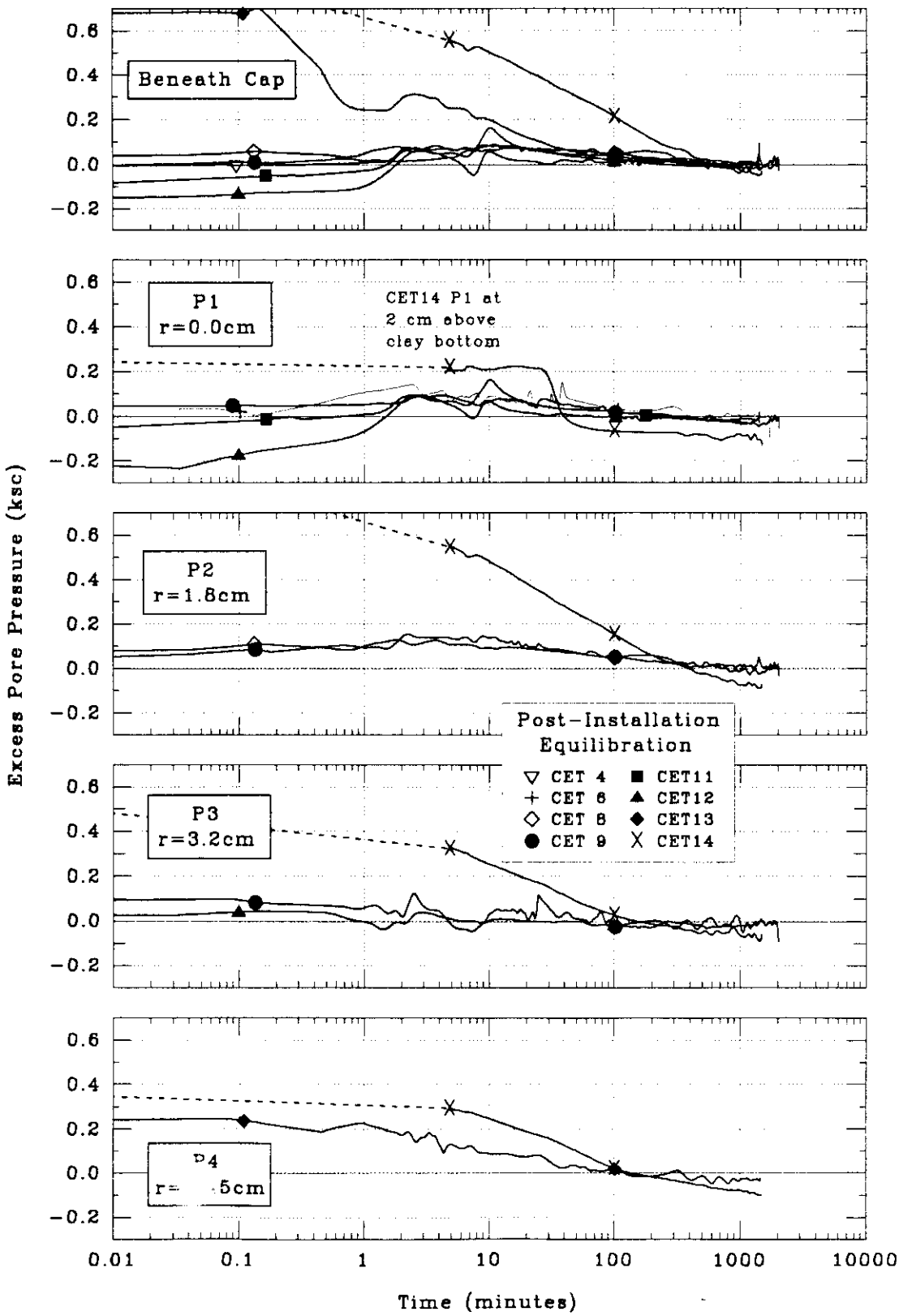

Figure 5.28 Measured Excess Pore Pressure Beneath Cap and by P1-P4 During Post-Installation Equilibration for CET4,8-9,11-14

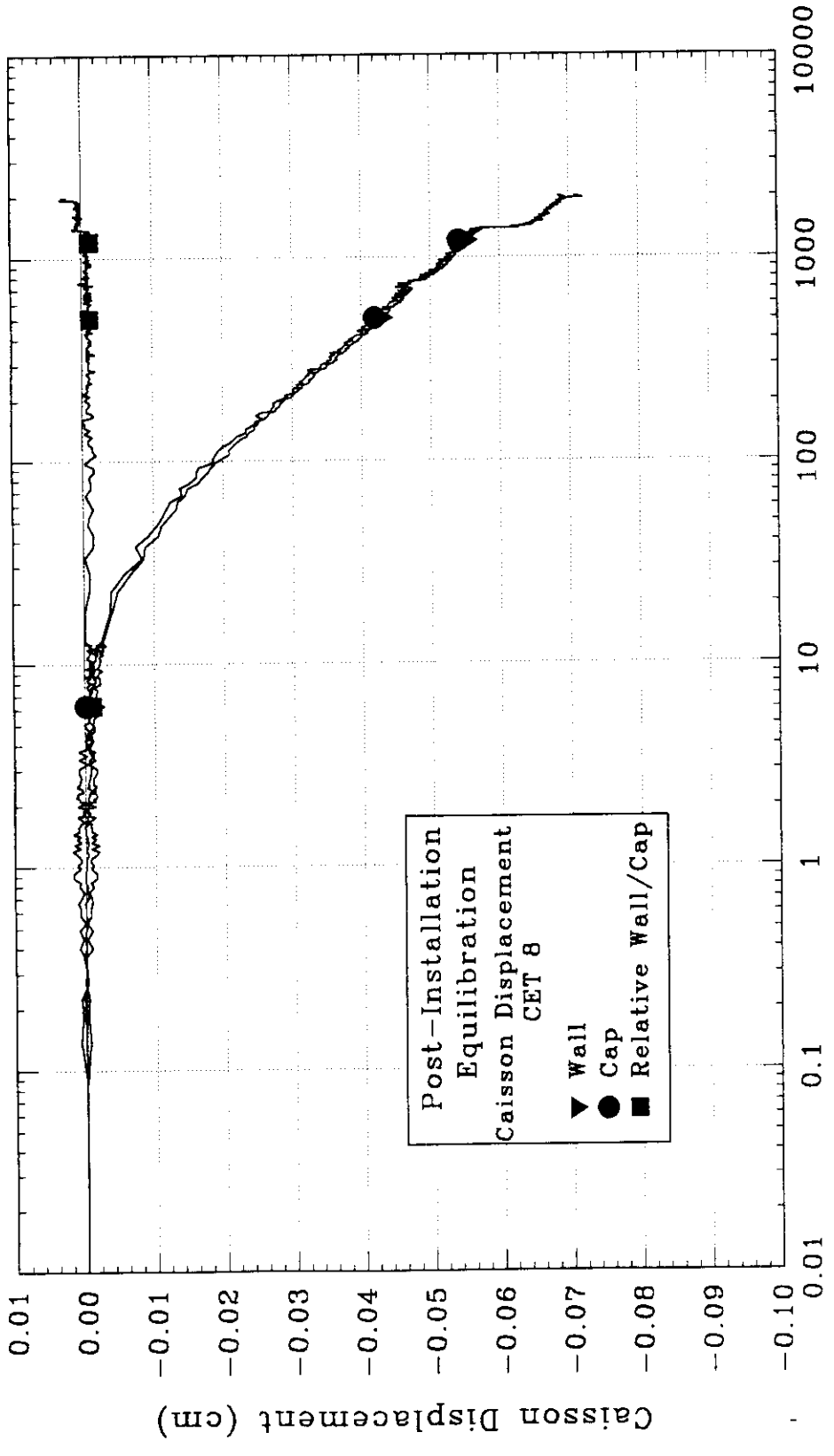

Figure 5.29 Measured Caisson Settlement During Post-Installation Equilibration for CET8

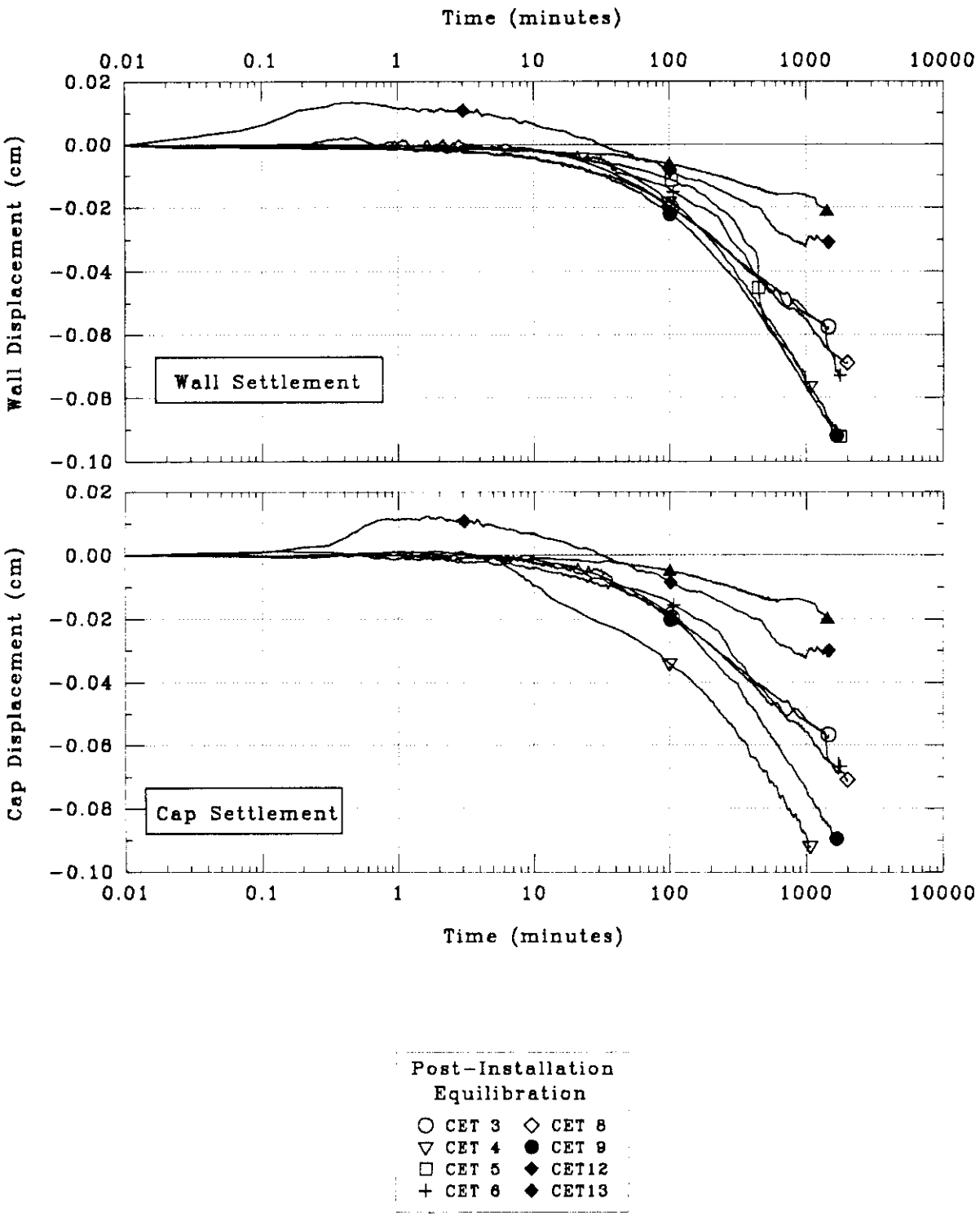

Figure 5.30 Measured Wall and Cap Settlement During Post-Installation Equilibration for CET3-6,8-9,12-13

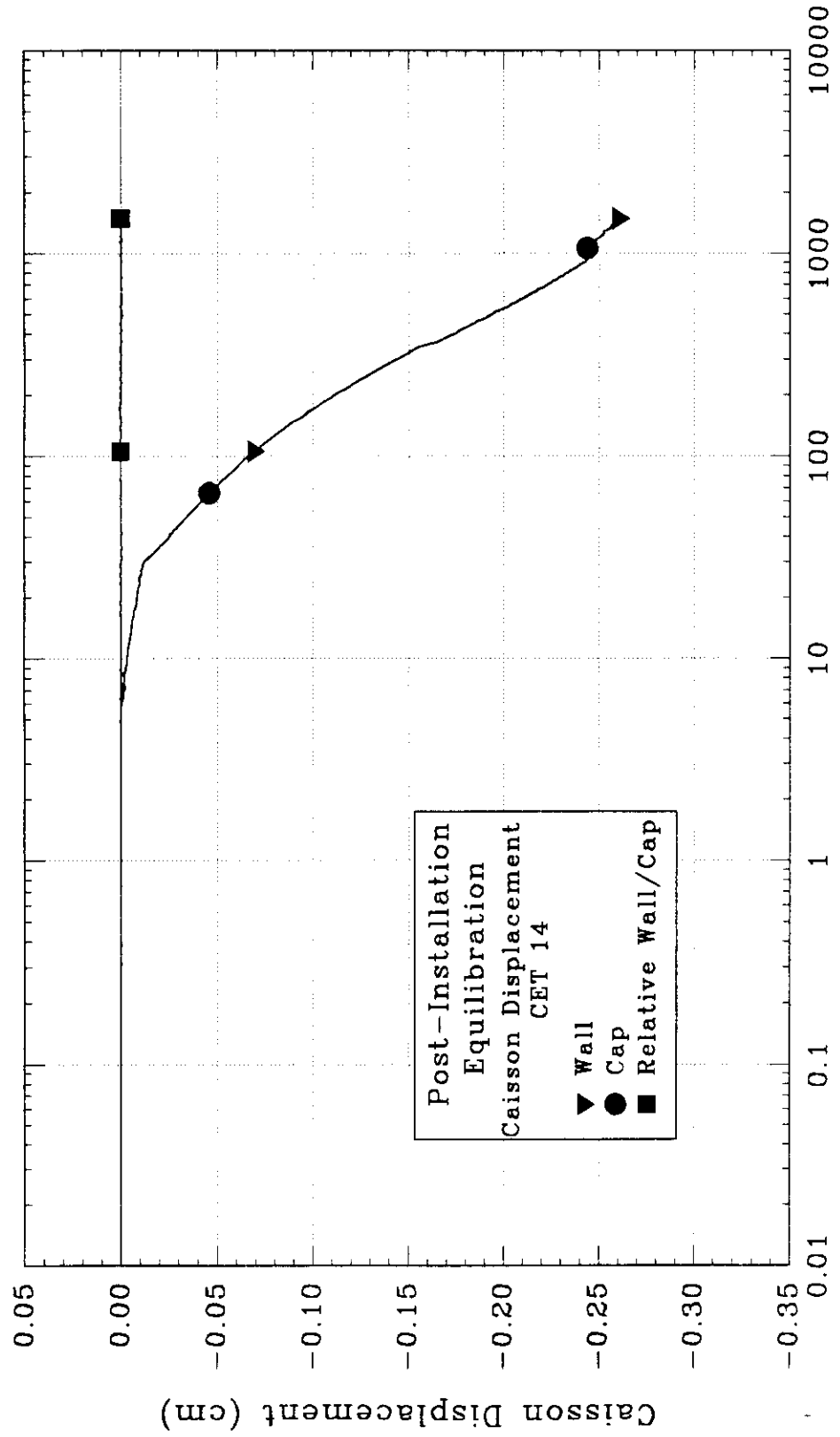

Figure 5.31 Measured Caisson Settlement During Post-Installation Equilibration for CET14

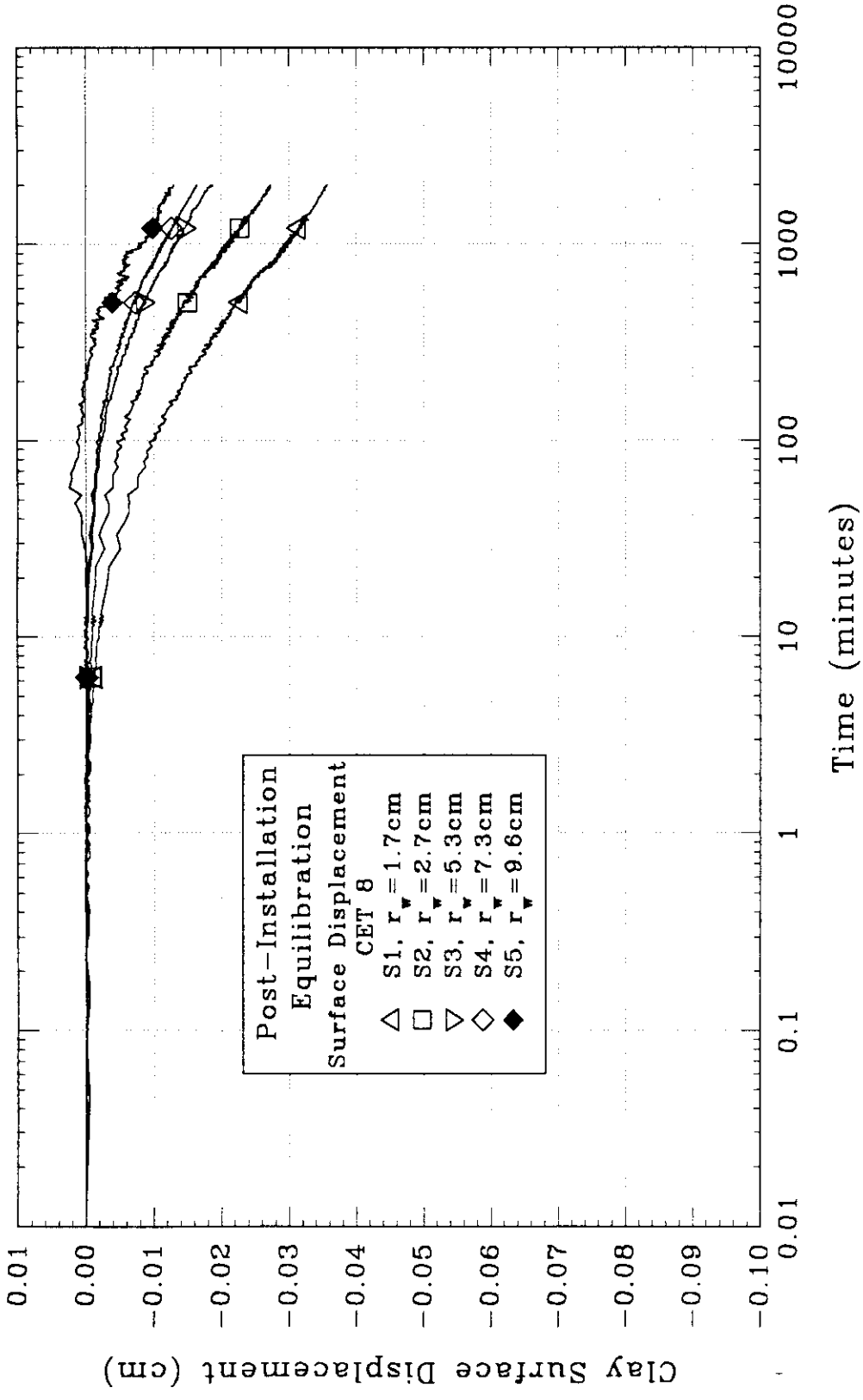

Figure 5.32 Measured Soil Surface Displacement at Five Radial Locations During Post-Installation Equilibration for CET8

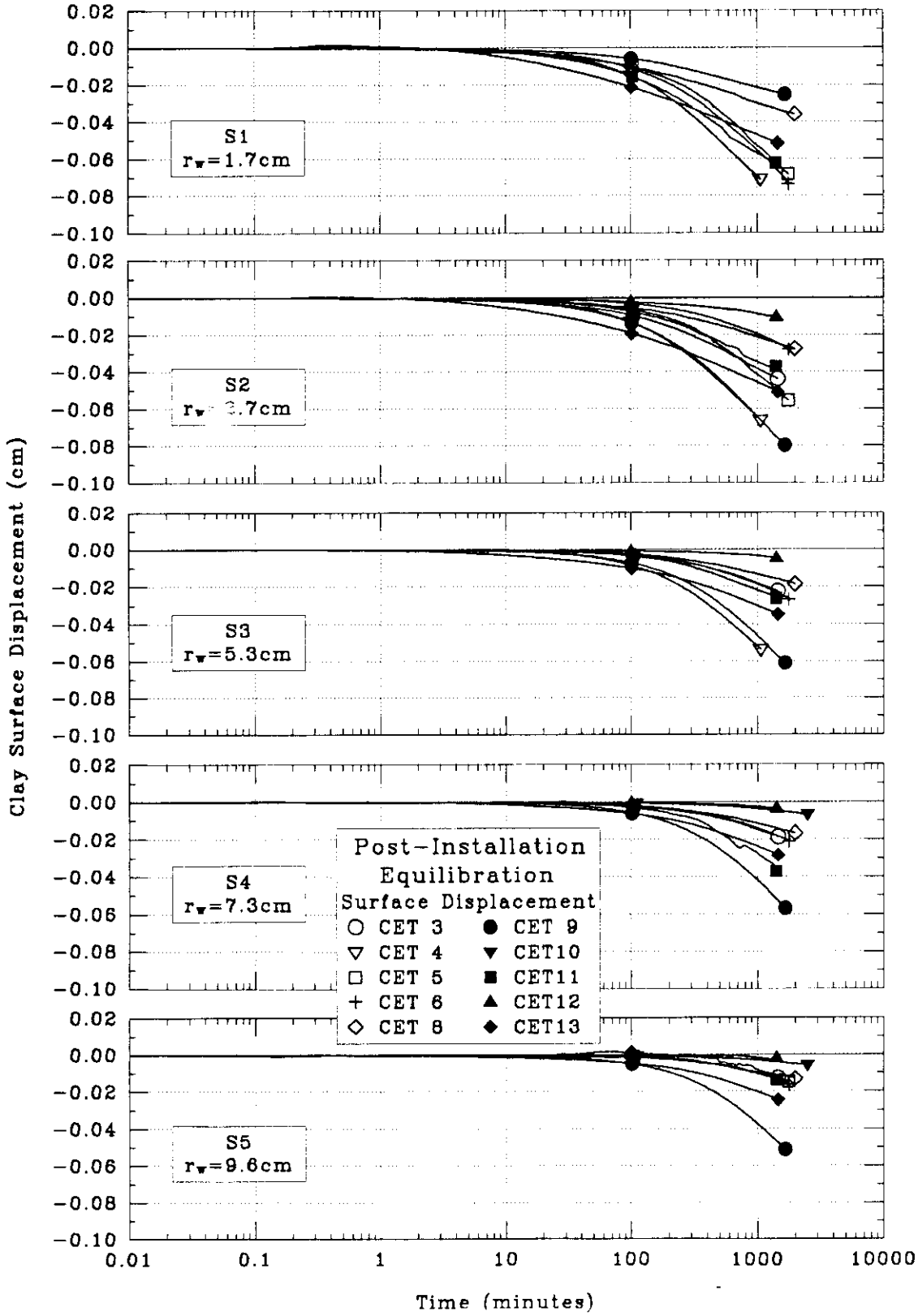

Figure 5.33 Measured Soil Surface Displacement by S1-S5 During Post-Installation Equilibration for CET3-6,8-9,11-13

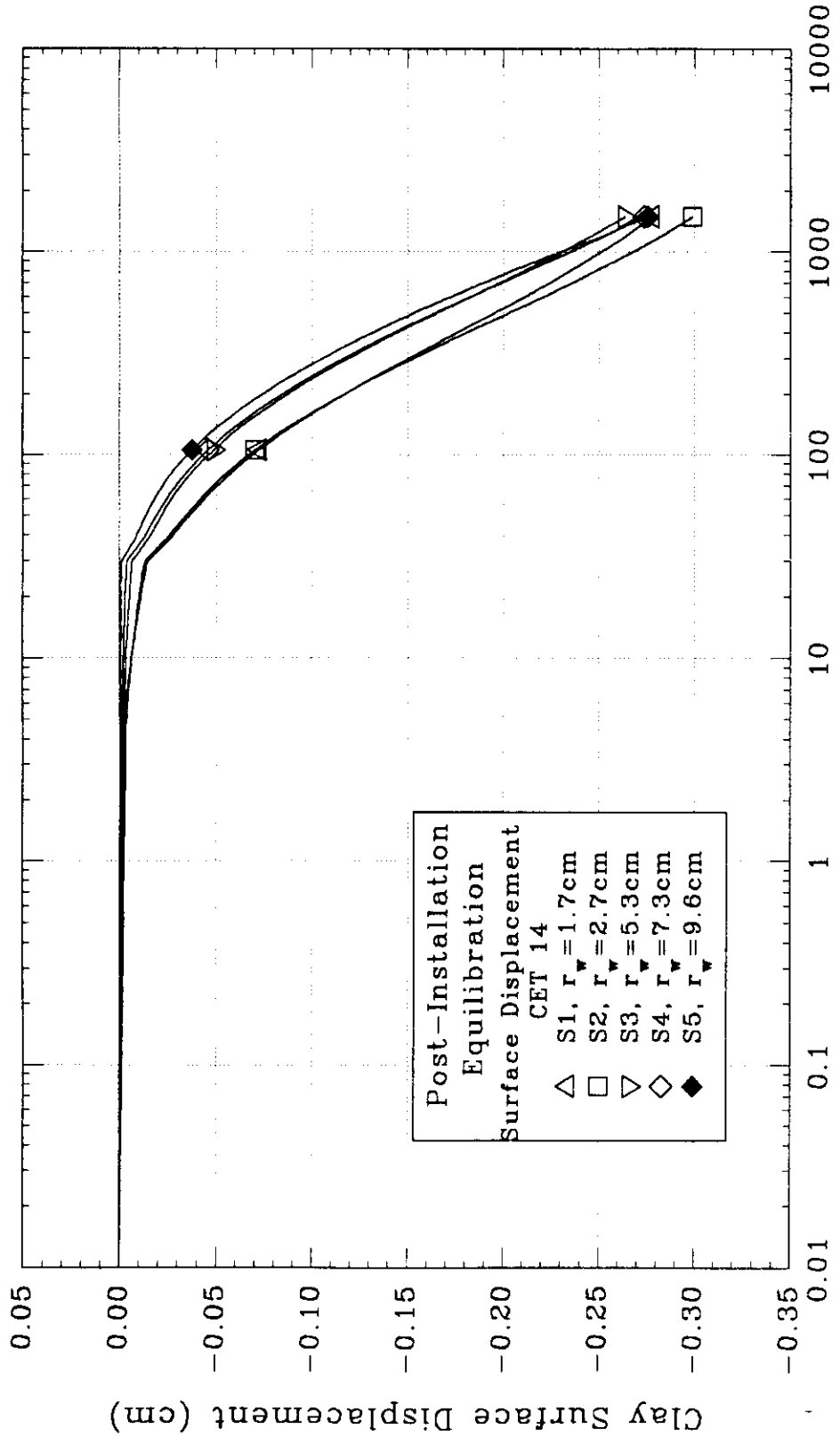

Figure 5.34 Measured Soil Surface Displacement at Five Radial Locations During Post-Installation Equilibration for CET14

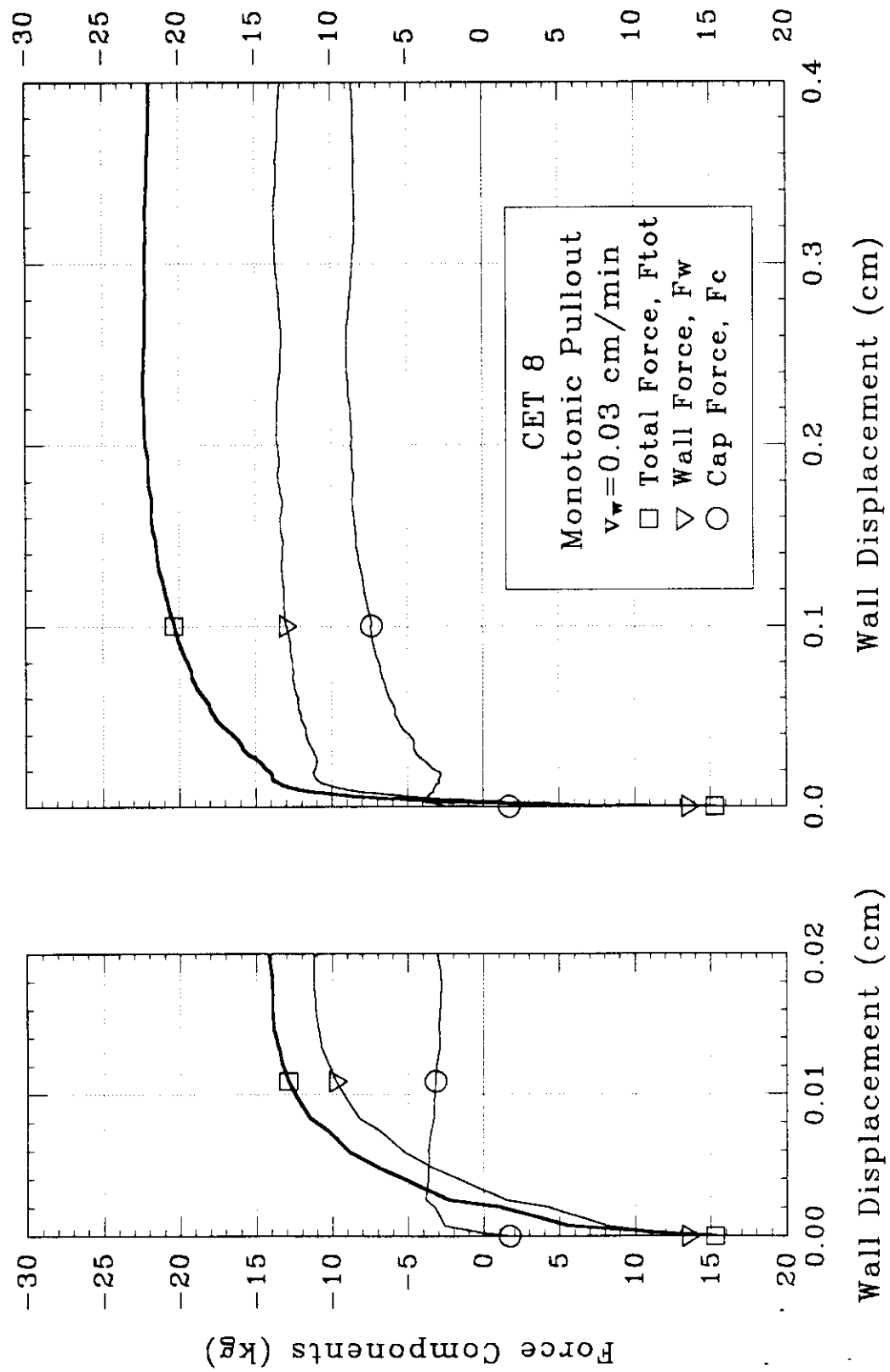

Figure 5.35 Measured Force Components During Monotonic Pullout 1 for CET8

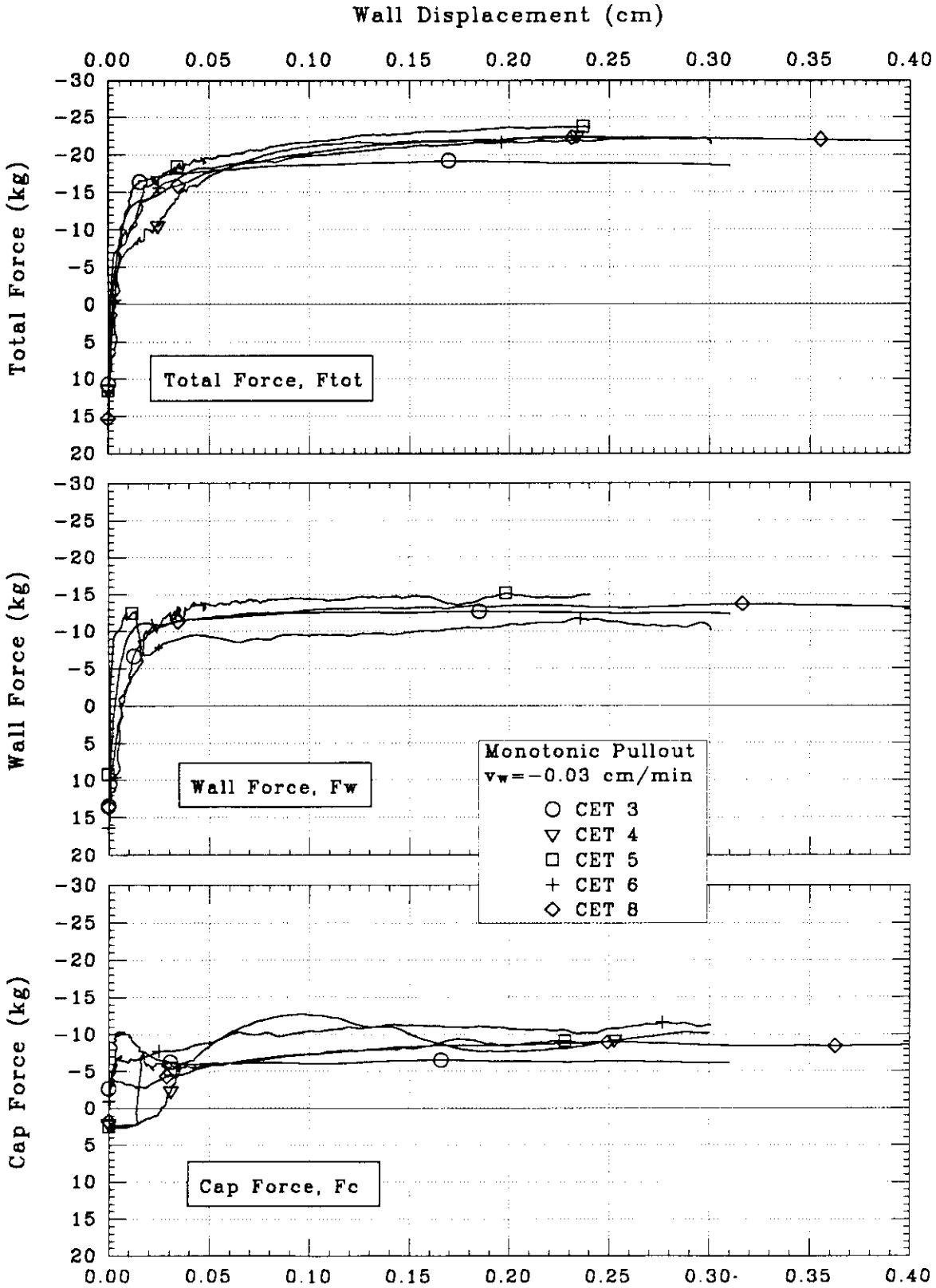

Figure 5.36 Measured Total, Wall, and Cap Force on Caisson During Monotonic Pullout 1 for CET3-6,8

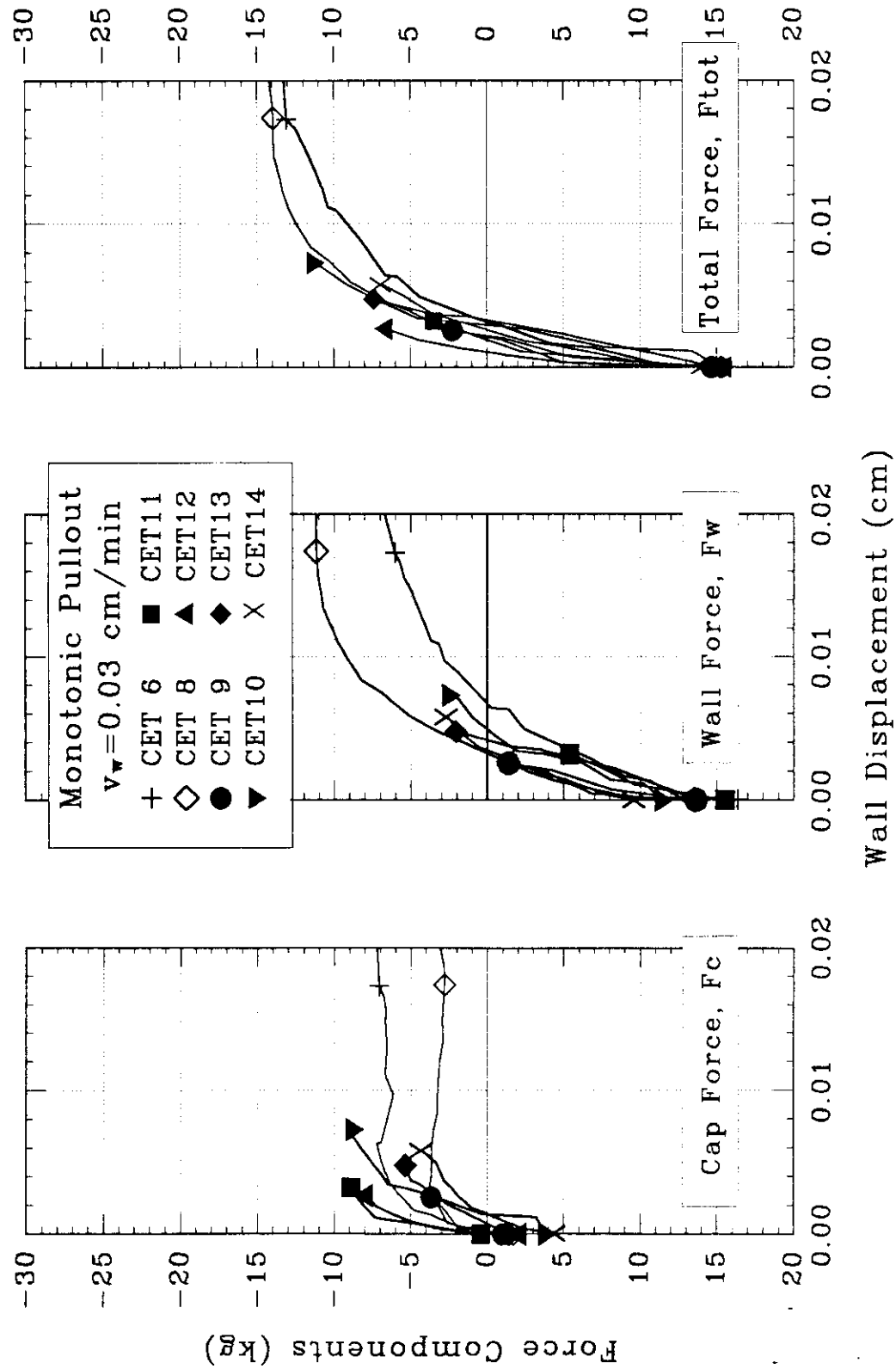

Figure 5.37 Measured Force Components During Early (0.0 to 0.02 cm) Monotonic Pullout 1 for CET6,8-14

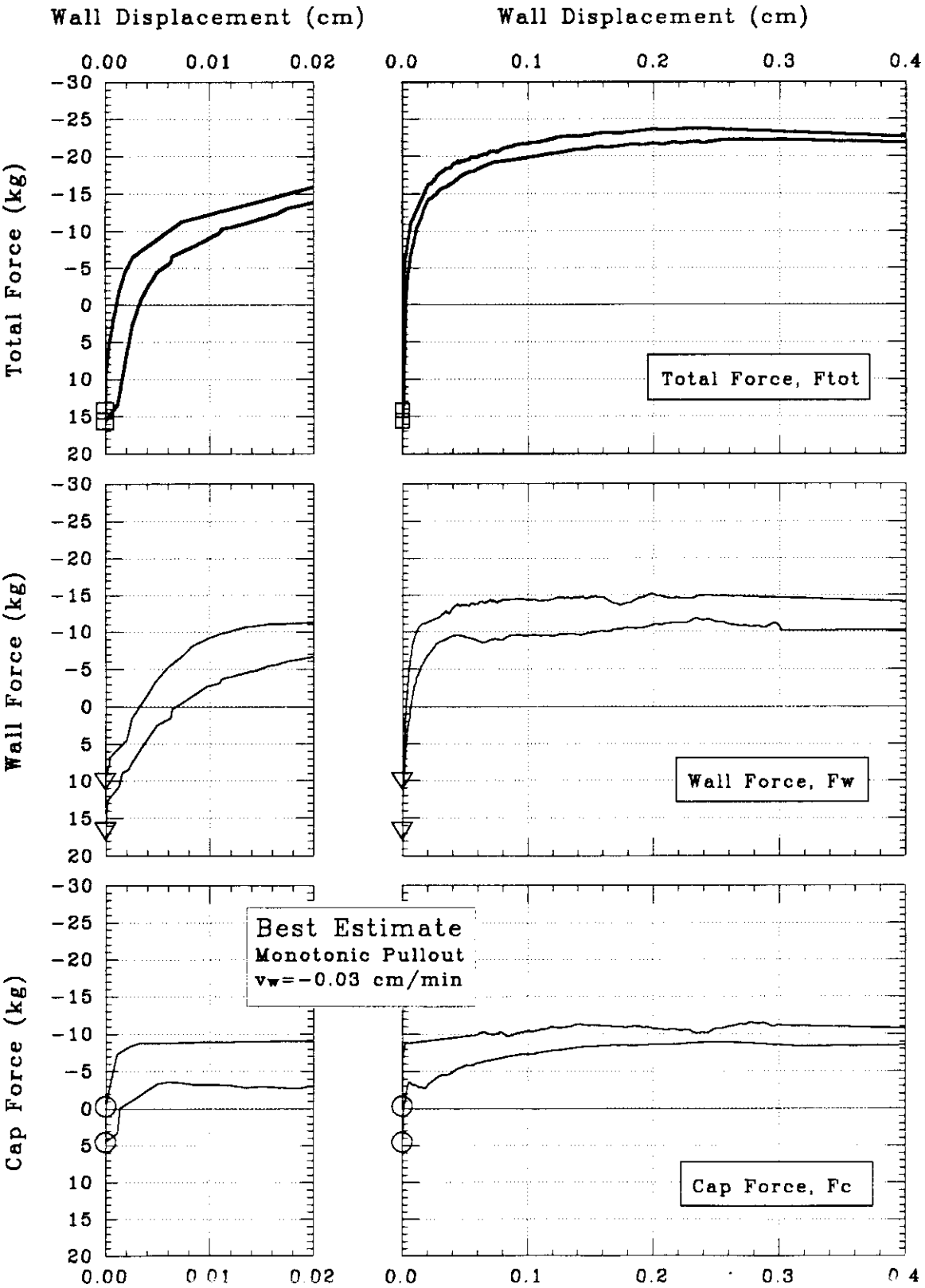

Figure 5.38 Best Estimate of Total, Wall, and Cap Force versus Wall Displacement During Monotonic Pullout 1

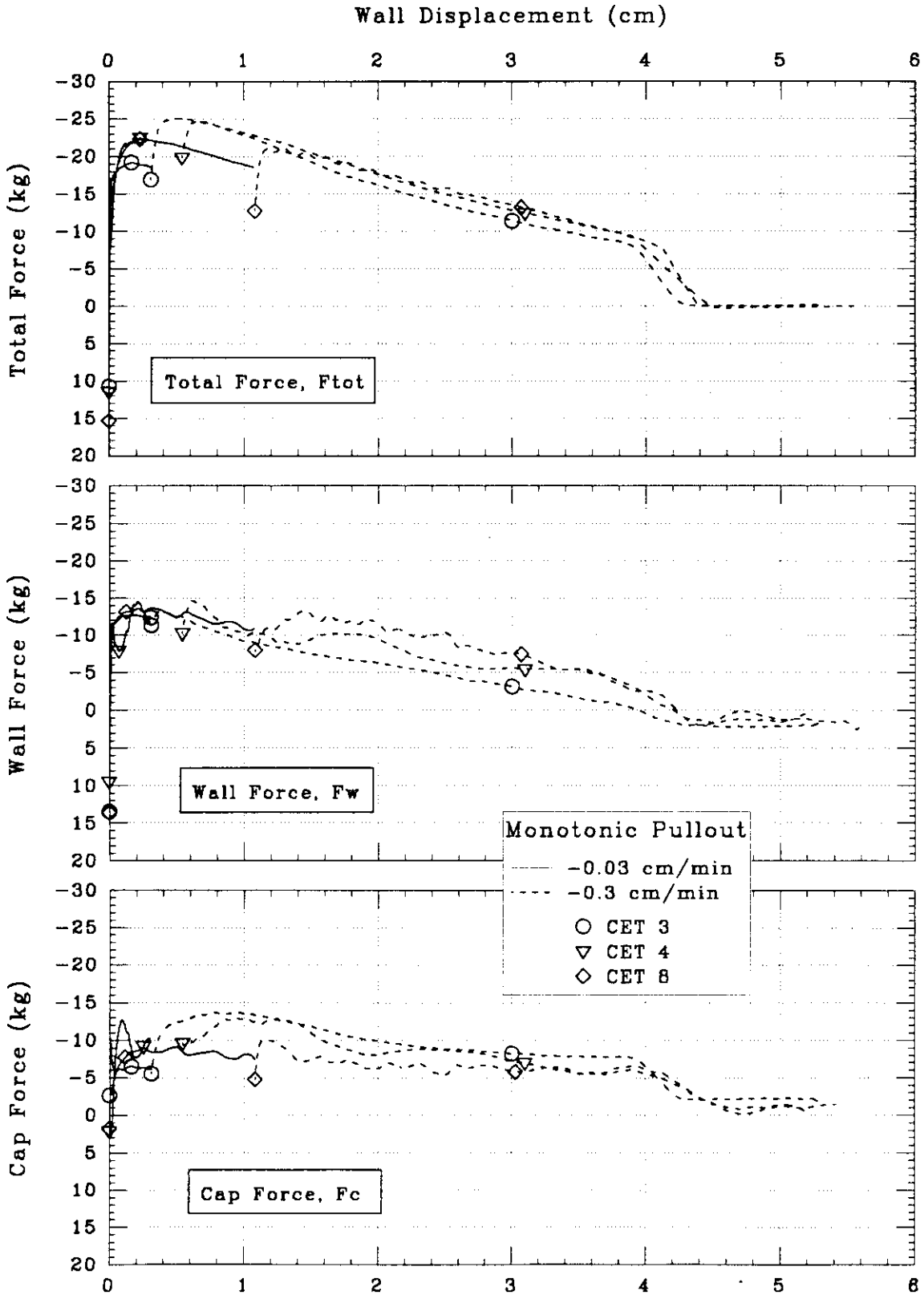

Figure 5.39 Measured Total, Wall, and Cap Force on Caisson During Monotonic Pullout 1 at Two Pullout Rates for CET3-4,8

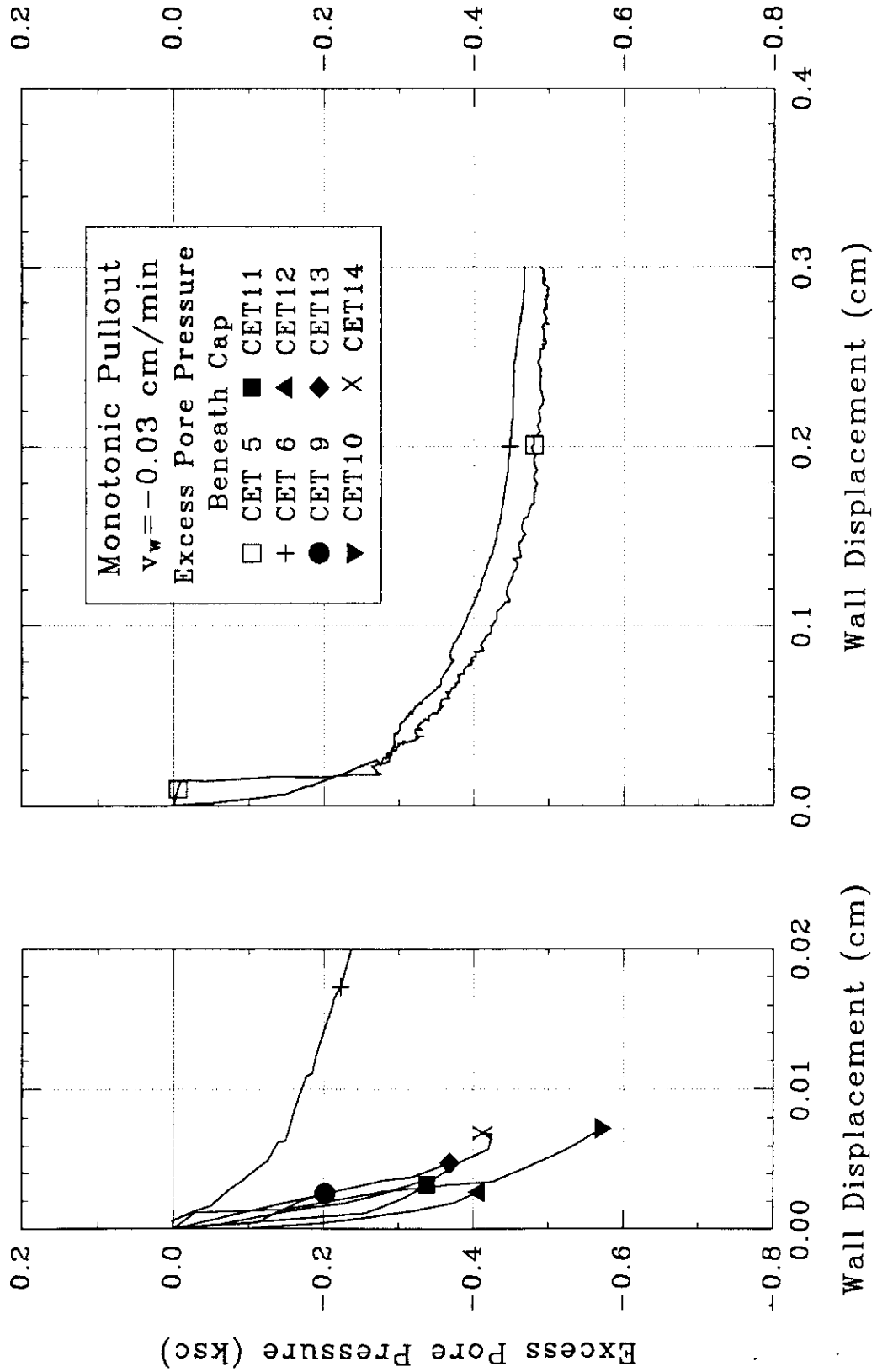

Figure 5.40 Measured Excess Pore Pressure Beneath Cap During Monotonic Pullout 1 for CET5-6,9-14

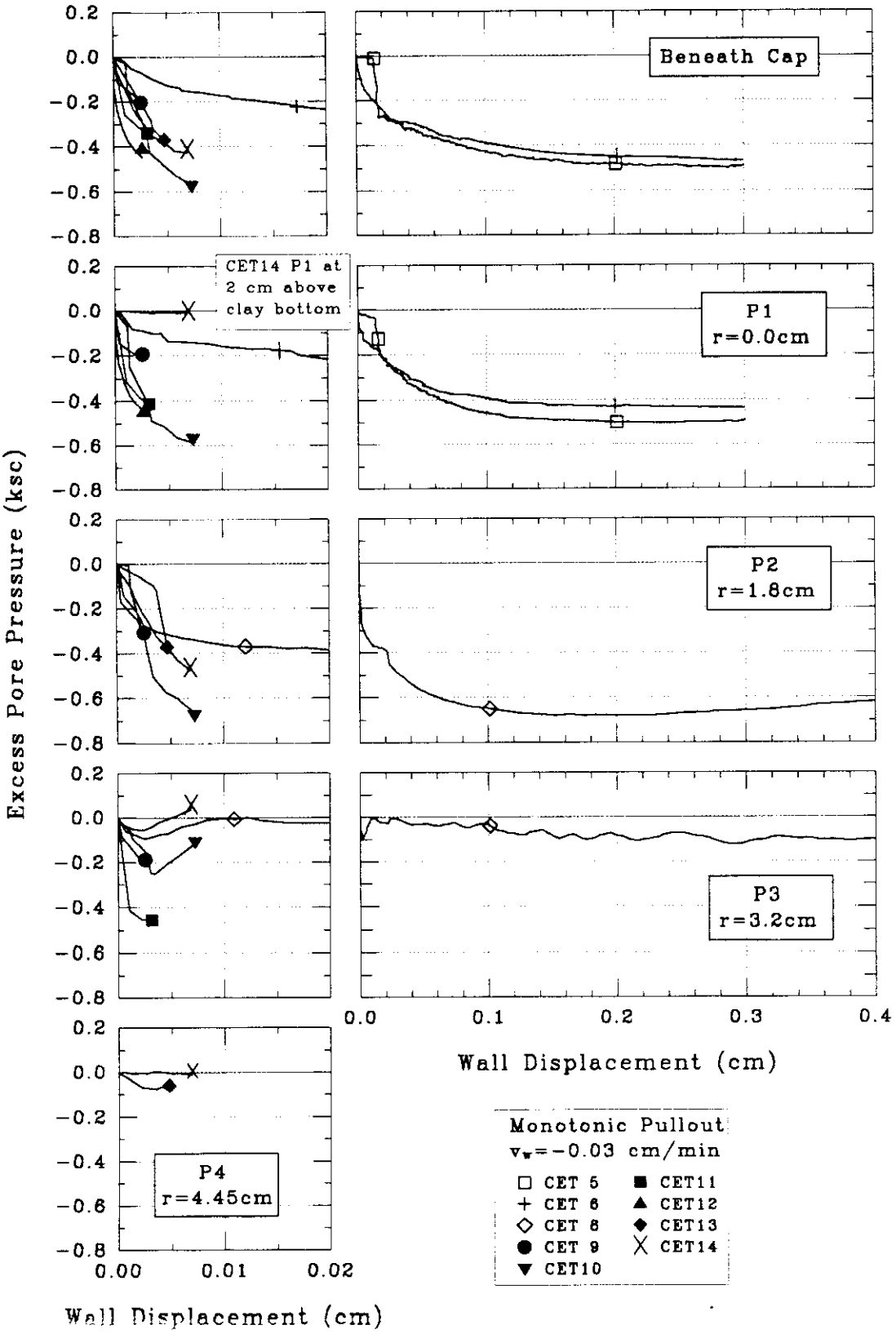

Figure 5.41 Measured Excess Pore Pressure Beneath Cap and by P1-P4 During Monotonic Pullout 1 for CET5-6,9-14

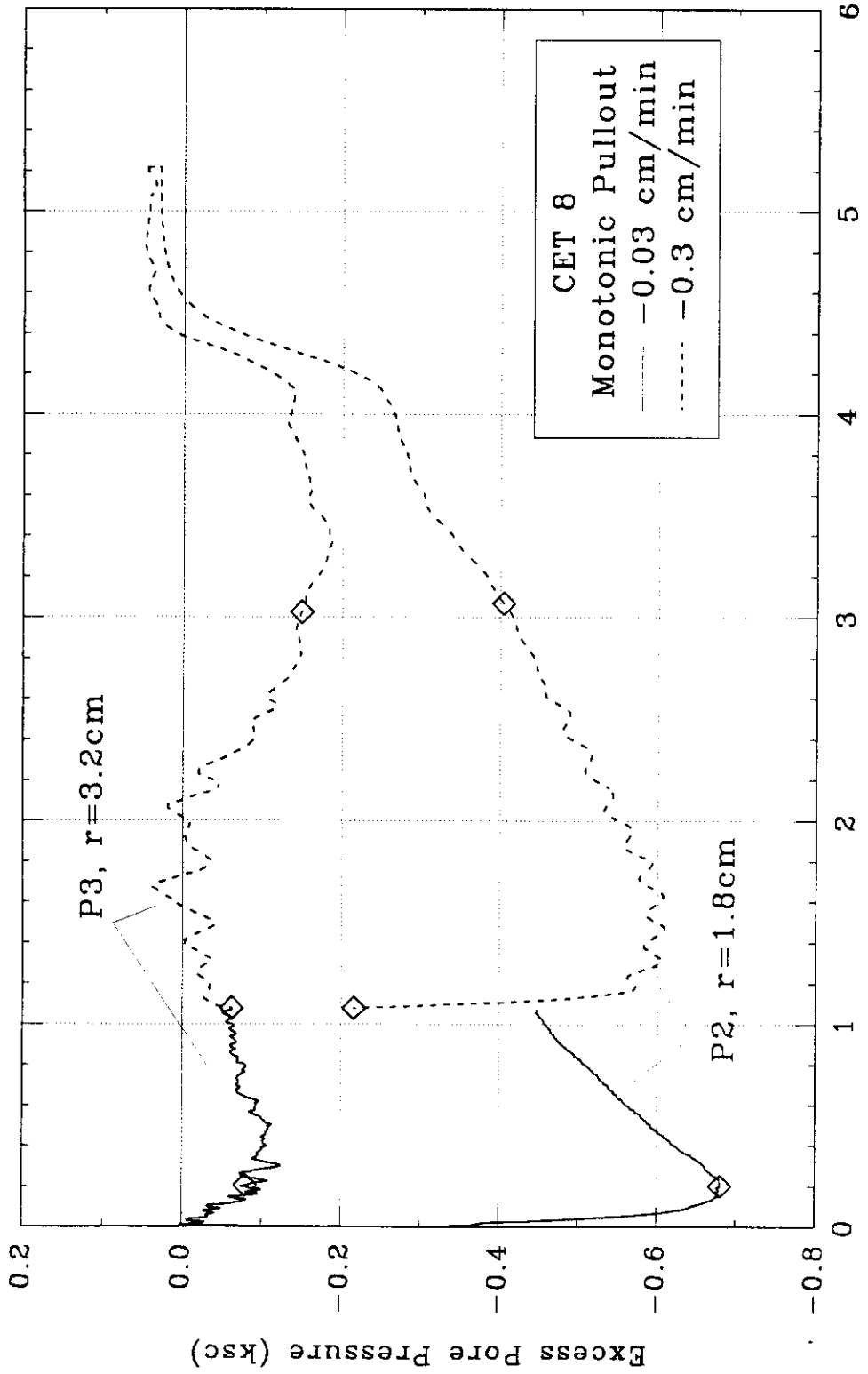

Figure 5.42 Measured Excess Pore Pressure by P2-P3 During Monotonic Pullout I at Two Pullout Rates for CET8

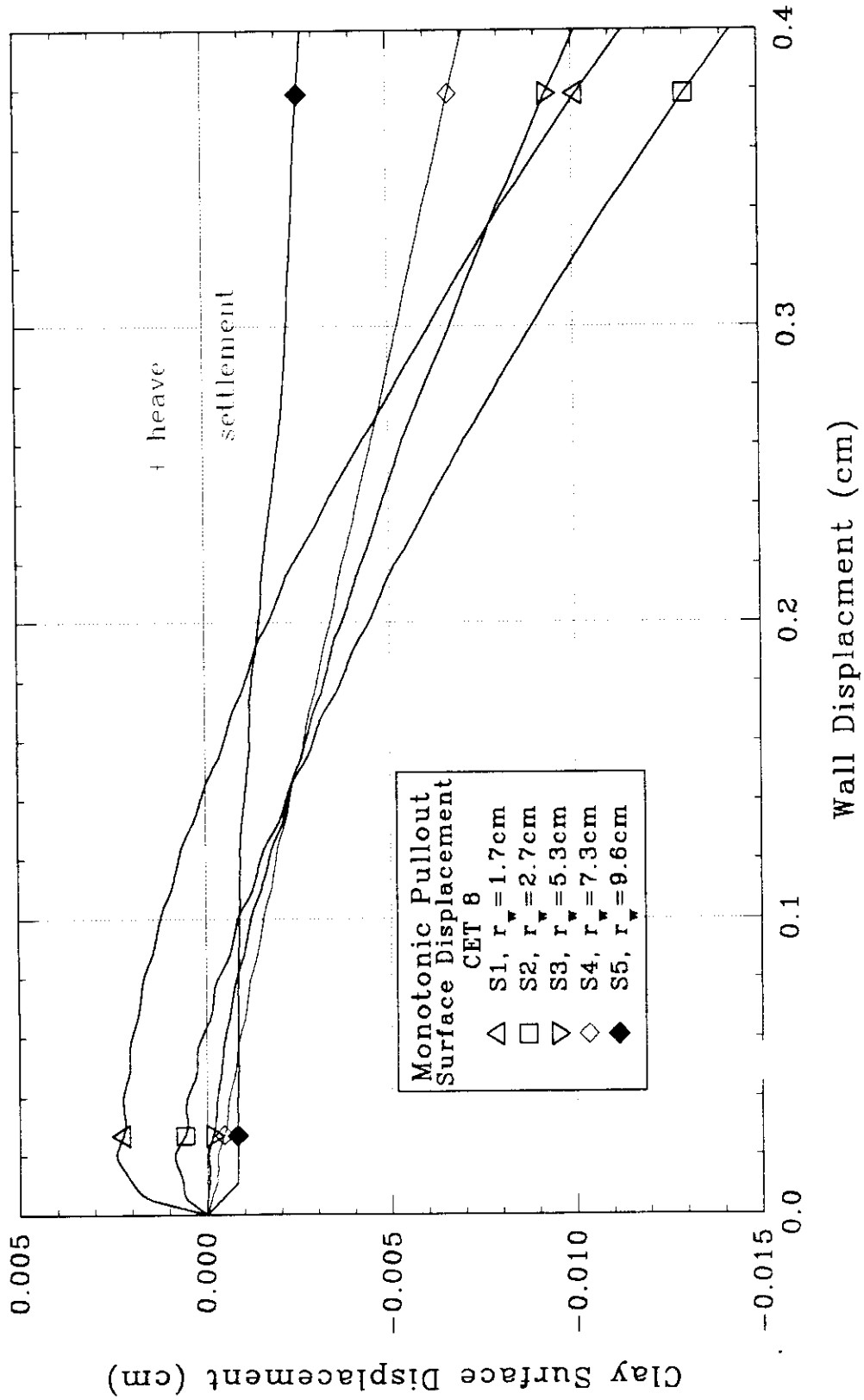

Figure 5.43 Measured Soil Surface Displacement at Five Radial Locations During Monotonic Pullout 1 for CET8

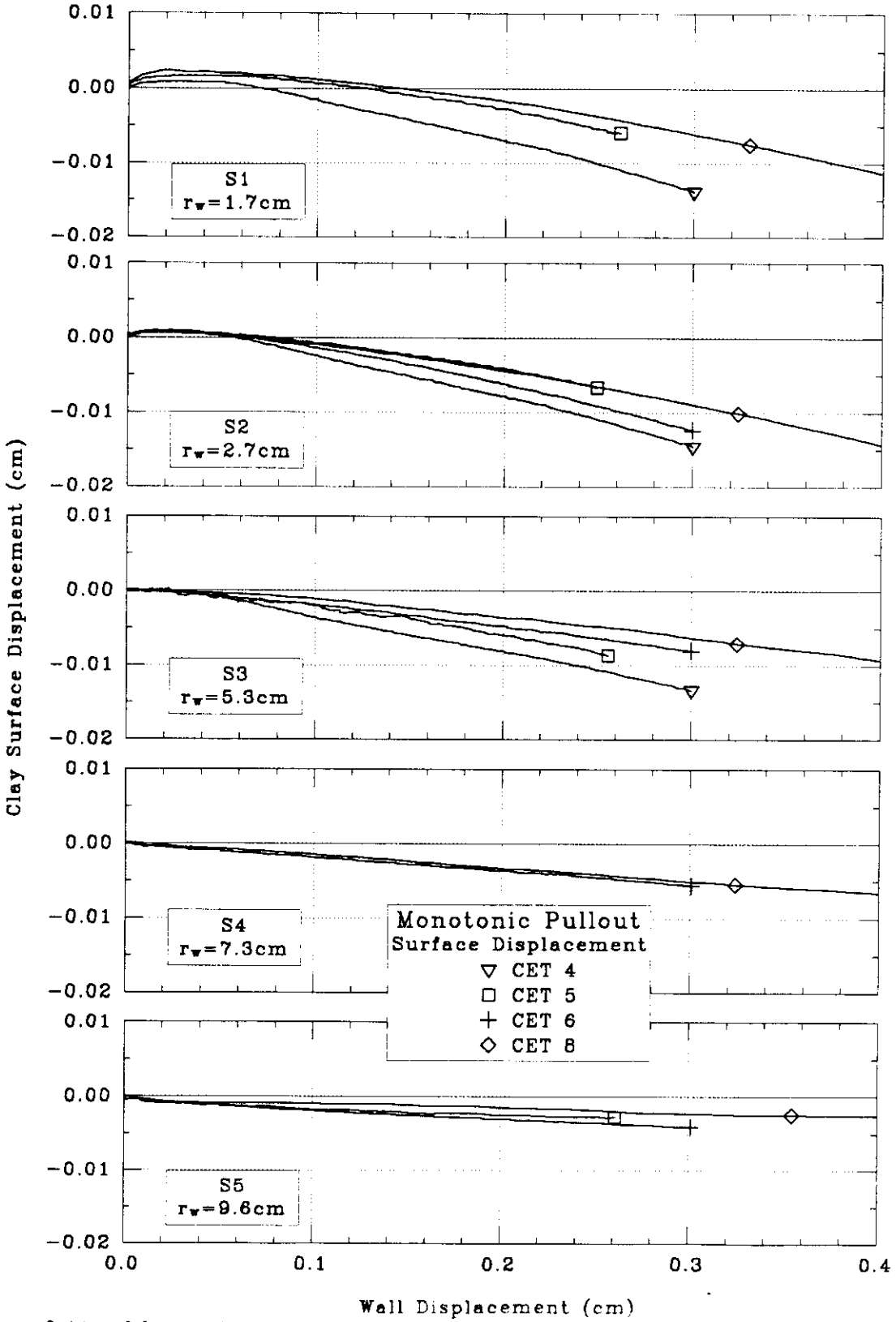

Figure 5.44 Measured Soil Surface Displacement by S1-S5 During Monotonic Pullout 1 for CET4-6,8

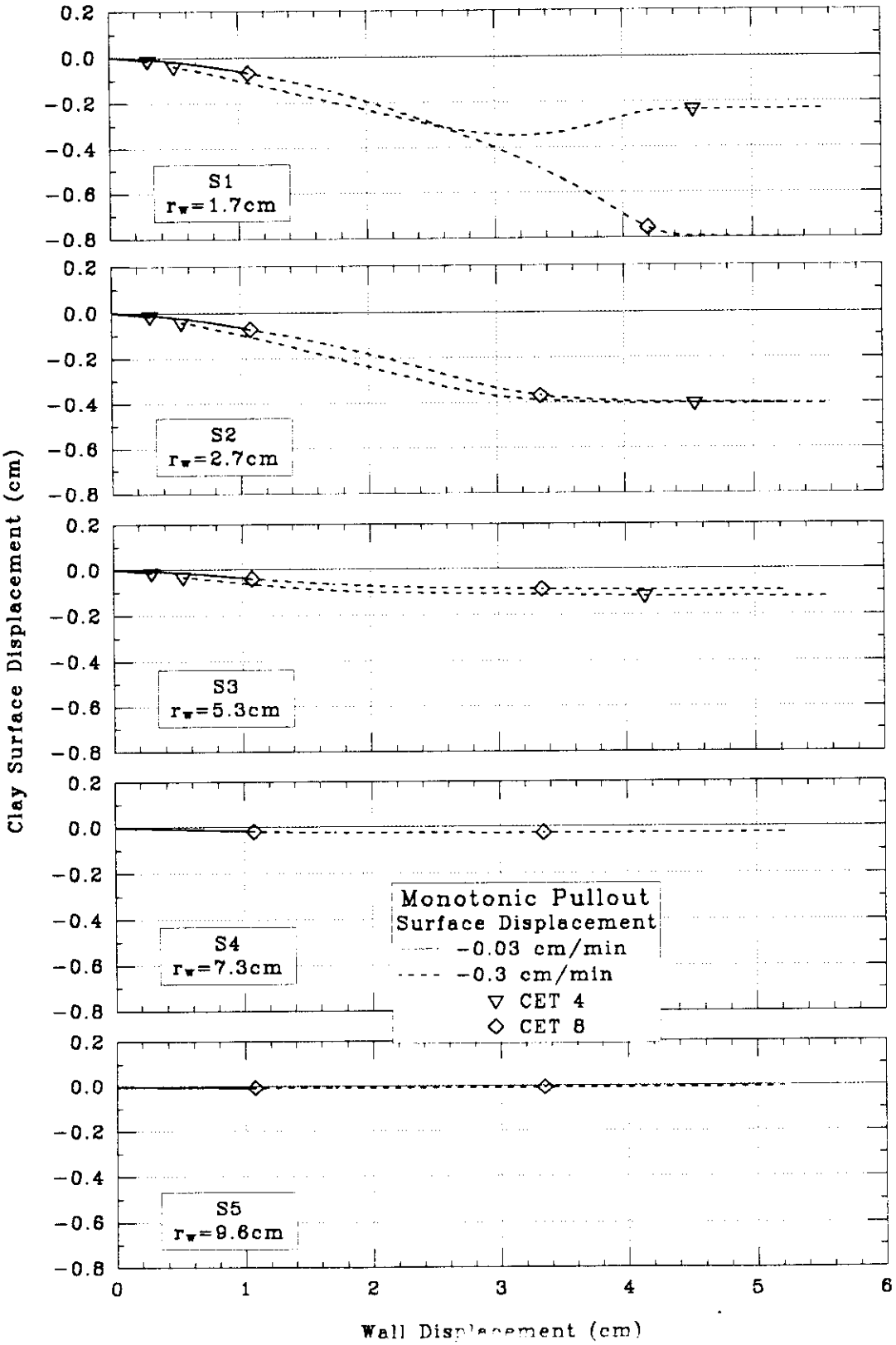

Figure 5.45 Measured Soil Surface Displacement by S1-S5 During Monotonic Pullout 1 at Two Pullout Rates for CET4,8

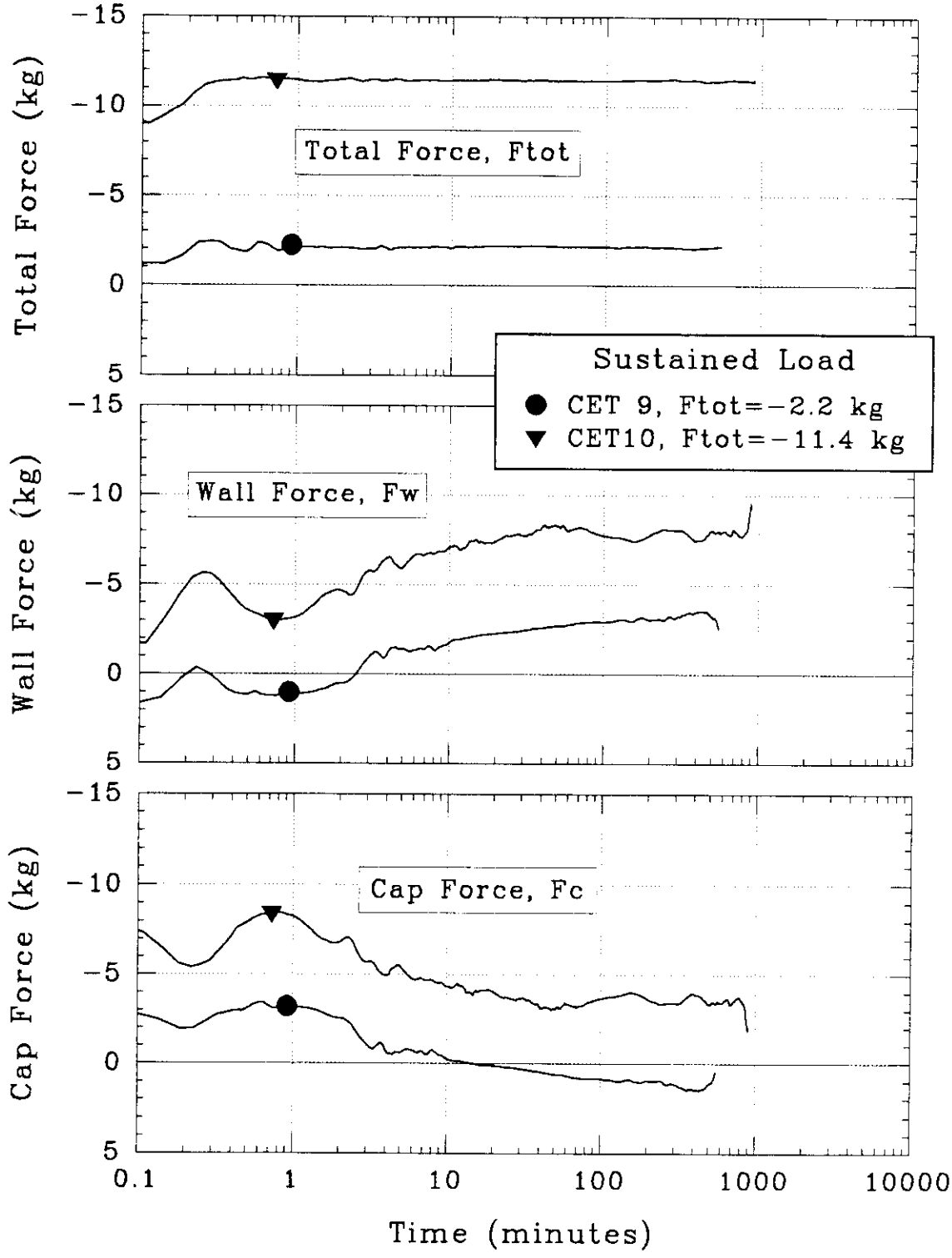

Figure 5.46 Measured Force Components During Sustained Load for CET9,10

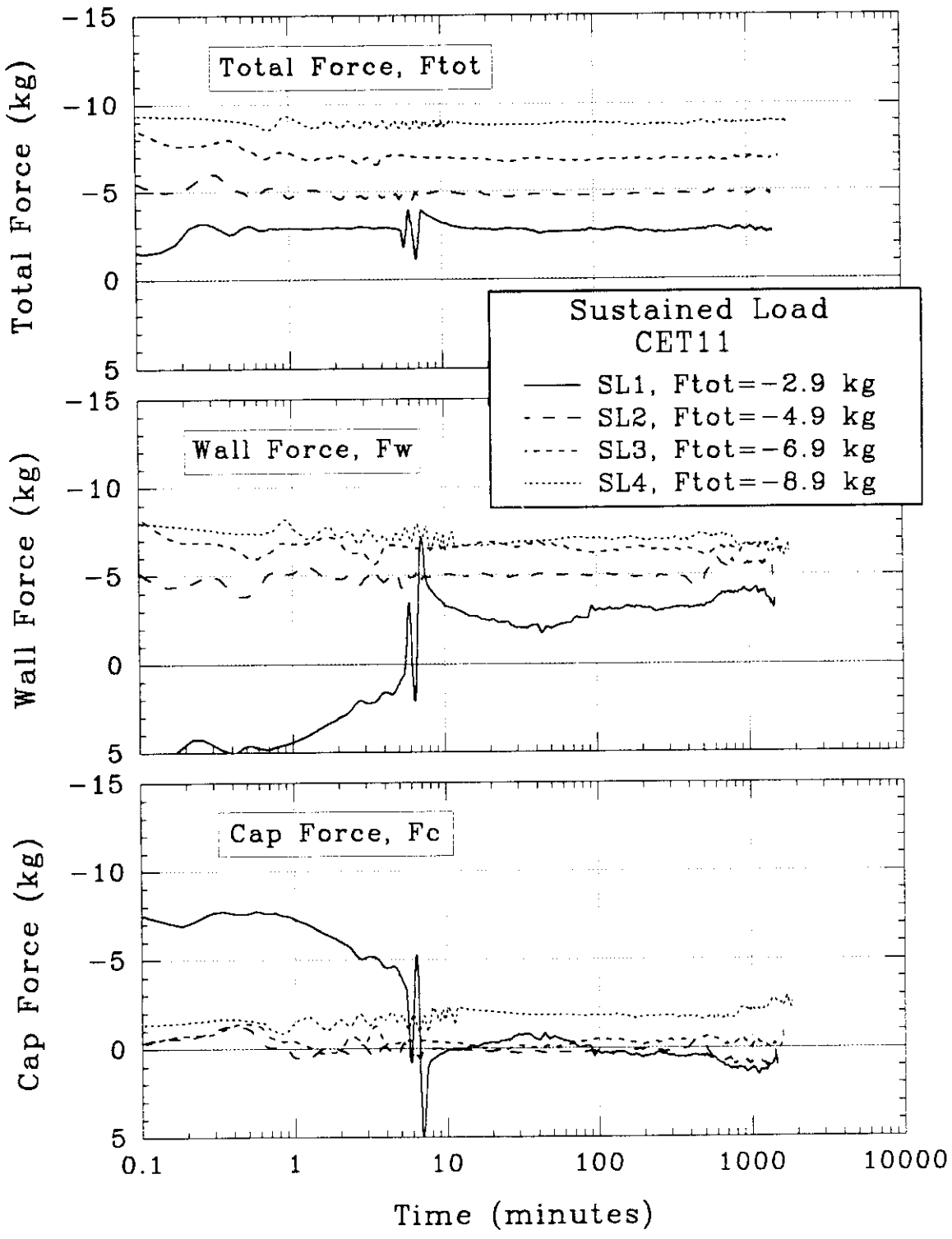

Figure 5.47 Measured Force Components During Sustained Load for CET11

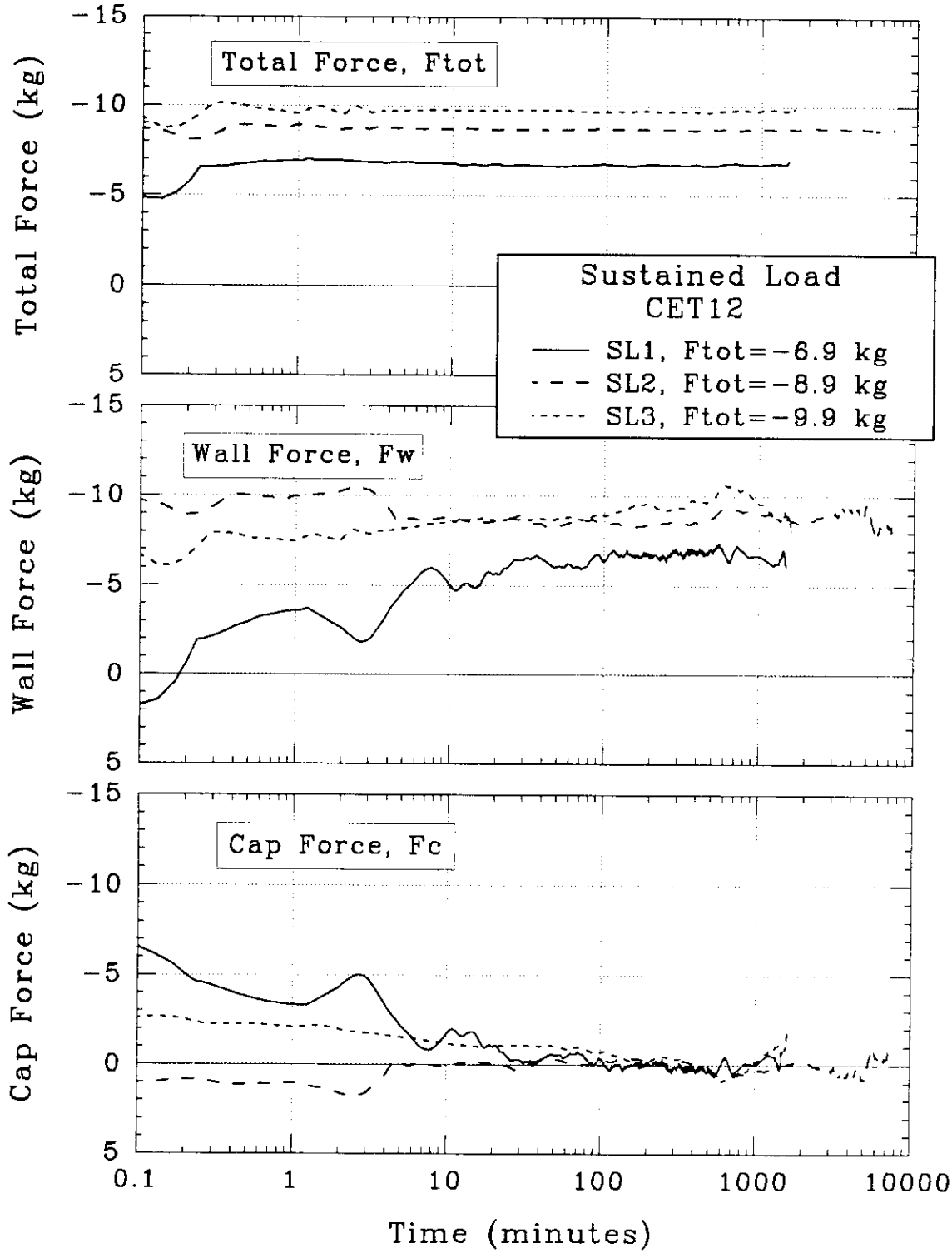

Figure 5.48 Measured Force Components During Sustained Load for CET12

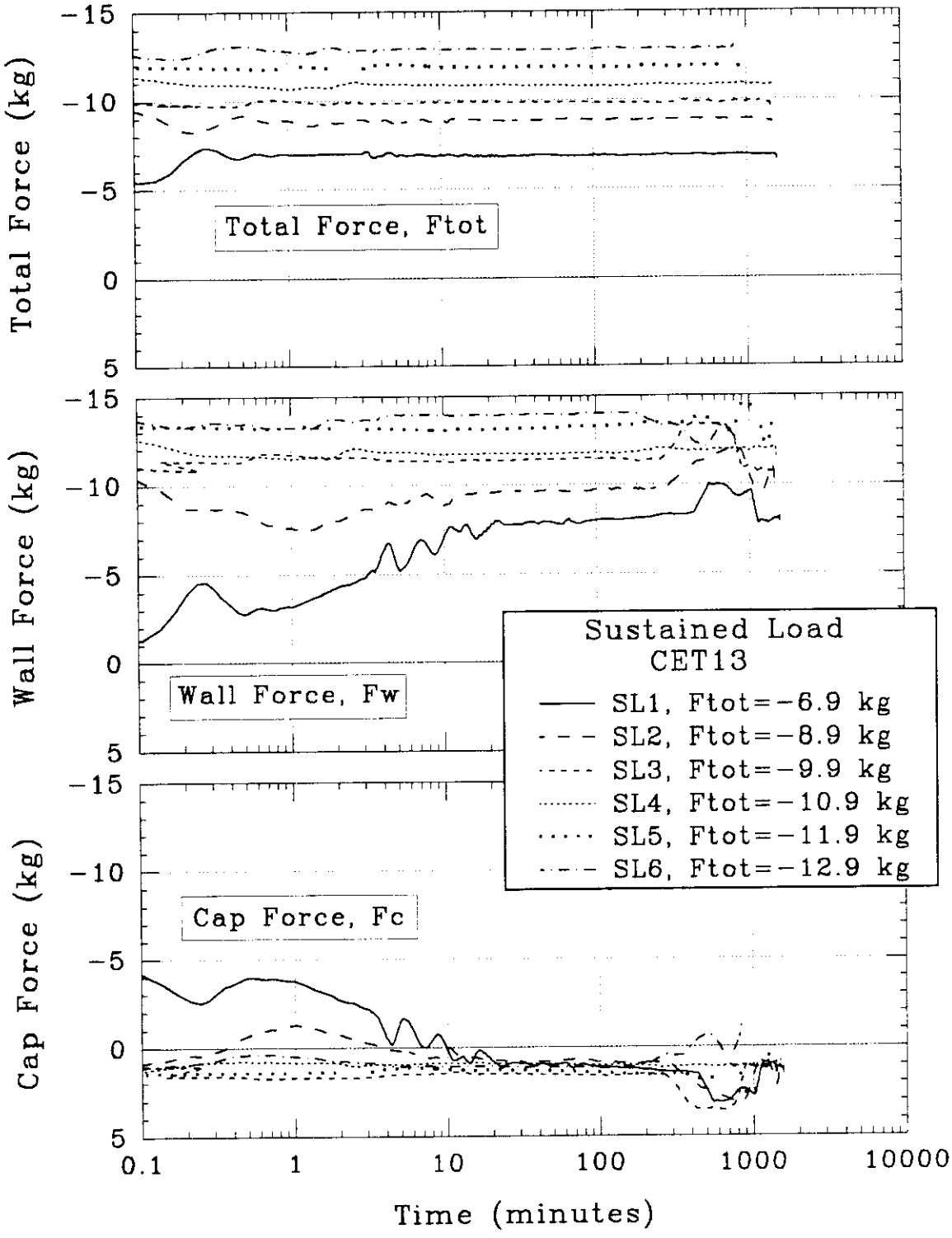

Figure 5.49 Measured Force Components During Sustained Load for CET13

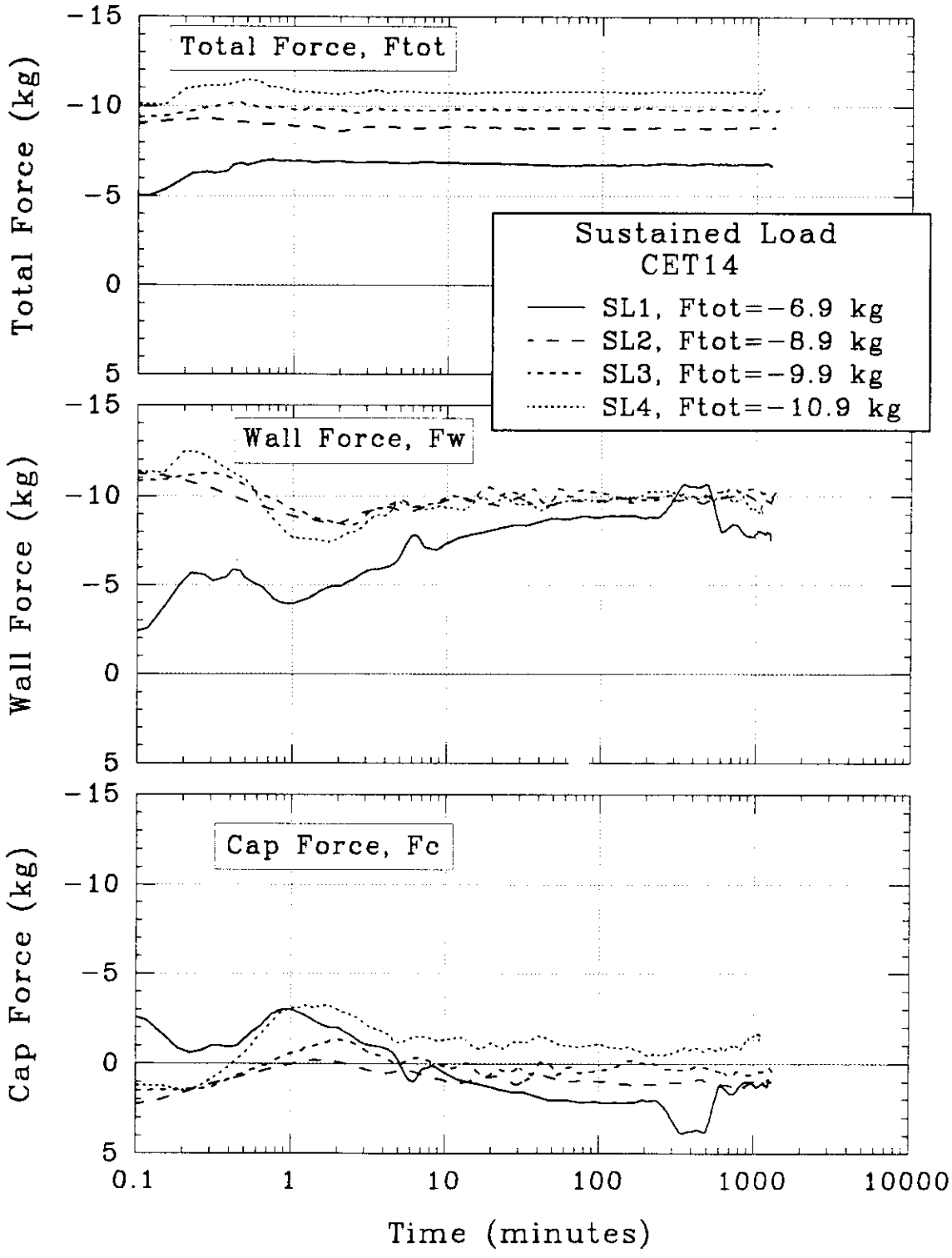

Figure 5.50 Measured Force Components During Sustained Load for CET14

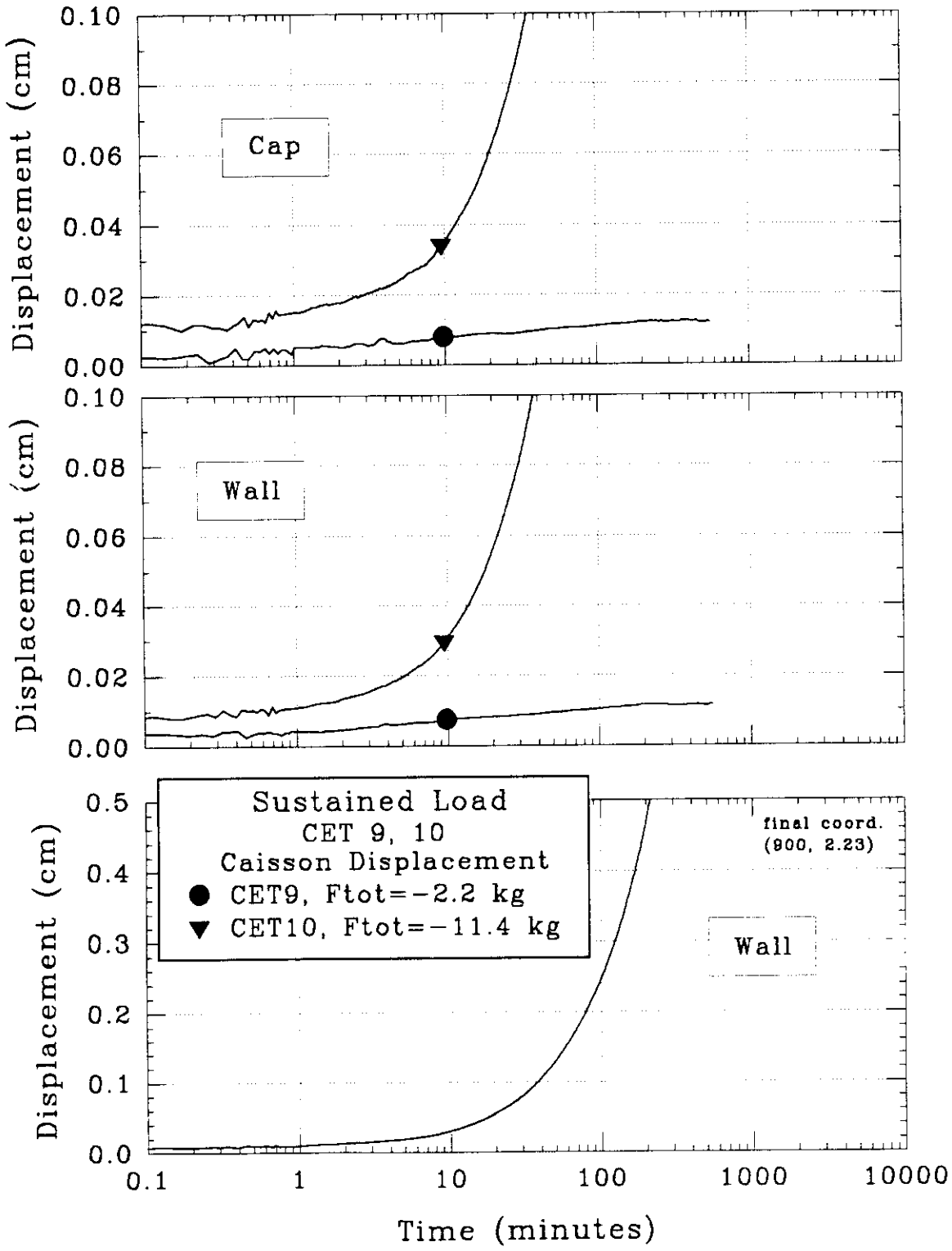

Figure 5.51 Measured Caisson Displacement During Sustained Load for CET9,10

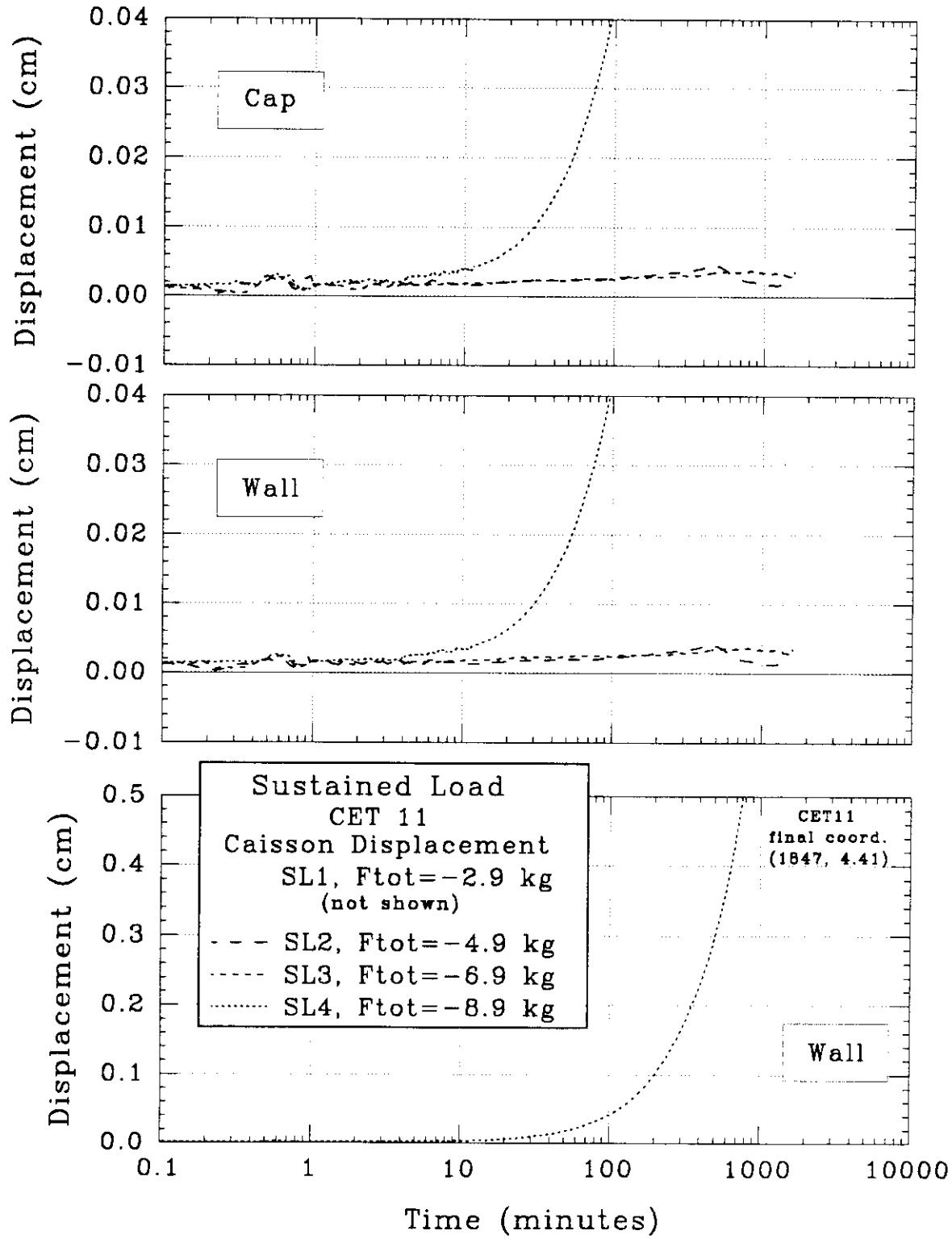

Figure 5.52 Measured Caisson Displacement During Sustained Load for CET11

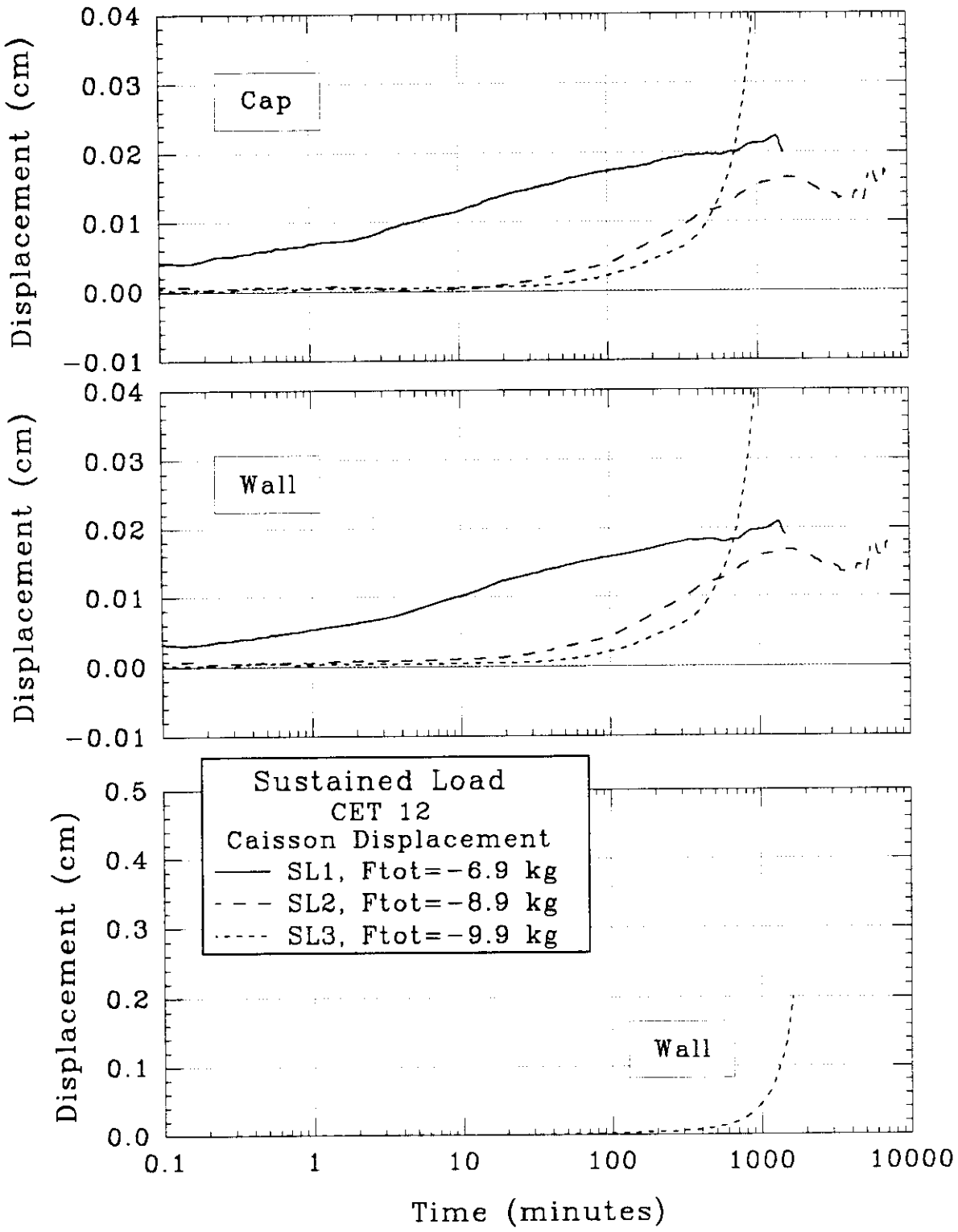

Figure 5.53 Measured Caisson Displacement During Sustained Load for CET12

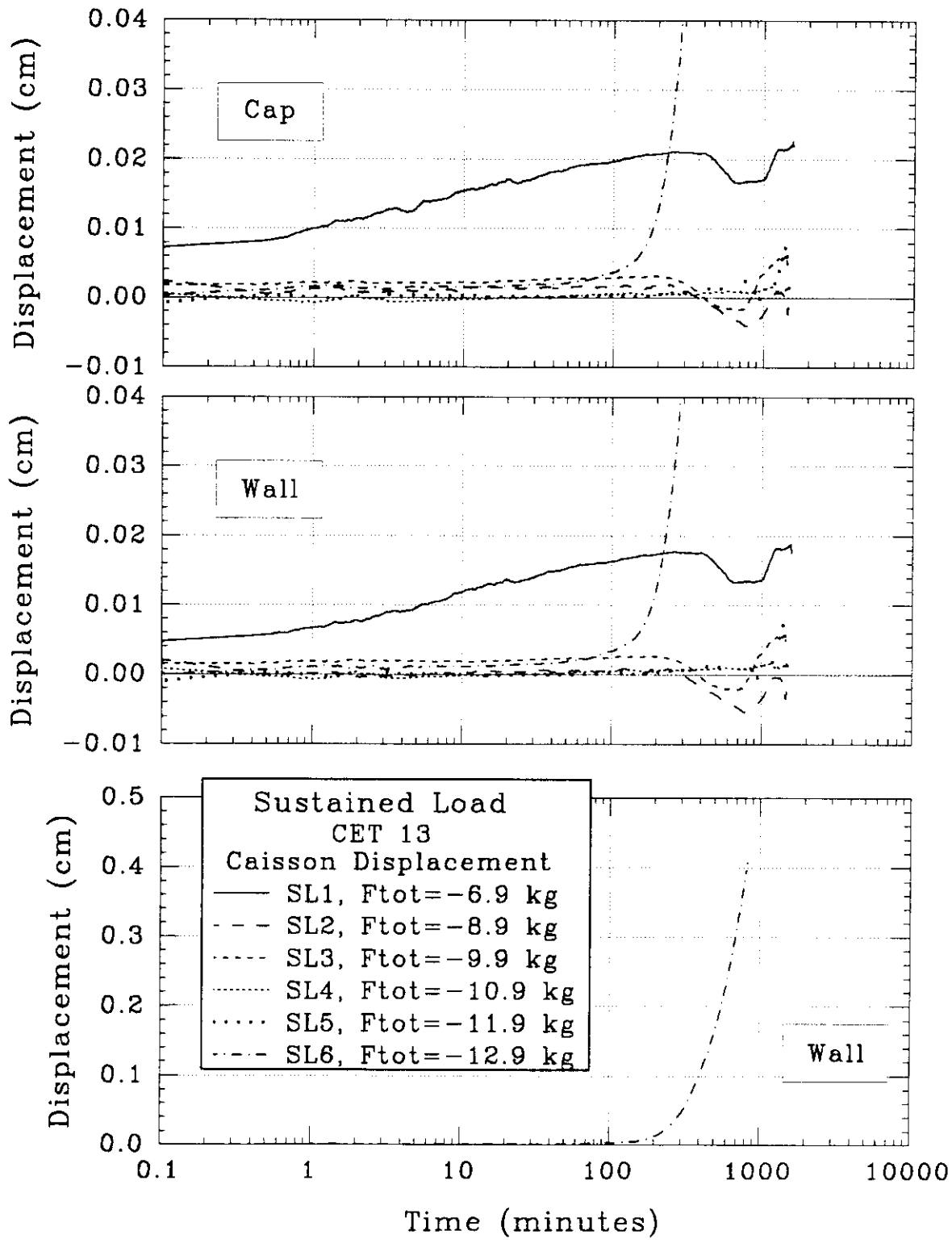

Figure 5.54 Measured Caisson Displacement During Sustained Load for CET13

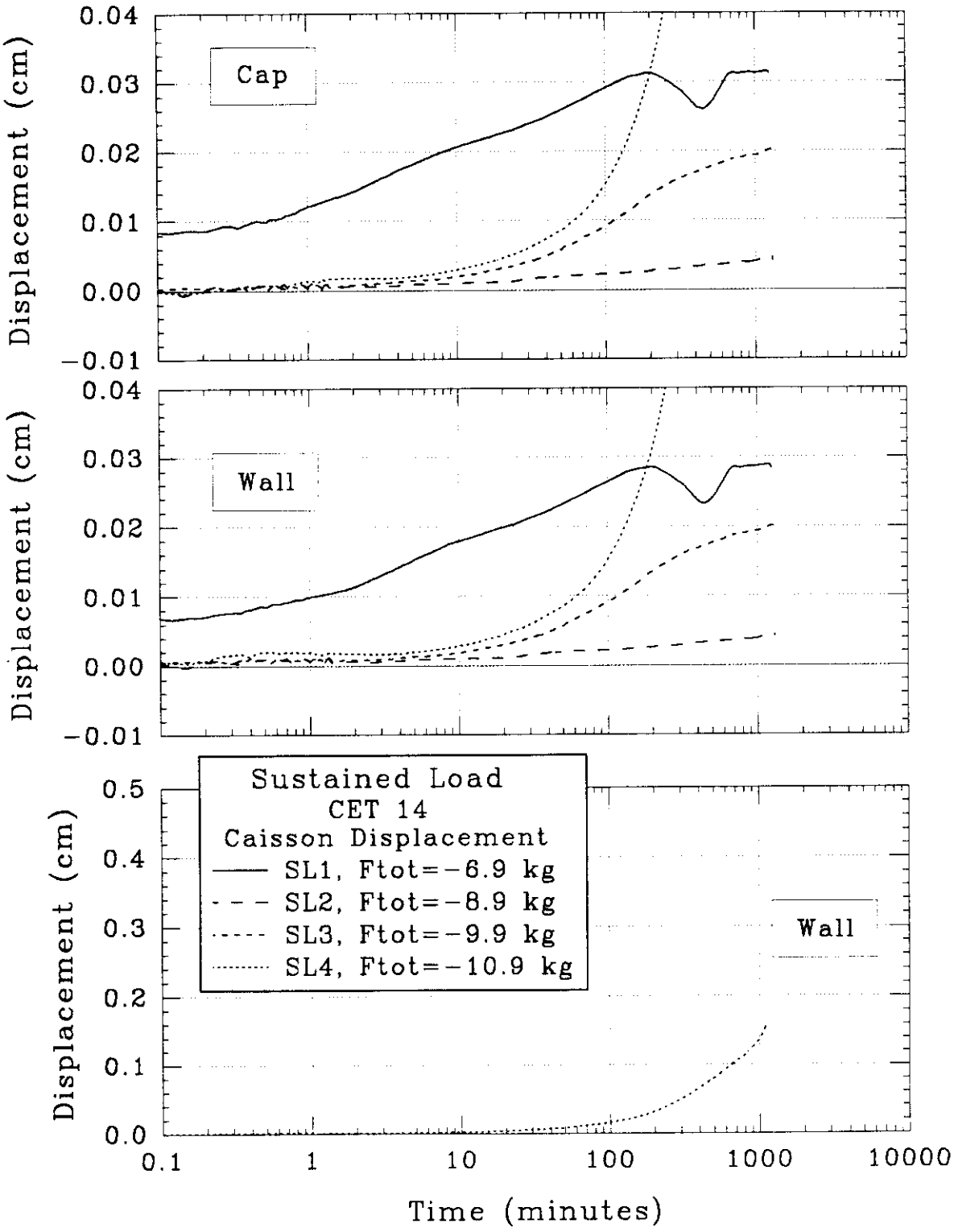

Figure 5.55 Measured Caisson Displacement During Sustained Load for CET14

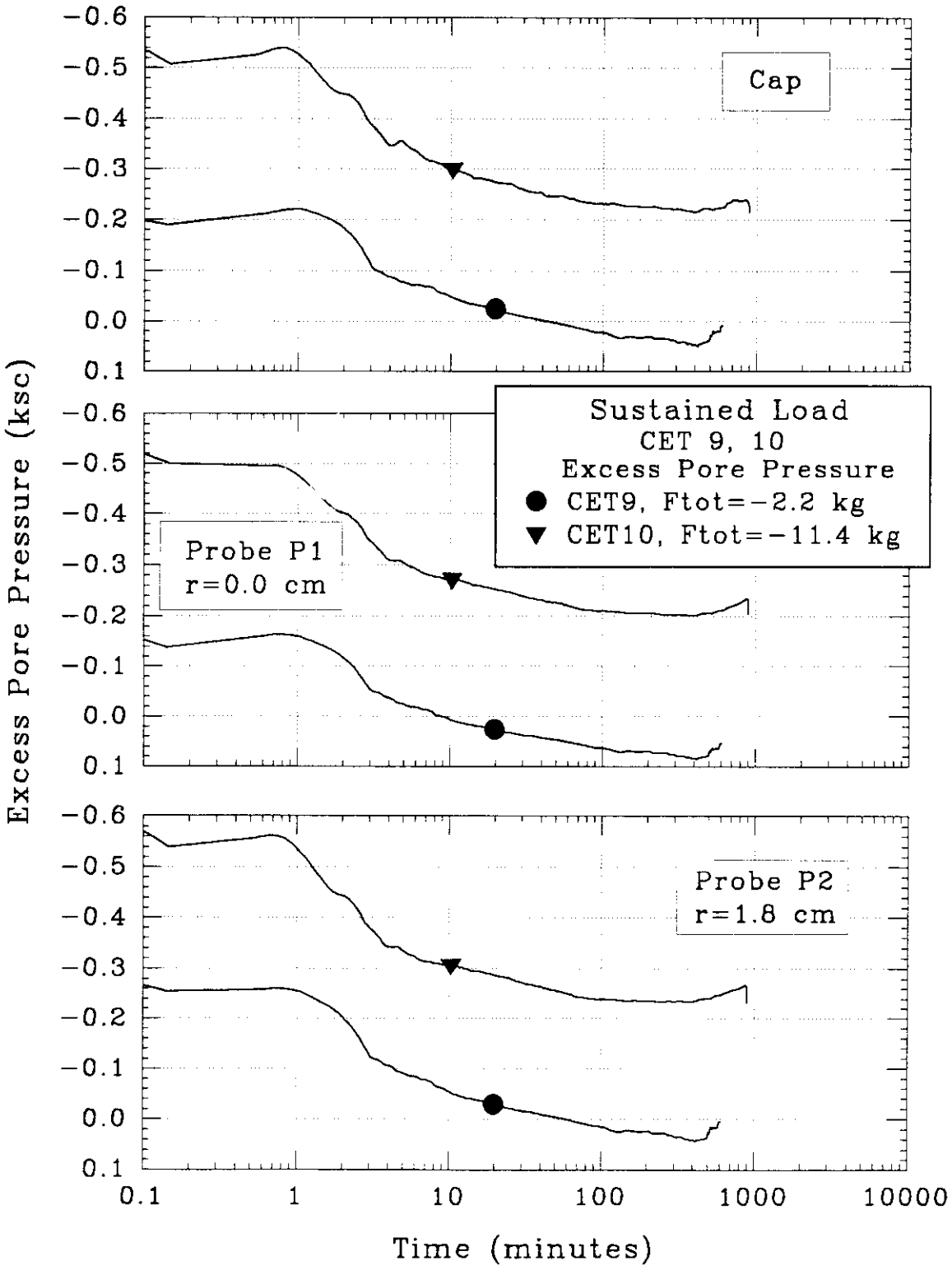

Figure 5.56 Measured Excess Pore Pressure Beneath Cap and by P1-P3 During Sustained Load for CET9,10

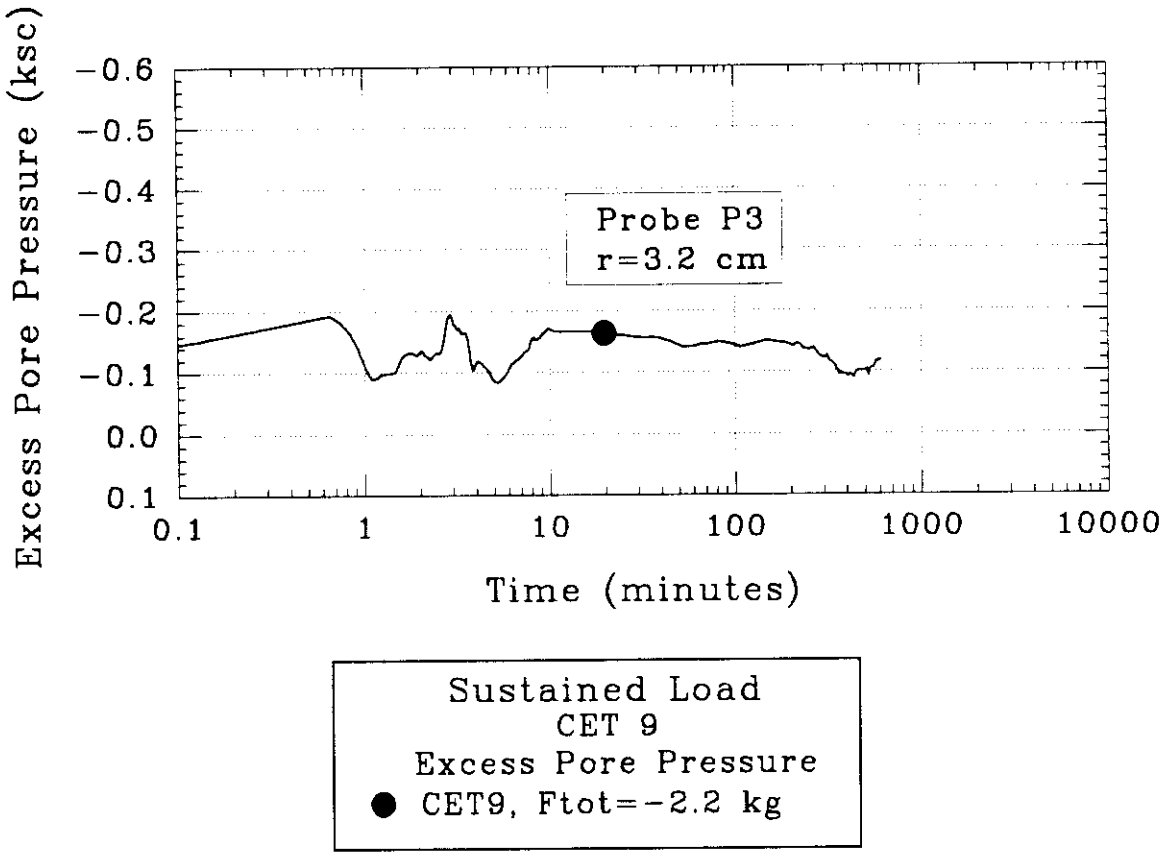

Figure 5.56 (cont.) Measured Excess Pore Pressure Beneath Cap and by P1-P3 During Sustained Load for CET9,10

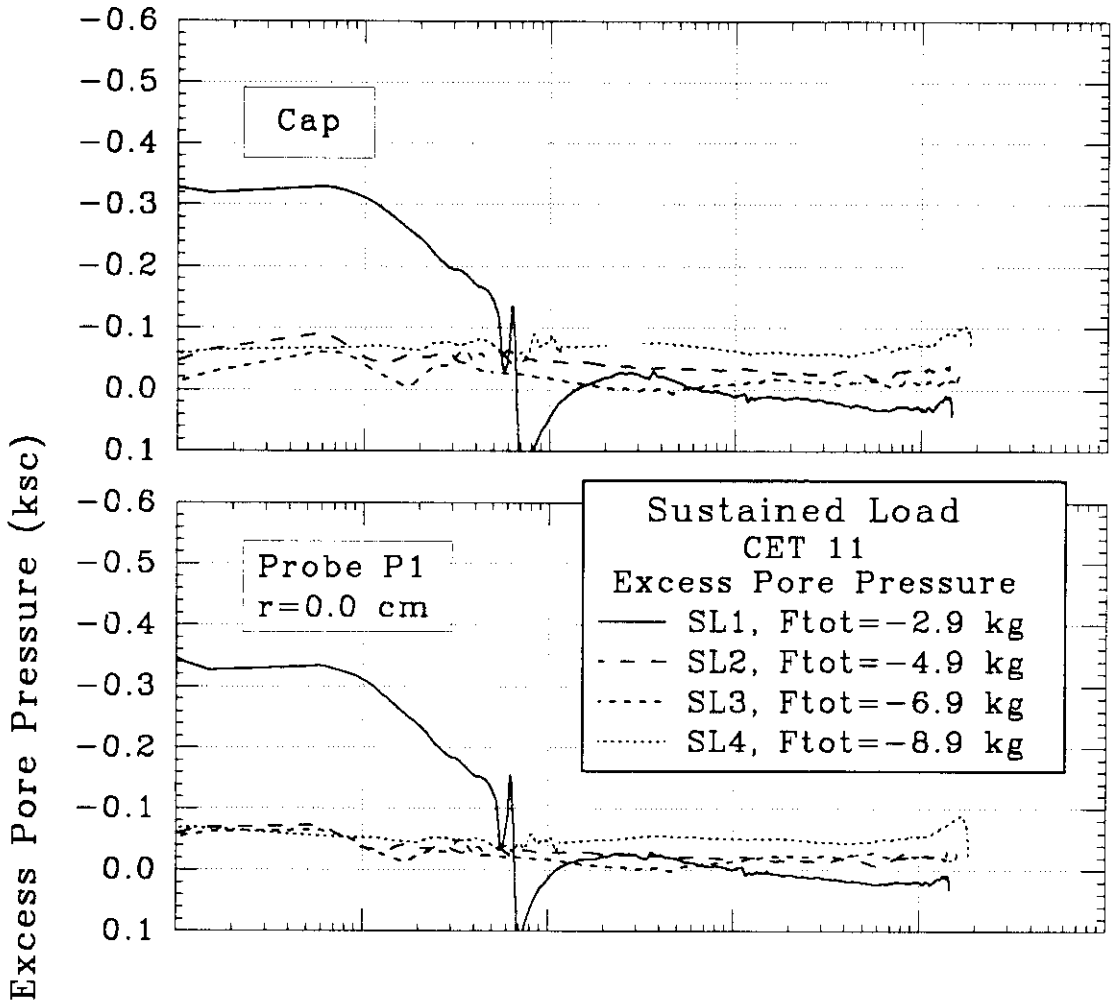

Figure 5.57 Measured Excess Pore Pressure Beneath Cap and by P1 During Sustained Load for CET11

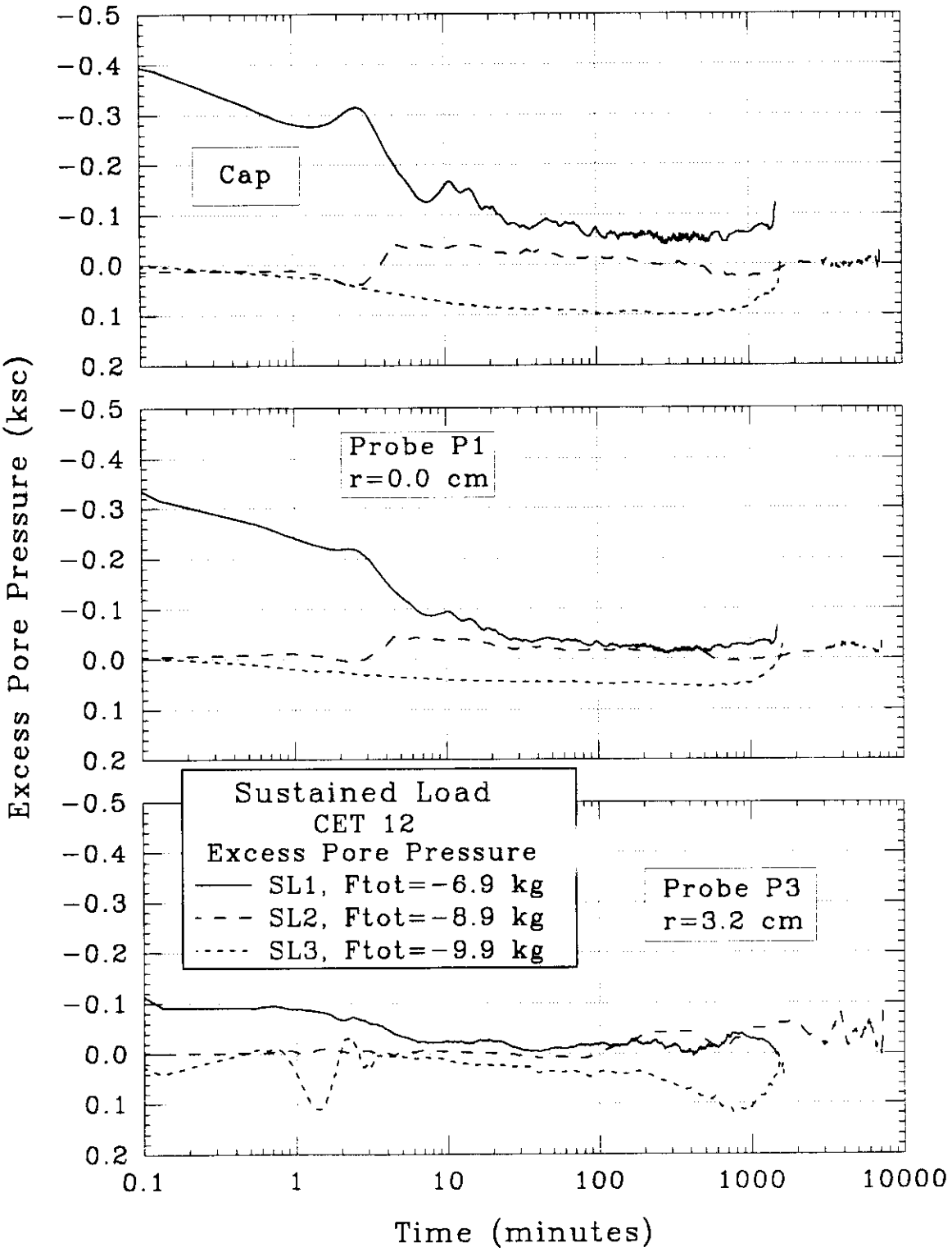

Figure 5.58 Measured Excess Pore Pressure Beneath Cap and by P1-P4 During Sustained Load for CET12

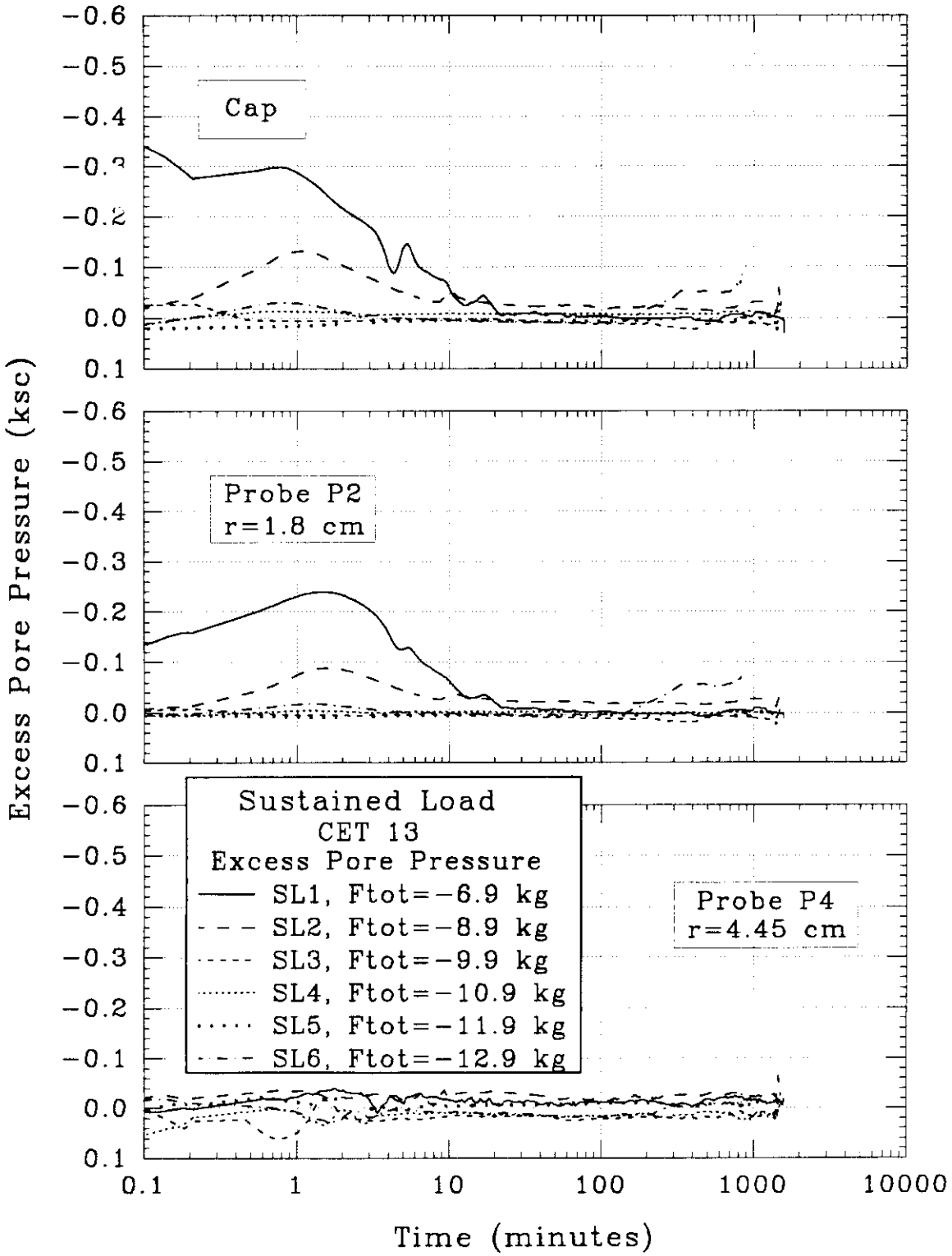

Figure 5.59 Measured Excess Pore Pressure Beneath Cap and by P1-P4 During Sustained Load for CET13

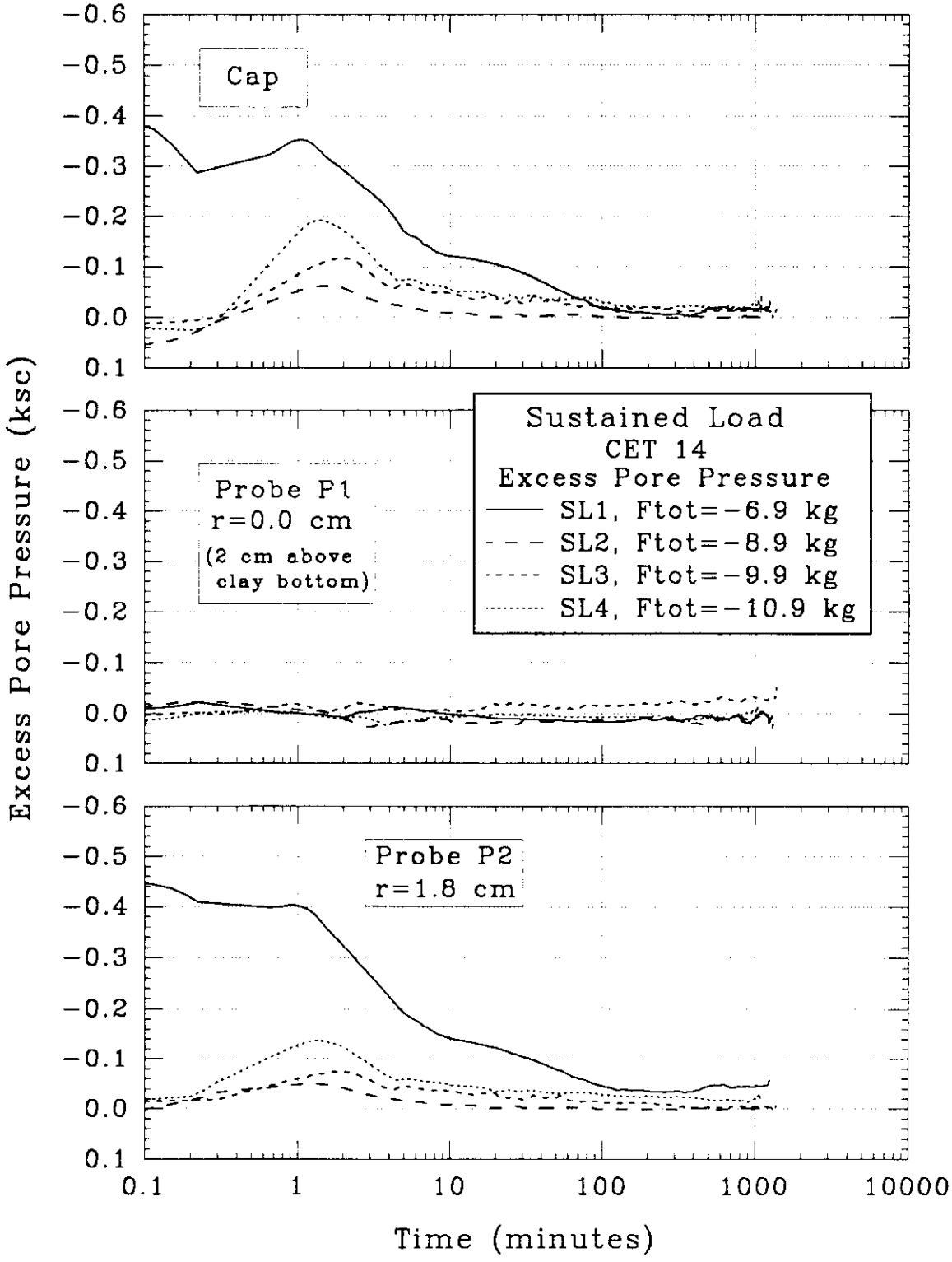

Figure 5.60 Measured Excess Pore Pressure Beneath Cap and by P1-P4 During Sustained Load for CET14

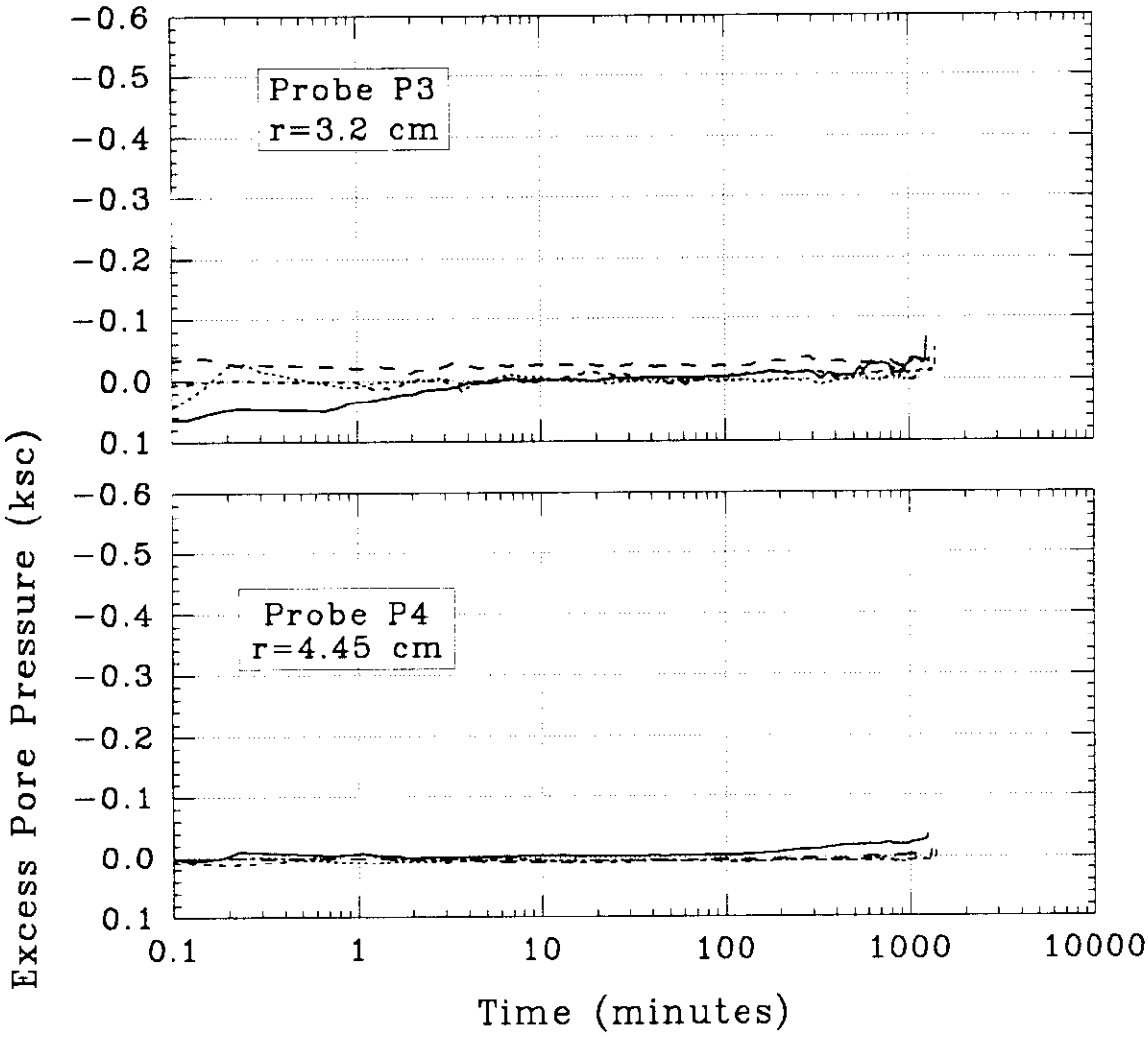

Figure 5.60 (cont.) Measured Excess Pore Pressure Beneath Cap and by P1-P4 During Sustained Load for CET14

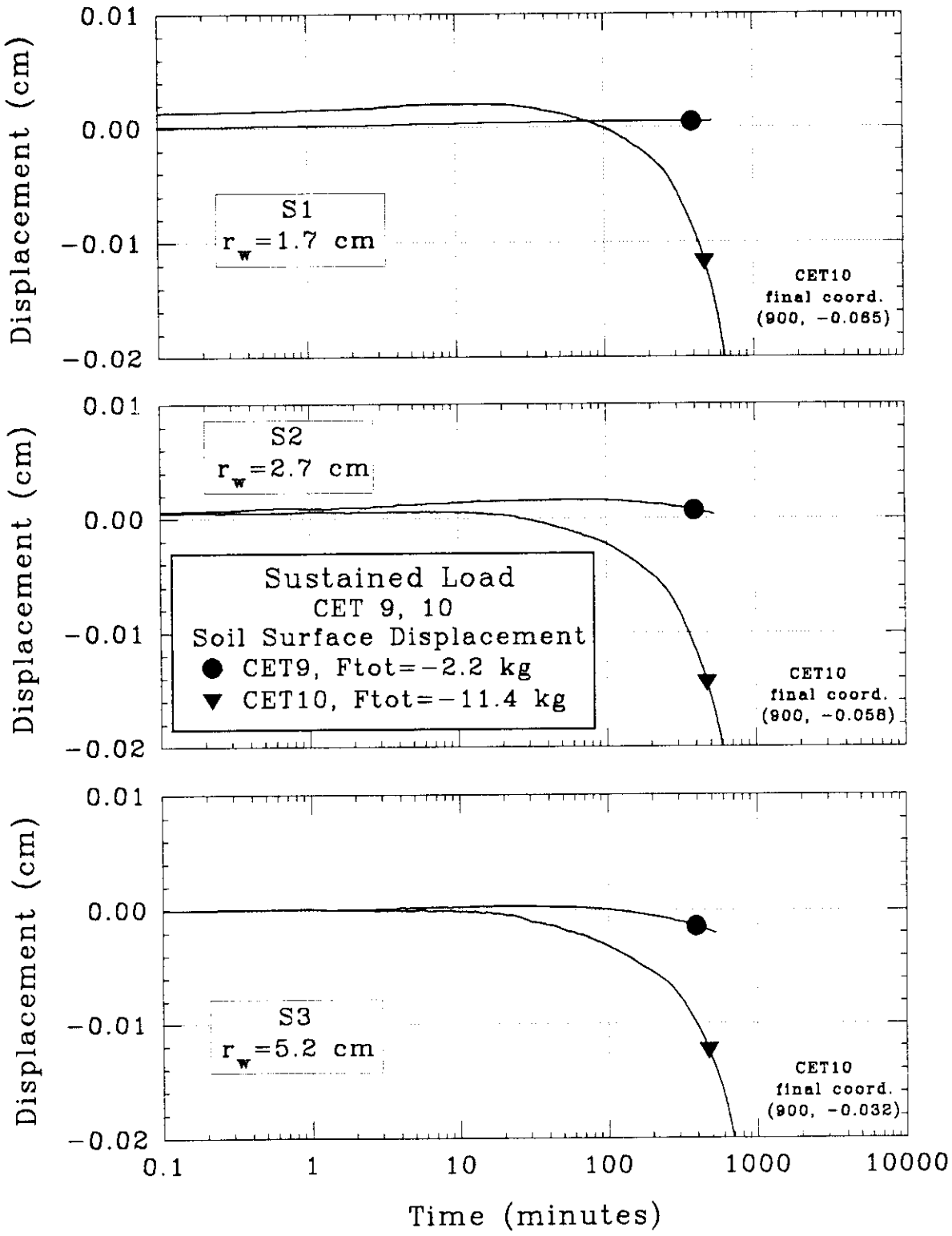

Figure 5.61 Measured Soil Surface Displacement by S1-S5 During Sustained Load for CET9,10

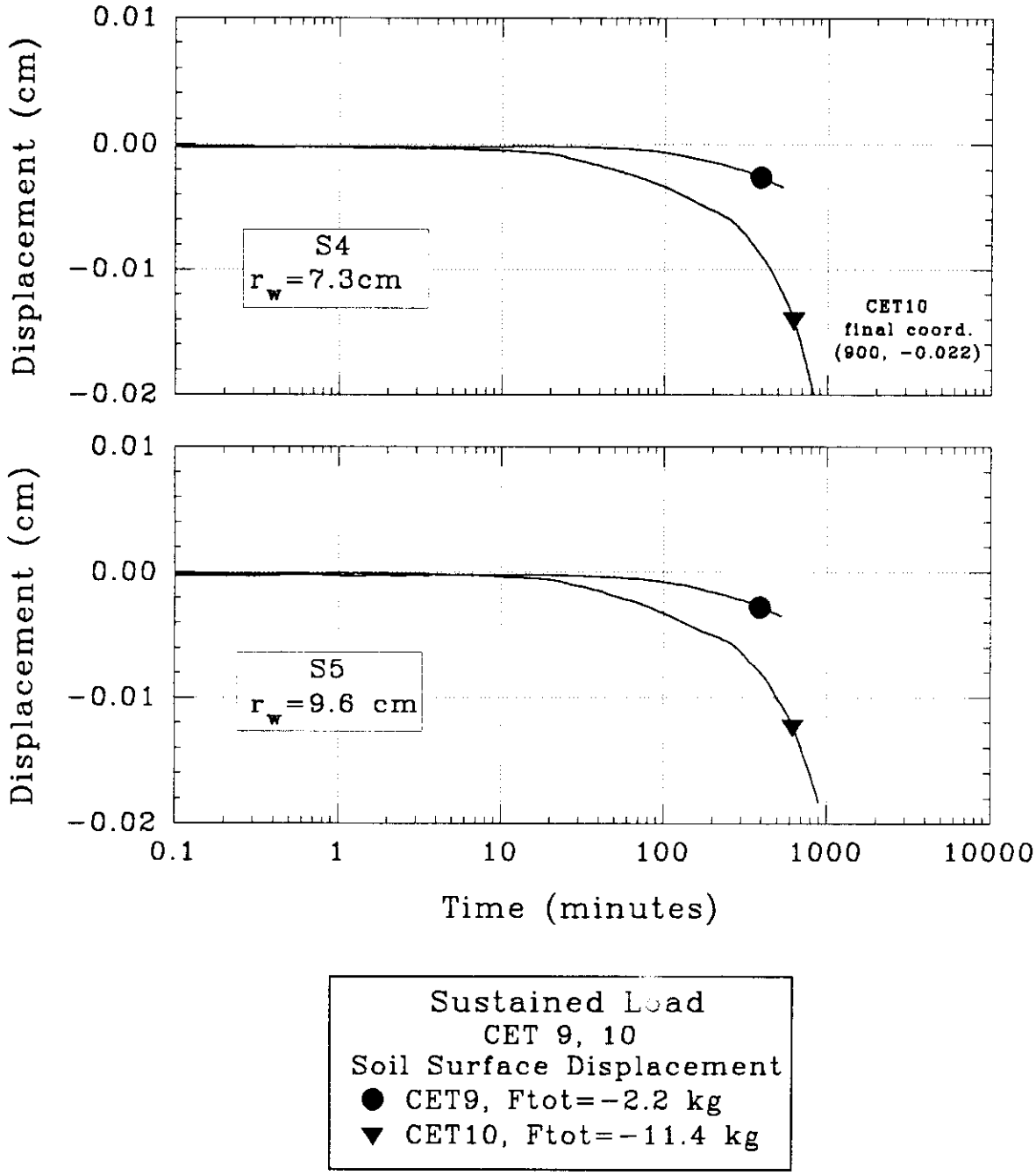

Figure 5.61 (cont.) Measured Soil Surface Displacement by S1-S5 During Sustained Load for CET9,10

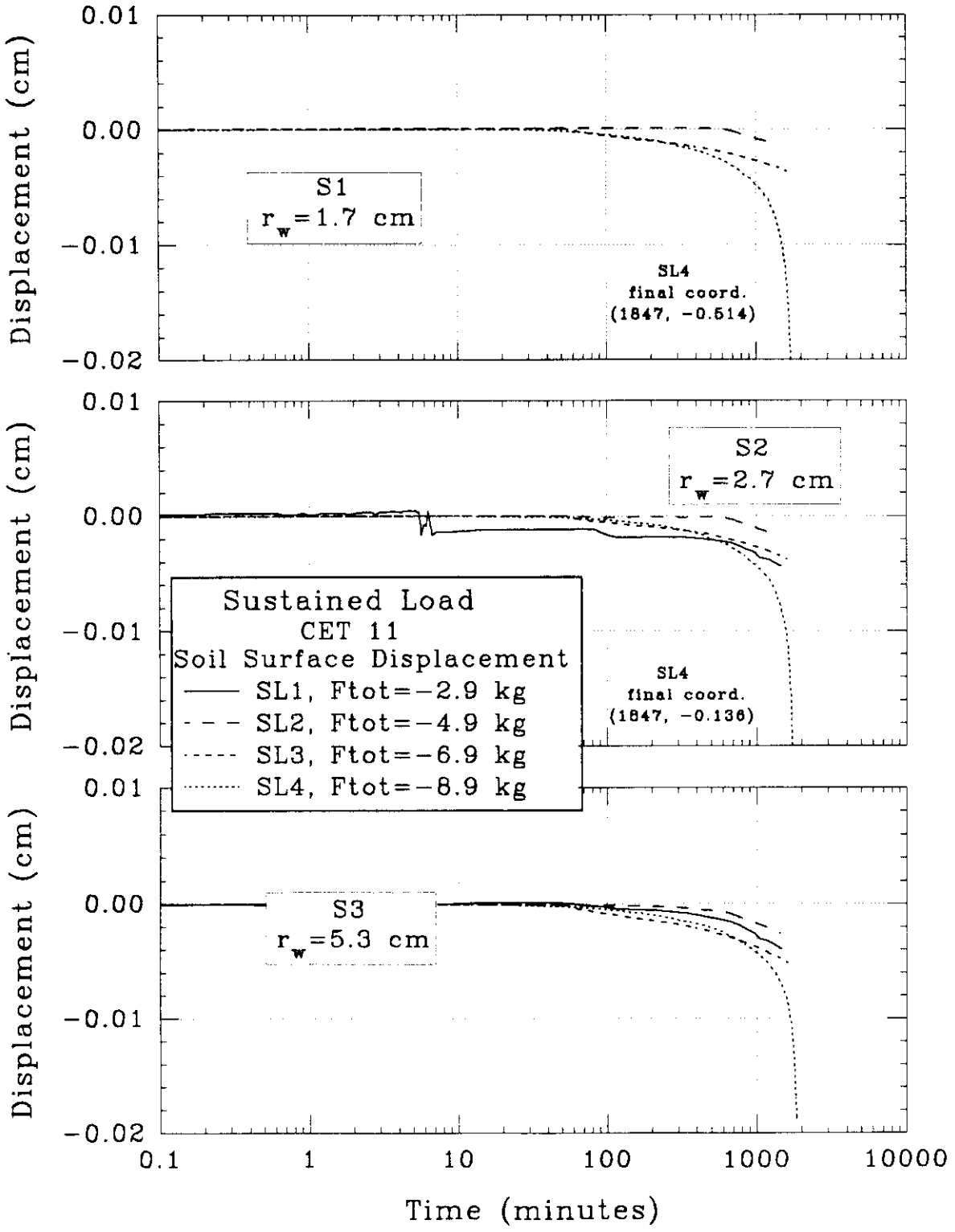

Figure 5.62 Measured Soil Surface Displacement by S1-S5 During Sustained Load for CET11

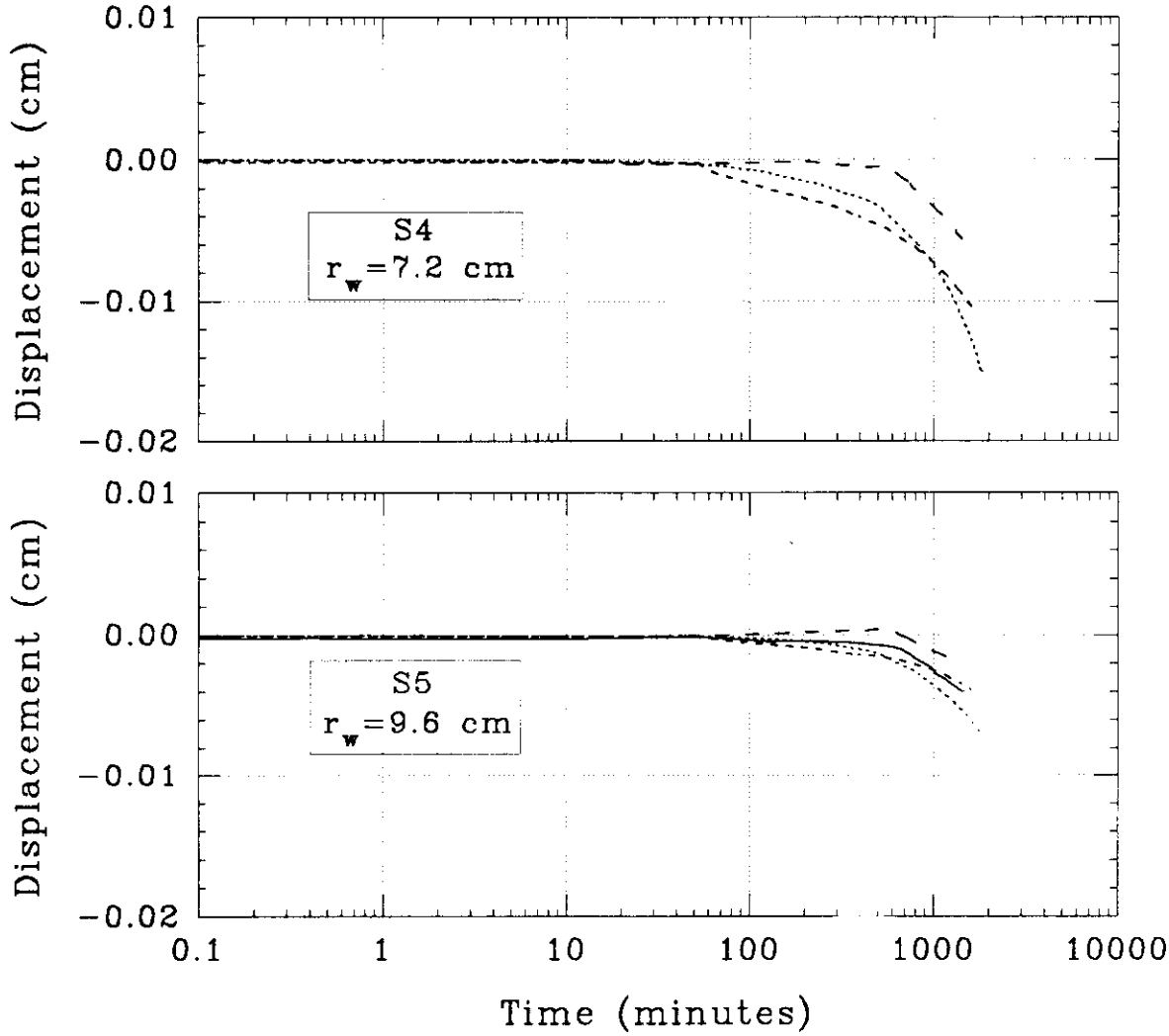

Figure 5.62 (cont.) Measured Soil Surface Displacement by S1-S5 During Sustained Load for CET11

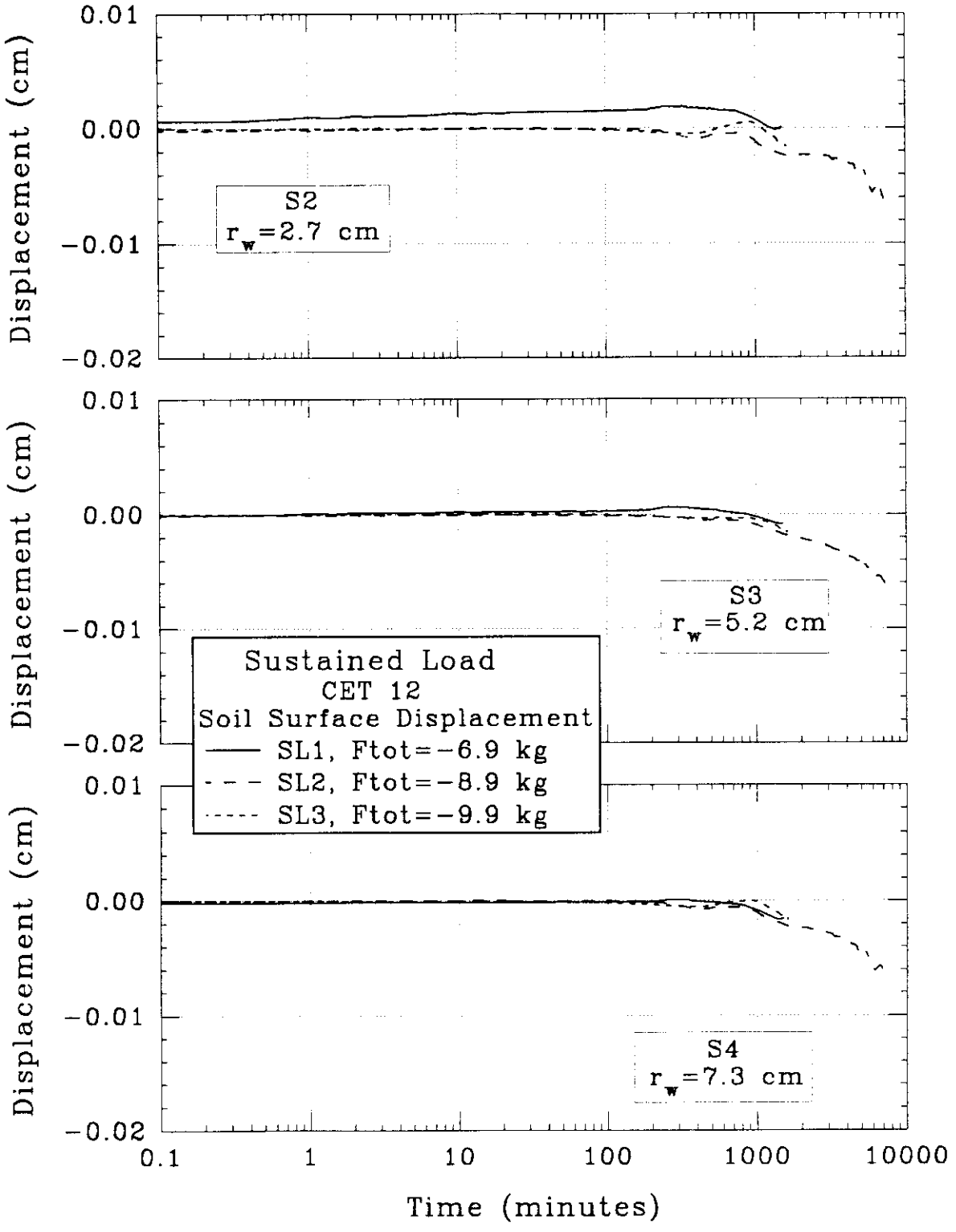

Figure 5.63 Measured Soil Surface Displacement by S2-S5 During Sustained Load for CET12

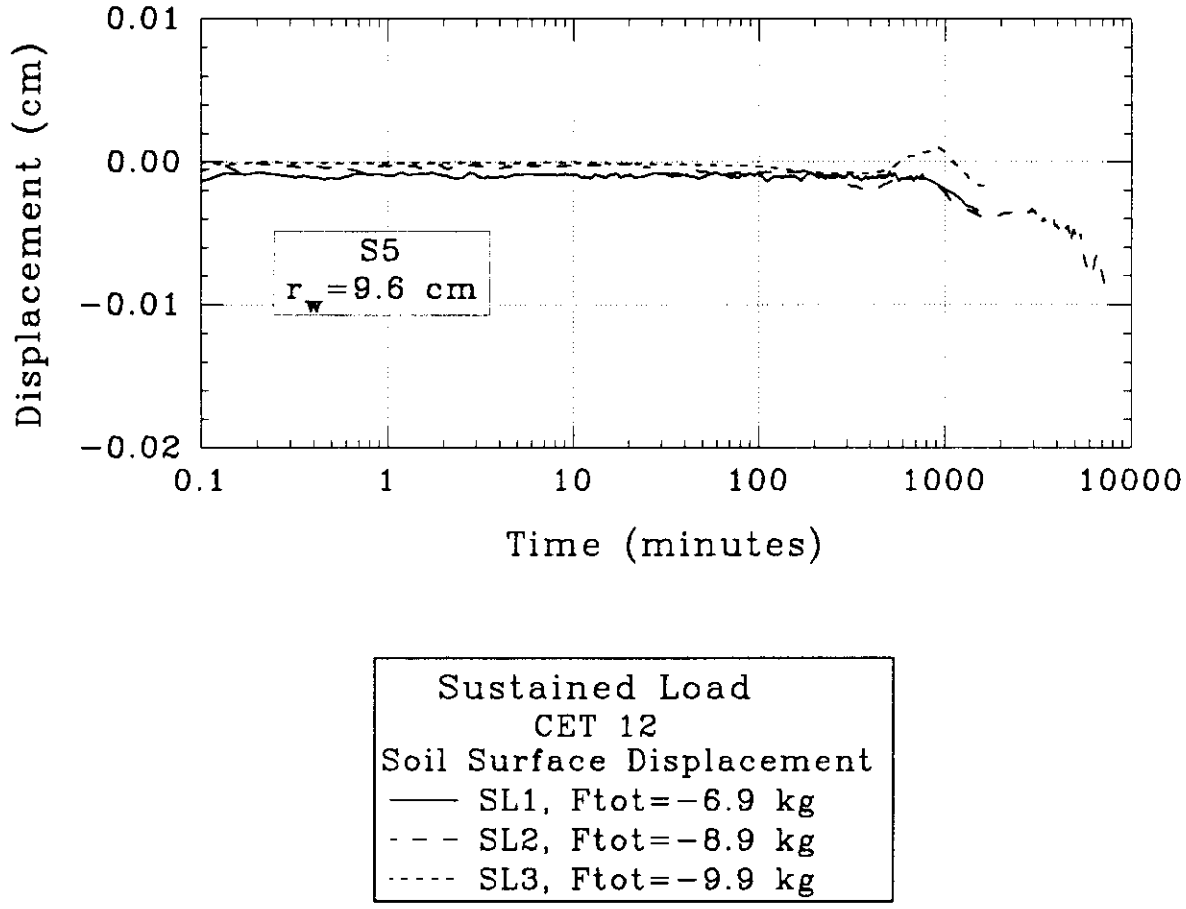

Figure 5.63 (cont.) Measured Soil Surface Displacement by S2-S5 During Sustained Load for CET12

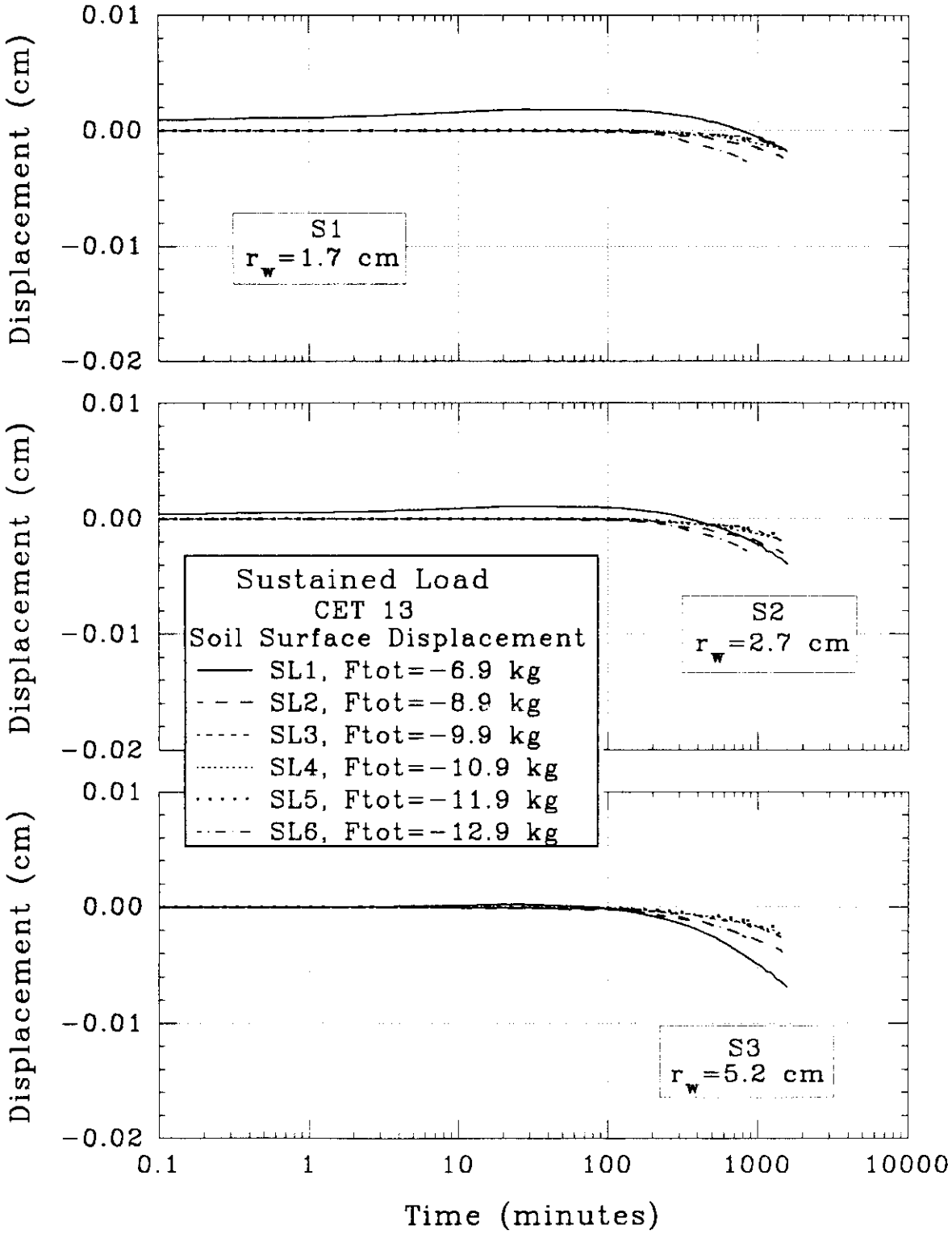

Figure 5.64 Measured Soil Surface Displacement by S1-S5 During Sustained Load for CET13

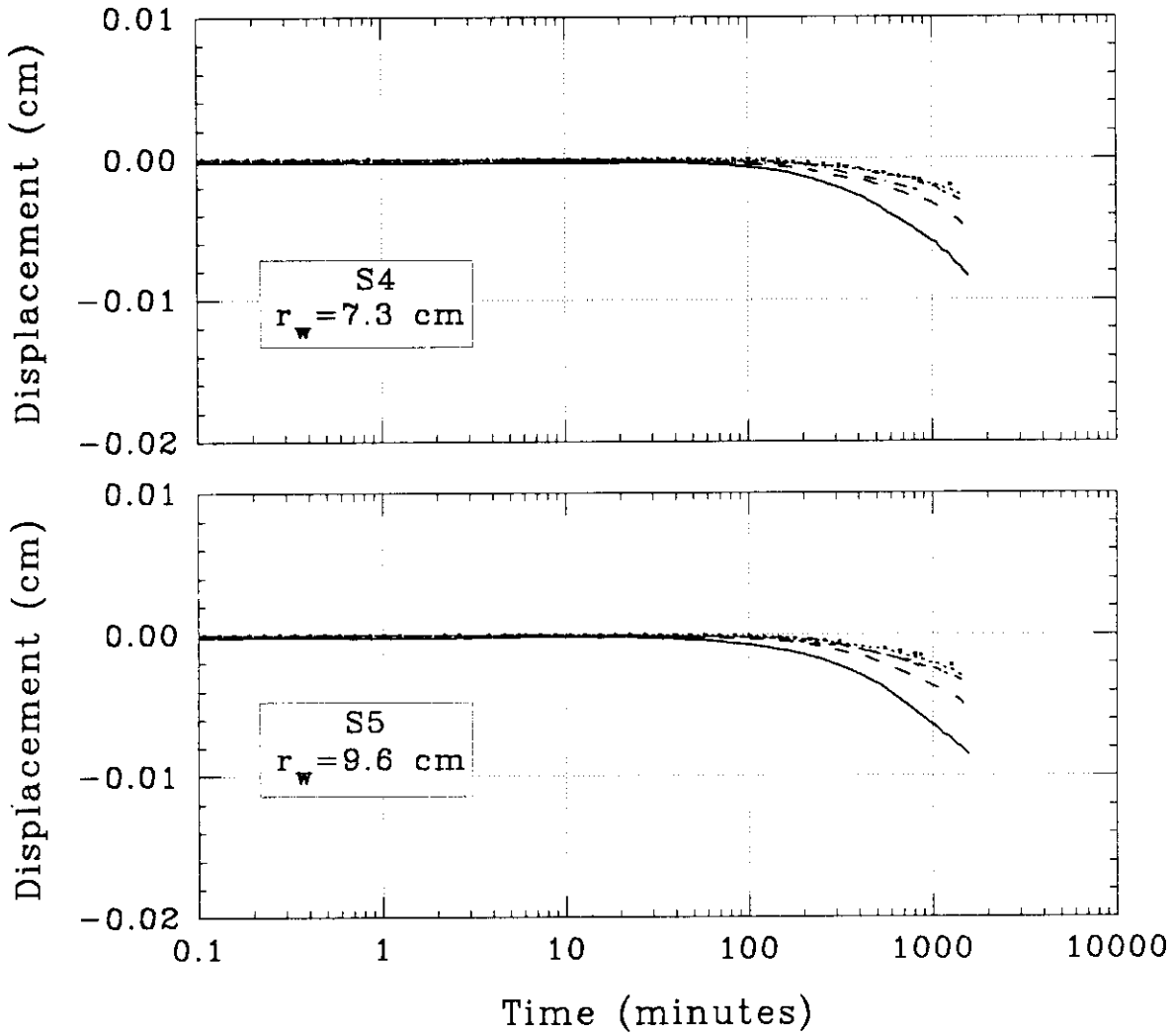

Figure 5.64 (cont.) Measured Soil Surface Displacement by S1-S5 During Sustained Load for CET13

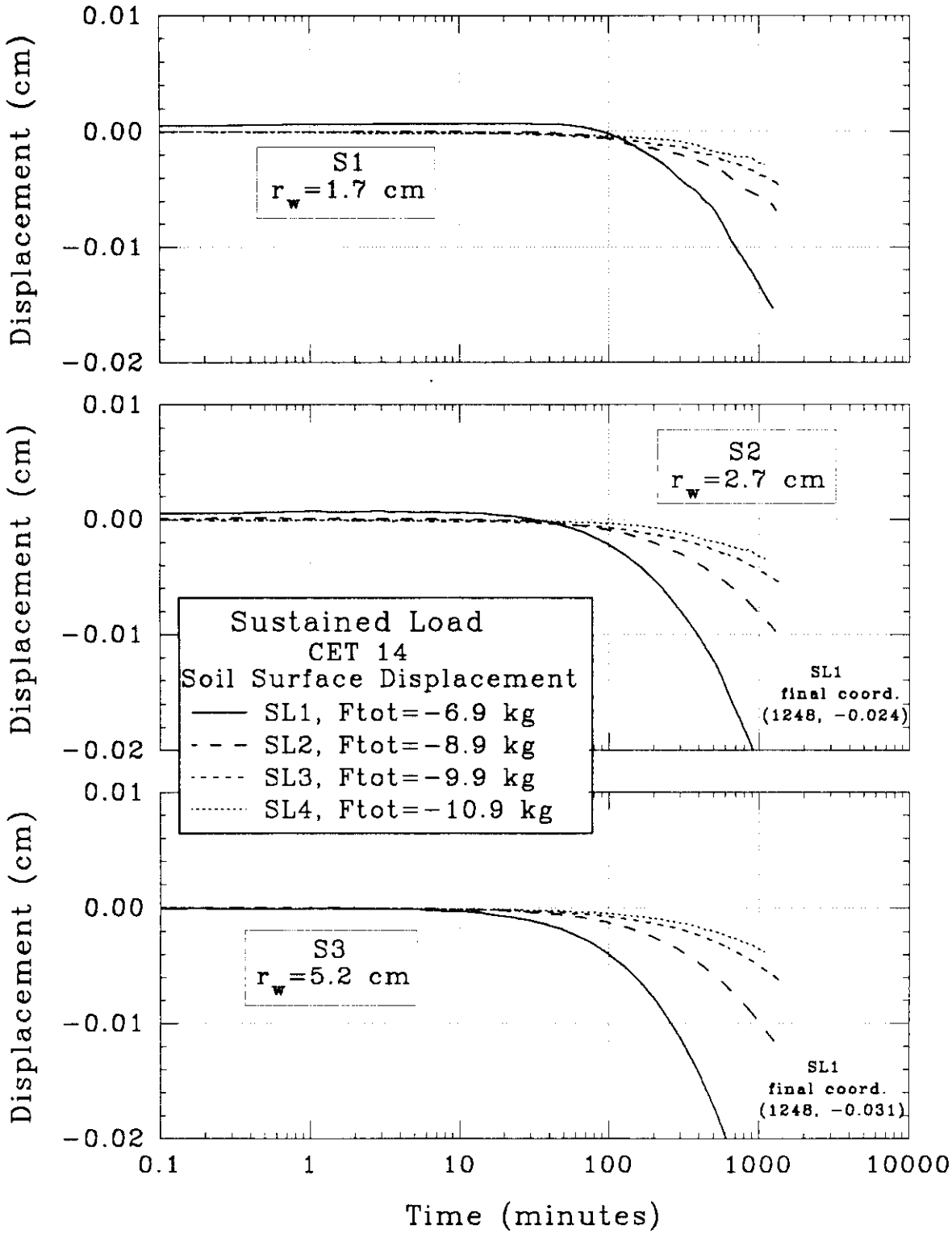

Figure 5.65 Measured Soil Surface Displacement by S1-S5 During Sustained Load for CET14

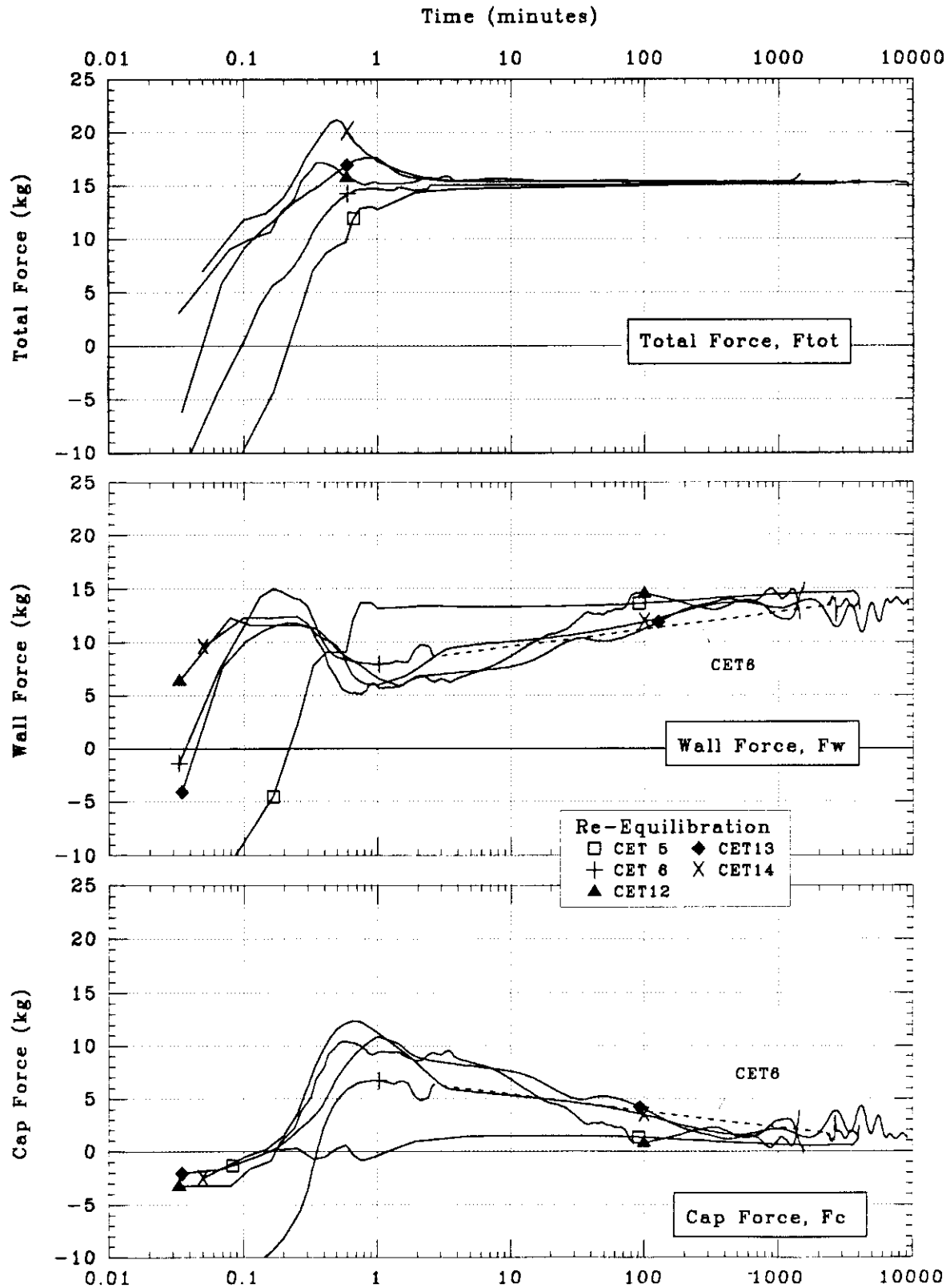

Figure 5.66 Measured Total, Wall, and Cap Forces on Caisson During Re-Equilibration for CET5-6,12-14

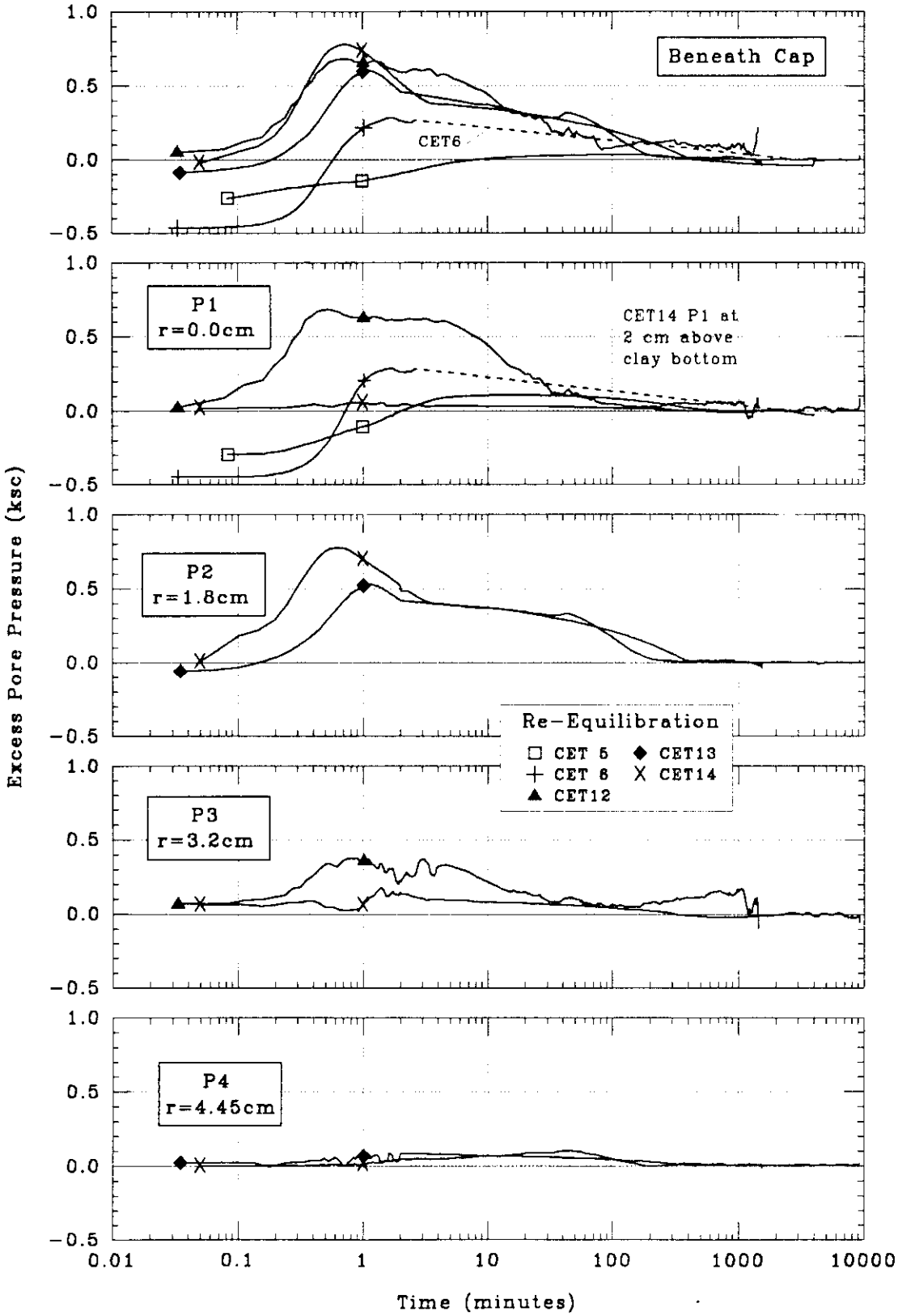

Figure 5.67 Measured Excess Pore Pressure Beneath Cap and by P1-P4 During Re-Equilibration for CET5-6,12-14

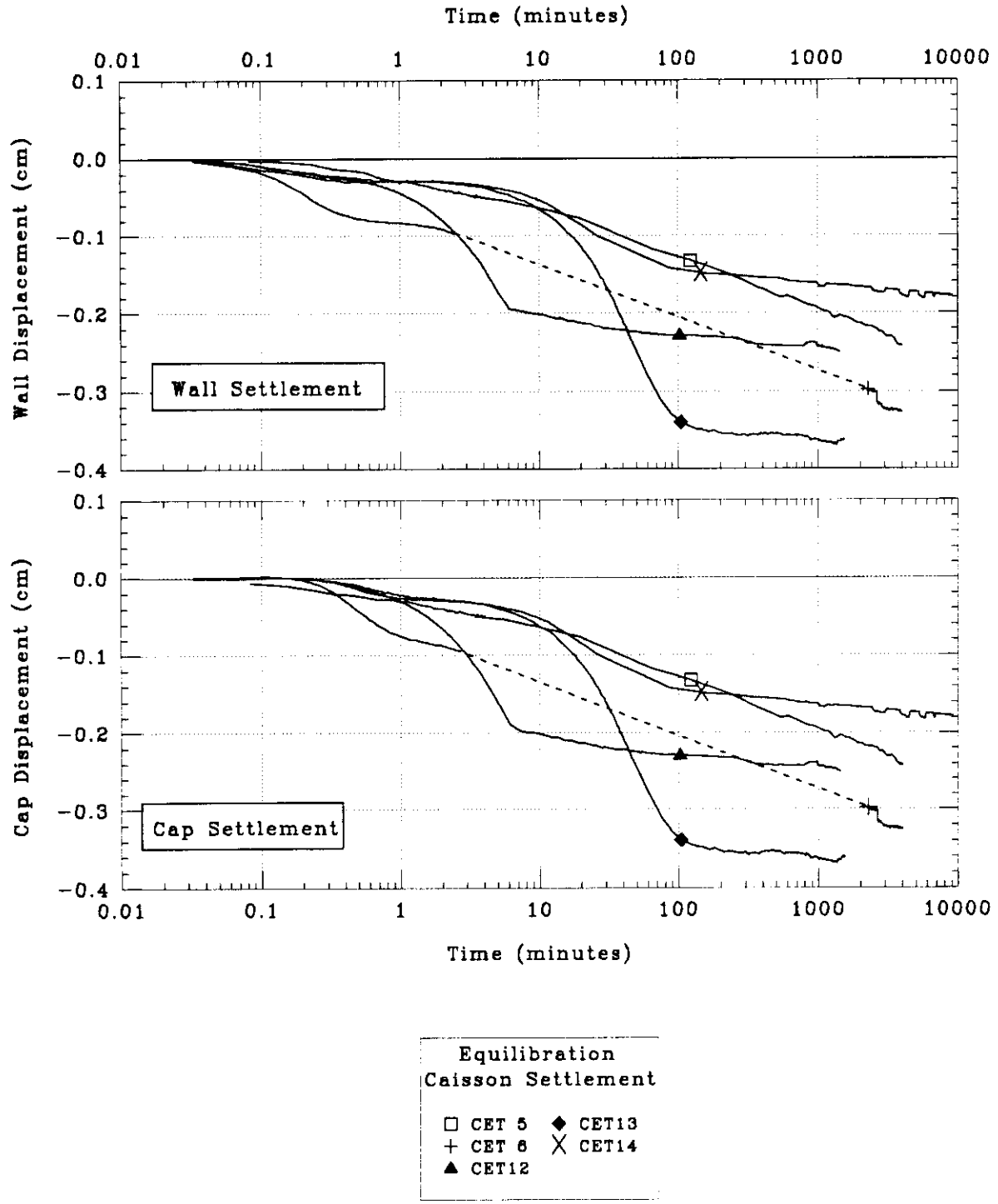

Figure 5.68 Measured Wall and Cap Settlement During Re-Equilibration for CET5-6,12-14

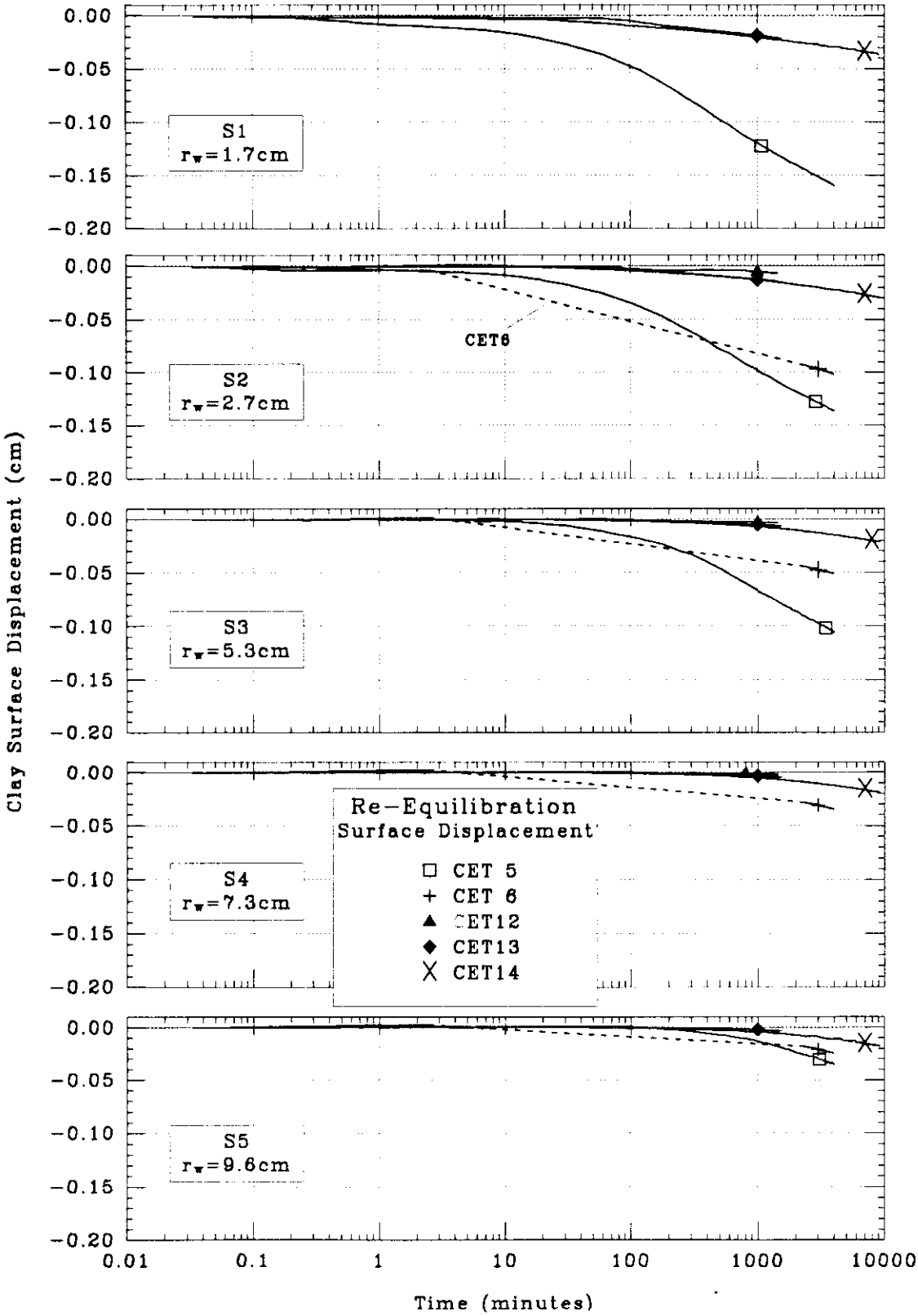

Figure 5.69 Measured Soil Surface Displacement by S1-S5 During Re-Equilibration for CET5-6,12-14

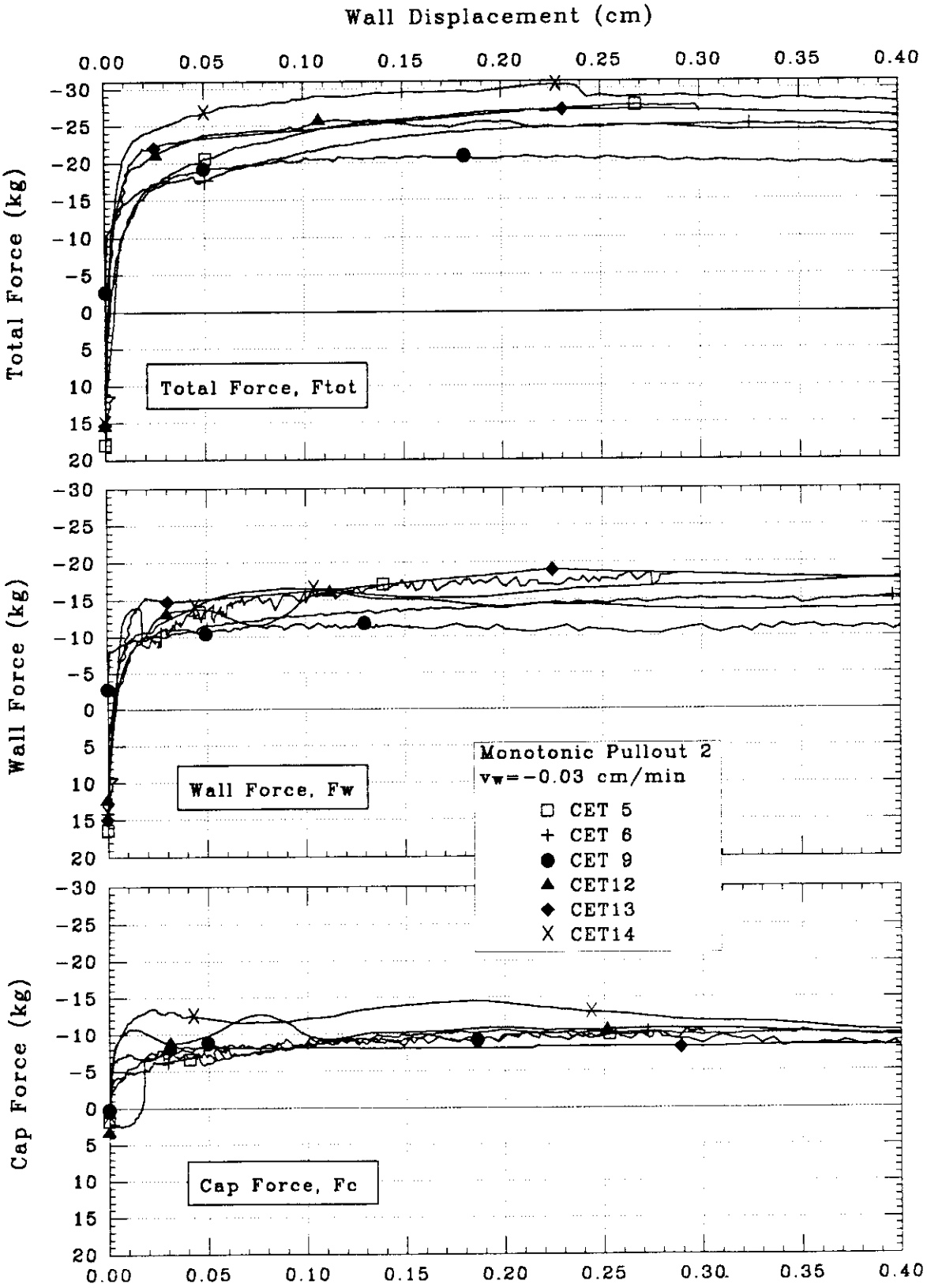

Figure 5.70 Measured Total, Wall, and Cap Force on Caisson During Monotonic Pullout 2 for CET5-6,9,12-14

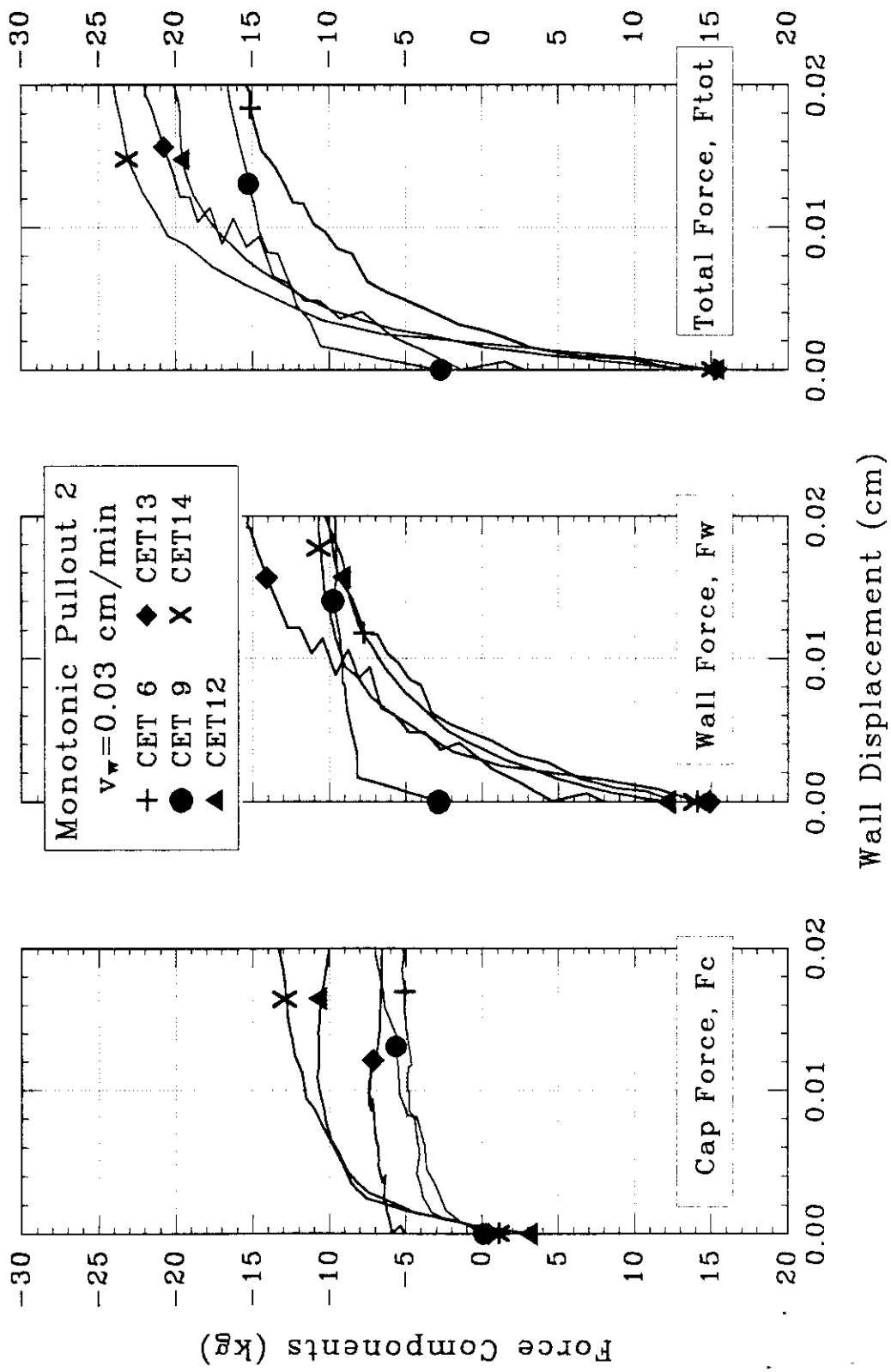

Figure 5.71 Measured Force Components During Monotonic Pullout 2 for CET6,9,12-14 (0.0 - 0.02 cm)

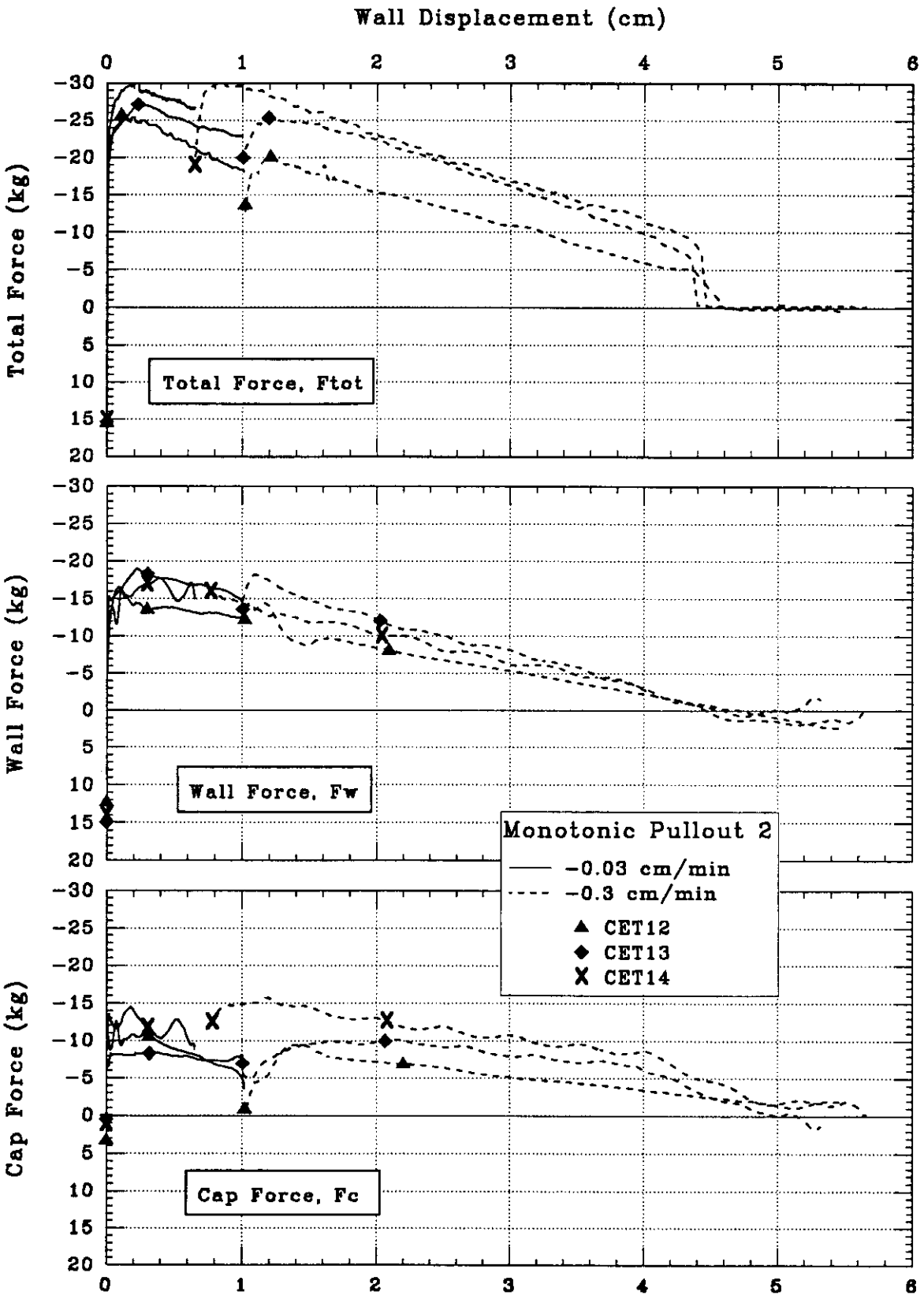

Figure 5.72 Measured Total, Wall, and Cap Force on Caisson During Monotonic Pullout 2 at Two Pullout Rates for CET12-14

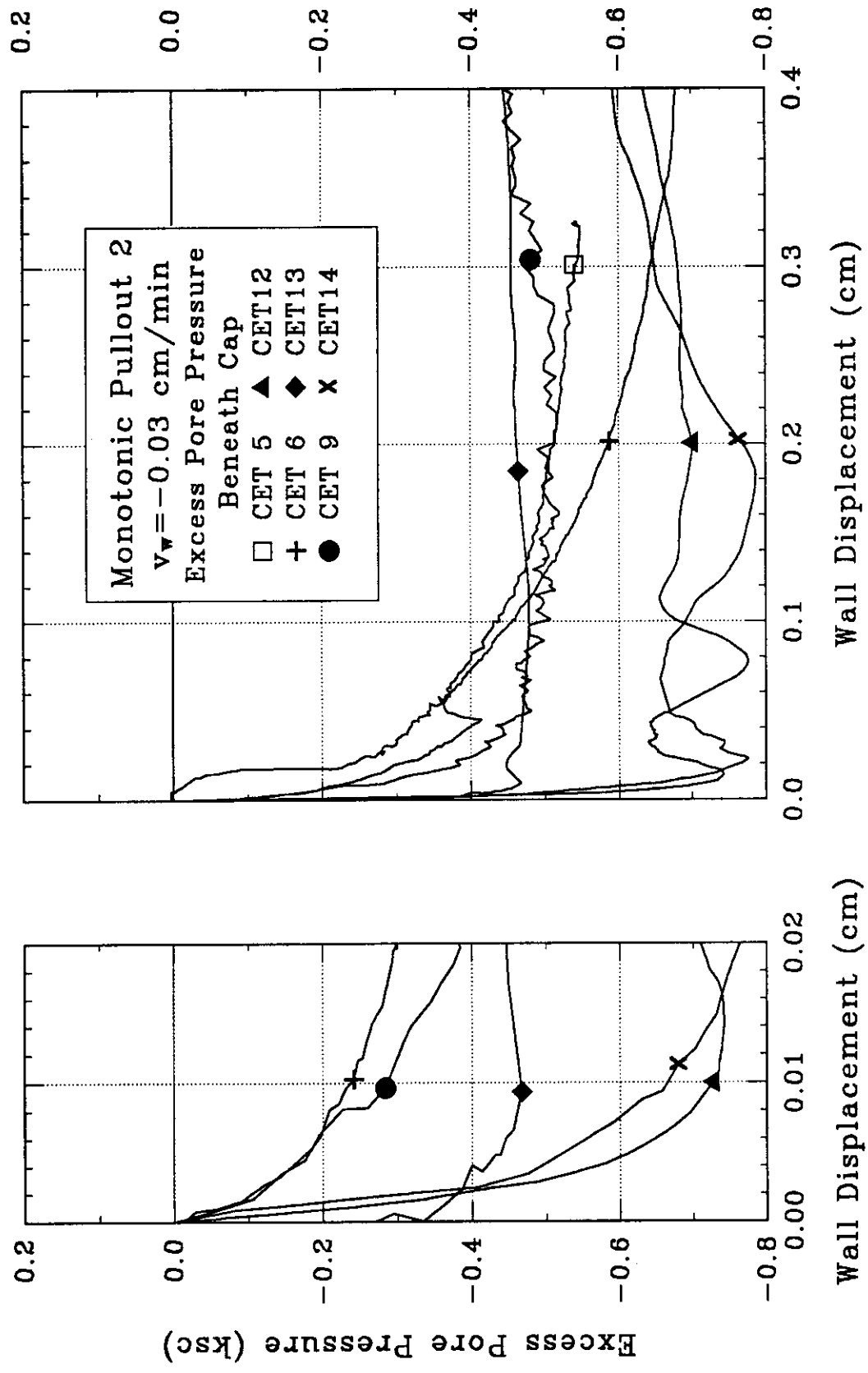

Figure 5.73 Measured Excess Pore Pressure Beneath Cap During Monotonic Pullout 2 for CET5-6,9,12-14

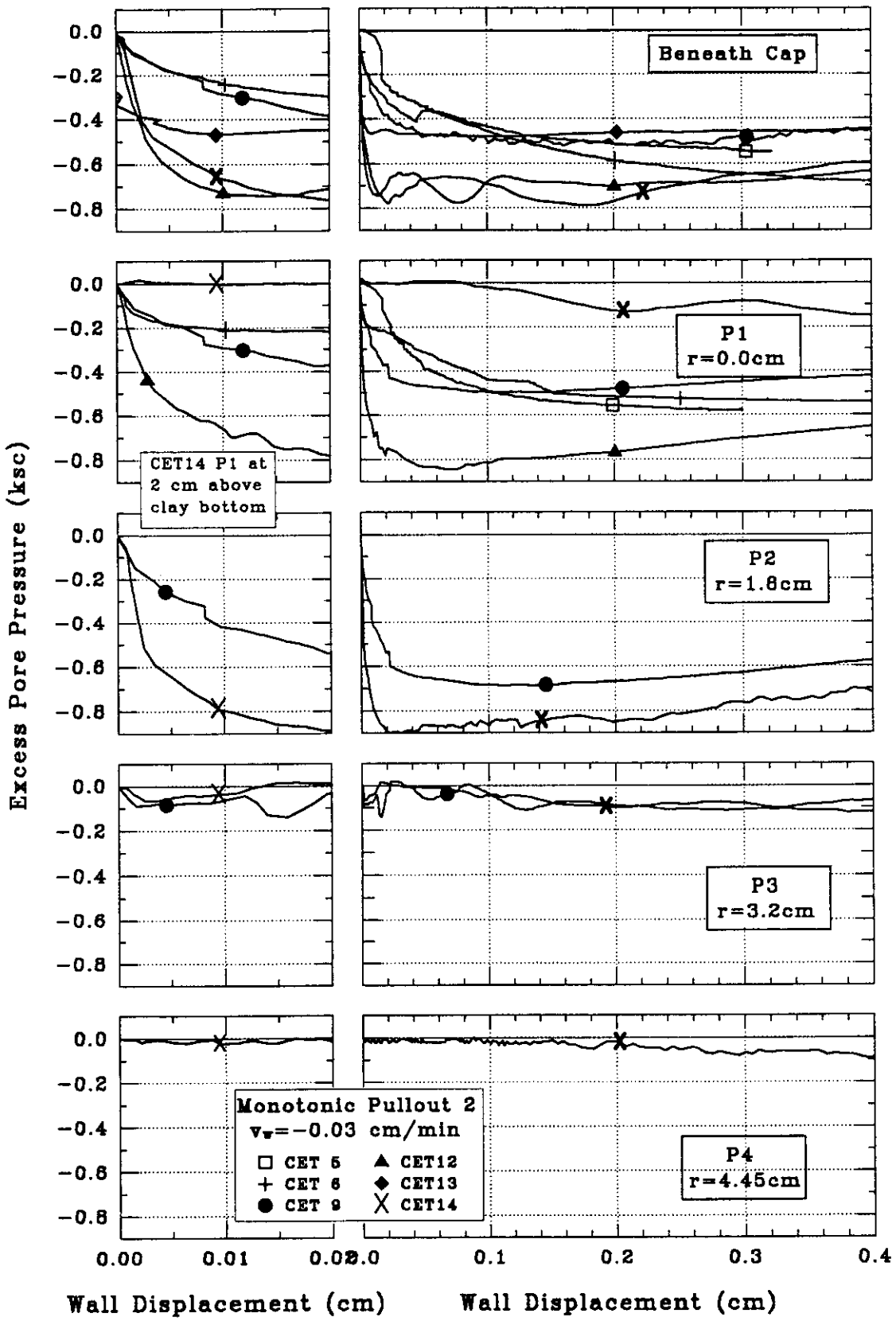

Figure 5.74 Measured Excess Pore Pressure by P1-P4 During Monotonic Pullout 2 for CET5-6,9,12,14

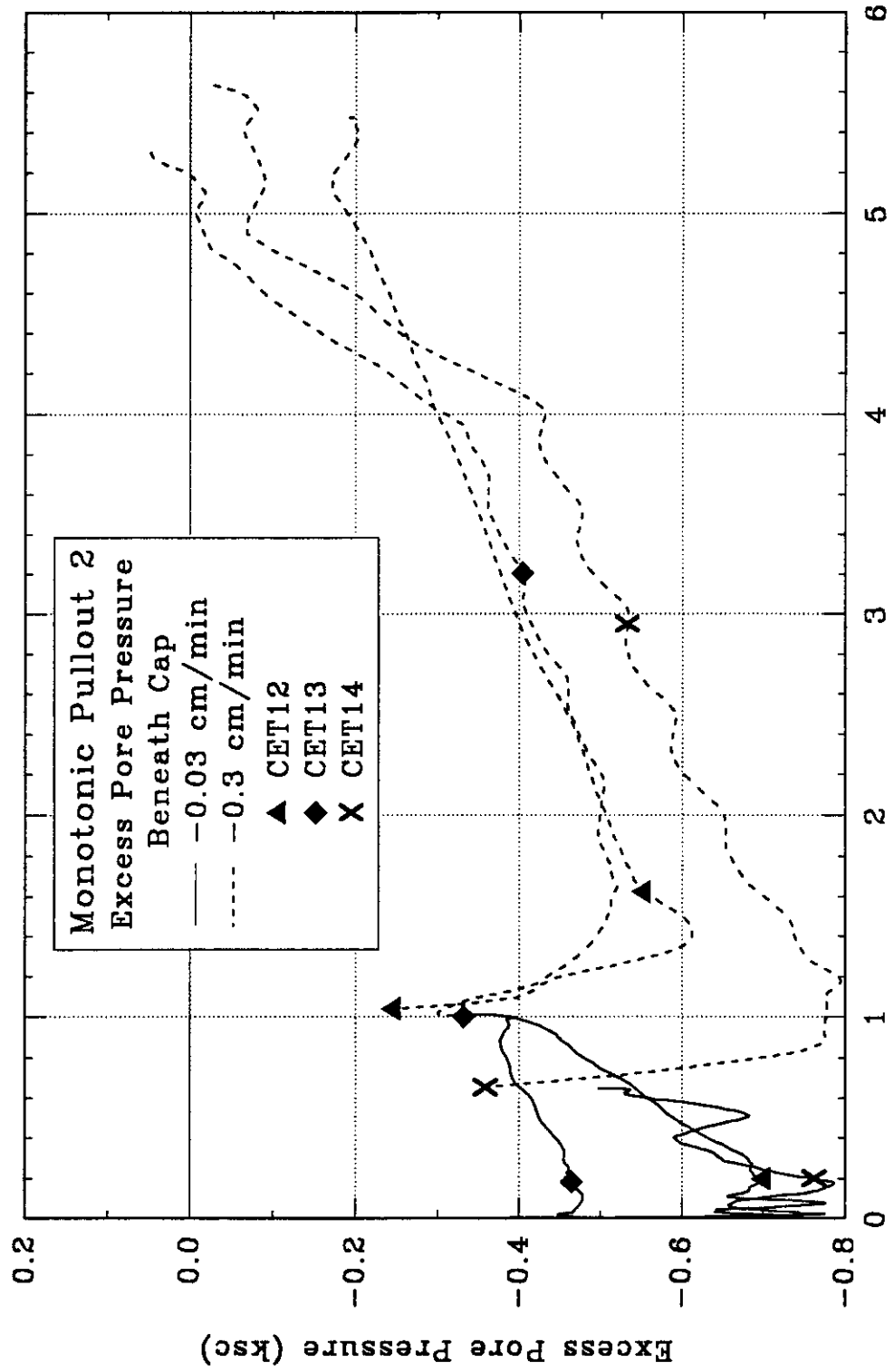

Figure 5.75 Measured Excess Pore Pressure Beneath Cap During Monotonic Pullout 2 at Two Pullout Rates for CET12-14

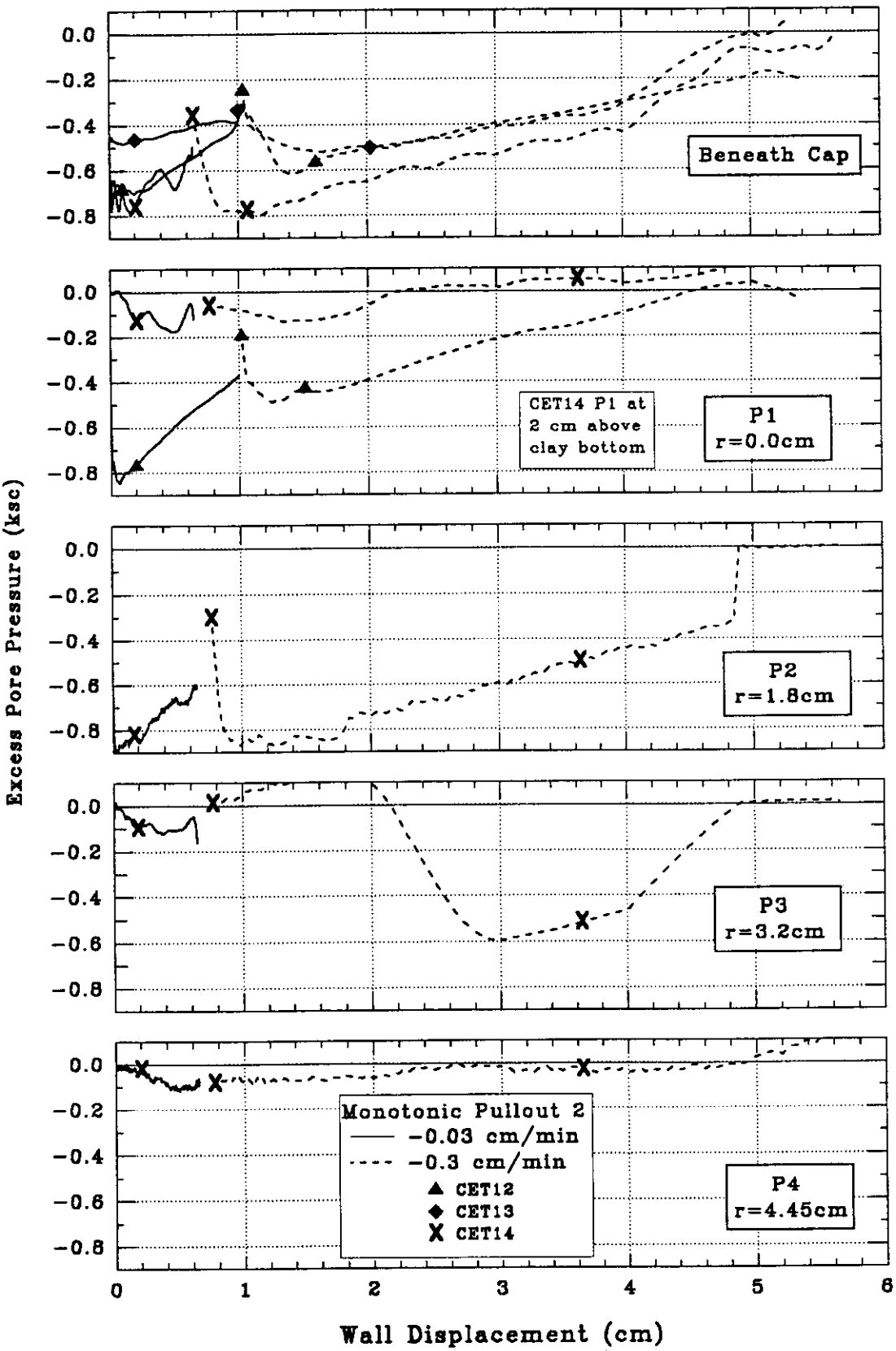

Figure 5.76 Measured Excess Pore Pressure by P1-P4 During Monotonic Pullout 2 at Two Pullout Rates for CET12,14

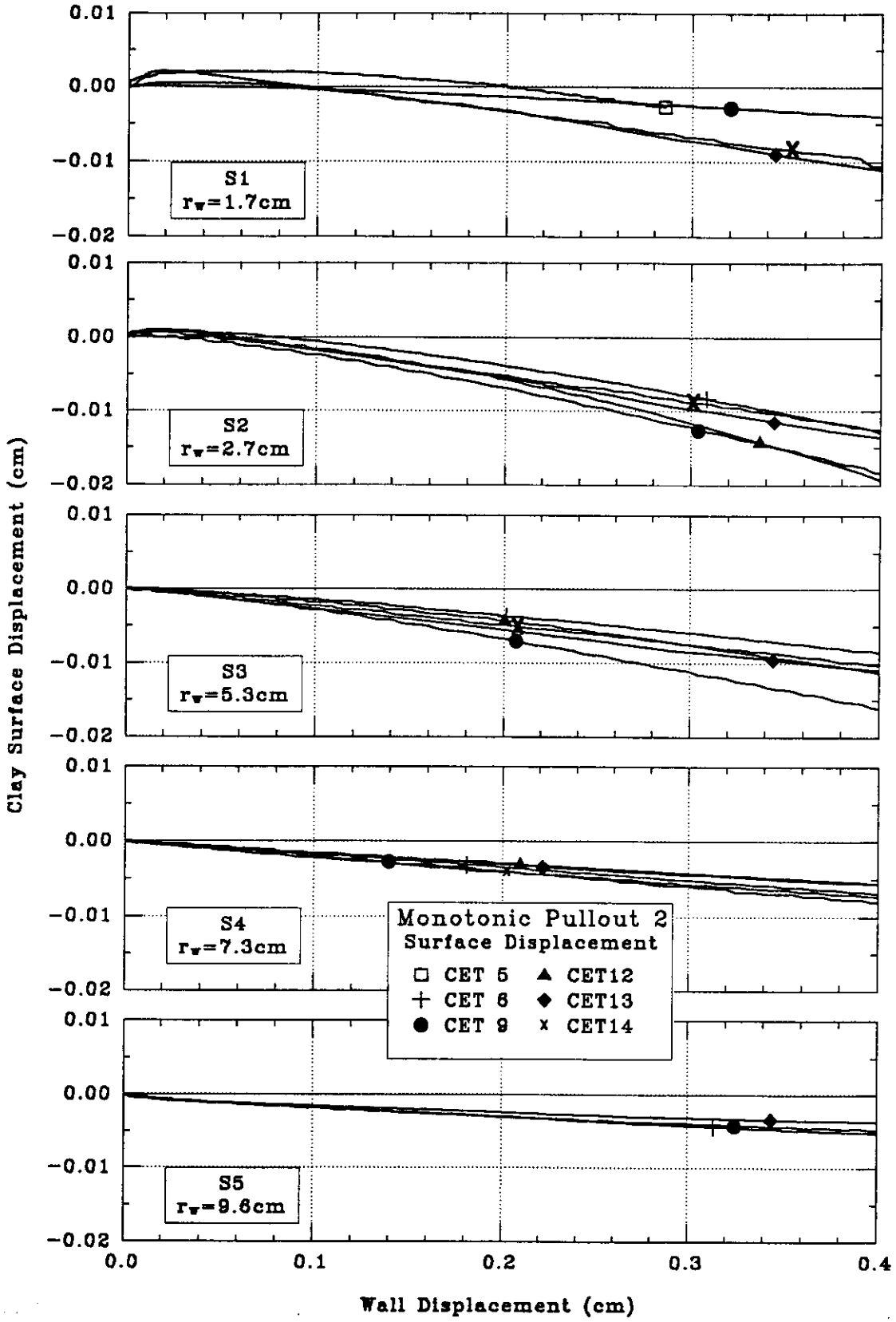

Figure 5.77 Measured Soil Surface Displacement by S1-S5 During Monotonic Pullout 2 for CET5-6,9,12-14 (Wall Tip Displacement, z_w=0 to 0.4 cm)

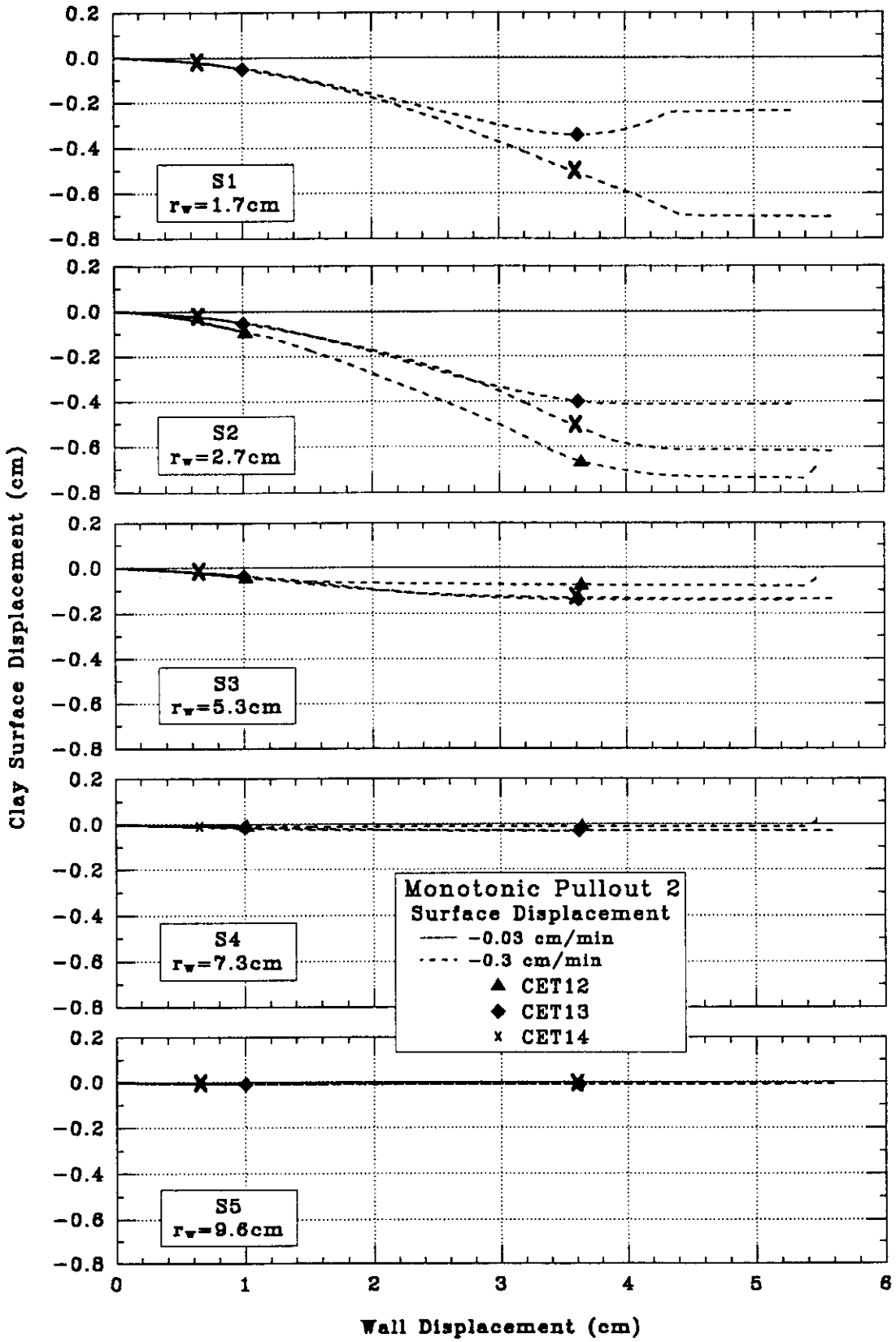

Figure 5.78 Measured Soil Surface Displacement by S1-S5 During Monotonic Pullout 2 at Two Pullout Rates for CET12-14

6. ANALYSIS OF CAISSON BEHAVIOR IN AXIAL TENSILE LOADING

6.1 INTRODUCTION

This chapter describes the axial load performance of single caisson cells in clay, based on numerical experiments using finite element analyses which incorporate advanced effective stress modeling of soil behavior. The analyses focus on two critical loading conditions for TLP anchorage applications, 1) quasi-static, continuous (monotonic) tensile loading to failure occurring within a relatively short time, such that there is relatively little migration of pore fluid within the surrounding soil (i.e. undrained shearing); and 2) long-term caisson response under sustained tensile loading, where re-distribution of soil resistance forces are associated with dissipation of load-induced excess pore pressures. The main goal of the analyses is to develop a clear understanding of the interactions between the caisson and the soil which control the relative magnitudes of the wall and cap reaction forces. The principal parameters of interest in this study are the shear strength and deformation properties of the soil, and the geometry of the caisson cell. The analyses make a number of important assumptions:

1. Caisson installation causes no disturbance of the surrounding soil (i.e. no deformations or change of in-situ stresses, pore pressures, or soil properties). In practice, the caisson anchorage will be installed through a combination of self-weight penetration and underbase suction. These processes will cause undrained shearing of the surrounding soil and will induce excess pore water pressures in low permeability clays. After installation, there will also be a period of re-equilibration involving dissipation of the excess pore pressures and concomitant changes in effective stresses. These processes are exactly analogous to pile set-up effects studied in previous research (Kavvadas, 1982; Chin, 1986; Whittle, 1987). It was the original intention of this research to simulate installation disturbance for caisson anchorages. However, this is not currently possible due to limitations in the existing strain path penetration models, which are restricted to conditions of steady, deep penetration. Recently, Sagaseta et al (1995) have extended the Strain Path Method (SPM; Baligh, 1985) to include the effects of the mudline on the deformations caused by shallow caisson penetration. These new SSPM (Shallow Strain Path Method; cf. Section 2.3) analyses offer a more realistic framework for modeling caisson installation (particularly behavior inside the soil plug) which will be used in future studies of caisson performance. Quantitative applications of the current analyses for wished-in-place caissons should be viewed with caution, although subsequent comparisons (sections 7.4, 7.5) show that they are capable of providing reasonable predictions of (1-g and centrifuge) model test data. The primary goal of these analyses is to develop a fundamental understanding of the geotechnical factors affecting the performance of full-scale caisson anchors in clay.

2. The analyses assume that the shear resistance at all soil-structure interfaces is controlled by the strength of the soil adjacent to the interface (i.e., no special interface elements are used in the finite element model). Similarly, there is no physical separation between the soil and caisson (at points below the lid of the caisson or the tip of the caisson walls). Instead, the interface stiffness and strength are controlled by effective stresses within the soil adjacent to the interface. This assumption is consistent with previous work done on friction piles in BBC (Azzouz et al., 1990).

Most of the analyses have been performed using the MIT-E3 soil model (Whittle, 1987; Whittle & Kavvadas, 1994) in order to represent, as reliably as possible, the generalized effective stress-strain-strength properties of typical marine clays. Section 6.2 illustrates the role of soil modeling by comparing predictions of monotonic axial load behavior for one caisson geometry using the Modified Cam Clay (MCC: Roscoe and Burland, 1968) and MIT-E3 soil models. Thereafter, Section 6.3 presents results of a parametric study (using MIT-E3) which examines the effects of wall length, L, and cell diameter, B, on the caisson response in monotonic axial loading. The analyses assume that the soil is K_0-normally consolidated (constant OCR = 1 soil profile) with input parameters corresponding to properties of Boston Blue Clay. Further results have also been obtained for one reference cell geometry for 1) properties corresponding to Empire Clay (Azzouz and Baligh, 1984; Whittle and Baligh, 1988), a typical high plasticity gulf of Mexico clay; and 2) an overconsolidated soil profile with constant OCR = 2.0.

One of the major factors controlling the current design of caisson anchorage is the long-term holding capacity for sustained tensile loads. Section 6.4 analyzes the re-distribution of wall and cap reaction forces which occurs when the caisson is subject to sustained tensile loads. The results provide insight on the mechanism of load transfer caused by the release of the underbase suction pressures, and relate the long-term load capacity to caisson geometry.

6.2 EFFECT OF SOIL MODEL FOR UNDRAINED AXIAL LOADING OF CAISSONS

6.2.1 Finite Element Model

This section presents the results of numerical experiments which evaluate the undrained, axial loading of a wished-in-place caisson using the MCC and MIT-E3 soil models. The analyses assume a 'base case' reference caisson geometry with wall length, L = 20m, outside diameter, B = (= 2R) = 20m, and wall thickness, 2w = 0.5m (i.e. aspect ratio R/w = 40, and embedment ratio L/B = 1.0). Figure 6.1 shows the finite element model of the caisson.

The soil is discretized using 404 triangular finite elements with mixed interpolation of displacement and pore pressure (T15-3; i.e., 15 displacement and 3 pore pressure nodes pre element; Section 2.2), with the mesh extending vertically to a distance z = 800m and laterally to r = 150m (i.e. z/B = 20 below the caisson, and r/B = 7.5 beyond the caisson wall).

The caisson is embedded in a deep clay layer with buoyant unit weight, γ_b=8.2 kN/m^3, and with soil model input parameters corresponding to K_0-normally consolidated Boston Blue Clay (cf. Table 6.1). Figure 6.2 compares predictions of shear stress-strain behavior from the two soil models with laboratory data from undrained triaxial and direct simple shear tests on K_0-normally consolidated BBC.

The measured data in triaxial compression and extension tests (Fig 6.2) show important aspects of the stress-strain-strength anisotropy of BBC. In compression tests, the undrained shear strength ratio, $s_{uTC}/\sigma'_{v0} = 0.33$ is mobilized at relatively small shear strains ($\gamma \approx 0.5\%$), and there is significant post-peak undrained brittleness. Much lower shear strengths, $s_{uTE}/\sigma'_{v0} = 0.18$, are mobilized in extension tests at large shear strains ($\gamma > 5$-10%). The MIT-E3 model describes very accurately these characteristic features of the measured stress-strain-strength behavior. In contrast, the MCC model predicts a unique shear strength in both triaxial compression and extension modes of shearing ($s_{uTC}/\sigma'_{vc} = 0.33$, based on parameters selected from triaxial tests), which is only mobilized for shearing to large strain, critical state conditions. The model also greatly underestimates the measured shear stiffness, especially in the extension mode of shearing, where predictions of linear stress-strain behavior reflect the elastic response for stress states inside the yield surface.

Figure 6.2b shows similar comparisons for undrained Direct Simple Shear tests (DSS) in a Geonor apparatus, in which the direction of applied principal strains is fixed at 45° to the vertical, while the direction of the principal stresses rotates during shearing. The measured data show an undrained strength ratio τ_{ff}/σ'_{vc}=0.20. The MIT-E3 model matches closely the measured stress-strain-strength properties, while MCC greatly overestimates the undrained shear strength, and grossly underestimates the stiffness for $\gamma \leq 1\%$.

Both MCC and MIT-E3 soil models assume normalized soil properties. Hence, the shear stiffness and undrained shear strength for the base case analysis (OCR = 1 soil profile) are proportional to the in-situ vertical effective stress, σ'_{vc} (= $\gamma'_o z$). Figure 6.1 shows the undrained shear strength profiles (s_{uTC}, s_{uDSS}, and s_{uTE}) for the MIT-E3 soil model alongside the FE model of the prototype caisson. Along the outside wall of the caisson the undrained shear strength ranges from s_{uDSS} = 0 to 33kPa along the outside wall, while the strength in triaxial extension at the base of the caisson s_{uTE}(z=20m) ≈ 26kPa. The corresponding reference strengths for MCC are s_{uDSS} = 0 to 60kPa and s_{uTE}(z=20m) ≈ 53kPa.

The caisson is modeled as an elastic material with total unit weight, γ = 18kN/m^3, Young's Modulus E_p = 3.4x10^4 MPa, and Poisson's ratio, ν = 0.2, using solid, 15-noded triangular

elements (T15) with cubic-interpolation of displacements. The selected elastic properties and wall thickness correspond to a heavily reinforced concrete section[1].

The caisson is loaded in tension assuming that the cap is perfectly rigid, such that all points on the cap undergo equal increments of vertical displacement. There is no separation between the lid and soil surface inside the plug and no slippage allowed between the caisson walls and the adjacent soil. Undrained conditions are approximated by using an artificial time frame for the loading sequence.

6.2.2 Results for the MCC Model

Figure 6.4 shows the cap, wall and total force components as functions of the vertical caisson displacement to a maximum value, $\delta_v = 0.5$m (i.e., $\delta_v/B = 2.5\%$). The wall force reaches a maximum resistance, $F_w \approx 49$MN at $\delta_0 = 0.25$ - 0.3m, while the cap force (underbase suction) continues to increase almost linearly with δ_v and shows no sign of reaching a limiting value over the displacement range reported in the analysis. At $\delta_v = 0.5$m, the cap force represents 69% of the mobilized total caisson resistance ($F_{TOT} = 156$MN). This result is consistent with experimental data which show that relatively large displacements are necessary to mobilize maximum caisson resistance. For example, Cauble (1996) reports $\delta_v/B \approx 10\%$ at maximum resistance from laboratory tests on miniature caissons (CET cell: Section 5.6). Clukey and Morrison (1993) show $\delta_v/B \approx 4\%$ at peak load from their centrifuge model tests.

Figure 6.4a shows the excess pore pressures relative to the underbase suction at a pullout displacement, $\delta_v = 0.5$m. The excess pore pressure is uniform inside the caisson ($\Delta u/\Delta u_{cap} \geq 90\%$ at the tip elevation) and forms a large zone of reduced pore pressures beneath the caisson. The analyses show significant excess pore pressures ($\Delta u/\Delta u_{cap} = 5\%$) along the centerline at a depth z/L = 3.5 (Fig. 6.4a). In prototype field situations drainage horizons within the vertical soil profile can significantly influence the excess pore pressure fields. The analyses also show negligible pore pressures occurring around the exterior wall of the caisson.

The assumption of perfect suction contact between the soil and caisson cap ensures that there are very small shear distortions within most of the soil plug, which displaces vertically with the caisson. Figure 6.4b shows the distribution of vertical strains in the soil along the centerline of the caisson. The results show strain gradients at the base of the caisson from $\varepsilon_v = 0.2\%$ at the tip elevation, to a maximum tensile strain, $\varepsilon_v \approx -2.2\%$ at z = 30m (i.e,. z/L = z/B = 1.5). The predicted strain levels decline very slowly with depth ($\varepsilon_v \approx -0.1\%$ at z = 100m).

---

[1] A rolled steel caisson with $E_s = 2.5 \times 10^5$ MPa (36000 ksi) and B = 20m has the same axial stiffness as the base case geometry using a wall thickness $t_s = 0.5(E_p/E_s) = 6.8$cm (2.68in).

Figure 6.5 summarizes normalized values of the radial effective stress and shear tractions (τ/σ'_{v0} and σ'_r/σ'_{v0}) acting along the inside and outside walls of the caisson at $\delta_v = 0.5$m. The full undrained shear strength of the soil is mobilized along the outside wall surface (in a direct simple shear mode) over the full embedded length of the caisson. There are minimal shear tractions acting on the inside wall of the caisson at $z \leq R$ where the underbase suction ensures that the soil plug displaces with the caisson. However, shear stresses increase towards the tip of the caisson, reaching, mobilizing a resistance $\tau/\sigma'_{v0} \approx 0.3$ at the tip elevation. These shear forces constitute a significant proportion of the total wall force (approximately 23%).

Figure 6.6 gives more information on the mobilization of shear stresses within the clay at $\delta_v = 0.5$m in the form of contours of the triaxial and direct simple shear stresses, $q/\sigma'_{v0} = (\sigma_v - \sigma_h)/2\sigma'_{v0}$, τ/σ'_{v0}, respectively. Below the base of the caisson, shearing occurs in a triaxial extension mode, however, the strains levels at this displacement are barely sufficient to cause yielding (cf. Figs. 6.2, 6.4b) of the clay.

6.2.3 MIT-E3 Analysis for Base Case Geometry

The analysis of the base case caisson geometry has also been performed using the MIT-E3 model with input parameters for K_0-normally consolidated BBC (Table 6.1). Figure 6.7 plots the load-displacement response of the caisson together with the wall and cap forces and their contribution to the total resistance. The results show the following:

1. The MIT-E3 model predicts a much higher initial caisson stiffness than previously shown for MCC (Fig. 6.3). There is a distinct yield in the total force-displacement response beyond which the total force continues to increase almost linearly with displacement, reaching a value of $F_{TOT} = 98.1$MN at a displacement of $\delta_v = 0.5$m. The analysis does not predict a limit load for the caisson. The wall and cap forces also show a very stiff initial response, with a yield occurring at $\delta_v \approx 0.05$m. Thereafter, the wall force reaches a limiting value, $F_w = 30$MN at $\delta_v \geq 0.1$m and all subsequent changes in the total resistance are due to increases in the cap force.
2. The MIT-E3 model predicts that relatively small displacements ($\delta_v < 0.1$m) are necessary to mobilize a maximum wall resistance, $F_w = 30$MN. The wall force remains almost constant for continued vertical caisson displacement to $\delta_v = 0.5$m. Figure 6.9 shows the distribution of the normalized shear and normal tractions (τ/σ'_{v0} and σ'_r/σ'_{v0}) on the inside and outside walls of the caisson at $\delta_v = 0.5$m. Along the outside wall, the interface tractions are consistent with the expected undrained direct simple shear behavior, with maximum shear resistance $\tau/\sigma'_{v0} = 0.2$. Hence, the outside wall of the caisson contributes $F_{wo} \approx 22$MN to the total wall resistance. The remaining fraction of the wall force (i.e. 8MN) derives from friction along the inside wall. Figure 6.10 shows that shear tractions along the inside wall decrease from the tip and are negligible at $z < 5$m. At $\delta_v = 0.5$m, the maximum shear traction inside the plug is

approximately $\tau/\sigma'_{v0} \approx 0.14$. Small changes in σ'_r/σ'_{v0} confirm (Fig. 6.9a) there is no shear failure of soil along the inner wall of the caisson. Very small increases in F_w for $\delta_v > 0.1$m (Fig. 6.9) are due to the mobilization of additional shear resistance along the inside wall of the caisson.

Figure 6.8 compares the centerline pore pressure rations and vertical strains with results ($\Delta u/\Delta u_{cap}$, ε_v) from the MCC analysis at the same cap displacement, $\delta_v = 0.5$m. Although both models predict similar magnitudes and locations of the maximum tensile strain below the base of the caisson ($\varepsilon_v \approx -2.5\%$ at $z \approx 30$m for MIT-E3 in Fig. 6.8b), there are significant differences in the strain distributions predicted by the two models. The strain field is much more localized in the MIT-E3 analysis due to its representation of small strain non-linear stiffness properties[2]. The soil model has minimal effect on the distribution of excess pore pressures predicted along the centerline of the caisson (Fig. 6.8a).

The representation of anisotropic stress-strain-strength properties in MIT-E3 makes the interpretation of stress conditions around the caisson more complex. Figure 6.10 shows contours of the normalized shear stress components q/σ'_{v0}, τ/σ'_{v0} for comparison with results presented for MCC (cf. Fig. 6.6). The failure mechanisms are very similar for the two analyses, showing full mobilization of shear tractions on the outside surface of the wall, while much larger cap displacements are required to mobilize the undrained shear strength in triaxial extension below the base of the caisson.

6.2.4 Undrained Capacity of Suction Caissons

The preceding calculations have found that relatively large cap displacements are necessary to mobilize the full capacity of prototype caissons in undrained, axial loading (pullout) conditions. Therefore, it is difficult to estimate the caisson capacity reliably from non-linear finite element analyses[3]. The section review two alternative methods of computing the caisson capacity using 1) limit equilibrium methods, and 2) numerical calculations of upper and lower bound limit loads.

6.2.4.1 Limit Equilibrium Calculation for Base Case Geometry

Several authors have used limit equilibrium calculations to estimate the undrained pullout capacity of caissons in clay. For example, Clukey and Morrison (1993) have proposed that the ultimate capacity of the caisson can be estimated as the sum of the external wall friction, F_{ESF}, and the 'reverse' bearing capacity, F'_{REB}:

$$F_{TOT} = F_{ESF} + F'_{REB} \qquad (6.1)$$

---

[2] The importance of non-linear shear stiffness is well known in settlement analyses for shallow foundations (e.g., Burland & Burbridge, 1983).

[3] Complete analyses will require a large strain formulation together with special interface elements.

If this calculation is applied to the base case geometry and BBC soil properties (as modeled by MIT-E3), then the external shaft resistance is given by:

$$F_{ESF} = \pi B L \bar{s}_{uDSS} = 400\pi(16.4) = 20.6MN \tag{6.2}$$

and $\bar{s}_{uDSS}$ is the average shear strength in undrained direct simple shear (at z = 10m).

This calculation is approximately 70% of the predicted maximum wall force at $\delta_v/t > 0.3m$ in the MIT-E3 analysis (Fig. 6.8), due to the development of shear tractions on the inside wall of the caisson.

There are no closed-form analytical expressions for the bearing capacity of an embedded cylinder in a non-homogeneous clay, however, F'_{REB} can be estimated from the plasticity solutions for a surface strip footing on a non-homogeneous clay layer given by Davis and Booker (1973), together with empirical correction factors proposed by Kulhawy et al. (1983):

$$\begin{aligned} F'_{REB} &= A_b F\left\{(2+\pi)\, s_{ub} + \frac{\rho B}{4}\right\} \alpha_c\, \alpha_d \\ &= 314[m^2]\; 1.1\left\{5.14(34.4[kPa]) + \frac{1.64(20)\;[kPa]}{4}\right\}(1.2)(1.13) = 86.6MN \end{aligned} \tag{6.3}$$

where F = 1.1 is estimated from Figure 6.11 (from Davis and Booker, 1973), s_{ub} = 34.4 kPa is the undrained strength in triaxial extension (from Fig. 6.1) at a depth, z = 30m (i.e., at B/2 below the tip of the caisson, as recommended by Kulhawy et al., 1983; Clukey & Morrison, 1993), $\rho = ds_u/dz$ = 1.64 kPa/m is the strength variation with depth (in an average DSS shear mode), α_c = 1.2 and α_d= 1.13 are empirical correction factors for cylindrical geometry and embedment depth using expressions presented by Kulhawy et al. (1983)[4].

According to equation 6.1, the total caisson capacity for the base case geometry, F_{TOT} = (20.6 + 86.6) = 107.2MN[5]. According to this estimate, the caisson has mobilized almost 92% of its ultimate capacity in finite element calculations at δ_v = 0.5m (Fig. 6.7).

Although the preceding calculation is very simple and easy to perform, there is no way of validating the computed capacity (other than physical model testing). Indeed, the correction factors represent a significant factor in the calculations (36% modification!), while the selection of the reference undrained strength for equation 6.3 is backfitted to available model test data. These types of problem are common to limit equilibrium methods (which generally involve a search procedure to locate the critical failure surface), and certainly restrict their use as a method of validating finite element calculations.

---

[4]Calculations using the assumptions of Clukey & Morrison (1993) give F_{base} = 1750 MN. In this case, base capacity is calculated via $F_{base}=qA_c = N_c S_{uTE}\alpha_c\alpha_d A_c = (5.14)S_{uTE}(1.20)(1.26)(314m^2)$, where N_c is the bearing capacity factor, α_c is the shape factor for a cylinder, α_d is the depth factor for B/L=1, and A_c is the cross-sectional area at the base of the caisson.

[5] A similar calculation for the MCC properties gives, F_{TOT} = 38 + 178 = 216MN.

6.2.4.2 Numerical Limit Analysis for Base Case Geometry

An alternative method for computing the caisson capacity, that uses numerical solutions of upper and lower bound limit loads, is summarized in Section 2.4. The analyses use finite element methods to discretize the problem geometry and interpolate the field variables (stresses and velocities for lower and upper bound calculations, respectively), and linear programming methods to formulate and optimize the collapse loads. The calculations require no search procedure, and can be applied to generalized strength profiles, caisson cell geometries and loading directions (cf. section 7.4.5). However, the current programs (Ukritchon, 1995) are restricted to plane strain problems, and assume an isotropic undrained shear strength criterion for the clay (Tresca yield).

Figures 7.12 and 7.13 summarize the lower and upper bound limit analyses for the base case caisson geometry. The analyses assume an average undrained strength ratio, $s_u/\sigma'_{v0} = 0.20$, such that the strength gradient of the clay, $\rho = 1.64$kPa/m. The caisson is represented by a series of rigid beam and joint elements[6] (Ukritchon, 1996), and full adhesion is allowed along all soil-structure interfaces.

The lower bound analysis maximizes the vertical force, Q_L, that can be applied to the caisson cap, while maintaining a statically admissible stress field. Note that the symbol Q [f/l] is introduced to represent the forces per unit width in all planar analyses in order to distinguish these calculations from the forces obtained for axisymmetric geometries, F [f]. Figure 7.12 summarizes the predictions of the lower bound stress field, with a collapse load, $Q_L = -5993$kN/m. The lower bound analyses maximizes the zone of failure in the soil (cf. Fig. 7.12d). Forces on the cap and sidewalls can be computed directly from vertical equilibrium (using the lower bound stress fields), $Q_c = -4950$kN/m and $Q_w = -1043$kN/m, respectively.

The upper bound collapse load is computed by minimizing the external work of the applied load on the caisson necessary to generate a failure mechanism in the clay (using the principle of virtual work). The analysis solves the upper bound collapse load $Q_U = -6510$kN/m, and generates a kinematically admissible velocity field, Figure 7.13. The upper bound calculation shows that there is no failure within the plug, while the zone of basal failure extends to a maximum depth, $z \approx 35$m. Outside the caisson, the velocity field indicates a local zone of shear along the wall, which is separated from movements associated with the basal failure mechanism (the latter extends to a distance $x \approx 55$m at the ground surface).

The true collapse load for the base case can now be bounded by, $-5993 \leq Q \leq -6510$ kN/m (i.e., accuracy of ±4.3%). In order to apply these analyses for an axisymmetric geometry, the results must be scaled to reflect differences in the relative surface areas of the cap and side walls. Throughout the remainder of this chapter, this is accomplished as follows:

---

[6] The programs have the capability to model structural failure in bending, shear and axial loading.

$$\text{Lower Bound:} \quad F_{TOT} = F_c + F_w = \pi \left\{ \left(\frac{Q_c}{Q}\right)\frac{B}{4} + \left(\frac{Q_w}{Q}\right)\frac{B}{2} \right\} Q \tag{6.4}$$

where (πB/4) and (πB/2) are the scaling dimensions for the cap and wall respectively

For the base case geometry, the lower bound collapse load is then:

$$F_{TOT} = \pi \left\{ \left(\frac{4950}{5993}\right)\frac{20}{4} + \left(\frac{1043}{5993}\right)\frac{20}{2} \right\} (-5.993) = -110.5\text{MN}$$

Assuming that the ratio of the upper and lower bound collapse loads is not affected by the caisson geometry (i.e., $Q_U/Q_L = F_U/F_L$), then the predicted capacity is in the range $-110.5 \le F_{TOT} \le -120.0$MN. Furthermore, the numerical limit analyses are also able to give estimates of the limiting wall and cap forces, $-32.8 \le F_w \le -35.6$MN, and $-77.8 \le F_c \le 84.5$MN. These calculations cannot be expected to match exactly the results of the axisymmetric finite element analyses (which include anisotropic stress-strain-strength properties of BBC using the MIT-E3 model). However, Figure 6.7 shows the computed collapse loads do tie in very closely with the finite element solutions and hence, provide a reasonable basis for estimating the axial pullout load capacity of caissons in clay.

6.2.4.3 Generalization of Collapse Loads for Offshore Caissons in Clay

After demonstrating the effectiveness of the numerical limit analyses for estimating the capacity of the base case caisson geometry, further calculations have been carried out to generalize the results for other (thin-walled) caisson geometries. All of these analyses assume profile where the undrained shear strength of the clay, $s_u = \rho z$, where z is the depth below the mudline. Figure 7.14 summarizes the lower and upper bound collapse loads (values of Q_U, Q_L are also tabulated in Table 6.2) as functions of the caisson embedment ratio, B/L. The collapse loads are presented in a normalized format $Q/\rho(B/2+L)^2$, such that the results converge to the existing solutions of Davis & Booker (1973) for surface footings ($L/B \rightarrow 0$), and to the limiting skin friction of a deep wall when $L/B \rightarrow 0$.

Figures 6.15-6.18 compare the lower and upper bound solutions for caissons with embedment ratios, L/B = 3, 0.25. The mechanism of collapse for the deep caisson is similar to the base case geometry, with no failure of soil inside the plug and a large lateral zone of yielding associated with basal failure. In contrast, failure extends inside the caisson at low embedment ratios (L/B = 0.25; Fig. 6.18), with a much smaller failure zone in the surrounding soil.

Table 6.3 and Figure 6.19 summarize the limiting wall and cap forces obtained from the lower bound analyses at the selected embedment ratios. These data (Q, Q_c/Q, Q_w/Q) can then be used to estimate the capacity of axisymmetric caissons by scaling the surface areas using equation 6.4. This procedure is used to calculate reference caisson capacities for comparison with the parametric study of caisson performance in the next section.

6.3 PARAMETRIC ANALYSIS OF UNDRAINED AXIAL LOADING

6.3.1 Cell Geometry

Table 6.4 summarizes the analyses that have been performed to study the effects of the caisson geometry on the undrained axial load response. The two principal parameters of interest are the wall length, L, and the outside cell diameter, B. The parametric study has considered combinations of B = 10 to 40m and L = 5 to 120m, with embedment ratios in the range L/B=0.5 to 3.0. Each of these calculations has assumed a constant wall thickness, t = 0.5m, with elastic properties corresponding to reinforced concrete ($E = 3.4 \times 10^4$ MPa, $\nu = 0.2$). These parameters are equivalent (i.e., with the same axial stiffness, EA) to a steel caisson ($E = 2.5 \times 10^5$ MPa; $\nu = 0.2$) with wall thickness, t_s = 6.8cm. Assuming that there is no installation disturbance, the wall thickness has very little effect on the undrained axial load response of the caisson. Table 6.4 summarizes the force components at a reference displacement, δ_v = 0.5m, including three tests with the same primary dimensions (B = 20m, L = 20m) but with wall thickness' 2w = 0.1m, 0.5m, and 2.0m (U-15, U-2, U-16). For this (rather extreme) range of wall thickness', there is almost no effect on the predicted forces, confirming previous assumptions that the wall is effectively rigid. The excess pore pressure at the cap is a function of the displacement δ_v and is effectively independent of the wall thickness. Hence, reductions in the cap force at a given value of δ_v in Figure 6.20 are solely related to variations in the basal area of the cap, A_b, with wall thickness.

6.3.2 Effect Of Wall Length

The effects of caisson wall length can be established by comparing the results from a series of analyses with B = 20m and L = 10, 20, 30, 40 and 60m (i.e. L/B=0.5, 1.0, 1.5, 2.0, and 3.0; tests U1, U3-U6 in Table 6.4) in Figure 6.20a. In all cases the calculations have been continued to a maximum vertical cap displacement, δ_v = 0.5m (δ_v /B = 2.5%).

It is immediately apparent that all of the load-displacement curves have the same characteristic form. In each case, there is a well defined yield point at $\delta_y \approx$ 0.1m, which is effectively independent of wall length. Further displacement of the caisson occurs with small increases in the wall resistance. The cap response is initially highly non-linear, with stiffness similar to the wall, but continues to harden almost linearly with displacements $\delta_v > 0.1$m. The initial cap stiffness is notably smaller than the wall stiffness for the small embedment ratio L/B = 0.5 (Fig. 6.20b).

Results for the shallowest embedment ratio (L/B = 0.5) show a maximum wall force, $F_w \approx$ 7MN, that represents only 18% of the total caisson resistance (F_{TOT} = 39MN), while the cap force carries more than 70% of the load at small displacements. For intermediate caisson embedment depths (L/B = 1.5, 2.0) the cap force carries more than 50% of the load at relatively large

displacements (δ_v > 0.1-0.2m) where the wall force is already fully mobilized. At the largest embedment ratio (L/B = 3.0; Fig. 6.20a) the wall force remains the major component, carrying more than 60% of the load at δ_v = 0.5m.

Figure 6.20b summarizes the total, wall, and cap forces as functions of the wall length at δ_v = 0.1m and 0.5m. The figure also includes reference values of caisson capacity from the numerical limit analyses (section 6.2.4.3), and the external wall force F_{ESF} from conventional limit equilibrium calculations (eqn. 6.2). These figures show clearly the hardening of both the cap and wall resistance forces as functions of the cap displacement. For L ≥ 20m, the cap resistance is a linear function of the embedment depth (at a given δ_v), and reflects the modeling of the soil profile in which both the stiffness and undrained shear strength of the clay increase linearly with depth. The cap force does not reach a limiting resistance, but increases almost linearly for displacements δ_v = 0.1 - 0.5m. Table 6.4 reports the tangent cap stiffness at δ_v = 0.5m for all of the geometries considered in the parametric study:

$$K_c = \frac{\Delta F_c}{\Delta \delta_c} \tag{6.5}$$

and the magnitude of the cap force can be computed from the linear relation:

$$F_c = f_{c0} + K_c\, \delta_v \tag{6.6}$$

where f_{c0}, K_c are dimensional empirical constants.

As expected, the wall force increase is proportional to $[L^2]$ (i.e., surface area of the shaft). In all cases, the computed wall force is larger than F_{ESF} at δ_v = 0.5m due to shear tractions inside the soil plug (and tensile forces at the wall tip). The ratio $F_w(0.5)/F_{ESF}$ decreases from 1.36 at L/B = 0.5, 1.0 to 1.06 at L/B = 3.0. These results confirm that significant shear tractions only occur close to the base of the soil plug for undrained loading at small cap displacements.

The comparisons between the non-linear finite element and numerical limit loads, suggest that 85 - 90% of the total capacity is mobilized at δ_v = 0.5m for caissons with shallow wall embedment (L ≤ 20m), but this ratio drops to less than 70% for L = 60m. One of the underlying reasons for this trend is that the lower bound limit calculation predicts much higher wall forces than are computed by the finite element analysis. This comparison should be regarded with caution pending more reliable limit analyses for axisymmetric geometries.

6.3.3 Effect Of Caisson Diameter

An analogous series of analyses have been performed for caissons of fixed wall length, L = 20m and diameters, B=10, 20 and 40m (i.e. L/B=0.5, 1.0, and 2.0; cases U9, U2, U11 respectively in Table 6.4). These analyses show the same characteristic load-deformation features described previously for δ_v ≤ 0.5m. However, there are obvious differences in the relative magnitude of the cap and wall forces (Table 6.4). Figure 6.22 summarizes the forces for each

diameter at displacements, δ_v =0.1m and 0.5m, corresponding to the approximate yield point in the overall behavior, and the maximum displacement for each analysis. As expected, the wall force is a linear function of B (i.e., proportional to the surface area). However, the computed values of F_w at δ_v = 0.5m are much larger (almost 50%) than values of F_{ESF} for largest diameter caisson with B = 40m, indicating the increased role played by shear resistance along the inside surface of the wall.

The magnitude and development of the cap force for $\delta_v \geq 0.1$m can be approximated by the linear relation given in eqn. 6.6 with parameters listed in Table 6.4. Figure 6.23 presents the values f_{c0}, K_c for all of the caisson geometries considered in this study (Table 6.4) as unique functions of the interior surface area of the caisson. These results are useful for estimating the mobilization of the cap force for interpolated caisson geometries.

6.3.5 Effect of Stress History

The most likely application of caissons for TLP anchorage will occur in deep water sites where the marine sediments are normally to lightly overconsolidated. Recent data from a number of sites in the Gulf of Mexico has found that one possible mechanism for overconsolidation is the occurrence of overpressures and deposits (creating upward flow in the clay, referred to as 'shallow water flow'). This section illustrates the effects of stress history on the undrained axial load response (base case geometry) for a caisson installed in an overconsolidated BBC with OCR = 2.0.

Figure 6.23 compares predictions of the MIT-E3 model with laboratory data for BBC in undrained triaxial and direct simple shear tests at OCR=2.0. The figure shows that there is very good agreement between the predicted and measured stress-strain-strength behavior in all three modes of shearing. Table 6.5 compares the predicted values of the key engineering properties of BBC at OCR's = 1.0 and 2.0. The undrained shear strength ratio, s_u/σ'_{vc}, at OCR = 2.0 is 70 - 90% higher than at OCR = 1.0 (in extension and DSS shear modes). The cap stiffness of the caisson is primarily related to the shear stiffness in the triaxial extension shear mode. Table 6.4 shows that the non-linear secant shear modulus, G_{sec}/σ'_{v0}, at OCR = 2.0 is typically 12 - 25% higher than the stiffness of the normally consolidated clay at three characteristic strain levels.

Figure 6.24 compares the load-deformation response for the base case cell geometry in BBC at OCR's = 1.0 and 2.0. The two analyses show qualitatively very similar mobilization of the wall and cap forces with cap displacement. However, the total caisson resistance, wall force and cap force are consistently 30 - 33% higher for the analysis at OCR = 2.0 at the reference displacement δ_v = 0.5m. As in the previous analyses, there is a well-defined displacement corresponding to yield of the wall force ($\delta_v \approx$ 0.1m), with a maximum wall resistance, $F_w \approx$ 40MN. The maximum wall force is only very slightly higher than the expected limiting shear resistance on the outside wall of the caisson (F_w/F_{ESF} = 1.01; for s_{uDSS}/σ'_{v0} = 0.40, Table 6.5).

Figure 6.25 shows that this result is coincidental, and only arises because larger caisson displacements are necessary to mobilize the shear resistance along the outside wall of the caisson at OCR = 2.0.

6.3.6 Effect of Soil Type

The most probable sites for the future application of TLP anchorage using suction caissons are at deep water sites in the Gulf of Mexico. The engineering properties of typical Gulf of Mexico clays differ significantly from those of Boston Blue Clay used in the previous analyses. The most reliable basis for evaluation caisson performance in typical Gulf of Mexico clays the extensive previous research on soil properties and pile performance at the Empire site in Louisiana. Lutz (1985) has reported an extensive program of laboratory tests on the highly plastic Empire Clay ($I_p \approx 60\%$), whose characteristic index properties are similar to other Gulf of Mexico clays. Azzouz and Morrison (1988) have compared field measurements on a miniature instrumented pile shaft (PLS cell) at both the Empire and MIT test sites (BBC in Saugus, MA). Whittle and Baligh (1988) have selected model input parameters and performed detailed analyses of the pile shaft performance at both sites.

This section presents results of undrained axial loading for a caisson (base case geometry) installed in a soil with properties corresponding to K_0-normally consolidated Empire Clay. The effects of soil type can then be established through comparisons with previous analyses for BBC.

Figure 6.26 compares MIT-E3 predictions with laboratory data for K_0-normally consolidated Empire Clay in undrained triaxial compression and extension and direct simple shear tests. Model input parameters where previously reported by Whittle and Baligh (1988) and are listed in Table 6.1. The measured undrained strength ratio ranges from $s_{uTE}/\sigma'_{vc} = 0.19$ to $s_{uTc}/\sigma'_{vc} = 0.24$, and the clay has a much lower shear stiffness than BBC (Table 6.5). The MIT-E3 model gives an excellent description of the undrained compression and direct simple shear tests, but overestimates the shear stiffness in extension at shear strains $|\varepsilon_v - \varepsilon_h| < 5\%$.

Figure 6.27 compares the model predictions of undrained shear behavior for BBC and Empire Clay. The following points should be noted:

1. The Empire Clay has a much higher initial lateral effective stress than BBC ($K_0 = 0.62$ and 0.48, respectively).
2. The largest differences occur in the triaxial compression shear mode, where the undrained strength ratio of Empire Clay ($s_{uTC}/\sigma'_{vc} = 0.24$) is actually less than the shear stress for BBC ($[1-K_0]/2 = 0.26$).
3. The undrained shear strength of Empire Clay in triaxial extension is slightly higher than that predicted for BBC ($s_{uTE}/\sigma'_{vc} = 0.16$ and 0.14 respectively), and only 6% less than BBC in direct simple shear (see Table 6.4).

4 The secant shear modulus of Empire Clay is much lower than BBC at small strain levels (by a factor or 2-3 times, for $\gamma \leq 0.01\%$; Table 6.5). However, for $\gamma \geq 0.1\%$, the differences in secant stiffness are less than 50%.

Figure 6.28 compares the undrained axial load-displacement response for the base case caisson geometry in Empire Clay and BBC. The total caisson resistance, F_{TOT} = 69MN, at the reference displacement (δ_v = 0.5m) is approximately 30% smaller than that obtained in the BBC analyses.

The initial cap stiffness of Empire Clay is much lower than that of BBC, and there are large differences in the mobilization of the cap force for $\delta_v < 0.1$m. However, for displacements, $\delta_v \geq$ 0.3m, the cap force follows the same linear relation described previously (eqn. 6.6) with a stiffness, K_c = 64MN/m approximately 30% below that of BBC. These results are consistent with differences in the undrained triaxial extension behavior described above.

The mobilization of the wall force occurs much more gradually for the Empire Clay, with no distinct yield point. The wall resistance hardens to F_w=24.5MN at δ_v =0.5m, which is more than 25% larger than the limiting external skin friction (F_{ESF}). Relatively small differences in the maximum wall force are consistent with the similarities in the undrained direct simple shear strengths of BBC and Empire Clay (Table 6.5).

Figures 6.29a and b compare the excess pore pressure ratios, $\Delta u/\Delta u_{cap}$ and vertical tensile strain along the centerline of the caisson at δ_v =0.5m. The results show that the distributions of pore pressure ratios and vertical strains are practically identical for both BBC and Empire Clay (although there are large differences in the magnitudes of Δu_{cap}) in spite of large differences in the stress-strain-strength properties of those two materials. This result confirms previous observations that the strain distribution is largely controlled by the incompressibility constraint (undrained conditions) and can be estimated independent of the soil properties (i.e., the problem is kinematically controlled). The differences in the magnitudes of the pore pressures are due to controlled by the shear stiffness, initial K_0 conditions and effective stress paths predicted for the two types of soil.

6.4 SUSTAINED TENSILE LOADING

6.4.1 Introduction

The previous section has described the axial load-deformation response of the caisson for short-term, tensile loading in low permeability clay. The caisson performance is controlled by the reaction forces which develop through friction, mainly along the outside walls of the caisson, and by suction pressures (i.e. negative excess pore pressures) beneath the caisson cap. For short-term loading, there is no migration within the soil skeleton, and hence, the response of the caisson is controlled by the undrained shear stiffness and strength of the underlying soil (and by the rigidity

of the caisson itself). When tensile forces are sustained over a long period of time, the excess pore pressures generated beneath the lid of the caisson will dissipate, and load will transfer from the cap to the walls of the caisson. For long-term, fully drained conditions, there are no excess pore pressures within the soil plug and reaction forces must be provided by the shear resistance along the inside and outside wall-soil interfaces.

For TLP anchorage applications, the design storms have an overall duration ranging from 6hrs to several days during which time at least partial drainage can occur beneath the caisson. In prototype applications of TLP caisson anchors in the North Sea (Christopherson et al., 1992), all of the sustained tensile loads are supported by dead-weight ballast applied to the top of the caisson. Clearly, this is a conservative design philosophy which ignores the long-term capacity of the caisson.

This section describes a series of analyses which have been performed in order to develop a fundamental understanding of the mechanisms controlling caisson response to sustained tensile loads. The results provide preliminary guidance on the long-term drained capacity of the caisson and the time frame required to dissipate excess pore pressures within the soil plug (i.e. release of underbase suction). The analyses make the following assumptions:

1. The tensile loads are initially applied over a short time frame such that there is no drainage within the surrounding soil (i.e., undrained; Section 6.3). Specified load levels are then maintained until either there is full dissipation of the underbase excess pore pressures or caisson failure occurs when the applied force exceeds the available reaction forces.
2.. The soil response to sustained loading is modeled as a process of coupled consolidation. The non-linear stiffness of the soil skeleton is controlled by the MIT-E3 soil model with initial effective stresses and soil properties described previously from undrained loading in BBC, while fluid flow is controlled by Darcy's law (within the ABAQUS finite element program). All of the analyses in this section assume a constant, isotropic coefficient of permeability[7], k = 1.0×10^{-8} cm/sec. The simulation assumes that there is no physical separation between the caisson cap and the soil surface. Table 6.5 summarizes the load conditions, caisson geometry and key output variables used in the study of sustained loading. All of the calculations assume deformation and strength properties of K_0-normally consolidated BBC.

6.4.2 Caisson Response at Selected Levels of Sustained Tensile Load

An initial series of four sustained load simulations were performed for the base case geometry (B = 20m, L = 20m, 2w = 0.5m), at F_{TOT} = 20.5, 46.5, 57.5, and 75MN. Figure 6.30 shows the overall load-displacement response for these tests (labeled I-IV) together with the

[7] Field permeability data for BBC at the Saugus site (Morrison, 1984), with OCR = 1.0- 1.2 measure k = 2×10^{-8} - 1×10^{-7}cm/sec.

backbone curve for undrained loading (which defines the initial displacements, δ_0). Sustained loading at levels I and II caused significant additional vertical displacement of the caisson (at I, δ_0 = 0.01m, δ_f = 0.068m; at II, δ_0 = 0.05m, δ_f = 0.29m) before reaching a final drained equilibrium condition. At levels III and IV, failure occurs at cap displacements $\delta_0 \approx$ 0.48m.

Figure 6.31 shows the development over time of the cap displacement, wall and cap forces, and excess pore water pressures inside the caisson (points A and B are located on the caisson centerline at the cap and the elevation of the caisson tip, respectively) for load level I. The results show that there is almost no cap displacement until t = 1 day after the load is applied, and no change in underbase pore pressure (at point A) until t = 1.75 days. The time corresponds to the 'breakthrough' point at which the cap force is first affected by partial drainage in the underlying clay. Time t_0 corresponds to the onset of load-transfer from the cap to the caisson wall force. The time lag between the pore pressure response at A and the tip (point B) is associated with the drainage occurring over the embedded length of the caisson.

For $t > t_0$, the subsequent pore pressure response at A is characterized by an 'S'-shaped dissipation curve. Most of the excess pore pressures dissipate between one and ten days after load application. The maximum dissipation rates (du/dlog t) occur at $t_{50} \approx$ 3 days, when the excess pore pressure ratio [1-($\Delta u/\Delta u$)] = 50%. The maximum displacement and load transfer rates also occur at t = 2-3 days. Long-term dissipation of excess pore pressures closely resembles an exponential time decay function. The reference time for 90% consolidation ([1-($\Delta u/\Delta u$)] = 0.9 at point A, t_{90} $\approx$ 30 days, after which time only small changes in F_w and F_c occur, and stable equilibrium is reached for t > 300 days. However, there are significant cap displacements occurring for t = 30-300 days.

Figure 6.32 shows the distribution of the normalized shear tractions on the inside and outside walls of the caisson at t = 0 (first load application), 30 days (t_{90}), and 300 days. At t = 0, there is almost uniform mobilization of the shear strength along the outside walls of the caisson (τ_{rz}/σ'_{v0} = 0.08-0.10; i.e. τ_{rz}/s_{uDSS} = 38-45%). For z/L < 0.5, there is almost zero shear along the inside caisson wall, and only small shear stresses towards the base of the soil plug ($\tau_{rz}/\sigma'_{v0} \rightarrow$ 0.05). When the loading is sustained to t_{90}, 90% of the cap force redistributes to the walls of the caisson, shear stresses on the outside wall increase to τ_{rz}/σ'_{v0} = 0.16 - 0.17, and reach similar stress levels at the base of the soil plug. Only small load transfer occurs for t > 30 days ($\Delta F \approx$ 1MN). The results in Figure 6.32 show that most of this load transfers to the inside wall of the caisson, giving a large increase in the mobilized shear traction over the full length of the caisson.

Figure 6.33 presents the time-dependent response for load level II, F_{TOT} = 46MN (Fig. 6.30). After load application, there is a 3 day delay (t_0 = 3 days) before underbase excess pore pressures start to dissipate. This breakthrough time also marks the onset of vertical displacements and load transfer from the cap to the wall. Most of the subsequent displacements occur over two

well-defined time intervals, t = 3 - 20 days and t = 40 - 150 days, giving the unusual appearance of a double 'S'-shaped curve. This response suggests that there are two separate mechanisms of soil-caisson interaction. Figure 6.33b shows that most of the load-transfer from the cap to the wall occurs during the second displacement phase (t = 40 - 150 days), after which the caisson approaches a stable equilibrium configuration with $F_c \rightarrow 0$MN and $F_w \rightarrow F_{TOT}$. The underbase excess pore pressures dissipate very slowly (compared to previous results for load level I), with $t_{50} \approx 70$ days and $t_{90} \approx 125$ days.

Figure 6.34 shows the normalized shear tractions along the inside and outside walls of the caisson at t = 0, 30, and 300 days. During the time interval 0 to 30 days, the shear stresses on the outside wall increase almost uniformly from $\tau_{rz}/\sigma'_{v0} = 0.16$ to 0.20, while stresses inside the caisson increase towards the base of the soil plug. These results show that the first mechanism controlling displacements for t = 3-70 days comprises the transfer for load to the outside wall of the caisson where the full shear strength of the soil is mobilized. As the strength becomes fully mobilized, the tangential wall stiffness decreases rapidly (cf. Fig. 6.2, DSS behavior for BBC) and significant cap displacements can occur. The cap displacements also generate further excess pore pressures and hence, retard the dissipation occurring within the soil plug (giving a much larger value of t_{50}).

Once the shear strength is fully mobilized along the outside wall of the caisson, the cap displacement appears to stabilize (t = 20 - 40 days). The second phase of displacement occurs when the dissipation of excess pore pressures dominates the process, causing further transfer of load to the inside wall of the caisson. Figure 6.34 shows that the long-term equilibrium condition includes full mobilization of the shear strength along the inside wall of the caisson for z/L > 0.5.

Figure 6.35 shows the first sustained load (level III) where the caisson experiences failure. The caisson is held at a sustained load $F_{TOT} = 57$MN until failure occurs at t = 60 - 90 days. Failure in this case is defined as a breakdown of the analyses (due to extremely large incremental displacements), and can be seen quantitatively by the time-displacement plot in Figure 6.35a, where displacement rate increases exponentially beyond about 60 days.

Prior to failure, the caisson response exhibits many of the same features described for load level II. The initial breakthrough time occurs at t = 7 days, and displacements occur rapidly as the full shear strength is mobilized along the outside wall of the caisson (Fig. 6.36). The onset of the second displacement phase at t = 20 days is associated with transfer of cap forces to the inside wall and continues until the wall force reaches a maximum capacity, $F_w = 42$MN (Fig. 6.35b) [8]. Once the wall resistance is full mobilized, there is no mechanism available for shedding the remaining

[8] This result is very close to the theoretical maximum wall capacity, F_w=43.3MN, assuming full undrained DSS strength mobilized over the inner and outer wall surfaces.

cap force, F_c = 15:5MN, and displacements continue to occur with no further reduction in the underbase pore pressure. (i.e., the generation of excess pore pressures by cap displacement balances the dissipation rate within the soil).

Figure 6.37 shows the final sustained loading test at load level IV, F_{TOT} = 74MN, which also ended in caisson pullout. In this case, the full wall friction is already mobilized along the outside wall of the caisson during undrained loading. Thus the cap displacements correspond to the second mechanism described previously, with cap forces transferring to the inside wall of the caisson. There is a 10 day delay before breakthrough occurs, initiating the transfer of load. Thereafter, the wall force increases rapidly to a maximum F_w = 42MN at t = 35 days. The behavior of wall tractions over time can be seen in Figure 6.38; the caisson pulls out before wall forces are maximized on the inside wall.

Figures 6.39a and b summarize the wall and cap force-displacement relations for the sustained tensile load tests. These results show clearly that the long-term capacity of the caisson is controlled by a maximum wall resistance F_w = 42 - 46MN. The results also show that the caisson can safely resist sustained loads significantly larger than 46 MN for time periods t_0 = 3 - 10 days before underbase excess pore pressures begin to dissipate.

Geer (1996) gives further details of the effects of cell geometry on caisson response under sustained loading (results are summarized in Table 6.6).

Test Type	Parameter/ Symbol	Physical contribution/ meaning	Boston Blue Clay	Empire Clay
1-D Consolidation (Oedometer, CRS)	e_0	Void ratio at reference stress on virgin consolidation line	1.12	1.26
	λ	Compressibility of virgin normally consolidated clay	0.184	0.274
	C	Non-linear volumetric swelling behavior	22.0	24.0
	n		1.60	1.75
	h	Irrecoverable plastic strain	0.2	0.2
K_0-oedometer or K_0-triaxial	K_{0NC}	K_0 for virgin NC clay	0.48	0.62
	2G/K	Ratio of elastic shear to bulk modulus	1.05	0.86
Undrained Triaxial Shear Tests: OCR=1; CK_0UC	ϕ'_{TC}	Critical state friction angles in triaxial compression and extension	33.4^0	23.6^0
	ϕ'_{TE}		45.9^{0**}	21.6^0
	c	Undrained shear strength (geometry of bounding surface)	0.866	0.75
OCR=1; CK_0UE	S_t	Amount of post-peak strain softening in undrained triaxial compression	4.5	3.0
OCR=2; CK_0UC	ω	Small strain non-linearity in undrained shear	0.07	0.20
	γ	Shear induced pore pressure for OC clay	0.5	0.5
Resonant Column*	κ_0	Small strain compressibility at load reversal	0.001	0.0035
Drained Triaxial	ψ_0	Rate of evolution of anisotropy (rotation of bounding surface)	100.0	100.0

* Alternatively use field data from cross-hole shear wave velocity type tests.

** Recent data (Germaine, 1989) suggest $\phi'_{TE} \approx 35^0$.

Input Parameters for the MCC Model					
Parameter	e_0	λ	κ	ϕ'_{TC}	2G/K
BBC	1.12	0.184	0.034	33.4^0	1.05

Table 6.1 Input Parameters for BBC using the MIT-E3 and MCC Models

L/B	$\frac{Q}{\rho(B/2+L)^2}$		Bound
	UB.	LB.	(%)
0.0	1.020	0.980	4.0
0.125	3.507	3.117	11.8
0.25	4.704	4.313	8.7
0.5	4.999	4.553	9.3
0.75	4.687	4.331	7.9
1.0	4.411	4.060	8.3

B/L	$\frac{Q}{\rho(B/2+L)^2}$		Bound
	UB.	LB.	(%)
1	4.411	4.060	8.3
0.667	3.856	3.562	7.9
0.5	3.443	3.167	8.4
0.333	2.915	2.656	9.3
0.2	2.382	2.240	6.2
0.125	2.004	1.850	8.0
0	1.000	0.991	0.9

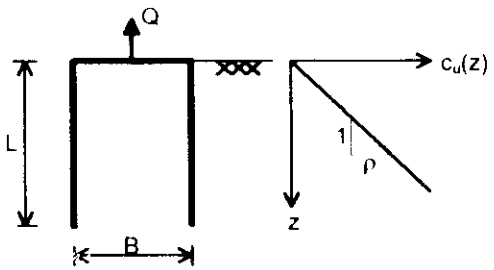

Table 6.2 Summary of Collapse Loads for Vertically Loaded Planar Caisssons

L/B	Total force $\frac{Q}{\rho(B/2+L)^2}$	Force on the cap $\frac{Q_c}{\rho(B/2+L)^2}$	Force on the side wall $\frac{Q_w}{\rho(B/2+L)^2}$	Q_c/Q (%)	Q_w/Q (%)
0	0.980	0.980	0.000	100.0	0.0
0.125	3.117	3.112	0.005	99.8	0.2
0.25	4.313	4.296	0.018	99.6	0.4
0.5	4.553	4.244	0.310	93.2	6.8
0.75	4.331	3.823	0.508	88.3	11.7
1	4.060	3.354	0.705	82.6	17.4

B/L	Total force $\frac{Q}{\rho(B/2+L)^2}$	Force on the cap $\frac{Q_c}{\rho(B/2+L)^2}$	Force on the side wall $\frac{Q_w}{\rho(B/2+L)^2}$	Q_c/Q (%)	Q_w/Q (%)
1	4.060	3.354	0.705	82.6	17.4
0.667	3.562	2.539	1.023	71.3	28.7
0.5	3.167	2.004	1.163	63.3	36.7
0.333	2.656	1.335	1.321	50.3	49.7
0.2	2.240	0.644	1.596	28.7	71.3
0.125	1.850	0.155	1.694	8.4	91.6
0	0.991	0.000	0.991	0.0	100.0

Table. 6.3 Summary of Wall and Cap Forces from Lower Bound Analyses of Planar Caissons

Case	B (m)	L (m)	2w (m)	Soil Conditions	Summary at δ_v = 0.5m			
					F_{TOT} (MN)	F_w/F_{TOT} (%)	f_{co} (MN)	K_c (MN/m)
U-1	20	20	0.5	Standard*	98	32	25	86
U-2	20	20	0.5	MCC, OCR = 1.0	155.3	31	27	162
U-3	20	10	0.5	Standard	49	9	11	42
U-4	20	30	0.5	Standard	145	421	33	100
U-5	20	40	0.5	Standard	203	50	40	118
U-6	20	60	0.5	Standard	335	60	56	156
U-7	10	5	0.5	Standard	19	5	5	26
U-8	10	10	0.5	Standard	24	14	7	30
U-9	10	20	0.5	Standard	38	31	10	32
U-10	10	30	0.5	Standard	58	46	14	34
U-11	40	20	0.5	Standard	160	17	55	158
U-12	40	40	0.5	Standard	410	49	105	180
U-13	40	80	0.5	Standard	1100	64	200	400
U-14	40	120	0.5	Standard	2080	71	300	590
U-15	20	20	0.1	Standard	86	37	-	-
U-16	20	20	2.0	Standard	100	31	-	-
U-17	20	20	0.5	OCR = 2.0	125	33	30	112
U-18	20	20	0.5	Empire, OCR = 1.0	69	35	13	64

* MIT-E3, BBC, OCR = 1.0

Table 6.4 Summary of Parametric Study for Undrained Axial Loading of Caissons

Property	Symbol	BBC OCR = 1.0	BBC OCR = 2.0	Empire Clay OCR = 1.0
Lateral Earth Pressure Ratio	K_0	0.48	0.57	0.62
1. Triaxial Compression:				
Undrained Strength Ratio	s_{uTC}/σ'_{v0}	0.33	0.58	0.24
Strain to Peak Strength	$\varepsilon_{ap}(\%)$	0.2	0.7	1.4
2. Direct Simple Shear:				
Undrained Strength Ratio	s_{uDSS}/σ'_{v0}	0.21	0.40	0.20
3. Triaxial Extension:				
Undrained Strength Ratio	s_{uTE}/σ'_{v0}	0.14	0.24	0.16
Secant Shear Moduli	$G_{0.001}/\sigma'_{v0}$	520	590	185
at	$G_{0.01}/\sigma'_{v0}$	330	390	140
γ =0.001, 0.01, 0.1%	$G_{0.1}/\sigma'_{v0}$	120	150	75

*Note: $s_{uDSS}/\sigma'_{v0} \equiv \tau_h/\sigma'_{v0}$

Table 6.5 Normalized Engineering Properties of BBC from MIT-E3 Soil Model

Case	B (m)	L (m)	2w (m)	Soil Conditions	F_{tot} (MN)	F_0 (MN)	δ_0 (m)	δ_f (m)
S-1	20	20	0.5	Standard*	98	20	0.01	0.068
S-2	20	20	0.5	Standard	98	46	0.05	0.29
S-3	20	20	0.5	Standard	98	57	0.1	failure
S-4	20	20	0.5	Standard	98	74	0.25	failure
S-5	20	10	0.5	Standard	49	12	0.01	0.25
S-6	20	10	0.5	Standard	49	20	0.1	failure
S-7	20	40	0.5	Standard	203	110	0.1	0.27

* MIT-E3, BBC, OCR = 1.0

Table 6.6 Summary of Sustained Loading Analyses

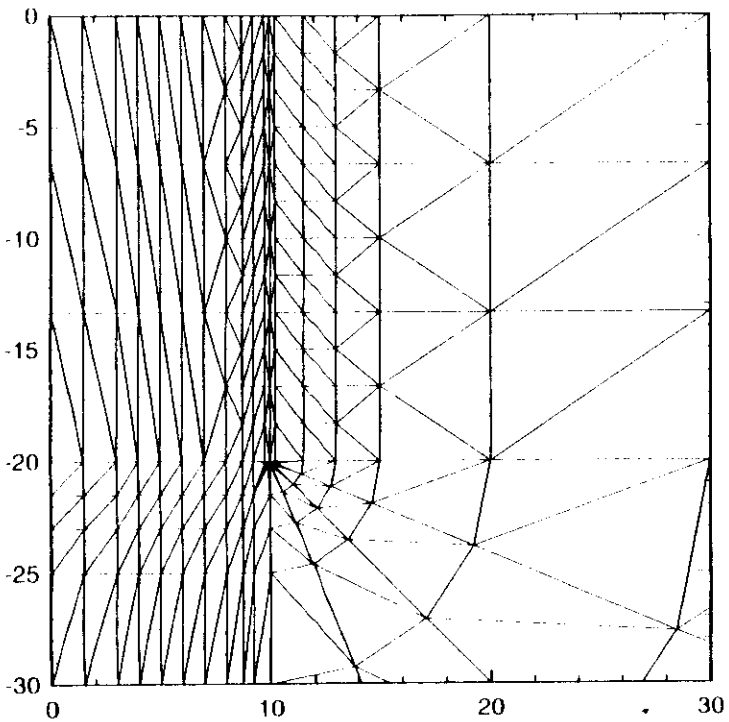

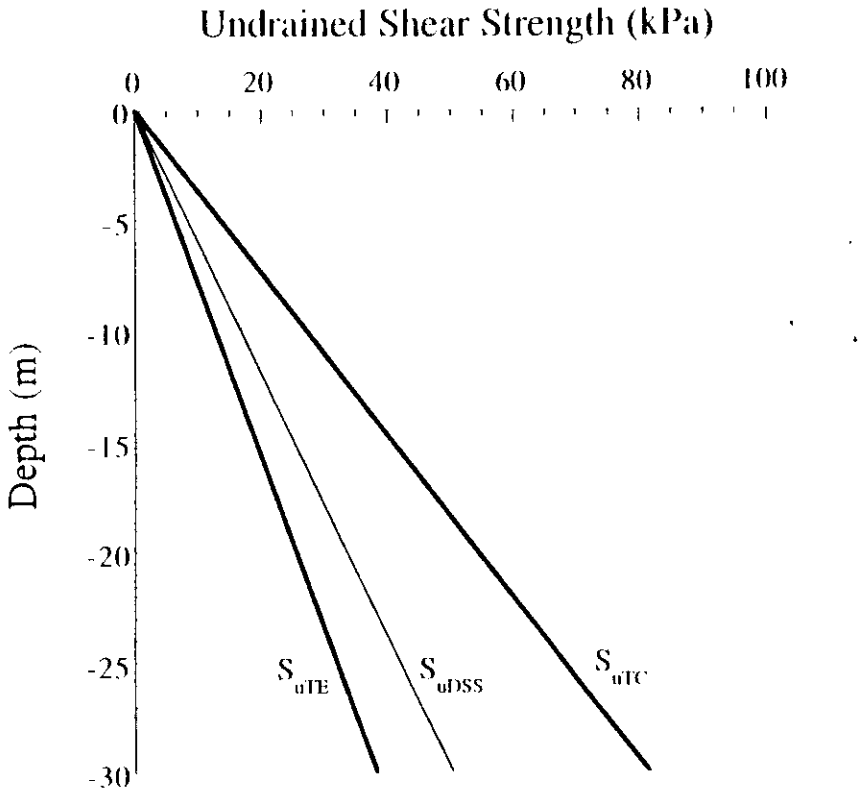

Suction Caisson Material Properties:
E = 3.4×10^4 MPa
ν = 0.2
γ = 18kN/m^3

Finite Element Mesh:
491 Elements (15-noded triangles)
404 Soil Elements, 87 Caisson Elements
4272 Nodes
8600 DOF

Element Types:
Caisson: UEL type U18, 15 noded triangles, 15 displacement nodes, 0 pore pressure nodes, 16 integration points
Soil: UEL type U17, 15-noded triangles, 15 displacement nodes, 3 pore pressure nodes, 16 integration points

Figure 6.1 Details of Finite Element Mesh and Shear Strength Profile of Clay for Base Case Analyses

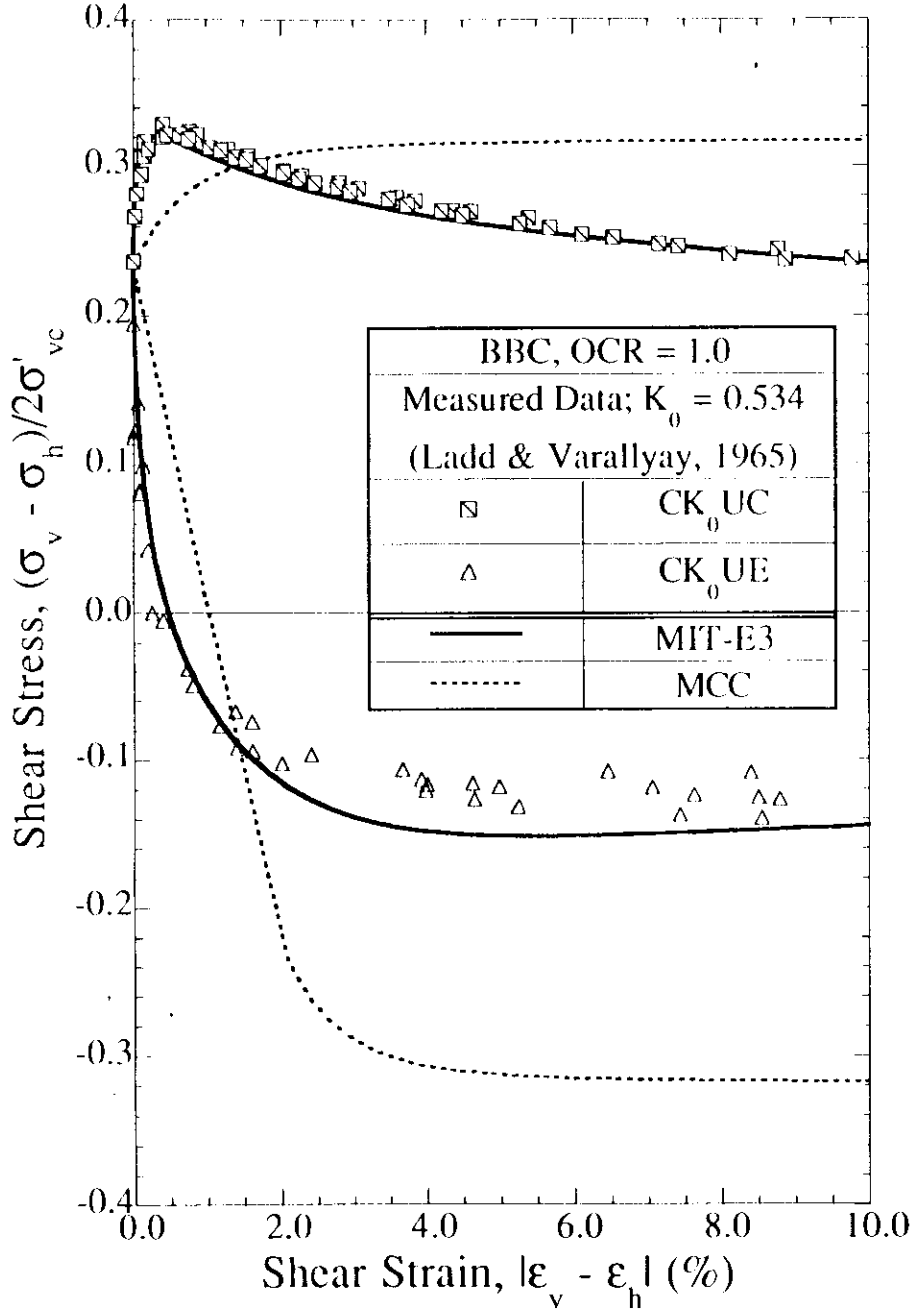

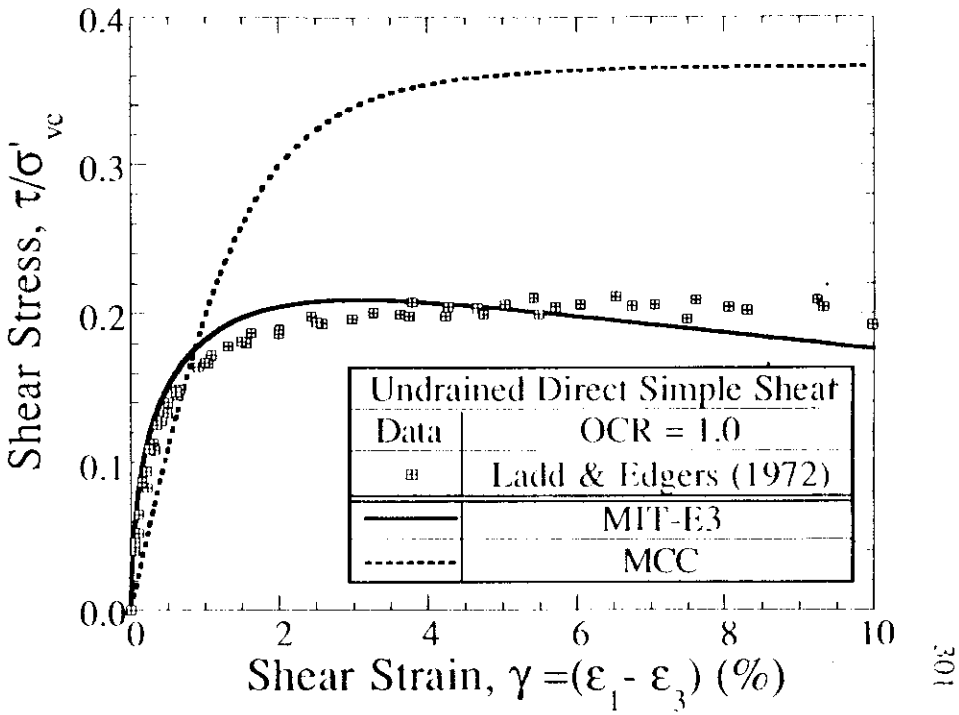

Figure 6.2 Comparison of Predicted and Measured Undrained Shear Behavior of K_0-Normally Consolidated BBC

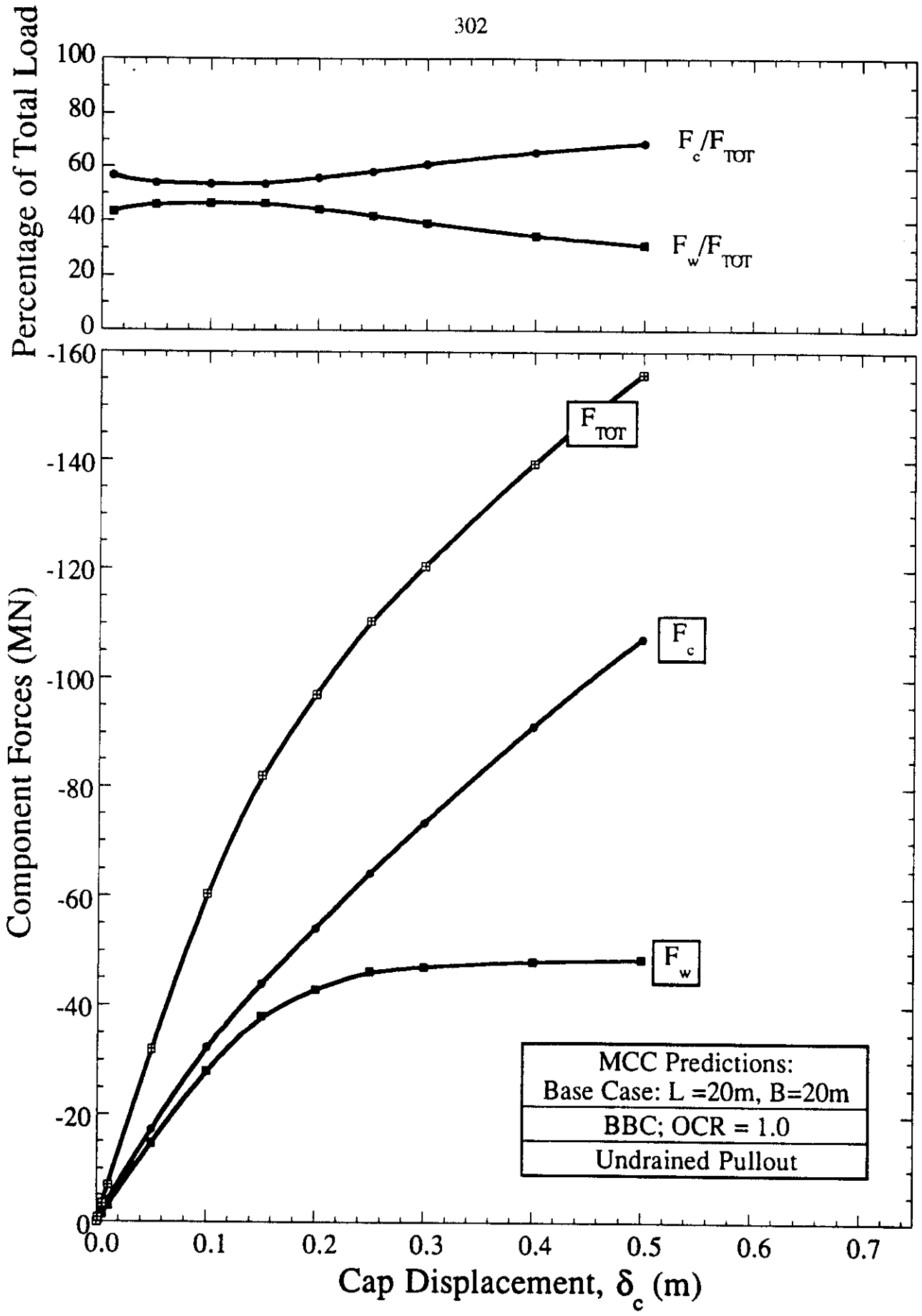

Figure 6.3 Predictions of Load-Deformation Response for Base Case Geometry using the MCC Soil Model

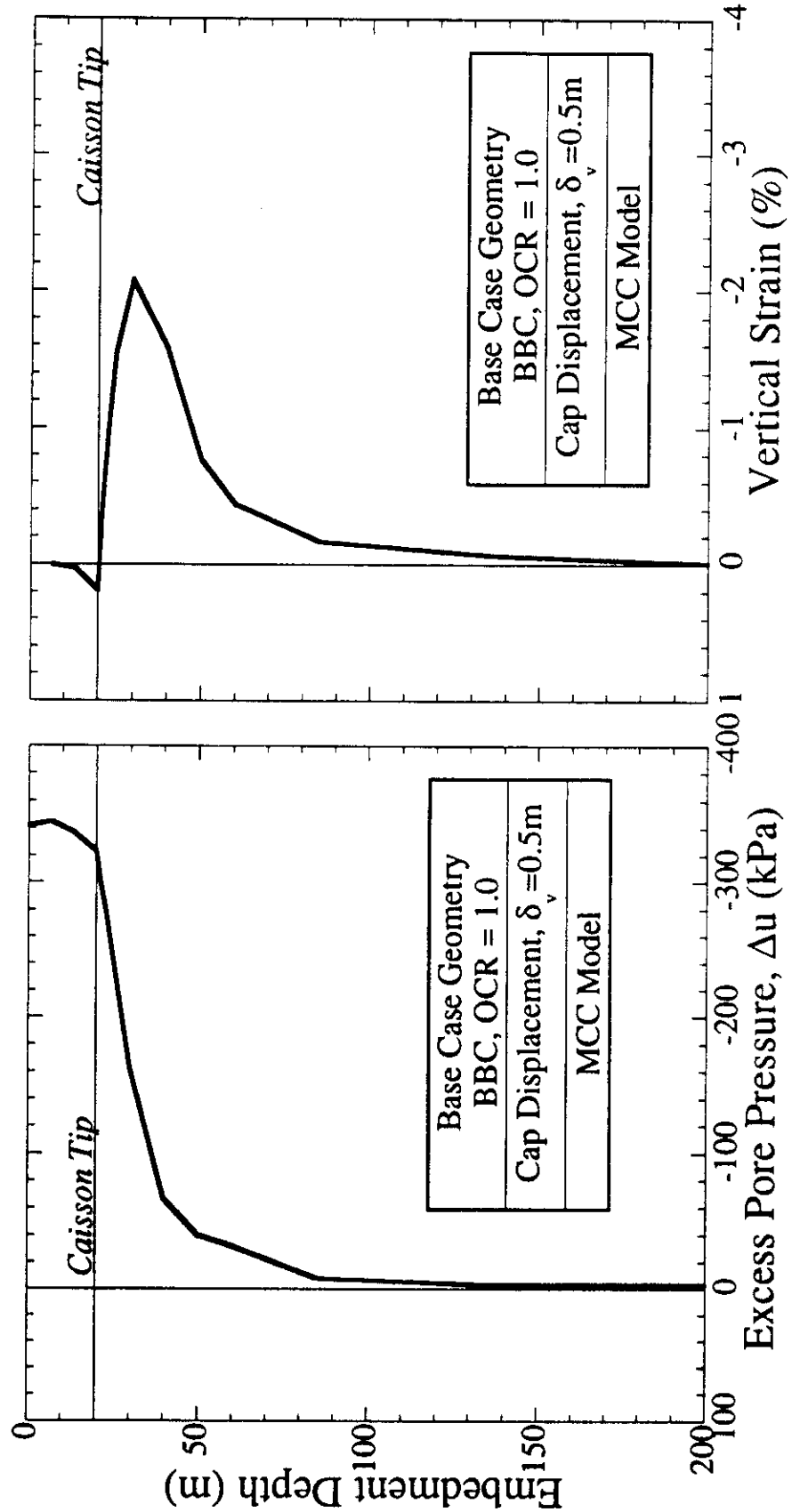

Figure 6.4 Excess Pore Pressure and Vertical Strains from Base Case Analysis with MCC Soil Model

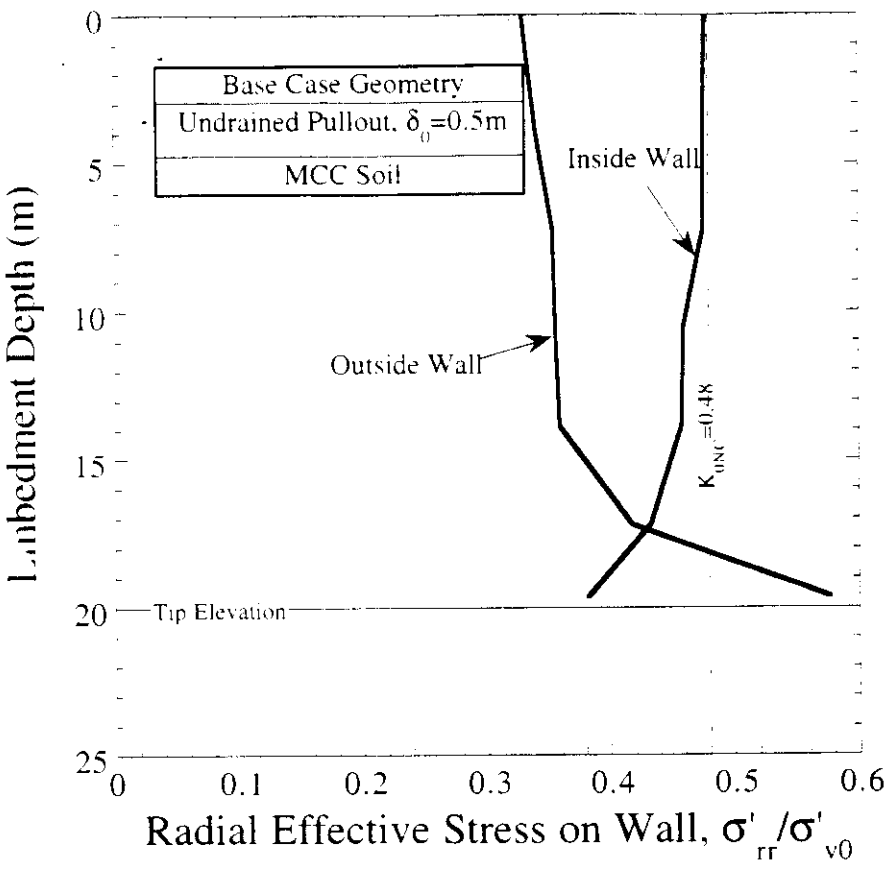

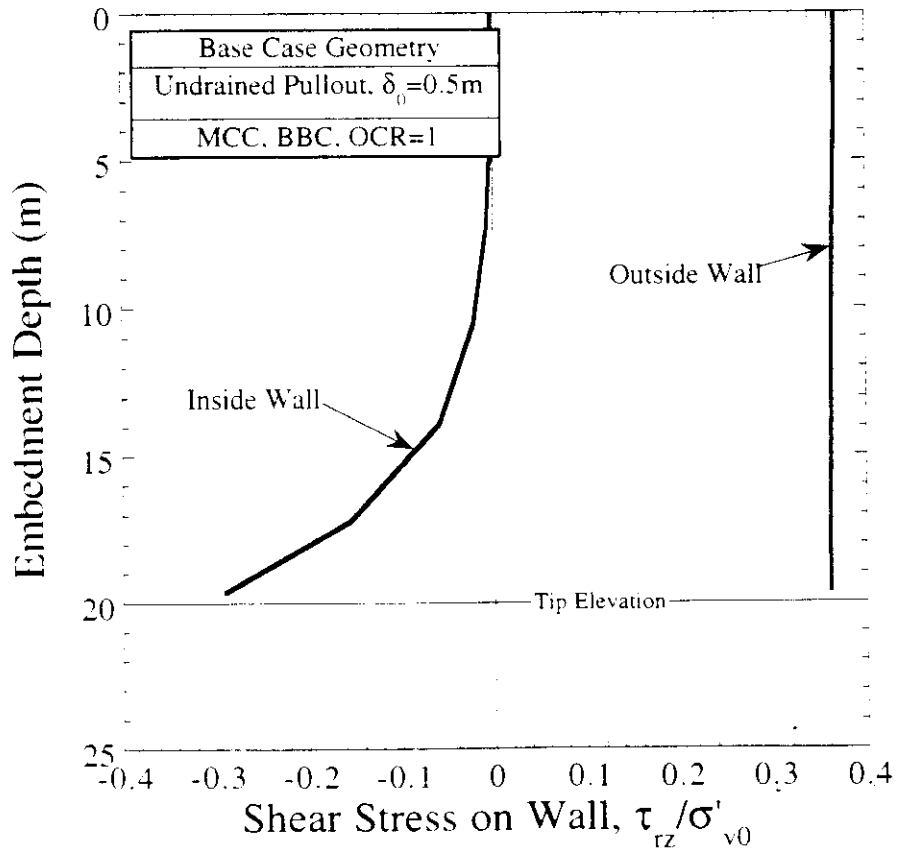

Figure 6.5 Radial Effective Stress and Shear Tractions on Caisson Wall for Base Case Analysis with MCC Soil Model

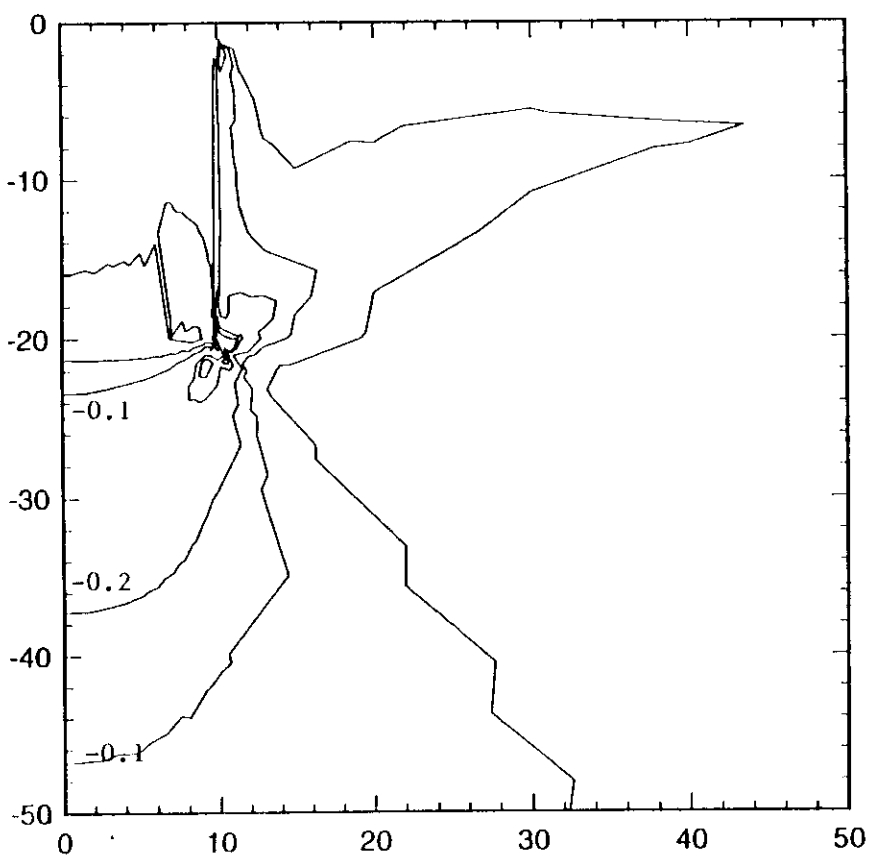

a) Triaxial Shear Stress, $q/\sigma'_{v0} = (\sigma_v - \sigma_h)/2\ \sigma'_{v0}$

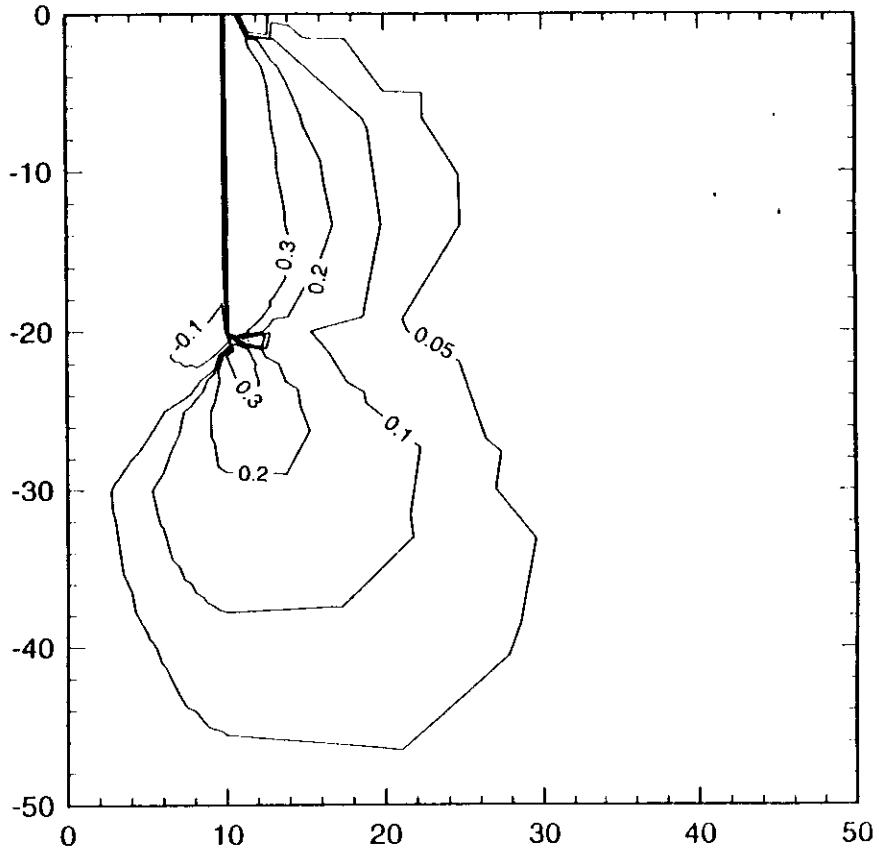

b) Direct Shear Stress τ/σ'_{v0}

Figure 6.6 Contours of Shear Stresses for Base Case Analysis with MCC Soil Model

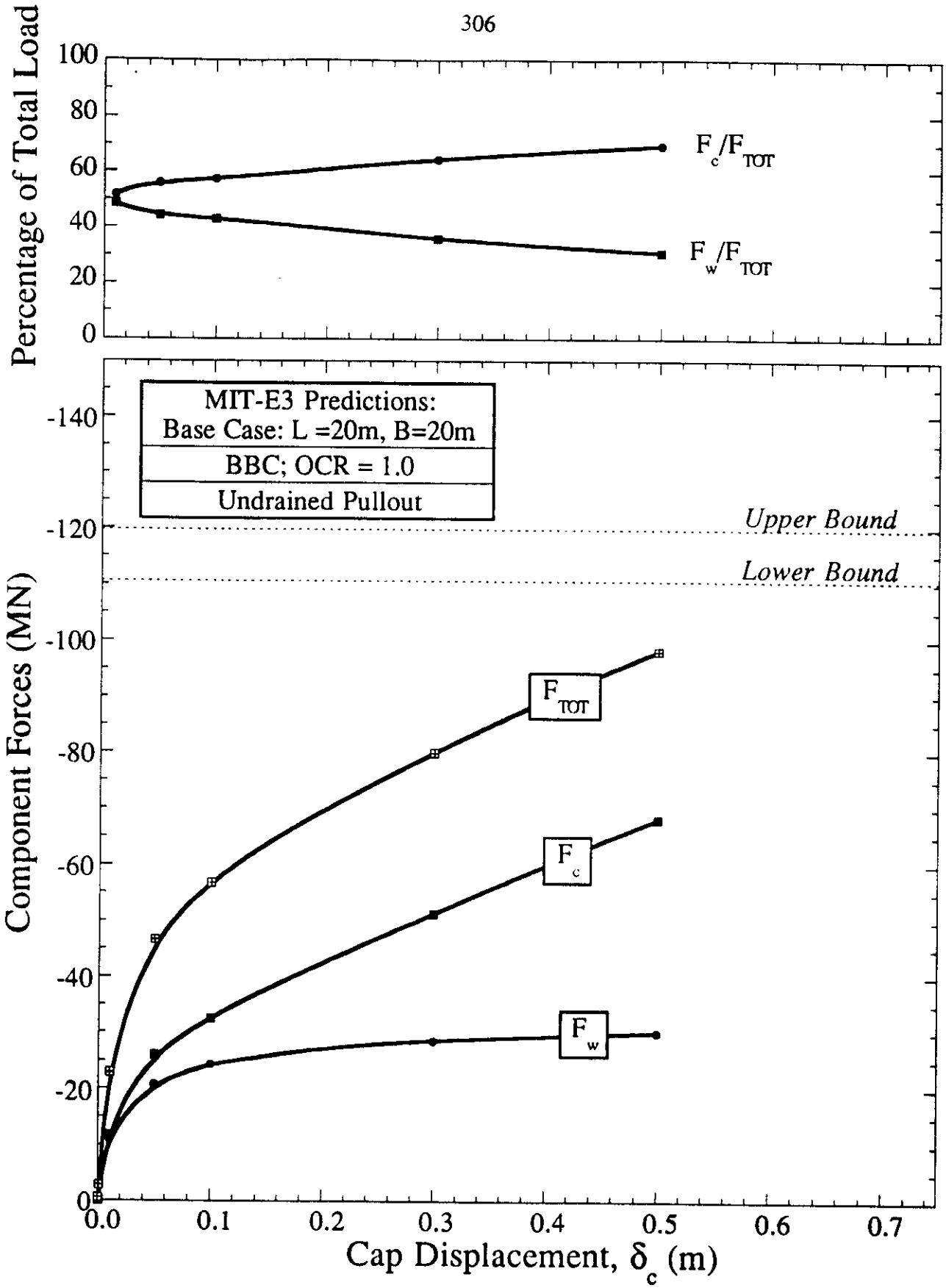

Figure 6.7 Predictions of Load-Deformation Response for Base Case Geometry using the MIT-E3 Soil Model

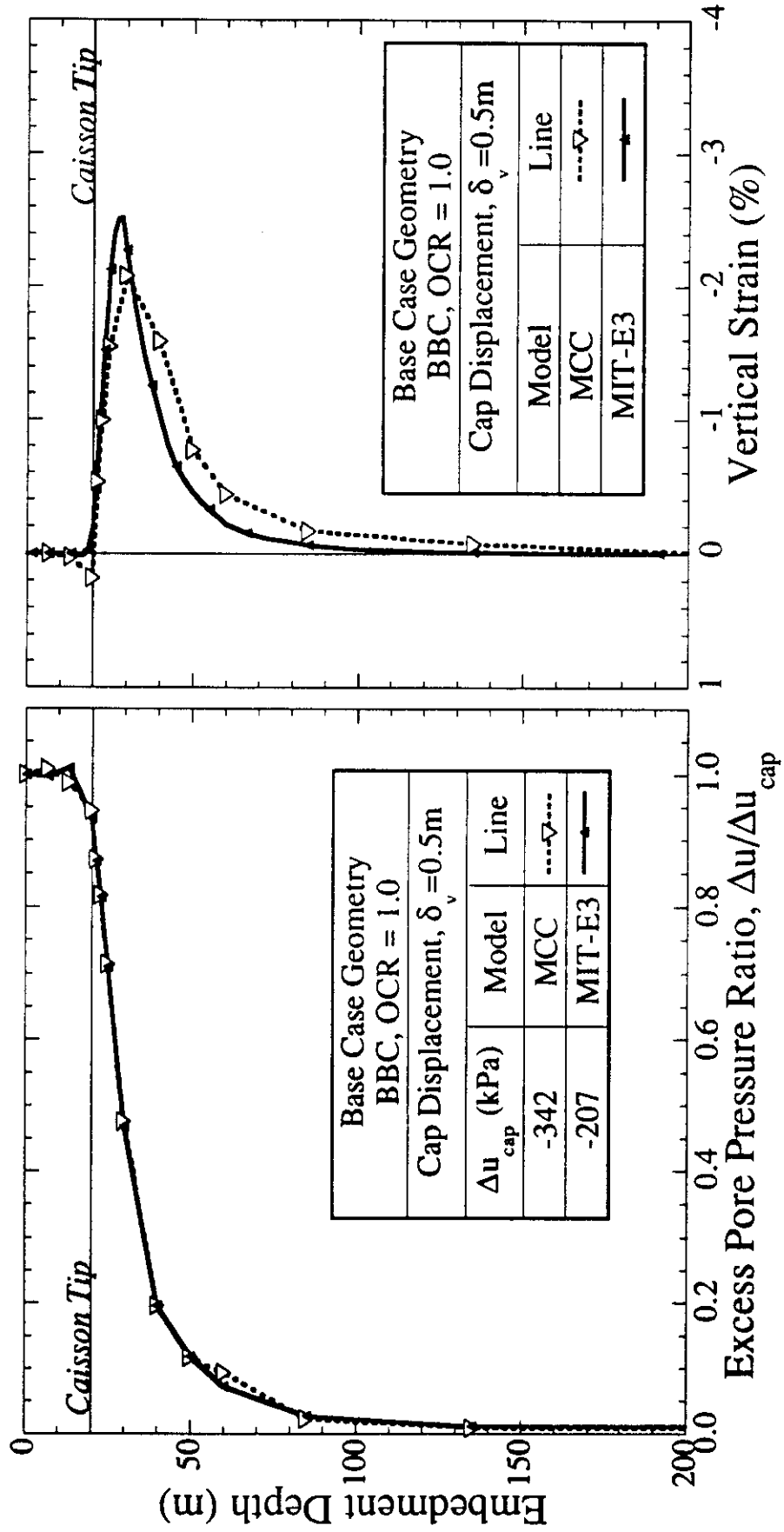

Figure 6.8 Excess Pore Pressure and Vertical Strains from Base Case Analysis with MIT-E3 Soil Model

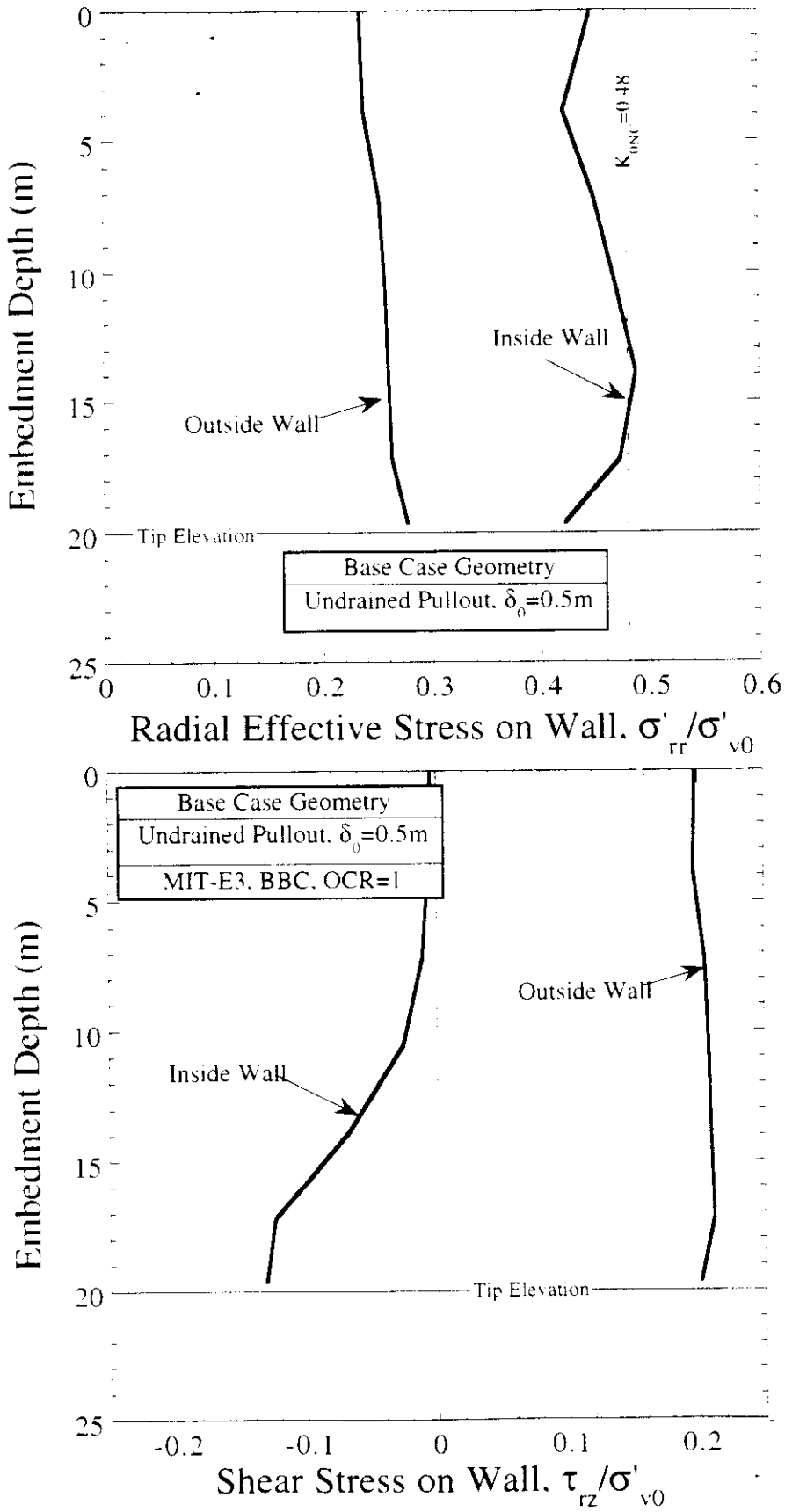

Figure 6.9 Radial Effective Stress and Shear Tractions on Caisson Wall for Base Case Analysis with MIT-E3 Soil Model

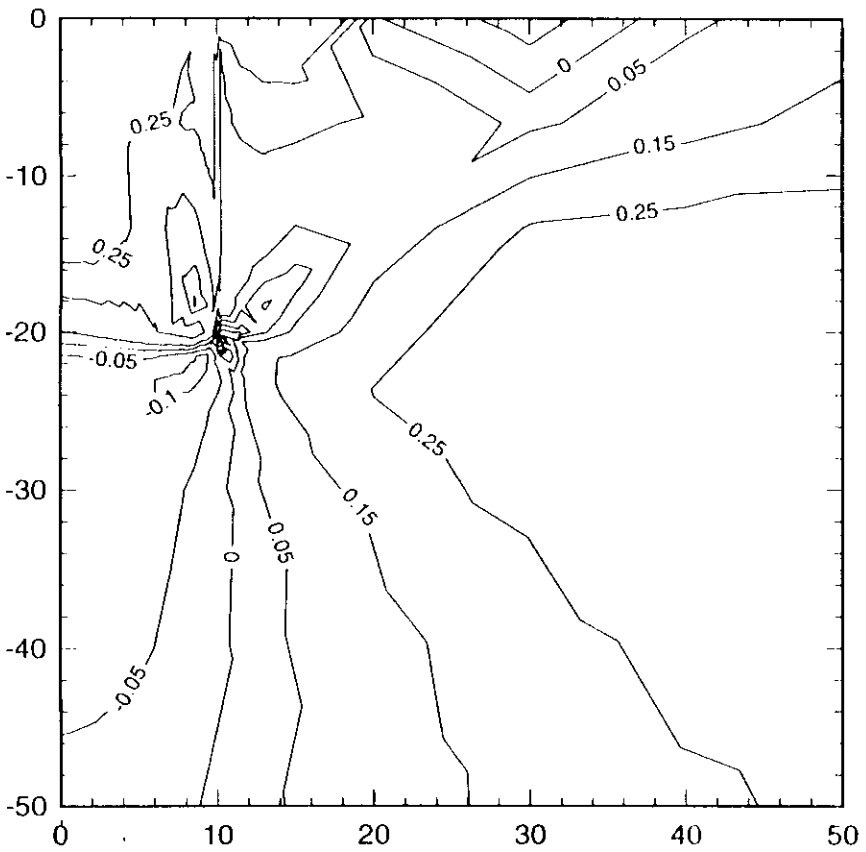

a) Triaxial Shear Stress, $q/\sigma'_{vo} = (\sigma_v - \sigma_h)/2\ \sigma'_{vo}$

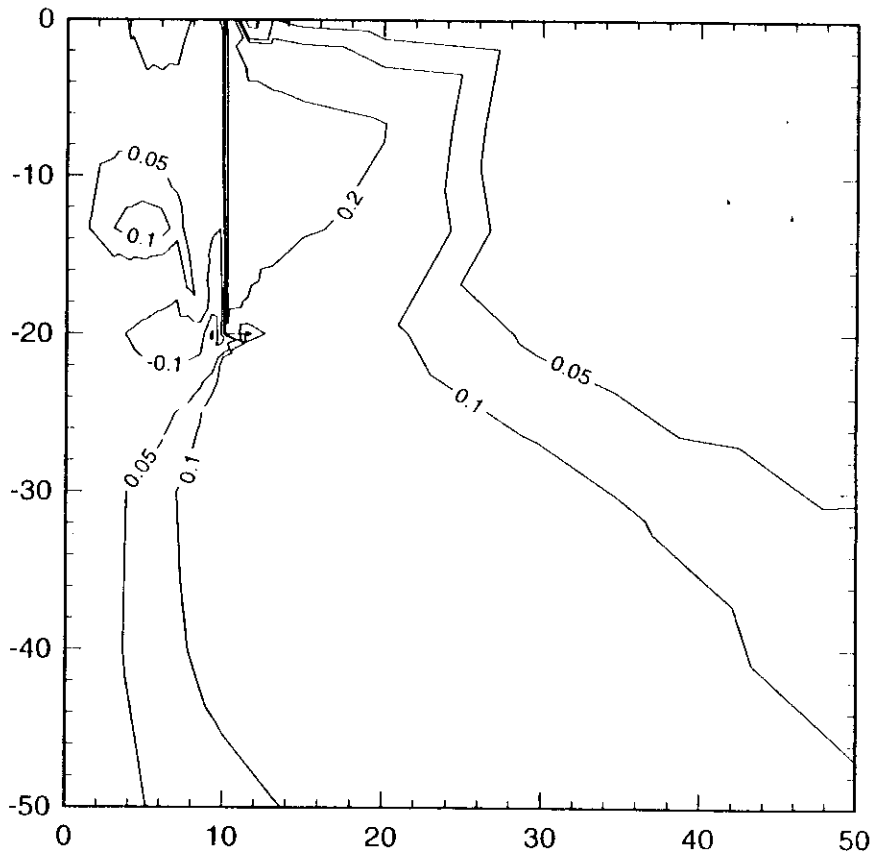

b) Direct Shear Stress τ/σ'_{vo}

Figure 6.10 Contours of Shear Stresses for Base Case Analysis with MIT-E3 Soil Model

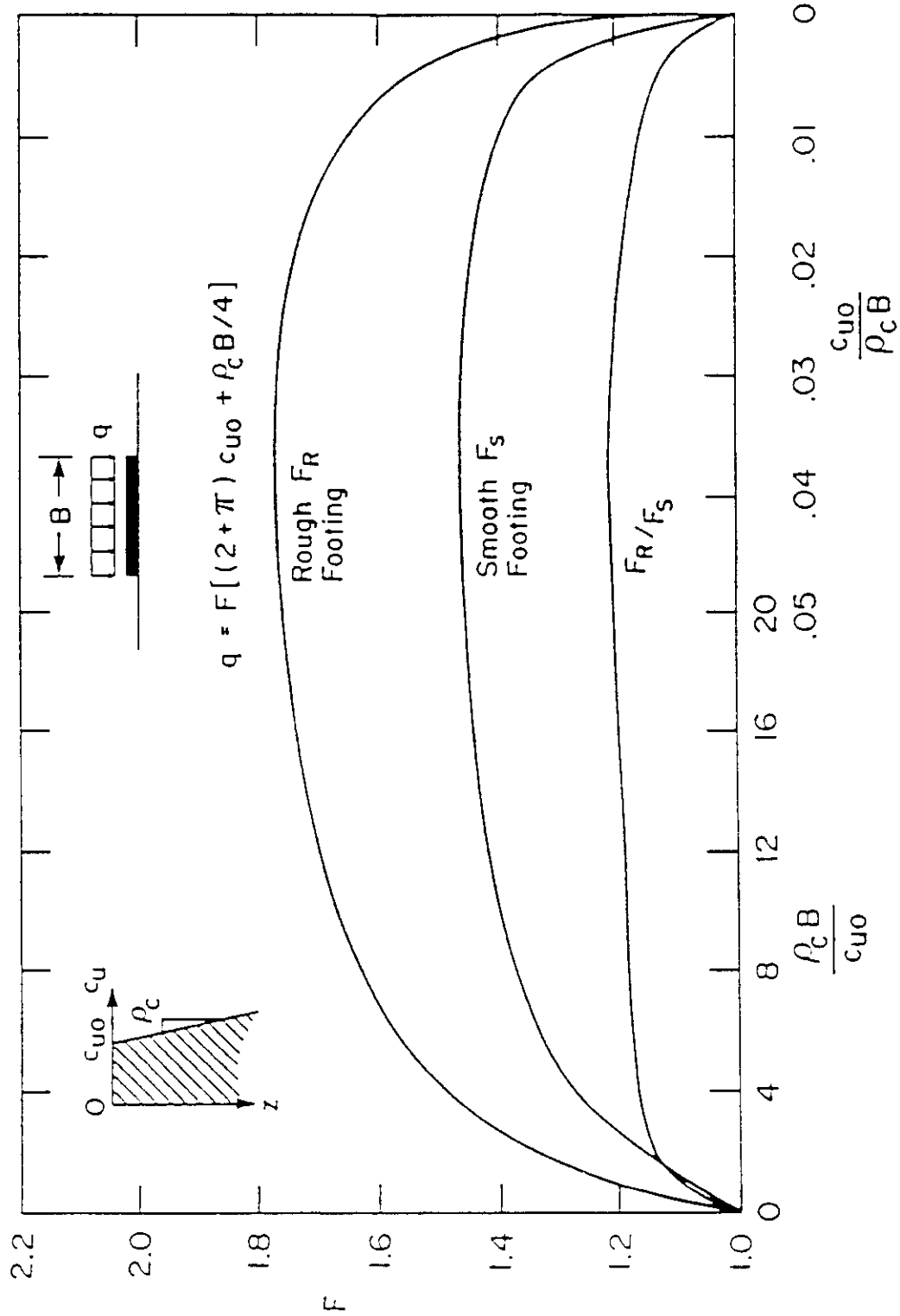

Figure 6.11 Bearing Capacity Factors for Footings on Non-Homogeneous Clay (Davis & Booker, 1973)

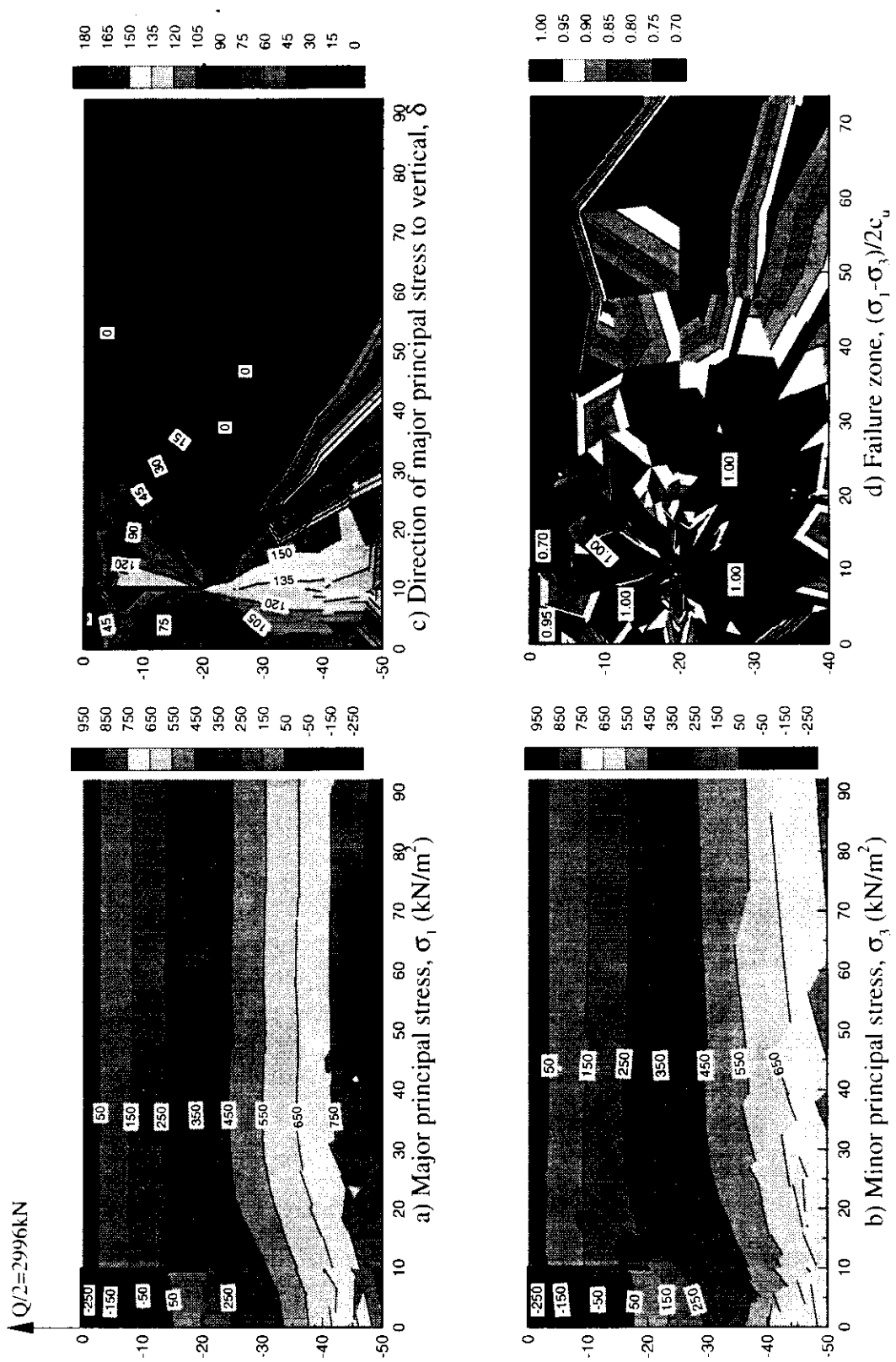

Figure 6.12 Results of Lower Bound Analysis for Base Case Caisson Geometry

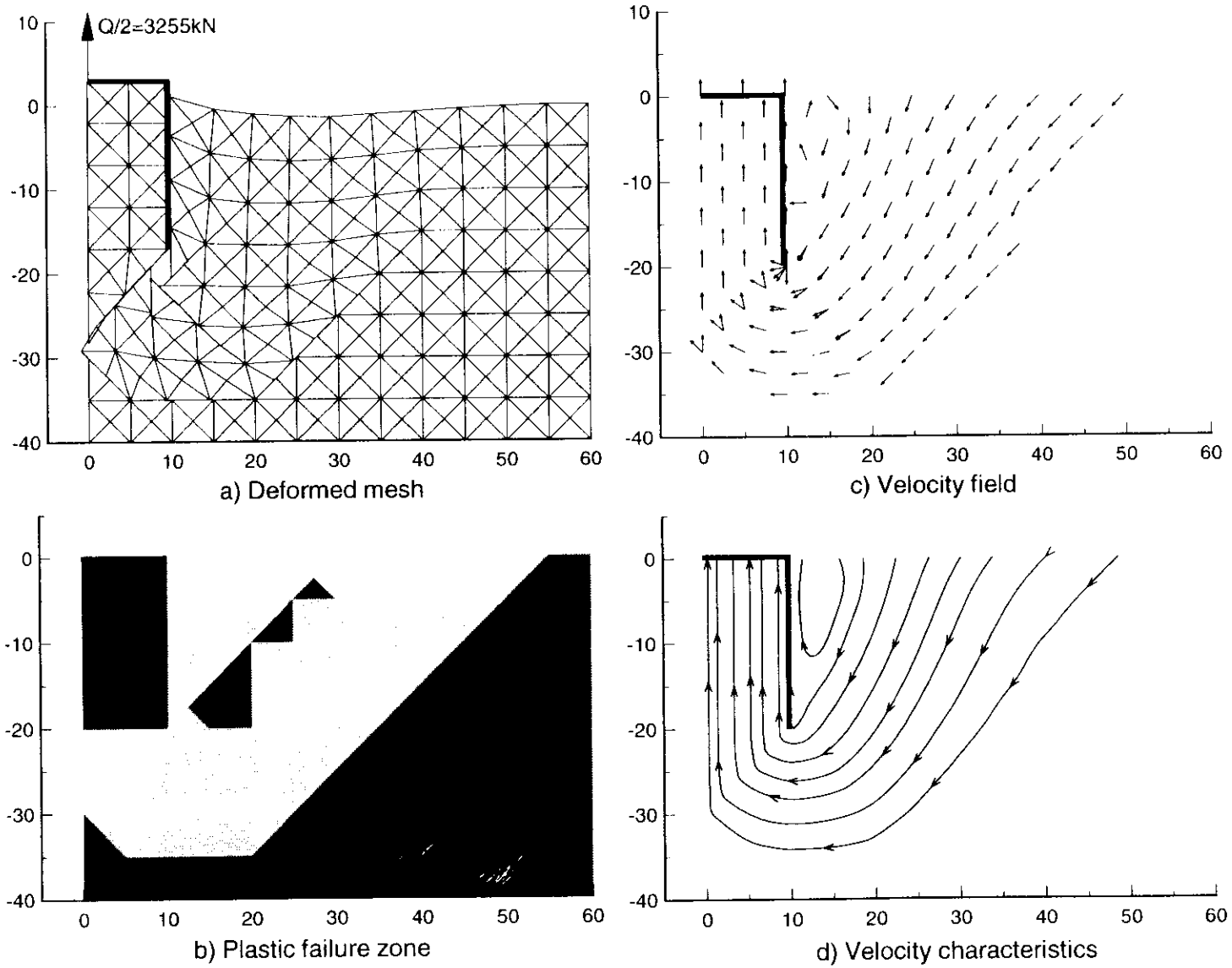

Figure 6.13 Results of Upper Bound Analysis for Base Case Caisson Geometry

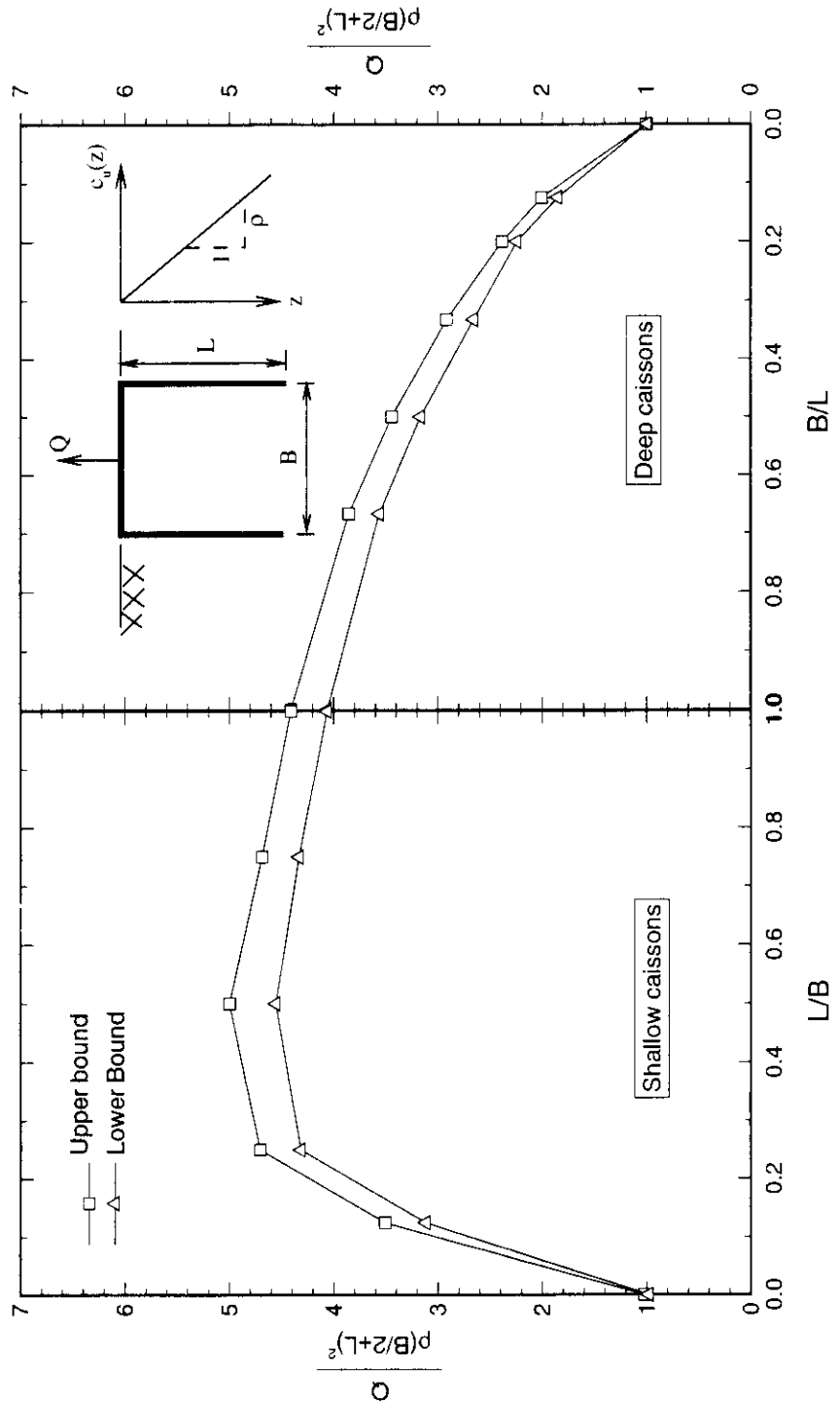

Figure 6.14 Pullout Loads from Planar Limit Analyses of Caissons in Non-Homogeneous Clay

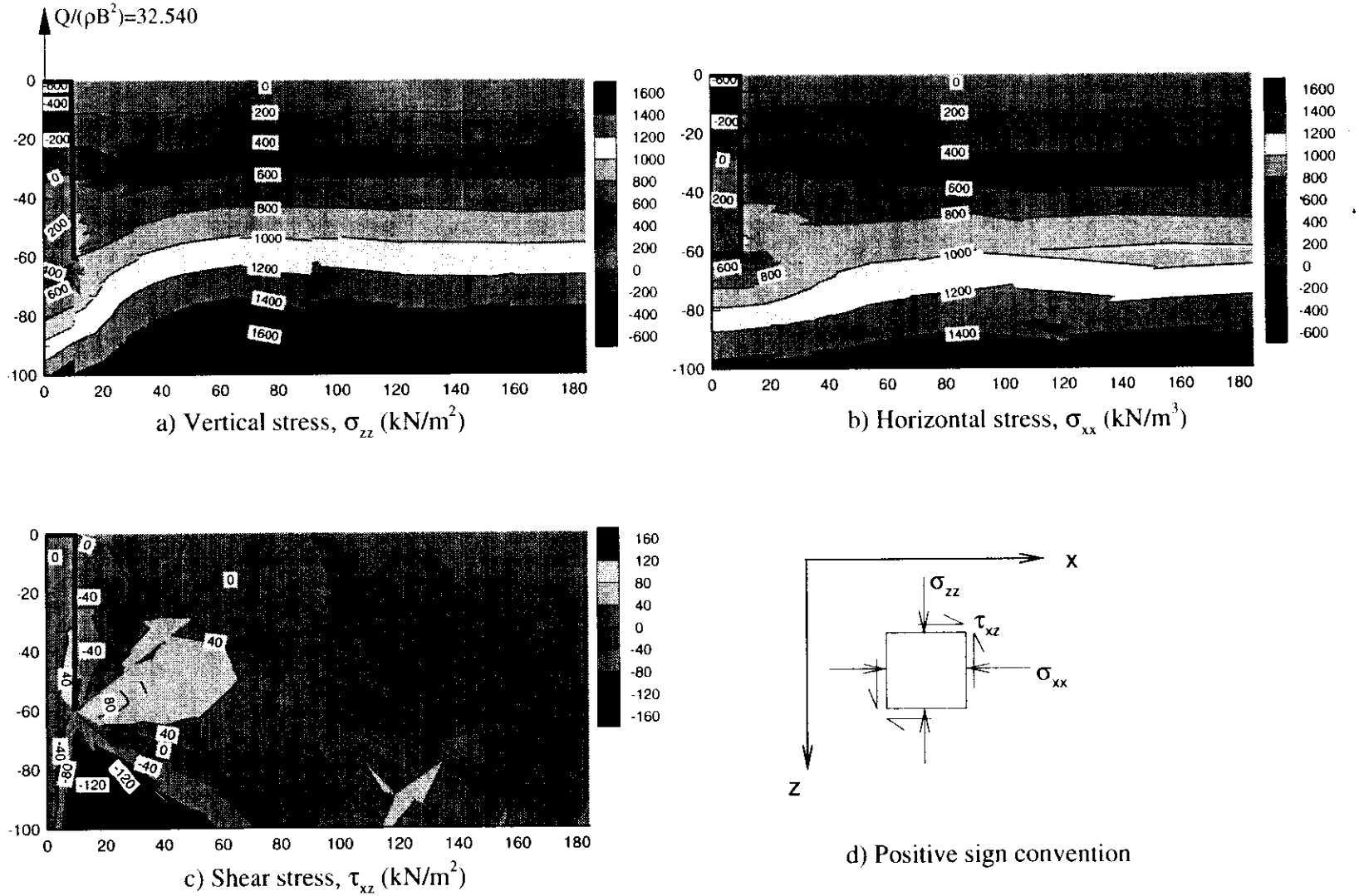

Figure 6.15 Results of Lower Bound Analysis of a Deep Caisson with Embedment Ratio, L/B = 3

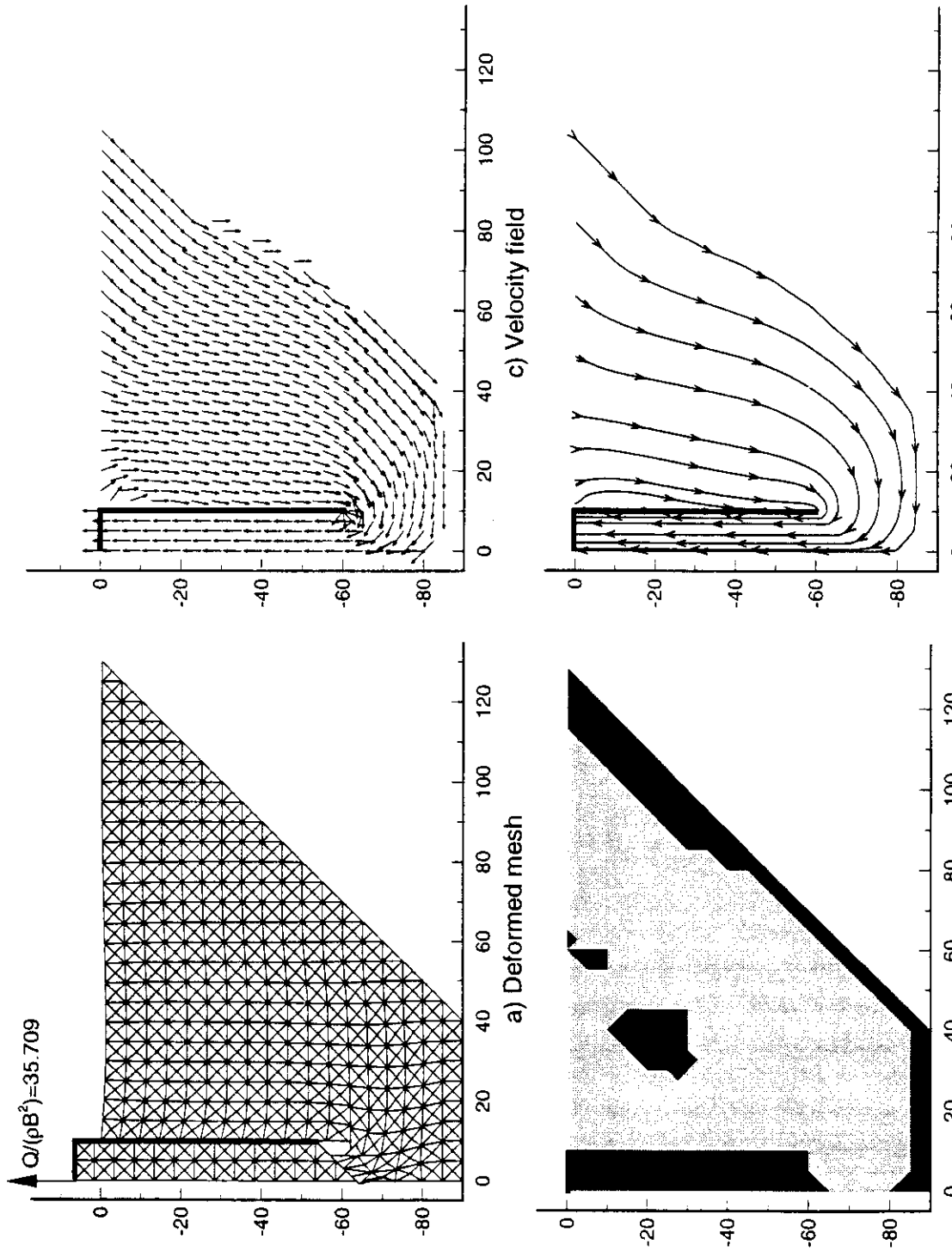

Figure 6.16 Results of Upper Bound Analysis of a Deep Caisson with Embedment Ratio, L/B = 3

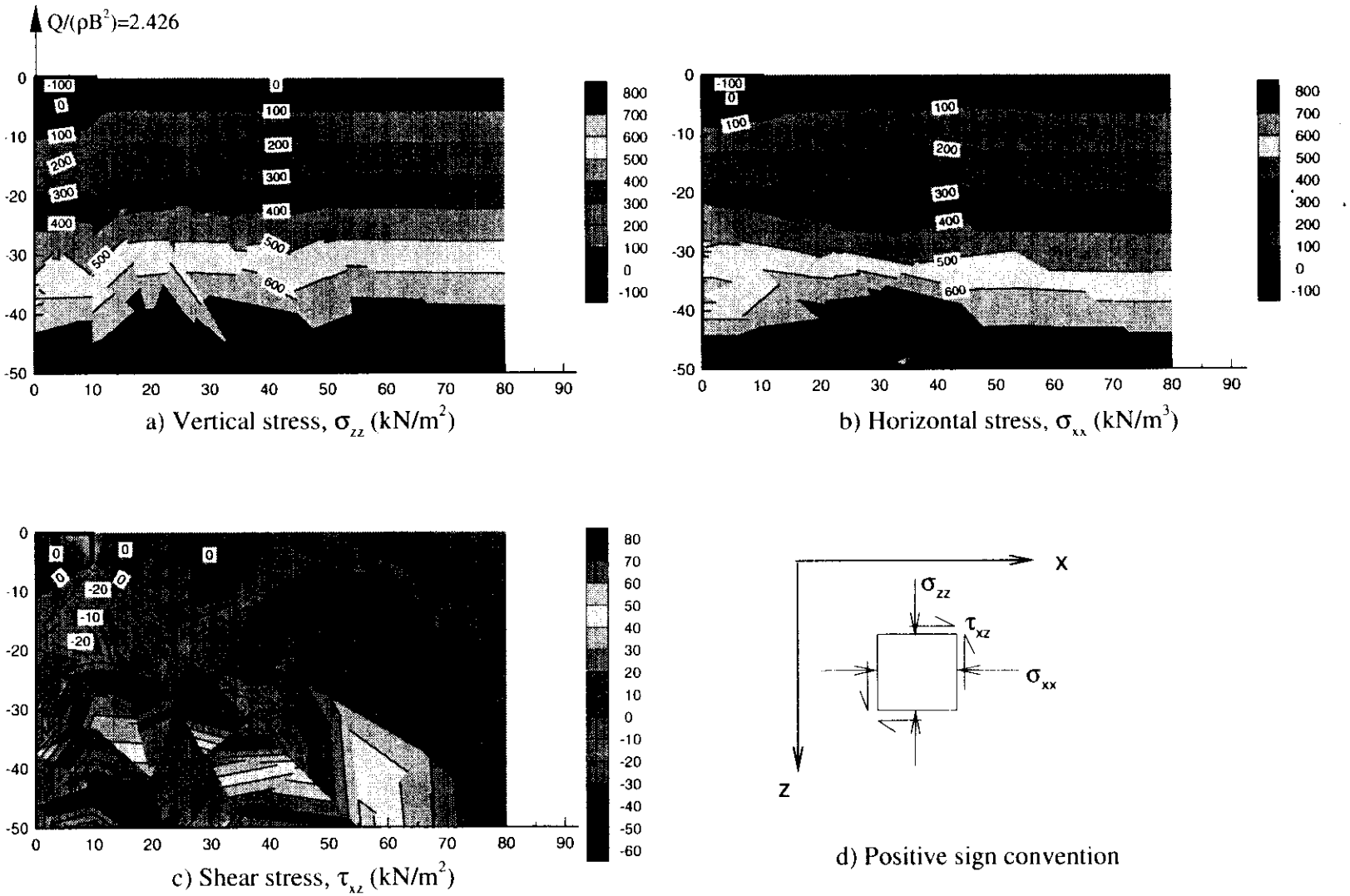

Figure 6.17 Results of Lower Bound Analysis of a Shallow Caisson with Embedment Ratio, L/B = 0.25

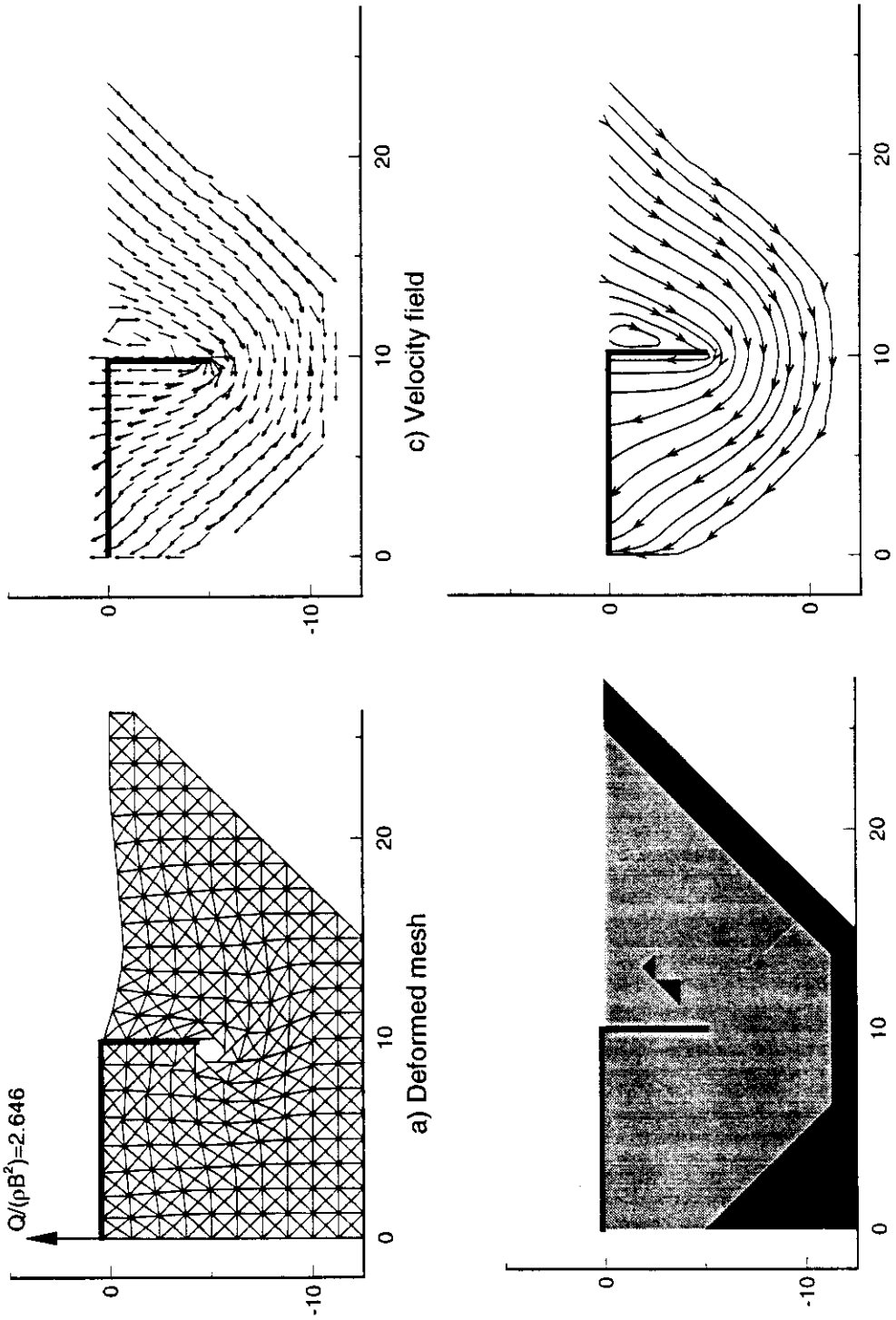

Figure 6.18 Results of Upper Bound Analysis of a Shallow Caisson with Embedment Ratio, L/B = 0.25

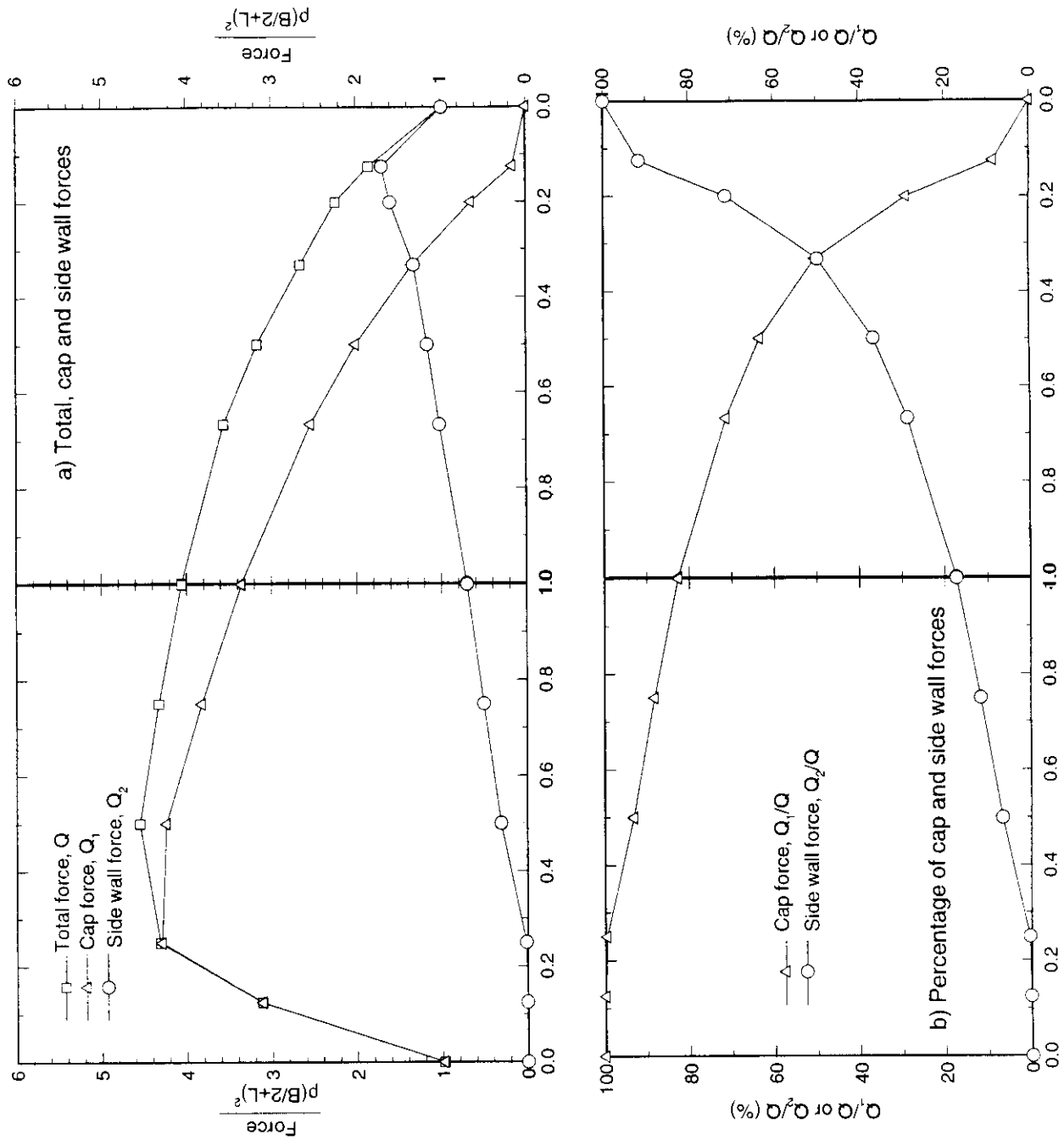

Figure 6.19 Lower Bound Calculations of Wall and Cap Forces for Planar Caissons in Non-Homogeneous Clay

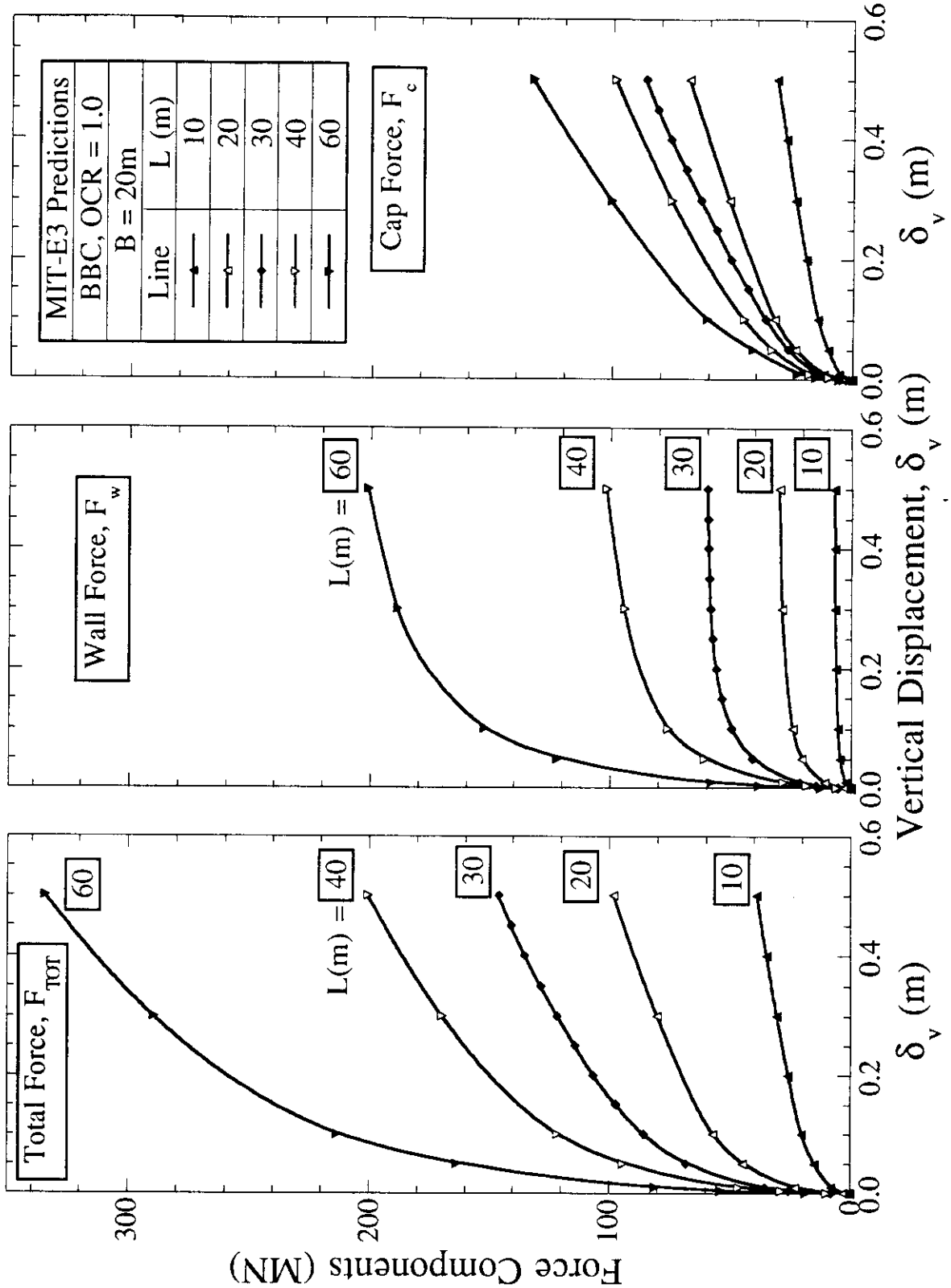

Figure 6.20a Effect of Wall Length on Predicted Load-Deformation Response

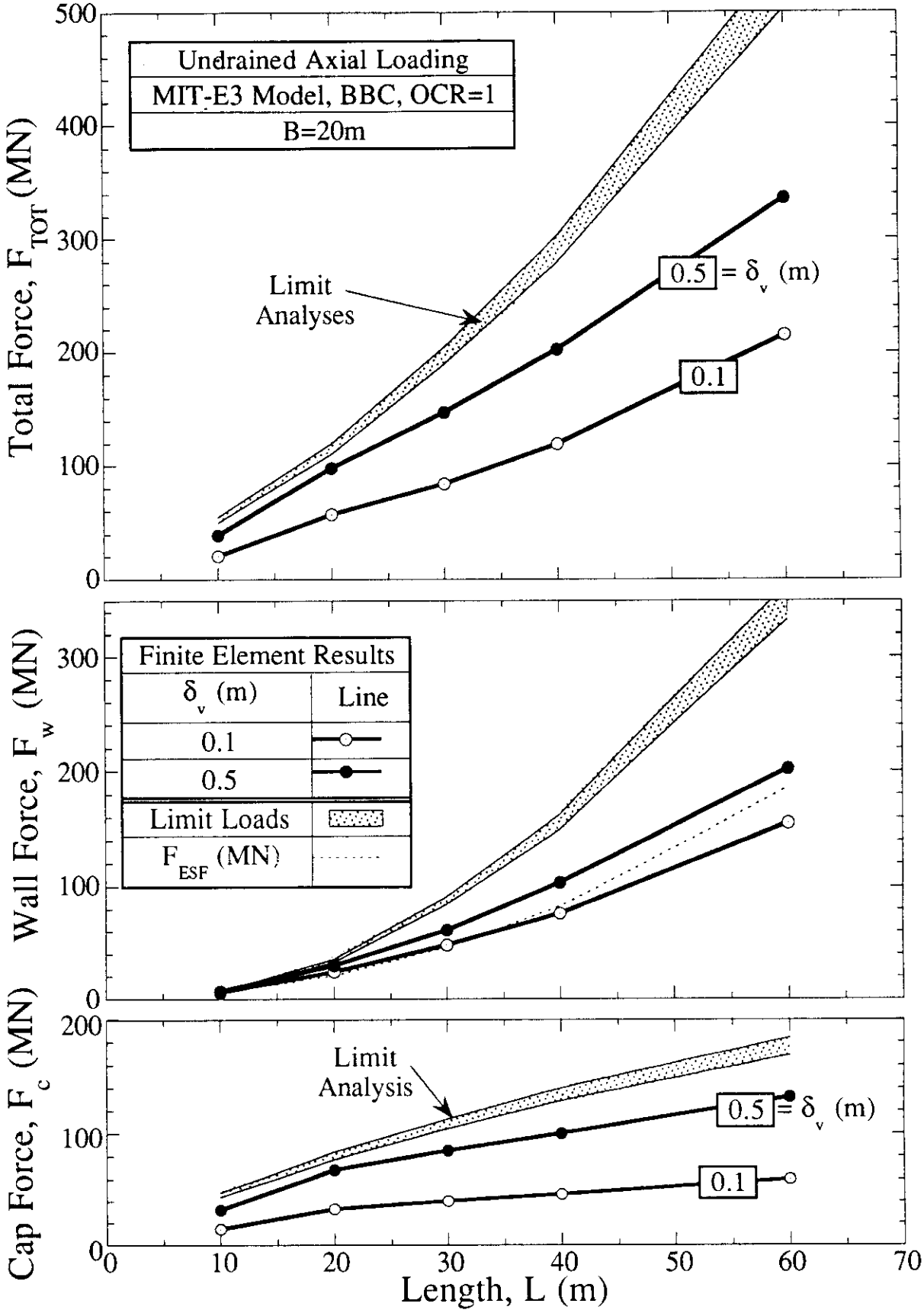

Figure 6.20b Effect of Wall Length on Mobilization of Total, Wall and Cap Forces

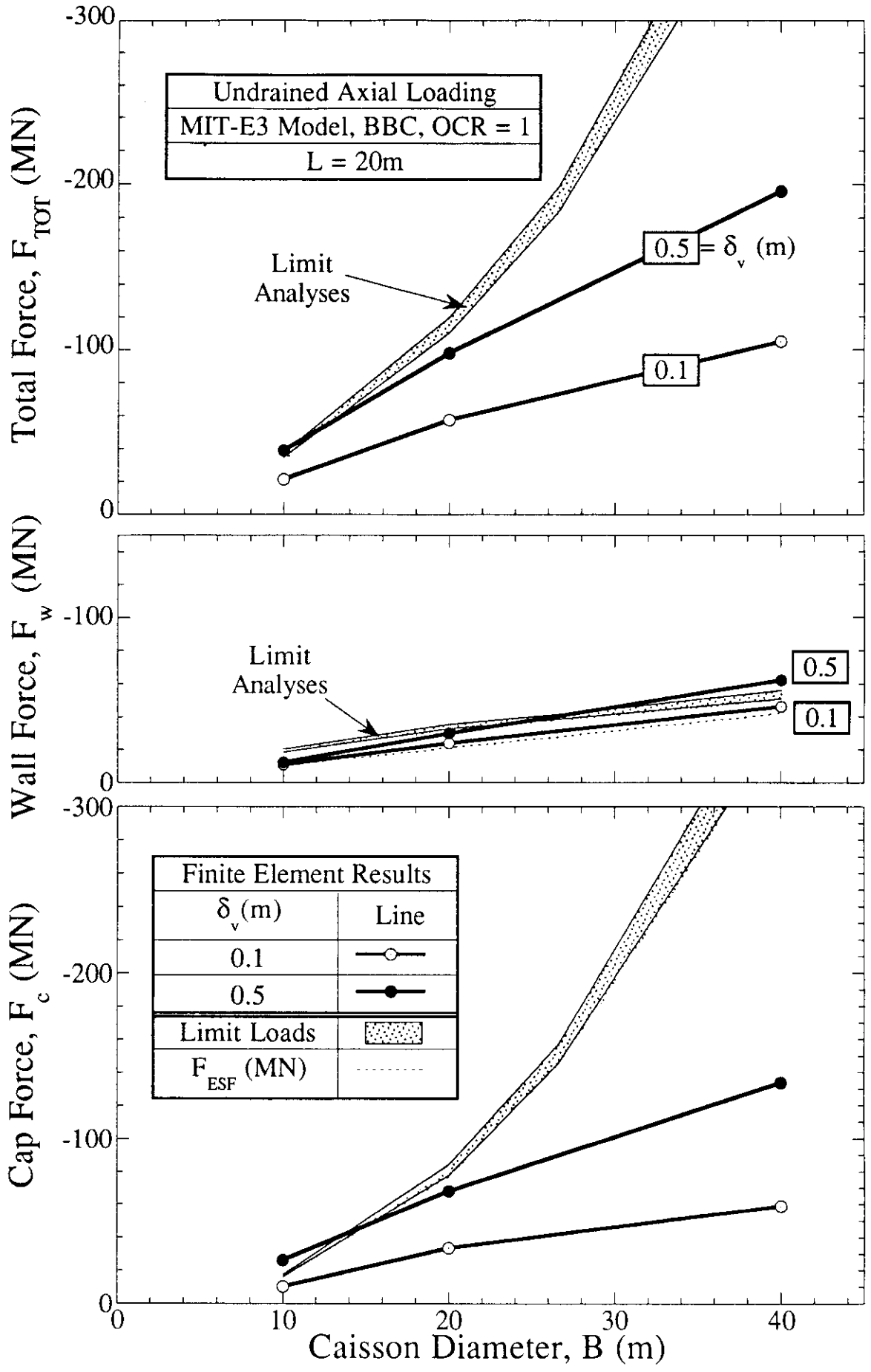

Figure 6.21 Effect of Caisson Diameter on Mobilization of Total, Wall and Cap Forces

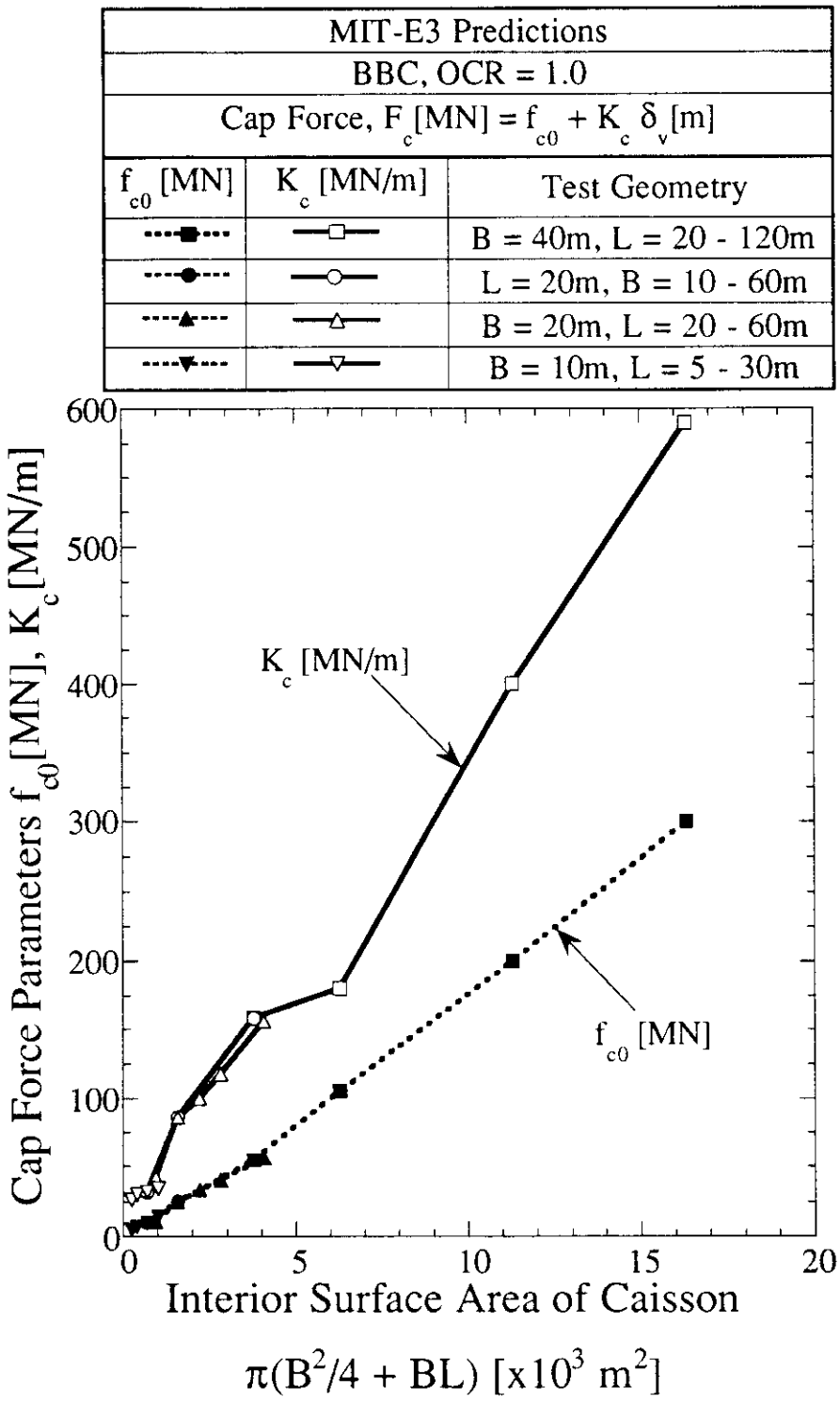

Figure 6.22 Parameters for Estimating the Cap Force-Displacement Behavior of Caissons in BBC

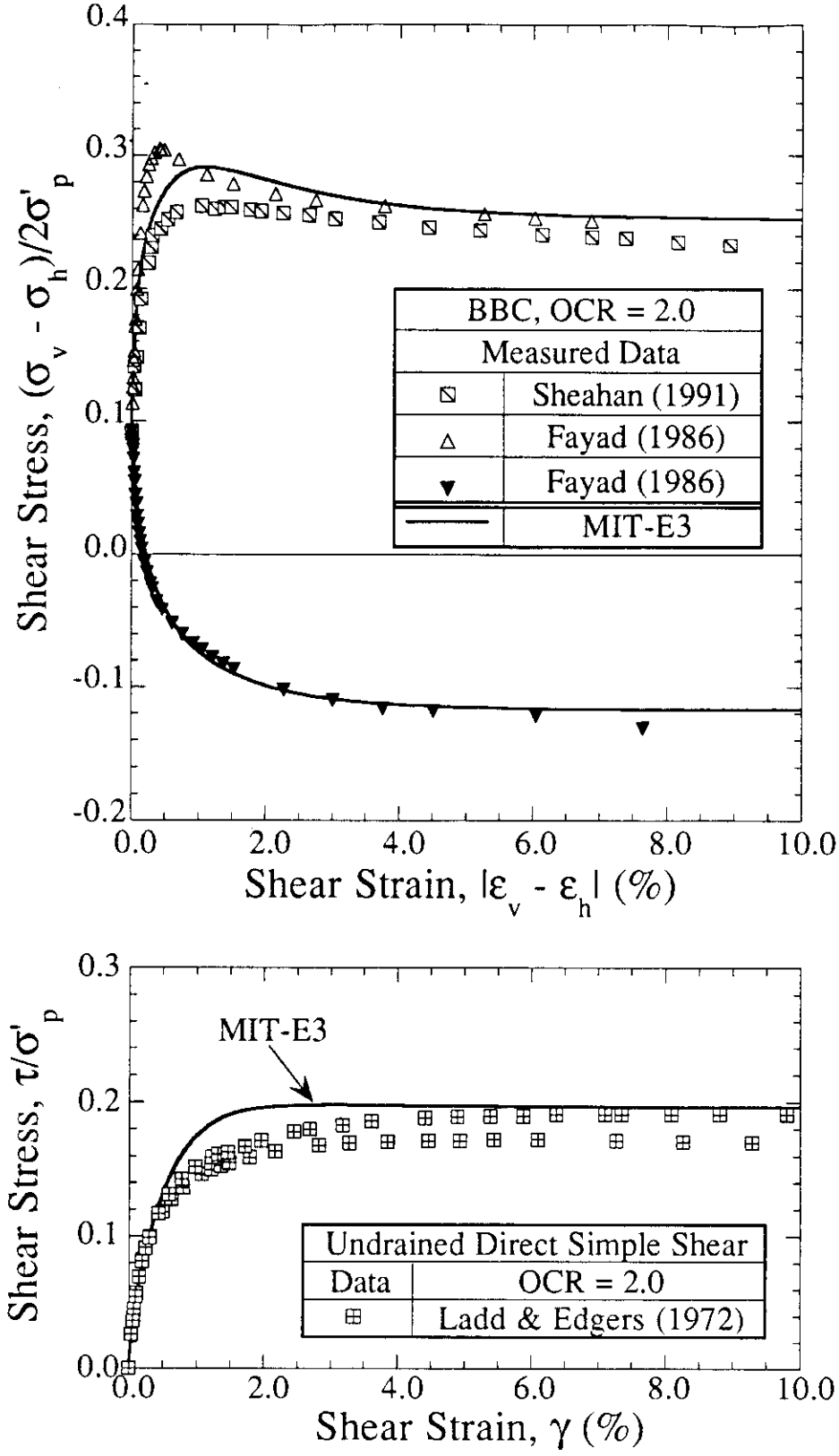

Figure 6.23 Comparison of Predicted and Measured Undrained Shear Behavior of BBC at OCR = 2.0

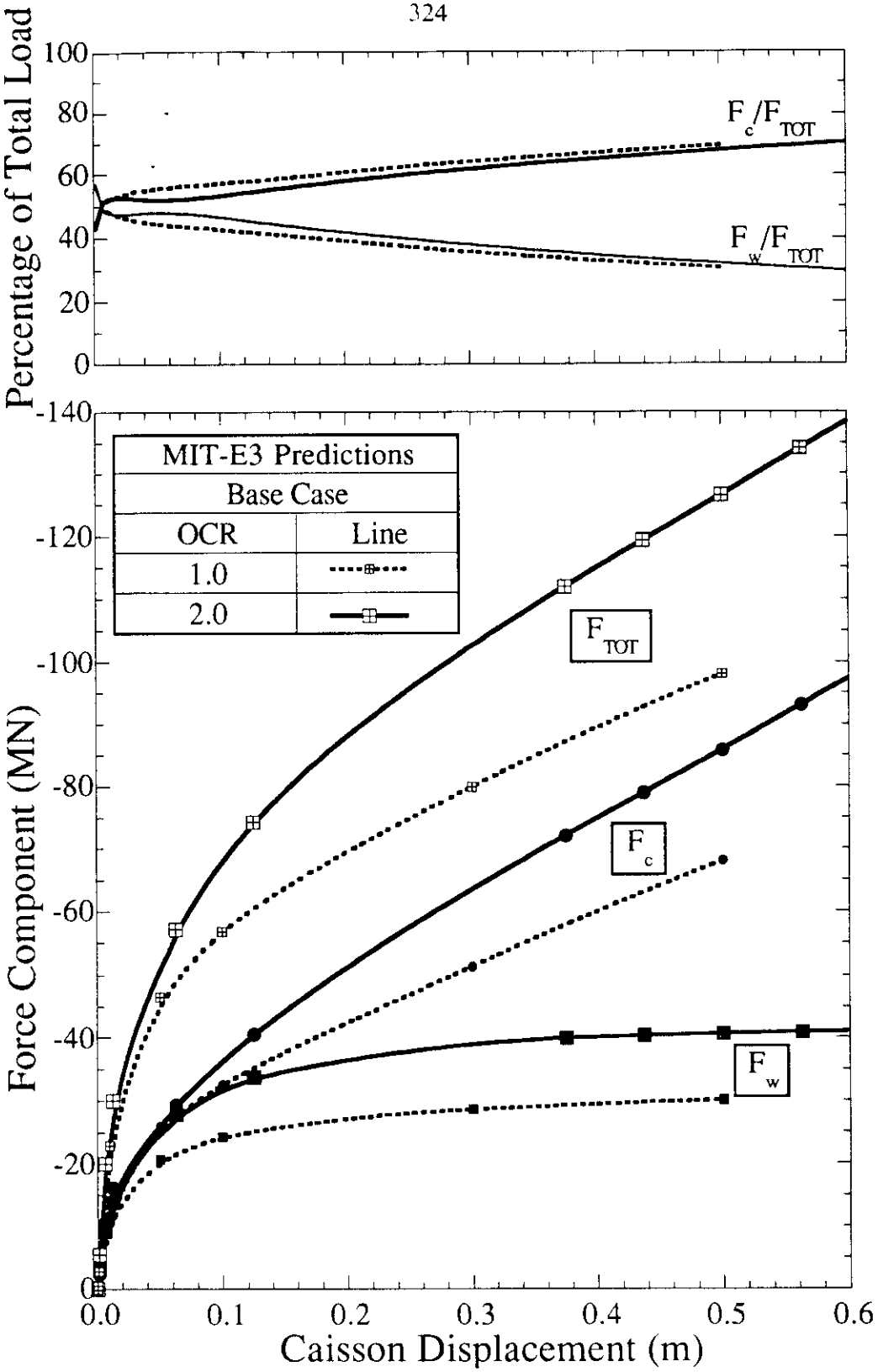

Figure 6.24 Comparison of Predicted Load-Deformation Response in BBC at OCR = 1.0 and 2.0 for Base Case Geometry

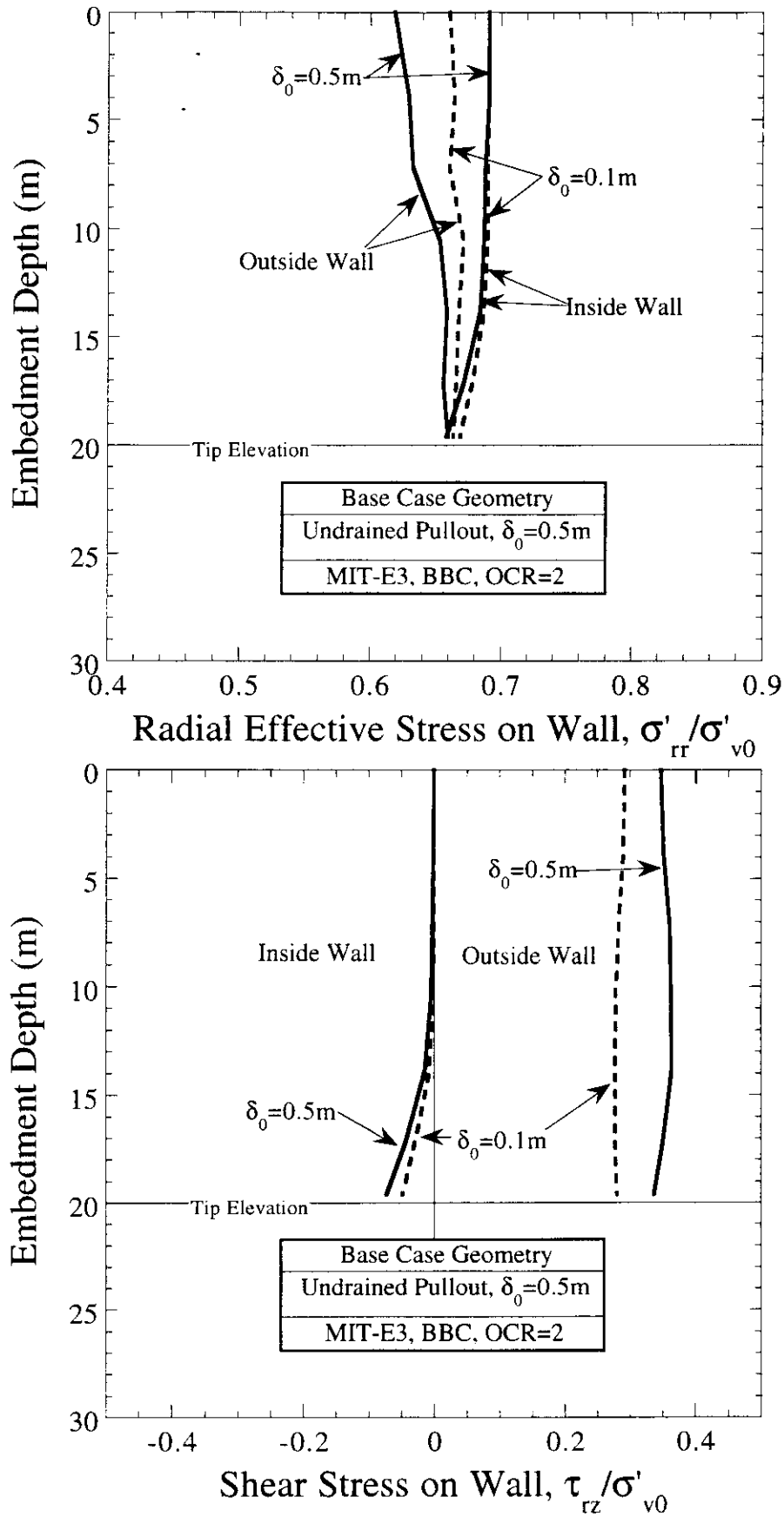

Figure 6.25 Radial Effective Stress and Shear Tractions on Caisson Wall in BBC at OCR = 2.0 for Base Case Geometry

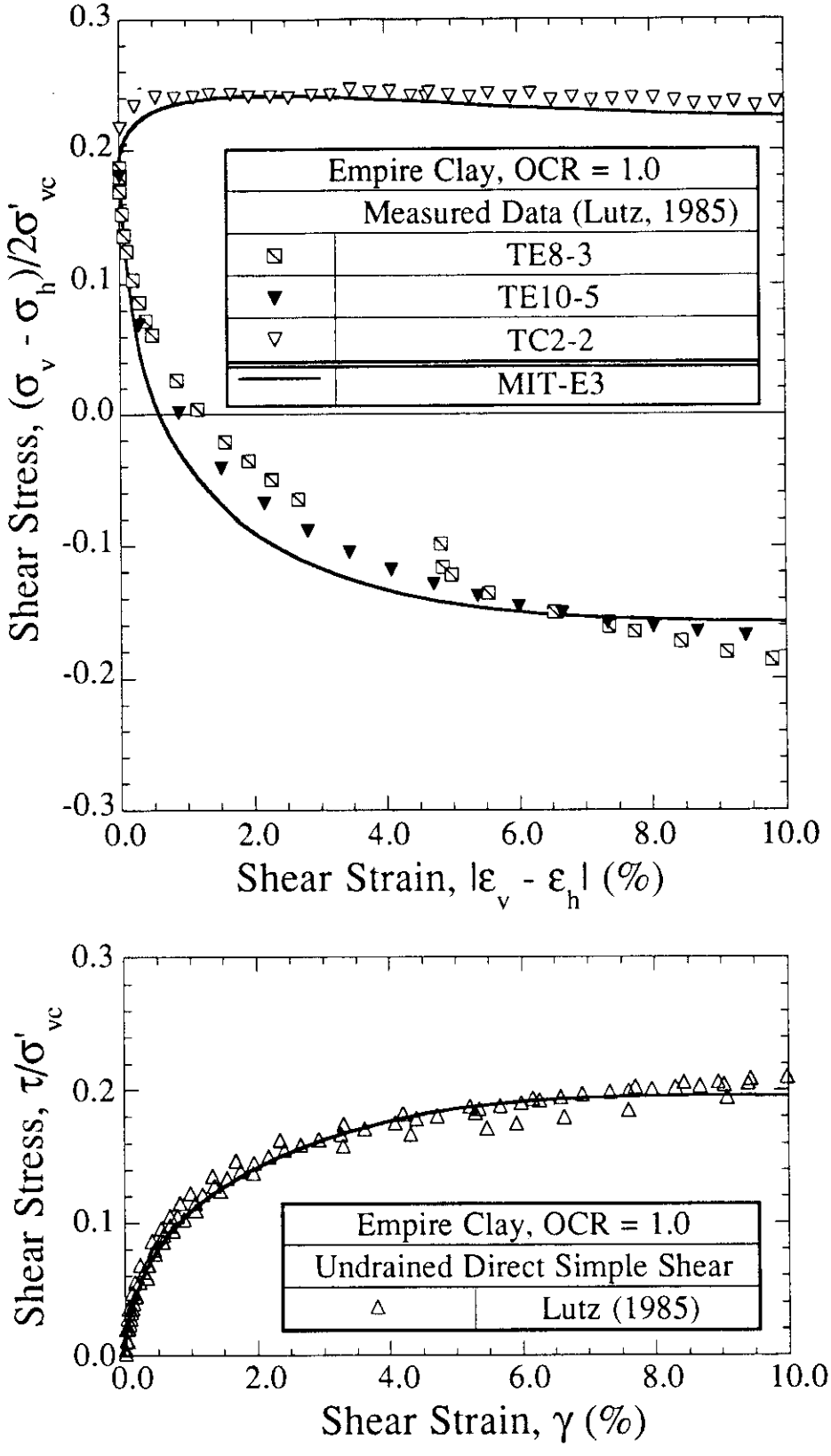

Figure 6.26 Comparison of Predicted and Measured Undrained Shear Behavior for K_0-Normally Consolidated Empire Clay

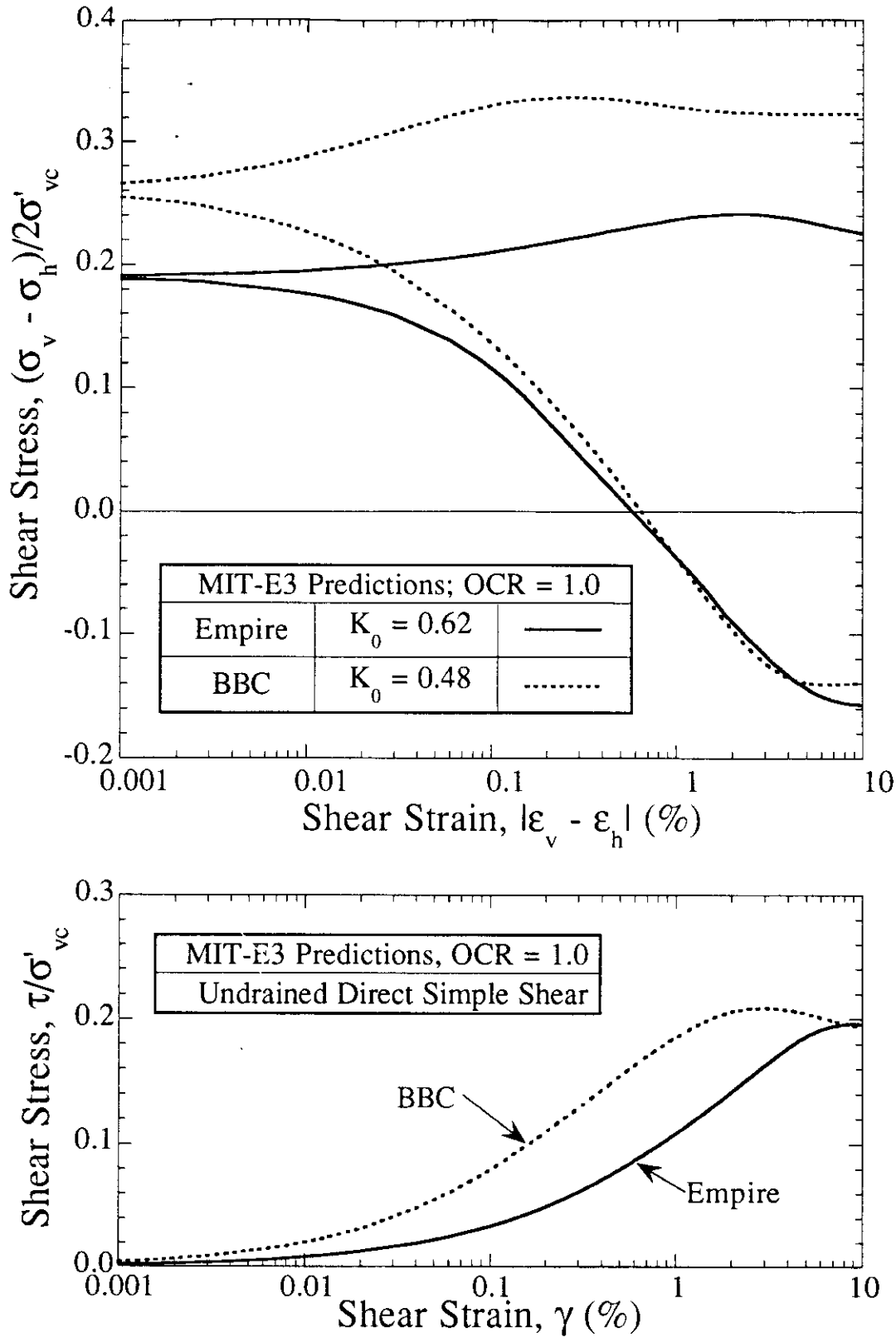

Figure 6.27 Comparison of Undrained Shear Stress-Strain Behavior Predicted by MIT-E3 for BBC and Empire Clay

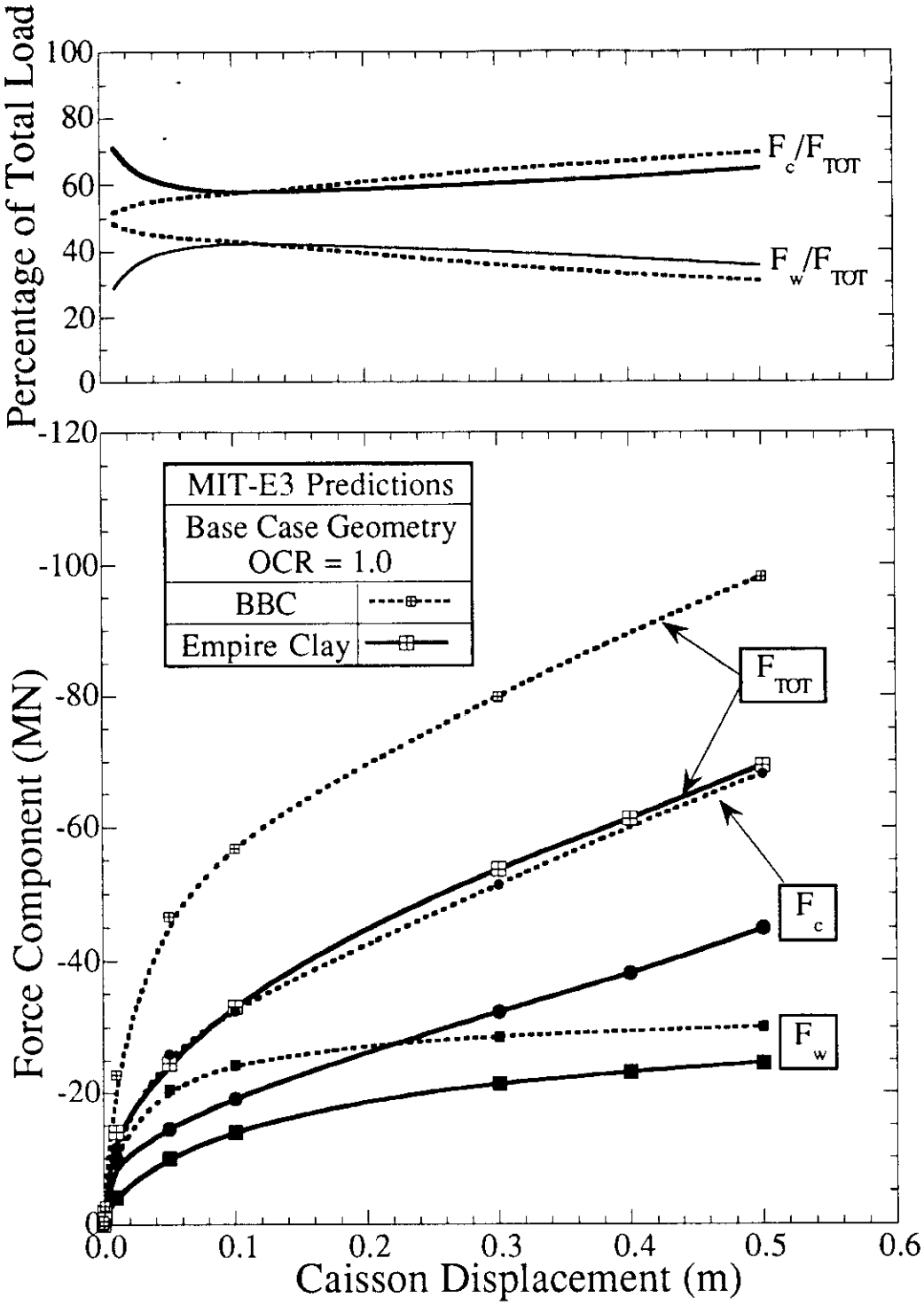

Figure 6.28 Comparison of Predicted Load-Deformation Response for Base Case Caisson Geometry in Normally Consolidated BBC and Empire Clay

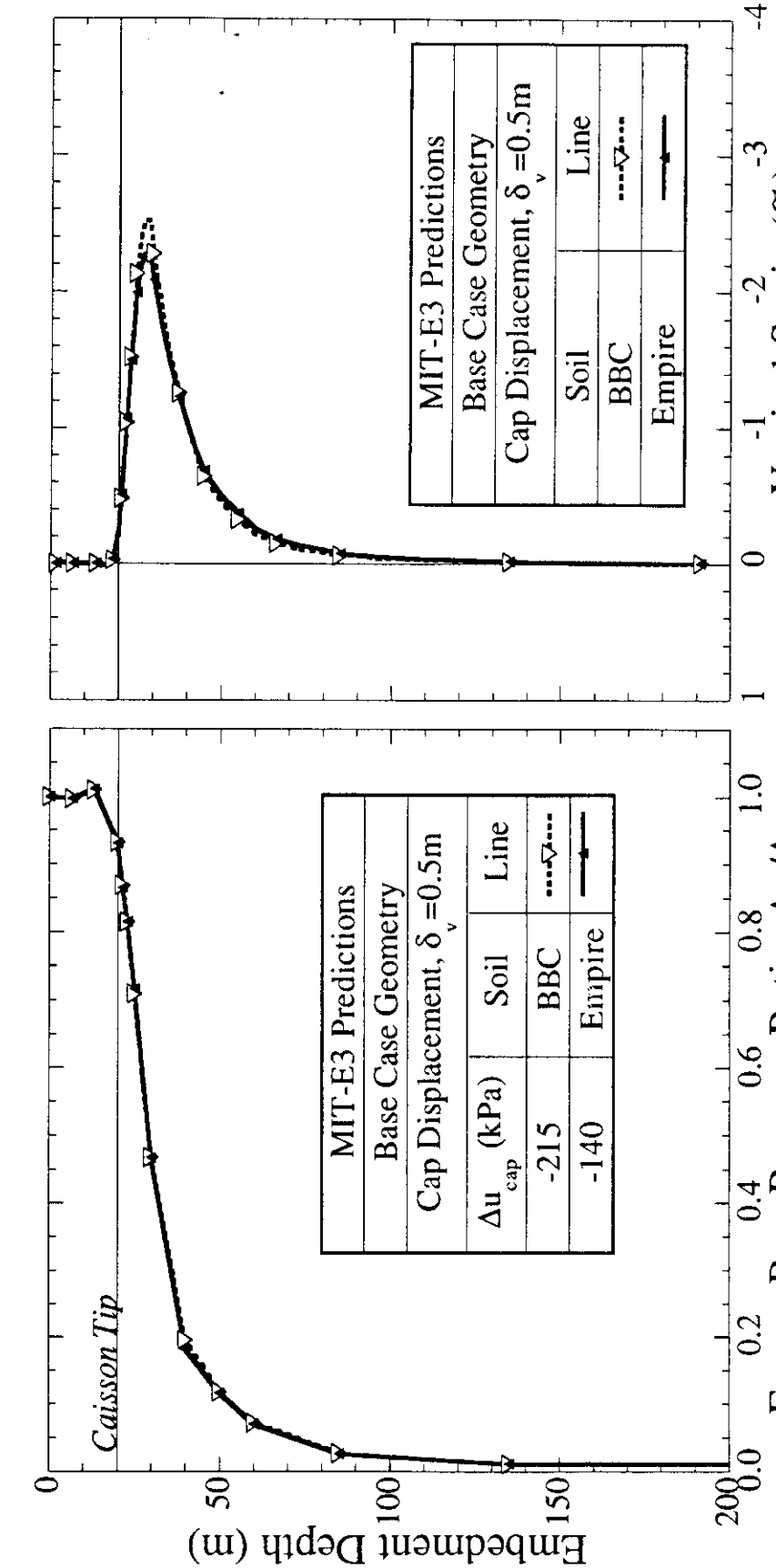

Figure 6.29 Excess Pore Pressure Ratio and Vertical Strains Predicted for Base Case Caisson Geometry in in Normally Consolidated BBC and Empire Clay

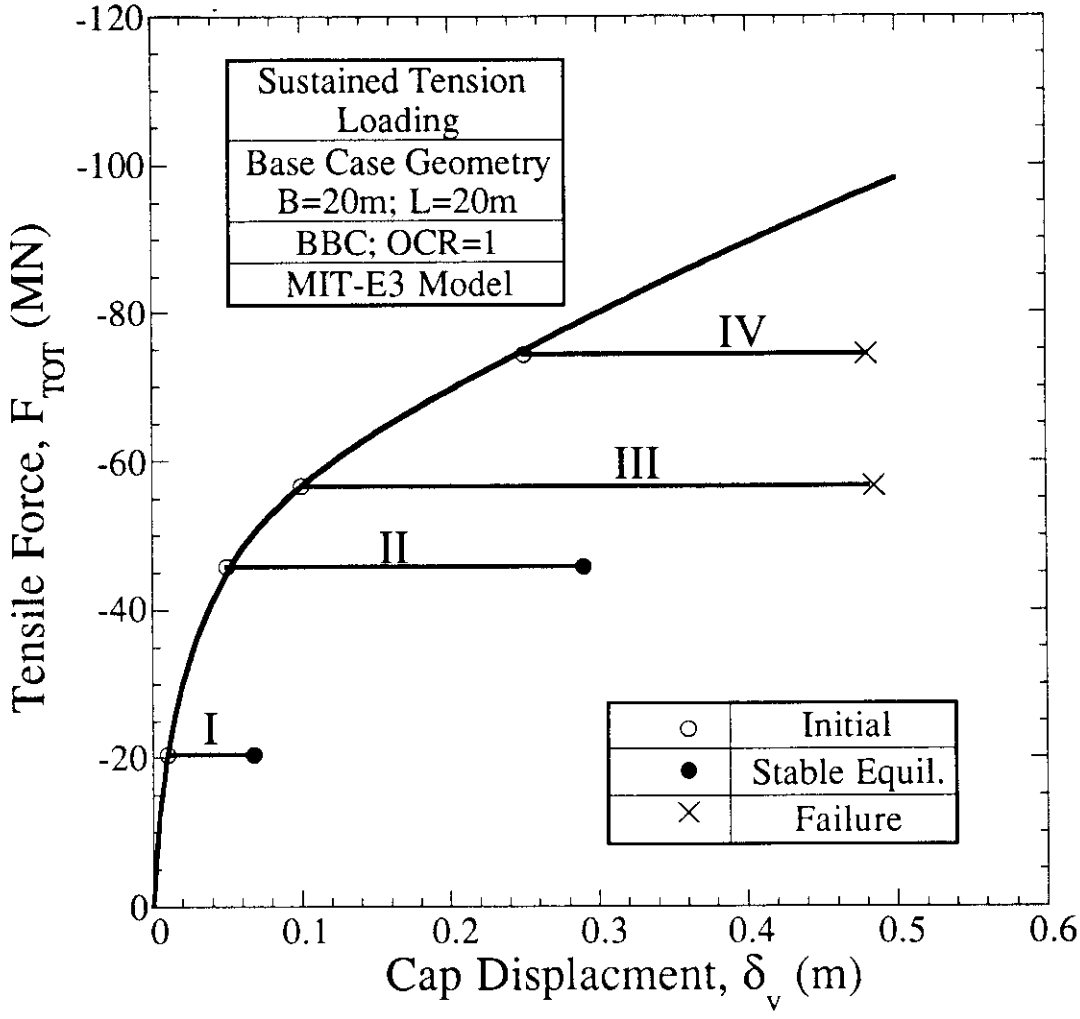

Figure 6.30 Summary of Load-Deformation Response for Four Sustained Load Tests with Base Case Caisson Geometry

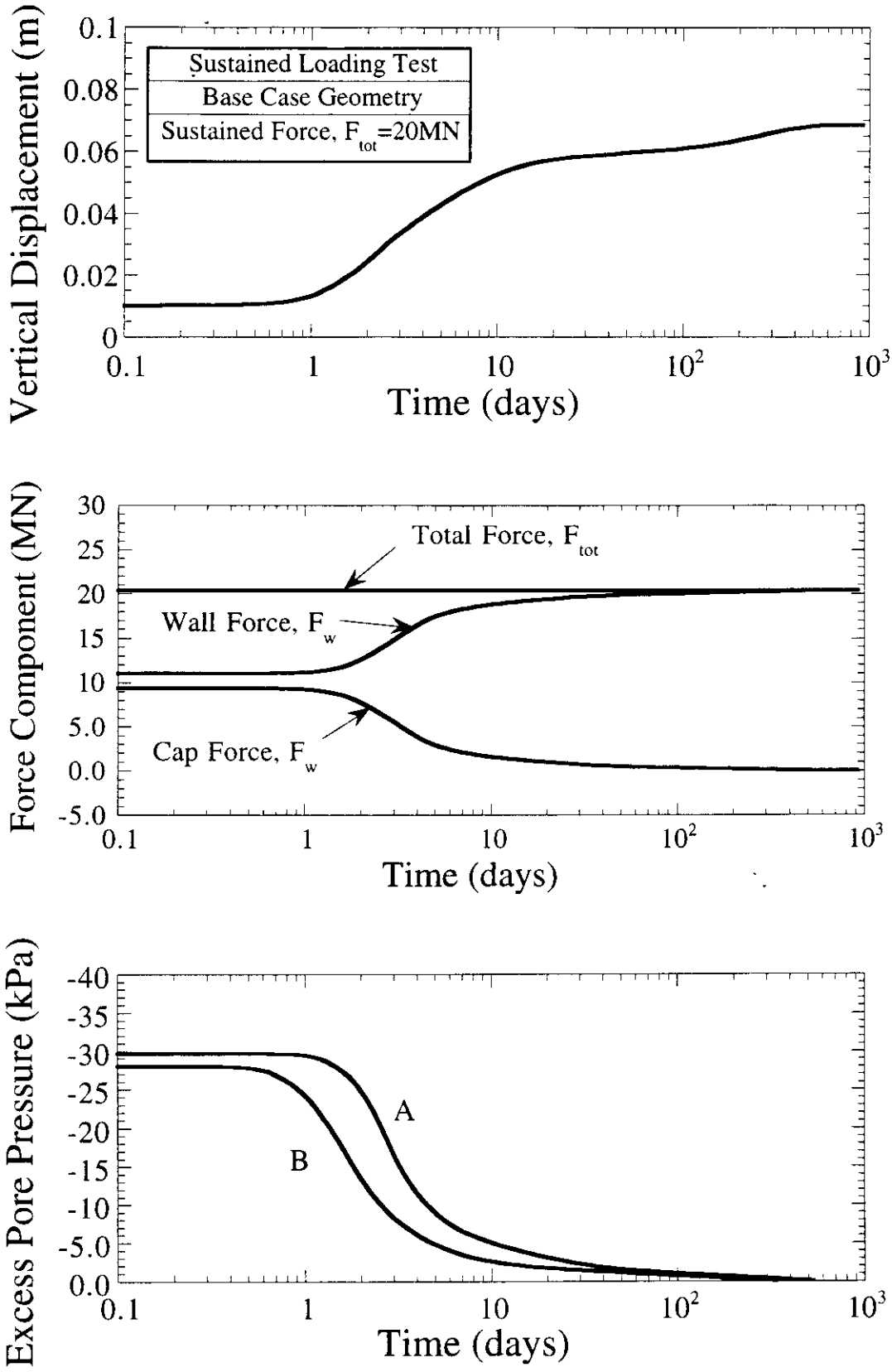

Figure 6.31 Time Dependent Response at Load Level I for the Base Case Geometry

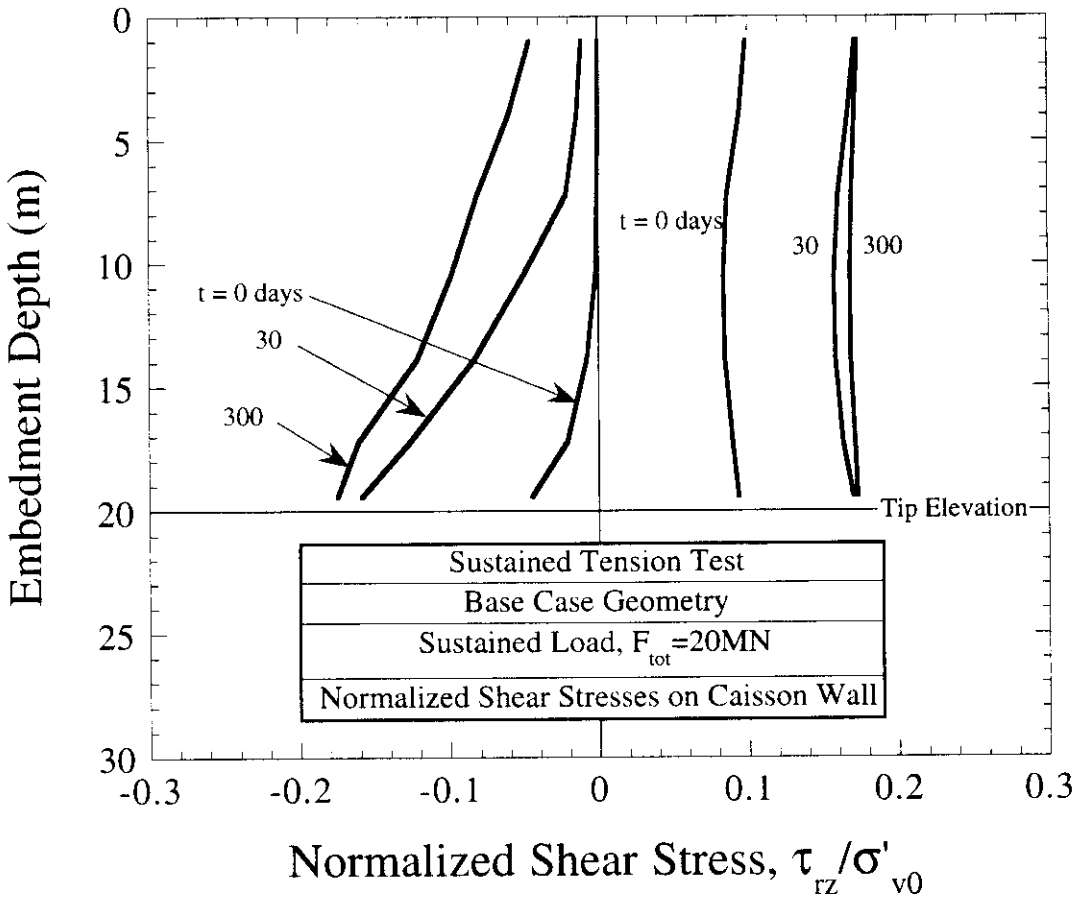

Figure 6.32 Development of Wall Shear Tractions During Sustained Loading at Level I

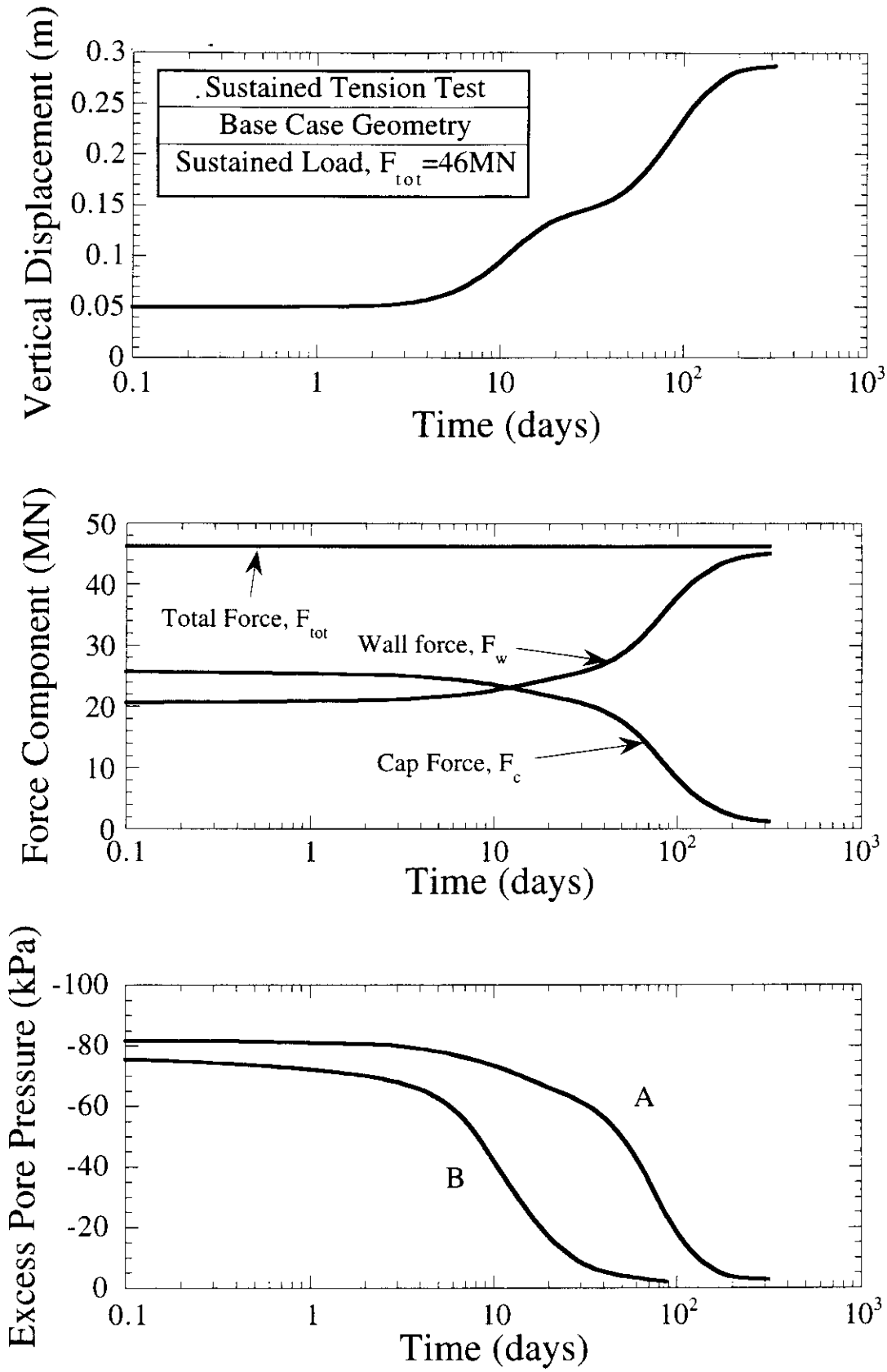

Figure 6.33 Time Dependent Response at Load Level II for the Base Case Geometry

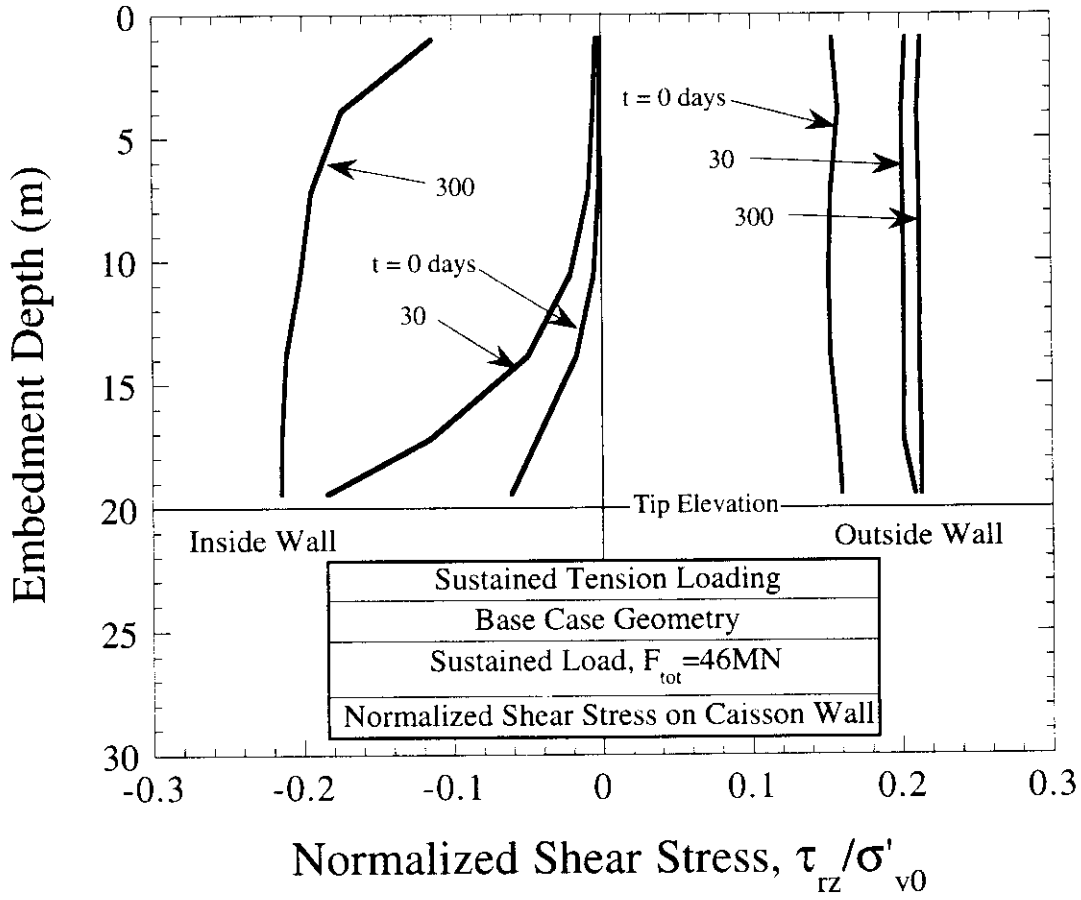

Figure 6.34 Development of Wall Shear Tractions During Sustained Loading at Level II

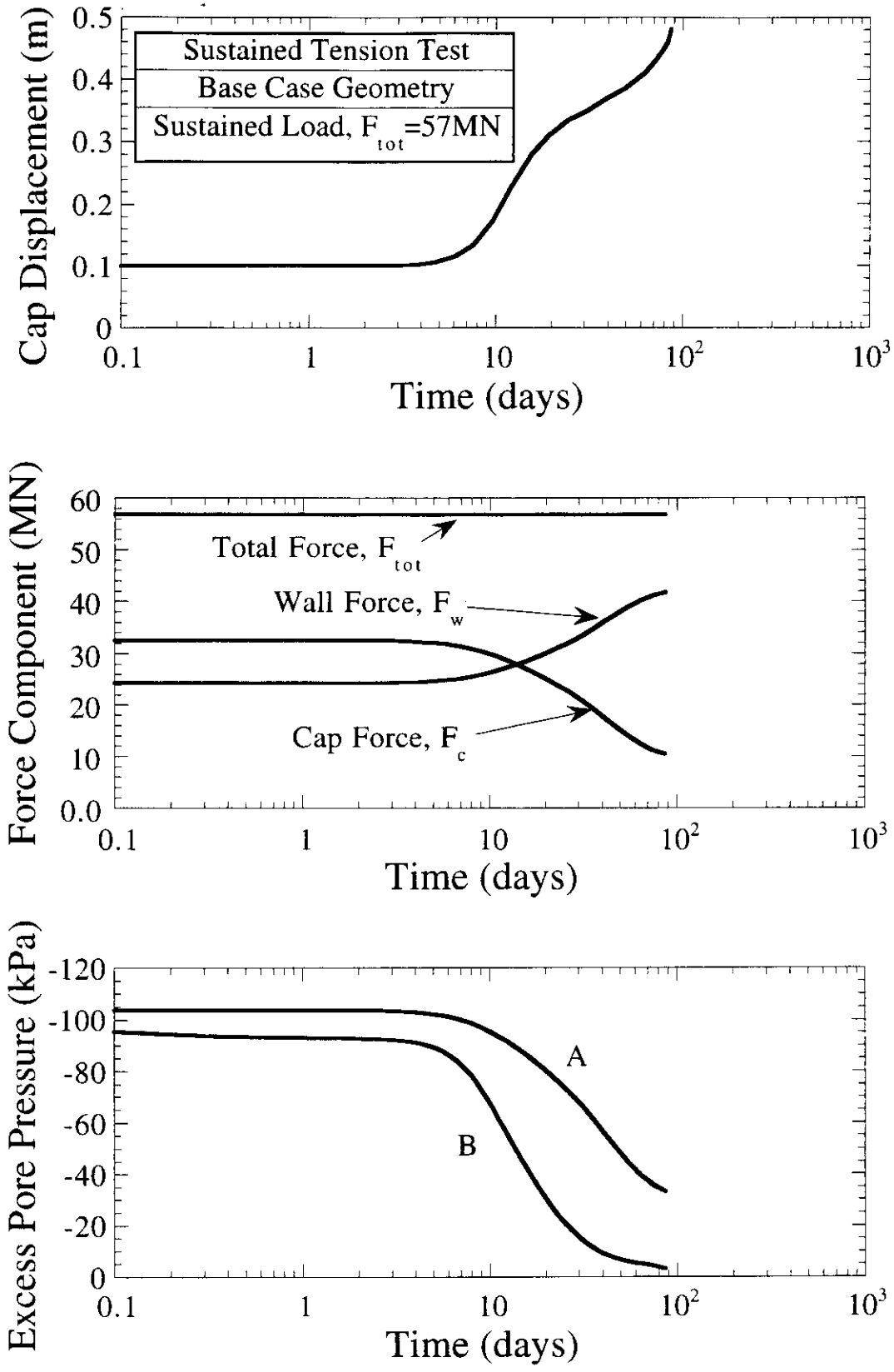

Figure 6.35 Time Dependent Response at Load Level III for the Base Case Geometry

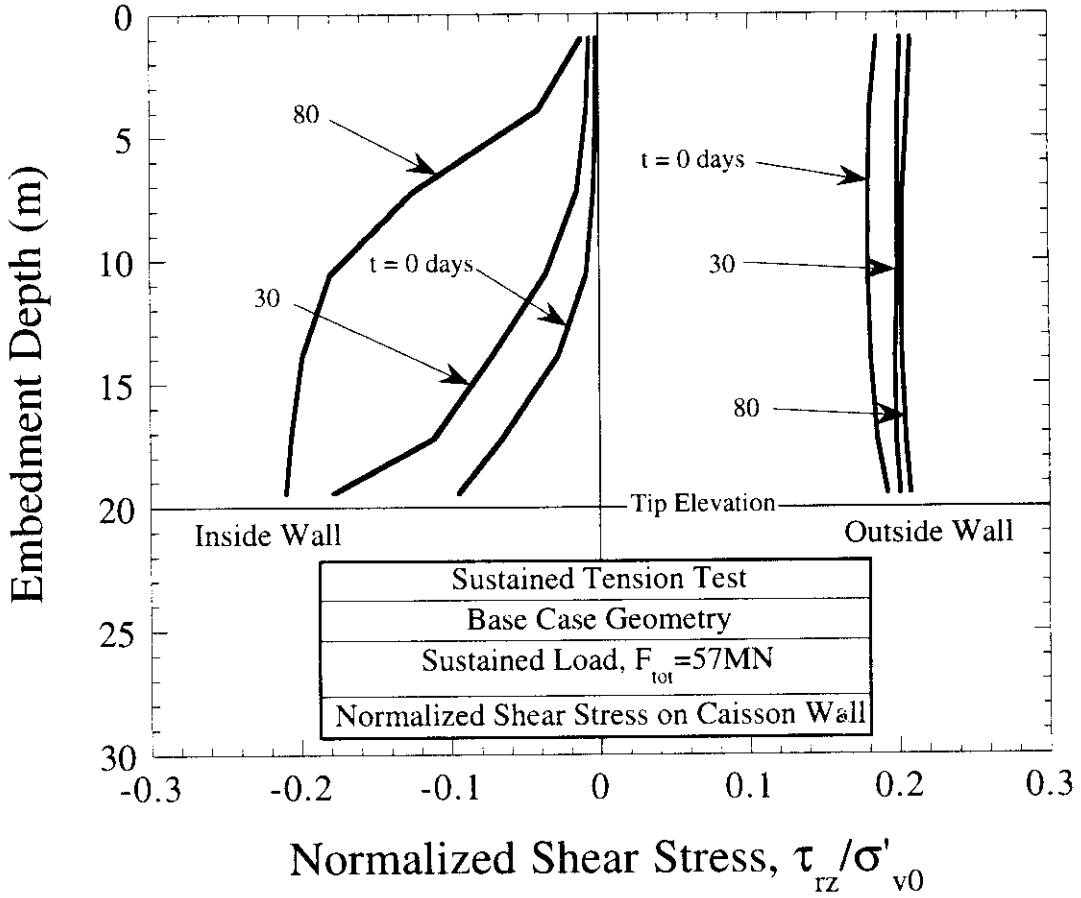

Figure 6.36 Development of Wall Shear Tractions During Sustained Loading at Level III

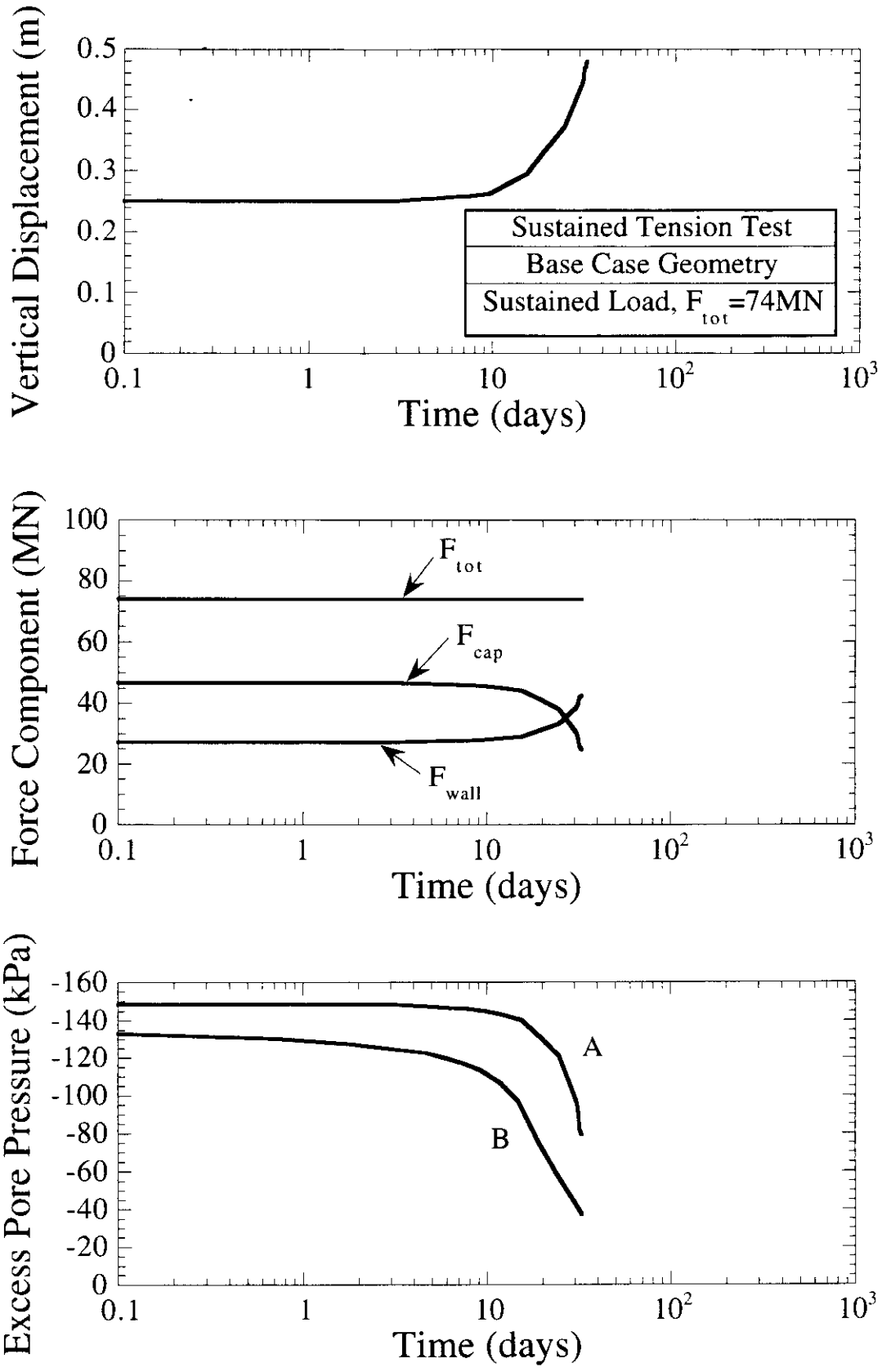

Figure 6.37 Time Dependent Response at Load Level IV for the Base Case Geometry

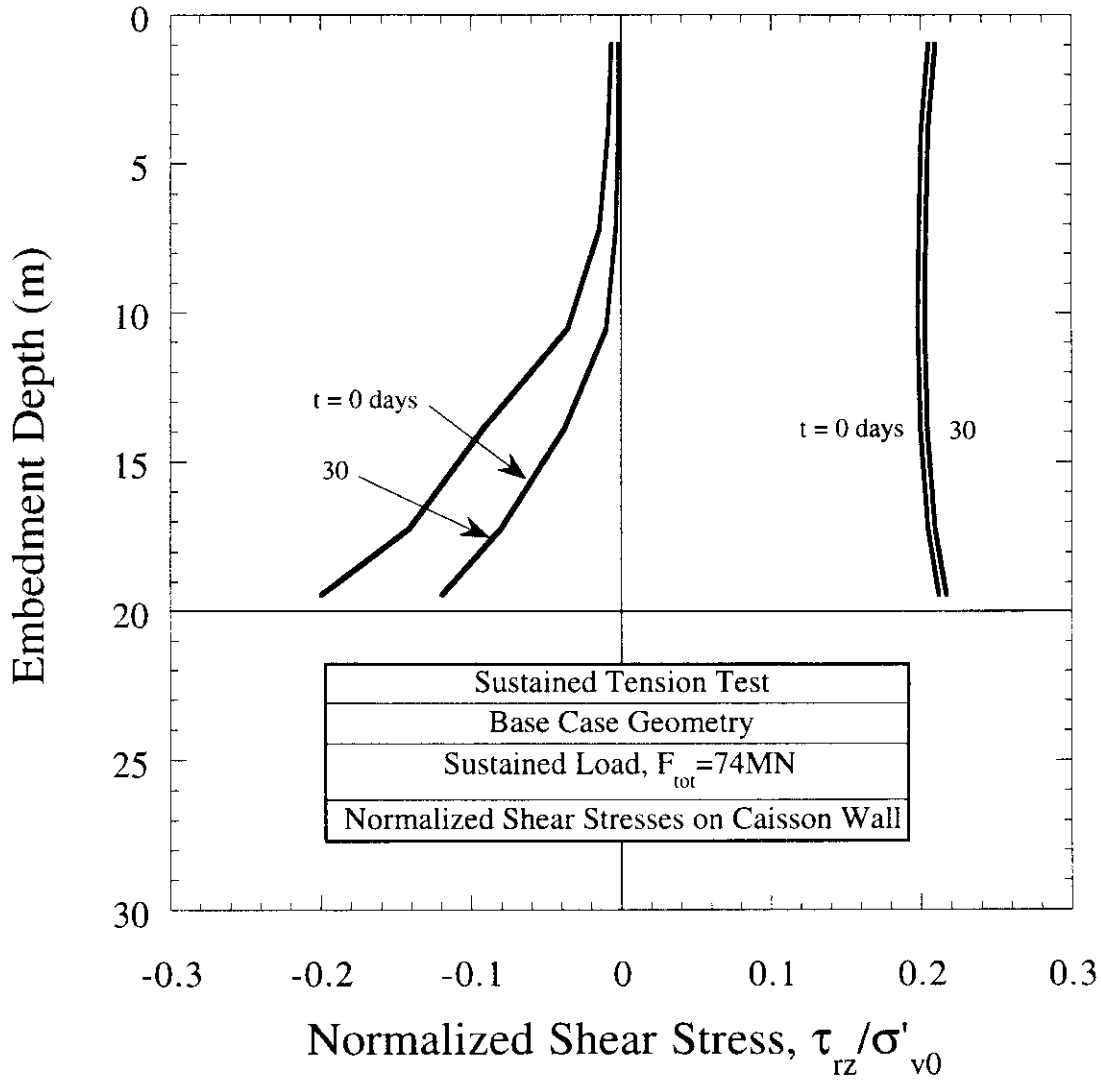

Figure 6.38 Development of Wall Shear Tractions During Sustained Loading at Level IV

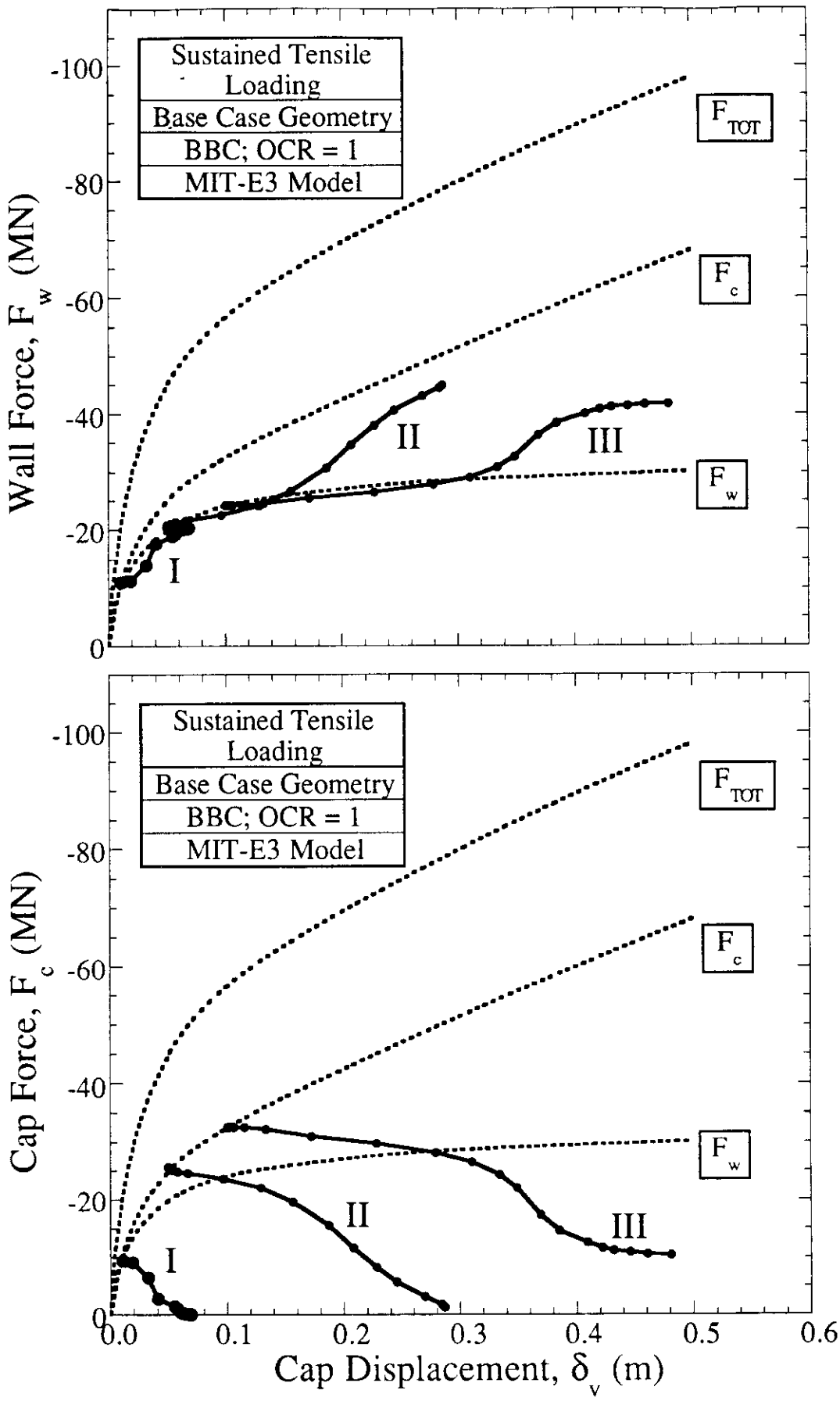

Figure 6.39 Summary of Cap and Wall Forces for Sustained Load Tests on Base Case Geometry

7. EVALUATION OF MEASURED CAISSON PERFORMANCE

7.1 INTRODUCTION

This chapter draws together an understanding of caisson behavior by comparing results of experimental measurements with analytical predictions during the successive phases of installation, set-up, monotonic (undrained) and sustained axial loading.

The CET experiments provide the most detailed information on the installation disturbance caused by underbase suction, while additional data were recorded in centrifuge model tests performed on thick-walled, open-ended piles (Hjortnaes-Pedersen and Bezuijen, 1992a, b). Section 7.2 compares measurements of soil deformations during installation with theoretical predictions based on the new SSPM analyses (Section 2.3, Sagaseta et al., 1995). In contrast to previous studies of deep pile penetration, deformations of the clay surface account fully for the volume displaced by the walls of the CET model caisson during penetration. The interpretation of the measured penetration forces relies on existing SPM solutions and empirical methods.

Section 7.3 reviews the measurements of equilibration in the CET experiments including the dissipation of pore pressures, load transfer and clay deformations. All of these tests are equilibrated with no net change in total vertical stress at the clay surface (there is no self-weight component of the penetration).

Section 7.4 compares and evaluates finite element predictions of monotonic axial load (undrained pullout) response for the CET and EPR centrifuge model (test f8) caissons. The analyses consider wished-in-place initial conditions (i.e., no installation disturbance) and focus on the load-deformation response at small cap displacements. The section also considers other methods of estimating undrained collapse loads for caissons in clay using numerical limit analyses (cf. Section 2.4). The section includes calculations for other caisson model experiments performed by EPR (including tests g9 and 119) and NGI (Andersen et al., 1993) with inclined static loading.

Section 7.5 compares finite element predictions with the measured response of the CET model caisson in sustained tensile loading. These data represent the first detailed measurements relating to the release of underbase suction pressures.

7.2 INSTALLATION PHASE

7.2.1 Installation Disturbance Due to Underbase Suction

At field scale, prototype caisson anchors will be installed through a combination of gravity penetration (due to the buoyant self-weight) and underbase 'suction' (achieved by reducing water pressures beneath the lid of the caisson). For example, the Concrete Foundation Templates (CFT) for the Snorre TLP (Christophersen et al., 1992) penetrated 10m under their buoyant self-weight, and were then assisted by underbase suction to reach a target penetration depth of 12m. Similarly,

the model caisson tests performed by NGI at the Lysaker site (Andersen et al., 1993a) reached 0.77m out of a 0.82m total skirt penetration depth due to the self-weight of the model. Installation of the EPR centrifuge model caissons was achieved primarily by applying dead weight surcharge loads with minor assistance from underbase suction.

One of the original goals of this project was to evaluate the effects of installation disturbance for suction caissons and to compare and contrast this behavior with the driven penetration of long, open-ended piles (cf. Whittle & Baligh, 1988). The two principal issues to be addressed are 1) the effects of the proposed caisson geometry (diameter to wall thickness ratio, referred to as B/t or R/w[1]) and proximity of the stress-free ground surface (embedment to diameter ratio, L/2R); and 2) characterize the penetration mechanisms associated with installation by underbase suction. Although the design of the CET experiments can address both of these issues, the experiments performed to date have focused on a single caisson geometry (R = 2.54cm, L/R ≈ 1.0, R/w = 34). The standard installation procedure used in the CET experiments simulates installation by underbase suction with no self-weight penetration. This is achieved (see Section 3.4) by balancing the forces applied to the top cap and side-wall components of the two-piece model caisson: The specimen is initially consolidated with the cap and side-wall resting on the ground surface and a uniform vertical effective stress, σ'_v = 0.75ksc applied across the top surface of the clay element (cf. Fig. 3.8), corresponding to a total compressive force on the caisson, F_{TOT} = 15.2kg. The tests impose a controlled wall penetration (at a specified displacement rate $\dot{\delta}_w$ = 0.03cm/min) and counterbalance the increments of wall force with equal and opposite decrements of cap force ($\Delta F_c = -\Delta F_w$, hence $\Delta F_{TOT} \approx 0$). Figure 7.1 compares the installation force measurements from 4 standard CET tests (CET-8, 9, 11, 12; all rated as high quality, Section 5.2) installed using underbase suction, with one experiment (CET-13) where the caisson wall is jacked into the clay by increasing the wall force, F_w. The results show the following:

1. The standard installation procedure maintains a constant total force in the range, F_{TOT} = 15-17kg throughout penetration, while the total force required to reach a wall tip penetration of 5.1cm in CET-13, F_{TOT} = 37.5kg (i.e., $\Delta F_{TOT} \approx$ 22.3kg).
2. There is significant scatter in the wall and cap forces measured in the 4 standard CET tests during the first 0.5cm of penetration. This behavior reflects both the physical transition from shallow indentation to deep penetration of the wall, and experimental problems arising from friction between the wall and cap components of the model caisson. Inter-component friction[2] is the most probable source of local maxima and minima in the wall and cap forces, respectively, which occur at wall tip penetrations 0.2-0.3cm. Test CET-12 shows particularly

[1] w is the half wall-thickness, R the outside radius of the caisson. This notation is preferred as it avoids later confusion with later notation which uses t for time.

[2] Section 5.3 shows that it is very difficult to control the inter-component friction in the CET experiments.

large deviations (up to ±5kg) from the other three tests during the first 2cm of penetration. This behavior is also most probably related to inter-component friction and is not considered typical in the subsequent interpretation of behavior.

The wall forces increase almost linearly with depth for tip penetrations exceeding 0.7cm, and can be represented by the expression:

$$F_w = F_0 + f'_w \delta_w \qquad (7.1)$$

where F_0 is the intercept at $\delta_w = 0$, and the f'_w is the average gradient of the wall force (i.e., $\Delta F_w/\Delta\delta_w$) over the range $1 \leq \delta_w \leq 5$cm. The measured data show $F_0 = 10.5$kg for all 4 standard tests and $f'_w = 1.23$ - 1.64kg/cm. The cap force decreases almost linearly over the same range of tip penetration depths, reaching a minimum value at the final depth, $F_c = -2 \pm 2$kg.

3. The cap force remains constant in CET-13, while the wall is jacked into position. The measured wall force in CET-13 is very similar to data from standard installation tests (underbase suction) for the first 0.5cm of penetration. Thereafter, the data show a linear increase in resistance with depth but CET-13 carries a higher wall load than the standard tests ($F_0 = 12.4$kg, $f'_w = 2.11$kg/cm).

Throughout the installation process, pore pressures are measured below the cap of the model caisson (cf. Fig. 3.6). Figure 7.2 summarizes these data for the same subset of CET experiments. The data from 3 tests (CET-8, 9, 11) are very consistent, while much lower excess pore pressures are obtained in CET-12 and are presumably related to differences in the measured cap and wall forces noted above. At the start of penetration there are small negative pore pressures beneath the cap (Δu = 0 to -0.1ksc), these increase during the first 0.7cm of penetration to a maximum positive value, $\Delta u \approx 0.2$ksc, and then decrease almost linearly with depth such that $\Delta u \approx$ 0ksc at the final embedment depth. Two pore pressure probes embedded within the clay and inside the caisson (P1 and P2, Figure 7.3) show a similar pattern of behavior. A third probe P3, Fig. 7.3) located close to the outside wall of the caisson confirms that penetration by underbase suction generates minimal excess pore pressures within the surrounding clay. In contrast when the wall is jacked into position (test CET-13), the cap pore pressures increase to $\Delta u = 0.6$ksc during the first 1cm of penetration but then remain almost constant as penetration proceeds to 5cm (maximum Δu = 0.68ksc).

The average vertical total stress is obtained from the measured cap force ($\bar{\sigma}_b = F_c/A_b$, where $A_b = 18.02\text{cm}^2$ is the cross-sectional area of the cap) assuming no frictional force is transferred from the cap to the wall[3], as shown in Figure 7.2b. Finally, the vertical effective stress

[3] Results in chapter 4 show that the frictional force is less than 2kg. Hence, by ignoring friction, the average cap stress may be in error by up to 0.11ksc.

at the cap-soil interface can be estimated from $\sigma'_v = \overline{\sigma}_b - \Delta u$[4]. The results in Figure 7.2c show that the vertical effective stress in all four tests installed with underbase suction decreases from an initial condition, $\sigma'_v = 0.75$ksc, to $\sigma'_v \approx 0$ksc at a wall tip penetration of approximately 1cm, and remain almost constant thereafter. The small negative effective stresses computed in these tests are not physically possible, but are an artifact of the assumptions used in computing σ'_v. The measurements for CET-13 show qualitatively very similar changes in effective stress with penetration depth when the wall is jacked into the clay, reaching a minimum, $\sigma'_v \approx 0.1$ksc.

Figure 7.4 summarizes the caisson cap displacements as functions of the wall tip penetration. There are surprisingly large variations in the cap movements measured in the four tests installed with standard underbase suction. However, three of the four tests generate a net upward displacement, $\delta_c = 0.52$ - 0.60cm (much larger values occur in CET-12) at the final embedment depth, which represent approximately 82-94% of the volume displaced by the wall (the figure includes the reference line, $\delta_c = \delta_w A_w / A_c$, corresponding to 100% of the displaced volume). At small wall tip penetrations ($\delta_w \leq$ 1cm) the measurements range from almost no cap movement (CET-11) to approximately 50% of the displaced volume. Thereafter, the rates of cap displacement vary widely among the four tests and often exceed the rate of volume displaced by the wall. The measurements show very similar net heave movements of the cap in test CET-13 ($\delta_c =$ 0.52cm), where installation is achieved by jacking the wall. This result is particularly surprising as the cap initially moves downwards during the first 1cm of penetration.

A series of up to 5 displacement transducers measured vertical deformations of the clay surface during installation of the model caissons in the CET apparatus. Figure 7.5 shows that these displacements are very small. For installation by underbase suction, measurements at S1 and S2 register small settlements of the surface (maximum $\delta_0 \approx -0.004$cm), while test CET-13 induces small amounts of heave (maximum $\delta_0 \approx 0.008$cm) which correlate closely with the cap movements observed in Figure 7.4. These results are consistent with previous observations that most of the displaced soil moves inside the caisson independent of the force system used during installation.

7.2.2 Interpretation of Installation Forces

The force measurements are difficult to interpret at small penetration depths due to factors such as inter-component friction. However, the data clearly show a transition to a well defined conditions where the wall and cap forces vary linearly with wall tip penetration (for $\delta_w \geq 1.0$cm). It is then possible to relate the coefficients F_0 and f'_w in eqn. 7.1 to a constant tip resistance (bearing stress) and average interface friction, respectively:

---

[4] This calculation assumes that the measured pore pressures are also approximately uniform at all points below the cap. Note that the pore pressure transducer has a surface area of 3.80 cm^2 and represents only 21% of the total area of the cap.

It is conventional practice in geotechnical engineering to relate the tip resistance to the undrained shear strength through a bearing capacity factor, N_c, where:

$$\frac{(q_{ult} - \sigma_{v0})}{\sigma'_{v0}} = N_c \frac{s_u}{\sigma'_{v0}} \qquad (7.2)$$

where q_{ult} is the stress at the wall tip, $q_{ult} = F_0/A_w$, the cross-sectional area of the wall, A_w = 2.248cm^2, $\sigma_{v0} = \sigma'_{v0}$ = 0.75ksc are the initial (consolidation) vertical total and effective stresses, and s_u/σ'_{v0} is the undrained strength ratio.

The CET experiments measure a normalized net tip resistance factor, $(q_{ult} - \sigma_{v0})/\sigma'_{v0}$ = 5.23 for installation by underbase suction, and a slightly higher value, $(q_{ult} - \sigma_{v0})/\sigma'_{v0}$ = 6.36 for CET-13. In comparison, field measurements of net tip resistance factors from piezocone tests in K_0-normally and lightly overconsolidated BBC (OCR = 1.0 - 1.2) range from 2.5 - 4.0. Theoretical predictions for closed-ended piles, based on the Strain Path Method and MIT-E3 model (at OCR = 1.0) range from 2.5 - 2.6 (Aubeny, 1992). Thus, the tip resistance for a thin-walled open-ended pile is significantly higher than that for the closed-ended penetrometer geometries considered in previous investigations.

Assuming a reference undrained strength ratio for K_0-normally consolidated RBBC in triaxial compression, s_{uTC}/σ'_{vc} = 0.32 (Sheahan, 1991), the resulting tip resistance factor, N_c = 16.3 (N_c = 19.9 for CET-13).

The gradient of the wall force in 'deep' penetration f'_w (eqn. 7.1) is related to the frictional resistance acting along the wall-soil interface. Assuming that there is similar mobilization of the undrained shear strength of the clay at all points along the inside and outside surfaces of the wall, then the average skin friction can be computed from $f_s = f'_w/2\pi(R_i + R_0)$ = 0.040 - 0.053 ksc for model caissons installed by underbase suction (where R_i = 2.395cm and R_0 = 2.54cm are the inside and outside radii of the caisson wall, respectively). The conventional skin friction β-factor is then obtained by normalizing with respect to the consolidation vertical effective stress, such that $\beta = f_s/\sigma'_{v0}$ = 0.053 - 0.071. This skin friction is clearly much lower than the undrained shear strength ratio of K_0-normally consolidated RBBC in direct simple shear, s_{uDSS}/σ'_{vc} = 0.205 (Ladd 1991), and hence $\alpha = f_s/s_{uDSS}$ = 0.26 - 0.35. The shaft friction is significantly higher in CET-13 (f_s = 0.068, β = 0.091, and α = 0.44).

The measured values of skin friction are in very good agreement with previous predictions for undrained deep penetration of open and closed-ended piles in BBC using the Strain Path Method and MIT-E3 model (β = 0.073 - 0.096; Whittle & Baligh, 1988; Whittle, 1992).

7.2.3 Interpretation of Ground Deformations by SSPM

The proximity of the stress free ground surface plays an important role in estimating the disturbances caused by caisson installation for the geometries of interest in this study, where the

total penetration depth is similar in magnitude to the cell diameter. Section 2.3 summarizes the development of a new method of analysis, referred to as the Shallow Strain Path Method (SSPM; Sagaseta et al., 1995), for predicting the ground deformations caused by undrained penetration of piles and caissons as functions of the embedment depth. The SSPM formulation combines the Strain Path Method developed by Baligh (1985) for steady, deep penetration in clays, with the work of Sagaseta (1985) for estimating deformations near the stress-free ground surface. Solutions for open-ended caissons are based on results for the simple tube geometry (Section 2.3.1) with nominal aspect ratio, R/w. Detailed observations show that the shaft radius of the simple tube is not exactly constant, but expands with distance from the tip especially at points close to the free surface. Section 2.3.1 describes approximate closed-form expressions for estimating ground surface heave around a straight-walled cylindrical caisson based on SSPM solutions for the simple tube geometry. These inherent clearance corrections factors become very significant for estimating the vertical displacements within the soil plug, especially for thick-walled caissons (small R/w), but have minimal impact on predictions of surface heave in the surrounding soil.

Figures 7.6 and 7.7 compare SSPM predictions of the surface heave profile at the final embedment depth (i.e., L/R ≈ 1) and vertical displacements of the cap during penetration with measured data from the CET experiments. The total predicted heave within the caisson ranges from δ_z/w = 1.2 - 1.7, increasing to 2.3 - 3.0 when the inherent clearance is included in the analysis. The measured cap displacements are much larger than the predictions (δ_z/w = 7.1 - 8.9 at L/R = 1, Fig. 7.6) for installation by both underbase suction (CET-8, 9, 11, 12) and wall jacking (CET-13). Furthermore, the measurements show much larger rates of cap displacement for wall tip penetration, δ_w > 1.0cm (Fig. 7.7). Outside of the caisson (Fig. 7.6) the analyses predict surface heave movements across the entire CET cell ($\delta_z/w \approx 1.5$ on the outside wall of the caisson), while the experimental data show very small net displacements of the original surface[5].

Discrepancies between SSPM predictions and the CET data are most probably caused by differences in the boundary stresses applied at the surface of the clay element. The SSPM analyses assume a stress-free ground surface, while the clay surface in the CET experiments is consolidated under a vertical effective stress, σ'_{v0} = 0.75ksc. During installation (by either underbase suction or wall jacking), there is a large reduction in the effective stress below the lid of the caisson (cf. Fig. 7.2) and hence, the undrained shear resistance at the top of the soil plug is much lower than that outside the caisson. This mechanism can then explain why almost the entire volume of soil displaced by wall penetration moves inside the caisson. Thus, the CET data cannot be used to evaluate predictions of ground deformations from the proposed SSPM analyses.

---

[5] The differences between predicted and measured displacements inside and outside the caisson are consistent with assumptions of undrained penetration (i.e., no volume change).

7.2.3.1 SSPM Predictions for Delft Centrifuge Tests

There is very little published data on ground movements caused by penetration of open-ended piles or caissons in clay. However, some useful results are available from two centrifuge tests[6] carried out by Delft Geotechnics (Hjortnaes-Pedersen and Bezuijen, 1992a, b). These tests reproduce a prototype thick-walled, open-ended caisson with length, L = 36.0m., outside radius, R = 6.525m., and wall thickness 2w = 1.275 m (Fig. 7.8). The caisson has a very small aspect ratio (R/w = 9.235) compared to the geometries being considered for TLP suction anchors ($40 \leq R/w \leq 200$). The caissons are jacked into a layer of Speswhite kaolin at an average rate of 0.78 cm/min. Vertical displacements of the ground surface are measured throughout penetration at the centerline axis (r/w = 0) and at a distance of about one pile radius from the wall (r/w = 19.3).

Figure 7.9 compares the surface displacement profile predicted by the SSPM analysis (at the final embedment depth, L/R = 5.52) with the measured heave inside and outside the pile. There is excellent agreement between predicted and measured displacements at both locations, however, it should be noted that the clearance correction represents a very significant factor in the computed heave inside the caisson. In these experiments, the measured heave of the soil plug ($\delta_z/w = 6 - 8$) corresponds to 20-26% of the volume displaced by the wall of the caisson. Figure 7.10 compares the predicted and measured surface displacements as functions of the wall tip penetration depth, h/w. These results confirm that the inherent clearance controls the magnitudes of ground deformations inside the tube. The proposed correction factor affects both the magnitude and rate of soil heave with penetration. The corrected solutions are in excellent agreement with the measured data and confirm that the proposed method of analysis can provide a reliable framework for interpreting ground deformations due to open-ended caisson penetration.

7.3 EQUILIBRATION PHASE

After installation, all of the model caissons were allowed to equilibrate at a constant total force, F_{TOT} = 15.2kg (i.e., statically equivalent to the initial consolidation effective stress σ'_{vc} = 0.75ksc) for a period of between 18 and 33hours. Figure 7.11 summarizes the cap displacements, component forces and excess pore pressures as functions of time for three tests CET-9, 12 and 13. Two of these tests (CET-9, 12) were installed by underbase suction (with $\Delta F_{TOT} = 0$), while the third (CET-13) was jacked into position by loading the wall (the additional surcharge load is removed at the start of equilibration).

There is a small re-distribution of loads between the wall and cap forces in tests CET-9, 12 which occurs within a period of 3-10mins after installation. The cap sheds the small initial tensile loads (F_c = -1 to -3kg) and thereafter applies a small compressive force, $F_c \approx$ 1kg, while the wall

[6]The tests were carried out at centrifugal accelerations of N = 150g and 300g.

transmits almost all of the compressive force to the soil. The cap pore pressures follow the signature of the cap force very closely, stabilizing in the range $\Delta u = 0.05 \pm 0.025$ksc within 3-10mins. These small positive excess pore pressures remain beneath the cap for an extended period of time, dissipating very slowly due to the low hydraulic gradient.

There is negligible displacement of the caisson (cap) during the first 10mins of equilibration. However, for t > 100mins, the rate of cap settlement is proportional to *log* t, generating displacements up to 0.12cm by the end of the equilibration period. Further observations (Section 5.5.4) show that the rates of settlement are approximately constant across the surface of the CET chamber (but vary significantly between tests) and are therefore caused by secondary compression of the clay. Estimated rates of secondary compression for CET-9, 12 are $C_\alpha = d\varepsilon_v/d(log\ t) = 0.0049,\ 0.0016$, respectively, which are much lower than the expected secondary compression rates for K_0-normally consolidated BBC ($C_\alpha = 0.026C_c \approx 0.01$; Mesri & Hayat, 1993).

The results for CET-13 show a number of important effects related to the installation procedure. The installation surcharge load ($\Delta F_{TOT} \approx 23$kg; cf. Fig. 7.1) is removed at the start of the equilibration phase, generating a small upward movement of the cap. Initially the wall and cap forces are approximately equal in magnitude ($F_w \approx F_c = 7.6 \pm 1.5$kg), with an excess pore pressure, $\Delta u = 0.25$ - 0.3ksc measured below the cap. At the end of equilibration, the force distribution is almost identical to the case of standard underbase installation ($F_w \approx 14$kg, $F_w \approx 1.0$kg). However, the re-distribution of the component forces and dissipation of excess pore pressures occurs over a much longer timeframe, with $t_{50} \approx 15$mins and $t_{90} \approx 150$mins. The measured cap settlement during this period is very similar to behavior measured in other CET tests, and is most probably caused by secondary compression of the clay.

For prototype offshore caissons, installation will occur through a combination of self-weight penetration and underbase suction. The CET experiments confirm that the re-equilibration of stresses and pore pressures associated with the underbase suction mode of penetration occurs relatively rapidly with minimal consolidation of the soil. Equilibration times for prototype caissons will be controlled by consolidation due to the buoyant self-weight of the structure (and applied ballast), with drainage path length related to the embedment depth of the wall, L, and cell radius, R.

7.4 UNDRAINED AXIAL LOADING TO FAILURE

7.4.1 Results of CET Tests

This section summarizes the measurements of undrained (short-term) tensile load capacity and load-displacement response for selected CET model caisson tests. The experiments can be sub-divided into two main groups:

1. First time pullout tests (MP1; Fig. 5.2), which are performed after the caisson is allowed to equilibrate for at least 24hrs after installation at the original applied load, F_{TOT} = 15.2kg. The first time pullout experiments include: a) tests which are loaded directly to failure at a specified cap displacement rate, $\dot{\delta}_c$ = 0.03cm/min (CET-3 - 8); and b) caissons which are partially loaded to a prescribed tensile load level (CET 9 - 13, $\dot{\delta}_c$ = 0.03cm/min), prior to a sequence of sustained load tests (cf. Fig. 5.2).
2. Subsequent pullout tests (MP2; Fig. 5.2), in which the model caisson is loaded directly to failure after a sequence of sustained load tests (CET-9, 12, 13). The initial equilibrium conditions in these experiments depends on the preceding stage of sustained loading.

Figure 7.12 summarizes the total, wall and cap force-displacement responses for first time loading up to failure (line weights in this figure correspond to the assessment of test quality given in Section 5.2.4). Figure 7.13 shows data from the same test series at small cap displacements ($\delta_c \leq 0.02$cm). The model caissons have a well defined tensile load capacity, F_{TOT} = -23±1kg, which is mobilized at a cap displacement, δ_c = 0.2±0.05cm (comparable to the wall thickness, 2w = 0.145cm). At the start of the experiments, the wall carries more than 90% of the total (compressive) force acting on the caisson. Tensile loading generates a maximum wall resistance, F_w = -13.5±1.5kg (i.e., 60% of the total capacity), which also occurs at $\delta_c \approx$ 0.2cm. There is more scatter in the measurements of the cap force. However, most of the tests show a very stiff initial load response (Fig. 7.13) with a yield load, F_c = -6±2kg at $\delta_c \approx$ 0.002cm, increasing slightly with continued loading to a maximum cap resistance F_c = -8±2kg. Figure 7.14 shows the best estimate of the load-displacement responses derived from the first time pullout tests.

Pore pressures are measured directly beneath the cap and independently by two probes, P1 and P2, located within the caisson at a depth, z ≈ 2.5cm (i.e., 0.5L; Fig. 3.18). Probe P1 is positioned close to the centerline, while P2 is close to the inside wall of the caisson. Figure 7.15 summarizes the pore pressures measured at these three locations inside the model caisson:

1. Reliable pore pressure data are only available for three first time tests loaded to failure (CET-5, 6, 7[7]). These data show negative excess pore pressures increasing to maximum Δu_c = -0.52±0.05ksc at cap displacements δ_v = 0.2 - 0.3cm. Probe P1 measures a very similar range of pore pressures (at this same displacement), while average excess pore pressures at P2, $\Delta u_2 \approx$ -0.65ksc.
2. Data from partially loaded caisson tests (CET-9 through 14) show a much stiffer pore pressure response than earlier tests (notably CET-5, 6), mobilizing excess pore pressures in the range $\Delta u_c \approx \Delta u_1$ = -0.5±0.1ksc at small cap displacements, $\delta_v \leq$ 0.01cm. These differences in measured cap pore pressures are most probably related to the procedure used to fill the thin

[7] The last progress report (Whittle et al., 1995) discusses problems associated with cavitation of the cap pore pressure transducer in CET-8.

annular space created by the O-ring seal between the cap and wall components of the model caisson (cf. Section 4.3.1). Improvements in the probe designs have also improved the response times of P1 and P2 in the later tests (cf. Section 4.6.2).

3. Figure 7.16 shows that the excess pore pressures (Δu_c) beneath the cap are in close agreement with the average underbase total stress (computed directly from the applied cap force, $\overline{\sigma}_b = F_c/A_b$). Indeed, detailed comparisons for individual tests show that $|\overline{\sigma}_b - \Delta u_c| \leq 0.1$ksc and which is consistent with estimated O-ring friction forces of up to 2kg acting between the cap and wall of the caisson (Section 4.3.2).

Figure 7.17 shows data from pore pressure probes P3 and P4, located outside of the caisson. These transducers measure relatively small pore pressures ($\Delta u = 0.0 \pm 0.1$ksc) for $\delta_v \geq 0.01$cm.

Figure 7.18 compares the load-deformation measurements from three subsequent pullout tests with the behavior observed in first time loading. Two of these tests (CET-12, 13[8]) were subjected to a sequence of sustained tensile loadings and were then re-consolidated at the original total force, $F_{TOT} = 15.2$kg, for more than 24hrs prior to undrained pullout. The third test (CET-9) was loaded to failure after equilibration at a small sustained tensile load ($F_{TOT} = -2.2$kg). The load capacity for tests CET-12 and 13, $F_{TOT} = -24 \pm 2$kg, is approximately 10% higher than the average value estimated from the series of first time test, and is mobilized at $\delta_v = 0.04$-0.1cm. In contrast, CET-9 has a slightly lower capacity ($F_{TOT} \approx 20$kg) than the first test series, with peak resistance occurring at $\delta_v \approx 0.1$cm. Detailed observations of the wall and cap forces show similar comparisons between the first time and subsequent pullout tests. However, the overall conclusion from Figure 7.18 is that the caisson capacity, maximum wall and cap forces are very well bounded in the CET experiments. Section 5.9.2 shows that measurements of excess pore pressures from the subsequent pullout tests are also very consistent with the behavior described for first time loading.

7.4.2 Interpretation of CET Model Caisson Capacity

7.4.2.1 Limit Equilibrium

Caisson capacity is usually estimated by limit equilibrium methods (cf. Clukey & Morrison, 1993; Andersen et al., 1993; Fuglsang & Steensen-Bach, 1991). For undrained axial loading, the conventional assumption is that the soil plug moves with caisson. Hence, the ultimate capacity of the caisson can be obtained as the sum of the external wall friction and the reverse end-

[8] There is minimal difference in undrained load-deformation response that can be related to differences in the installation procedures. However, it should be noted that both CET-12 and CET-13 are equilibrated at the same value of F_{TOT} and hence, the CET experiments do not include the additional consolidation associated with the self-weight of a prototype caisson.

bearing acting over the full basal area (footprint) of the caisson (Fig. 7.19). Following the notation of Clukey and Morrison (1993) this is written as:

$$F_{TOT} = F_{ESF} + F'_{REB} \tag{7.3}$$

The usual procedure for estimating F_{ESF} is to assume that: 1) the caisson wall is relatively inextensible, such that $F_{ESF} = f_s A_e$, where $A_e = 2\pi RL$ is the external surface area of the caisson; 2) the limiting skin friction f_s is equated with the undrained shear strength of the soil adjacent to the wall-soil interface; and 3) the clay fails in a mode of undrained Direct Simple Shear, s_{uDSS}. The CET experiments are all performed in specimens of K_0-normally consolidated RBBC with undrained strength ratio, $s_{uDSS}/\sigma'_{vc} = 0.2$ (Ladd, 1991), and consolidation effective stress, σ'_{vc}= 0.75ksc. Thus the best estimate of external skin friction is given by:

$$F_{ESF} = 2\pi(2.54)(5.1)(0.75)(0.205) \ = 12.5\text{kg} \tag{7.4}$$

The computed external wall friction ties in very closely with the band of maximum wall forces mobilized in the CET experiments (F_w = -13.5±1.5kg). This agreement may be considered fortuitous as there are no data to confirm the distribution of shear tractions along the inside and outside wall of the CET model caissons.

The reverse end-bearing is computed based on the conventional bearing capacity formula (for strip footings) together with empirical factors to account for the embedment and axisymmetric geometry of the caisson. Clukey and Morrison (1993) follow design equations given by Kulhawy et al. (1983):

$$F'_{REB} = q'_b A_b = N_c s_u \alpha_c \alpha_d A_b \tag{7.5}$$

where A_b is the cross-sectional area of the base, the bearing capacity factor, N_c = 5.14 (for homogeneous clay), α_c and α_d are empirical factors accounting for the cross-sectional shape of the caisson and the depth of embedment. For the CET model caisson, α_c = 1.20, and , α_d = 1.26 (Kulhawy et al., 1983).

For tensile loading of the caisson, the reverse end-bearing capacity is controlled by the undrained shear strength in an undrained triaxial shear mode, s_{uTE}. For K_0-normally consolidated RBBC, Sheahan (1991) measures an undrained strength ratio, $s_{uTE}/\sigma'_{vc} = 0.16$. Hence, the best estimate of the reverse end-bearing capacity is given as:

$$F'_{REB} == (5.14)\,(0.12\text{ ksc})\,(1.20)(1.26)(20.27\text{ cm}^2) = 18.9\text{kg} \tag{7.6}$$

and the expected total caisson capacity by this calculation, F_{TOT} = (12.5 + 18.9) = 31.4kg.

It is clear that the computed F_{TOT} is much larger (35%) than the measured caisson capacity and that the likely source of this discrepancy is related to the calculation of reverse end-bearing.

7.4.2.2 Numerical Limit Analysis

An alternative (independent) calculation of the caisson capacity can be carried out using numerical limit analyses (cf. Section 2.4; Ukritchon, 1995; Ukritchon et al., 1996). These

calculations give rigorous lower and upper bounds on the true collapse load using finite element discretization and linear programming optimization methods (after Sloan, 1988a; and Sloan and Kleeman, 1994). The current programs are restricted to plane strain problems (the same restriction applies to limit equilibrium calculations of bearing capacity), with an isotropic Tresca failure criterion for the clay ($s_u = [\sigma_1 - \sigma_3]/2$), but do also include beam and joint elements which are capable of simulating failure conditions in a caisson structure. Figure 7.20 shows the spatial discretization and boundary conditions used to represent the CET model caisson in the lower bound limit calculation. This analysis assumes there is no transfer of shear force or bending moment at the junction of the caisson cap and wall. The soil is assigned an average undrained shear strength equivalent, $s_u = s_{uDSS} = 0.205(0.75) = 0.15$ksc, with full adhesion permitted along all soil-structure interfaces. The lower bound caisson capacity, found by maximizing the total vertical force acting on the cap and wall, $Q_L = -0.64$kg/mm width. Figure 7.21 shows that the total caisson resistance comprises 1) forces on the inside and outside surfaces of the wall, $Q_w = (Q_{wi} + Q_{wo} = (0.146 + 0.133) = 0.259$kg; 2) the surcharge pressure on the lid of the caisson, $Q_s = \sigma_{v0}B = 0.381$kg/mm; and 3) the underbase reaction force of the soil on the cap, $Q_c = -0.02$kg/mm.

The upper bound collapse load is computed from the principle of virtual work, assuming that the caisson cap and wall are rigid and displace together vertically. The program minimizes the total vertical force on the caisson for the spatial discretization shown in Figure 7.20, generating an upper bound collapse load, $Q_U = -0.70$kg/mm width. Thus, the true collapse load, Q is bounded by, $-0.64 \leq Q \leq -0.70$ kg/mm (i.e., a 9% range of uncertainty).

The lower bound analysis produces a statically admissible stress field. Figure 7.21 shows the zone of yield around the caisson, $q/s_u = (\sigma_1 - \sigma_3)/2s_u$, the average total pressure, $p/s_u = (\sigma_1 + \sigma_3)/2s_u$, and δ, the direction of the major principal stress to the vertical. The stress field mobilizes the full shear strength of the soil at most points within the CET cell ($q/s_u = 1$). The lowest pressures occur close to the base of the caisson ($p/s_u = -1$) where the clay fails in an extension mode of shearing ($\delta = 90^0$). Failure in undrained direct simple shear ($\delta = 135^0, 45^0$) occurs at points along the outside wall of the caisson and extends to the base of the cell (at $x \approx B$).

Figure 7.22 shows the mechanism of failure predicted by the upper bound analysis together with velocity trajectories, indicating the directions of soil movements, and the zone of yielding within the CET cell. These results show that there is no failure within the soil plug (and a conical region beneath the wall tip). However, the zone of yielding covers most of the CET cell extending to both the base and side walls. Slip occurs at the external wall-soil interface, and most of the soil surface moves downwards in the computed failure mechanism.

In order to estimate the collapse load of the CET model caisson, the results of the planar limit analyses must be scaled to account for the axisymmetric geometry. Two alternative (approximate) methods for doing this scaling are as follows:

(Al-Tabaa & Wood, 1987). Although laboratory data for kaolin (notably the 'Spetstone' variety) have played a major role in establishing critical state theories of soil behavior, there is much data to show that the engineering properties of kaolin are not typical of most natural clays (e.g., Rossato et al., 1992). Furthermore, there is a surprising lack of reliable laboratory test data from which to select model properties. In large part, this is due to variations in the types/grades of kaolin which have been used by different laboratories. For example, the quoted index properties for Speswhite kaolin range from w_L = 58-84%, and w_p = 34-45%. An extensive literature search has been conducted in order to locate sufficient test data for Speswhite kaolin from which to select input parameters for the MIT-E3 model. Table 7.1 summarizes the selected input parameters which were obtained from the following sources:

1. The most comprehensive study of compression behavior and permeability characteristics are reported by Al-Tabbaa (1987). Figures 7.28a and b illustrate the selection of the parameters e_0, λ, C and n from 1-D compression tests. The unload-reload cycles performed in these tests also provide information for calibrating the bounding surface parameter, h (Table 7.1).
2. Values of K_{0NC} = 0.65 - 0.70 are relatively consistent among the various reference sources. However, quoted values of the elastic Poisson's ratio range from ν' = 0.25 to 0.35 (i.e., 2G/K = 1.2, 0.66; Table 7.1).
3. Atkinson et al. (1986) report results of undrained and drained triaxial compression and extension tests on K_0-normally consolidated kaolin. Unfortunately, the published data[15] focus on the evaluation of critical state conditions and do not give adequate information at axial strain levels, $|\varepsilon_a| < 1\%$. Tatsuoka and Kowhata (1994) reports very detailed stress-strain measurements from a single CK_0UC test, separately plotted in overlapping strain ranges (0 -> 0.01%, 0 -> 0.1%, 0 -> 1.0%, 0 -> 10%). Unfortunately, there is a significant difference in the large strain friction angles reported by Tatsuoka and Kowhata (1994) and Atkinson et al.(1986) ($\Delta\phi'_{TC} = 5^o$; Fig. 7.29a) which represents a major source of uncertainty. The current analyses use $\phi'_{TC} = 20^o$ (= ϕ'_{TE}) which appears to give a reasonable average of the two tests in Figure 7.29a. The effective stress paths are then used to select the parameters c, s_t in Table 7.1 following procedures recommended by Whittle & Kavvadas (1994).
4. The small strain stiffness[16] parameter and non-linearity at small shear strains are represented by the parameters κ_0 and ω (Table 7.1). Both of these parameters have been found by matching the stress-strain properties reported by Tatsuoka and Kowhata (1994). Figure 7.29b shows that the selected stiffness parameters give an excellent match to the experimental data.

---

[15]The original data were not available at the time of writing.

[16]Values of G_{max} can also be obtained from dynamic measurements reported by Viggiani (1992).

The two remaining parameters (γ and ψ_0) have been left at default values. The first parameter only affects the behavior of overconsolidated clay, while the second requires measurements of the effective stress path in a drained strain path test which are not available.

Figures 7.29a and b show the MIT-E3 simulations of CK_0UC and CK_0UE tests for Speswhite kaolin at OCR's =1.0, 2.0 using the parameters listed in Table 7.1 together with the measured data at OCR =1.0. At OCR = 1.0, the comparisons between computed and measured behavior show that the selected input parameters provide a good match to the effective stress path and stress-strain behavior in undrained triaxial compression, with undrained shear strength, $s_{uTC}/\sigma'_p = 0.23$ mobilized at an axial strain, $\varepsilon_{af} \approx 1.5\%$. Thereafter, the model predictions represent a compromise between the data reported by Atkinson et al. (1986) and Tatsuoka and Kowhata (1994). In the extension mode, the model matches the measured effective stress path at small shear strains but underpredicts the undrained shear strength reported by Atkinson et al. (1986). It is likely that much of this discrepancy arises due to necking in the laboratory tests.

Figures 7.30a and b compare MIT-E3 predictions with measured behavior in undrained direct simple shear tests (CK_0UDSS). Again the database for Speswhite kaolin is rather incomplete and inconsistent. Airey and Wood (1987) report data for K_0-normally consolidated kaolin from tests performed in both the Geonor device (standard equipment used at MIT) and Cambridge Simple Shear Apparatus (CSSA). More recently Ampadu and Tatsuoka (1994) have reported data from constant volume Torsional Shear Hollow Cylinder (TSHC) tests. In principle, these tests replicate conventional undrained direct simple shear tests. However, there are no published comparisons to show that the data are reliable. Figure 7.30a shows that the effective stress paths measured by Ampadu and Tatsuoka (1994) are relatively consistent with the data reported by Airey and Wood (1987) at OCR = 1.0, although the TSHC data give a lower undrained shear strength (which is mobilized at a lower stress obliquity, τ/σ'_v). The MIT-E3 model predicts an undrained shear strength $s_{uDSS}/\sigma'_p = 0.184$ which is 5-10% higher than the measured data. The obliquity mobilized at peak strength, $\psi = 17.5^0$, is very similar to that measured by Airey and Wood (1987) in the Geonor device. At OCR = 2.2, the MIT-E3 model gives quite reasonable predictions of the data reported by Ampadu and Tatsuoka (1994). The measured shear stress-strain data in Figure 7.30b have been digitized directly from the publications and are not reliable at strain levels, $\gamma < 0.5\%$. The MIT-E3 predictions are in very reasonable agreement with the CSSA data reported by Airey and Wood (1987), in which the maximum shear stress is mobilized at $\gamma \approx 10\%$. In contrast, the TSHC data show a very much softer response with peak shear strength mobilized at strain levels $\gamma > 20\%$. This large discrepancy between the experimental data from different devices suggests possible limitations in the TSHC simulation of CK_0UDSS tests.

Table 7.2 compares the engineering properties predicted by MIT-E3 for Speswhite kaolin, Boston Blue Clay and Empire Clay (a high plasticity Gulf of Mexico clay). The shear stiffness (G_{max}) of Speswhite kaolin is an order of magnitude smaller than BBC and significantly lower than that of Empire clay. However, its normally consolidated compressibility (λ) is similar to BBC but is much less compressible than Empire clay. The undrained shear strengths of kaolin are up to 40% smaller than that of BBC but are only 10% less than that of Empire clay. Therefore, the principal differences between Speswhite kaolin and Empire clay are in the deformation and permeability properties.

7.4.4.3 Predictions of Axial Load-Deformation and Caisson Capacity

The non-linear finite element analysis simulates the EPR centrifuge model at prototype scale. The analysis assumes that the kaolin is K_0-normally consolidated with hydrostatic pore pressures and a buoyant unit weight, γ_b = 7.3kN/m^3. Stress-strain-strength properties of the kaolin are modeled using the MIT-E3 model with input parameters listed in Table 7.1. The analysis assumes: i) that the caisson is wished-in-place; ii) the wall is modeled as an elastic material, while the cap is perfectly rigid; iii) there is no separation between the cap and the underlying soil plug and no slippage between the caisson wall and the surrounding soil; iv) the ground surface and base of the clay are free draining boundaries with zero excess pore pressures; and v) the caisson is loaded at a constant rate of vertical displacement.

Figure 7.31b summarizes the predicted and measured axial load-deformation response for the EPR centrifuge model caisson. The experimental data (test f8) generate a maximum pullout resistance, F_{TOT} = -110MN at a vertical displacement, $\delta_v \approx$ 1.5m, with a total time to failure, $t_f \approx$ 4hrs at prototype scale (t_f = 150secs at model scale). In comparison, the finite element analysis is restricted to relatively small displacements, mobilizing a resistance F_{TOT} = -78MN at δ_v = 0.2m. The predicted caisson resistance is approximately 10% lower than the measured value at this final displacement, with 44% of the load carried by the cap.

There are no direct measurements of wall and cap forces in the centrifuge model. However, Figure 7.31a shows pore pressure data from 5 transducers located within and below the base of the caisson. The pore pressures inside the soil plug (PI-151, P-5018, P-5068, P-5069) are similar in magnitude and decrease monotonically to a minimum value Δu = 300 - 360kPa at failure (assuming a water depth of 32.5m, the cavitation pressure, Δu_{cav} = -(32.5)(9.81) -75 = -394kPa). The predicted cap pore pressures decrease almost linearly for $\delta_v \leq 0.2$, and are in good agreement with the measured data over this range of displacements. These results provide indirect support that the predicted magnitudes of the cap force.

The finite element analysis predicts that the maximum wall force, F_w = 42MN is mobilized at δ_v =0.2m (Fig. 7.31a). Figure 7.32 shows the corresponding distribution of surface tractions

along the inner and outer surfaces of the wall. Shear tractions at all points along the outside of the wall reach the limiting undrained shear strength of K_0-normally consolidated kaolin ($s_{uDSS}/\sigma'_{vc} \approx 0.18$), while much smaller shear forces develop over the lower third of the inside surface. These results are consistent with previous calculations for prototype caissons in Chapter 6.

Overall, the finite element predictions of load-deformation response are in surprisingly good agreement with the measured centrifuge data, given the absence of reliable stiffness properties for the speswhite kaolin.

Finite element predictions of the ultimate caisson capacity[17] involve relatively small displacements of the structural system ($\delta/2R \leq 10\%$), but very large local shear strains which require more refined modeling of the soil-structure interfaces than have been attempted in this project. Instead, numerical limit analysis offer a direct approach for estimating the caisson capacity. Figures 7.33 and 7.34 summarize the lower and upper bound predictions for a planar representation of the EPR centrifuge model caisson under axial loading. The analyses assume an isotropic undrained strength ratio for the clay, $s_u/\sigma'_{vc} = 0.2$ and hence, simulate a profile in which the undrained shear strength increases linearly with depth ($s_u \approx 44$kPa at the base of the caisson, based on the prototype stresses). The caisson wall and cap are rigidly connected together (in contrast to the CET model caisson).

The upper bound analysis (Fig. 7.34) predicts a failure mechanism across the base of the caisson, extending across the full width of the test chamber, with $Q_u = -6.90$MN/m. The lower bound stress field also shows very small shear stresses within the soil plug, while the full shear strength of the clay is mobilized along the outer wall and below the base of the caisson. The lower bound collapse load, $Q_L = -6.44$MN/m, comprises a maximum wall resistance, $Q_w = -2.47$MN/m and a cap force, $Q_c = -3.97$MN/m. Overall, the analyses provide a very well bounded estimate of the collapse load, $-6.44 \leq Q \leq -6.90$MN/m. The most reliable way to apply these solutions for an axisymmetric caisson geometry is to scale the wall and cap forces separately to account for the relative surface areas of the caisson cap and wall (internal and external surfaces). In this calculation, the lower bound wall force, $F_{wL} = Q_w(\pi B/2) = -2.47(23.88) = -59.0$MN[18]; and the cap force, $F_{cL} = Q_c(\pi B/4) = -3.97(11.94) = -47.4$MN and hence, the lower bound collapse load for the caisson, $F_{TOT} = -106.4$MN. Assuming that the ratio of Q_U/Q_L is unaffected by the geometry, then the total caisson capacity is in the range $-106.4 \leq F_{TOT} \leq -113.5$MN. Figure 7.31 confirms that these calculations give excellent predictions of the measured caisson capacity in test f8.

---

[17] A crude estimate of the experimental collapse load can be obtained from Fig. 7.35b using the predicted maximum wall force, and assuming that the limiting cap force is controlled by the theoretical cavitation limit. In this case, $F_{TOT} = 42+(0.394A_b) = 112$MN, which matches very closely to the measured data (where $A_b = 17.6$m^2).

[18] Note that the limit analysis predicts a wall force which is 33% higher than that from the finite element model. Part of this difference is due to variations in the undrained shear strength in the two calculations.

7.4.5 Caisson Capacity with Inclined Loading

The principal focus of this research relates to caisson performance under axial loading conditions. However, for prototype TLP applications[19], critical loading conditions are likely to occur when the platform is offset from the foundation (in a storm) and the tether loads are inclined to the vertical (typically at 5-10^0). The EPR centrifuge experiments (test g10) and NGI field tests (Andersen et al., 1993) both include measurements of caisson response for inclined static loading conditions.

Inclined loading represents a major challenge for non-linear finite element analysis as it requires either a full three-dimensional model or a simplified two-dimensional representation (treating planar loading with axisymmetric geometry; e.g. Lai & Booker, 1993) to model the complete load-deformation response. In principal, there are similar geometric problems for the numerical limit analyses. However, it has been conventional practice in geotechnical engineering to use planar limit equilibrium calculations to compute collapse loads for generalized loading conditions (e.g., Janbu, 1985[20]). This section illustrates predictions of collapse for inclined static loading of the centrifuge model caissons and the NGI field test (4 caisson unit) using planar numerical limit analyses. Although the results should be interpreted with caution, they demonstrate the power and flexibility of numerical limit analyses and provide encouragement for further development of these methods.

Figure 7.35 summarizes results of limit analyses for the EPR centrifuge model caisson loaded at an inclination angle, i = 6^0 to the vertical. Loading is applied through a pin connection at the top of the cap (Fig. 7.35a) approximately 8.5m above the ground surface (at prototype scale). The analysis assume that there is no yielding of the caisson structure and hence, it is modeled by a series of rigid line elements. The computed lower and upper bound loads for the planar section define the collapse load within ±6%, such that -5.39 ≤ Q ≤ -6.06MN/m. Figure 7.37 shows the mechanism of collapse, which involves a rigid body rotation centered at a point on the front wall of the caisson at a depth of 22m. The ground surface in front of the caisson heaves, while the trailing edge settles. The extent of the soil yield around the caisson is smaller than that predicted for axial loading (cf. Fig. 7.34) and again there is no yielding inside the plug. The lower bound analyses provide detailed predictions of the force distributions acting on the leading and trailing walls of the caisson (Fig. 7.36).

Unfortunately, it is difficult to scale the results of planar limit analyses for cases where the lateral wall resistance constitutes a significant fraction of the total caisson capacity. The calculation in Figure 7.35 separates the vertical and horizontal components of the wall force and vertical cap resistance, leading to a best estimate of the collapse load, -88.4 ≤ F_{TOT} ≤ -98.7MN. Hence, the

---

[19] Lateral loading is the critical loading condition for caissons used to anchor spar-type platforms.

[20] For shallow foundations, the side wall resistance is usually not considered in the bearing capacity calculations.

7.5 BEHAVIOR OF CAISSONS UNDER SUSTAINED TENSILE LOADING

7.5.1 Experimental Data

Section 5.6 presents complete measurements of the CET model caisson response under sustained tensile loads (i.e., constant tensile total force F_{TOT}) from tests CET-9 through CET-14. This program of tests was designed to investigate the long-term capacity of the model caisson, and the time frame required for release of the underbase suction pressures. All of these CET tests are initially equilibrated under a total compressive load, F_{TOT} = 15.2kg (statically equivalent to the in-situ consolidation effective stress, σ'_{v0} = 0.75ksc). The experimental program includes two single stage sustained loading tests (CET-9, 10) and four multi-stage tests (CET-11, 12, 13, and 14). Figure 7.41 summarizes the component force-cap displacement data from all six experiments. The load increments (ΔF_{TOT} = -17.4 to -26.6kg[22]) applied in the first stage of each test are much larger than those used in subsequent stages (ΔF_{TOT} = -1 -2kg) and hence, generate much larger cap forces and excess pore pressures. Therefore, the following paragraphs distinguish between behavior measured in the first stage and subsequent stages of sustained tensile loading.

Figures 7.42, 7.43 and 7.44 summarize the three characteristic time dependent responses of the CET model caisson in sustained tensile loading:

1. Stable response. Figure 7.42 shows the cap displacement, force components and excess pore pressures inside the caisson as functions of time (from the start of tensile load application) for the first stage of test CET-11 with F_{TOT} = -2.7kg. At the start of this load stage, the cap carries a tensile force, $F_c \approx$ -7kg, while the wall remains in compression. The cap sheds this initial tensile load onto the wall within approximately 8mins, and thereafter, $F_w \approx F_{TOT}$. The excess pore pressures inside the caisson follow very closely the cap force, and measure $\Delta u \approx$ 0ksc for t > 8 mins. The load transfer process generates very small displacements of the cap (< 0.01cm). However, fluctuations in the applied forces (at t= 6-8mins and t = 60-70mins) cause an uncontrolled jump in the measurements of δ_v (the data strongly suggest that the LVDT transducer becomes stuck temporarily). However, for t > 100mins, the data again appear to be reliable (matching closely the trend prior to t = 6mins) with very small cap displacements.
2. Failure in the first stage of sustained loading (overshoot condition). The first stage of CET-10 fails under a total tensile load, F_{TOT} = -11.4kg, Figure 7.43. The tensile cap force decreases from a maximum initial value, $F_c \approx$ -9kg, to a minimum, $F_c \approx$ -3kg, at t ≈ 40-60mins after load application. During this same time period, the wall force increases to a maximum resistance $F_w \approx$ 8kg and then remains constant. At t = 50mins, the vertical displacement of the cap δ_v = 0.01cm, and the excess pore pressure inside the caisson, Δu = -0.27ksc. Thereafter, the caisson continues to displace at a nearly constant velocity (for t = 50-500mins, $\dot{\delta}_v$ =

[22] e.g. For CET-10, the first tensile load level, F_{TOT} = -11.4kg and hence, ΔF_{TOT} = -11.4 - 15.2 = -26.6kg.

0.00216cm/min) with almost no further change in the excess pore pressure inside the caisson. These results suggest that the soil plug remains in contact with the cap and hence, failure occurs below the base of the caisson.

3. Failure in a multi-stage sustained load test. Figure 7.44 summarizes the measurements of failure in the 4th stage of sustained tensile loading for CET-11. This stage applies a small (2kg) incremental load to reach a total sustained tensile load, F_{TOT} = -9.3kg. Most of the applied load increment is carried by the cap force (generating a small but significant excess pore pressure, Δu = -0.075ksc). In contrast to the previous examples, there is almost no load transfer between the cap and wall. Instead, large cap displacements with minimal change in the component forces or excess pore pressures (there is a small cap acceleration, $\ddot{\delta}_v \approx 3x10^{-6}$cm/min^2 for t > 200mins).

Figures 7.43 and 7.44 report values of the limiting wall resistance, F_w = -8, -7kg, respectively from sustained tensile tests. These results are well below the average capacity of the wall measured in the Series 1 undrained pullout tests (cf. Fig. 7.41) and suggest that there is a significant change in either the magnitude of the shear force mobilized along the inside wall of the caisson and/or the mode of failure (e.g., failure occurring within the soil plug rather than below the base of the caisson). However, data from three other multi-stage sustained load tests (CET-12-14) give limiting wall forces, F_w = -10 to -13kg, which match more closely the Series 1 undrained pullout tests (cf. Fig. 7.41). Thus, there remains some uncertainty in the long-term capacity of the CET model caissons based on the measured limiting wall friction, F_w = -10±3kg.

Figure 7.45 shows the dissipation of excess pore pressure ratios from the first stage of sustained tensile loading. Five of the six tests reach stable long term equilibrium conditions (with effectively zero excess pore pressure and cap velocity), while incomplete pore pressure dissipation in test CET-10 corresponds to failure (cf. Fig. 7.43). For the stable tests, there are wide fluctuations in pore pressures at early stages of dissipation ($\Delta u/\Delta u_i > 0.8$) and large differences in the measured data for $\Delta u/\Delta u_i \leq 0.4$. However, the time for 50% consolidation is relatively well bounded, t_{50} = 3.5 - 6.0mins.

7.5.2 Finite Element Simulation of Sustained Loading for CET Model Caisson

This section illustrates finite element predictions for sustained tensile loading of the CET model caisson. The calculations are based on the previous assumption that the caisson is wished-in-place and therefore, cannot replicate the load histories for the experiments described above (due to differences in the initial cap and wall forces and system stiffness at small displacements). Figure 7.46 compares predictions of force displacement behavior from a 4-stage sustained loading test with the undrained axial load response computed previously. The corresponding sustained load time functions are given in Figure 7.47 in terms of a dimensionless time factor, $T = \sigma'_{vc}kt/\gamma_w R^2$,

where the consolidation effective stress, σ'_{vc}, and permeability, k are constants used in the calculations.

The test sequence applies load increments of increasing magnitude, generating an overshoot type failure at the 4th stage with F_{TOT} = -24.2kg (Fig. 7.46). The cap carries 40-50% of the incremental loads applied in Stages 1, 2 and 3. Figure 7.47c shows that full dissipation of the excess pore pressures occurs within a time factor, $T \leq 10^{-4}$, for each of these three stages. The sustained load sequence generates accumulates much smaller cap displacements (δ_v < 0.02cm at failure) than the actual experiments, as the numerical analysis applies a much smaller net change in total force to the model caisson (i.e., F_{TOT} = 0kg initially). Staged loading increases the apparent stiffness of the wall force. This is due to two factors, 1) the small load increments in Stages 1 and 2; and 2) the large small strain shear stiffness of MIT-E3 in undrained shearing. The analysis predicts that a limiting wall force, F_w = -15kg, which is slightly larger than that computed for monotonic, undrained axial loading.

Further analyses are now required, using larger first stage load steps (Geer, 1996), to compare model predictions with the measured pore pressure dissipation in CET experiments (cf. Fig. 7.41).

Test Type	Parameter/ Symbol	Physical contribution/ meaning	Boston Blue Clay	Empire Clay	Speswhite Kaolin
1-D Consolidation (Oedometer CRS etc.)	e_0	Void ratio at reference stress on virgin consolidation line	1.12	1.26	1.353
	λ	Compressibility of virgin normally consolidated clay	0.184	0.274	0.200
	C	Non-linear volumetric swelling behavior	22.0	24.0	1.75
	n		1.6	1.75	1.35
	h	Irrecoverable plastic strain	0.2	0.2	1.0
K_0 -oedometer or K_0 -triaxial	K_{0NC}	K_0 for virgin normally consolidated clay	0.48	0.62	0.70
	2G/K	Ratio of elastic shear to bulk modulus (Poisson's ratio for initial unload)	1.05	0.86	0.66
Undrained Triaxial Shear Tests:	ϕ'_{TC}	Critical state friction angles in triaxial compression and extension (large strain failure criterion)	33.4^0	23.6^0	20.0^0
	ϕ'_{TE}		45.9^0	21.6^0	20.0^0
OCR=1; CK_0UC	c	Undrained shear strength (geometry of bounding surface)	0.86	0.75	0.525
OCR=1; CK_0UE	s_t	Amount of post-peak strain softening in undrained triaxial compression	4.5	3.0	2.0
OCR=2; CK_0UC	ω	Non-linearity at small strains in undrained shear	0.07	0.20	5.0
	γ	Shear induced pore pressure for OC clay	0.5	0.5	0.5
Shear wave velocity*	κ_0	Small strain compressibility at load reversal	0.001	0.0035	0.00855
Drained Triaxial	ψ_0	Rate of evolution of anisotropy (rotation of bounding surface)	100.0	100.0	100.0

* Either from laboratory tests (resonant column), wave propagation in triaxial specimens (piezo or bender elements), or field cross-hole tests.

Table 7.1 Input Parameters for Speswhite Kaolin using the MIT-E3 Model

Engineering Property	Boston Blue Clay	Empire Clay	Speswhite Kaolin
λ	0.184	0.274	0.200
G_{max}/σ'_{v0}	1100	210	75
s_{uTC}/σ'_{v0}	0.323	0.241	0.228
ε_{af} (%)	0.20	1.40	1.50
$q(10\%)/s_{uTC}$	0.721	0.923	1.00
ϕ'_{TC}	33.4^0	23.6^0	20.0^0
s_{uTE}/σ'_{v0}	0.18	0.20	0.105
s_{uDSS}/σ'_{v0}	0.205	0.200	0.184
k ($x10^{-8}$cm/sec)	8.0[§]	1.0[§]	14*

[§] For natural clays at e ≈ 1.0

* Average permeability of clay in EPR test chamber (e = 1.3, σ'_v = 180kPa).

Table 7.2. MIT-E3 Predictions of Deformation and Strength Properties of K_0-Normally Consolidated Clays

Condition	Parameter	Boston Blue Clay	Empire Clay	Speswhite Kaolin
Pile Installation	$\Delta u_i/\sigma'_{v0}$	1.20	1.05	0.99
	K_i	0.08	0.23	0.23
Radial Consolidation	T_{50}	0.116	0.083	0.20
	K_c	0.37	0.61	0.71
In-Situ Stress:	K_0	0.48	0.62	0.70

Table 7.3 Comparison of MIT-E3 Predictions for Shaft Parameters of Piles Installed in Three K_0-Normally Consolidated Clays

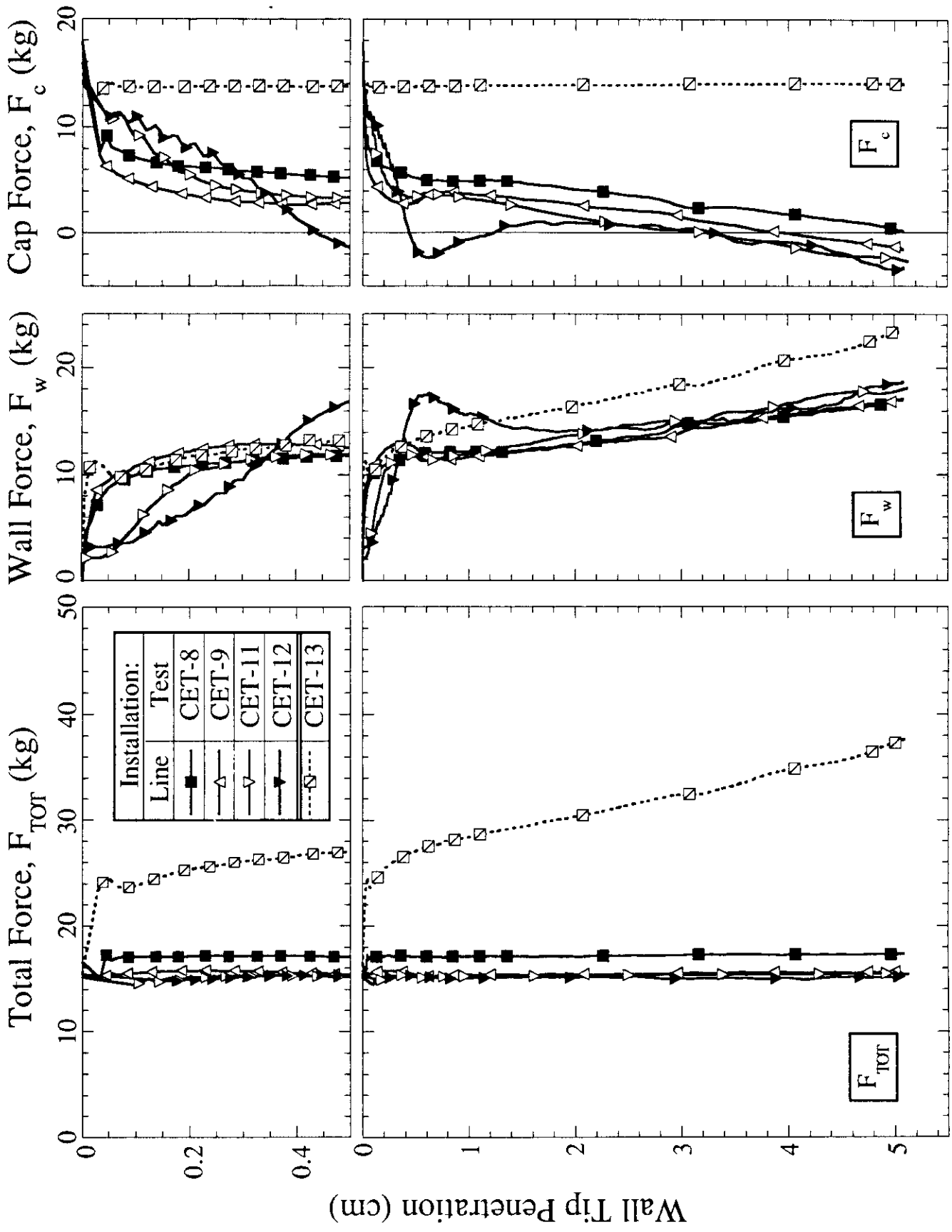

Figure 7.1 Summary of CET Penetration Force Measurements

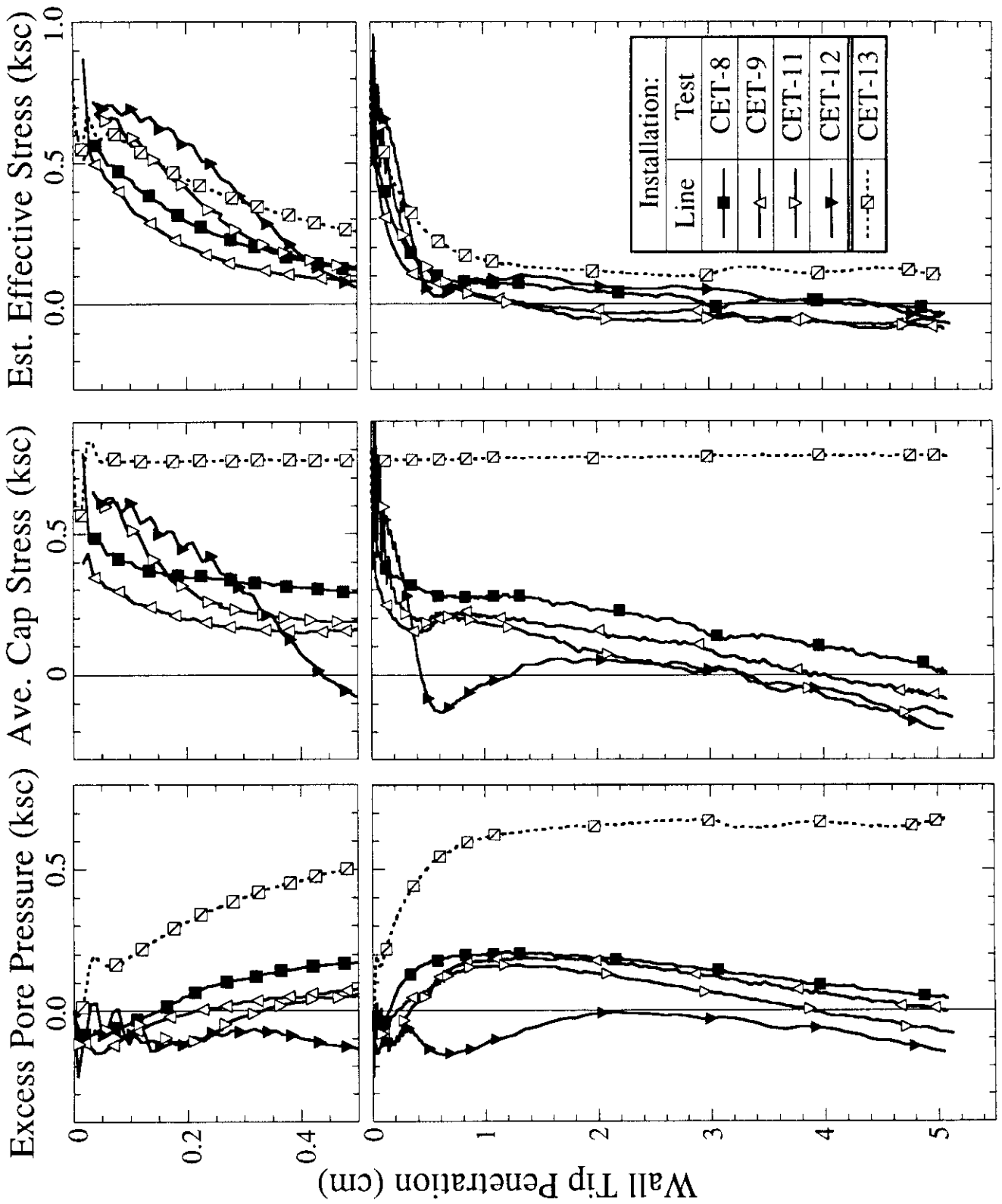

Figure 7.2 Stress Conditions Beneath Caisson Cap in CET Penetration Tests

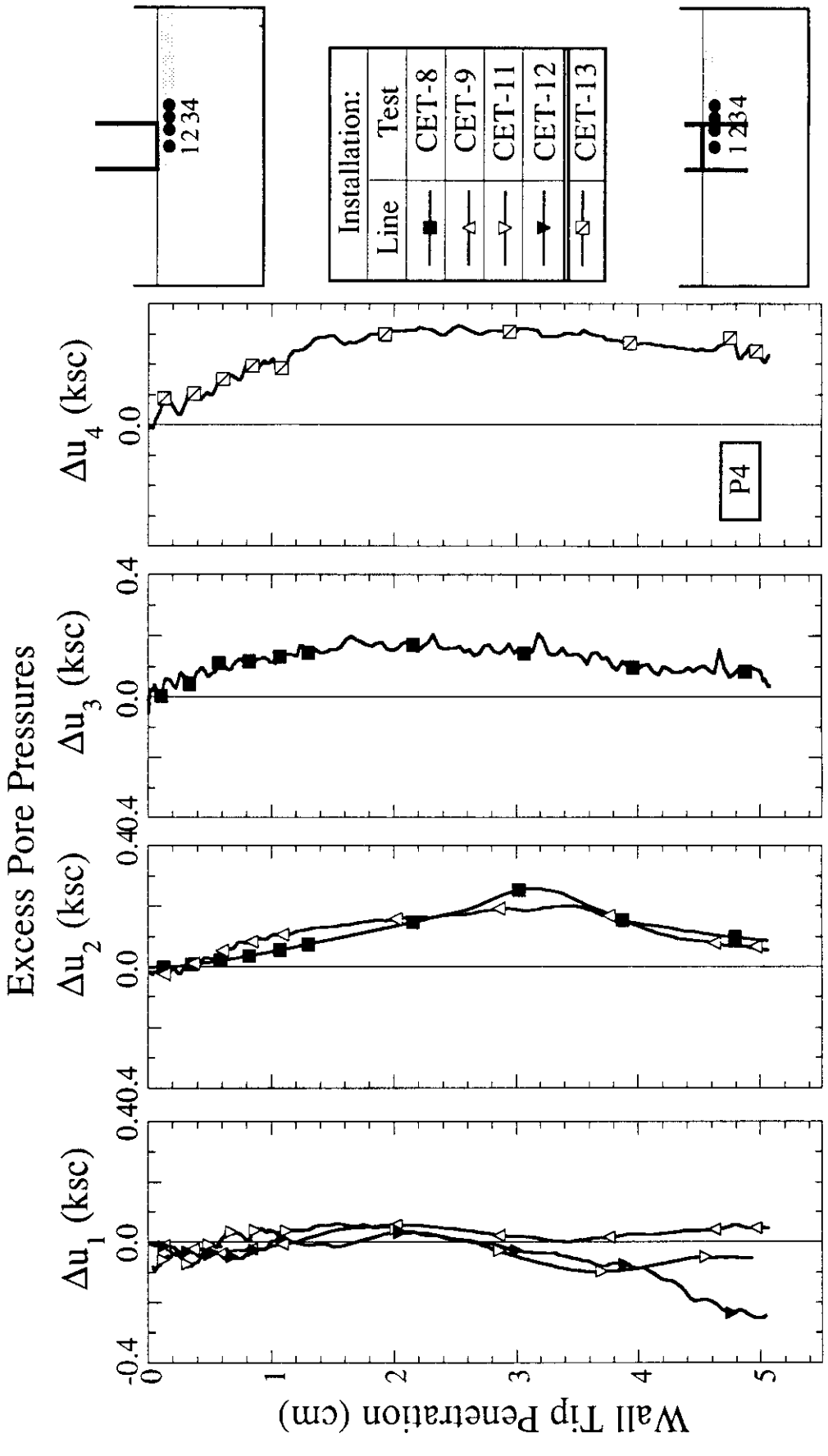

Figure 7.3 Summary of Pore Pressures in Clay During Penetration of CET Model Caisson

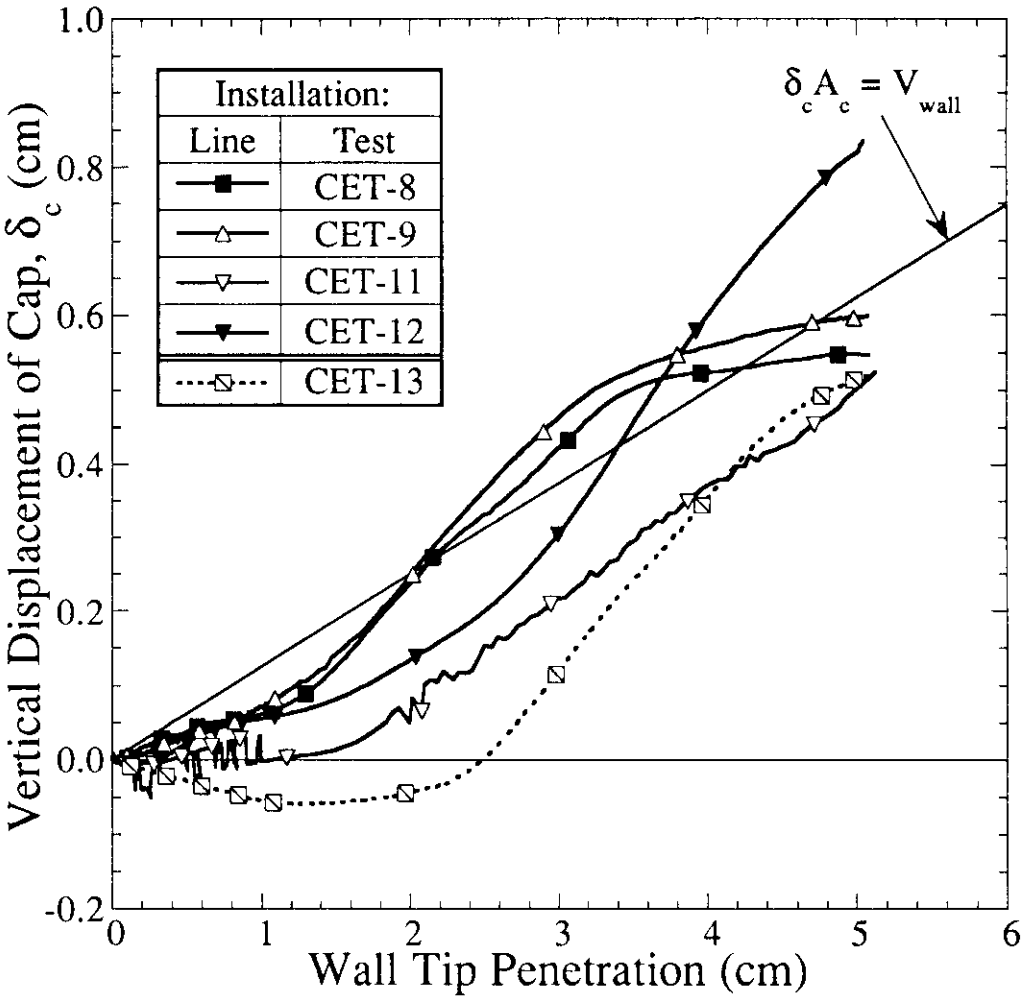

Figure 7.4 Summary of CET Cap Displacements During Caisson Installation

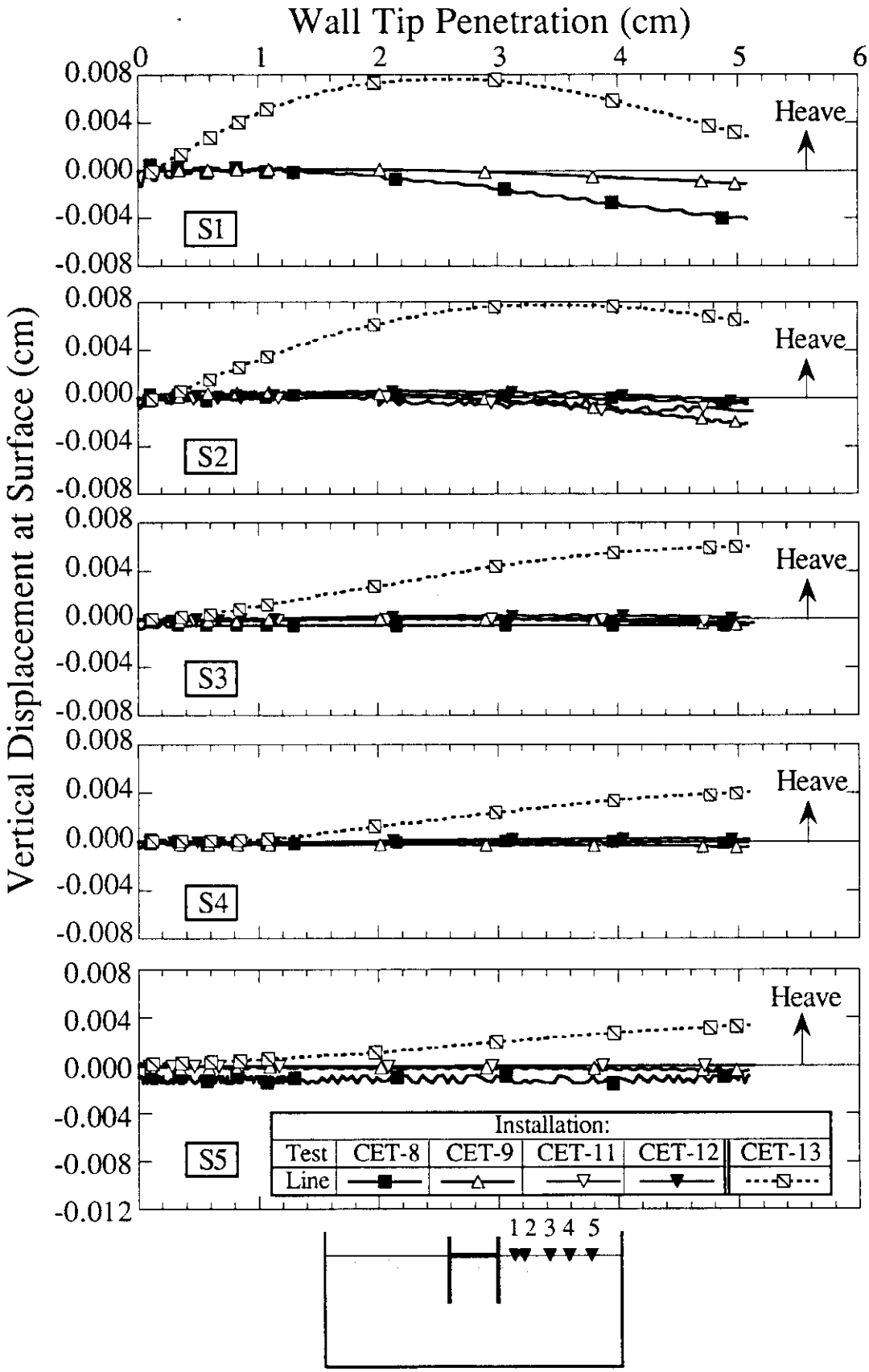

Figure 7.5 Summary of CET Clay Surface Displacements During Caisson Installation

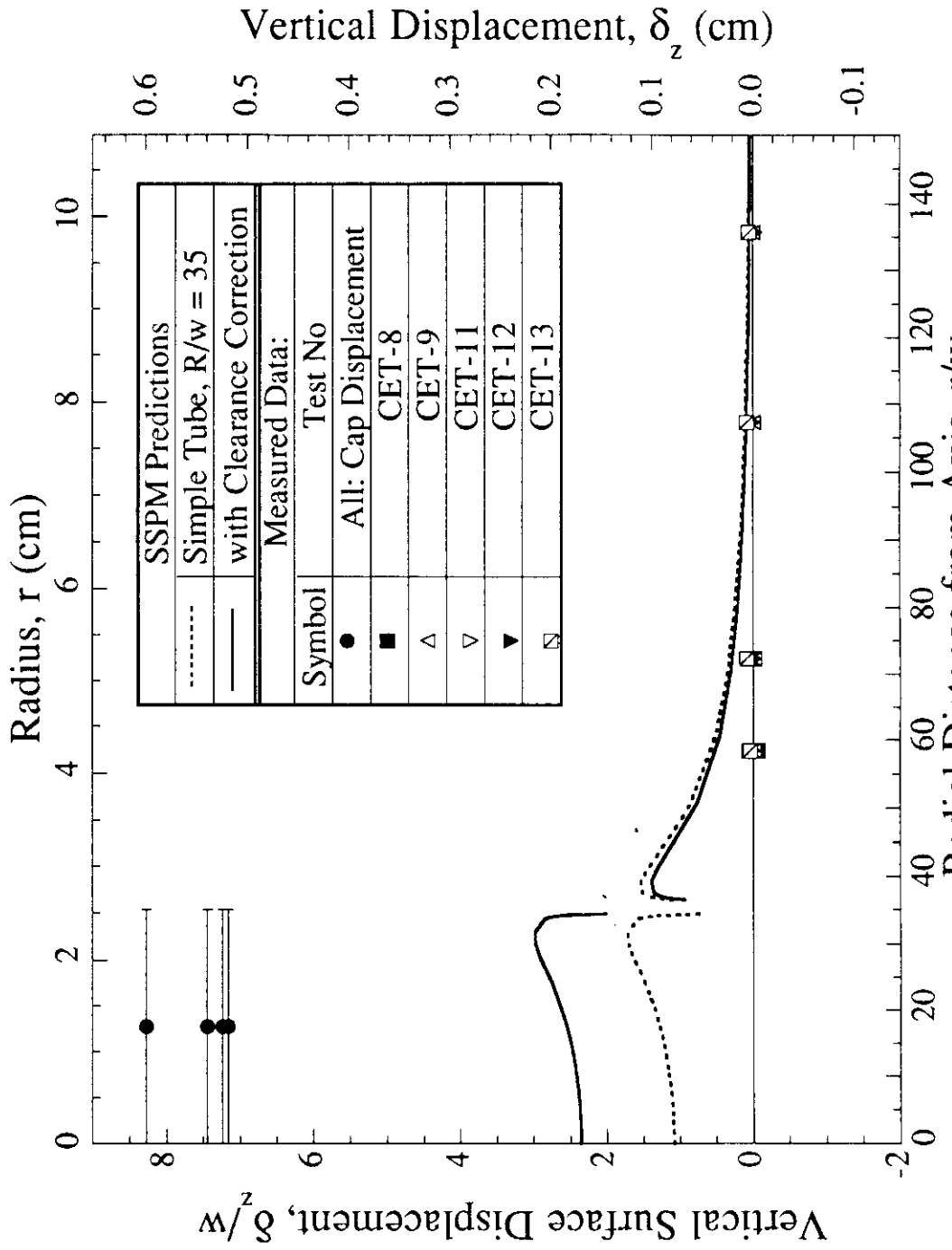

Figure 7.6 Comparison of Predicted and Measured Surface Heave in CET Cell at End of Installation

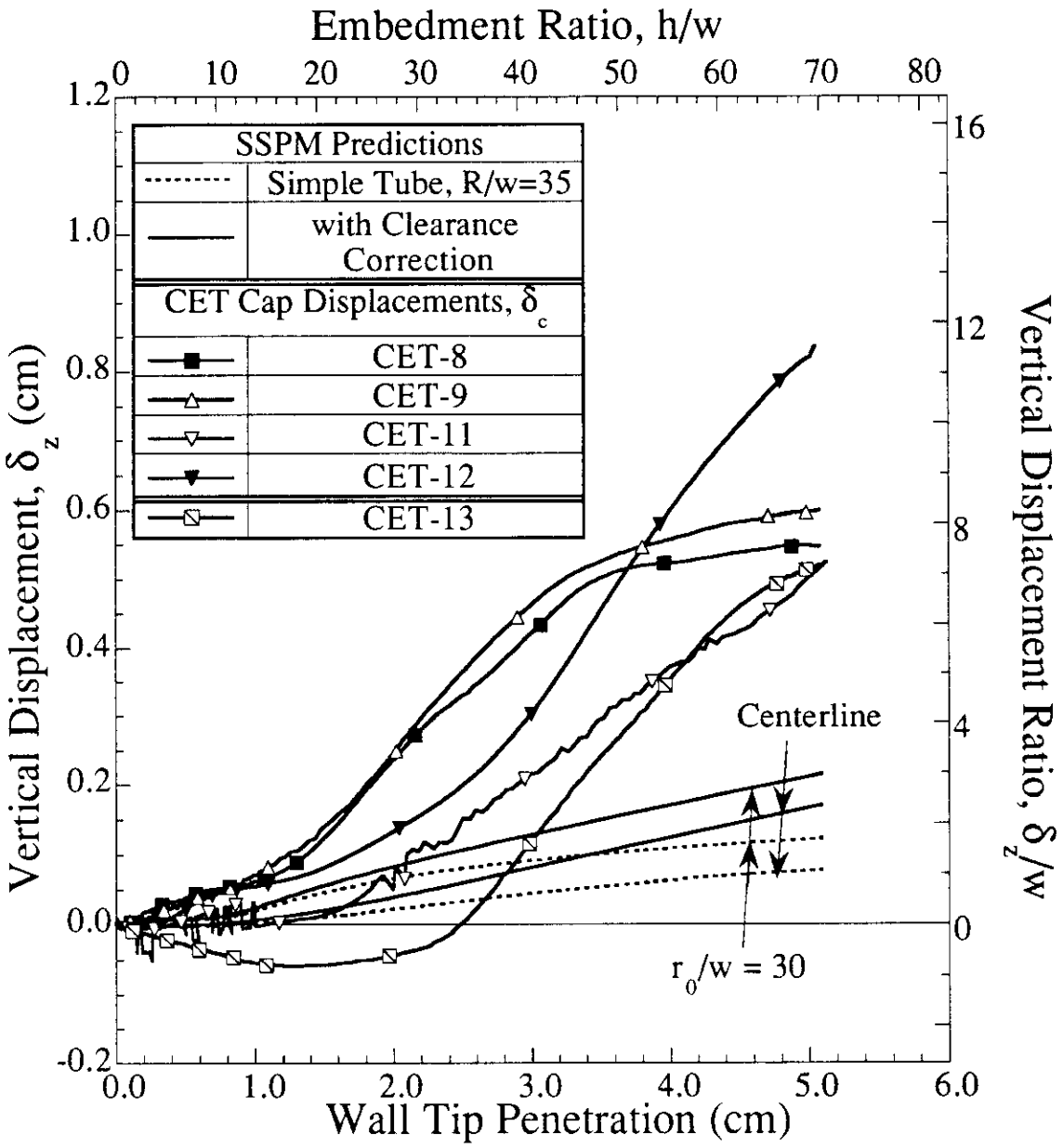

Figure 7.7 Comparison of Predicted and Measured Surface Displacements During CET Caisson Penetration

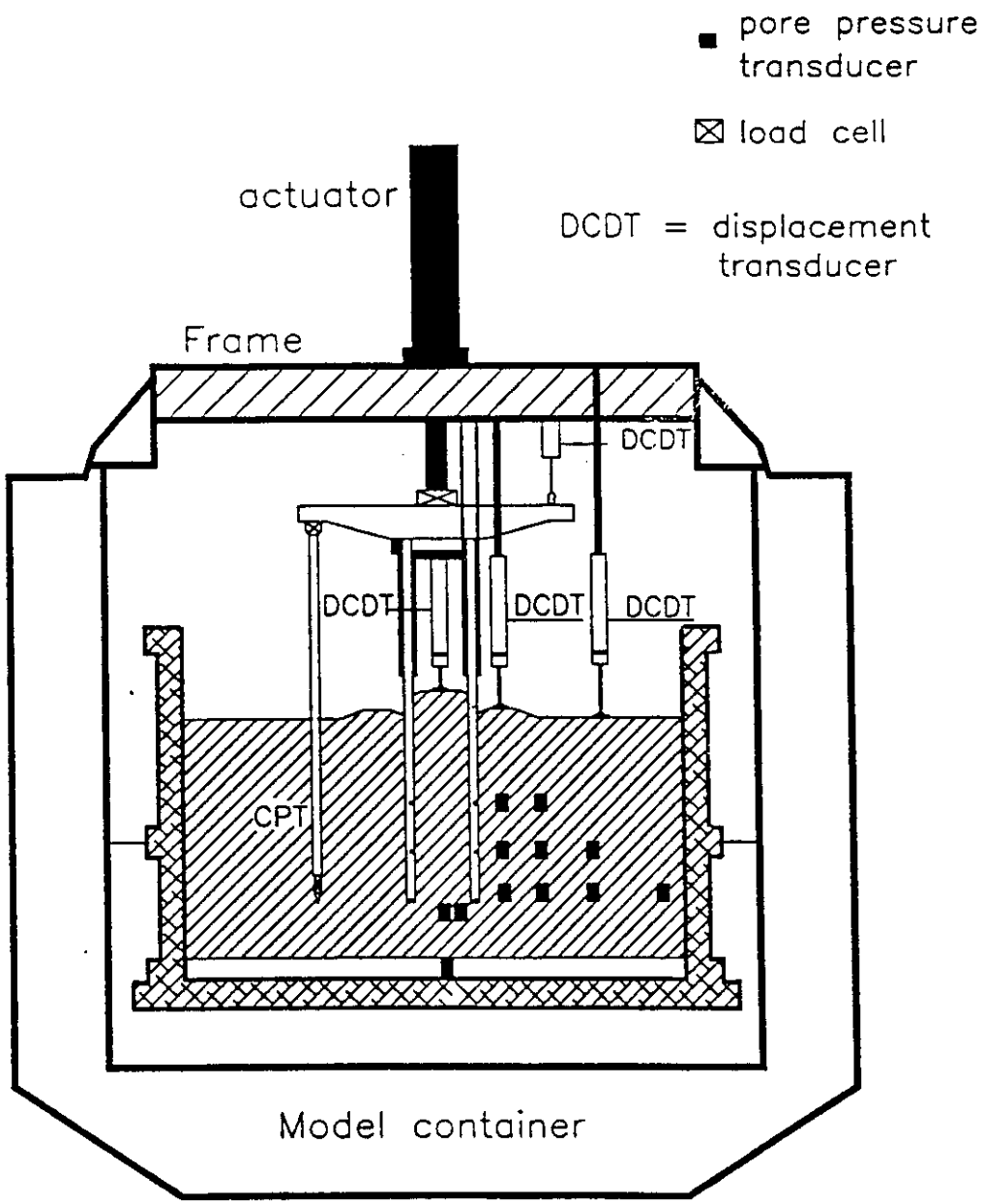

Figure 7.8 Delft Geotechnics Centrifuge Model of Thick-Walled Open-Ended Pile (from Hjortnaes-Pedersen & Bezuijen, 1992)

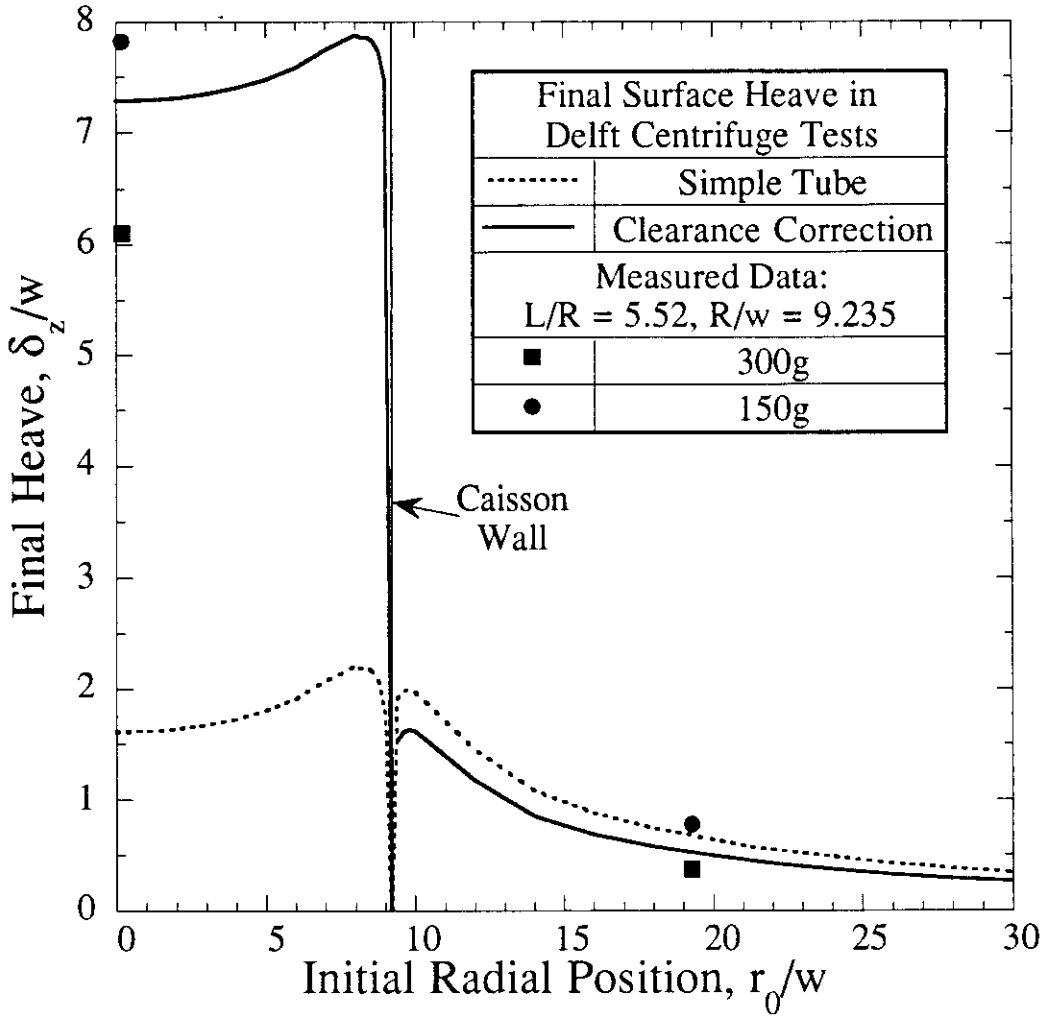

Figure 7.9 Comparison of Predicted and Measured Surface Heave Profile in Delft Centrifuge Test

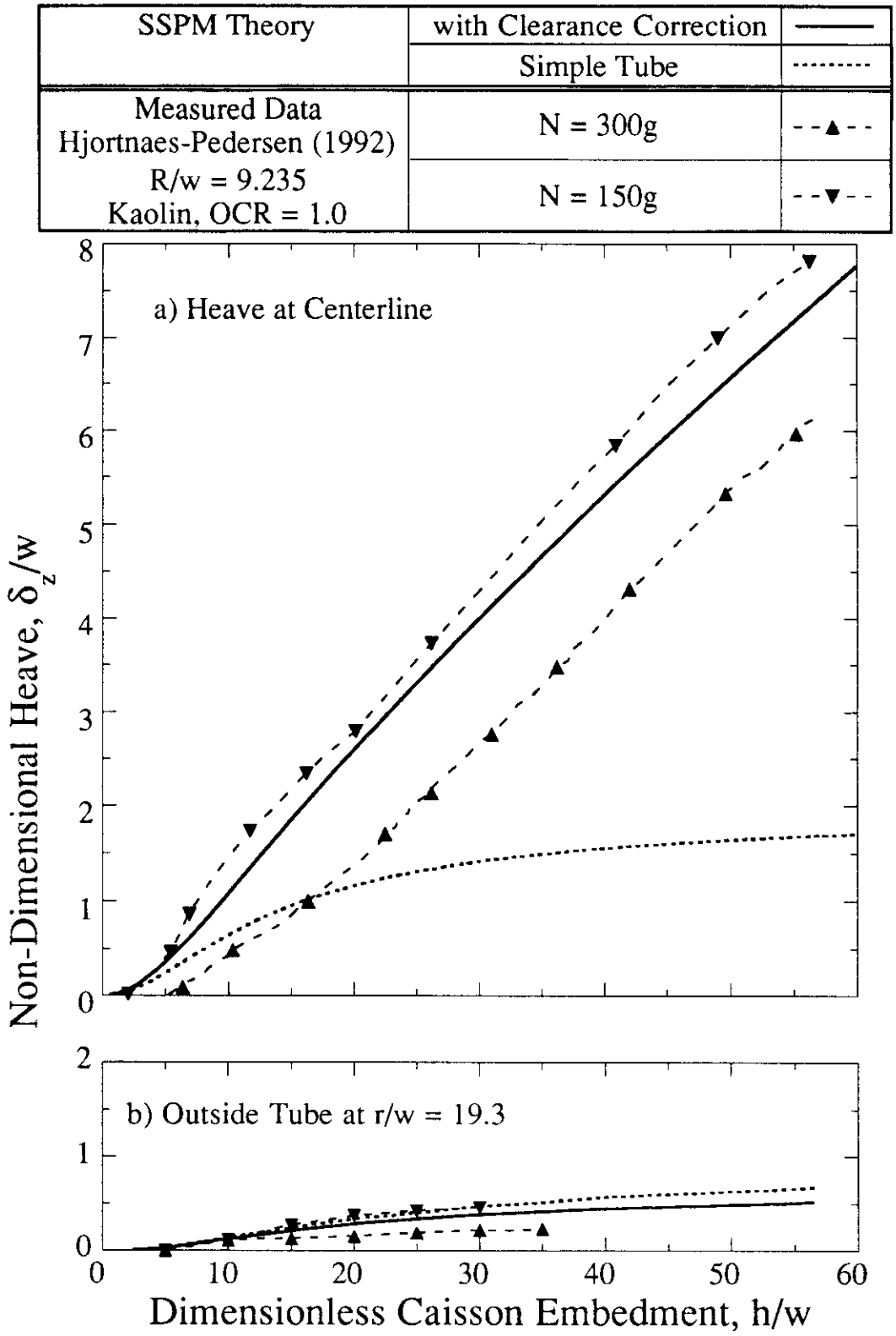

Figure 7.10 Comparison of Predicted and Measured Surface Displacements During Penetration of Thick-Walled Open-Ended Pile in Delft Centrifuge Tests

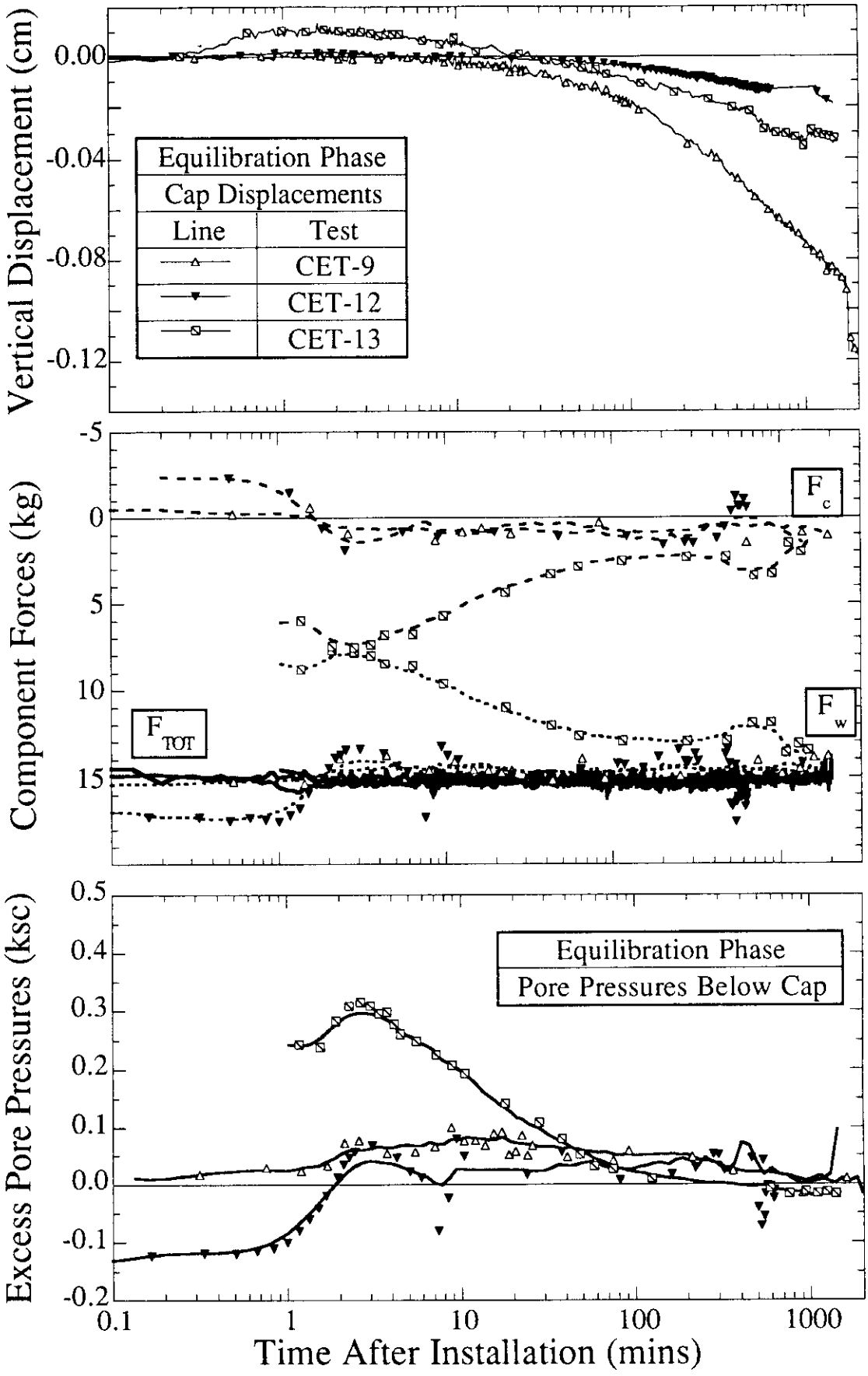

Figure 7.11 Summary of Equilibration Data for CET Model Caissons

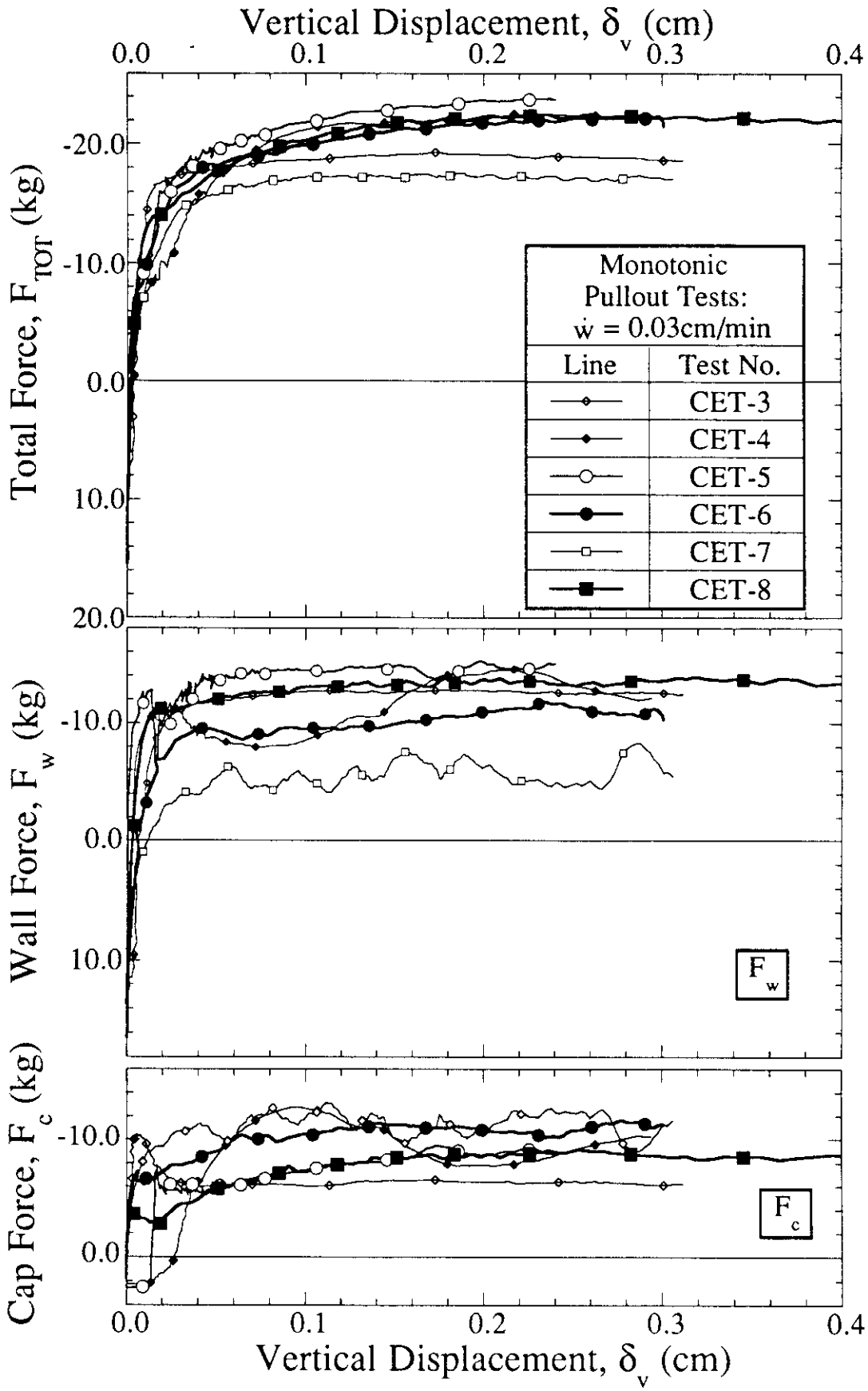

Figure 7.12 Summary of CET Model Caisson Behavior in First Time Axial Pullout Tests

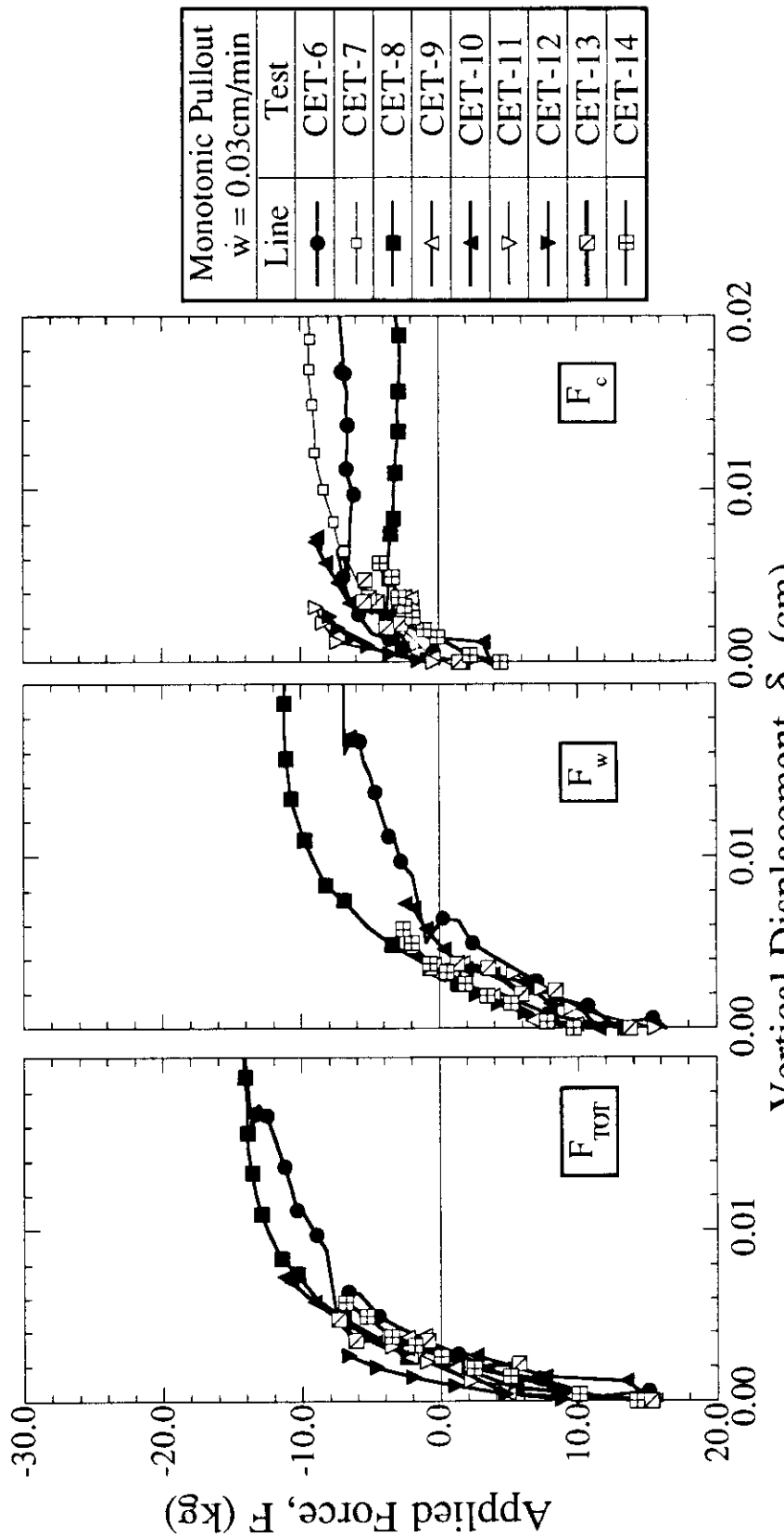

Figure 7.13 Behavior of CET Model Caissons in Axial Pullout Tests at Small Displacements

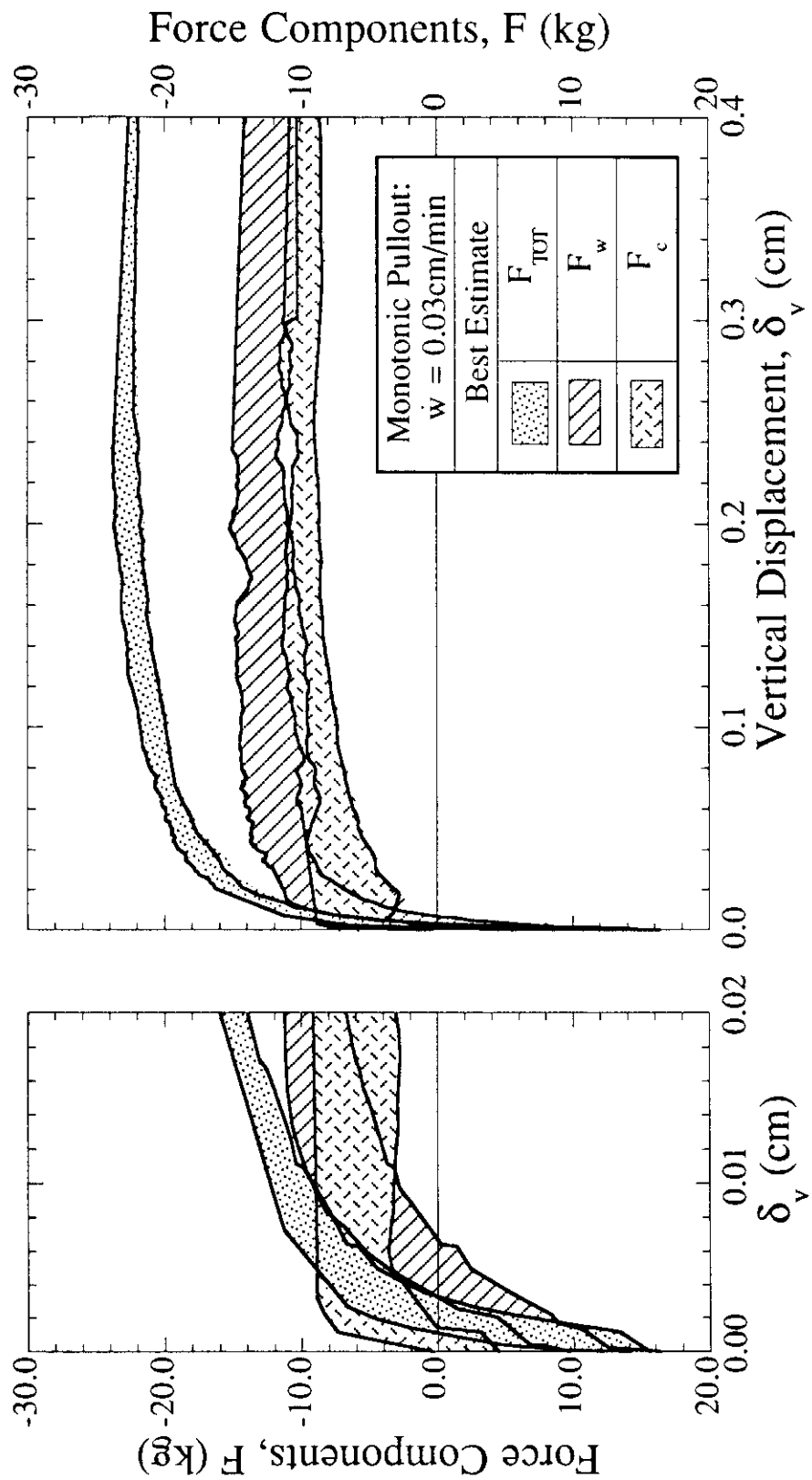

Figure 7.14 Best Estimate of Force-Displacement Behavior in First Time Axial Pullout Tests

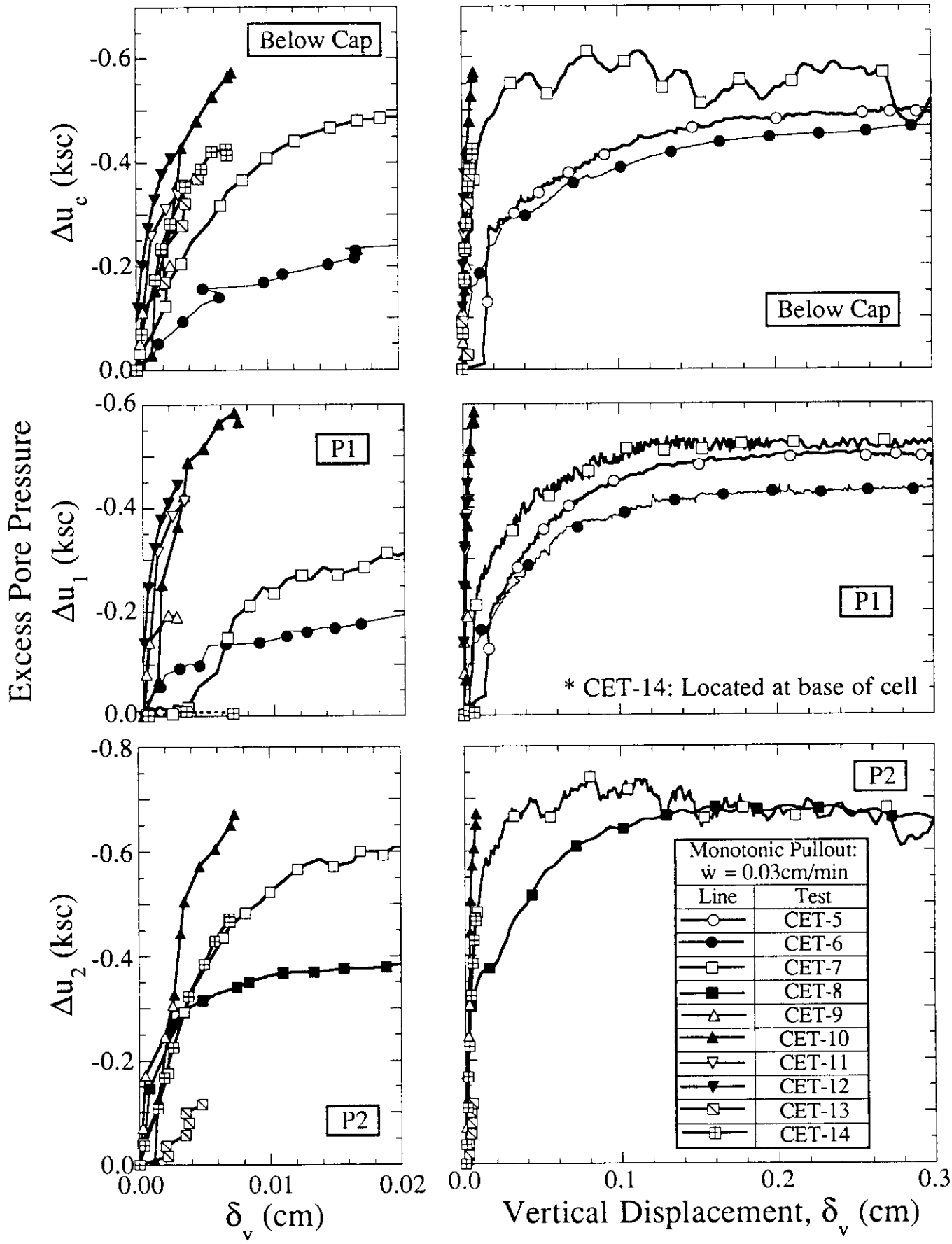

Figure 7.15 Measurements of Pore Pressures Inside CET Model Caissons During First Time Axial Pullout

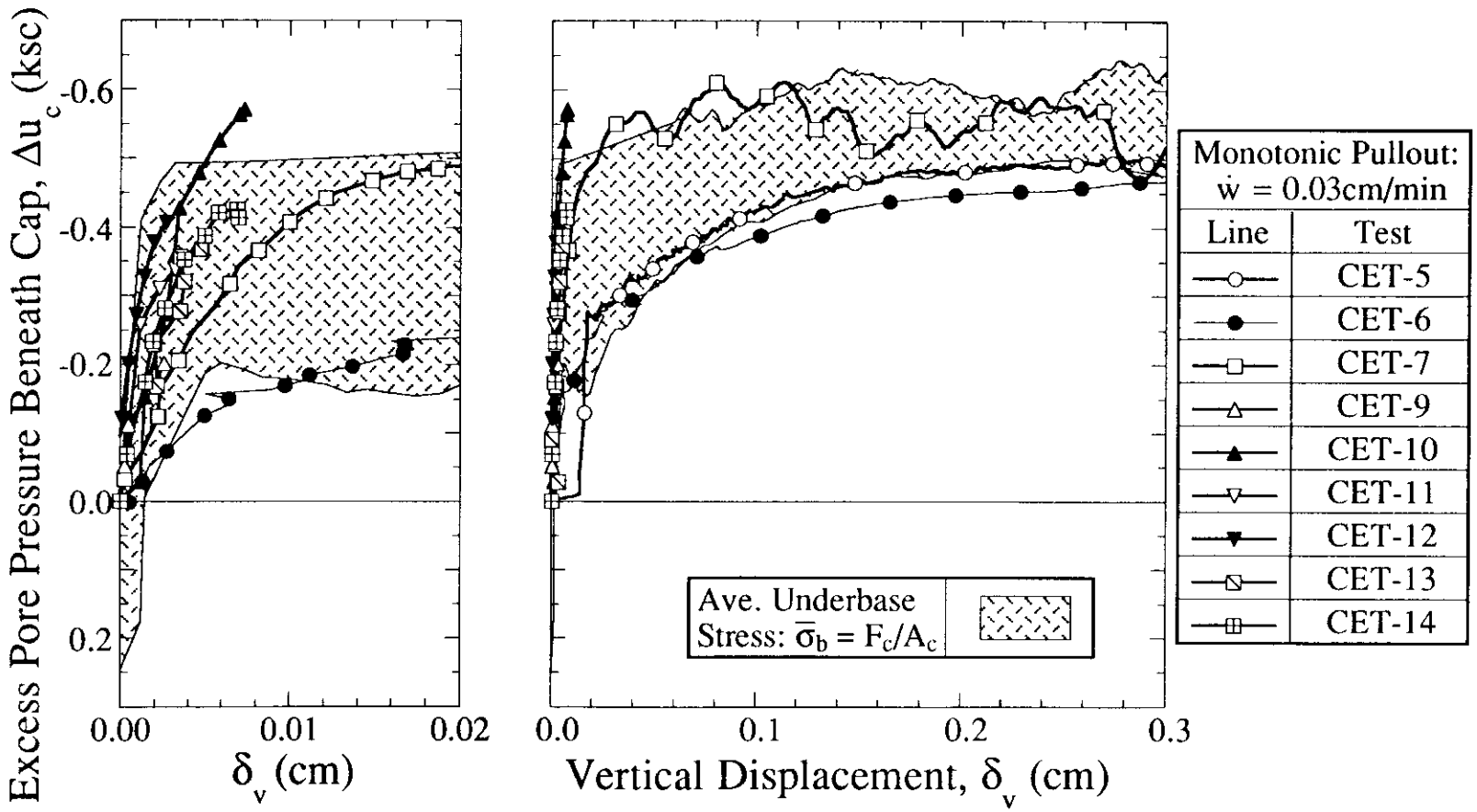

Figure 7.16 Comparison of Average Total Stresses and Excess Pore Pressures Below Cap in First Time Axial Pullout Tests

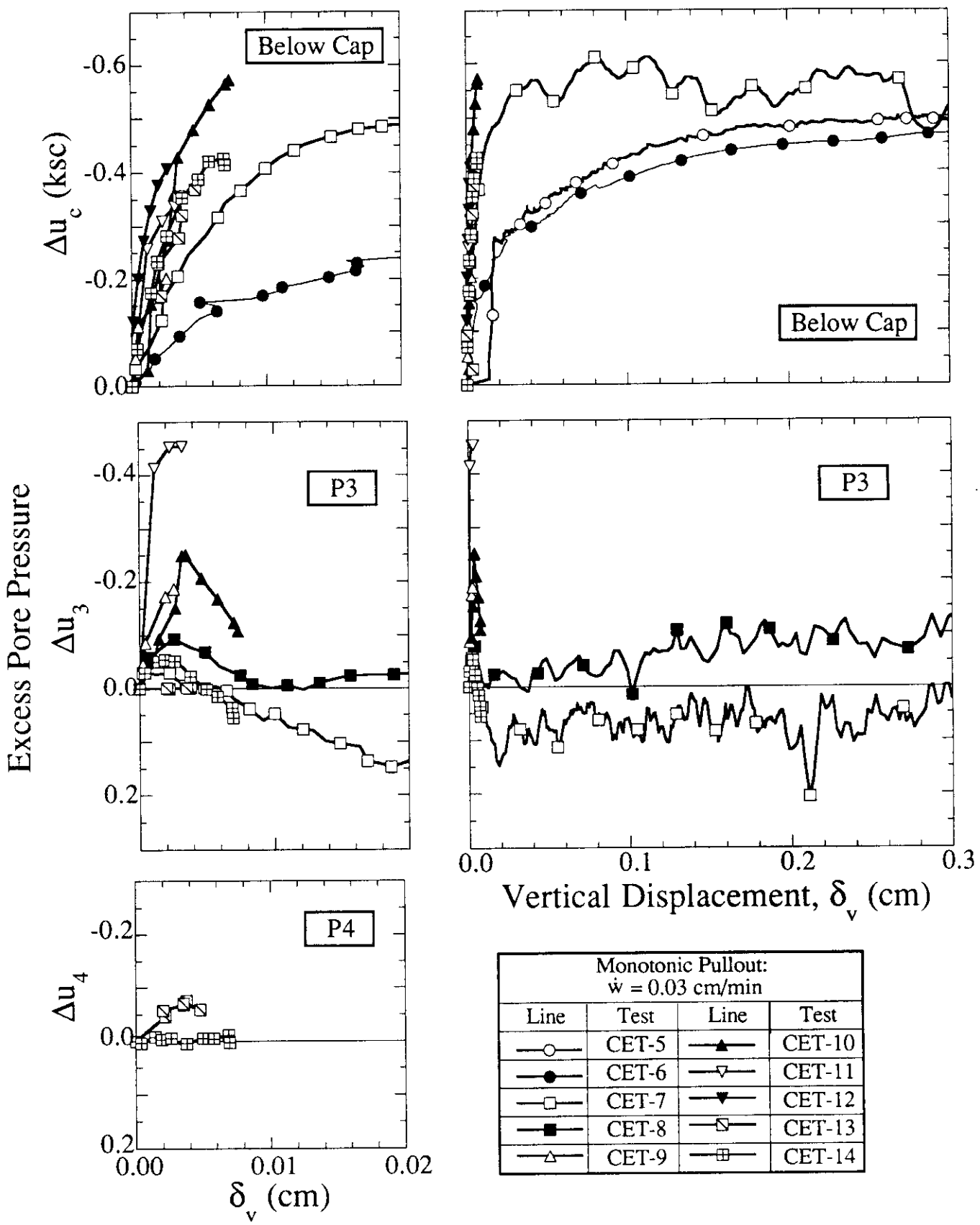

Figure 7.17 Measurements of Pore Pressure Outside CET Model Caissons During First Time Axial Pullout

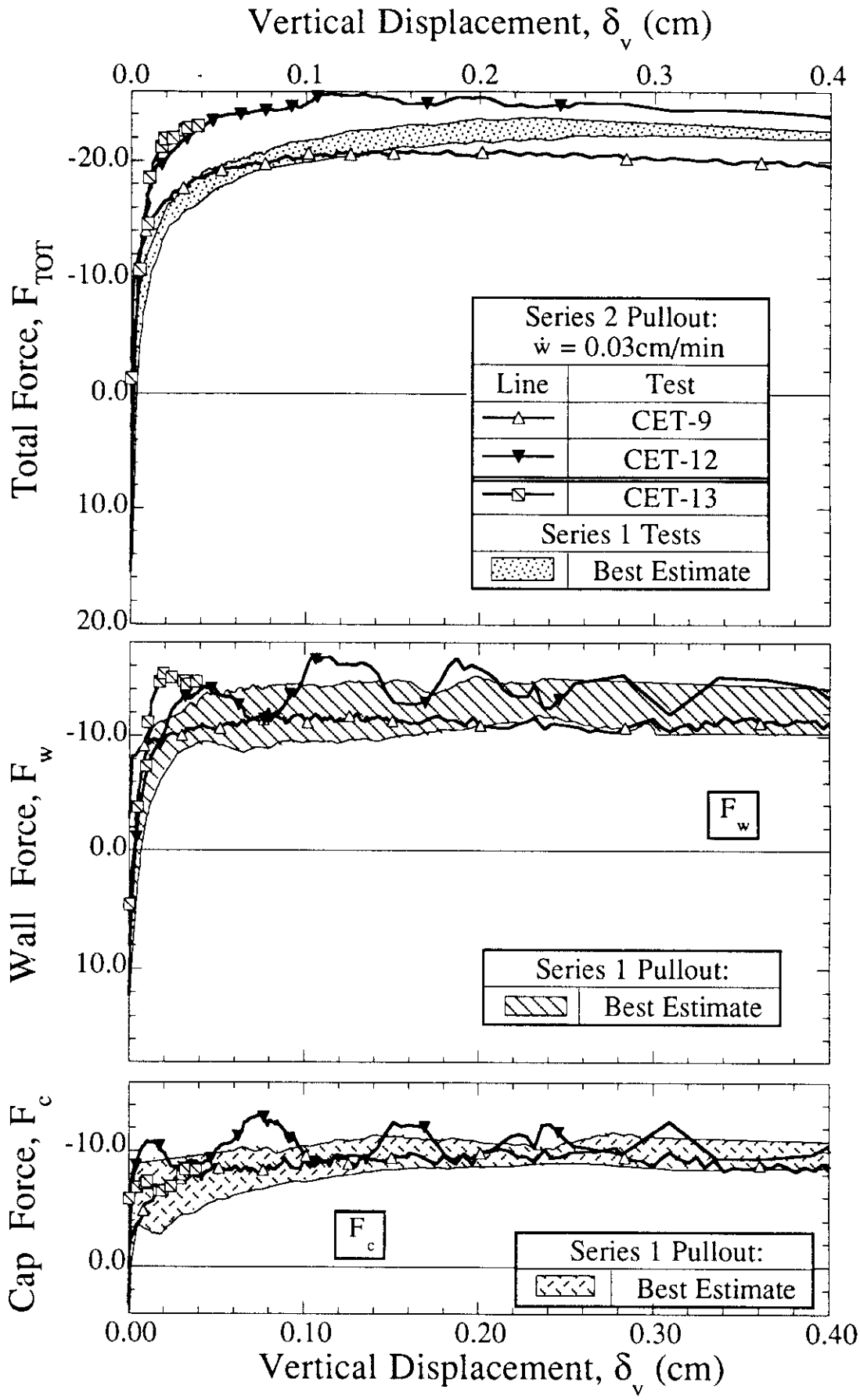

Figure 7.18 Comparison of Force-Deformation Response of CET Model Caissons in First and Second Time Axial Pullout Experiments

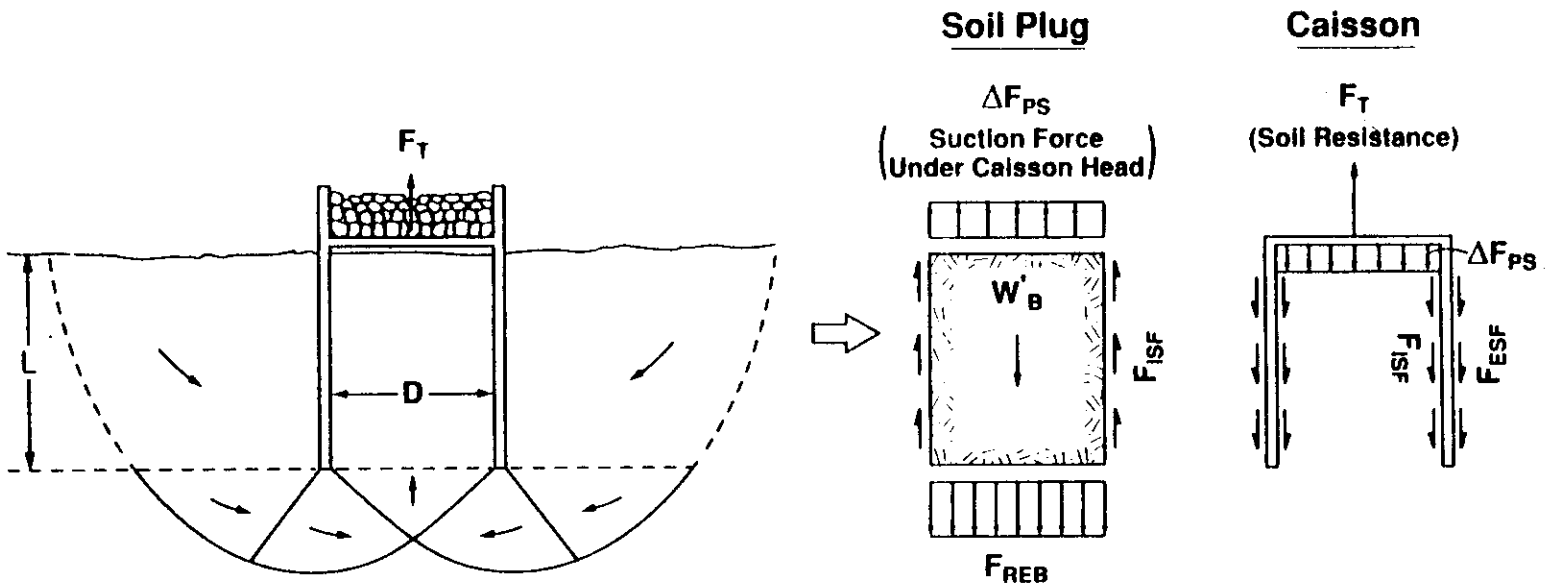

$$\Delta F_{PS} + F_{ISF} = W'_B + F_{REB}$$

$$F_{ISF} = (W'_B + F_{REB}) - \Delta F_{PS}$$

$$F_{ISF} = F'_{REB} - \Delta F_{PS}$$

Where:

$$F_T = \Delta F_{PS} + F_{ISF} + F_{ESF}$$

$$F_T = F'_{REB} + F_{ESF}$$

Figure 7.19 Static Equilibrium for Vertically Loaded Suction Anchors (from Clukey & Morrison, 1993)

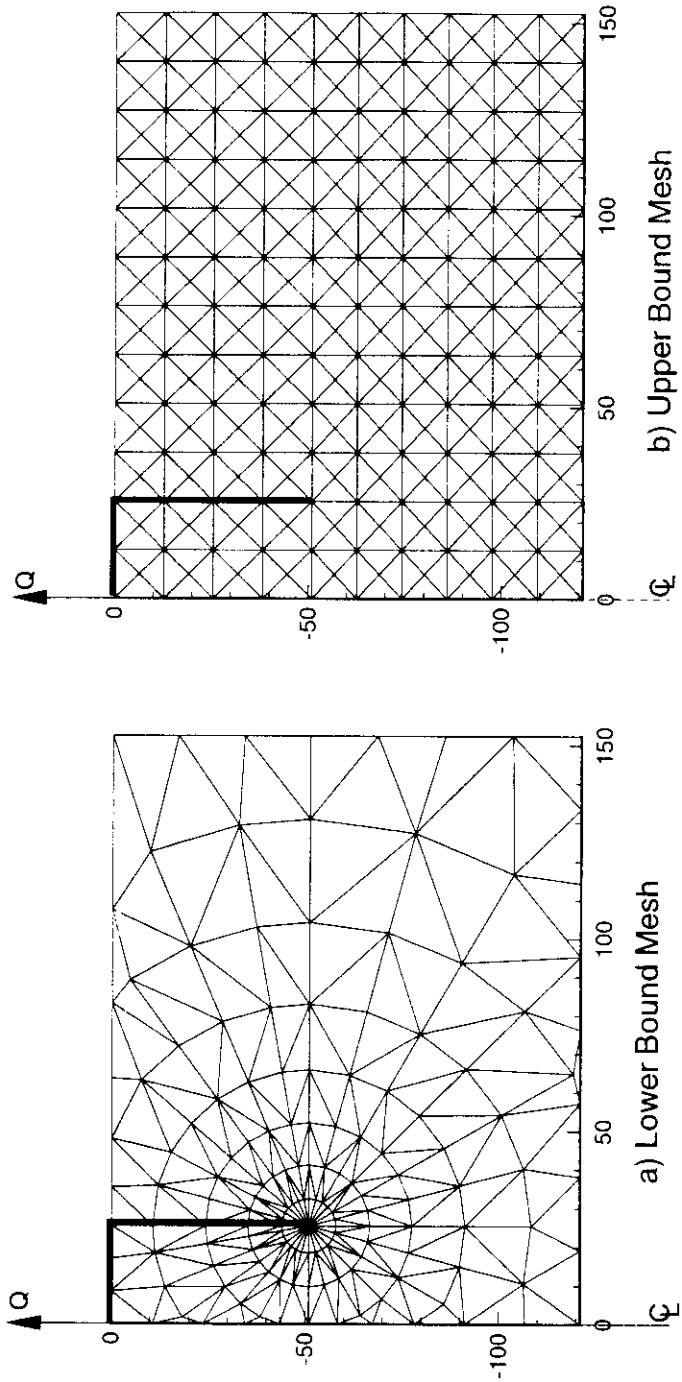

Figure 7.20 Spatial Discretization of CET Cell for Numerical Limit Analyses

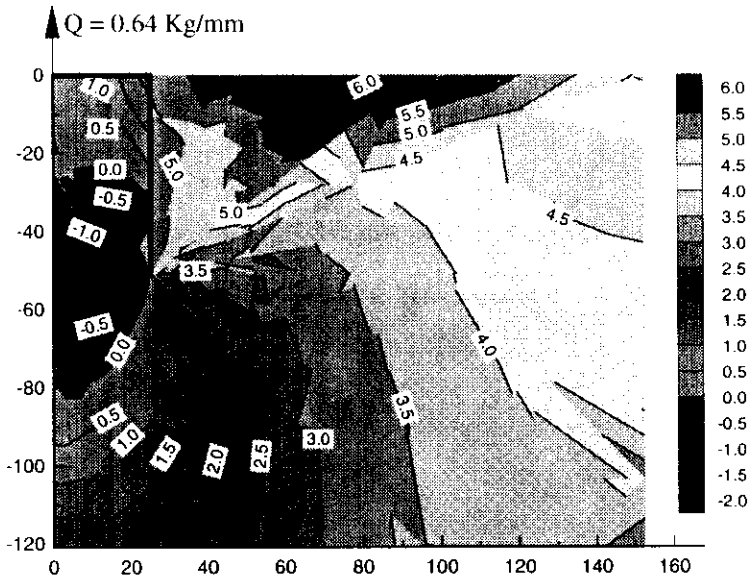

a) Mean stress, $(\sigma_1+\sigma_3)/2c_u$

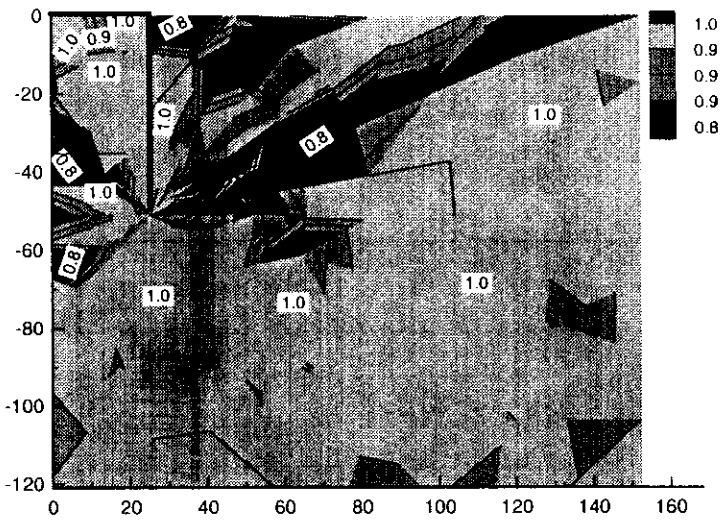

b) Shear stress, $(\sigma_1-\sigma_3)/2c_u$

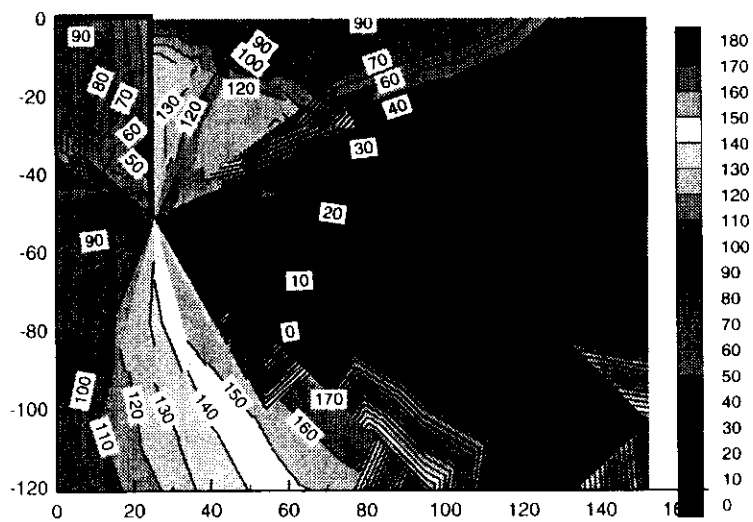

c) Direction of major principal stress to vertical, δ (deg, cw)

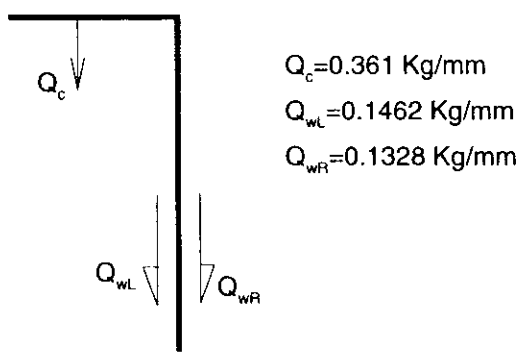

d) Reaction forces on caisson

Figure 7.21 Results of Lower Bound Analysis for CET Model Caisson

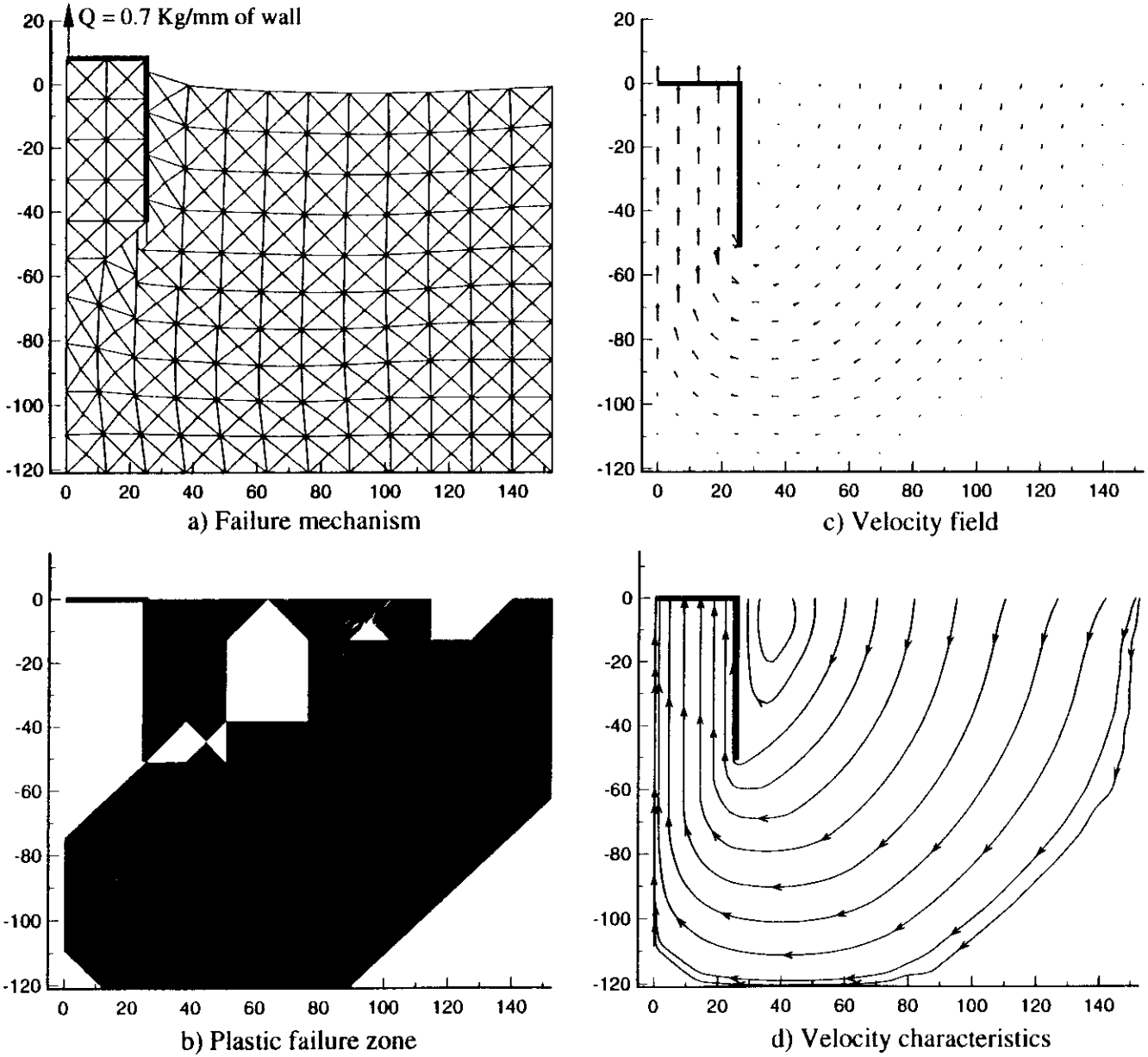

Figure 7.22 Results of Upper Bound Analysis for CET Model Caisson

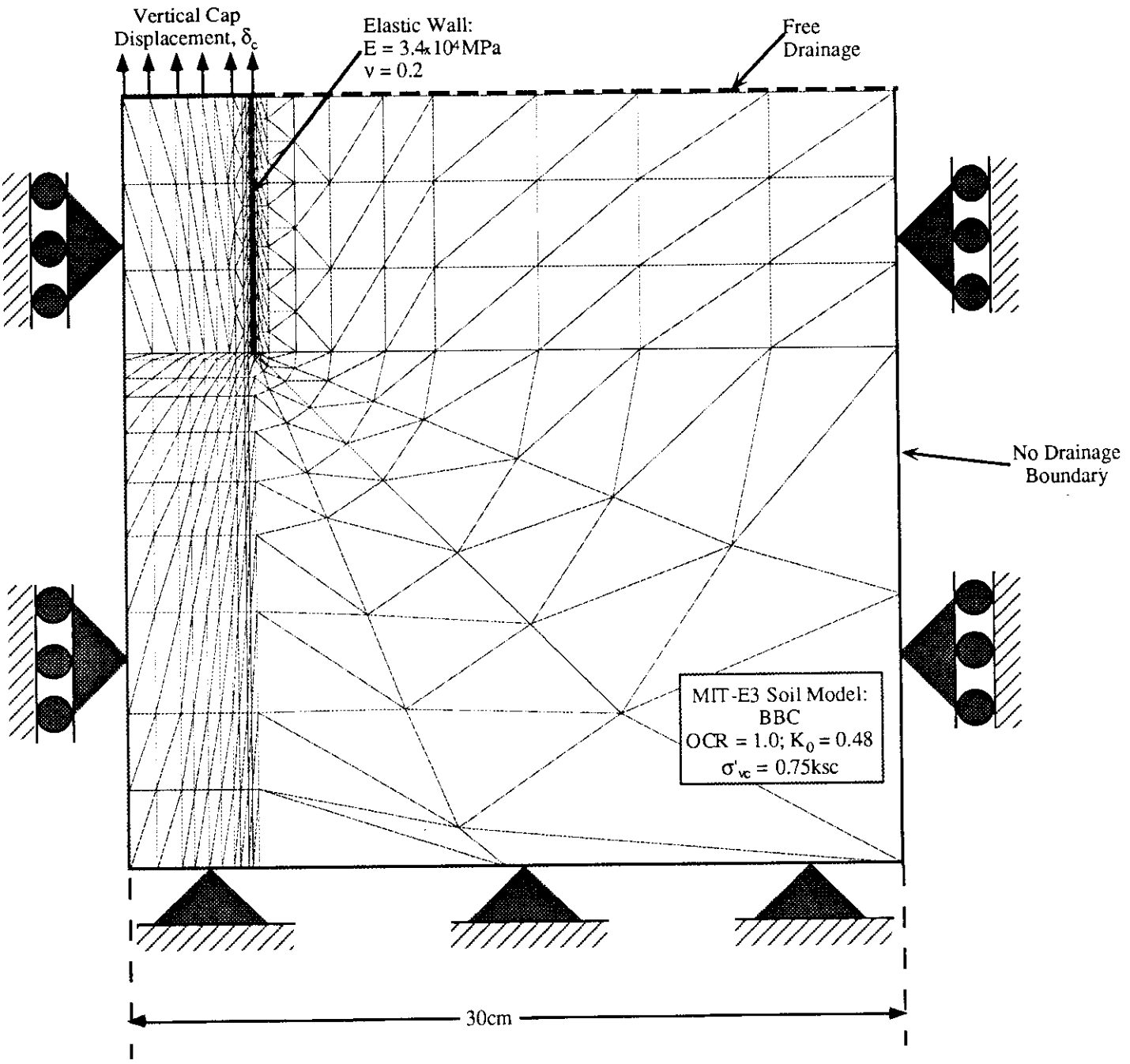

Figure 7.23 Finite Element Mesh and Boundary Conditions for Finite Element Analysis of CET Tests

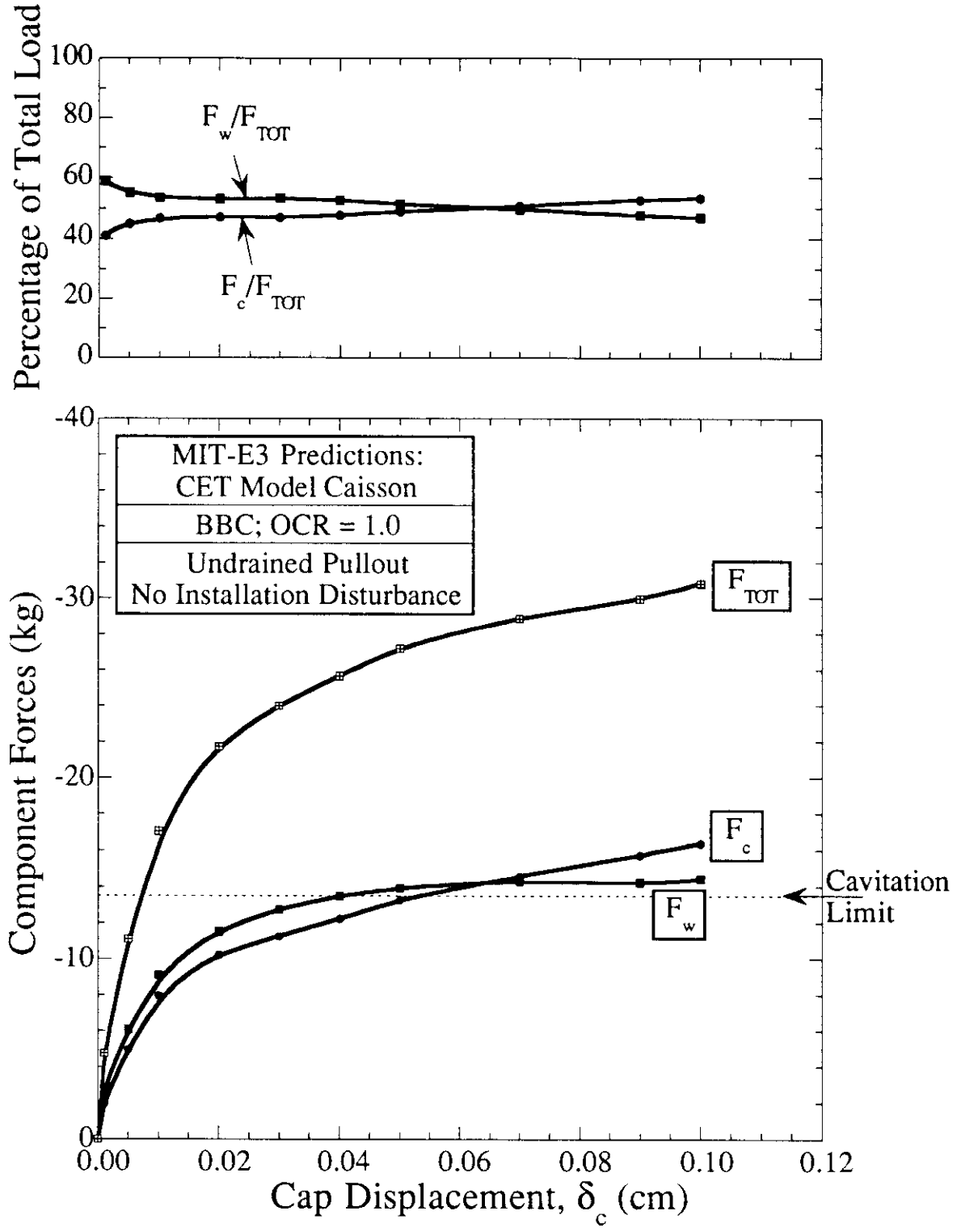

Figure 7.24 Finite Element Predictions of Undrained Axial Load-Deformation Response for CET Model Caisson

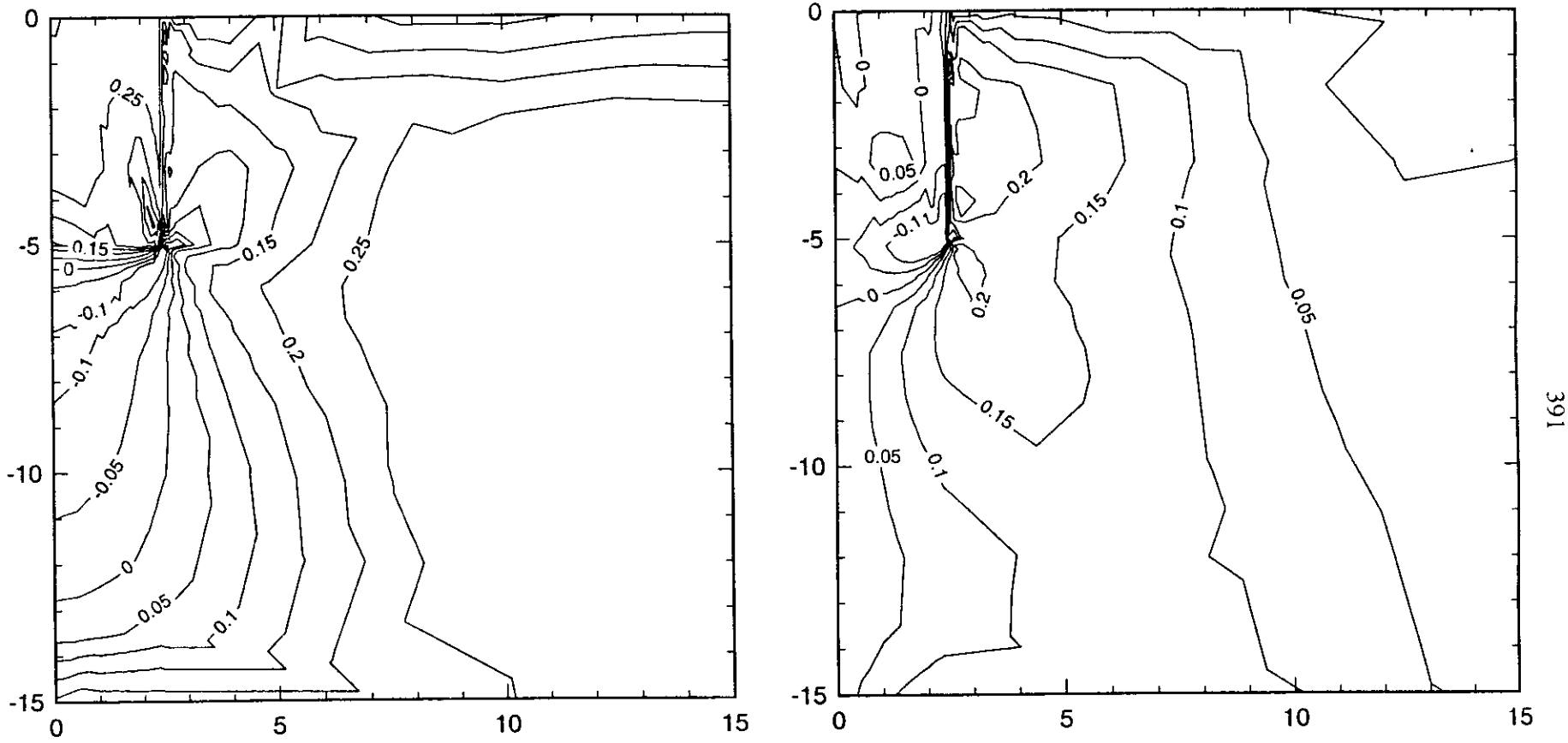

a) Triaxial Shear Stress, q/σ'_{v0}

b) Direct Simple Shear Stress, τ/σ'_{v0}

Figure 7.25 Finite Element Predictions of Displacements, Shear Stresses and Pore Pressures for Undrained Axial Loading of CET Model Caisson at $\delta_v = 0.1$cm

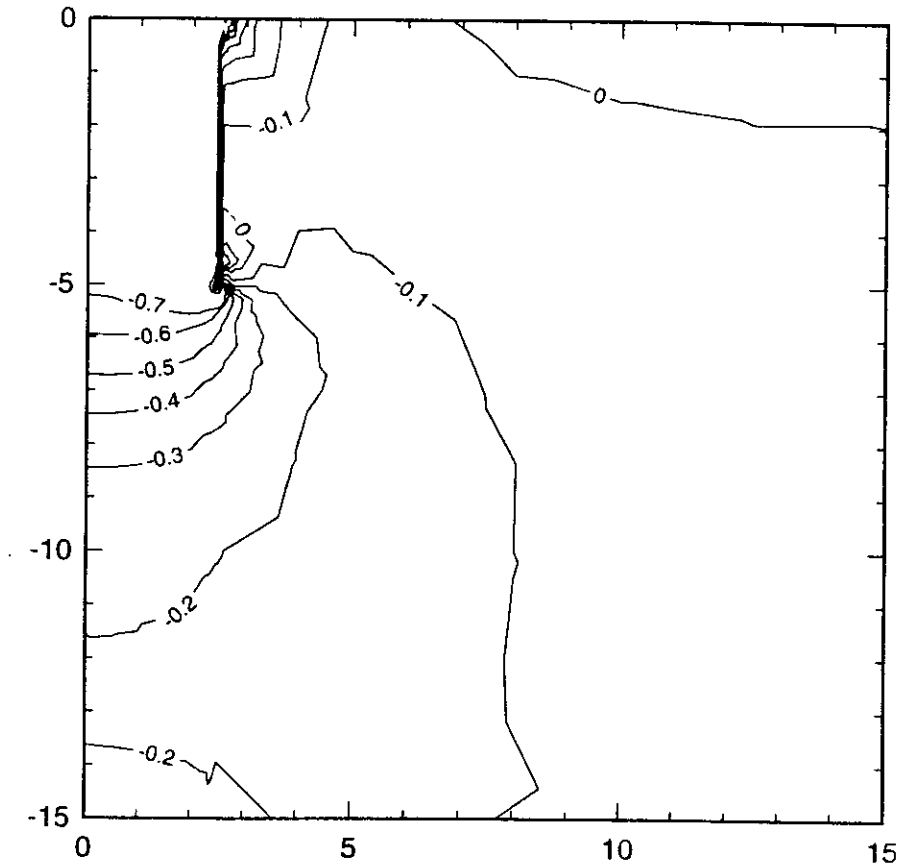

c) Excess Pore Pressures $\Delta u/\sigma'_{v0}$

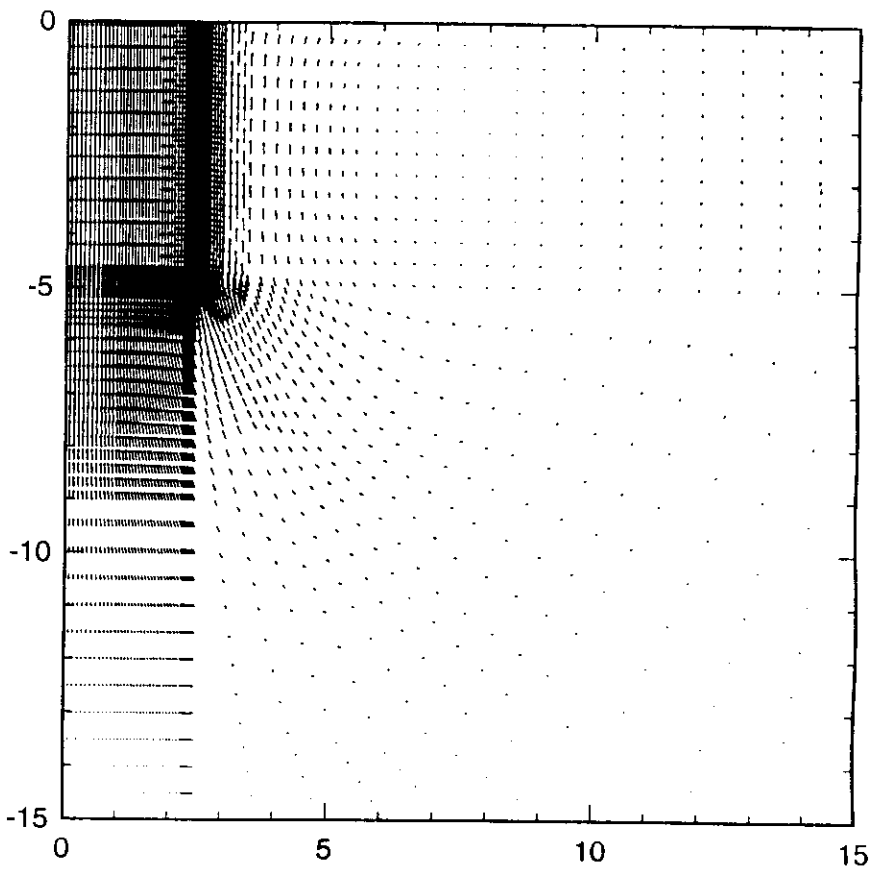

d) Displacements

Figure 7.25 Finite Element Predictions of Displacements, Shear Stresses and Pore Pressures for Undrained Axial Loading of CET Model Caisson at $\delta_v = 0.1$cm

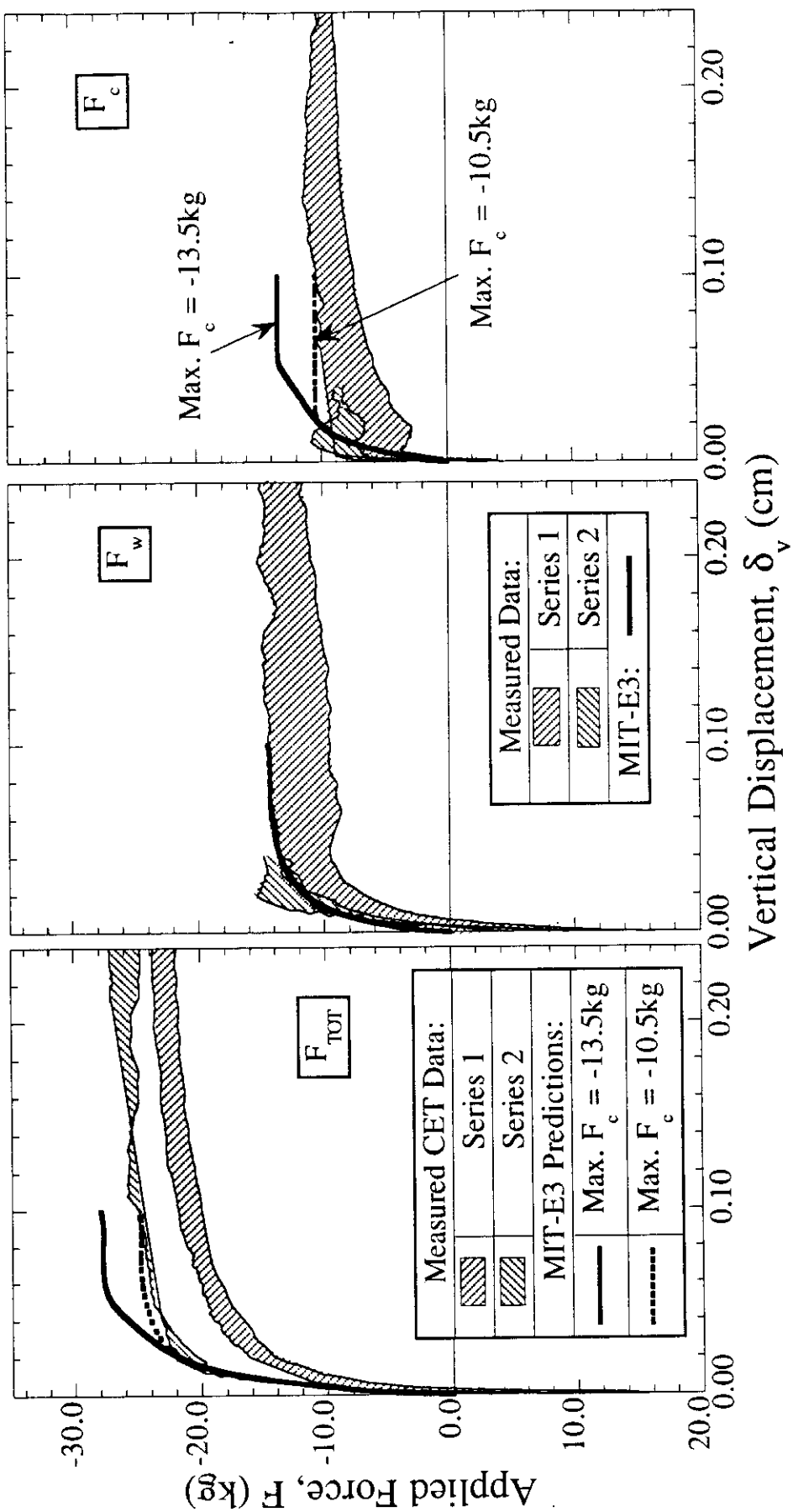

Figure 7.26 Comparison of Predicted and Measured Force-Displacement Behavior for Axial Pullout of CET Model Caissons

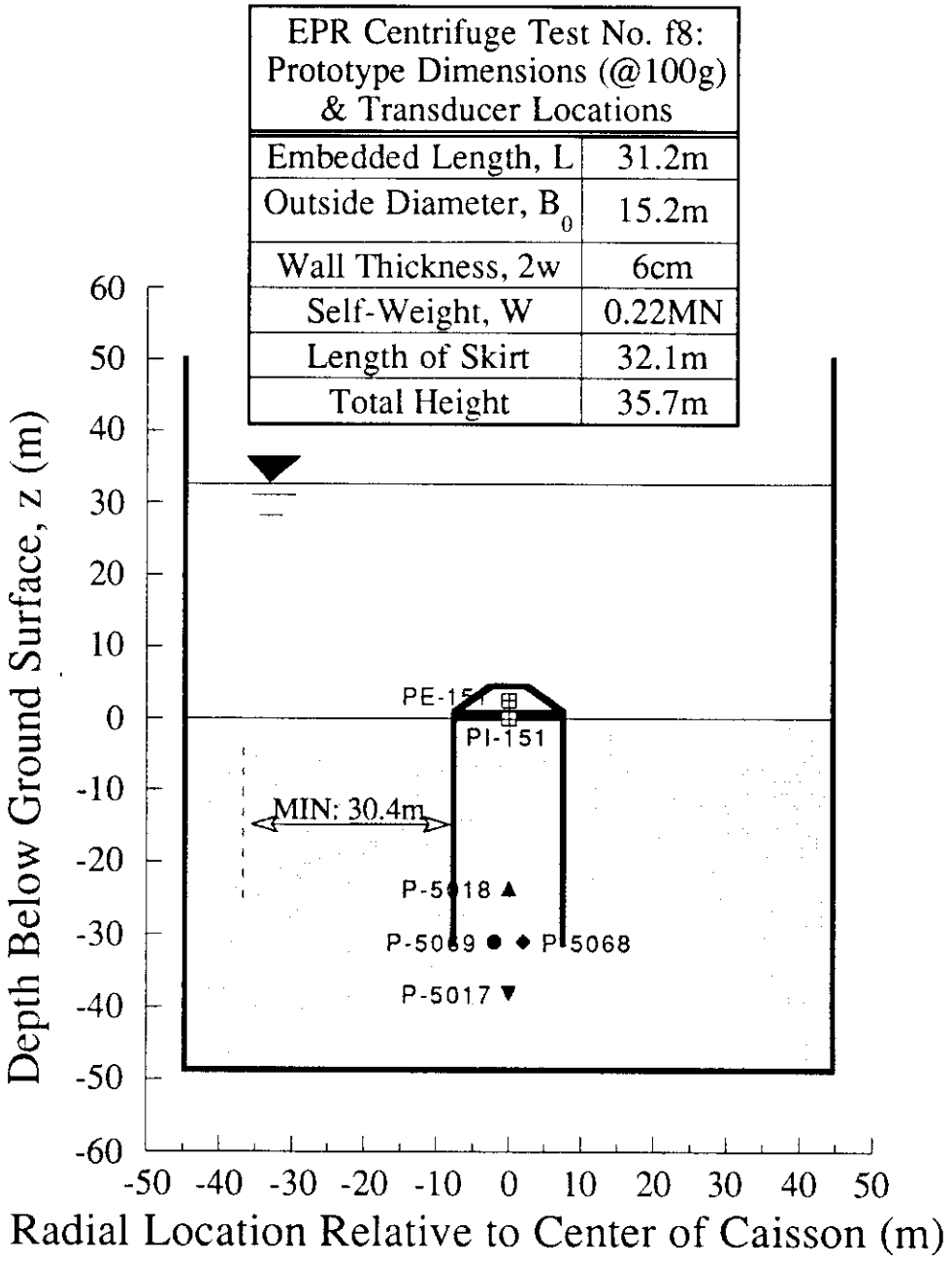

Figure 7.27 Geometry and Instrumentation for EPR Centrifuge Model Caisson Experiments

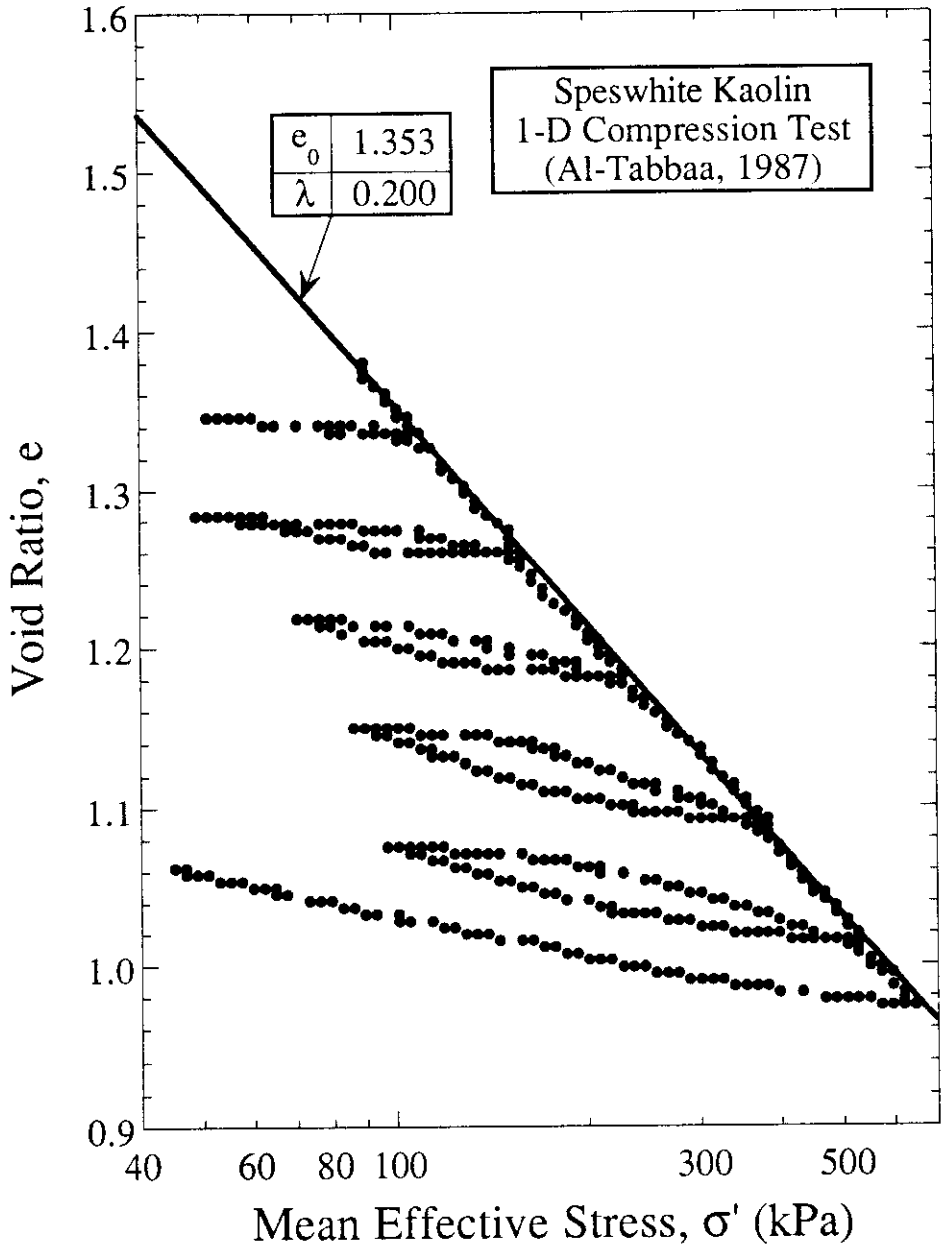

Figure 7.28a. One-Dimensional Compression Behavior of Speswhite Kaolin

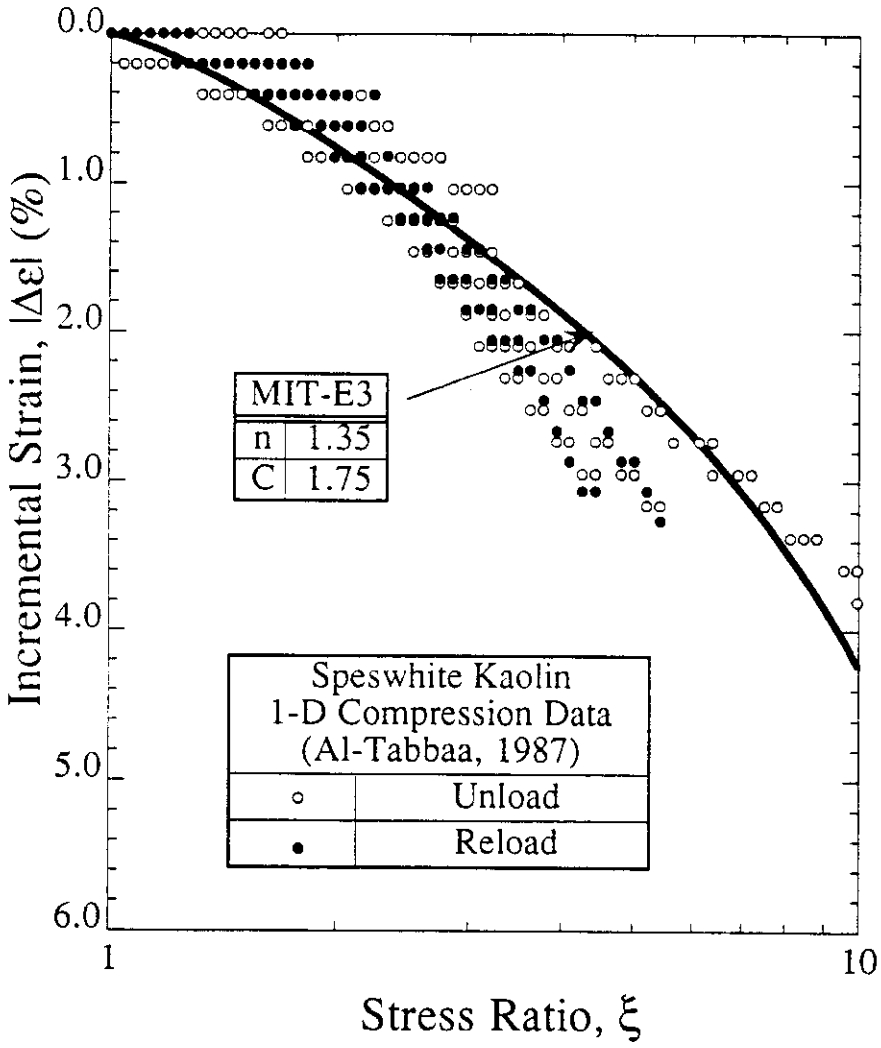

Figure 7.28b. One-Dimensional Swelling Behavior of Speswhite Kaolin

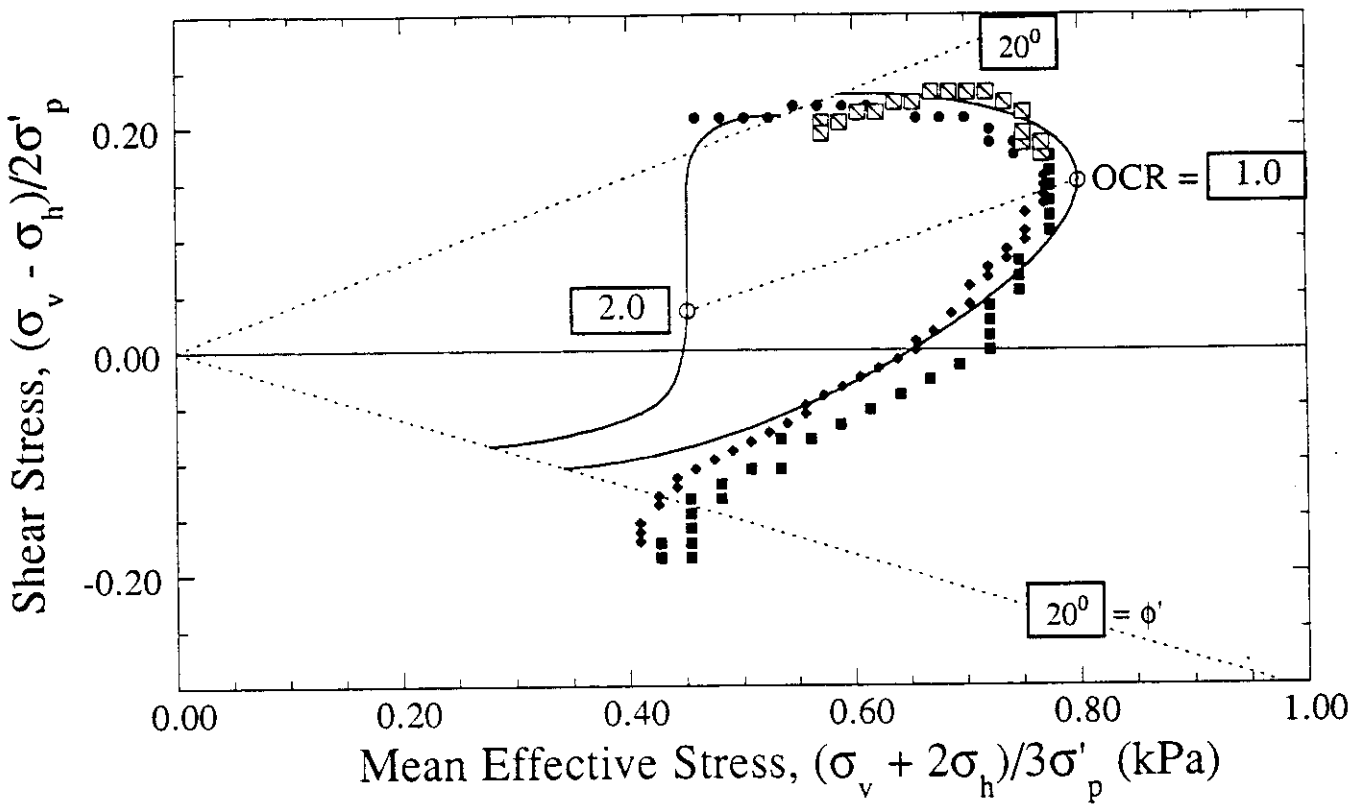

Speswhite Kaolin: Triaxial Test Data				
Test No.	Symbol	σ'_p (kPa)	K_{0NC}	Source:
C6	•	265	0.65	Atkinson et al. (1988)
E5	■	217	0.66	"
E6	◆	354	0.66	"
AU	▨	387	0.70	Tatsuoka (1994)
MIT-E3 Predictions	———		0.70	

Figure 7.29a. Comparison of Computed and Measured Effective Stress Paths in Undrained Triaxial Shear Tests on K_0-Consolidated Kaolin

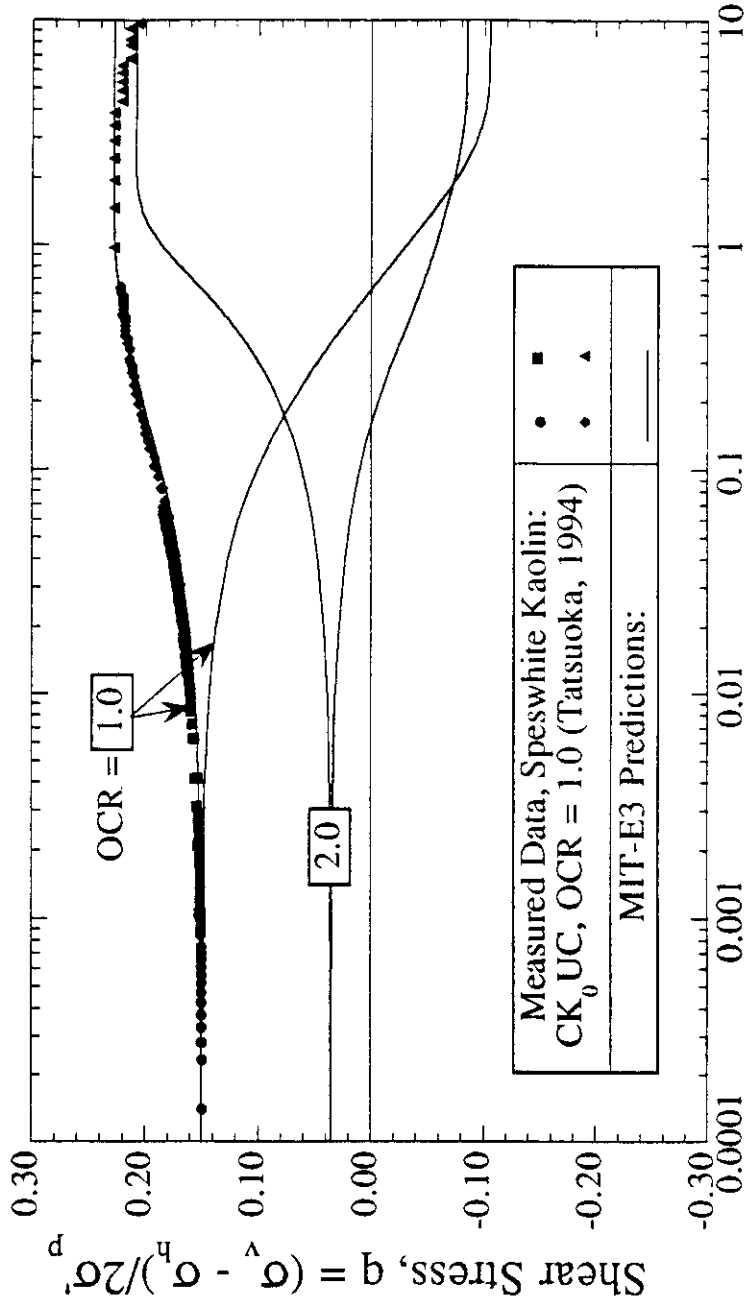

Figure 7.29b. Comparison of Computed and Measured Shear Stress-Strain Behavior in Undrained Triaxial Tests on K_0-Consolidated Kaolin

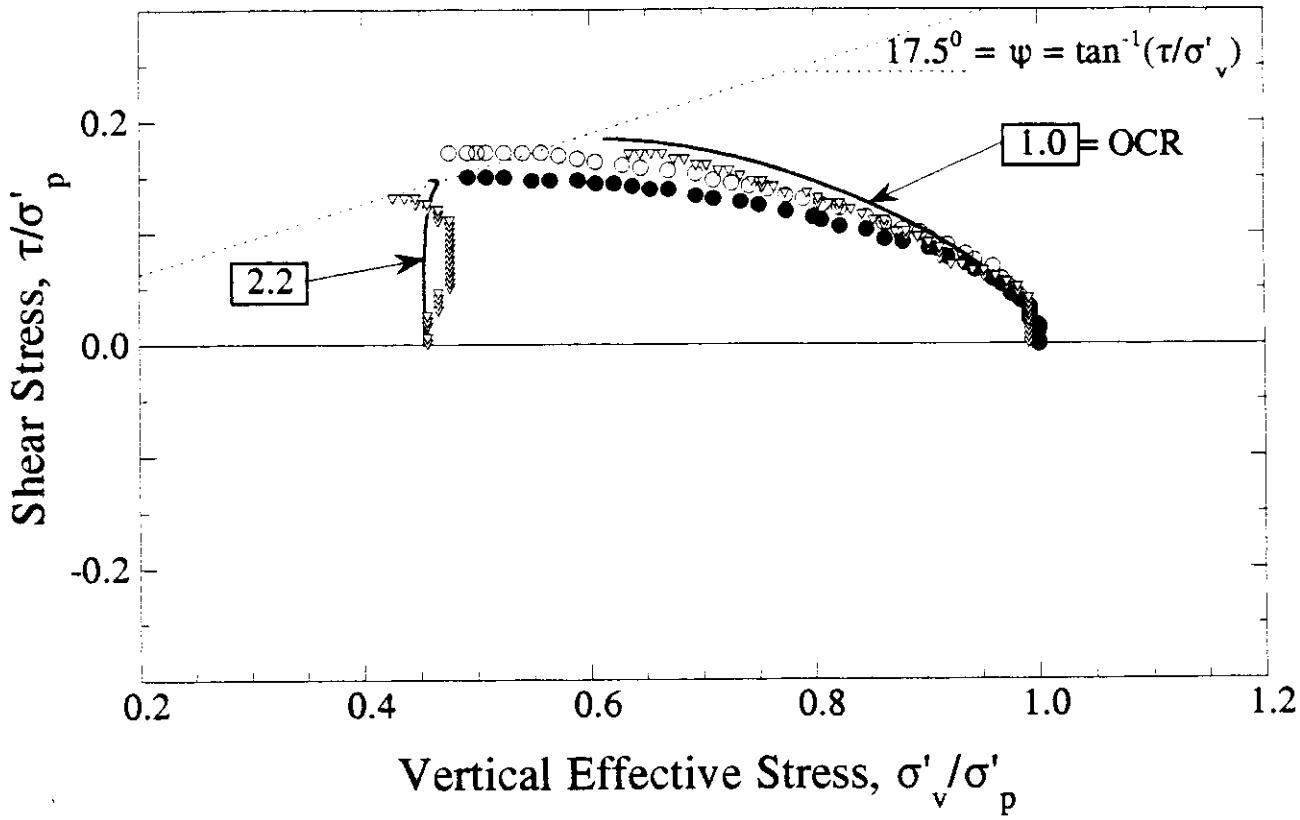

Measured Data: Speswhite Kaolin		
Symbol:	Device:	Source:
○	CSSA (Core)	Airey & Wood (1987)
●	Geonor	Airey & Wood (1987)
▽	TSHC	Ampadu & Tatsuoka (1994)
———	MIT-E3 Predictions	

Figure 7.30a. Comparison of Predicted and Measured Effective Stress Paths for Undrained Direct Simple Shear Tests on Speswhite Kaolin

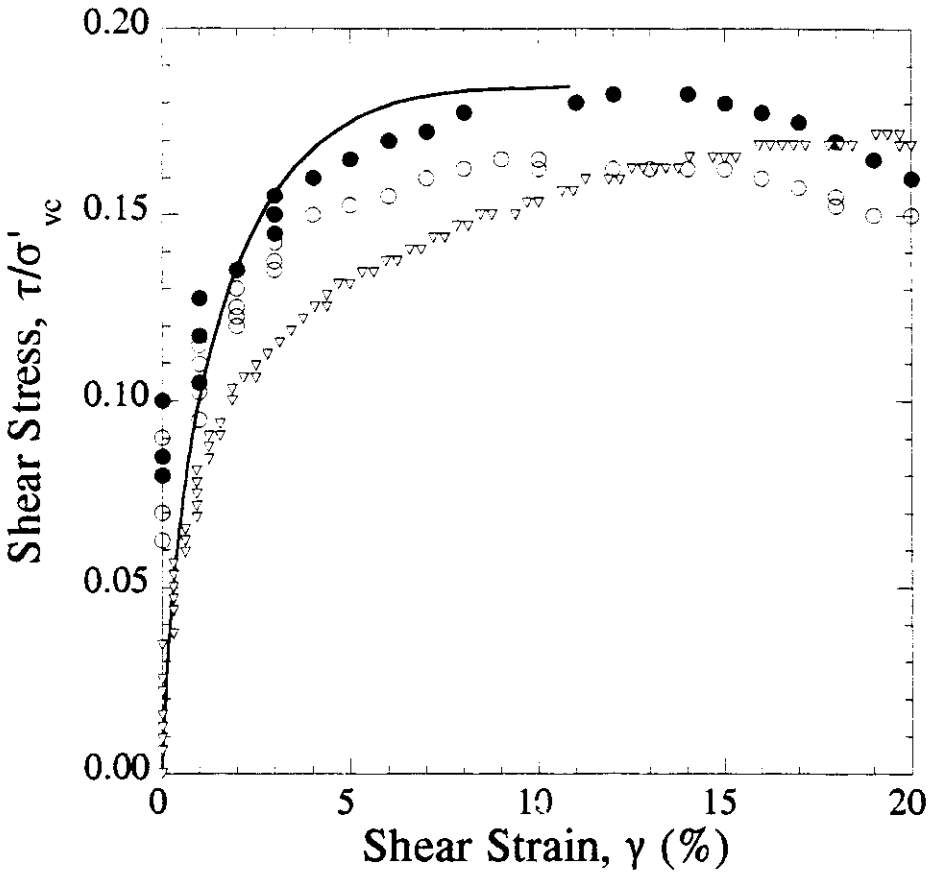

Measured Data: Speshwite Kaolin (OCR = 1.0)		
Symbol:	Device:	Source:
○	CSSA (Av.)	Airey & Wood (1987)
●	CSSA (core)	Airey & Wood (1987)
▽	TSHC	Ampadu & Tatsuoka (1994)
——	MIT-E3 Predictions	

Figure 7.30b. Comparison of Predicted and Measured Shear Stress-Strain Behavior for Undrained Direct Simple Shear Tests on Speswhite Kaolin

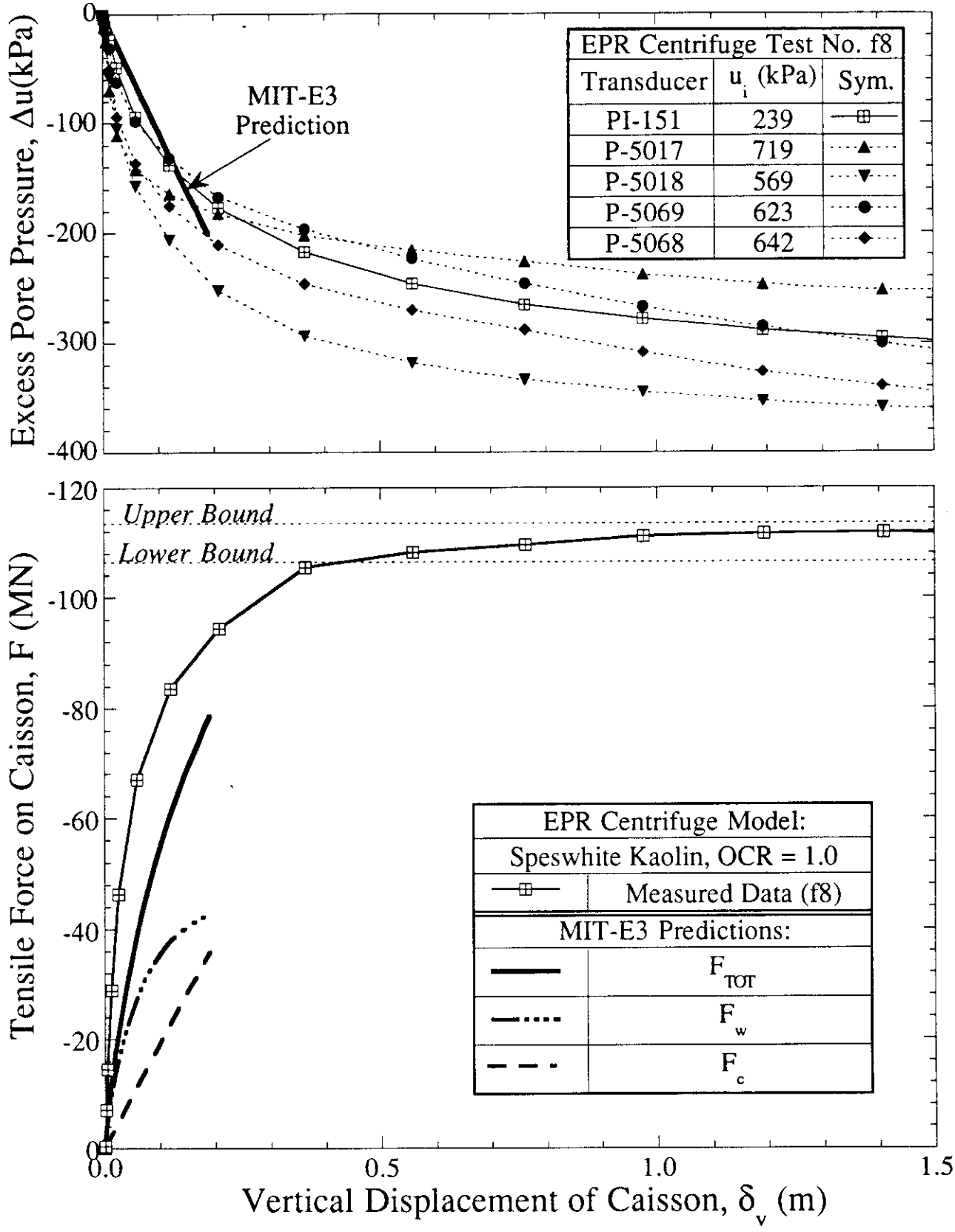

Figure 7.31 Comparison of Predicted and Measured Behavior for Axial Pullout of EPR Centrifuge Model Caisson: a) Pore Pressures Inside Caisson; b) Force-Displacement Response

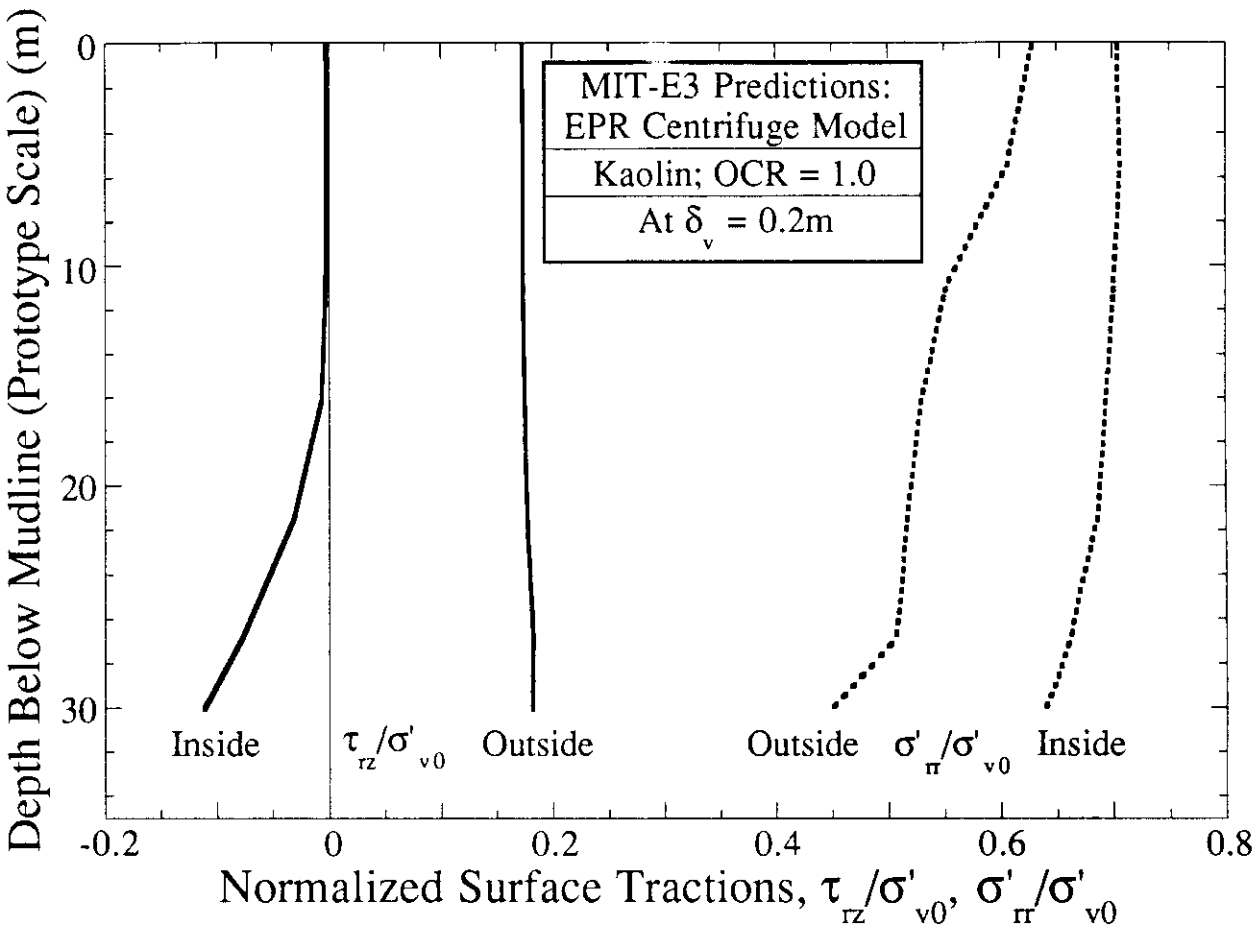

Figure 7.32 Finite Element Prediction of Surface Tractions on Wall of EPR Centrifuge Model

Caisson at δ_v = 0.2m

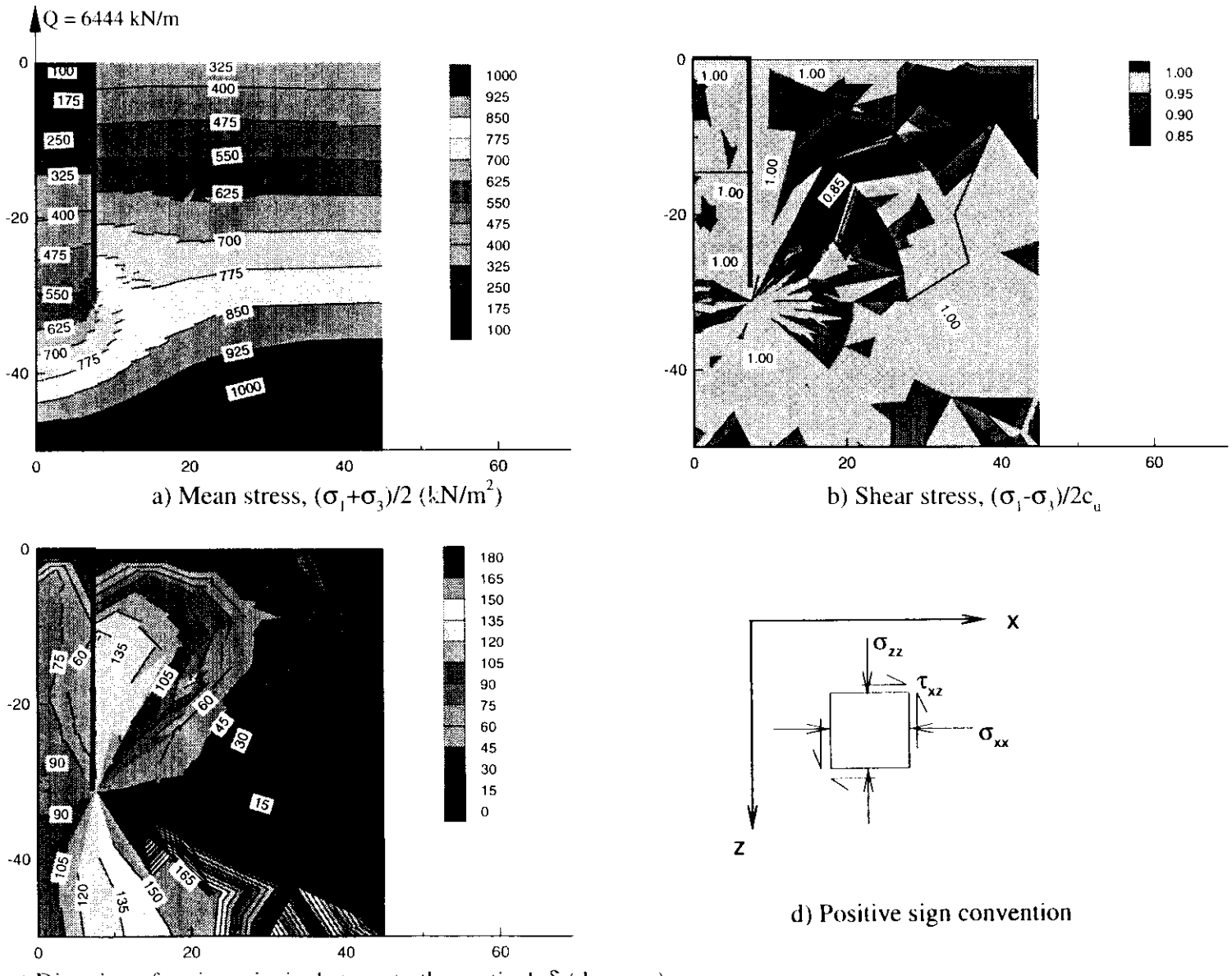

Figure 7.33 Lower Bound Limit Analysis for Axial Pullout of EPR Centrifuge Model Caisson

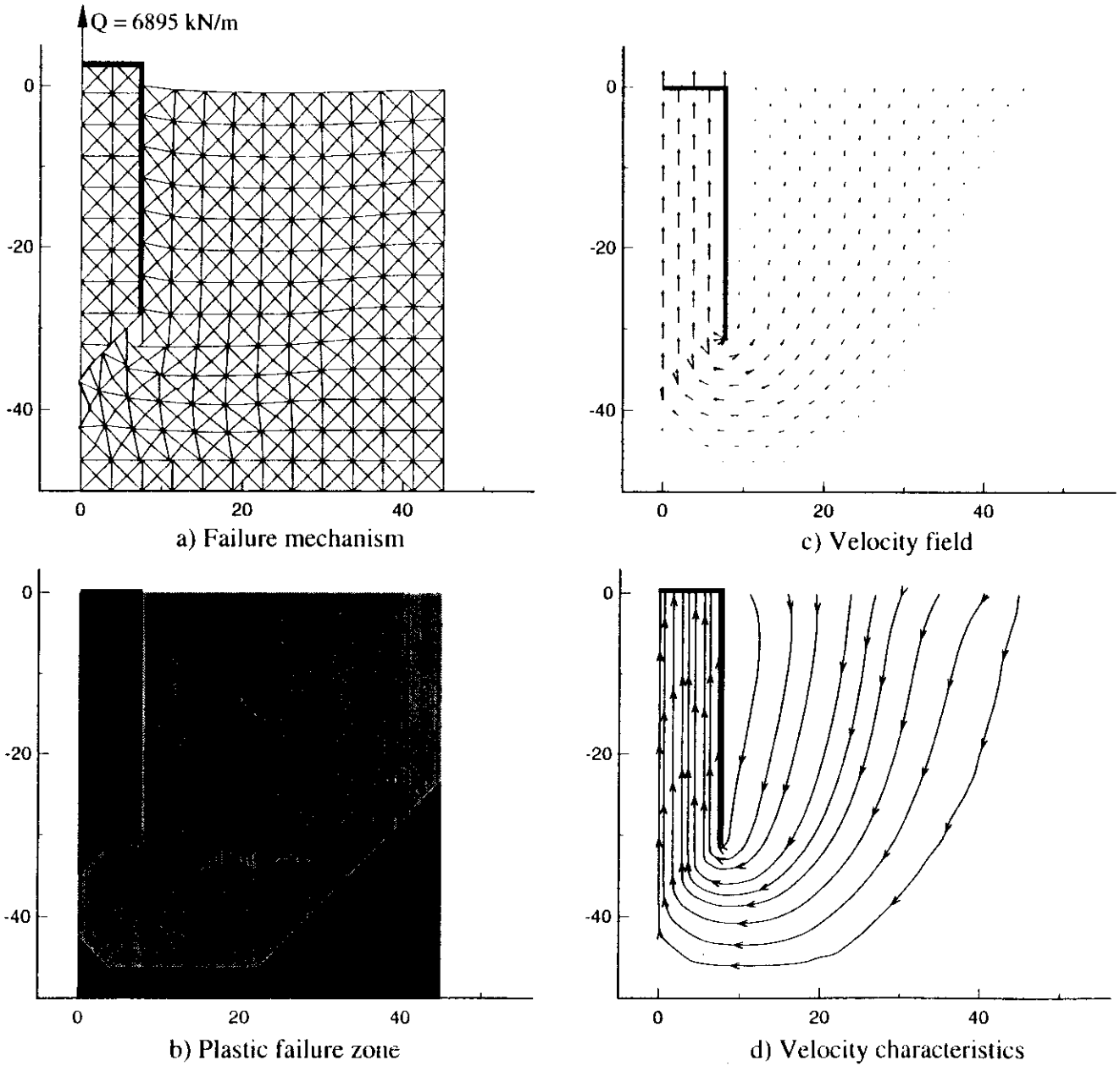

Figure 7.34 Upper Bound Limit Analysis for Axial Pullout of EPR Centrifuge Model Caisson

Numerical Solutions

Upper Bound	Q_U = 6056 kN/m
Lower Bound	Q_L = 5387 kN/m
Average	Q_{ave} = 5722 kN/m
Bound	11.70%

Net Reaction Forces on Caisson (Lower Bound Results)

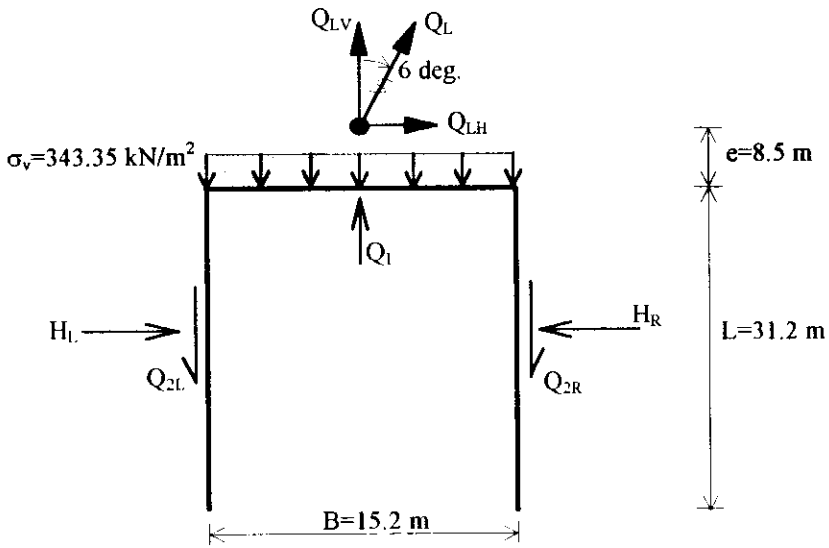

Vertical Components

Q_{LV} =	5357 kN/m
Q_1 =	1888 kN/m
Q_{2L} =	1163 kN/m
Q_{2R} =	864 kN/m
σ_v (B) =	5218 kN/m

Horizontal Components

Q_{LH} =	563 kN/m
H_L =	6250 kN/m
H_R =	6813 kN/m

Figure 7.35 Calculation of Lower Bound Inclined Loads for EPR Centrifuge Model Caisson

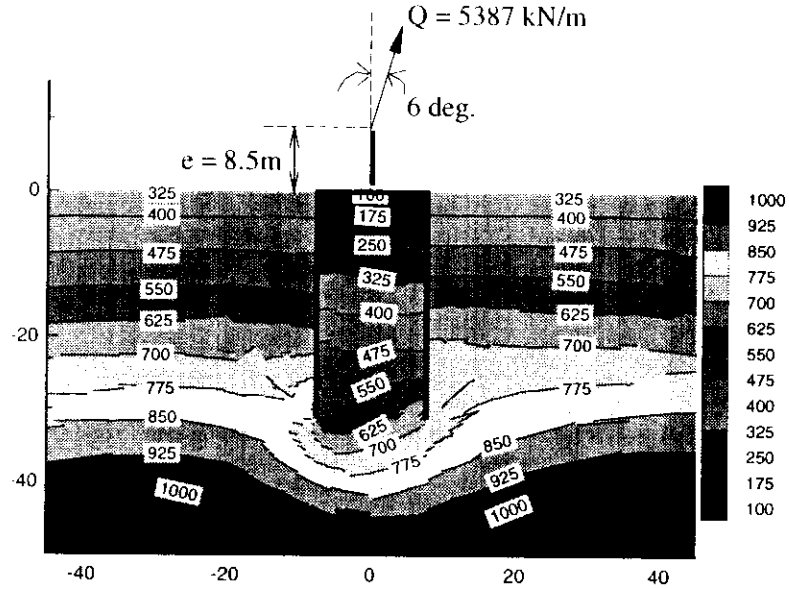

a) Mean stress, $(\sigma_1+\sigma_3)/2$ (kN/m^2)

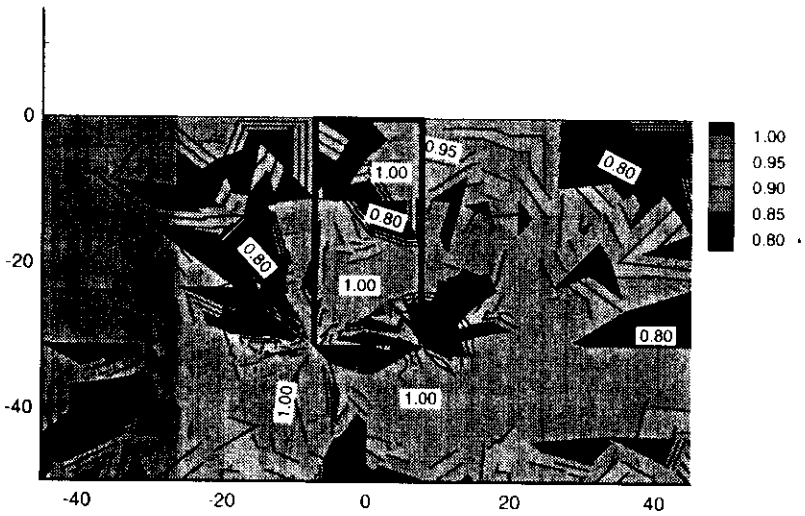

b) Shear stress, $(\sigma_1-\sigma_3)/2c_u$

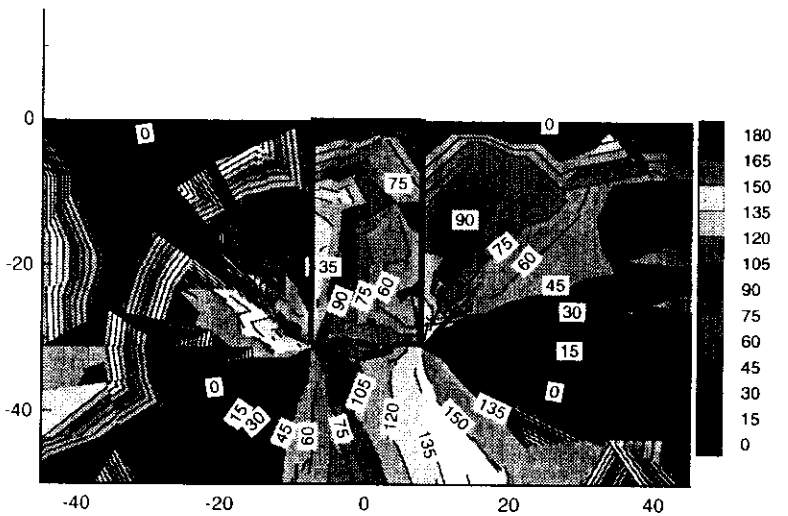

c) Direction of major principal stress to the vertical, δ (deg,cw)

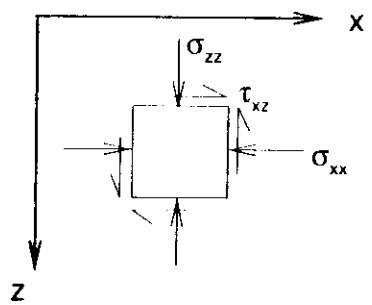

d) Positive sign convention

Figure 7.36 Results of Lower Bound Limit Analysis for Inclined Pullout of EPR Centrifuge Model Caisson

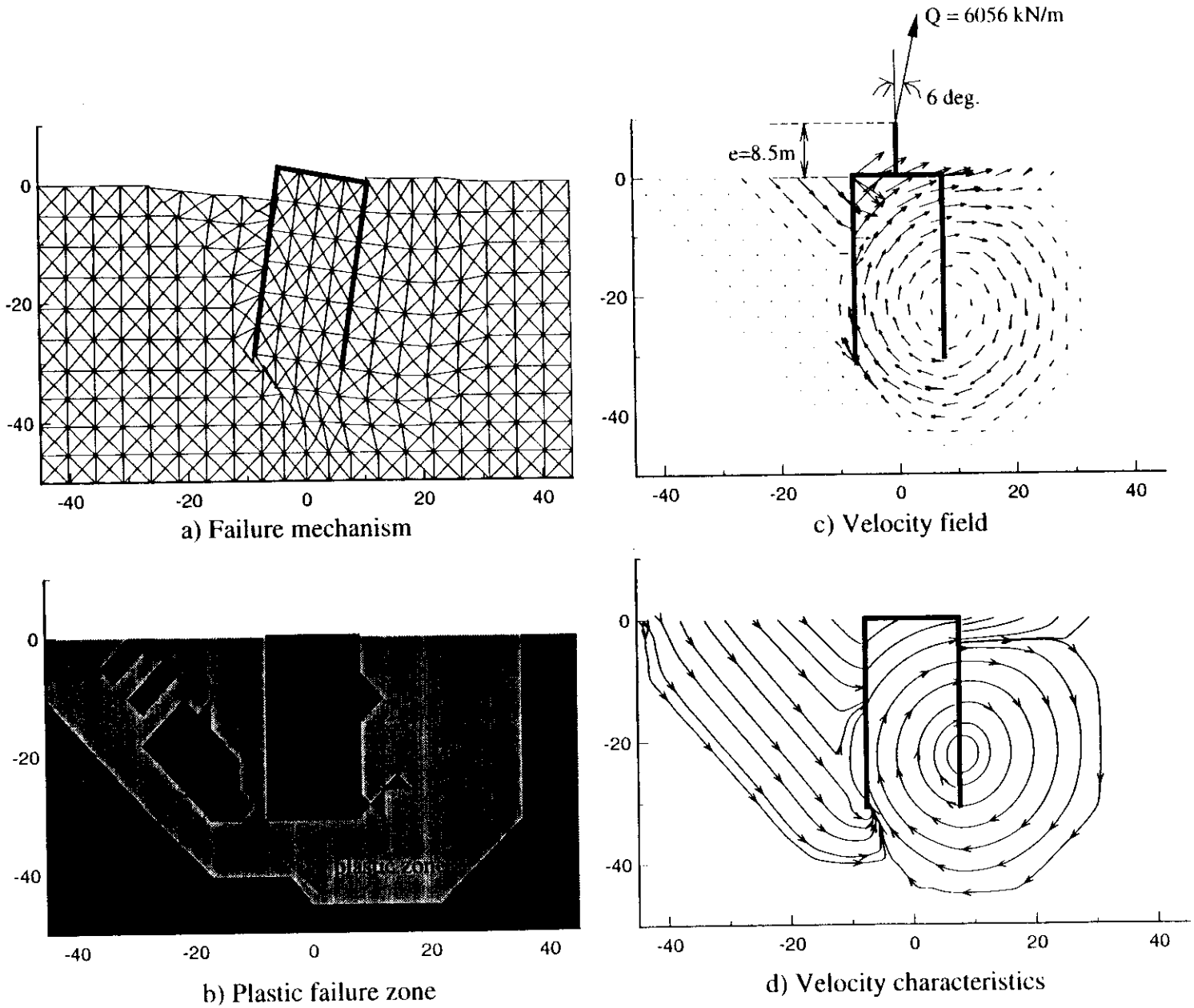

Figure 7.37 Results of Upper Bound Limit Analysis for Inclined Pullout of EPR Centrifuge Model Caisson

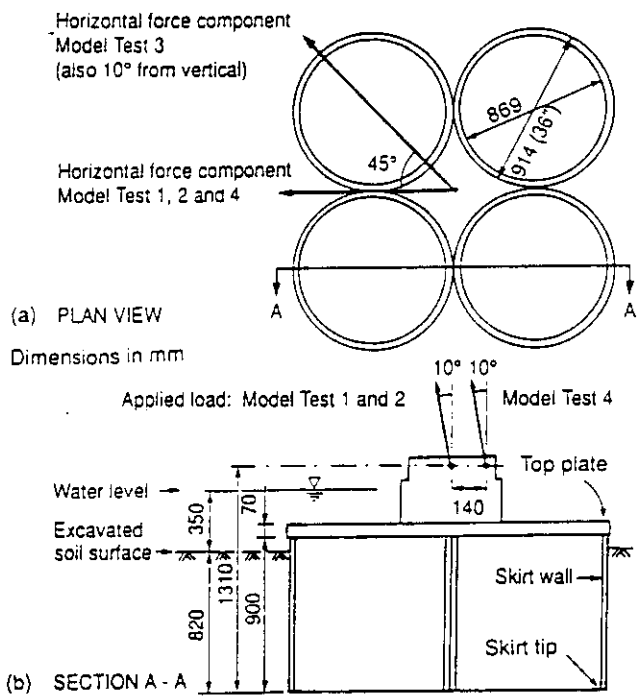

Figure 7.38a. NGI Four Cell Caisson Model (Dyvik et al., 1993)

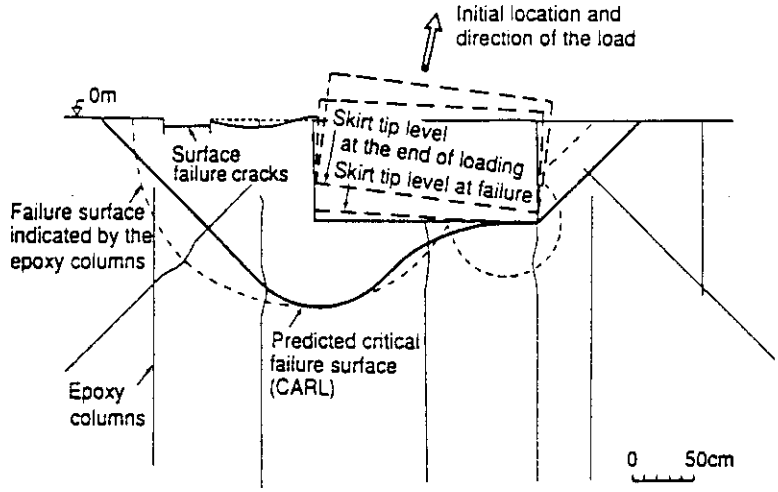

Figure 7.38b. Prediction and Observation of Failure in NGI Caisson Test (Andersen et al., 1993)

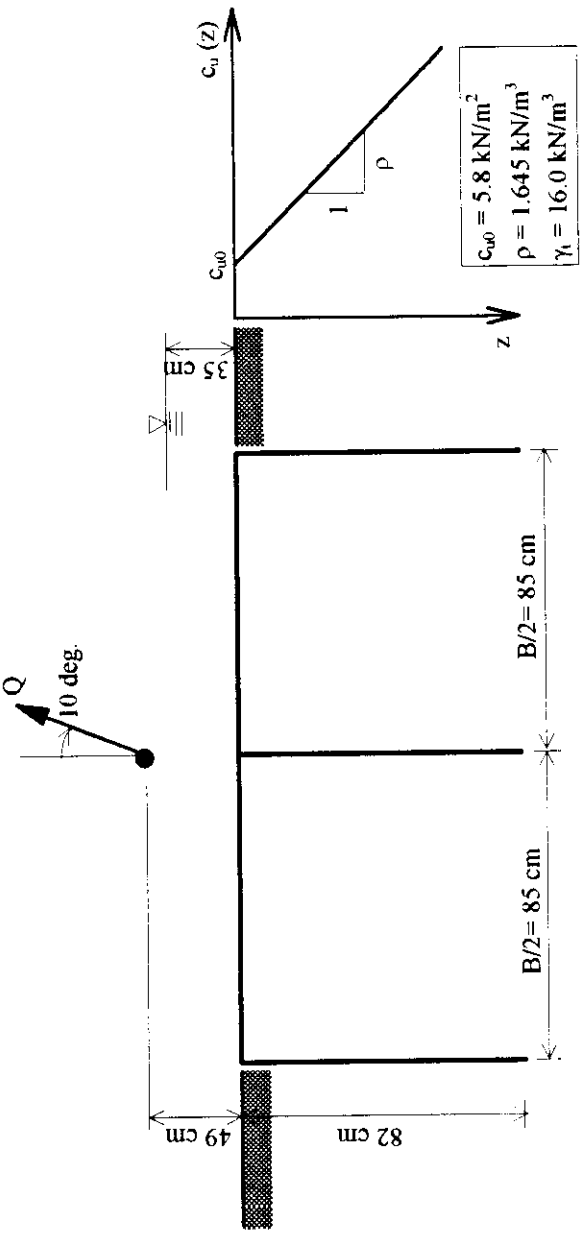

Numerical Solutions	
Upper Bound	Q_U = 0.852 kN/cm
Lower Bound	Q_L = 0.782 kN/m
Bound	8.50%
Axisymmetric Approximation	
Upper Bound	$F_U = Q_U$ (B) = 145 kN
Lower Bound	$F_L = Q_U$ (B) = 133 kN

NGI Results	
Field Test	F = 137.7 kN
LEM, i = 7.5°	F = 138 kN
LEM, i = 10.0°	F = 128 kN

Figure 7.38c. Input Conditions and Interpretation of Results from Numerical Limit Analysis of NGI Field Test

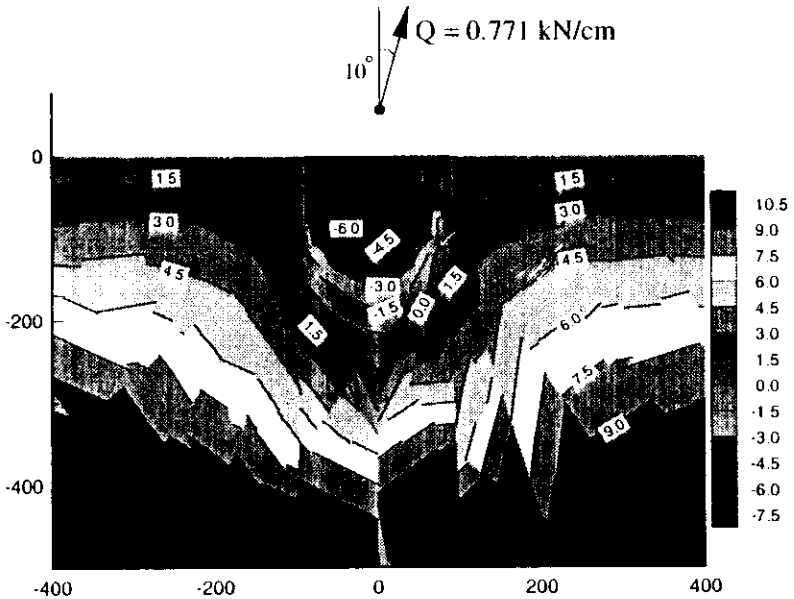

a) Vertical stress, σ_{zz}/c_{u0}

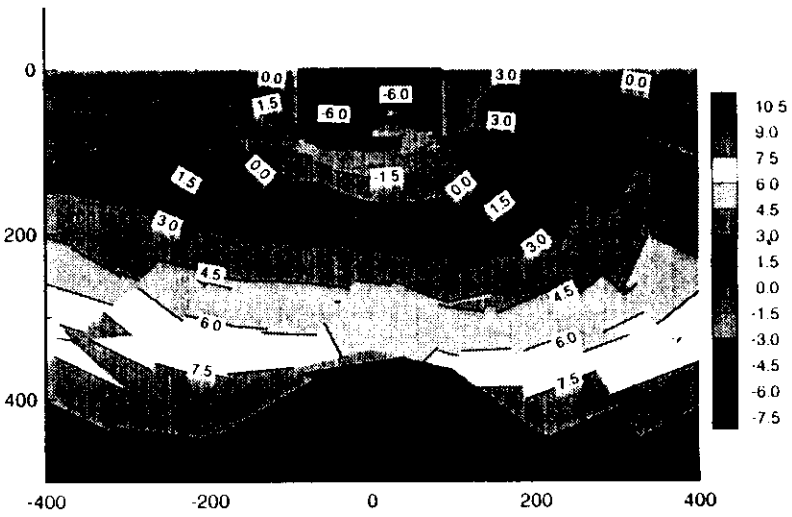

b) Horizontal stress, σ_{xx}/c_{u0}

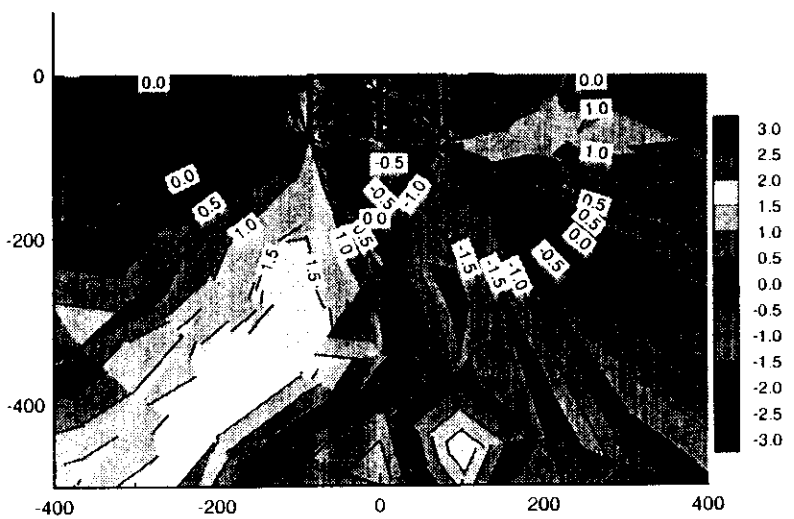

c) Shear stress, τ_{xz}/c_{u0}

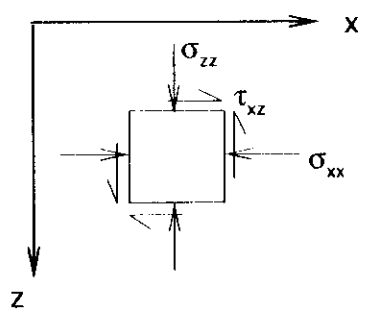

d) Positive sign convention

Figure 7.39 Results of Lower Bound Limit Analysis for Inclined Loading of NGI Field Test

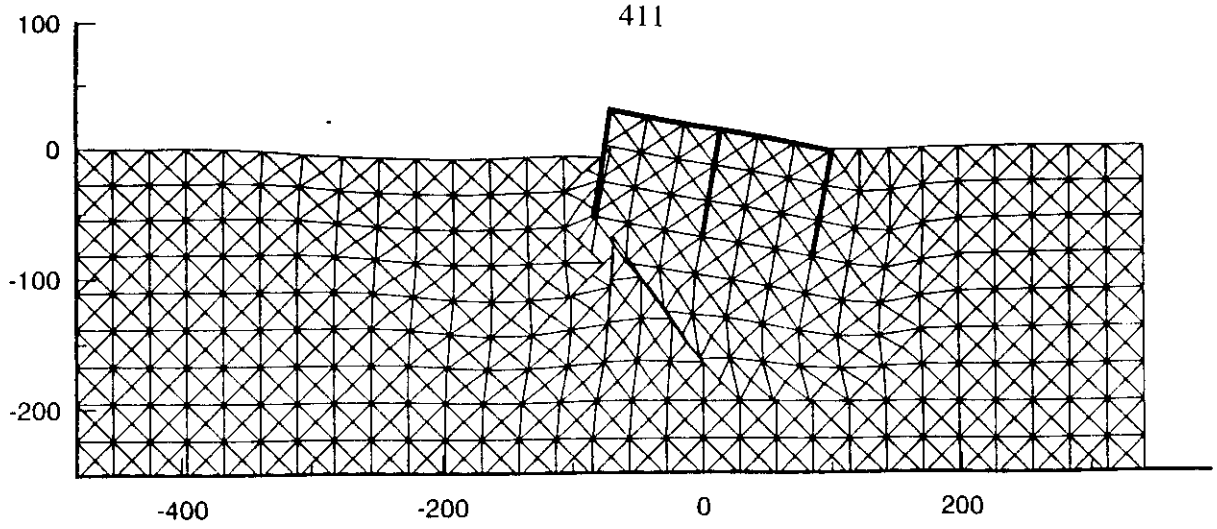

a) Failure Mechanism

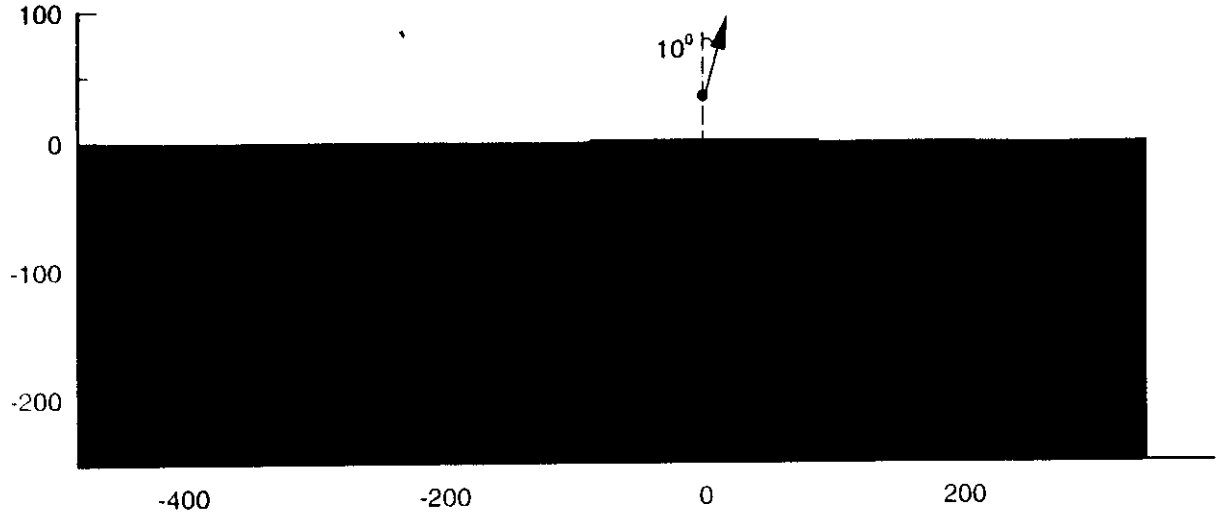

b) Plastic Failure Zone

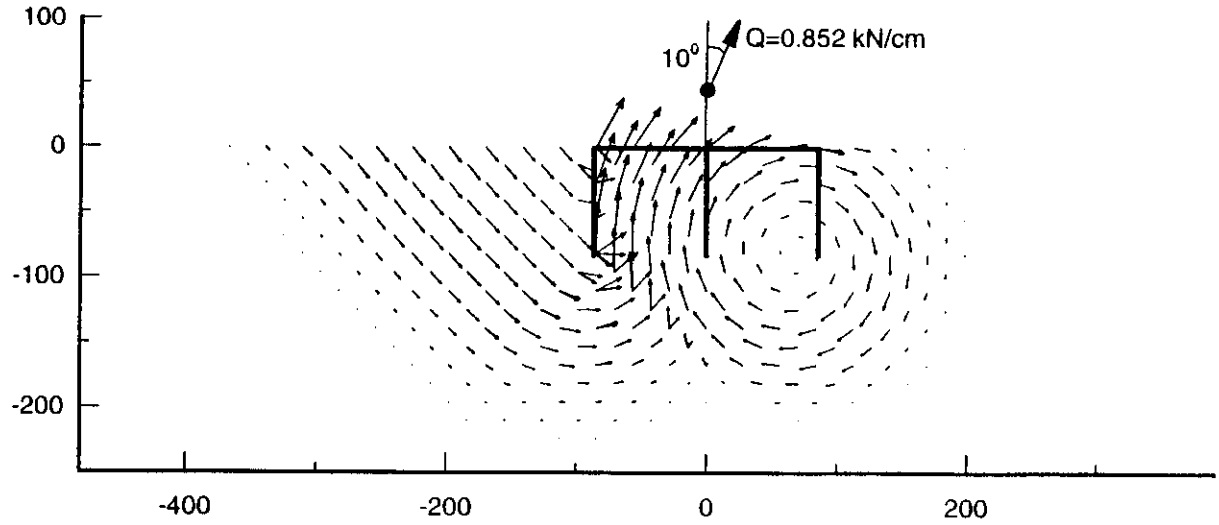

c) Velocity Field

Figure 7.40 Results of Upper Bound Limit Analysis for Inclined Loading of NGI Field Test

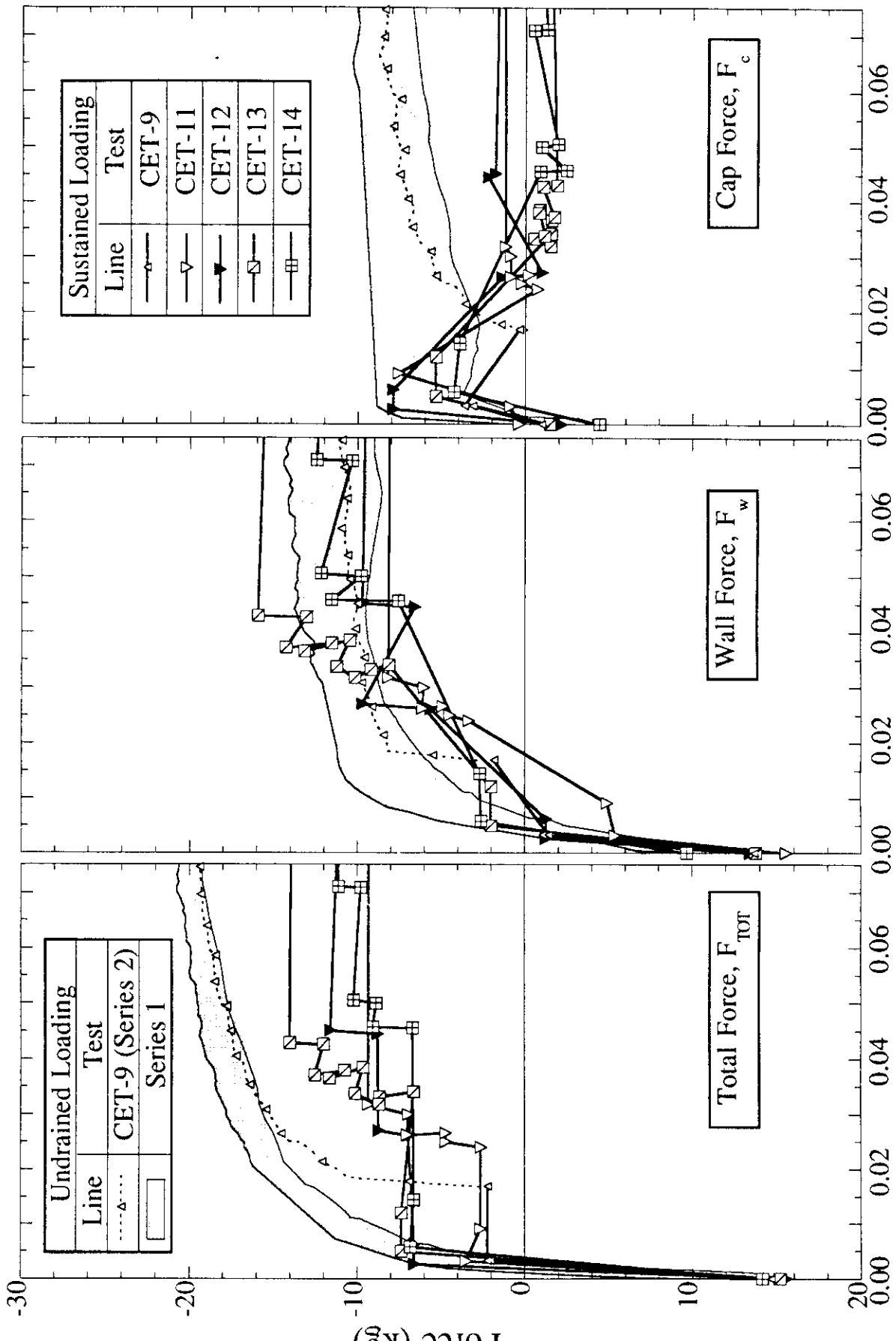

Figure 7.41 Summary of Force-Deformation Measurements for Sustained Tensile Loading of CET

Model Caisson

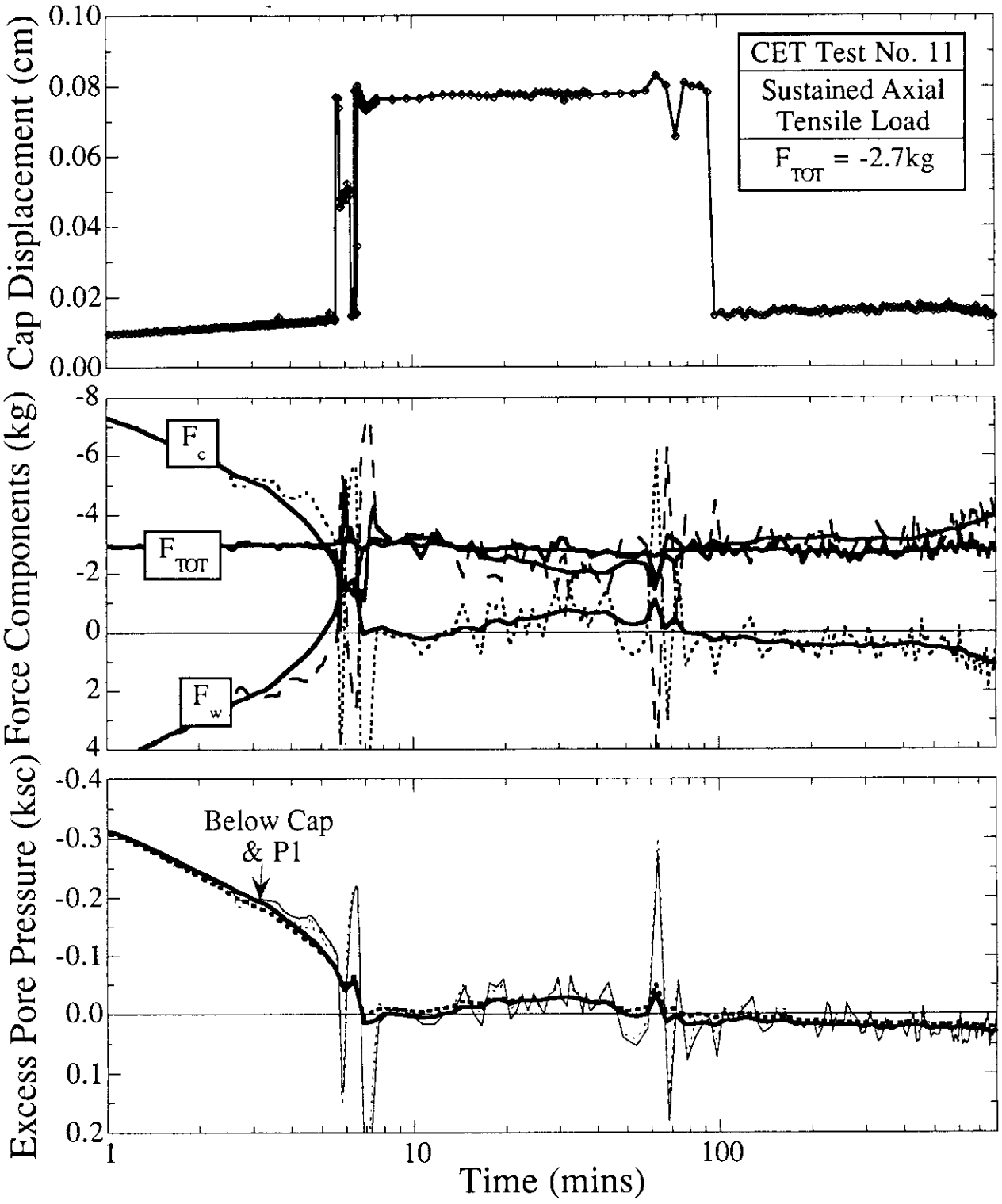

Figure 7.42 Typical Stable Behavior of CET Model Caisson Under Sustained Tensile Loading

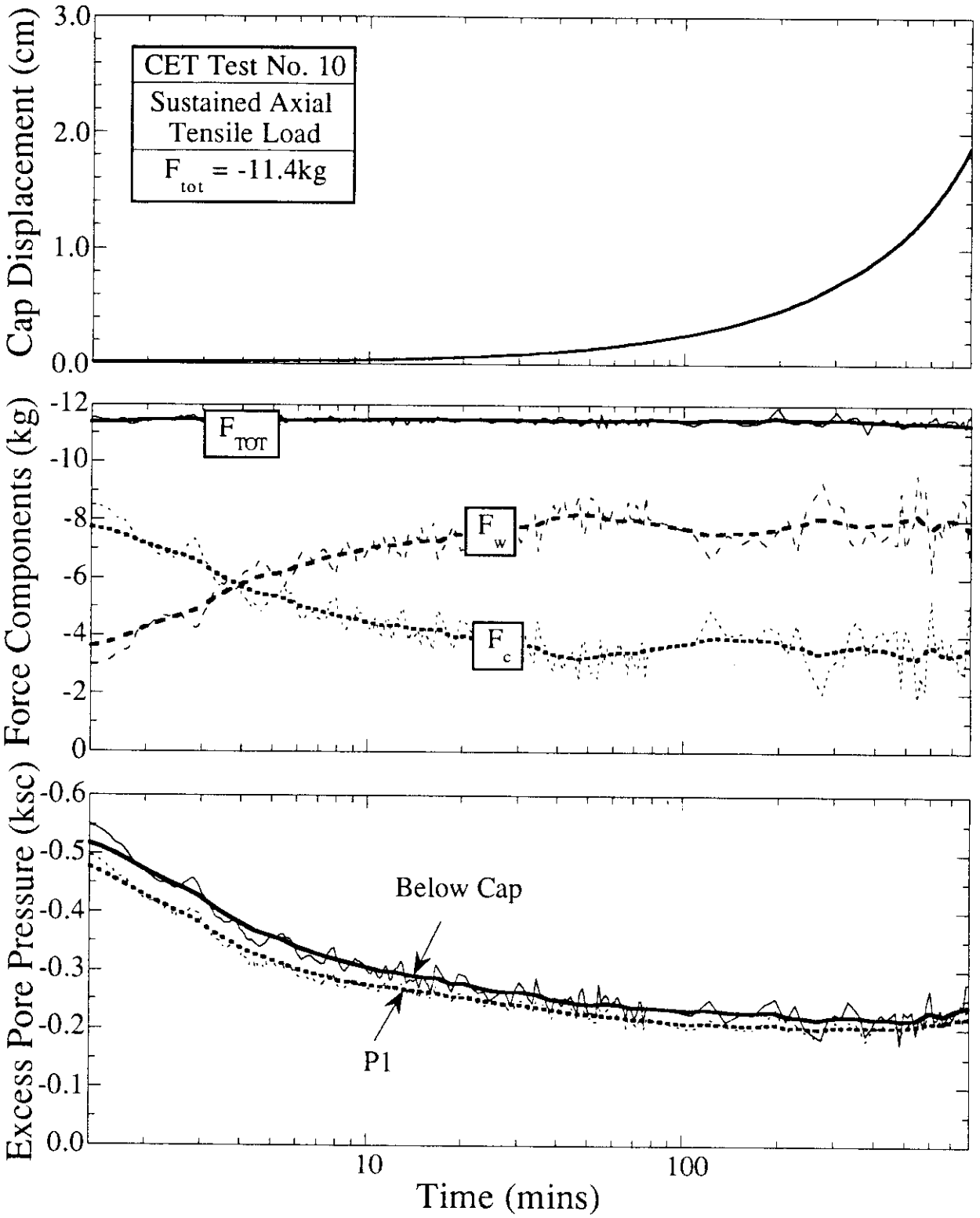

Figure 7.43 Failure of CET Model Caisson in First Stage Sustained Tensile Load Test

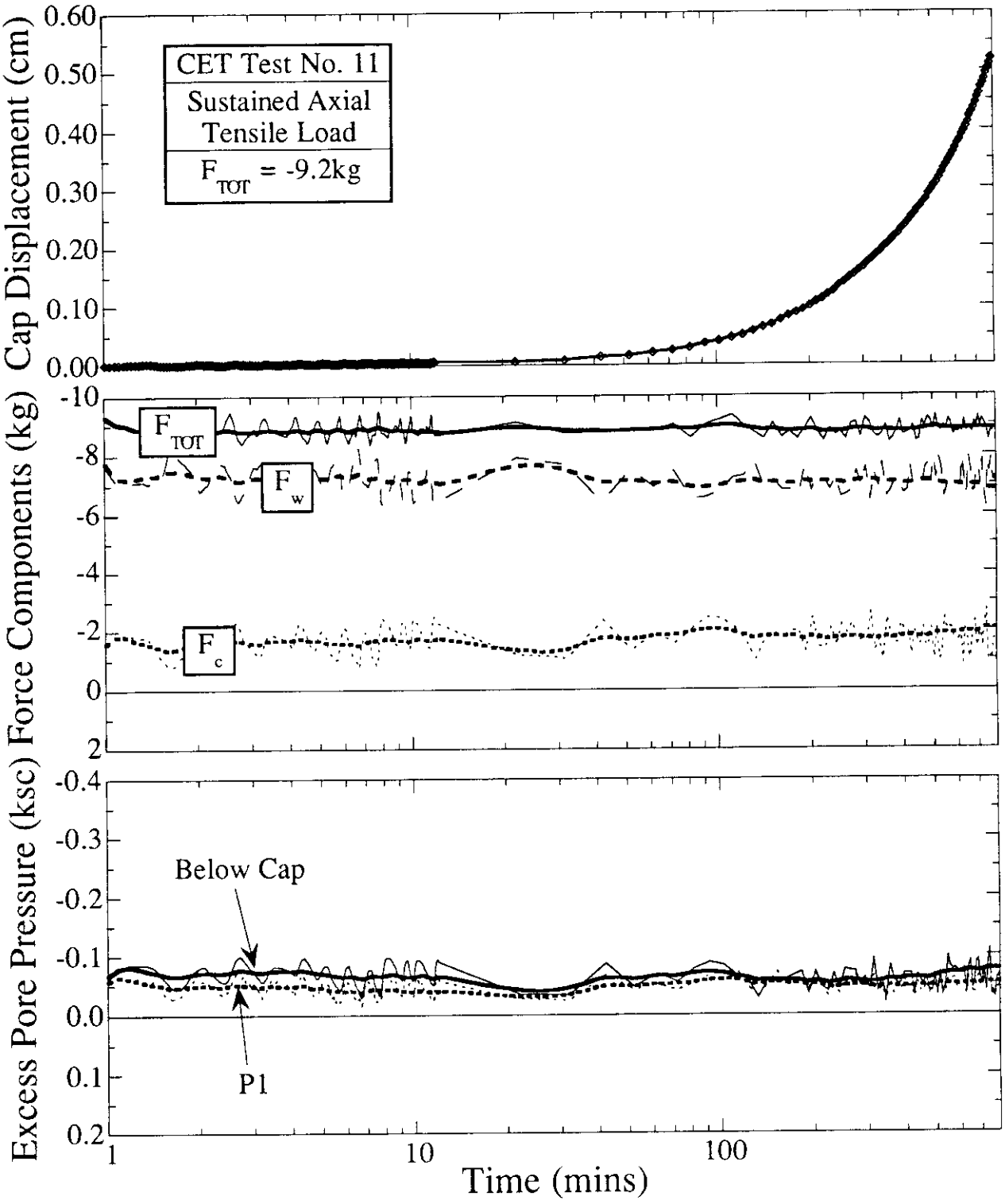

Figure 7.44 Failure of CET Model Caisson in Subsequent Sustained Tensile Load Test

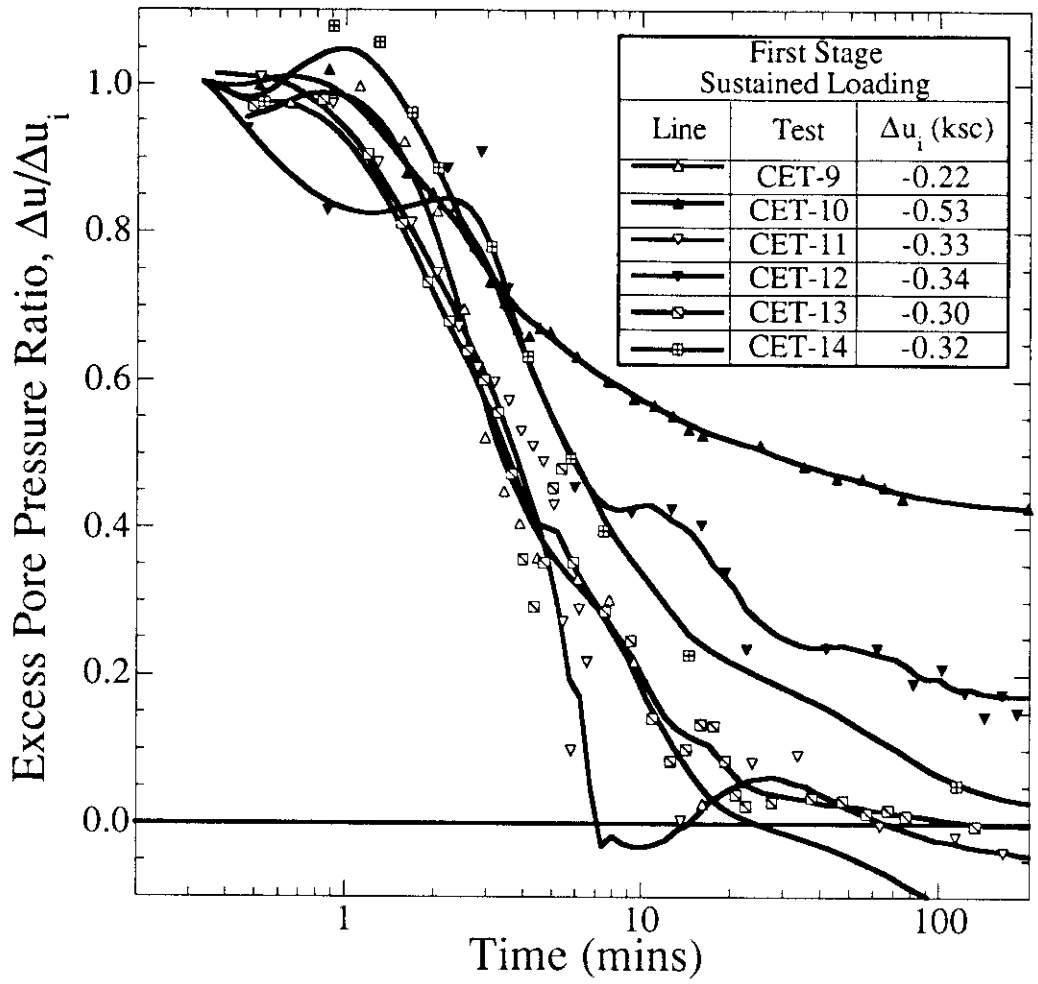

Figure 7.45 Measurements of Pore Pressure Dissipation During First Stage of Sustained Tensile Loading

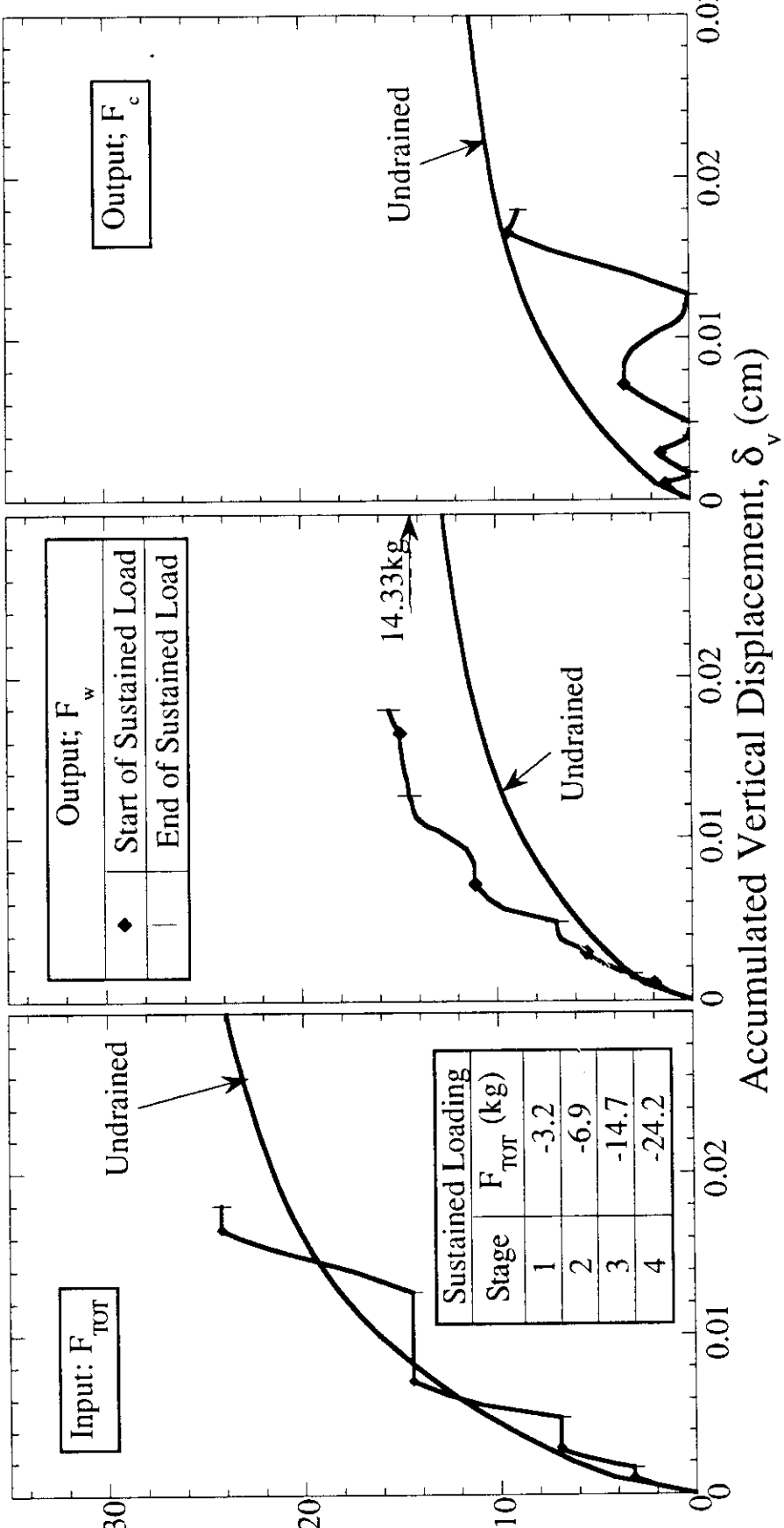

Figure 7.46 Finite Element Prediction of CET Model Force-Displacement Response in Four-Stage Sustained Tensile Load Test

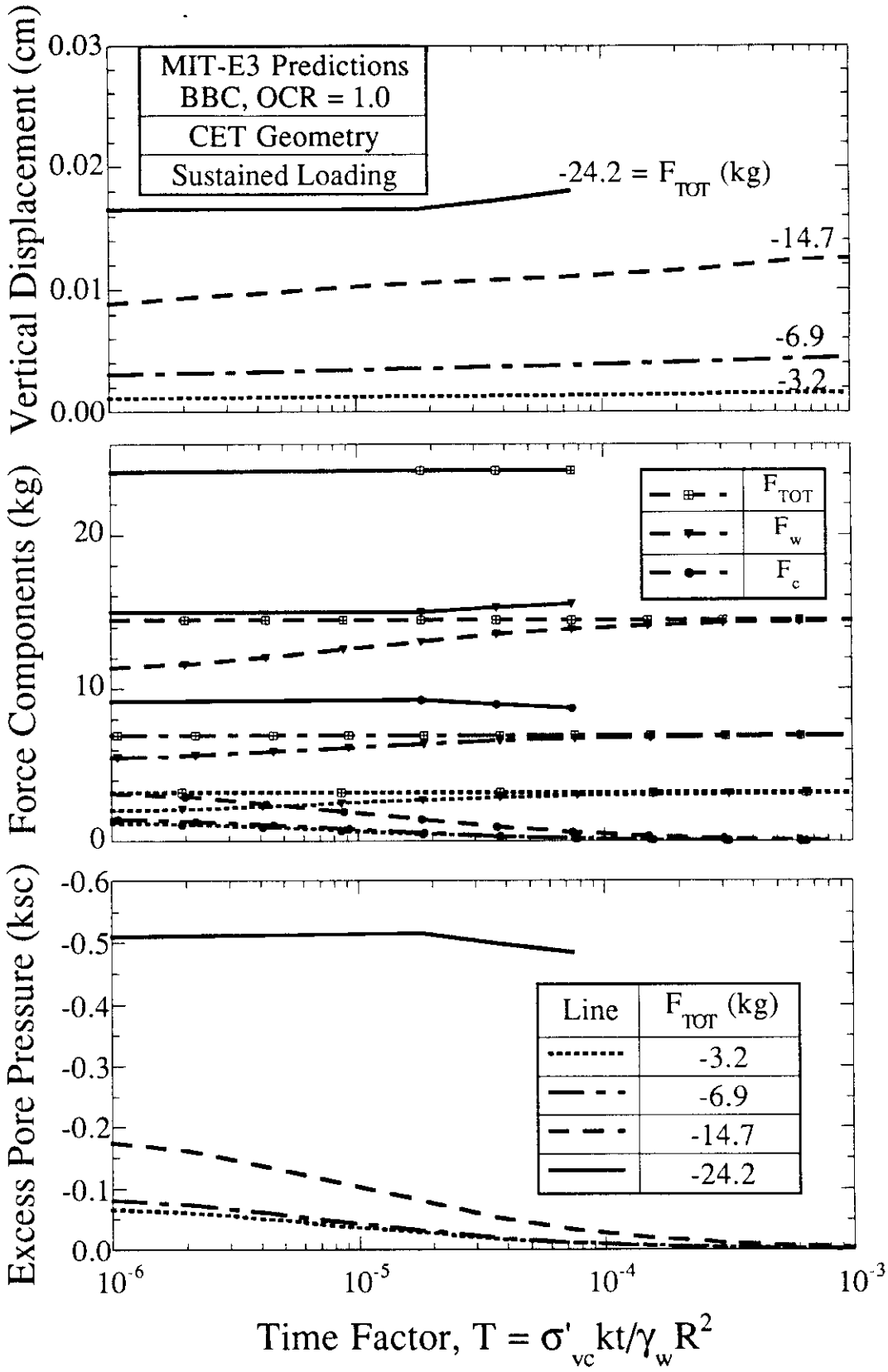

Figure 7.47 Summary of Predicted CET Model Caisson Response in Sustained Tensile Load Tests

8. SUMMARY AND CONCLUSIONS

8.1 SUMMARY

This report describes the main findings of a three year, joint industry funded research project which addresses geotechnical problems associated with the design of large diameter caissons as permanent anchors for tension leg platforms in deep water applications. The work focuses on the axial load response of single caisson cells in clay for short-term (undrained) pullout and sustained tensile loading conditions. The results of this project also form the basis of two Ph.D. theses (Cauble, 1996; Geer, 1996) which are still in progress.

The principal questions addressed during the course of this research were:

1. The measurement and interpretation of penetration forces and ground deformations for caisson installation by underbase suction.
2. The measurement and prediction of soil reaction forces for axial loading including i) the mechanisms controlling the generation and release of (passive) underbase suction pressures; and ii) the frictional resistance along the inside and outside walls of the caisson.
3. The effects of the cell geometry and soil properties on the expected behavior of prototype caissons.

The following sections summarize the main tasks that have been carried out in the course of this project relating to 1) the development and application of analytical methods, 2) laboratory measurements of behavior for a miniature caisson; 3) evaluation and validation of analytical predictions using available experimental data.

8.1.1 Analytical Framework

This project is predicated on the concept that reliable predictions of caisson performance can be achieved through the development of a systematic analytical framework that can predict changes in the soil stresses and properties occurring through the phases of caisson installation, equilibration and TLP loading conditions. Previous research has applied this methodology successfully to study the set-up and capacity of driven, friction piles in clay (Whittle & Baligh, 1988; Azzouz et al., 1990; Whittle, 1992). The original strategy for this project was to apply the same methods of analysis for caisson geometries, a task which involves integrating: 1) strain path analyses of installation disturbance (Baligh, 1985) for deep penetration of piles in clay; 2) MIT-E3 (Whittle, 1987), a generalized effective stress soil model with well documented capabilities for predicting the non-linear and anisotropic stress-strain behavior of soft clays; and 3) ABAQUS, a commercial finite element program, capable of solving non-linear coupled flow-deformation problems with user-defined soil models. However, difficulties encountered during the first year of this project (Whittle & Germaine, 1993), have completely re-shaped the direction and progress of

the analytical research, requiring more extensive development of new analytical methods for caissons as follows:

1. Undrained analyses of axisymmetric piles and caissons causes severe numerical difficulties in the finite element analyses. These difficulties arise due to the constraints imposed by material incompressibility on the displacement interpolation functions. These problems were solved by implementing a new library of finite elements, with high order interpolation of displacements (after Sloan & Randolph, 1982), in the ABAQUS code[1]. Geer (1996) has validated these user element [UEL] sub-routines in combination with the MIT-E3 soil model, and has developed procedures for accurate non-linear analyses of undrained axial pullout and (consolidation due to) sustained tensile loading
2. Several severe difficulties were encountered in applying the original strain path method to caisson geometries including: 1) unreliable prediction of stresses and pore pressures inside the soil plug; 2) unrealistic predictions of ground surface deformations; and 3) numerical difficulties in integrating the steady SPM solutions as initial conditions in subsequent finite element analysis (cf. Teh & Houlsby, 1991). These problems have been addressed through the formulation of the Shallow Strain Path Method (SSPM; Section 2.3; Sagaseta et al., 1995). The SSPM analysis has been carefully validated for closed-ended piles as well as (open-ended) unplugged caisson penetration. The report by Sagaseta et al. (1995) shows that the SSPM analysis is capable of making reliable predictions of ground movements due to pile installation.
3. In principle, the calculation of undrained caisson capacity can be achieved by non-linear finite element methods. However, the results presented in this report show that relatively large cap displacements are necessary to mobilize the full base resistance of the underlying clay. Alternative calculations of capacity rely on approximate limit equilibrium methods[2]. This project has implemented numerical techniques for solving (rigorous) upper and lower bound collapse loads (for rigid perfectly-plastic materials) for general planar soil-structure problems (Ukritchon, 1996). These numerical analyses provide an independent calculation of caisson capacity for comparison with results of the finite element analyses.

Chapter 6 describes in detail the application of the proposed non-linear finite element analyses for predicting the performance of prototype, single-cell caissons for both undrained pullout and sustained tensile loading conditions. All of the finite element analyses in this report are based on the assumption that the caissons are wished-in-place (i.e., no change in the soil stresses

---

[1] Several commercially available geotechnical finite element programs (PLAXIS, CRISP-90) have also implemented these types of element.

[2] All of these calculations are based on solutions of plane strain problems, with empirical correction factors for axisymmetric geometries.

or properties due to installation), while SSPM calculations of disturbance have been used to evaluate measurements of ground deformations during installation only (Section 7.2).

The finite element calculations all assume a non-homogeneous profile where the undrained shear strength and stiffness of the clay increase linearly with depth (the MIT-E3 soil model is used throughout). The majority of the finite element analyses focus on a base case condition, comprising a caisson with 20m wall length and cell diameter, installed in a deep layer of K_0-normally consolidated Boston Blue Clay. Further parametric calculations have been carried out to identify the effects of 1) the caisson geometry (wall length and cell diameter); 2) the stress history (OCR) of the clay; and 3) the type of clay. The latter includes calculations for a caisson installed in a deep layer of K_0-normally consolidated Empire clay (with properties typical of deepwater, Gulf of Mexico clays). The undrained load-deformation responses from the finite element analyses are compared with capacities computed by limit equilibrium and numerical limit analyses. Simplified procedures are presented for interpreting the cap and wall forces of prototype caissons from the finite element solutions.

Caisson stability in sustained tensile loading relies on the transfer of the underbase suction forces to the caisson wall. Finite element analyses have studied the mechanisms controlling the release of underbase suction pressures at selected tensile load levels in Section 6.4.

8.1.2 Experimental Behavior of CET Model Caissons

Reliable experimental data are essential for validating analytical predictions of caisson performance. However, it is very difficult to design experiments which a) scale accurately all of the parameters affecting caisson performance (including gravity stresses and stress gradients, consolidation and flow properties of the soil), and b) generate sufficient reproducible, high quality data to validate key aspects of model predictions. This project has supplemented the data available from centrifuge model and field tests with results from 'element tests' on miniature caissons, through the development of the Caisson Element Test (CET) apparatus. Chapters 3 and 4 describe the design, construction and evaluation of the CET cell, while Chapter 5 presents results from a series of 14 experiments[3].

The design of the CET apparatus includes five separate components: 1) A pressurized, rigid-walled test chamber (30cm inside diameter), which contains the resedimented clay specimen (with pre-test heights ranging from 12-14cm). The top surface of the clay is sealed by a rubber membrane, and the specimen is confined at a constant total vertical stress of 0.75ksc. All of the tests use resedimented, normally consolidated Boston Blue Clay. 2) A two-piece model caisson, which enables independent control of the forces and displacements acting on the cylindrical

[3] The chapter actually presents results for approximately half of these experiments, while the remainder of the tests were necessary for debugging and refining the equipment and test procedures.

sidewall and cap. The experiments use one standardized caisson geometry[4], comprising a 0.15cm thick wall with outside diameter 5.1cm, which penetrates to a total depth of approximately 5.1cm. 3) The mechanical driving system that controls movements of the caisson cap and wall (and also the chamber air pressure). The final cell design uses linear ball screw actuators with in-line compression springs to eliminate lashback at load reversals. 4) The control system of primary transducers and software which provide continuous automated feedback, for controlling the displacements and/or forces applied to the cap and sidewall of the model caisson. The control software comprises a menu-driven series of modules which simulate caisson installation, consolidation, axial pullout, sustained tensile loading etc. 5) The instrumentation package which provides input signals for feedback control and data for test interpretation. In addition to wall and cap forces and displacements, the CET experiments include measurements of surface displacements, pore pressures beneath the cap and (at 3-4 locations) within the clay.

The CET experimental test program focused on the following main issues: 1) measurement of penetration forces and ground displacements for installation by underbase suction; 2) the timeframe required for the equilibration after caisson installation; 3) the pullout capacity and axial load-deformation response in monotonic loading to failure; 4) the time dependent caisson response for (single stage and multi-stage) sustained tensile loads; and 5) the axial pullout response following a re-equilibration period.

8.1.3 Evaluation of Predicted and Measured Caisson Behavior

Chapter 7 reviews the current understanding of caisson behavior through comparison of predicted and measured behavior using data from the CET experiments, as well as centrifuge models and field tests. The chapter uses the proposed SSPM analysis to interpret ground deformations caused by installation of the CET model caissons and compares penetration forces with previous experimental and analytical results.

Finite element predictions of undrained axial load-deformation response are compared directly with measured data in the CET cell, assuming that there is no installation disturbance. The development of a finite element model for the EPR centrifuge test (f8) has required careful selection of MIT-E3 input parameters to represent the properties of Speswhite kaolin. Numerical limit analyses have also been used to estimate the capacity of the CET and centrifuge model caissons. Further calculations of limit loads have been carried out to demonstrate the potential of the these analyses for studying problems of inclined loading (the predictions are compared to centrifuge model and a field test data).

---

[4] The caisson has a rounded tip geometry.

The chapter shows qualitative comparisons between finite element predictions and CET data from sustained tensile load tests.

8.2 CONCLUSIONS

This section summarizes the main findings of this research pertaining to each of the major aspects of caisson performance.

8.2.1 Caisson Installation and Equilibration

The majority of the CET experiments simulate installation by underbase suction, by balancing the increments of force required for wall penetration, with equal and opposite decrements of load applied to the caisson cap (i.e., $\Delta F_{TOT} = 0$, there is no contribution of self-weight to the penetration). The penetration process can be sub-divided into three phases: 1) shallow penetration ($\delta_w \leq 0.2$cm - similar to the wall thickness) requiring a large increment of wall force ($\Delta F_w \approx 10$kg); 2) a transitional regime ($0.2 < \delta_w < 1.0$cm) where test variability is most probably caused by inter-component friction, and 3) a steady condition where the wall force increases linearly with depth (and there is a corresponding decrease in the force on the cap). Measurements of pore pressure beneath the cap during this third phase show that there is almost zero effective stress at the top of the soil plug during this third phase of penetration (compared to an initial condition, $\sigma'_{v0} = 0.75$ksc throughout the specimen). Surprisingly large upward vertical displacements of the cap ($\delta_c \approx 0.5$ - 0.6cm) during penetration balance very closely the volume of soil displaced by the wall, while there are almost no vertical displacements of the surrounding ground surface. In one of the experiments (CET-13), wall penetration was achieved by surcharge loading. This experiment required a significant increment of force to achieve full penetration of the wall ($\Delta F_{TOT} \approx 23$kg vs initial total force $F_{TOT} = 15.2$kg), and generated large pore pressures within the caisson and in the surrounding soil. In spite of these large differences in applied forces, the test shows very similar overall cap displacements and estimated vertical effective stress at the top of the soil plug, $\sigma'_v \leq$ 0.1ksc. These data suggest that deformations in the CET cell are effectively independent of the force system used to achieve penetration.

The gradients of wall force during the third phase of penetration can be equated with a constant limiting value of the skin friction (mobilized along the inner and outer surface of the wall). Backfigured skin friction ratios, $\beta = f_s/\sigma'_{v0} = 0.053$ - 0.071 are much lower than the undrained shear strength of BBC but are consistent with previous strain path analyses of deep penetration for thin-walled open-ended piles (Whittle & Baligh, 1988).

The proposed Shallow Strain Path Method (SSPM) is capable of predicting the surface displacements caused by caisson penetration providing the calculations account for the inherent clearance (deviation of the simple tube geometry from a straight cylindrical caisson wall). The

analyses greatly underestimate the cap displacements measured in the CET experiments, and also predict a significant surface heave in the surrounding soil. However, further comparisons were carried with results of centrifuge model tests performed by Delft Geotechnics. These data were obtained for penetration of thick-walled, open-ended caissons (R/w ≈ 9) in kaolin. The SSPM analyses gave excellent predictions of ground surface movements both inside and outside the caisson. These results suggest that differences between the CET data and SSPM predictions are related to confining pressures imposed in the CET cell (the SSPM analysis assumes a stress-free ground surface).

After penetration, all of the CET model caissons were allowed to equilibrate at the same initial total force (i.e., F_{TOT} =15.2kg) for 18-33hrs. Apart from a small re-distribution of cap and wall forces that occurs within 10mins, the process of underbase suction generates negligible consolidation within the clay. In contrast, much longer equilibration times occur in CET-13 (t_{90} ≈ 150mins) are associated with dissipation of excess pore pressures remaining after the surcharge load is removed. At the end of equilibration, the cap carries a very small compressive load (less than 2kg)[5], while the remaining 85% of the load is applied to the wall (this is almost a complete reversal of the load distribution at the start of the experiment). The large difference in load distribution within the caisson has a major effect on the subsequent caisson stiffness in pullout experiments.

8.2.2 Undrained Axial Pullout Behavior

8.2.2.1 Measurement and Prediction for CET Model Caissons

The axial load-deformation behavior has been measured in CET pullout experiments performed at the end of equilibration, and in a second series of tests following various histories of sustained tensile loading (the tests were all performed at constant rate of cap displacement, $\dot{\delta}_c$ = 0.03cm/min). The maximum caisson capacity, F_{TOT} = -23±1kg occurs at a cap displacement δ_c = 0.2±0.05cm, when there is also full mobilization of the wall resistance (F_w = -13±1.5kg). The data show a very stiff initial load response with a yield in the cap force at δ_c ≈ 0.002cm. Finite element analyses using the MIT-E3 model give excellent predictions of the wall resistance versus cap displacement, and also show a very stiff initial cap response (with yield at δ_c ≈ 0.02cm). However, the analyses assume a perfect contact between the soil and caisson cap such that the wall force continues to increase (harden) with cap displacement. In principle, the analyses should be truncated when the cap force reaches the theoretical cavitation limit of the CET experiments (i.e., Δu = -0.75ksc), corresponding to a maximum cap force, F_c = -13.5kg. In practice, the measured cap force never reaches this limit (although cavitation was measured in at least one experiment,

[5] This results also implies that there are very low effective stresses within the soil plug at the end of equilibration.

CET-8). Low cap resistance measurements in the CET cell may be related to air trapped in the annular space between the caisson cap and wall. However, further experimentation is still necessary to confirm this explanation.

8.2.2.2 Finite Element Predictions of Prototype Caisson Behavior

Finite element analyses of undrained axial load-deformation response have been carried out for prototype caisson dimensions (L = 10 - 60m, B = 10 -40m) in deep deposit of normally consolidated clay (with BBC properties). These analyses predict a well defined yield of the wall and cap resistance forces at $\delta_c \approx 0.1$m, after which the hardening of the caisson resistance is controlled by further mobilization of cap forces. The analysis show that there are relatively well defined limits to the maximum wall resistance in undrained loading, with between 5 to 35% of this capacity deriving from shear tractions acting on the inside surface of the wall. Shear tractions on the exterior surface of the wall match closely the behavior expected from simple limit equilibrium calculations (assuming failure of the soil in an undrained direct simple shear mode), and therefore predictions of wall stiffness can also be obtained from simple engineering models.

For displacements $\delta_c > 0.1$m, the predicted cap forces can be approximated as linear functions of the cap displacement with tangential stiffness related to the interior surface area of the soil plug. At a given cap displacement, the analyses predict very similar distributions of tensile strain at all points below the caisson for widely differing soil models (MCC vs MIT-E3) and soil types (BBC vs Empire clay). This indicates that the mobilization of basal resistance is controlled primarily by the shear stiffness of the soil in an undrained triaxial extension mode of shearing.

Parametric calculations were performed for caissons of fixed diameter but increasing embedment length. As expected the limiting wall force is proportional to the surface area, and hence, increase in proportional to L^2, while the mobilized cap force varies almost linearly with depth (for profiles in which the clay stiffness also increases linearly with depth). Increases in the caisson diameter (with fixed wall length) generate linear increases in wall resistance, and also linear increases in the mobilized cap force at a given displacement.

A typical high plasticity Gulf of Mexico clay such as Empire clay, has a much lower shear stiffness than BBC and also a lower undrained shear strength in triaxial compression (with no strain softening). However, there are much smaller differences in the undrained shear strengths of the two clays in direct simple shear and triaxial extension modes. Hence, simple limit equilibrium calculations predict very similar pullout loads for the two clays. Finite element predictions show that the caisson resistance mobilized at a given displacement is typically 30% lower for Empire clay than BBC (for $\delta_c > 0.1$m), with no well defined yield in the wall resistance.

8.2.2.3 Measurement and Predictions for EPR Centrifuge Model

As part of this project, EPR provided data from three centrifuge model caisson tests performed in resedimented Speswhite kaolin. The thin-walled steel caissons have a prototype wall length, L = 31.2m, and radius, R = 7.6m. Finite element predictions have been carried out for one axial pullout experiment (test f8). The experimental data did not include sufficient laboratory tests data for selecting model input parameters. Instead, the input parameters have been selected from a compilation of published data on Speswhite kaolin, which notably did not include stiffness measurements in the undrained triaxial extension mode of shearing. The model tends to underestimate the measured caisson resistance by about 10% (for loading to a cap displacement of 20cm), while the predicted pore pressures are in good agreement with measurements from a series of 5 transducers inside the caisson (suggesting that the relative magnitudes of the cap and wall forces are also reasonably well described). The measured caisson capacity is only mobilized at a cap displacement, $\delta_c \approx 1.5$m, well beyond the reliable range of the small strain finite element analyses.

8.2.2.4 Caisson Capacity by Numerical Limit Analysis

Caisson capacity calculations are currently based on semi-empirical limit equilibrium methods, which either assume a given failure mechanism or search for the critical failure surface. Calculations for axial loading are currently based on calculations of reverse bearing capacity and exterior skin friction (e.g., Clukey & Morrison, 1993), while search schemes are used to locate critical failure surfaces for combined loading of footings (after Janbu, 1985). Numerical limit analyses offer and alternative method of calculation which mitigate the need for search routines and avoids arbitrary selection of failure mechanisms. The limit calculations used in this research do still have two important limitations: 1) they are restricted to planar problem geometries (such that careful scaling of the results is the only method available for estimating the capacity of axisymmetric caissons); and 2) they assume an isotropic strength criterion for the clay.

Limit capacity calculations have been carried out for all of the caissons considered in this study (including the parametric calculation in Chapter 6, the CET and EPR centrifuge models). The analyses predict much larger capacities for the CET model caissons (due to the low cap forces in these experiments) than are measured in the experiments, but are consistent with the limit equilibrium calculations. Limit analyses provide excellent bound on the measured pullout capacity of the EPR centrifuge model.

Section 7.4.5 shows further predictions of capacity for caissons with inclined loading (for planar sections). The computed upper and lower bounds for the EPR centrifuge model (at an inclination angle, $i = 6^0$) match the lowest of three capacities reported by Clukey and Morrison

(1993). Calculations for the NGI field tests (Dyvik et al., 1993; i = 10^0) are in excellent agreement with the measured capacity.

8.2.3 Behavior Under Sustained Tensile Loading

The behavior of the CET model caissons in sustained tensile loading has been measured in a series of 5 experiments (CET-9 through 14). In each test, the first stage of sustained loading involved a large increment of total force, sufficient to mobilize significant suction resistance. The measured first stage data include tests where there is full release of this suction pressure, and the caisson reaches a stable equilibrium condition where the tensile load is carried by wall friction. In other tests, the applied tensile load exceeds the maximum wall resistance and displacements of the caisson are necessary to counteract the dissipation of pore pressures within the soil plug, leading to a pullout mechanism with residual excess pore pressures remaining in the soil plug. Multi-stage tests with small load increments establish that the maximum wall resistance for sustained tensile load is very similar to the limiting resistance measured in undrained pullout tests.

Detailed finite element calculations of sustained load behavior have been carried out for the base case prototype caisson geometry. These results show that the long term wall resistance is approximately 30% higher than that computed in undrained loading, due to increased mobilization of friction forces on the inside wall of the caisson[6]. The analyses show that the mechanisms of load transfer depend on the applied level of tensile loading, with surplus cap forces initially carried by frictional resistance on the outside wall of the caisson. Only when the maximum shear resistance is mobilized on the outside wall of the caisson do additional forces transfer to the inner wall surface. A key characteristic of the numerical predictions is the breakthrough time required before there is dissipation of the excess pore pressures beneath the lid of the caisson. The analyses for the base case geometry show breakthrough times ranging from t_0 = 1-7 days for a caisson in BBC. These observations have yet to be confirmed by experimental measurements.

[6] Note: Inside wall friction may be affected significantly by installation disturbance

REFERENCES

Al-Tabbaa, A. (1987) "Permeability and stress-strain response of Speswhite kaolin," PhD Thesis, Cambridge University.

Al-Tabbaa, A. & Wood, D.M. (1987) "Some measurements of the permeability of kaolin," Géotechnique, 37(4), 499-503.

Ampadu, S.K. & Tatsuoka, F. (1994) "A hollow cylinder torsional simple shear apparatus capable of a wide range of shear strain measurement," To appear, ASTM Geotechnical Testing Journal.

Airey, D.W. & Wood, D.M. (1987) "An evaluation of direct simple shear tests on clay," Géotechnique, 37(1), 25-35.

Andersen, K.H., Dyvik, R., Schrøder, K. Hansteen, O.E. & Bysveen, S. (1993) "Field tests of anchors in clay. II: Predictions and interpretation," ASCE, Journal of Geotechnical Engineering, 119(10), 1532-1549.

Atkinson, J.H., Richardson, D. & Robinson, P.J. (1986), "Compression and extension of K_0 normally consolidated kaolin clay," ASCE Journal of Geotechnical Engineering, 113(12), 1468-1482.

Aubeny, C.P. (1992) "Rational interpretation of in situ tests in cohesive soils," PhD Thesis, Department of Civil & Environmental Engineering, MIT, Cambridge, MA.

Azzouz, A.S & Baligh, M.M. (1984) "Behavior of friction piles in plastic Empire clay," Research Report R84-14, Dept. of Civil Engineering, MIT, Cambridge, MA. (3 Vols.)

Azzouz, A.S. & Morrison, M.J. (1988) "Field measurements on model pile in two clay deposits," ASCE Journal of Geotechnical Engineering, 114(1), 104-121.

Azzouz, A.S., Baligh, M.M. & Whittle, A.J. (1990) "Shaft resistance of piles in clay," ASCE Journal of Geotechnical Engineering, 116(2), 205-221.

Baligh, M.M. (1975), "Theory of deep site static cone penetration resistance," MIT Research Report R75-56, Department of Civil Engineering, MIT, Cambridge, MA.

Baligh, M.M. (1985), "Strain Path Method," ASCE, Journal of Geotechnical Engineering, 111(9), 1108-1136.

Baligh, M.M. (1986) "Undrained deep penetration: I. Shear stresses," Géotechnique, 36(4), 471-485.

Baligh, M.M. & Kavvadas, M. (1980) "Axial static capacity of offshore friction piles in clays," MIT Research Report R80-32, Dept. of Civil Engrg., MIT, Cambridge, MA.

Baligh, M.M. & Levadoux, J-N (1980), "Pore pressure dissipation after cone penetration," Research Report R80-11, Dept. of Civil Engineering, MIT, Cambridge, MA.

Baligh, M.M., Azzouz, A.S. & Chin, C.T. (1987) "Disturbances due to 'Ideal' tube sampling," ASCE Journal of Geotechnical Engineering, 113(7), 739-757.

Berman, D.R. (1993) "Characterization of the engineering properties of Boston Blue Clay at the MIT campus," MS Thesis, Department of Civil & Environmental Engineering, MIT, Cambridge, MA.

Caquot, A. and Kérisel, J. (1948) Tables for the calculation of passive pressure, active pressure and bearing capacity of foundation, Gauthier-Villars, Paris.

Cauble, D.F. (1996) "Experimental measurements for a model suction caisson," PhD Thesis in progress, MIT, Cambridge, MA.

Chin, C.T. (1986) " Open-ended pile penetration in saturated clays," PhD Thesis, Dept. of Civil Enghineering, MIT, Cambridge, MA.

Christophersen, H-P. (1992) "The non-piled foundation systems of the Snorre field," Advances in Underwater Technology, Ocean Science and Offshore Engineering, Vol. 28: Offshore Site Investigation and Foundation Behavior, Society for Underwater Technology, pp. 433-451.

Christophersen, H.P., Bysveen, S. & Støve, O. (1992) "Innovative foundation system selected for Snorre field development," Proc. BOSS'92, Imperial College, London.

Clukey, E.C. & Morrison, M.J. (1993) "A centrifuge and analytical study to evaluate suction caissons for TLP applications in the Gulf of Mexico," Design and Performance of Deep Foundations: Piles and Piers in Soil and Soft Rock, ASCE, NY, 141-156

Clukey, E.C., Morrison, M.J., Garnier, J. & Corté, J.F. (1995) "The response of suction caissons in normally consolidated clays to cyclic loading," OTC Paper 7796.

Davis, E.H. & Booker, J.R. (1973) "The effect of increasing strength with depth on the bearing capacity of clays," Géotechnique, 23(4), 551-563

DeBorst, R. & Vermeer, P.A. (1984) "Possibilities and limitations of finite element for limit analysis," Géotechnique, Vol. 32, No. 2, 199-210.

DeJosselin DeJong, G. (1953) "Consolidation around pore pressuremeters," Journal of Applied Physics, 24(7), 922-928.

Dyvik, R., Andersen, K.H., Hansen, S.B. & Christophersen, H.P. (1993) "Field tests of anchors in clay. I: Description," ASCE, Journal of Geotechnical Engineering, 119(10), 1515-1531.

Esrig, M.I., Kirby, R.C., Bea, R.G. & Murphy, B.S. (1977) "Initial development of a general effective stress method for the prediction of axial capacity of driven piles in clay," Proc. 9th Offshore Technology Conf.,, Houston, 3, 495-506.

Fuglsang, L.D. & Steensen-Bach (1991) "Breakout resistance of suction piles in clay," Proc. Centrifuge'91, Boulder, CO., Balkema, 153-159.

Geer, M. (1996) "Analysis of pile and suction caisson behavior in axial loading," PhD Thesis in progress, MIT, Cambridge, MA.

Germaine, J.T. (1982) "Development of the directional shear cell for measuring cross-anisotropic properties," ScD. Thesis, Department of Civil & Environmental Engineering, MIT,

Cambridge, MA..

Gibson, R.E. (1963) "An analysis of system flexibility and its effect on time lag in pore-water pressure measurements," Géotechnique, 13, 1-11.

Griffiths, D.V. (1982) "Elasto-plastic analyses of deep foundations in cohesive soil," Intl. J. for Numerical and Analytical Methods in Geomechanics, 6, 211-218.

Hashash, Y.M.A. (1992) "Analysis of Deep Excavations in Clay", Ph..D. Thesis, Dept. of Civil Engrg., MIT, Cambridge, MA, 337p.

Henderson, E. (1994) "Evaluation of time response of pore pressure measurements," MS Thesis, Dept. of Civil & Environmental Engrg., MIT, Cambridge, MA.

Hjortnaes-Pedersen, A.G.I & Bezuijen, A. (1992a) "Skirt penetration in clay, Experiments in the Delft Geo-Centrifuge," Delft Geotechnics Report No. SE704841/1.

Hjortnaes-Pedersen, A.G.I & Bezuijen, A. (1992b) "Offshore skirt penetration in the geo-centrifuge," Proc. 7th Intl. Conf. on Behavior of Offshore Structure (BOSS'92), London..

Janbu, N. (1985) "Soil models in offshore engineering," Géotechnique, 35(3), 241-281.

Kavvadas, M.J. (1982) "Non-linear consolidation around driven piles in clay," PhD Thesis, Department of Civil Engineering, MIT, Cambridge, MA.

Kenney, T.C. (1964) "Sea level movements and geological histories of the post-glacial marine soils at Boston, Nicolet, Ottawa and Oslo," Géotechnique, 14(3), 203-230.

Kiousis, P.D., Voyiadjis, G.Z. & Tumay, M.T. (1988) " A large strain theory and its application in the analysis of the cone penetration mechanism," Intl. J. for Numerical and Analytical Methods in Geomechanics, 12, 45-60.

Kulhawy, F.H., Trautmann, C.H., Beech, J.F., O'Rourke, T.D., & McGuire, W. (1983) "Transmission line structure foundations for uplift-compression loading," EPRI Report EL-2870, Electric Power Research Institute, Palo Alto, CA.

Kutter, B.L., Sathialingam, N. & Herrmann, L.R. (1990) "Effects of arching on response time of miniature pore pressure transducers in clay," ASTM Geotechnical Testing Journal, 13(3), 164-178.

Ladd, C.C. (1991). "22nd Terzaghi Lecture: Stability evaluation during staged construction." ASCE, Journal of Geotechnical Engineering, 117(4), 540-615.

Lambe, T.W. & Whitman, R.V. (1969) Soil Mechanics, John Wiley & Sons., NY.

Lutz, D.G. (1984) "Predictions of the axial capacity of friction piles in Empire clays by means of the piezo-lateral stress call," MS Thesis, Department of Civil Engineering, MIT, Cambridge, MA.

Lysmer, J. (1970) "Limit analysis of plane problems in soil mechanics," ASCE Journal of the Soil Mechanics and Foundations Division, 96(SM4), 1311-1334.

Mesri, G. & Hayat, T.M. (1993) "The coefficient of earth pressure at rest," Canadian Geotechnical

Journal, 30(4), 647-666.

Nagtegaal, J. C., Parke, D.M. & Rice, J.R. (1974) "On numerically accurate solutions in the fully plastic range," Comp. Meth. Appl. Mech. Engrg., 4, 113-135.

O'Neill, D.A. (1985) "Undrained Strength Anisotropy of an Overconsolidated Thixotropic Clay." MS Thesis, Department of Civil & Environmental Engineering, MIT, Cambridge, MA.

Ortega, O.J. (1992) "Computer automation of the consolidated-undrained direct simple shear tests," MS Thesis, Department of Civil & Environmental Engineering, MIT, Cambridge, MA.

Prandtl, L. (1920). Über die Harte plastischer Körper. Nachr. K. Ges. Wiss. Gott., Math-Phys. Kl., 74-85.

Randolph, M.F., Carter, J.P., & Wroth, C.P. (1979) "Driven piles in clay - the effects of installation and subsequent consolidation," Géotechnique, 29(4), 361-393.

Roscoe, K.H. & Burland, J.B. (1968), "On the Generalized Behaviour of Wet Clays," Engineering Plasticity, Cambridge University Press, 535-609.

Rossato, G., Ninis, N.L. & Jardine, R.J. (1992) "properties of some kaolin-based model clay soils," ASTM Geotechnical Testing Journal, 15(2), 166-179.

Sagaseta, C. (1987) "Analysis of undrained deformation due to ground loss," Géotechnique, 37(3), 301-320.

Sagaseta, C.,.Whittle, A.J., & Santagata, M. (1994) "Deformation analysis of shallow penetration in saturated clay," MIT Research Report R94-09, Department of Civil & Environmental Engineering, MIT, Cambridge, MA.

Seah, T-H. (1990) "Anisotropy of resedimented Boston Blue Clay," PhD Thesis, Department of Civil & Environmental Engineering, MIT, Cambridge, MA.

Sheahan, T.C. (1991) "An experimental study of the time-dependent undrained shear behavior of resedimented clay using automated stress path triaxial equipment," ScD Thesis, Department of Civil & Environmental Engineering, MIT, Cambridge, MA.

Sheahan, T.C. & Germaine, J.T. (1992) "Computer automation of conventional triaxial equipment," ASTM Geotechnical Testing Journal, 15(4), 311-322.

Sinfield, J.V. (1994) "An experimental investigation of sampling disturbance effects in resedimented Boston Blue Clay, MS Thesis, Department of Civil & Environmental Engineering, MIT, Cambridge, MA.

Sloan, S. W., & Randolph, M.F. (1982) "Numerical prediction of collapse loads using finite element methods," Intl. J. for Numerical and Analytical Methods in Geomechanics, 6(1), 47-76.

Sloan, S.W. (1988a) "Lower bound limit analysis using finite elements and linear programming," Intl. Journal for Numerical and Analytical Methods in Geomechanics, 12, 61-77.

Sloan S. W. (1988b). "A.steepest edge active set algorithm for solving sparse linear programming problems." Int. J. Numer. Anal. Methods in Geomech., 26(12), 2671-2685.

Sloan, S.W. & Kleeman, P.W. (1995) "Upper bound limit analysis using discontinuous velcotiy fields," Computer Methods in Applied Mechanics and Engineering, 127, 293-314.

Tatsuoka, F. & Kowhata, Y. (1994) "Stiffness of hard soils and soft rocks in engineering applications," Proc. Intl. Symp. on Pre-failure Deformations Characteristics of Geomaterials (IS Hokkaido'94), 2, 227-336.

Teh, C-I & Houlsby, G.T. (1991) "An analytical study of the cone penetration test in clay," Géotechnique, 41(1), 17-35.

Terzaghi, K. (1943) Theoretical Soil Mechanics, John Wiley & Sons., New York.

Ukritchon, B. (1995) "Evaluation of numerical limit analyses by finite elements and linear programming," MS Thesis, Department of Civil & Environmental Engineering, MIT, Cambridge, MA.

Ukritchon, B. (1996) PhD Thesis in progress, MIT, Cambridge, MA.

van den Berg, P. (1994) "Analysis of soil penetration," PhD Thesis, Delft University of Technology..

Vesic, A.S. (1972) "Expansion of cavities in an infinite soil mass," ASCE J. of Soil Mechs. and Found. Engrg. Div., 98(3), 265-290.

Whittle, A.J. (1987), "A constitutive model for overconsolidated clays with application to the cyclic loading of friction piles," Sc.D. Thesis, Dept. of Civil Engrg., MIT, Cambridge, MA, 641p

Whittle, A.J. (1992) "Assessment of an effective stress analysis for predicting the performance of driven piles in clays," Advances in Underwater Technology, Ocean Science and Offshore Engineering Volume 28, Offshore Site Investigation and Foundation Behaviour, Society for Underwater Technology, London, 607-643.

Whittle, A.J. & Baligh, M.M. (1988) "Behavior of piles supporting tension leg platforms: Phase III" Research Report submitted to Joint Oil Industry.

Whittle, A.J. & Germaine, J.T. (1993) "Behavior of suction caisson foundations: Annual Technical Report September 1992 - September 1993," report submitted to MIT Sea Grant and Joint Oil Industry Consortium.

Whittle, A.J. & Kavvadas, M. (1994). "Formulation of the MIT-E3 constitutive model for overconsolidated clays." ASCE, Journal of Geotechnical Engineering, 120(1), 173-198

Whittle, A.J., Aubeny, C.P., Rafalovich, A., Ladd, C.C. & Baligh, M.M. (1991) "Interpretation of in-situ tests in cohesive soils using rational methods," Research Report R91-01, Dept. of Civil Engineering, MIT, Cambridge, MA.

Whittle, D.J., DeGroot, D.G., Ladd, C.C. and Seah, T-H. (1994) "Model prediction of the

anisotropic behavior of Boston Blue Clay," ASCE Journal of Geotechnical Engineering, 120(1), 199-224.

Whittle, A.J., Germaine, J.T., Cauble, D.F., Geer, M. & Santagata, M.K. (1994) "Behavior of suction caisson foundations: Annual Technical Report September 1993 - October 1994," report submitted to MIT Sea Grant and Joint Oil Industry Consortium

Zienkiewicz, O.C. & Cheung, Y.K. (1967) The finite element method in structural and continuum mechanics, McGraw-Hill, London.